frontiers | Research Topics

Gas hydrate appearance accumulation, exploration and exploitation in continental margins - volume 2

Edited by
Pibo Su, Wei Zhang, Zhifeng Wan, Lihua Zuo and Jinan Guan

Published in
Frontiers in Earth Science

ISSN 1664-8714
ISBN 978-2-83251-440-5
DOI 10.3389/978-2-83251-440-5

About Frontiers

Frontiers is more than just an open access publisher of scholarly articles: it is a pioneering approach to the world of academia, radically improving the way scholarly research is managed. The grand vision of Frontiers is a world where all people have an equal opportunity to seek, share and generate knowledge. Frontiers provides immediate and permanent online open access to all its publications, but this alone is not enough to realize our grand goals.

Frontiers journal series

The Frontiers journal series is a multi-tier and interdisciplinary set of open-access, online journals, promising a paradigm shift from the current review, selection and dissemination processes in academic publishing. All Frontiers journals are driven by researchers for researchers; therefore, they constitute a service to the scholarly community. At the same time, the *Frontiers journal series* operates on a revolutionary invention, the tiered publishing system, initially addressing specific communities of scholars, and gradually climbing up to broader public understanding, thus serving the interests of the lay society, too.

Dedication to quality

Each Frontiers article is a landmark of the highest quality, thanks to genuinely collaborative interactions between authors and review editors, who include some of the world's best academicians. Research must be certified by peers before entering a stream of knowledge that may eventually reach the public - and shape society; therefore, Frontiers only applies the most rigorous and unbiased reviews. Frontiers revolutionizes research publishing by freely delivering the most outstanding research, evaluated with no bias from both the academic and social point of view. By applying the most advanced information technologies, Frontiers is catapulting scholarly publishing into a new generation.

What are Frontiers Research Topics?

Frontiers Research Topics are very popular trademarks of the *Frontiers journals series*: they are collections of at least ten articles, all centered on a particular subject. With their unique mix of varied contributions from Original Research to Review Articles, Frontiers Research Topics unify the most influential researchers, the latest key findings and historical advances in a hot research area.

Find out more on how to host your own Frontiers Research Topic or contribute to one as an author by contacting the Frontiers editorial office: frontiersin.org/about/contact

Gas hydrate appearance accumulation, exploration and exploitation in continental margins - volume 2

Topic editors

Pibo Su — Guangzhou Marine Geological Survey, China
Wei Zhang — Guangzhou Marine Geological Survey, China
Zhifeng Wan — Sun Yat-sen University, China
Lihua Zuo — Texas A&M University Kingsville, United States
Jinan Guan — Guangzhou Institute of Energy Conversion, Chinese Academy of Sciences (CAS), China

Citation

Su, P., Zhang, W., Wan, Z., Zuo, L., Guan, J., eds. (2023). *Gas hydrate appearance accumulation, exploration and exploitation in continental margins - volume 2*. Lausanne: Frontiers Media SA. doi: 10.3389/978-2-83251-440-5

Table of contents

frontiers | Frontiers in Earth Science

TYPE Editorial
PUBLISHED 11 January 2023
DOI 10.3389/feart.2023.1121601

OPEN ACCESS

EDITED AND REVIEWED BY
Sabine Schmidt,
Centre National de la Recherche Scientifique (CNRS), France

*CORRESPONDENCE
Pibo Su,
spb_525@sina.com
Jinan Guan,
guanja@ms.giec.ac.cn
Zhifeng Wan,
wanzhif@mail.sysu.edu.cn
Wei Zhang,
zwgmgs@foxmail.com

SPECIALTY SECTION
This article was submitted to Marine Geoscience, a section of the journal Frontiers in Earth Science

RECEIVED 12 December 2022
ACCEPTED 04 January 2023
PUBLISHED 11 January 2023

CITATION
Su P, Guan J, Wan Z, Zhang W and Zuo L (2023), Editorial: Gas hydrate appearance, accumulation, exploration and exploitation in continental margins. *Front. Earth Sci.* 11:1121601. doi: 10.3389/feart.2023.1121601

Editorial: Gas hydrate appearance, accumulation, exploration and exploitation in continental margins

Pibo Su[1]*, Jinan Guan[2]*, Zhifeng Wan[3]*, Wei Zhang[1]* and Lihua Zuo[4]

[1]Sanya Institute of South China Sea Geology, Guangzhou Marine Geological Survey, Sanya, China, [2]Key Laboratory of Gas Hydrate, Guangzhou Institute of Energy Conversion, Chinese Academy of Sciences, Guangzhou, Guangdong Province, China, [3]School of Marine Sciences, Sun Yat-sen University and Southern Marine Science and Engineering Guangdong Laboratory (Zhuhai), Zhuhai, China, [4]Department of Mathematics, Texas A&M University-Kingsville, Kingsville, TX, United States

KEYWORDS

continental slope, sedimentary properties, combustible ice, gas accumulation, offshore gas hydrate, deep petroleum system, resource prediction

Editorial on the Research Topic
Gas hydrate appearance, accumulation, exploration and exploitation in continental margins

Gas hydrate (GH) is so fascinating whether in exploring natural principle of geological evolution or for pursuing economic benefits of human sustainable development. GH plays an essential role in global carbon cycle and climate change. Two prominent events, the Paleocene–Eocene thermal maximum (PETM) and the three submarine Storegga Slides off Norway's continental shelf, are typical consequences subjected to GH dissociation with scales from global continental to local shelf (Paull et al., 2007; Ruppel and Kessler, 2017). Spanning from cold Alaska and Siberia permafrost zones, to busy merchant nautical routes in warm seas, like the north South China Sea (SCS), Nankai Trough, northeast India Ocean, and northern Gulf of Mexico, many governments and petroleum companies pay great interests on utilizing the huge resource potential of GHs.

Our Research Topic is divided into two format-separate and content-coherent volumes, aims to deepen theoretical cognition and broaden technological applications on the exploration and exploitation of GH-bearing sediments, including the appearance, accumulation, and abundance. A total of 30 research papers and abstracts publishing in this topic present exciting and distinguishing detections and conceptions on understanding the properties of GHs.

General natural principles of geology, geochemistry and geophysics are extensively adopted to explore GH-related system in fields. Ai et al. (2022), Feng C. et al., Feng J. et al. (2022), and Kong et al. (2022) focus on the records of methanogenesis and anaerobic oxidation of methane in shallow sediments and investigate related methane seepage activities in northern SCS. Li H. et al. (2022), Liang et al. (2022), Liu et al., Song et al. and Xing et al. (2022) use *in-situ* seismic and logging data and drilling cores to investigate the existence and characteristics of GH in sediments. In addition, many authors theoretically evaluate the influence of sedimentary geological structure on the accumulation of free gases and hydrates (Fan et al., 2022; Liao et al.; Luo et al., 2022; Ren et al., 2022; Zhang et al.; Zhong et al., 2022).

This topic exhibits some novel engineering methods and technological improvement for exploiting GH reservoirs. A thermodynamic plot to calculate the whole heat consumption of

GH dissociation through gas production and assess free gas proportion is proposed by Li Z. et al. A high pressure rotating water jets technology is presented to promote the efficiency of gas production in low-permeability hydrate-bearing sediments (Li. S et al.). Wei et al. (2022a) and Wu et al. (2022) conceive structure and parameter group optimization proposals to economically extract gas from hydrate reservoirs. Wei et al. (2022b) and Pei et al. (2022) summarize recent progresses on the drilling techniques on hydrate-bearing sediments and reveal geotechnical behaviors when drilling fluid invading associated layers through experimental studies.

Thanks for the hard work of all authors and reviewers in our topic Research Topic. Fruitful achievements are acquired for enhancing insightful learning on natural GH layers in continental margins, including diverse aspects in theory, numerical simulation, and experimental observation. However, continued work based on the idea of geological-engineering integration is required to accurately predict reservoir potential and environmentally and friendly utilize the resource. Finally, we sincerely appreciate the immense help from the editorial board of Frontiers in Earth Science.

Author contributions

All authors are editors for "Gas Hydrate Appearance Accumulation, Exploration and Exploitation in Continental Margins."

Conflict of interest

The authors declare that the research was conducted in the absence of any commercial or financial relationships that could be construed as a potential conflict of interest.

Publisher's note

References

Ai, X., Zha, R., Lai, Y., Yang, T., and Su, P. (2022). Pore-water geochemical gradients of sulfate, calcium, magnesium, and iodide correlated with underlying gas hydrate potential: A case study of the shenhu area, south China sea. *Front. Earth Sci.* 10, 882207. doi:10.3389/feart.2022.882207

Fan, Q., Li, Q., Zhou, S., Li, L., Zhu, Z., and Lv, X. (2022). Source-reservoir characteristics and accumulation of gas chimney-type gas hydrates in Qiongdongnan Basin, northern South China Sea. *Front. Earth Sci.* 10, 880471. doi:10.3389/feart.2022.880471

Feng, J., Luo, M., Liang, J., Yang, S., Wang, H., and Li, N. (2022). Possible links with methane seepage and gas hydrate dynamics inferred from authigenic barite records in the northern south china sea. *Front. Earth Sci.* 10, 968504. doi:10.3389/feart.2022.968504

Kong, Y., Lei, H., Cheng, W., Wang, B., Pan, F., and Huang, F. (2022). Shifting microbial communities perform anaerobic oxidation of methane and methanogenesis in sediments from the Shenhu area of northern south China sea during long-term incubations. *Front. Earth Sci.* 10, 1014976. doi:10.3389/feart.2022.1014976

Li, H., Liu, J., Qu, C., Song, H., and Zhuang, X. (2022). A method for calculating gas hydrate saturation by dual parameters of logging. *Front. Earth Sci.* 10, 986647. doi:10.3389/feart.2022.986647

Liang, J., Meng, M., Liang, J., Ren, J., He, Y., Li, T., et al. (2022). Drilling cores and geophysical characteristics of gas hydrate-bearing sediments in the production test region in the Shenhu sea, South China sea. *Front. Earth Sci.* 10, 911123. doi:10.3389/feart.2022.911123

Luo, D., Cai, F., Li, Q., Yan, G., Sun, Y., Li, A., et al. (2022). Geophysical evidence for submarine methane seepage on the Western slope of Okinawa Trough. *Front. Earth Sci.* 10, 985597. doi:10.3389/feart.2022.985597

Paull, C. K., Ussler, W., and Holbrook, W. S. (2007). Assessing methane release from the colossal Storegga submarine landslide. *Geophys. Res. Lett.* 34, L04601. doi:10.1029/2006gl028331

Ren, J., Xu, L., Shi, W., Yang, W., Wang, R., He, Y., et al. (2022). Shallow overpressure formation in the deep water area of the Qiongdongnan Basin, China. *Front. Earth Sci.* 10, 922802. doi:10.3389/feart.2022.922802

Ruppel, C. D., and Kessler, J. D. (2017). The interaction of climate change and methane hydrates. *Rev. Geophys.* 55, 126–168. doi:10.1002/2016RG000534

Pei, J., Wei, N., Zhang, B., Zhao, J., Kvamme, B., Coffin, R. B., et al. (2022). Imitating the effects of drilling fluid invasion on the strength behaviors of hydrate-bearing sediments: An experimental study. *Front. Earth Sci.* 10, 994602. doi:10.3389/feart.2022.994602

Wei, N., Qiao, Y., Liu, A., Zhao, J., Zhang, L., Xue, J., et al. (2022a). Study on structure optimization and applicability of hydrocyclone in natural gas hydrate exploitation. *Front. Earth Sci.* 10, 991208. doi:10.3389/feart.2022.991208

Wei, N., Pei, J., Zhao, J., Zhang, L., Zhou, S., Luo, P., et al. (2022b). A state-of the-art review and prospect of gas hydrate reservoir drilling techniques. *Front. Earth Sci.* 10, 997337. doi:10.3389/feart.2022.997337

Wu, L., Zhang, T., Zhang, H., Sui, Y., Yu, X., and Miao, M. (2022). Economic evaluation of production capacity for natural gas hydrate industrial exploitation in the South China Sea. *Front. Earth Sci.* 10, 990562. doi:10.3389/feart.2022.990562

Xing, D., Fan, Y., Lu, H., Lu, C., Zhang, P., and Li, H. (2022). A combined method for gas-bearing layer identification in a complex sandstone reservoir. *Front. Earth Sci.* 10, 942895. doi:10.3389/feart.2022.942895

Zhong, G., Feng, C., Wang, Y., Cheng, S., Sun, M., Yi, H., et al. (2022). Fault bounded models of oil–Gas and gas–Hydrate accumulation in the Chaoshan Depression, the South China Sea. *Front. Earth Sci.* 10, 965898. doi:10.3389/feart.2022.965898

frontiers | Frontiers in Earth Science

ORIGINAL RESEARCH
published: 02 June 2022
doi: 10.3389/feart.2022.911123

Drilling Cores and Geophysical Characteristics of Gas Hydrate-Bearing Sediments in the Production Test Region in the Shenhu sea, South China sea

Jin Liang[1,2,3], *Miaomiao Meng*[1,2,3]*, *Jinqiang Liang*[1,2,3], *Jinfeng Ren*[1,2,3]*, *Yulin He*[1,2,3], *Tingwei Li*[1,2,3], *Mengjie Xu*[1,2,3] *and Xiaoxue Wang*[1,2,3]

[1]*Southern Marine Science and Engineering Guangdong Laboratory (Guangzhou), Guangzhou, China,* [2]*MLR Key Laboratory of Marine Mineral Resources, Guangzhou Marine Geological Survey, Ministry of Natural Resources, Guangzhou, China,* [3]*National Engineering Research Center of Gas Hydrate Exploration and Development, Guangzhou, China*

OPEN ACCESS

Edited by:
Jinan Guan,
Chinese Academy of Sciences (CAS), China

Reviewed by:
Qinggguo Meng,
Qingdao Institute of Marine Geology (QIMG), China
Qinghai Xu,
Yangtze University, China

***Correspondence:**
Miaomiao Meng
18811309981@126.com
Jinfeng Ren
jf_ren@163.com

Specialty section:
This article was submitted to Marine Geoscience, a section of the journal Frontiers in Earth Science

Received: *02 April 2022*
Accepted: *02 May 2022*
Published: *02 June 2022*

Citation:
Liang J, Meng M, Liang J, Ren J, He Y, Li T, Xu M and Wang X (2022) Drilling Cores and Geophysical Characteristics of Gas Hydrate-Bearing Sediments in the Production Test Region in the Shenhu sea, South China sea. Front. Earth Sci. 10:911123. doi: 10.3389/feart.2022.911123

Gas hydrate production testing was conducted in 2017 in the Shenhu Area in the northern part of the South China Sea, and unprecedented success was achieved. In order to obtain gas production and physical properties of gas hydrate reservoirs in the study area and determine the location of test production wells, the seismic and logging data and drilling cores were analyzed in detail, the physical characteristics of the sediments, faults, gas components, and reservoir were studied. The results show that 1) the gas hydrates are diffusion type, with reservoirs dominated by clayey silt sediments, and the gas hydrate-bearing layers are characterized by soup-like, porridge-like, cavity, and vein structures; 2) the resistivity and acoustic velocity of gas hydrate formation are significantly higher than those of the surrounding sediments, while the neutron porosity, density, and natural gamma are slightly lower; the Bottom Simulating Reflectors (BSRs) in seismic profiles exhibit the exist of gas hydrates; 3) gas chimneys and faults are well-developed beneath the BSRs, and hydrocarbon gases can easily migrate into the gas hydrate reservoirs in areas with stable temperature and pressure conditions; 4) the gas hydrate saturation is high, the highest saturation in site W17 was up to 76%, with an average of 33%; while the highest saturation in site W19 was up to 68%, with an average of 31%. The gas source is considered as mixed gas of thermogenic gas and microbial gas. By comparing the core samples and geophysical characteristics of sites W17 and W19 in the study area and calculating the thickness, distribution area, and saturation of the hydrate deposition layer, it was found that site W17 is characterized by a thick layer, large area, high saturation, and good sealing, and thus, site W17 was established as the test production site. The development of gas chimney and faults provides pathways for the upward migration of deep gas, and the gas migrates to gas hydrate stable zone in forms of diffusion, water soluble and free state, forming high saturation of diffusion gas hydrates.

Keywords: gas hydrates, gas hydrate-bearing sediments, geophysical characteristics, saturation, gas source

INTRODUCTION

Natural gas hydrates (hereinafter referred to as hydrates) mainly exist in the shallow sedimentary strata in marine continental margins and permafrost regions in alpine areas on land (Kvenvolden and Lorenson, 2001; Collett, 2002, 2010; Klauda and Sandier, 2005; Demirbas, 2010; Chong et al., 2016). Under high pressure and low-temperature conditions, they are cage structure compounds composed of an ice lattice and adsorbed natural gas molecules (Booth et al., 1994; Wang et al., 2006; Wang et al., 2014). In recent years, gas hydrate reservoirs closely related to levee facies have been discovered by exploration or drilling in several sea areas around the world (Boswell et al., 2012; Lee and Collett, 2012).

At present, the geophysical characteristics of hydrate-bearing sediments has been studied by many experts and scholars (Liang et al., 2013; Yu et al., 2014). Compared with the surrounding unconsolidated sediments, pure hydrates are considered to have the physical properties of a high acoustic velocity and resistivity and low density. The high acoustic velocity of hydrates changes the seismic reflection characteristics of the sedimentary strata, forming a strong amplitude Bottom Simulating Reflector (BSR), weak amplitude blank zone, and bottom reverse polarity from that of the seafloor on seismic reflection profiles (Wang et al., 2005; Liang et al., 2014). Under the sufficient gas supply, suitable migration channels, and storage space, the distribution of natural gas hydrate stability zone is only related to the temperature and pressure of the sedimentary strata. Therefore, when the sedimentary strata are inclined on the continental slope or in the shallow seabed, the BSR on the seismic profile usually obliquely crosses the sedimentary strata (Paull et al., 1991; Kvenvolden, 1993; Liang et al., 2016). On the logging curve, gas hydrate-bearing strata usually has obvious high resistivity and high acoustic velocity (Hyndman and Davis, 1992; Liang et al., 2013). In addition, since gas hydrates are usually formed in sedimentary layers with relatively large pores, the neutron porosity is slightly higher and the spontaneous potential value is relatively small (Kawasaki et al., 2011; Boswell et al., 2012; Lee and Collett, 2012). The density of hydrate-bearing formations is usually only slightly lower, but for relatively pure and massive hydrates, the density log value can be significantly lower (Lee et al., 1993; Walter et al., 1999; Liang et al., 2006). These results play a guiding role in general surveys and detailed surveys of hydrates, but due to the limitations of the available data (usually only seismic data and a small amount of logging data), and the lack of verification of cores, lithologic interpretation has the limitation of multiple solutions, and the gas hydrate occurrences cannot be finely characterized. Therefore, it is hard to accurately determine the experimental exploitation wells of natural gas hydrates.

In 2015, gas hydrate drillings were carried out before production test in the Shenhu area of the northern South China Sea. Logging while drilling was conducted at 19 drilling sites, and *in situ* measurements and coring were conducted at four sites. The logging data show that gas hydrates with different saturation were developed in the 19 sites. High saturation and very thick diffusion hydrate samples were acquired from the four drilling sites (Yang et al., 2015, Yang et al., 2017 S. X.; Zhong et al., 2017; Zhang et al., 2018).

In 2017, test drilling in the Shenhu area in the northern South China Sea were conducted by Guangzhou Marine Geological Survey. This test produced 309000 m^3 gas, with average daily gas production of more than 5000 m^3 and methane content of up to 99.5%. Before the location of production test drilling was determined, the lithological characteristics, vertical variation of gas hydrate-bearing sedimentary strata, gas hydrate saturation, reservoir thickness, and gas source should be cleared. Through detailed analysis of pressure cores and 3-D seismic and geophysical well logging data, gas hydrate-bearing sediments were finely characterized, overcoming the limitations and interpretation ambiguity that exist when only geophysical data are used and revealing the physical properties and storage characteristics of the hydrate-bearing sedimentary strata. The gas migration and accumulation characteristics were studied based on the regional geological structure and metallogenic conditions, and the location of the test well was finally determined. The great success of the production test verified the accuracy of the interpretation of the geophysical characteristics of gas hydrate-bearing sediments.

GEOLOGICAL SETTING

The study area is located in the continental slope zone in the Shenhu area in the northern part of the South China Sea (**Figure 1**), with a water depth range of 350–1750 m. The water depth contours are roughly parallel to the coastline. The measured heat flow in the Shenhu area is about 60–96 mW/m^2, and the average heat flow is about 76 mW/m^2. Compared with the heat flow in the Pearl River Mouth Basin in the northern part of the South China Sea, the average heat flow in the Shenhu area is about 5–6 mW/m^2 higher than those in the southern depression and central uplift in the Pearl River Mouth Basin, indicating that the hydrothermal activity within the deep strata in the Shenhu area is relatively active, and the velocity of the fluid migration in the strata is relatively fast. The seafloor temperature in the study area is about 2–4°C, the geothermal gradient of the seafloor sediments is about 46–68°C/km, and the water depth pressure of the seafloor is greater than 10 MPa. Therefore, the conditions of the hydrate accumulation in the study area are relatively stable (Zhang et al., 2017). The seafloor topography in the study area fluctuates greatly and the changes are relatively complex. The slope of the seafloor decreases slowly from north to south, and the average value of the sea floor slope gradient is about 18‰. Under the joint impact of the gravity current and submarine current, a submarine landslide is relatively well-developed in the study area, which is manifested by the alternating arrangement of dunes and troughs, forming a pattern of scour trenches and submarine ridges spreading in a nearly north-south direction. The formation and decomposition of the gas hydrates are closely related to the submarine landslide. The landslide is a favorable geological body for the formation and distribution of gas hydrates. The large amount of water and gas released during the decomposition of gas hydrates, which could result in the instability of the overlying strata and accelerates the submarine landslide.

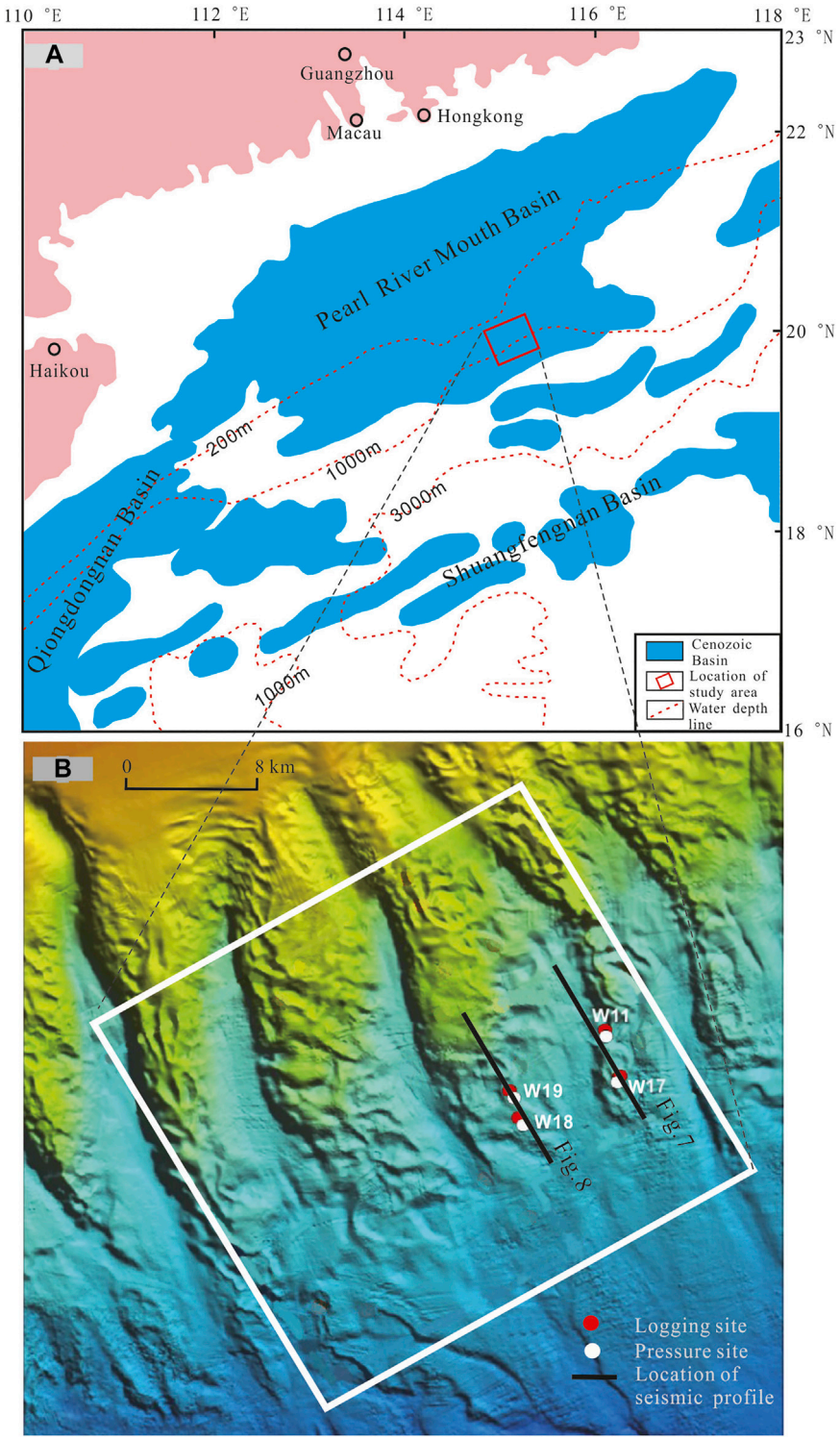

FIGURE 1 | Location of production testing and drilling sites in the pearl river mouth basin, south china sea. Note: the two black lines show the location of seismic profiles in **Figures 7**, **8** respectively.

There is an excellent correspondence between the seabed landslide and BSRs in the study area, and the BSRs can be seen clearly at the bottom of the landslide. The extremely high sedimentation rate in the Shenhu Sea area has resulted in a very thick sedimentary layer. The research area is located in the Baiyun Depression, which has a large area and a very thick sedimentary

layer. It is the main hydrocarbon generation and expulsion depression in the Shenhu area, with TOC content in the range of 0.50–1.52%, and Ro content in the range of 0.6–1.3%, and it has very favorable conditions for the formation of hydrates. The upper strata in the study area are mainly argillaceous deposits with relatively low sand contents, high organic matter contents, and low thermal maturity. Therefore, large quantities of biogas are easily generated, and hydrate orebodies can be formed under certain temperature and pressure conditions. Neritic detrital and bathyal clastic sedimentary substrata are relatively well-developed. Their sediment organic matter contents are higher. The organic matter in the eastern Pearl River Mouth Basin near the study area is in mature or highly mature stage (Ro = 1.3–2.5%), and in the local area, the organic matter has entered the overly mature stage. This has resulted in oil and gas formation (i.e., cracking gas and thermogenic gas), providing abundant thermogenic gas for hydrate formation (Zhang et al., 2014; He et al., 2008; 2013). In addition, the neotectonic movement led to the plastic flow of thick over pressurized mud, forming a large-scale diapir active zone, resulting in the abnormal development of mud diapirs, gas chimneys, faults and vertical fissures, and providing favorable gas-bearing fluid migration and transport channels for gas hydrate formation in the study area (He et al., 2014; Zhang et al., 2017).

DATA AND METHODS

In 2015, Logging While Drilling (LWD) was conducted at 19 drilling sites by the China Geological Survey (CGS) in the hydrate production test area in the Shenhu Sea, and pressure coring was conducted at 4 sites (**Figure 1**). The logging parameters mainly included resistivity, bit resistivity imaging, p-wave acoustic time difference, full-wave logging and neutron, density, well diameter, and natural gamma logging. After the sample coring, *in-situ* temperature and formation pore pressure dispersion tests were performed. The geochemical analysis of the samples was conducted in the field. The logging data revealed that various amounts of gas hydrates existed in the 19 sites, and the core samples directly proved that gas hydrates filled the pore spaces of the formation in the study area. Among the 19 sites, sites W11, W17, and W19 have the most obvious gas hydrate characteristics. Sites W11 and W17 are located close to each other and have similar geophysical properties. In this study, sites W17 and W19 were taken as examples to analysis the logging characteristics of gas hydrates. In addition, the quasi-3-D seismic data collected by the Fendou 4 (research vessel) in the research area in 2008 were used. The original surface element size was 12.5 m × 50 m, the number of receiving channels was 192, the channel spacing was 12.5 m, the gun spacing was 25 m, the minimum offset was 125 m, the sampling rate was 1 ms, the recording length was 5 s, and the cable and source-sink depth was 5 m. The Source capacity was 160 Cu. in, and the working pressure was 2000 Psi. In terms of seismic data processing for gas hydrate characteristics, prestack noise suppression, deconvolution and multiple wave suppression are mainly used to achieve high SNR, high resolution and high fidelity processing effect.

RESULTS

Characteristics of Gas Hydrate-Bearing Sediments

Through the observation of drilling cores, it was found that gas hydrates are closely related to the medium-coarse sediments and fractures. The high saturation gas hydrates mainly occur as pore-filling, blocky, and vein forms in the medium-coarse sediments and small fractures. However, the core and lithological analysis of sediment samples from the study area indicates that gas hydrates accumulated and occur in the fine-grained sediments, and the gas hydrates are uniformly distributed within the sediments (**Figures 2**, **3**). The gas hydrate-bearing sediments can be divided into four lithologic types: siliceous-bearing calcareous clayey silt, calcareous and siliceous-bearing clayey silt, calcareous silt, and calcareous clayey silt. Most of the free gas accumulates in the gas hydrate stability zone in the form of diffuse deposits, and a small part migrates along the faults. In the study area, gas chimneys are developed below the BSR, but the faults are not developed above the BSR, so diffusive gas hydrates are easily formed. Shallow biogenic gas and deep thermogenic gas enters the bottom of the hydrate stability zone, and then, they diffuse and are stored in the sediment pores. Because there are no fractures, it is easy for a stable gas hydrate accumulation area with an uneven distribution to form. The core samples from 1465 to 1475 m (water depth) and core infrared images taken at 1490–1510 m in site W17 (**Figure 2**) show that the main lithology is calcareous clay medium-coarse silt, and the hydrates in this depth interval often occur as dispersed fine particles. The sedimentary structures include vein, soup-like, and porridge-like occurrences (**Figure 2**). Low temperature anomalies (10–12°C) were observed in the core samples due to hydrate decomposition. The gas hydrates are evenly distributed in the sediment pore space. **Figure 3** shows core samples from 1418 to 1426 m (water depth) in site W19 and the core infrared image was taken at 1424–1438 m. Strong gas swelling phenomenon and cavity and congee core structures formed during the decomposition of the hydrates were observed after the cores arrived in the lab. The core from this section was obtained from the gas hydrate enrichment layer. Through pressure relief and degassing treatment, a large amount of gas was collected. The infrared image scanning of the core revealed a low temperature region (10–12°C) with a geothermal gradient of 5.58°C/100 m. The core from site W19 is mainly composed of calcareous nodular silt. The gas migrated upward through the migration channels formed by the gas chimneys, and abundant inorganic substances were gathered in this area, which promoted the enrichment of microorganisms and other calcium-rich substances, forming calcareous nodular silt.

The chemical properties and gas sources of hydrates are reflected by the gas composition and carbon isotopic characteristics of the gas hydrates (Chen et al., 2002; Fu et al., 2011; Fang et al., 2019). The methane contents of the gas samplesare greater than 98.5%, while ethane and propane are about 1 and 0.5%, respectively, but high

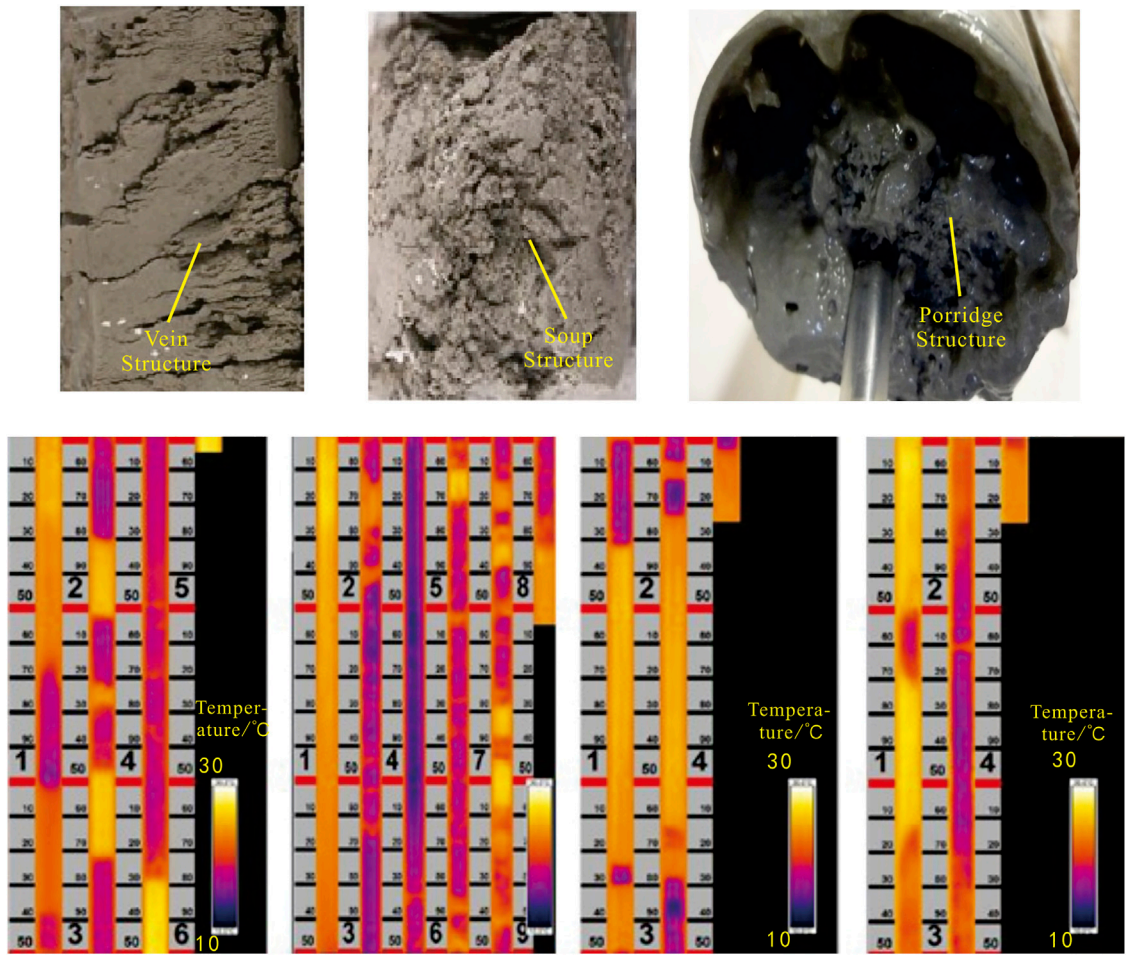

FIGURE 2 | Characteristics of gas hydrates and gas hydrate-bearing sediments at site W17 based on drilling cores and infrared scanning images.

concentrations of ethane and propane were detected in the fractured gas (gas extracted from the core expansion fracture) and pressure release gas in the pressure cores from sites W17 and W19 (**Figure 4**).

The $C_1/(C_2+C_3)$ value for the fissure gas and air release slowly decreases with increasing depth in site W17, and the $C_1/(C_2+C_3)$ values are around 800 (**Figure 4A**). At the top of the bottom interface of the gas hydrate reservoir, the values exhibit mutation at around 206 m. The $C_1/(C_2+C_3)$ values of the gas samples from the hydrate reservoir are less than 300, and the ethane and propane contents slowly increase with increasing depth. In addition, mutations occur near 206 m at the top of the bottom interface of the gas hydrate reservoir, and the concentration is more than 104 ppm, which is higher than the ethane and propane contents. Presumably, the gas source of the hydrates is mainly a mixture of thermogenic gas (thermal) and microbial gas. The decrease of propane content below 206 m may the result of lateral gas migration and accumulation near 206 m to form gas hydrate. An abrupt change in the $C_1/(C_2+C_3)$ values was observed at the top of the hydrate reservoir interface in site W19 (**Figure 4B**), the $C_1/(C_2+C_3)$ values within the reservoir decreased with increasing depth, the $C_1/(C_2+C_3)$ values of the gas samples from the hydrate reservoir are less than 300, and the propane content is higher than the ethane content near the top boundary of the gas hydrate reservoir. It is speculated that the gas hydrate reservoir in site W19 was mainly formed from a mixture of thermogenic gas and microbial gas. In addition, the carbon isotope compositions of the methane gas from sites W17 and W19 are −45‰ to −80‰, and the methane/ethane ratio is 90–1000; this further indicates that the gas source is mainly a mixture of thermogenic gas and microbial gas (**Figure 5**).

Logging Characteristics of Gas Hydrates

Gas hydrate reservoirs can be identified by analyzing the logging characteristics of the sedimentary strata. The distribution of the gas hydrates in the sedimentary layer can be estimated effectively using the multi-means exploration technology of geophysical logging (Lu et al., 2008; Liang et al., 2010; Liang et al., 2017a). The gas hydrate reservoirs with different types or different saturations have different logging responses: the resistivity and acoustic velocity in gas hydrate reservoirs are significantly higher than those of the surrounding sediments, while the neutron porosity, density, and natural gamma are slightly lower, and the acoustic velocity, density, and neutron

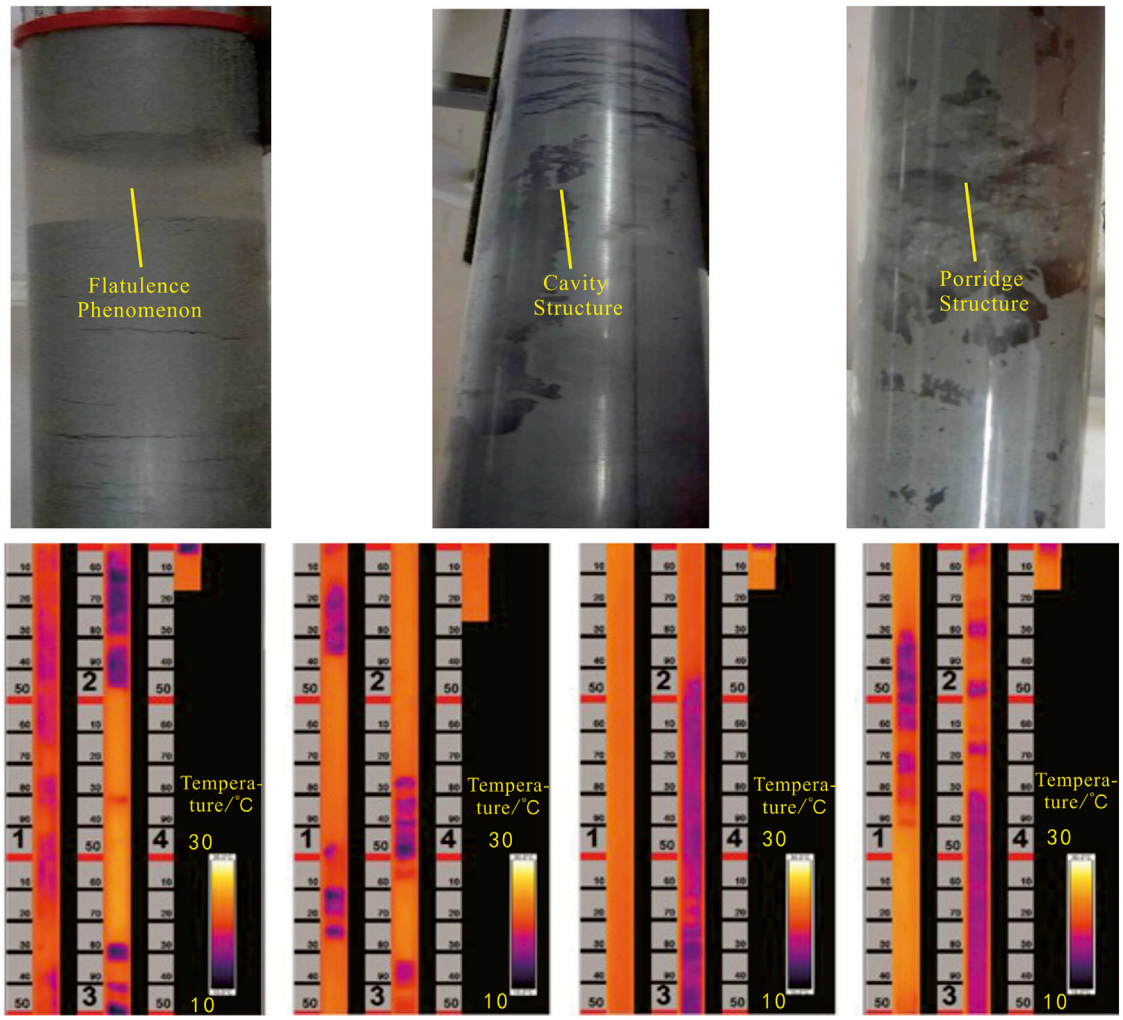

FIGURE 3 | Characteristics of gas hydrates and gas hydrate-bearing sediments at site W19 based on drilling cores and infrared scanning images (Zhang et al., 2017).

porosity are significantly lower (Wang et al., 2003; Mo et al., 2008; Liang et al., 2017b).

Site W17 is located in the southeastern part of the study area, at the bottom of the northern continental slope of the South China Sea, with a water depth of 1249 m and a maximum well depth of 319 m. The logging curve for site W17 shows that the abnormal characteristics of "two highs and three lows" values of the logging curves are obvious in the 1460–1522 m section (**Figure 6**). The acoustic velocity increases rapidly from 1460 m to 1522 m and reaches the highest value of 2295 m s^{-1} at 1490 m. The upper part of the density curve is relatively gentle, with little change. The lower part is the 1510–1522 m section, in which the lowest density is 1.72 g cm^{-3}. The resistivity curve starts at 1460 m and changes in a wavy shape with increasing depth. It also exhibits the abnormal features of low values at both ends and large values in the middle. The maximum resistivity value is 4.6 Ω m. The neutron porosity decreases due to the filling of the sediment pores with hydrates and/or free gas. The porosity curve begins to decrease slowly at 1460 m, with a minimum porosity value of 28%. The natural gamma logging curve is relatively flat overall, and there is no large mutation. It is concluded that the deposition near site W17 is relatively stable, and the grain size of the hydrate enrichment section is mainly medium silt to coarse silt (Liang et al., 2009; Guo et al., 2017; Yang et al., 2020). Obvious turbidity deposits are observed in this section of the channel on the seismic profile beside the well, which is speculated to be the levee facies of the turbidity current. The overall seismic signal is relatively continuous, and the strongly reflective hydrate-bearing sediment layer is located near the natural levee (**Figure 7**). According to the logging curve for site W17, it is speculated that there is a ~ 45 m thick hydrate sedimentary layer near the site, with the average saturation of 19.4%, and an ~ 12 m thick free gas layer beneath the hydrate layer, with the average saturation of 30.1%.

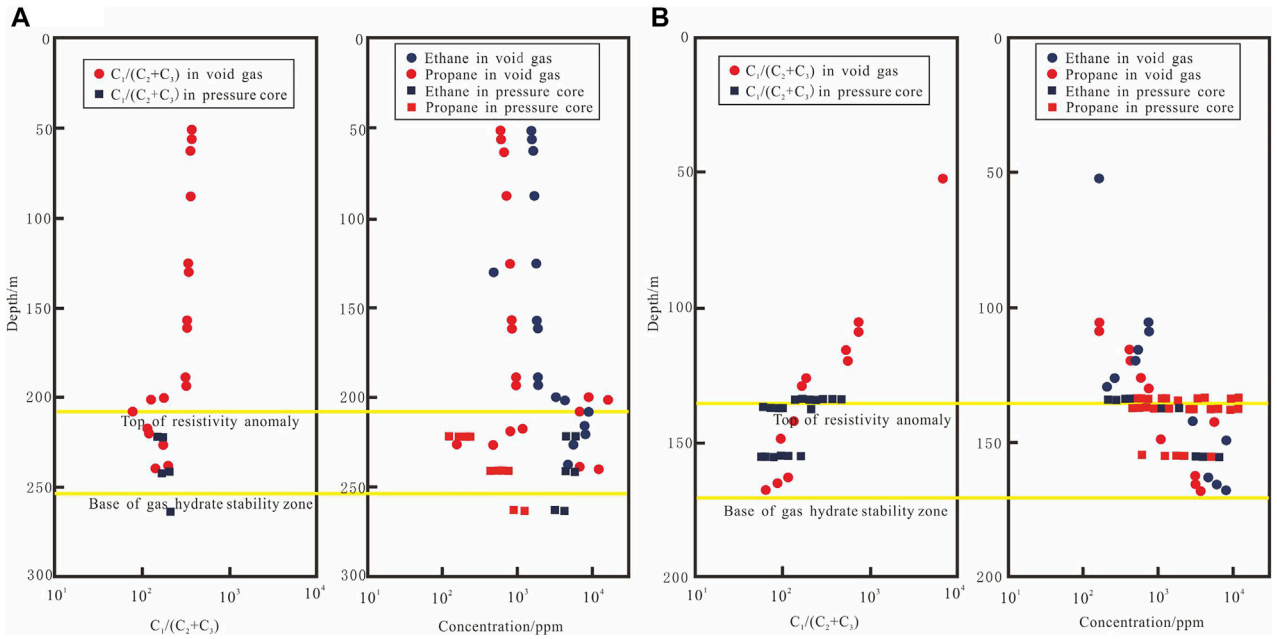

FIGURE 4 | Vertical variations in the gas compositions in sites W17 and W19.

Site W19 is located in the central and southern parts of the study area, and it is also at the bottom of the continental slope, with a water depth of 1274 m and a maximum well depth of 245 m. The logging anomaly at site W19 mainly shows that the acoustic velocity increases rapidly from 1788 m·s^{-1} from 1411 m–1432 m (**Figure 8**). It rapidly reaches 2522 m s^{-1}, and the highest value is 2790 m s^{-1}.

Then, it drops sharply to 1821 m s^{-1} at 1432 m. The acoustic velocity curve oscillates and decreases with increasing depth. The entire section of the density curve is relatively flat with little change, and there is no low segment that corresponds to the acoustic velocity curve. Therefore, it is speculated that the hydrates occur in the form of diffuse hydrates, and there is no obvious free gas layer under the hydrate-bearing sedimentary layer. The resistivity rises rapidly from 1 Ω m to 8 Ω m starting at 1411 m. The maximum value (8.67 Ω m) occurs at 1415 m, and then, it oscillates with increasing depth. The neutron porosity decreases due to the filling of the sediment pores with hydrates, and the minimum porosity value is 26%. The natural gamma logging curve decreases slightly in the hydrate formation (**Figure 7**), the effective thickness of gas hydrate layer is about 25 m and the average saturation is 30.4%. According to the core characteristics, there are three hydrate enrichment layers in site W19. The gas hydrates in the 1401–1403 m are mainly in fine silts and silts with relatively coarse grain size, and there are silts and muds interlayers with vertical discontinuity. Based on the seismic reflection characteristics, it can be concluded that the hydrates in this section are concentrated in the shallow natural gas layer of the slump body. In the 1412–1425 m and 1430–1438 m intervals, the granularity of the hydrate layer is low, the vertical continuity is good. It is a powdery sand-shale deposit, with a soup-like core structure and fracture development (**Figure 9**). For the hydrate layer with the relatively cluttered seismic reflection, it is speculated that the hydrate development channel is located in the slump. The hydrate layer with a wedge seismic reflection is most likely a silty turbidity deposit such as levee facies.

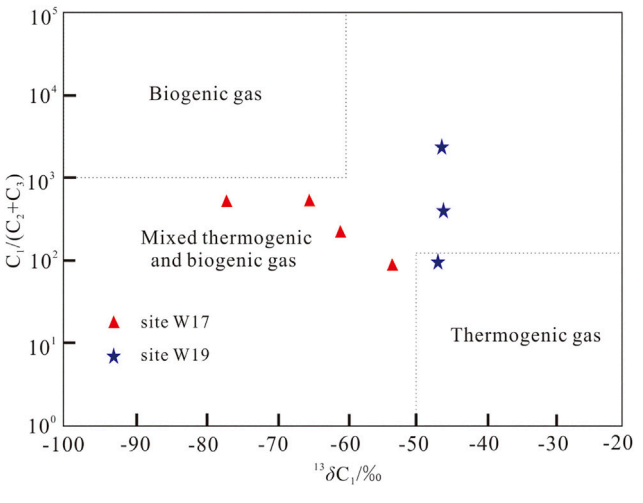

FIGURE 5 | Cross plot of methane carbon isotope ($\delta^{13}C_1$) and $C_1/(C_2+C_3)$ of gas hydrates.

Seismic Reflection and Gas Migration Characteristics of Hydrate Layer

The seismic exploration of the hydrates in the study area revealed that the bottom-simulating reflector is an important indicator of the hydrate content of the sedimentary strata (Santamarina et al., 2015;

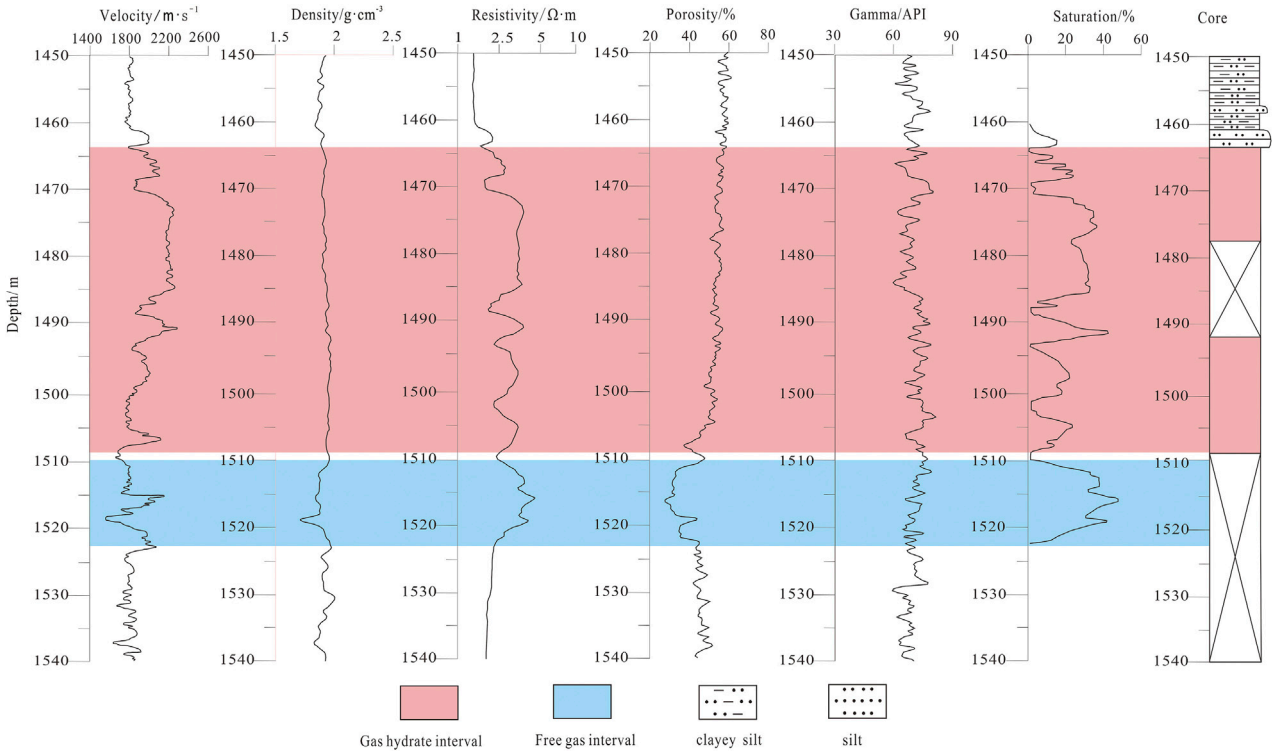

FIGURE 6 | Characteristics of well logging curves and lithology of site W17.

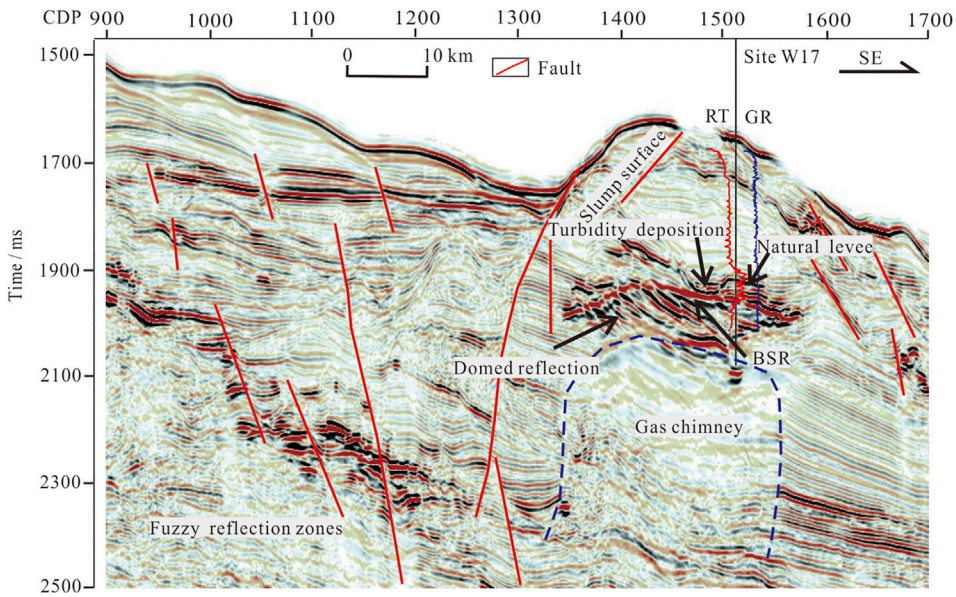

FIGURE 7 | The seismic reflection profile across site W17. The location of the seismic profile is shown in **Figure 1B**.

Sua et al., 2018; Shukla et al., 2019). It usually has a medium-strong amplitude and medium-high continuous reflection on the seismic profile, which is roughly parallel to the seafloor reflection. The BSR is usually oblique to the formation in the slope zone. If there is free gas in the formation, due to the large wave impedance difference between the hydrates and free gas, the seismic reflection is enhanced and an

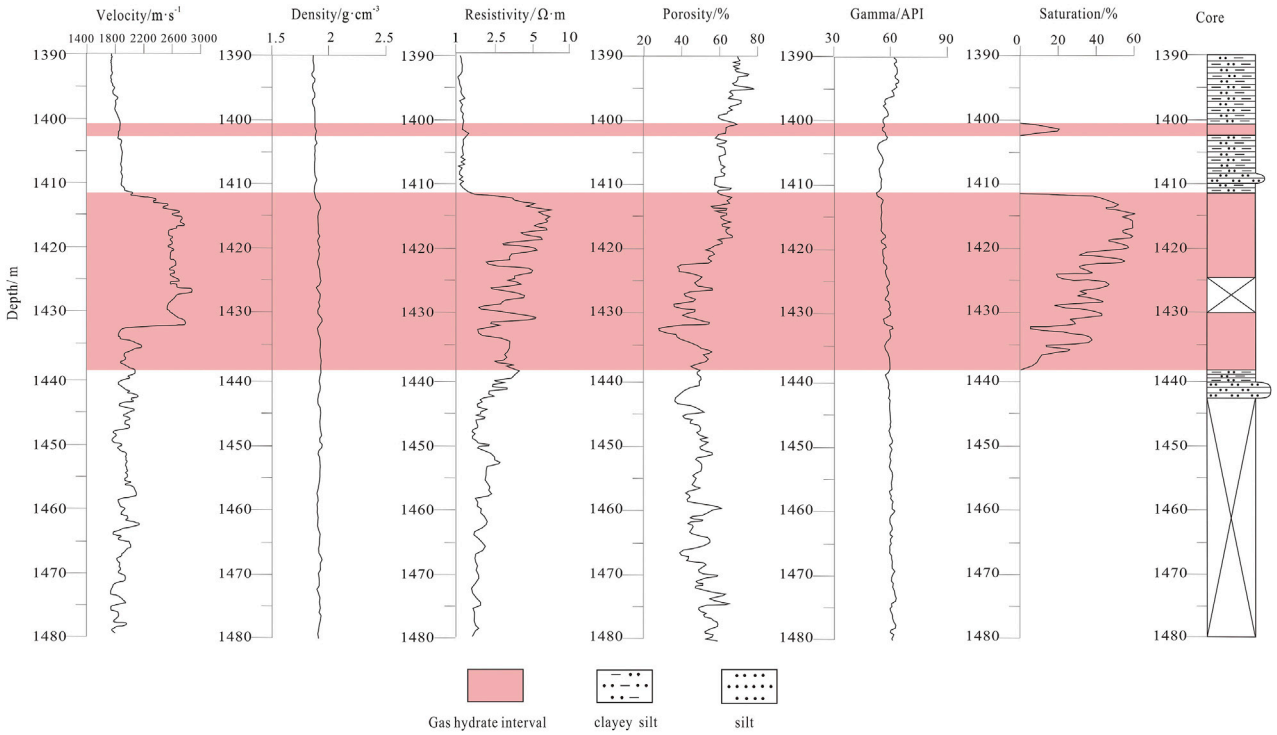

FIGURE 8 | Characteristics of well logging curves and lithology of site W19.

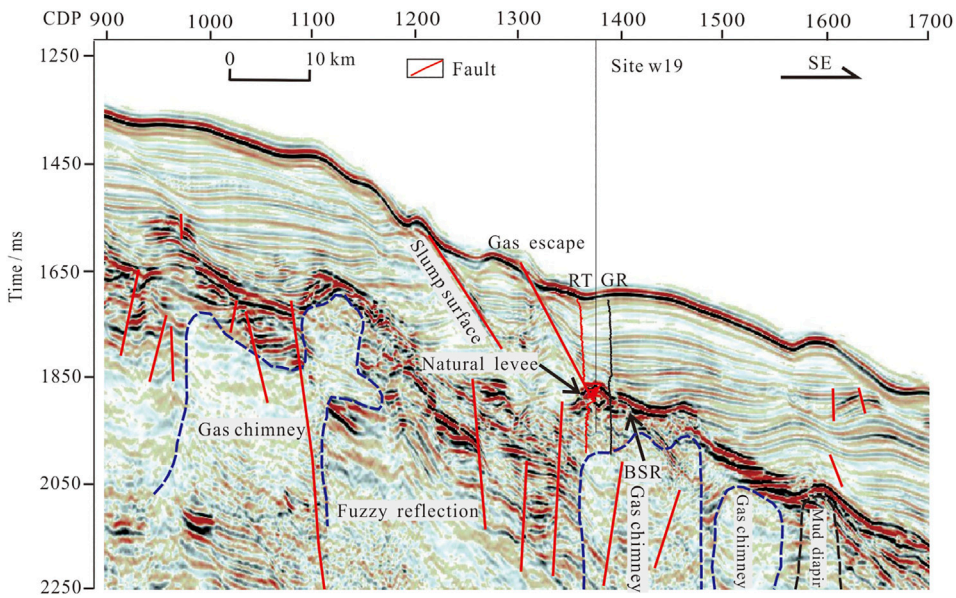

FIGURE 9 | The seismic reflection profile across site W19. The location of the seismic profile is shown in **Figure 1B**.

amplitude enhancer is formed (Su et al., 2014; Yang et al., 2017b; Zhang et al., 2020). The seismic wave velocity of the hydrate-bearing sedimentary layer is relatively high, so the reflection time is short, and the seismic event on the profile stretches upward; while the seismic wave velocity of the free gas-bearing stratum is relatively low and the reflection time is short, which causes downward stretching of the seismic event, forming an abnormal eyeball velocity amplitude structure (V'AMP). In addition, when the sedimentary formation

is filled with hydrates and is further cemented, the formation's pore space becomes uniform, and the seismic profile shows blank or weak amplitude zones. The waveform of the BSR subwave generally has a negative polarity, which is opposite to the waveform of the wave reflected by the seafloor, and the absolute value of the reflection coefficient is relatively large. These seismic reflection characteristics of hydrates can be used to identify the existence of hydrate-bearing deposits.

The BSR in the seismic profile cross site W17 has a medium-strong amplitude and medium-high continuity (**Figure 8**). There is an obvious amplitude gap above the BSR, and the formation had good ductility. The polarity of the BSR waveform is opposite to that of the submarine waveform. Under the temperature and pressure conditions, the BSR waveform cuts through the seismic event of the formation, and the seismic event exhibits an enhanced reflection, which has quite obvious BSR characteristics. An obvious domed reflection occurs below the BSR, this is due to the velocity amplitude anomaly augen structure, which is formed by the hydrates in the stable zone, with the upper interface causing the seismic reflection wave velocity to increase and the reflection time to shorten. On the seismic profiles, the seismic event bends upward, and the seismic wave velocity is lower due to the low amount of free gas, producing a prolonged reflection time under the gas hydrate stable zone. On the seismic profiles, the seismic event bending exhibits an obvious V'AMP phenomenon. The shallow deposits above the BSR are mound and sheet slump deposits, and the entire deposit is composed of mounds and sheets. The seismic event in the sedimentary layer exhibits an asymmetric wavy reflection structure and gradually migrates upward towards the continental slope. The high wave impedance (RT) value corresponds to the hydrate layer in the natural levee, and the gamma ray (RT) curve does not change much. The cap layer is developed above the BSR, a fracture pathway exists at the edge of the hydrate layer, and gas escapes to the seabed through this pathway. The reinforced reflection is obvious below the BSR, there is a lot of free gas, and the fault structure is developed below the BSR. There are large gas chimneys and many disorderly and fuzzy reflections on the seismic profile.

The BSR on the seismic profiles cross site W19 exhibits enhanced reflection, with the polar opposite to the bottom reflection polarity (**Figure 9**). The high wave impedance (RT) value corresponds to the gas hydrate layer in the natural embankment, while the low gamma ray value corresponds to the gas hydrate layer. On the seismic profile, the fractures are well developed on the left side of the BSR, and many disorderly and fuzzy reflections can be seen below the BSR, indicating that a large number of gas chimneys exist near site W19. The shallow deposits above the BSR are sheet-like and U-shaped slump deposits (Wu et al., 2003, Wu et al., 2007). Their overall distribution is sheet-like, and an obvious slip surface at the bottom of the slump deposit and erosion trough deposits above the BSR exist. The erosion trough deposits exhibit high frequency, medium amplitude, and U-shaped filling features on seismic reflection (**Figure 9**). In addition, faults that extending to the seafloor indicate gas escaping. The seismic profile below the BSR exhibits a medium frequency and medium amplitude, which is interpretated as submarine fan deposits in the upper Miocene.

Through many years of seismic and geological investigation and oil and gas exploitation in the Pearl River Mouth Basin, it has been shown that there are many natural gas fields in the Shenhu Sea area in the southern part of the basin, especially in the Baiyun sag, in which the natural gas distribution area is concentrated. That is, there is plenty of hydrocarbon gas in the deep layer near the study area. Under the effect of the formation pressure, the deep gas gradually migrates upward along the gas chimneys, unconformity surfaces, faults, fractures, and sandstone channels, and then, it gathers in the hydrate stability zone, which has suitable temperature and pressure conditions. There are several vertical fuzzy zones on the seismic reflection profile in the deep and central parts of the study area. These phenomena are gas chimneys formed by the movement of deep gas upward along the fractures, causing disturbance of the stratum. In addition, submarine canyon channel is an important migration pathway of terrigenous materials to the deep sea, and the formation and development of turbidity channels and levees are closely related to gas hydrate accumulation (Kuang et al., 2018). Channel-filling sediments is not only a good reservoir, but also a good gas migration and transport pathway, which is a dominant gathering place for gas hydrate formation and occurrence (Kuang and Guo, 2011; Davies et al., 2012).

Gas chimneys and fault structures are well developed near site W17, and there are gas chimneys under the BSR (**Figure 8**). Gas chimneys and deep faults are developed. The hydrocarbon gases in the middle and deep strata migrated to the seafloor along the dense fractures and faults and formed a hydrate layer with a high saturation under the low temperature and pressure conditions. There are also faults and gas chimney clusters near site W19, which are larger in scale than those at site W17 (**Figure 9**). Thermogenic gas migrates upward with the overpressure fluid through deep and large faults, and then, it migrates laterally along the conformable surfaces with appropriate porosity and permeability to form reservoirs in suitable stratigraphic traps and/or structures. Under the action of the fluid potential, part of the thermogenic gas continues to migrate into the shallow strata along the channels formed by the faults and fractures. Once the temperature and pressure conditions of the hydrocarbon gas in the fracture channels are suitable, a seepage hydrate is formed. In addition, the microbial gas in the shallow strata can migrate and accumulate through sediment pores or interlayer micro-fissures to form diffusive hydrates, and the microbial gas in the lower part of the gas hydrate stable zone can also migrate upward through gas chimneys, mud diapirs, and faults to form gas hydrates.

DISCUSSION

How is Gas Hydrate Production Test Site Selected?

The above analysis shows that gas hydrates in sites W17 and W19 belong to diffuse type. The reservoir properties of two sites show

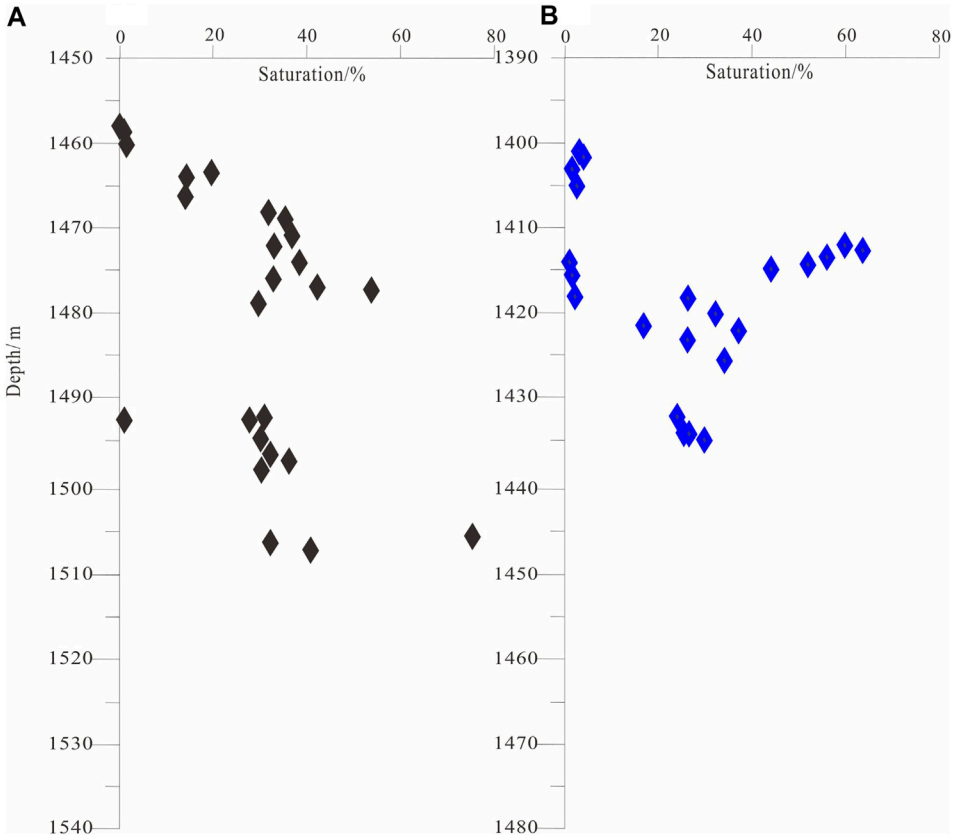

FIGURE 10 | Vertical variations in the gas hydrate saturation in sites W17 and W19.

similar permeability, porosities, and shale contents. The engineering geological conditions (e.g., water depth, bottom slope, reservoir depth, and engineering mechanics) conform to the conditions for gas hydrate exploration. The following questions are thus raised: why was site W17 chosen as the final test site rather than site W19? The reservoir saturation, reservoir thickness, and gas sealing ability of these two sites are analyzed and discussed below.The gas hydrate saturation was calculated from the desalination degree of the chloride ions in the pore water of the hydrate-bearing deposits from sites W17 and W19 (**Figure 10**). At site W17, the thickness of the gas hydrate-bearing sediment layer is about 45 m, and the maximum saturation is 76%, with an average of 33%. At site W19, the thickness of the gas hydrate-bearing sediment layer is about 25 m, and the maximum saturation is 68%, with an average of 31%. Through the seismic profile analysis and well logging curve calculation, the gas hydrate sediments in W17 site containing thicker, and higher saturation of gas hydrate, the W17 orebody area is 3 times than that of W19 orebody, and the resources of W17 orebody is 7 times higher than that of in W19 site. Beside the W17 orebody has good continuity reservoir, sealing layer, fault pathway at orebody edge. The logging curve shows that the thickness of the gas layer is 12 m and the average gas saturation is 30.1%, which can provide sufficient gas source for gas hydrate formation. The seismic profile shows that there is a large gas chimney structure under the gas layer, which is the upward migration channel of deep cracked gas and the gas source guarantee for the formation of free gas layer. While site W19 has thinner gas hydrate reservoirs, faults directly leading to the bottom of the seafloor above the BSR, and gas escape. Thus, site W17 was chosen for the hydrate exploration.

Why do Silty Clay Sediments Develop High Saturation of gas Hydrates?

The gas hydrates in the study area are mainly developed in or near the levee facies sediments. In this study, it was revealed that the sand-bearing sediments in the levee facies are relatively developed, and the sandy reservoir is a good sedimentary environment for gas hydrate formation (Riedel et al., 2011; Crutchley et al., 2017). Compared with muddy and silty mudstone sediments, the sandy sediments in the levee facies have more reservoir space due to their higher porosity and permeability (Su et al., 2018; Liang et al., 2019; Meng et al., 2021). Hydrocarbon gases tend to accumulate in strata with high porosities and permeabilities, which are more conducive to the formation of gas hydrates with higher saturation (Lu et al., 2011; Dai et al., 2012; Bahk et al., 2013). The core samples from sites W17 and W19 in the study area indicate that the hydrate deposits are fine-grained silty clay deposits. However, the highest gas

hydrate saturation at site W17 is 76%, with an average of 33%; while the highest gas hydrate saturation at site W19 is 68%, with an average of 31%. Both of these sites have high saturation. The gas hydrates in the study area are diffused within the fine-grained sediments, and it is difficult to form high saturation gas hydrates through diffusion migration alone because the capillaries with a high resistance need to be broken through before fluid migration can occur. Therefore, what caused the high saturation in the fine-grained silty clay sediments? Some studies have reported that the gas mainly reaches the gas hydrate stable zone via diffusion migration, water-soluble migration, and free migration through certain migration and transport channels (Collett et al., 2009). Post-drilling research in the study area revealed that the migration and transport pathways, such as gas chimneys, mud diapers, and faults, which play a key role in the accumulation of high saturation gas hydrates (Wang et al., 2014; Su et al., 2017). Gas chimneys and mud diapirs are identified in the lower part of the BSR, and faults are developed nearby, which should be the migration channel through which the deep gas-bearing fluid migrates into the gas hydrate stable zone. In addition, the study area is located close to the center of Baiyun Sag, and thermogenic gas from the deep part of the sag continuously migrates upward through the faults, diapirs, and gas chimneys, and then, it mixes with microbial gas. These mixed gases then migrate into the hydrate stable zone to form high saturation gas hydrates (Zhang et al., 2017).

CONCLUSION

Based on logging data, seismic data, drilling core data, gas composition and carbon isotope characteristics, and gas hydrate saturation data, the logging and geophysical characteristics and variations in the gas hydrate-bearing sediments were summarized.

1) the gas hydrates are diffusion type, with reservoirs dominated by clayey silt sediments, and the gas hydrate-bearing layers are characterized by soup-like, porridge-like, cavity, and vein structures;
2) the resistivity and acoustic velocity of gas hydrate formation are significantly higher than those of the surrounding sediments, while the neutron porosity, density, and natural gamma are slightly lower; the Bottom Simulating Reflectors (BSRs) in seismic profiles exhibit the exist of gas hydrates;
3) gas chimneys and faults are well-developed beneath the BSRs, and hydrocarbon gases can easily migrate into the gas hydrate reservoirs in areas with stable temperature and pressure conditions;
4) the gas hydrate saturation is high, the highest saturation in site W17 was up to 76%, with an average of 33%; while the highest saturation in site W19 was up to 68%, with an average of 31%. The gas source is considered as mixed gas of thermogenic gas and microbial gas.

By comparing the core samples and geophysical characteristics of sites W17 and W19 in the study area and calculating the thickness, distribution area, and saturation of the gas hydrate deposition layer, it was found that site W17 is characterized by a thick layer, large area, high saturation, and good sealing, besides, the gas sources are sufficient and gas migration pathway are well developed, thus site W17 was established as the test production site. The development of gas chimney and faults provides driving force for the upward migration of deep gas, and the gas migrates to gas hydrate stable zone in forms of diffusion, water soluble and free state, forming high saturation of diffusion gas hydrates.

DATA AVAILABILITY STATEMENT

The original contributions presented in the study are included in the article/Supplementary Material, further inquiries can be directed to the corresponding author.

AUTHOR CONTRIBUTIONS

JL: Investigation, Formal analysis, Writing—original draft. MM: Review and editing. JL: Supervision. JR: Supervision in Geology. YH: Investigation and seismic analysis. TL: Logging analysis. MX: Geophysical interpretation. XW: Figure drawing.

FUNDING

This work was supported by Key Special Project for Introduced Talents Team of Southern Marine Science and Engineering Guangdong Laboratory (Guangzhou) (No. GML2019ZD0105), Guangdong Province Marine Economic Development (Six Major Marine Industries) Special Fund Project (No. [2021] No. 58), and the National Natural Science Foundation of China (No. 42102144). the Geological Survey Project of China (No. DD20221705, No. DD20221700).

ACKNOWLEDGMENTS

Thank to those who contributed to the success of the China National Gas Hydrate Program Expeditions 3 (GMGS3). Editor Jinan Guan and two reviewers that provide constructive suggestions are gratefully appreciated. We also thank LetPub for its linguistic assistance during the preparation of this manuscript.

REFERENCES

Bahk, J.-J., Kim, D.-H., Chun, J.-H., Son, B.-K., Kim, J.-H., Ryu, B.-J., et al. (2013). Gas Hydrate Occurrences and Their Relation to Host Sediment Properties: Results from Second Ulleung Basin Gas Hydrate Drilling Expedition, East Sea. *Mar. Petroleum Geol.* 47, 21–29. doi:10.1016/j.marpetgeo.2013.05.006

Booth, J. S., Winters, W. J., and Dillon, W. P. (1994). Circumstantial Evidence of Gas Hydrate and Slope Failure Associations on the United States Atlantic Continental Margin. *Ann. N. Y. Acad. Sci.* 715 (1), 487–489. doi:10.1111/j.1749-6632.1994.tb38863.x

Boswell, R., Frye, M., Shelander, D., Shedd, W., McConnell, D. R., and Cook, A. (2012). Architecture of Gas-Hydrate-Bearing Sands from Walker Ridge 313, Green Canyon 955, and Alaminos Canyon 21: Northern Deepwater Gulf of Mexico. *Mar. Petroleum Geol.* 34 (1), 134–149. doi:10.1016/j.marpetgeo.2011.08.010

Chen, D. F., Chen, X. P., and Chen, G. Q. (2002). Geology and Geochemistry of Cold Seepage and Venting-Elated Carbonates. *Acta Sedimentol. Sin.* 20 (1), 34–40. (In Chinese with English abstract). doi:10.3969/j.issn.1000-0550.2002.01.007

Chong, Z. R., Yang, S. H. B., Babu, P., Linga, P., and Li, X.-S. (2016). Review of Natural Gas Hydrates as an Energy Resource: Prospects and Challenges. *Appl. Energy* 162, 1633–1652. doi:10.1016/j.apenergy.2014.12.061

Collett, T. S. (2002). Energy Resource Potential of Natural Gas Hydrates. *AAPG Bull.* 86 (11), 1971–1992. doi:10.1306/61eeddd2-173e-11d7-8645000102c1865d

Collett, T. S., Johnson, A. H., Knapp, C. C., and Boswell, R. (2009). American Association of Petroleum Geologists Memoir, Natural Gas Hydrates. *A Rev.* 89, 146–219.

Collett, T. S. (2010). Resource Potential of Gas Hydrates: Recent Contributions from International Research and Development Projects. *Pet. Geol. Conf. Ser.* 7, 1151–1154. doi:10.1144/0071151

Crutchley, G. J., Kroeger, K. F., Pecher, I. A., Mountjoy, J. J., and Gorman, A. R. (2017). Gas Hydrate Formation amid Submarine Canyon Incision: Investigations from new Zealand's Hikurangi Subduction Margin. *Geochem. Geophys. Geosyst.* 18, 4299–4316. doi:10.1002/2017gc007021

Dai, S., Santamarina, J. C., Waite, W. F., and Kneafsey, T. J. (2012). Hydrate Morphology: Physical Properties of Sands with Patchy Hydrate Saturation. *J. Geophys. Res. Solid Earth* 117, B11205. doi:10.1029/2012jb009667

Davies, R. J., Thatcher, K. E., Mathias, S. A., and Yang, J. (2012). Deepwater Canyons: An Escape Route for Methane Sealed by Methane Hydrate. *Earth Planet. Sci. Lett.* 323, 72–78. doi:10.1016/j.epsl.2011.11.007

Demirbas, A. (2010). Methane Hydrates as Potential Energy Resource: Part 2 - Methane Production Processes from Gas Hydrates. *Energy Convers. Manag.* 51 (7), 1562–1571. doi:10.1016/j.enconman.2010.02.014

Fang, Y., Wei, J. G., Wei, J., Lu, H., Liang, J., Lu, J. a., et al. (2019). Chemical and Structural Characteristics of Gas Hydrates from the Haima Cold Seeps in the Qiongdongnan Basin of the South China Sea. *J. Asian Earth Sci.* 182, 103924. doi:10.1016/j.jseaes.2019.103924

Fu, N., Lin, Q., and Liu, Y. L. (2011). Analysis on Potential Gas Source of Gas Hydrate from the Original Characteristics of Shallow Gas in the North of the South China Sea. *Geoscience* 25 (2), 332–339. (In Chinese with English abstract). doi:10.3969/j.issn.1000-8527.2011.02.017

Guo, Y. Q., Yang, S. X., Liang, J. Q., Lu, J. A., Lin, L., and Kuang, Z. G. (2017). Characteristics of High Gas Hydrate Distribution in the Shenhu Area, Northern Slope of South China Sea. *Earth Sci. Front.* 24 (4), 24–31. (In Chinese with English abstract). doi:10.13745/j.esf.yx.2016-12-28

He, J. X., Yan, W., Zhu, Y. H., Zhang, W., Gong, F., Liu, S. L., et al. (2013). Biogenetic and Sub-biogenetic Gas Resource Potential and Genetic Types of Natural Gas Hydrate in the Northern Marginal Basins of the South China Sea. *Nat. Gas. Ind.* 33 (6), 121–134. (In Chinese with English abstract). doi:10.3787/j.issn.1000-0976.2013.06.023

He, J. X., Yao, Y. J., Liu, H. L., and Wan, Z. F. (2008). Genetic Types of Natural Gas and Characteristic of the Gas Source Composition in Marginal Basins of the Northern South China Sea. *Geol. China* 35 (5), 1007–1016. (In Chinese with English abstract). doi:10.3969/j.issn.1000-3657.2008.05.020

He, Y., Zhong, G., Wang, L., and Kuang, Z. (2014). Characteristics and Occurrence of Submarine Canyon-Associated Landslides in the Middle of the Northern Continental Slope, South China Sea. *Mar. Petroleum Geol.* 57, 546–560. doi:10.1016/j.marpetgeo.2014.07.003

Hyndman, R. D., and Davis, E. E. (1992). A Mechanism for the Formation of Methane Hydrate and Seafloor Bottom-Simulating Reflectors by Vertical Fluid Expulsion. *J. Geophys. Res.* 97 (B5), 7025–7041. doi:10.1029/91jb03061

Jin, J., Wang, X., He, M., Li, J., Yan, C., Li, Y., et al. (2020). Downward Shift of Gas Hydrate Stability Zone Due to Seafloor Erosion in the Eastern Dongsha Island, South China Sea. *J. Ocean. Limnol.* 38, 1188–1200. doi:10.1007/s00343-020-0064-z

Kawasaki, T., Ukita, T., Fujii, T., Noguchi, S., and Ripmeester, J. A. (2011). Particle Size Effect on the Saturation of Methane Hydrate in Sediments - Constrained from Experimental Results. *Mar. Petroleum Geol.* 28 (10), 1801–1805. doi:10.1016/j.marpetgeo.2010.11.007

Klauda, J. B., and Sandler, S. I. (2005). Global Distribution of Methane Hydrate in Ocean Sediment. *Energy fuels.* 19 (2), 459–470. doi:10.1021/ef049798o

Kuang, Z. G., Fang, Y. X., Liang, J. Q., Lu, J. A., and Wang, L. (2018). Geomorphological-geological-geophysical Signatures of High-Flux Fluid Flows in the Eastern Pearl River Mouth Basin and Effects on Gas Hydrate Accumulation. *Sci. China (Earth Sci.* 61 (7), 914–924.

Kuang, Z. G., and Guo, Y. (2011). The Sedimentary Facies and Gas Hydrate Accumulation Models since Neogene of Shenhu Area, Northern South China Sea. *Earth Sci. — J. China Univ. Geosciences* 36 (5), 914–920. (In Chinese with English abstract). doi:10.3799/dqkx.2011.096

Kvenvolden, K. A. (1993). Gas Hydrates-Geological Perspective and Global Change. *Rev. Geophys.* 31 (2), 173–187. doi:10.1029/93rg00268

Kvenvolden, K. A., and Lorenson, T. D. (2001). The Global Occurrence of Natural Gas Hydrate. *Nat. Gas Hydrates Occur. Distribution, Detect.* 124, 3–18.

Lee, M. W., and Collett, T. S. (2012). Pore- and Fracture-Filling Gas Hydrate Reservoirs in the Gulf of Mexico Gas Hydrate Joint Industry Project Leg II Green Canyon 955 H Well. *Mar. Petroleum Geol.* 34, 62–71. doi:10.1016/j.marpetgeo.2011.08.002

Lee, M. W., Hutchinson, D. R., Dillon, W. P., Miller, J. J., Agena, W. F., and Swift, B. A. (1993). Method of Estimating the Amount of *In Situ* Gas Hydrates in Deep Marine Sediments. *Mar. Petroleum Geol.* 10 (5), 493–506. doi:10.1016/0264-8172(93)90050-3

Liang, J. Q., Wang, H. B., Su, X., Fu, S. Y., Wang, L. F., Guo, Y. Q., et al. (2014). Natural Gas Hydrate Formation Conditions and the Associated Controlling Factors in the Northern Slope of the South China Sea. *Nat. Gas. Ind.* 2 34 (7), 128–135. (In Chinese with English abstract). doi:10.3787/j.issn.1000-0976.2014.07.022

Liang, J. Q., Zhang, G. X., Lu, J. A., et al. (2016). Accumulation Characteristics and Genetic Models of Natural Gas Hydrate Reservoirs in the NE Slope of the South China Sea. *Nat. Gas. Ind.* 36 (10), 157–162. (In Chinese with English abstract). doi:10.3787/j.issn.1000-0976.2016.10.020

Liang, J., Wang, M. J., and Guo, Y. Q. (2006). Studies of Seismic Velocity about Gas Hydrate in North Slope of the South China Sea. *Geoscience* 20 (1), 123–129. (In Chinese with English abstract). doi:10.1007/s11769-006-0026-1

Liang, J., Wang, M. J., Lu, J. A., Wang, M. J., Liang, J. Q., and Su, P. B. (2010). Logging Response Characteristics of Gas Hydrae Formation in Shenhu Area of the South China Sea. *Geoscience* 24 (3), 506–514. (In Chinese with English abstract). doi:10.3969/j.issn.1000-8527.2010.03.014

Liang, J., Wang, J. L., Lu, J. A., Kang, D. J., Kuang, Z. G., and Yang, C. Z. (2017a). The Logging Response Character and its Geological Significance of Gas Hydrae Formation in Taixinan Basin. *Earth Sci. Front.* 24 (4), 32–40. (In Chinese with English abstract). doi:10.13745/j.esf.yx.2016-12-32

Liang, J., Wang, J. L., Yang, C. Z., Kang, D. J., Lu, J. A., and Liang, J. Q. (2017b). Geophysical Characteristics of Gas Hydrate Bearing Sediments in the Eastern Sea Area of the Pearl River Mouth Basin. *Nat. Gas. Ind.* 37 (2), 126–133. (In Chinese with English abstract). doi:10.3787/j.issn.1000-0976.2017.02.017

Liang, J., Wang, M. J., Lu, J. A., Liang, J. Q., Wang, H. B., and Kuang, Z. G. (2013). Characteristics of Sonic and Seismic Velocities of Gas Hydrate Bearing Sediments in the Shenhu Area, Northern South China Sea. *Nat. Gas. Ind.* 33 (7), 29–35. (In Chinese with English abstract). doi:10.3787/j.issn.1000-0976.2013.07.005

Liang, J., Wang, M. J., Wang, H. B., Lu, J. A., and Liang, J. Q. (2009). Relationship between the Sonic Logging Velocity and Saturation for Gas Hydrate in Shenhu Area, Northern Slope of South China Sea. *Geoscience* 23 (2), 217–223. (In Chinese with English abstract). doi:10.3969/j.issn.1000-8527.2009.02.004

Liang, J., Zhang, W., Lu, J. a., Wei, J., Kuang, Z., and He, Y. (2019). Geological Occurrence and Accumulation Mechanism of Natural Gas Hydrates in the Eastern Qiongdongnan Basin of the South China Sea: Insights from Site GMGS5-W9-2018. *Mar. Geol.* 418, 106042. doi:10.1016/j.margeo.2019.106042

Lu, H. L., Kawasaki, T., Ukita, T., Moudrakovski, I., Fujii, T., Noguch, et al. (2011). Particle Size Effect on the Saturation of Methane Hydrate in Sediments — Constrained from Experimental Results. *Mar. Petroleum Geol.* 28 (10), 1805. doi:10.1016/j.marpetgeo.2010.11.007

Lu, J. A., Yang, S. X., Wu, N. Y., Zhang, G. X., Zhang, M., and Liang, J. Q. (2008). Well Logging Evaluation of Gas Hydrates in Shenhu Area, South China Sea. *Geoscience* 22 (3), 447–451. (In Chinese with English abstract). doi:10.1016/S1876-3804(08)60015-4

Meng, M., Liang, J., Lu, J., Zhang, W., Kuang, Z., Fang, Y., et al. (2021). Quaternary Deep-water Sedimentary Characteristics and its Relationship with Gas Hydrate Accumulations in the Qiongdongnan Basin, Northwest South China Sea. *Deep-sea Res. Part I* 177. doi:10.1016/j.dsr.2021.103628

Mo, X. W., Lu, J. A., Sha, Z. B., et al. (2008). A New Method for Gas Hydrate Saturation Estimation Using Well Logging Data. *J. Jilin Univ. (Earth Sci. Ed.* 42 (4), 921–927. (In Chinese with English abstract).

Paull, C. K., Ussler, W., and Dillon, W. P. (1991). Is the Extent of Glaciation Limited by Marine Gas-Hydrates? *Geophys. Res. Lett.* 18 (3), 432–434. doi:10.1029/91gl00351

Riedel, M., Collett, T. S., and Shankar, U. (2011). Documenting Channel Features Associated with Gas Hydrates in the Krishna-Godavari Basin, Offshore India. *Mar. Geol.* 279, 1–11. doi:10.1016/j.margeo.2010.10.008

Santamarina, J. C., Dai, S., Terzariol, M., Jang, J., Waite, W. F., Winters, W. J., et al. (2015). Hydro-bio-geomechanical Properties of Hydrate-Bearing Sediments from Nankai Trough. *Mar. Petroleum Geol.* 66, 434–450. doi:10.1016/j.marpetgeo.2015.02.033

Shukla, K. M., Kumar, P., Kumar, P., and Yadav, U. S. (2019). Gas Hydrate Reservoir Identification, Delineation, and Characterization in the Krishna-Godavari Basin Using Subsurface Geologic and Geophysical Data from the National Gas Hydrate Program 02 Expedition, Offshore India. *Mar. Petroleum Geol.* 108, 185–205. doi:10.1016/j.marpetgeo.2018.10.019

Su, M., Sha, Z., Zhang, C., Wang, H., Wu, N., Yang, R., et al. (2017). Types, Characteristics and Significances of Migrating Pathways of Gas-bearing Fluids in the Shenhu Area, Northern Continental Slope of the South China Sea. *Acta Geol. Sin. - Engl. Ed.* 91 (1), 219–231. doi:10.1111/1755-6724.13073

Su, P. B., Liang, J. Q., Peng, J., et al. (2018). *Petroleum Systems Modeling on Gas Hydrate of the First Experimental.*

Su, P. B., Liang, J. Q., Sha, Z. B., and Fu, S. Y. (2014). Gas Sources Condition of Gas Hydrate Formation in Shenhu Deep Water Sea Zone. *J. Southwest Petroleum Univ. Sci. &Technology Ed.* 36 (2), 1–8. (In Chinese with English abstract). doi:10.11885/j.issn.1674-5086.2013.10.16.01

Sua, P., Lianga, J., Peng, J., Zhang, W., and Xu, J. (2018). Petroleum Systems Modeling on Gas Hydrate of the First Experimental Exploitation Region in the Shenhu Area, Northern South China Sea. *J. Asian Earth Sci.* 168, 57–76. doi:10.1016/j.jseaes.2018.08.001

Walter, S. B., Charles, K. P., and William, U. (1999). Global and Local Variations of Interstitial Sulfate Gradients in Deep-Water, Continental Margin Sediments: Sensitivity to Underlying Methane and Gas Hydrates. *Mar. Geol.* 159 (1-4), 131–154. doi:10.1016/s0025-3227(99)00004-3

Wang, H. B., Liang, J., Gong, Y. H., Huang, Y. Y., Liu, X. W., and Sha, Z. B. (2005). Estimation of the Heat Flow in the Northern of the South China Sea Based on the Seismic Data of Gas Hydrate. *Geoscience* 19 (1), 67–73. (In Chinese with English abstract). doi:10.3969/j.issn.1000-8527.2005.01.010

Wang, X., Collett, T. S., Lee, M. W., Yang, S., Guo, Y., and Wu, S. (2014). Geological Controls on the Occurrence of Gas Hydrate from Core, Downhole Log, and Seismic Data in the Shenhu Area, South China Sea. *Mar. Geol.* 357, 272–292. doi:10.1016/j.margeo.2014.09.040

Wang, X. J., Wu, S. G., and Liu, X. W. (2006). Factors Affecting the Estimation of Gas Hydrate and Free Gas Saturation. *Chin. J. Geophys.* 49 (2), 505–511. doi:10.1002/cjg2.853

Wang, Z. W., Li, Z. B., and Liu, J. H. (2003). Logging Identification and Evaluation Methods for Gas Hydrates. *Mar. Geol. Quat. Geol.* 23 (2), 97–102. (In Chinese with English abstract).

Wu, N. Y., Zhang, H. Q., Yang, S. X., Liang, J. Q., and Wang, H. B. (2007). Preliminary Discussion on Natural Gas Hydrate (NGH) Reservoir System of Shenhu Area, Northern South China Sea. *Nat. Gas. Ind.* 27 (9), 1–6. (In Chinese with English abstract). doi:10.3321/j.issn:1000-0976.2007.09.001

Wu, S. G., Gong, Y. H., Mi, L. J., Wang, Z. J., and Wang, X. J. (2010). Study on Hydrocarbon Leakage System and Associated Gas Hydrate Reservoirs in the Deepwater Basin of Northern South China Sea. *Geoscience* 24 (3), 433–440. (In Chinese with English abstract). doi:10.3969/j.issn.1000-8527.2010.03.003

Yang, C. Z., Luo, K. W., Liang, J. Q., Lin, Z. X., Zhang, B. D., Liu, F., et al. (2020). Control Effect of Shallow-Burial Deepwater Deposits on Natural Gas Hydrate Accumulation in the Shenhu Sea Area of the Northern South China Sea. *Nat. Gas. Ind.* 40 (8), 68–76. (In Chinese with English abstract). doi:10.3787/j.issn.1000-0976.2020.08.005

Yang, S. X., Lei, Y., Liang, J. Q., Holland, M., Schultheiss, P., Lu, J. A., et al. (2017a). "Concentrated Gas Hydrate in the Shenhu Area, South China Sea: Results from Drilling Expeditions GMGS3 & GMGS4," in Proceedings of 9th International Conference on Gas Hydrates, Denver (Paper), 105.

Yang, S. X., Liang, J. Q., Lu, J. A., Qu, C. W., and Bo, L. (2017b). New Understandings on Characteristics and Controlling Factors of Gas Hydrate Reservoirs in Shenhu Area on Northern Slope of South China Sea. *Earth Sci. Front.* 24 (4), 1–14. (In Chinese with English abstract). doi:10.13745/j.esf.yx.2016-12-43

Yang, S. X., Zhang, M., Liang, J. Q., Lu, J. A., Zhang, Z. J., and Melanie, H. (2015). Preliminary Results of China's Third Gas Hydrate Drilling Expedition: A Critical Step from Discovery to Development in the South China Sea. *Fire Ice* 15 (2), 1–5.

Yu, X., Wang, J., Liang, J., Li, S., Zeng, X., and Li, W. (2014). Depositional Characteristics and Accumulation Model of Gas Hydrates in Northern South China Sea. *Mar. Petroleum Geol.* 56, 74–86. doi:10.1016/j.marpetgeo.2014.03.011

Zhang, G. X., Liang, J. Q., Lu, J. A., Yang, S. X., Zhang, M., Xin, S., et al. (2014). Characteristics of Natural Gas Hydrate Reservoirs on the Northeastern Slope of the South China Sea. *Nat. Gas. Ind.* 34 (11), 1–10. (In Chinese with English abstract). doi:10.3787/j.issn.1000-0976.2014.11.001

Zhang, W., Liang, J., Lu, J. a., Wei, J., Su, P., Fang, Y., et al. (2017). Accumulation Features and Mechanisms of High Saturation Natural Gas Hydrate in Shenhu Area, Northern South China Sea. *Petroleum Explor. Dev.* 44 (5), 708–719. doi:10.1016/s1876-3804(17)30082-4

Zhang, W., Liang, J. Q., Su, P. B., Wei, J. G., Sha, Z. B., Lin, L., et al. (2018). Migrating Pathways of Hydrocarbons and Their Controlling Effects Associated with High Saturation Gas Hydrate in Shenhu Area, Northern South China Sea. *Geol. China* 45 (1), 1–14. (In Chinese with English abstract). doi:10.12029/gc20180101

Zhang, W., Liang, J., Wan, Z., Su, P., Huang, W., Wang, L., et al. (2020). Dynamic Accumulation of Gas Hydrates Associated with the Channel-Levee System in the Shenhu Area, Northern South China Sea. *Mar. Petroleum Geol.* 117, 104354. doi:10.1016/j.marpetgeo.2020.104354

Zhong, G., Liang, J., Guo, Y., Kuang, Z., Su, P., and Lin, L. (2017). Integrated Core-Log Facies Analysis and Depositional Model of the Gas Hydrate-Bearing Sediments in the Northeastern Continental Slope, South China Sea. *Mar. Petroleum Geol.* 86, 1159–1172. doi:10.1016/j.marpetgeo.2017.07.012

Conflict of Interest: The authors declare that the research was conducted in the absence of any commercial or financial relationships that could be construed as a potential conflict of interest.

Publisher's Note: All claims expressed in this article are solely those of the authors and do not necessarily represent those of their affiliated organizations, or those of the publisher, the editors and the reviewers. Any product that may be evaluated in this article, or claim that may be made by its manufacturer, is not guaranteed or endorsed by the publisher.

frontiers | Frontiers in Earth Science

ORIGINAL RESEARCH
published: 07 July 2022
doi: 10.3389/feart.2022.922802

Shallow Overpressure Formation in the Deep Water Area of the Qiongdongnan Basin, China

Jinfeng Ren[1,2], Litao Xu[3,4], Wanzhong Shi[3,4]*, Wei Yang[1,2], Ren Wang[3,4], Yulin He[1,2] and Hao Du[3,4]*

[1]Southern Marine Science and Engineering Guangdong Laboratory (Guangzhou), Guangzhou, China, [2]National Engineering Research Center of Gas Hydrate Exploration and Development, Guangzhou Marine Geological Survey, Guangzhou, China, [3]Key Laboratory of Tectonics and Petroleum Resources, The Ministry of Education, China University of Geosciences, Wuhan, China, [4]School of Earth Resources, China University of Geosciences, Wuhan, China

The scarcity of drilling in the deep water area of Qiongdongnan Basin restricts the cognition and prediction of overpressure. In this paper, a shallow zone of overpressure at the depth of 900–1,200 m below the sea floor in the deep water area was found by analyzing electronic logs, mud pressure (Mud pressure is a product of the height of the column of mud, density and gravity acceleration) and test pressure from drill stem testing (DST) and modular dynamic testing (MDT), and the interpretation of anomalous seismic interval velocities. The shallow overpressure is a newly observed geological phenomenon in the South China Sea for which the generation mechanisms are not well understood, despite similar observations and analyses elsewhere in the world. Two representative wells, one each located in the shallow water and the deep water areas, respectively were selected to investigate the vertical distribution of the shallow overpressure. The top of the overpressure in Well A in the shallow water area is about 2,111 m below sea floor, while the top of the overpressure in Well B in the deep water area is about 1,077 m below sea floor. A pressure coefficient (i.e., ratio of pore pressure to the normal hydrostatic pressure measured from the sea surface) profile was constructed from the shallow water area to the deep water area using the calibrated relationship between seismic interval velocities and pressure data from 30 wells. The distance between the top of the overpressure and the seabed is predicted to be between 900 and 1,200 m in the deep water area Basin. Disequilibrium compaction is the interpreted primary cause of the shallow overpressure and the results of basin modeling indicate that the shallow overpressure was generated since 5.5 Ma.

Keywords: shallow overpressure, overpressure prediction, overpressure distribution, generation mechanism, basin modeling, deep water area, qiongdongnan basin

OPEN ACCESS

Edited by:
Lihua Zuo,
Texas A&M University Kingsville, United States

Reviewed by:
Qinghai Xu,
Yangtze University, China
Ziye Lu,
Southwest Petroleum University, China

***Correspondence:**
Litao Xu
litaoxu001@163.com
Wanzhong Shi
shiwz@cug.edu.cn

Specialty section:
This article was submitted to Marine Geoscience, a section of the journal Frontiers in Earth Science

Received: *18 April 2022*
Accepted: *16 June 2022*
Published: *07 July 2022*

Citation:
Ren J, Xu L, Shi W, Yang W, Wang R, He Y and Du H (2022) Shallow Overpressure Formation in the Deep Water Area of the Qiongdongnan Basin, China. Front. Earth Sci. 10:922802. doi: 10.3389/feart.2022.922802

INTRODUCTION

Overpressure, pore pressures in excess of hydrostatic, plays a critical role in geologic processes, such as retarding organic-matter maturation and petroleum generation (Hao et al., 1995, 1998; Zou and Peng, 2001; Radwana et al., 2020; Wang et al., 2022), improving reservoir porosity by resisting consolidation (Ma et al., 2008), driving petroleum migration (Tang and Lerche, 1993; Liu et al., 2021) and natural hydraulic fracturing (Hao et al., 2002), and inducing submarine landslides (Cobbold et al., 2004; Zhang et al., 2015). The Qiongdongnan Basin (QDNB) is an overpressured basin in the

northern part of the South China Sea (Shi et al., 2013; Xu et al., 2017). Overpressure is an obvious geologic feature in the basin, where the maximum pressure coefficient from drill stem testing (DST) is as high as 2.27.

Shallow overpressure is a newly observed geological phenomenon in the Basin. Direct measurement in mudrocks from IODP Expedition 308 in the Gulf of Mexico using pore pressure penetrometers confirmed that overpressure can occur at depths of 0–600 m below the seafloor (Flemings et al., 2008; Binh et al., 2009; Long et al., 2011). Much study shows that the shallow overpressure has an important effect on submarine landslides (Dugan and Flemings, 2002; Flemings et al., 2008). Samples test from IODP Expedition 308 in the Gulf of Mexico shows that porosity varies from 80% at the seafloor to 37% at 620 m below the seafloor (Binh et al., 2009). These observations contradict the traditional thinking that overpressure is not possible in shallow formations with high porosity. Flemings et al. (2008) proposed that the high overpressures observed in IODP Expedition 308 were the result of rapid sedimentation of low permeability material from the ancestral Mississippi River. Porosity tests in the overpressure sections show that the values are high, greater than 37% in fact. The permeability values obtained from 14 consolidation tests ranged from 0.05 to 0.0001 mD under porosity conditions ranging from 33 to 47% (Binh et al., 2009). Long et al. (2011) proposed that rapid sediment consolidation near the seafloor at the IODP Expedition 308 location provided the fluid source to generate overpressure, despite the fact that these sediments have high porosity. These two opinions about the shallow overpressure formation share many similarities with the disequilibrium compaction mechanism for the generation of high pore pressures. Recent drilling indicates that shallow overpressure exists in the deep water area of the QDNB. The mechanism for the shallow overpressure in the QDNB has not been previously examined.

There are a number of papers published on overpressure generation mechanisms as a result of disequilibrium compaction (Dickinson, 1953; Skempton, 1970; Magara, 1975; Osborne and Swarbrick, 1997; Mondol et al., 2007; Tingay et al., 2009; Hua et al., 2021; Li et al., 2021), oil and gas generation (Timko and Fertl, 1971; Hedberg, 1974; Law and Dickinson, 1985; Spencer, 1987; Bredehoeft et al., 1994; Luo and Vasseur, 1996; Guo et al., 2010; Tingay et al., 2013), aquathermal pressuring (Barker, 1972; Bradley, 1975; Plumley, 1980; Sharp, 1983; Liu et al., 2019), fluid release during dehydration reactions (Powers, 1967; Schmidt, 1973; Magara, 1975; Li et al., 2016), vertical transfer of overpressures (Tingay et al., 2007), tectonic compression (Berry, 1973; Luo 2004; Luo et al., 2006; Zhang et al., 2021) and aquathermal expansion and clay dehydration (Luo and Vasseur, 1992; Osborne and Swarbrick, 1997; Wang et al., 2020). Disequilibrium compaction and oil and gas generation are believed to be the primary causes of overpressure in the young basins (Osborne and Swarbrick, 1997; Akrout et al., 2021). These reported overpressures all formed in the middle-deep formations of the basin. The mechanism of the shallow overpressure formation in the QDNB is investigated in this study.

The objectives of this article are 1) to document the characteristics of the overpressure distribution based on well-log and seismic analysis; 2) to determine the mechanism of the shallow overpressure formation in the QDNB. The method of revealing overpressure distribution we present can be applied around the world. Meanwhile, shallow overpressure was recognized as a common geological phenomenon, which provided a mechanism for submarine slope failures, fluid diapirs, and hydrocarbon migration. Revealing its distribution and genetic mechanism is of great significance for avoiding risk in construction and the prospecting of the shallow resource (e.g., natural gas hydrate).

GEOLOGICAL BACKGROUND

The QDNB is located in the northern part of the South China Sea (108°50′—111°50′ E, 16°50′—19°00′ N). The basin covers an area of about 45,000 km^2. The maximum thickness of Cenozoic sediments in the basin is in excess of 12,000 m (Wang et al., 2008; Wu et al., 2009). It can be divided into eight depocentres, namely the Yanan, Yabei, Songxi, Songdong, Ledong-Lingshui, Songnan-Baodao, Changchang and Beijiao sags (**Figure 1**). The basin underwent rifting from 50 to 21 Ma, thermal subsidence from 21 to 10.5 Ma, and then rapid subsidence from 10.5 Ma to the present. The break-up unconformity of T60 (21 Ma) divided the Cenozoic formations into two tectonic sequences. Faults are primarily distributed in the tectonic sequence of the region from the basement to the T60 horizon; the faults are seldom active in the sequences above the T60 horizon. The Eocene, Yacheng, Lingshui, Sanya, Meishan, Huangliu, Yinggehai, and Ledong formations (Fms.), can be identified with both geological and geophysical data (**Figure 2**). The basin has been filled by both continental and marine sequences. Continental facies dominated in the Eocene, whereas marine facies dominate from the Oligocene Yacheng formation (Fm.) to the present (**Figure 2**).

QDNB is world-famous for its notable high overpressure. There exists a widespread strong overpressure in the middle-deep formation throughout the entire basin (2,900–5,000 m) (Xu et al., 2017). The drilling analysis showed that the maximum pressure coefficient is over 2.27 (Shi et al., 2013; Xu et al., 2017). Overpressure is mainly generated by disequilibrium compaction, associated with anomalously high porosity (Dasgupta et al., 2016). The current pressure coefficient in the western area is greater than that in the eastern area (Shi et al., 2013).

The maximum water depth can reach 2,500 m in the deep water area. Paleontological data indicate that the water depth deepened gradually from 10.5 Ma onward. Several large oil and gas fields have been discovered in the shallow water regions in the northern part of the basin. However, exploration in the QDNB is now gradually extending into deep water areas.

DATA AND METHODS

This study employed three main approaches (**Figure 3**): 1) pore pressure test data and well-log analysis to confirm the presence of the shallow overpressure, 2) seismic velocities used to predict the shallow overpressure distribution, and 3) calculation of sedimentation rates and basin modeling to illustrate the shallow overpressure caused by the disequilibrium compaction.

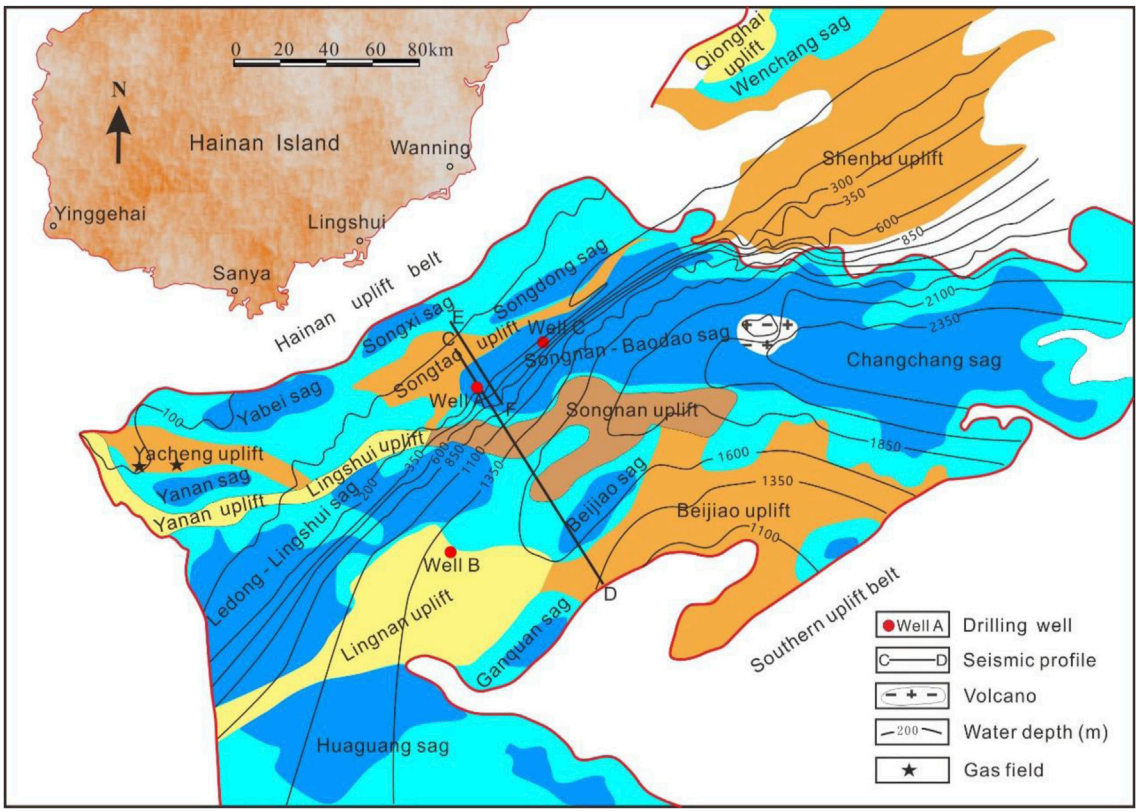

FIGURE 1 | Structural features of the Qiongdongnan Basin and the location of gas fields, wells, bathymetry and locations of seismic profiles (modified after Zhu, 2007). The units of bathymetry are in meters.

Well-Log Responses to Overpressure Distribution

Overpressure refers to pore pressure that is greater than the corresponding hydrostatic pressure (Dutta, 2002; Radwana et al., 2020). Pore pressure in sandstone can be directly measured using repeat formation testing (RFT), modular dynamic testing (MDT) or drill stem testing (DST), which are believed to be close to the actual pore pressure. Pore pressure in the mudstones is commonly estimated based on wire-line logging methods and the analysis of drilling parameters because pore-fluid pressure in mudstones usually cannot be measured directly because of their low permeability. However, a few pore pressure test data are not sufficient for an areal overpressure analysis, so they are supplemented with electronic logs with curve responses used to predict and analyze pressure as pore pressures in seals and the associated reservoir rocks are commonly equal (Guo et al., 2010). P-wave sonic, resistivity, density and mud pressure can provide information on rock and fluid properties that are indications of overpressure (Guo et al., 2010; Li et al., 2022). For the normally pressured sediments, mudstone parameters such as P-wave sonic, resistivity, and density fit exponential model (Singha and Chatterjee, 2014). Therefore, logging parameters of normally pressured mudstone were selected from drillings to fit the compaction trend guidelines.

Two representative wells A and B located in the shallow water and the deep water respectively were selected to show the vertical distribution of overpressure. **Figure 4** and **Figure 5** showed that the P-wave sonic, resistivity picked from mudstone and VSP velocity for Well A and Well B in the shallow water deviate from the compaction trend and increase or decrease respectively below the normal pressure zone. Meanwhile, the calculated mud pressure and testing pressure confirmed the existence of overpressure zone below the normal pressure zone. It can be confirmed that overpressure exists below about 2,300 m in Well A and 2,550 m in Well B (**Figure 4** and **Figure 5**). These show that the overpressure can be identified by the electric and P-wave sonic logs deviating from the normal trend of the compaction and that resistivity logs can be used to estimate the presence of overpressure in mudstones.

Seismic Data Responses to Overpressure Distribution

The technique of using a decrease in seismic velocity to predict overpressure has been widely used since the pioneering work of Pennebaker (1968). Since then, seismic velocity has remained the main way to predict overpressure, even though other techniques have subsequently been developed such as prestack amplitude inversion and poststack amplitude inversion (Kan and Swan,

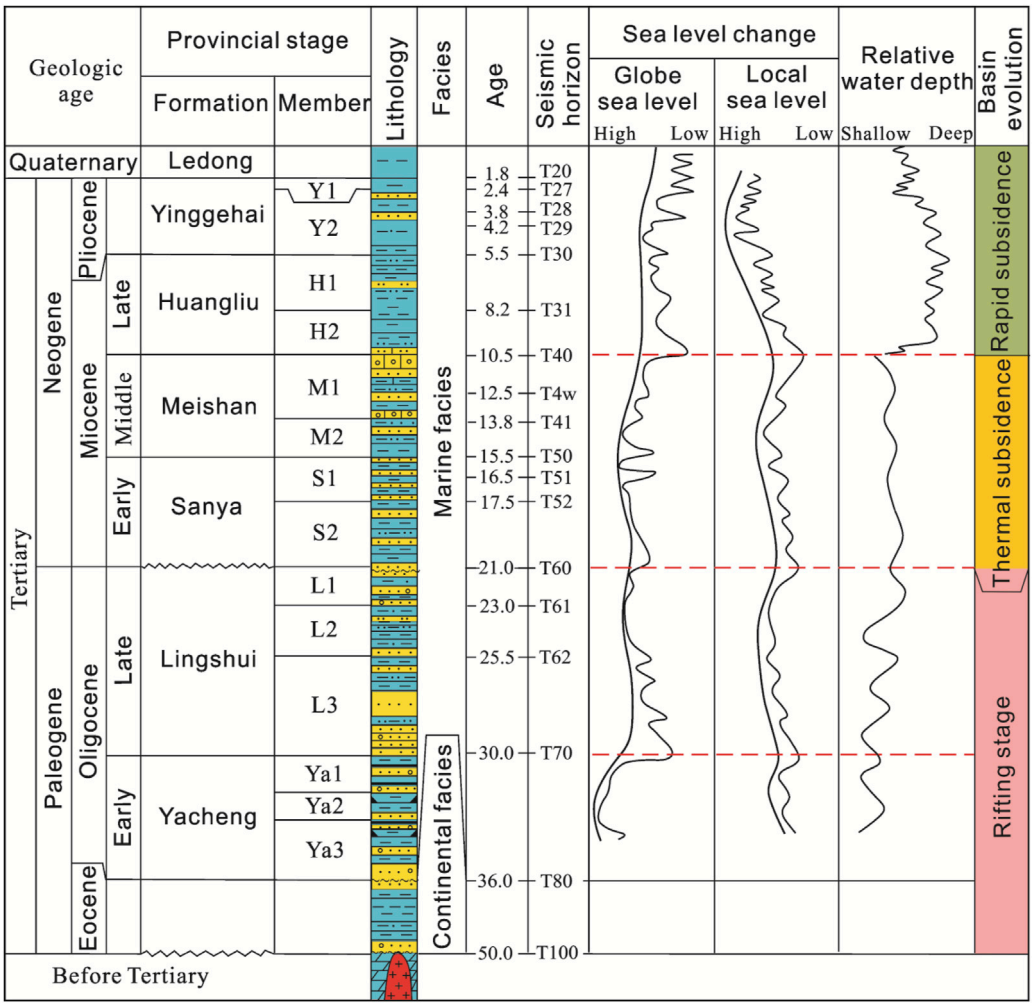

FIGURE 2 | Generalized stratigraphic column of the Qiongdongnan Basin showing age, seismic horizon, sea level curves (Zhu, 2007), water depth curves and basin evolution stages.

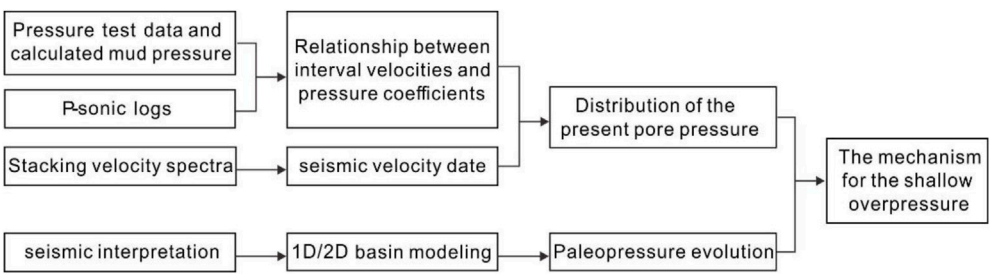

FIGURE 3 | The flow chart of studying the distribution and formation mechanism of the shallow overpressure in the QDNB.

2001; Dutta, 2002; Xu et al., 2017). In order to objectively characterize the subsurface seismic velocity distribution, high-quality stacking velocity spectra are selected to illustrate the velocity variation in profile C-D (**Figure 6**). The seabed is seen to stack best at a velocity of 1,500 m/s. The 2000 and 2,500 m/s isolines of the stacking velocity are developed further by analysis of the stacking velocity spectra. **Figure 6** shows that near the seafloor seismic wave velocities increase from 1,500 m/s to 2000 m/s (or to 2,500 m/s) over a thicker sedimentary section as water depth increases. This shows that

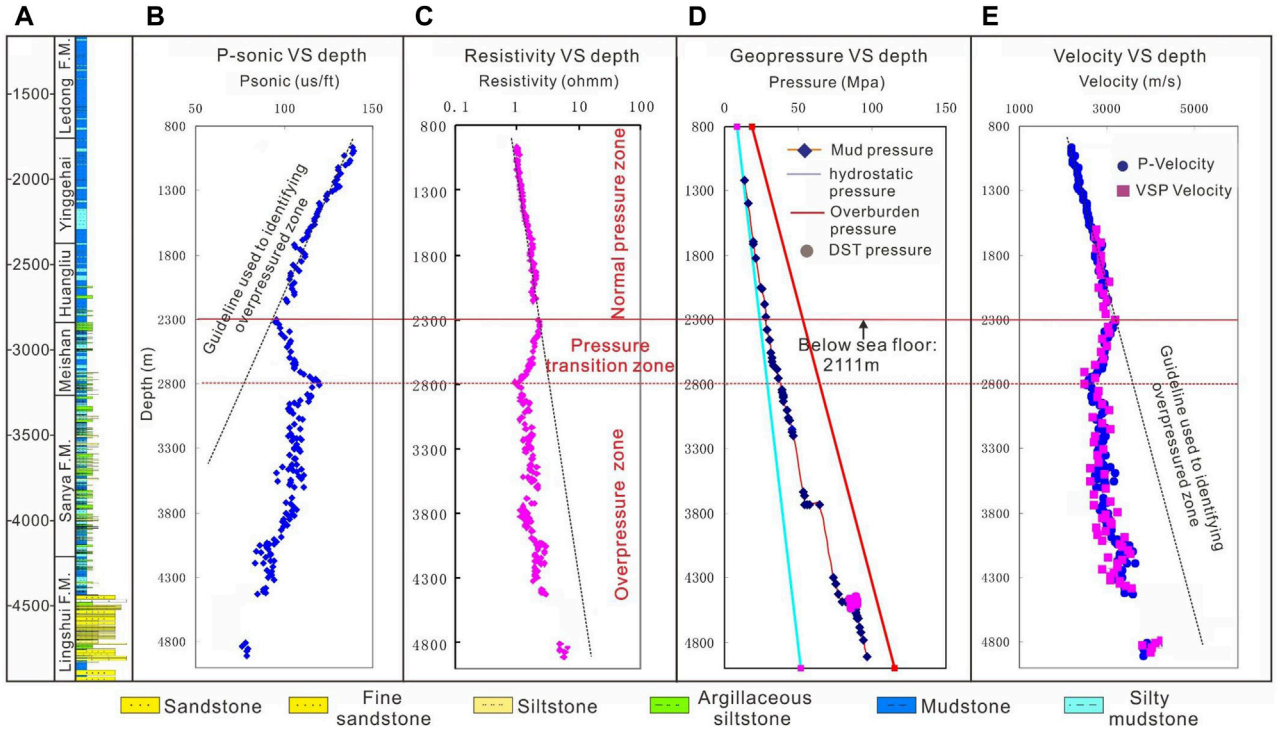

FIGURE 4 | (A) Lithologic profile of Well A **(B)** Pseudo log of sonic P-wave transit times for mudstone. The plot shows the deviation of transit time from the compaction trend below about 2,300 m. **(C)** Plot of log-derived resistivity values for mudstone showing deviation from the compaction trend below about 2,300 m. **(D)** Plot of calculated mud pressures and drill stem test pressures showing a corresponding positive deviation from hydrostatic pressure (overpressure) below about 2,700 m. **(E)** Seismic velocity (VSP velocity) and P-wave sonic velocity plots that show similar deviation from the compaction trend in the overpressure section, which supports the premise that seismic velocity can be used to predict overpressure. A zone of normal pressure is evident above 2,300 m, an apparent transition zone occurs from around 2,300–2,800 m, and the decrease in velocity below 2,800 m corresponds to the zone of overpressure. The water depth in Well A is 189 m. The well location is shown in **Figure 1**.

the seismic interval velocity in the uppermost seafloor will decrease dramatically as the seawater depth increases; this is in accordance with the Dix velocity transformation relationship for stacking velocities, RMS velocities and interval velocities (Dutta, 2002; Yuan et al., 2021). As a result, there appears to be shallow overpressure in the deep water area.

In order to further illustrate the distribution of overpressure, a pressure profile needs to be created by examining the relationship between interval velocities and pressure coefficients. In the past few decades, many methods have used seismic velocities to predict overpressure (Pennebaker, 1968; Eaton, 1972; Kan and Swan, 2001; Dutta, 2002; Sayers et al., 2002; Carcione et al., 2003; Abiola and Ayenuro, 2021; Prankada et al., 2021). **Figures 4**, **5** show that there exists a clear response between the overpressured interval and P-sonic curve, and indicate that overpressure can be predicted by the deviation of the seismic velocity, so the method of Eaton (1972) was selected to identify the position of overpressure in profile C-D. To use Eaton's method, the deviation of the velocity from the normal compaction velocity needs to be estimated. A normal velocity trend starting from the seabed was created based on P-velocity data from the 8 wells with the normal pressure (blue line) and the interval velocities calculated from the stacking velocities (red line) (**Figure 7A**). Pressure coefficients measured by DST data were selected to fit the relationship between the deviation of the velocity and the pressure coefficients (**Figure 7B**). The correlation coefficient between these two parameters can reach 0.79 (**Figure 7B**). According to this relationship, a pressure coefficient profile was then obtained for profile C-D (**Figure 8**).

Modeling of Overpressure

In order to ascertain the age of the shallow overpressure in the deep water parts of the QDNB, 1D modeling was carried out for the position MN at the profile C-D using the PetroMod software (**Figure 9**). The selected position for 1D modeling is far from the slope, so the effect of horizontal compressive stresses from the gravitational load of the clastic wedge on the generation of the shallow overpressure can be ignored. The input data for the basin modeling include age, lithology, erosion thickness, faults activity, heat flow, paleo water depth, kerogen type, TOC, and HI (Xu et al., 2017; Zhang and Li, 2021). Some of these parameters such as age, lithology, and paleo water depth are listed in **Figure 2**, **Figure 9A** and **Table 1**, respectively. The erosion thickness of T70, T60 and T40 are generally 100~250 m, 200~500 m, and 100~300 m, respectively. Fault activity can be identified by analyzing the faults distribution and comparing the Formation thickness between footwall block and hanging wall block. Active faults can be defined as high permeability channels in the

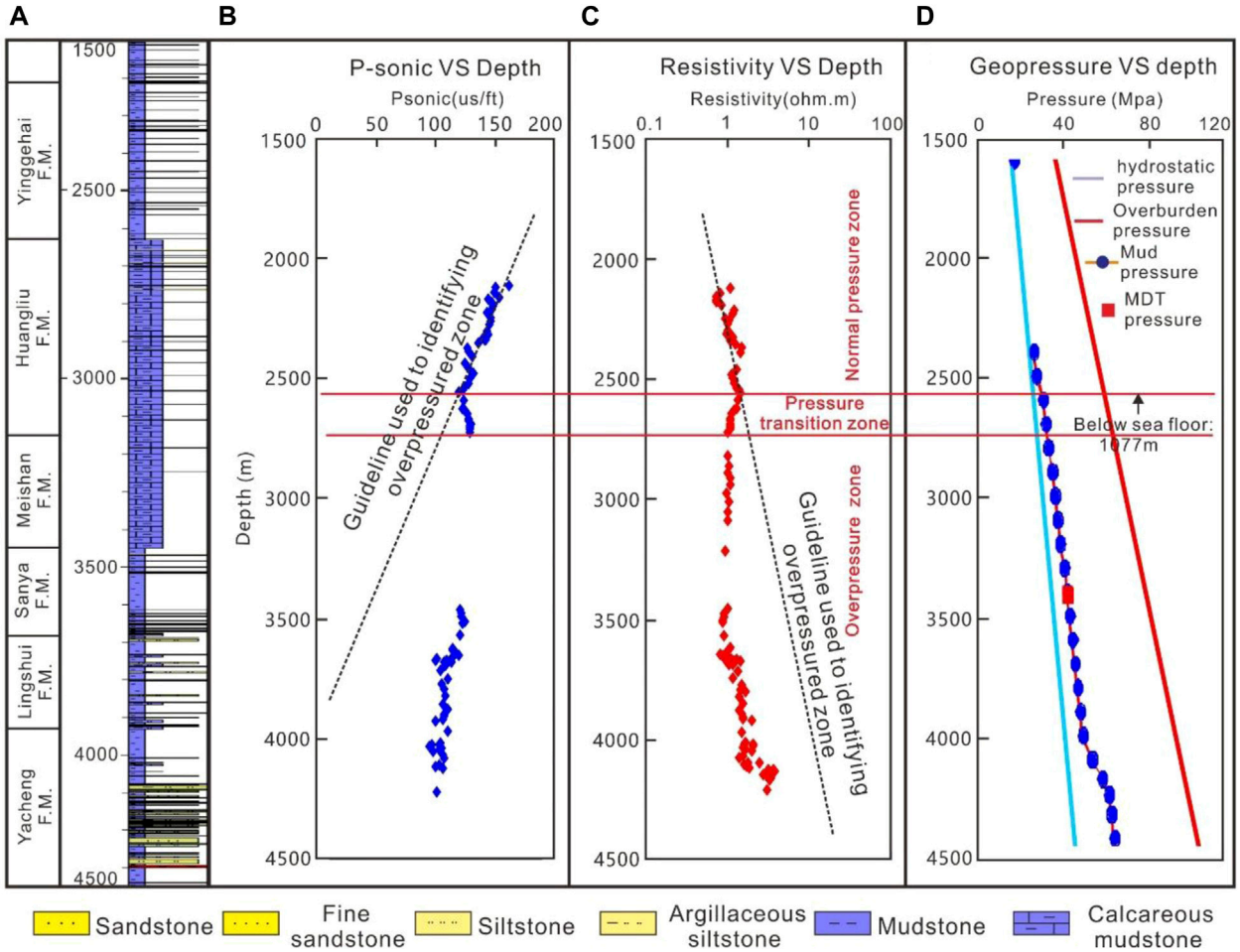

FIGURE 5 | (A) Lithologic profile of Well B **(B)** Pseudo log of sonic P-wave transit times for mudstone. The plot shows the deviation of transit time from the compaction trend below about 2,550 m. The P-wave sonic data at the depth of 2,750–3,450 m were not measured. **(C)** Plot of log-derived resistivity values for mudstone showing deviation from the compaction trend below about 2,550 m. **(D)** Plot of calculated mud pressures and MDT pressures showing a corresponding positive deviation from hydrostatic pressure (overpressure) below about 2,550 m. A normal pressure zone, a pressure transition zone and an overpressure zone can be identified. The water depth in Well B is 1,473 m. The well location is shown in **Figure 1**.

PetroMod software. Heat flow in the QDNB is 58.7–87.1 mW/m^2 with a tendency to increase from the continental shelf to the continental slope owing to the lithospheric/crustal thinning in the Cenozoic (Yuan et al., 2009). Shi et al. (2003) collected 592 heat flow measurements in the South China Sea and established a relationship between the heat flow and the age. Shi et al. (2003) report that the heat flow in the area selected for their study could be derived from the empirical function given by Parsons and Sclater (1977) as follows, and we assigned heat flow values at different stages using this function:

$$Q(t) = 472.34t^{-\frac{1}{2}}$$

Where Q is the heat flow; t is the age of the formation.

In order to understand the seawater depth variation over time in the QDNB, continuous samples from some wells in the shallow water area were collected and analyzed for foraminifer distributions (Zhu, 2007). This analysis indicates that the water depth in the QDNB has increased since 10.5 Ma (**Figure 2**). Because the wells sampled and tested lie in the shallow water area, the results cannot completely support the occurrence of the same processes in the deep water. However, it is known that continental margins are characterized by the slope break, an important feature that is used to separate shallow shelf and deeper slope waters. **Figure 10** shows that the slope break began forming about 5.5 Ma, and that the seawater depth was relatively constant in the QDNB before that time. By integrating the results of the slope break migration, seawater depth variations can be estimated based on a regularly varying velocity with depth. **Table 1** shows that the seawater depth in the deep water area dramatically deepened since 5.5 Ma. The paleotemperature parameters were calculated through the change of paleo water depths. The organic matter types are type II in Eocene and type III in Oligocene and Miocene (Zuo et al., 2022). The average contents of total organic carbon (TOC) in Eocene, Oligocene and Miocene are 1.5, 1.0 and 0.6%, respectively. The hydrogen

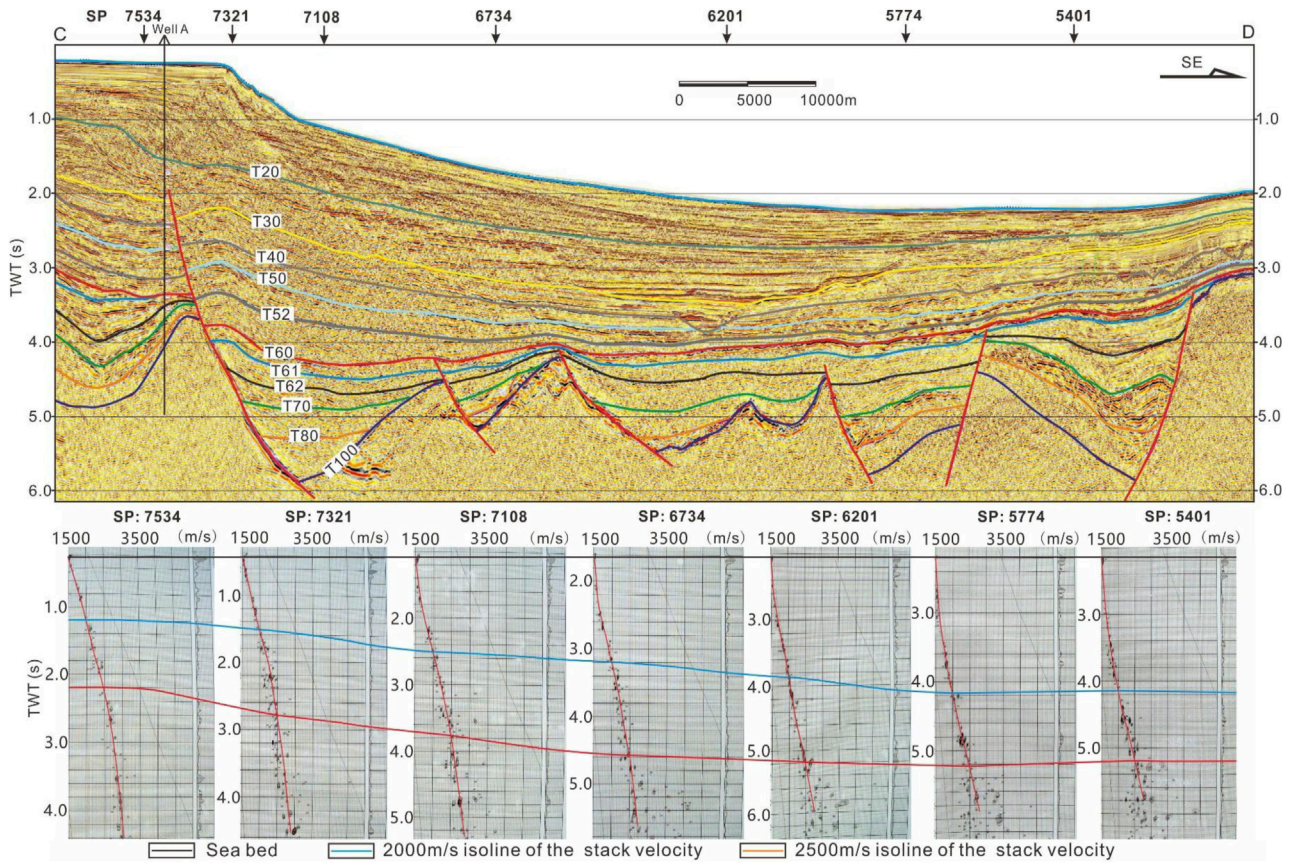

FIGURE 6 | Top interpreted seismic cross-section, showing the site of Well A and the selected points for the stacking velocity analysis. (Bottom) Selected stacking velocity spectra, and the 2000 m/s and 2,500 m/s isolines of the stacking velocity. The cross section location is shown in **Figure 1**.

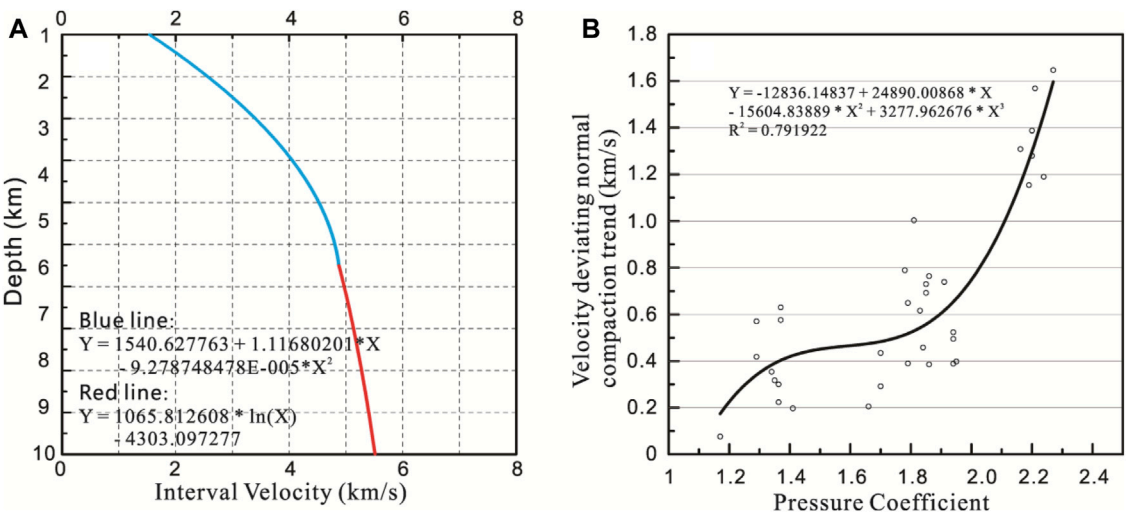

FIGURE 7 | (A) Reconstructed normal velocity trend starting from the seabed that is based on the P-velocity data from 8 wells characterized by the normal pressure (blue line) and the interval velocities calculated from the stacking velocities (red line). **(B)** Relationship between the velocity values deviating from the normal compaction trend and the pressure coefficient of wells in the Qiongdongnan Basin.

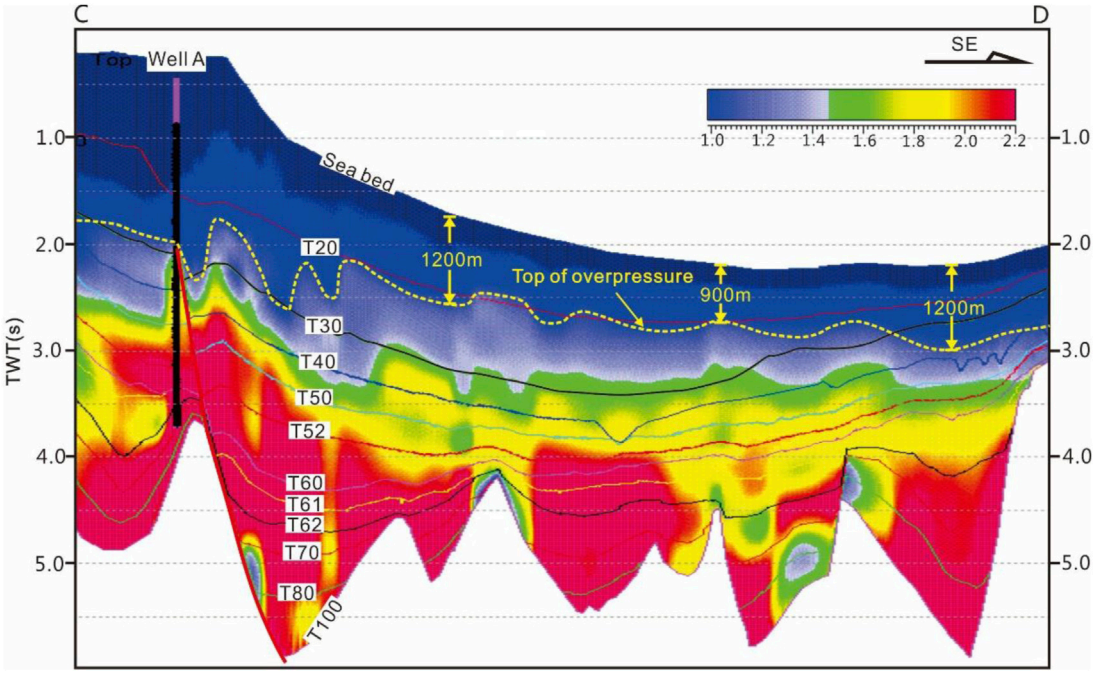

FIGURE 8 | Pressure coefficient profile and interpreted top of overpressure of cross section CD, which shows the position of shallow overpressure in the deep water area of the Qiongdongnan Basin. The cross section location is shown in **Figure 1**.

index (HI) values in Eocene, Oligocene and Miocene are 300 mg/g, 260 mg/g and 204 mg/g, respectively.

RESULTS AND DISCUSSION

Shallow Overpressure Presence in the Deep Water Area

The measured data from DST, P-sonic and resistivity logs are the most reliable indicator for overpressure. **Figure 4** shows that the P-wave sonic, resistivity picked from mudstone and VSP velocity for Well A in the shallow water deviate from the compaction trend and increase or decrease respectively below about 2,300 m. The calculated mud pressure and testing pressure show that overpressure exists below 2,300 m in Well A. The pressure coefficients measured by the drill stem test (DST) are 1.95, and 1.94 at the depth of 4,446 m and 4,475–4,508 m, respectively. **Figure 5** shows that the P-wave sonic and the resistivity for Well B in the deep water deviate from the normal compaction trend and increase or decrease respectively below about 2,550 m. There are no data at the depth of 2,750–3,450 m in **Figure 5B** because the P-wave sonic data at the depth of 2,750–3,450 m has not been measured, but the resistivity log clearly indicates a drop in resistivity (Rt) indicative of overpressure below about 2,550 m. Calculate pressures from mud weight (Mud pressure) and MDT pressures (test pressures) confirm the overpressured zone below about 2,550 m. The pressure coefficient measured by the modular dynamic tester (MDT) is 1.23 at the depth of 3,400 m. This measured pressure coefficient should be less than the true value because the pore-fluid pressure in the mudstones is very difficult to balance and to be directly measured because of their low permeability. Therefore, the normal pressure zone, pressure transition zone and overpressure zone can be identified according to the logs variation.

The water depth in Well A is 189 m and that in Well B is 1,473 m. If the water depth is subtracted from the total depth of Well A and Well B, the top of the overpressure in Well A is about 2,111 m below the sea floor, and that in Well B is about 1,077 m below sea floor. The present depth of the overpressure in the deep water area is shallower than the reported depth in the middle-deep formations of the basin and deeper than the depth reported by Flemings et al. (2008), Binh et al. (2009) and Long et al. (2011) in the Gulf of Mexico. This shows that there is a relatively shallow overpressure in the deep water area of the QDNB.

The top of overpressure for profile C-D can be identified according to the classification of the overpressure, as long as the pressure coefficient is greater than 1.27 (Hunt, 1990) (**Figure 8**). **Figure 4** shows that the top of the overpressure in Well A is at about 2,300 m. The top of the overpressure interpreted in **Figure 8** shows that the value in the Well A area is about 2.0 s, which converts to about 2,300 m using the VSP data from Well A. The comparison shows that there is a good agreement between the predicted top of the overpressure in **Figure 8** and the identified top of the overpressure in **Figure 4**. Secondly, the pressure coefficients from DST of Well A are 1.95, and 1.94 at the depth of 4,446 m and 4,475–4,508 m, respectively, which belong to the Lingshui Fm. The predicted pressure coefficient in the Lingshui Fm. shown in **Figure 8** is about 2.04, there exists a little bias between the predicted pressure

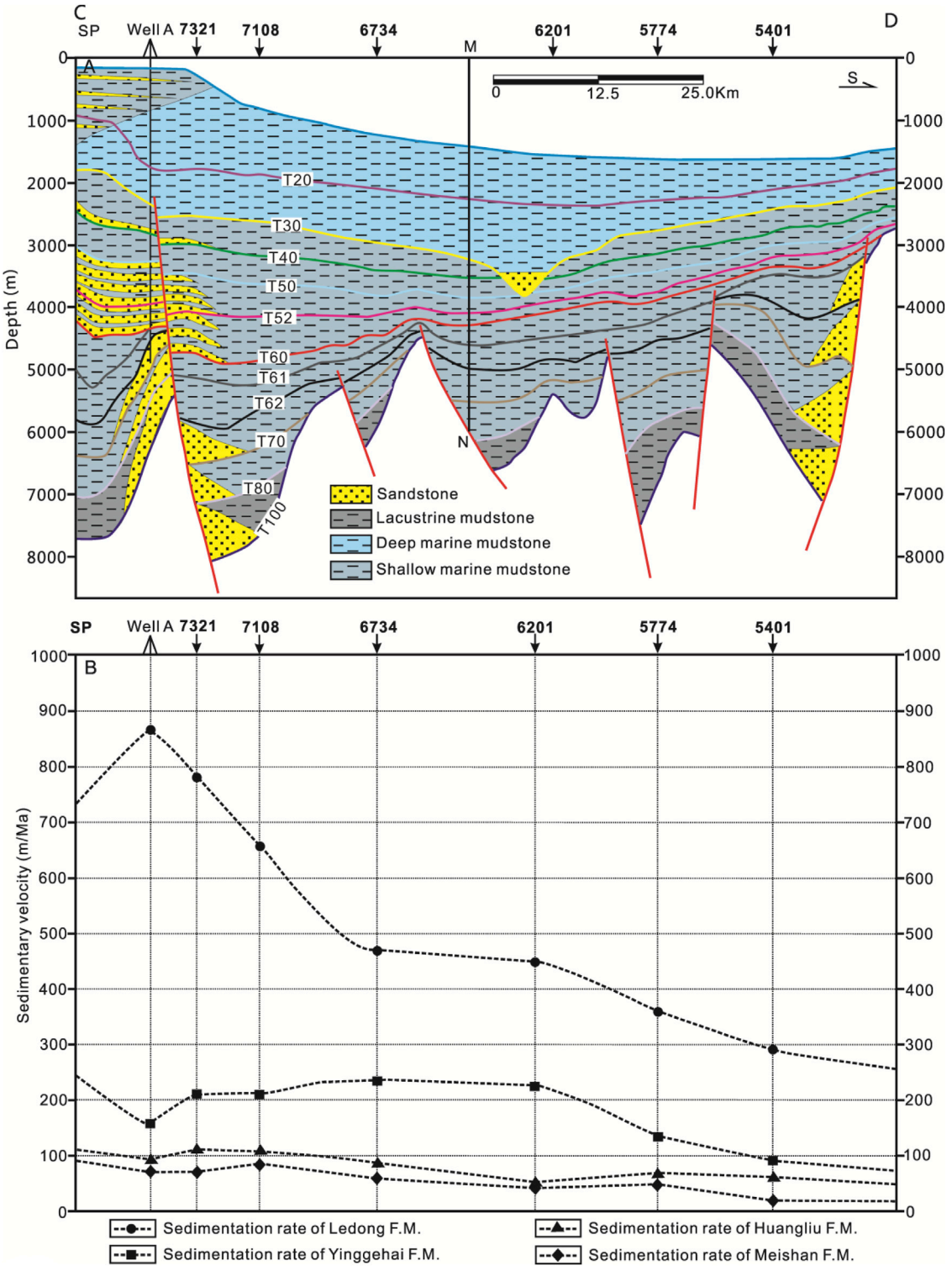

FIGURE 9 | (A) Lithologic cross-section of Profile CD. **(B)** Sedimentation rates of the different formations showing the sedimentation rates of the Ledong and Yinggehai Formations were greater than other Formations. The cross section location is shown in **Figure 1**.

coefficient and the actual test pressure coefficient. This comparison indicates that the pressure coefficient profile shown in **Figure 8** can be used to analyze the overpressure distribution. **Figure 8** shows that the distance from the seafloor to the top of overpressure is greater in the shallow water than that in the deep water. **Figure 9A** shows that there

TABLE 1 | Parameters for 1D modeling.

Name	Base Depth (m)	Strata Thickness (m)	Erosion Thickness (m)	Water Depth (m)	Alignment Lithology
water depth	1,410	1,410		1,410	
Ledong	2,268	858		1,410	Mudstone
Yinggehai	3,253	985		1,047	Mudstone
Huangliu	3,597	344		300	Mudstone
Meishan	3,941	344		100	Mudstone
SY1	4,195	254		70	Mudstone
SY2	4,428	233		40	Mudstone
LS1	4,789	361	100	0	Mudstone
LS2	5,088	299		50	Mudstone
LS3	5,317	229		40	Mudstone
Yacheng	6,033	716		30	Mudstone

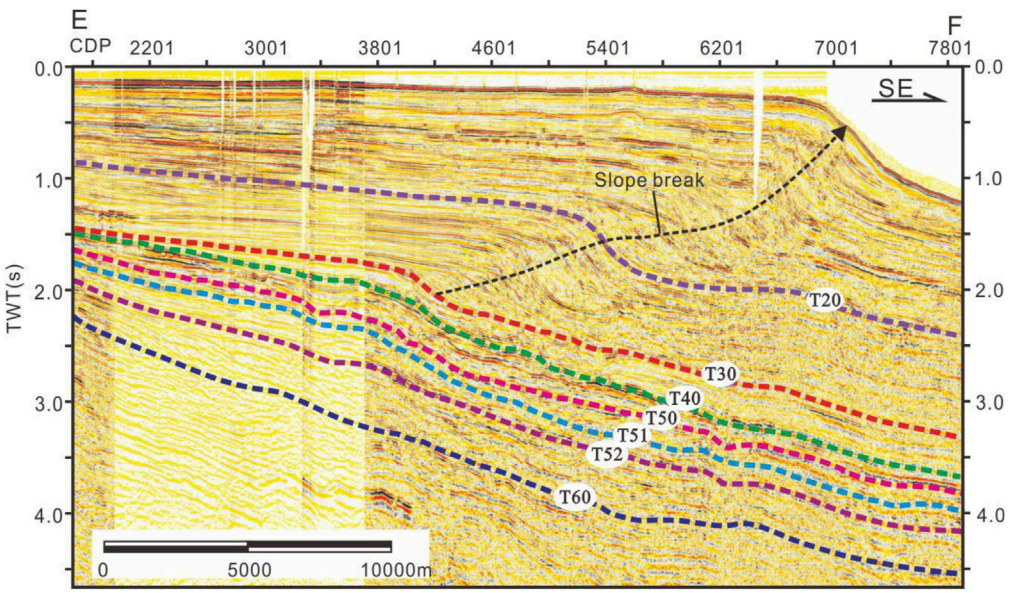

FIGURE 10 | Seismic cross-section showing the position of the prominent slope break that formed during deposition of the Yinggehai and Ledong Formations, in response to a dramatic deeping of seawater around 5.5 Ma. The location of the cross section is shown in **Figure 1**.

are differences in sedimentary facies between the shallow water and deep water. The higher permeability of sediments in shallow water is conducive to pressure relief, and the activation of faults at the edge of the basin can also lead to the reduction of pressure, which may be the reason why the distance from the seafloor to the top of overpressure is greater in the shallow water than that in the deep water. This indicates that shallow overpressure exists in the deep water, where the top of overpressure is about 900–1,200 m into the seafloor. There is a very good agreement between drilling data and seismic data response to the shallow overpressure.

Mechanisms of Shallow Overpressure Generation

As mentioned above, disequilibrium compaction and oil and gas generation are believed to be the primary causes of overpressure in sedimentary basins (Osborne and Swarbrick, 1997; Hua et al., 2021; Li et al., 2021). In an extensional tectonic setting such as the QDNB, tectonic compression is not a probable mechanism for overpressure development (Zhang et al., 2021). Although there exists a possible effect of the horizontal compressive stresses from the components of the clastic wedge weight at the slop on the generation of the shallow overpressure in the zones of the slope or near the base of the slope, this effect only limits the zones of the slope or near the base of the slope. **Figure 1** shows that Well B locates in about 1380 m of water depth right at the plain of the basin indicated by the big space of contours rather than at the slop or base of the slope, where is in the Lingnan uplift formed before 21.0 Ma and covered by the Sanya, Meishan, Huangliu, Yinggehai and Ledong Fms., so disequilibrium compaction is primarily controlled by the overburden pressure rather than the horizontal stress. Secondly, if the horizontal stress act on the

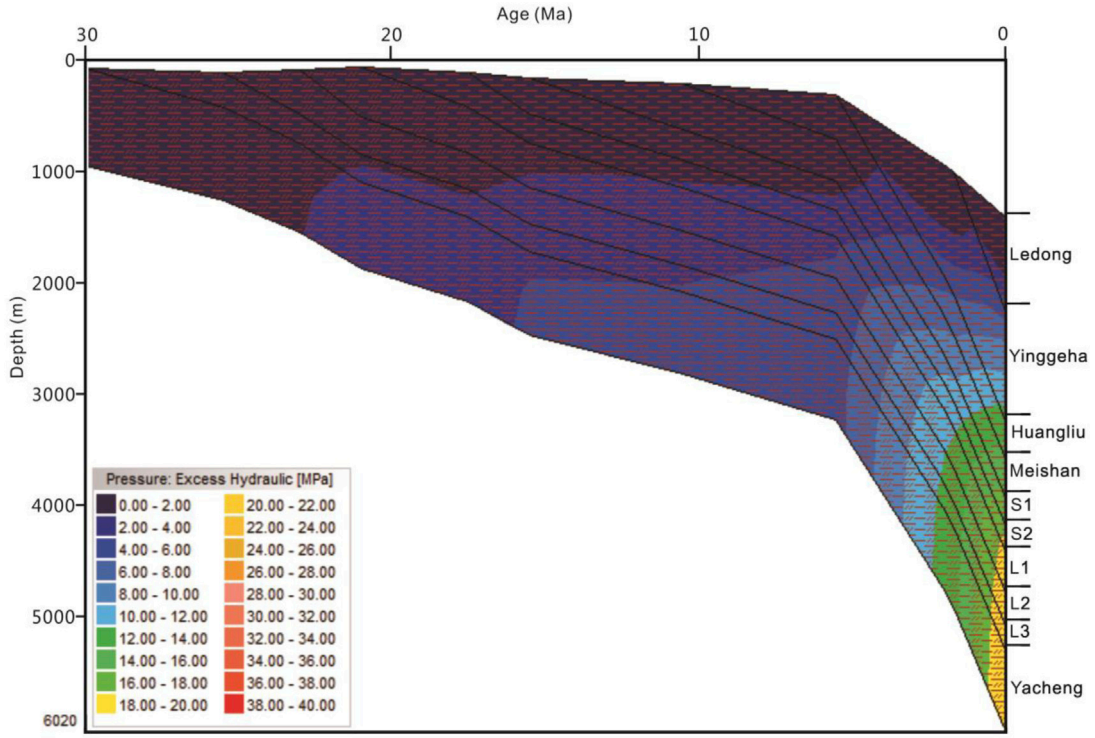

FIGURE 11 | Modelling of the evolution of excess pressure at position MN in **Figure 8**, Based on this model overpressure was generated beginning approximately 5.5 Ma.

formation drilled by well B, it is much less than the overburden pressure. The horizontal stress is one of the components of the weight contributed by the interval of 180–1380 m of the clastic wedge above Well B, if the slop angle is about 10°, then the maximum horizontal stress calculated based on the trigonometric function equals about the weight of 208 m Formation. The overpressure top of Well B is about 1,077 m below sea floor, so the vertical stress is equivalent to the weight of 1077 m Formation. The comparison between the horizontal stress and the overburden pressure shows that maximum stress is still overburdened pressure, therefore, the disequilibrium compaction is controlled by the overburden pressure rather than the horizontal stress. These indicate that the effect of the horizontal compressive stresses from the gravitational load of the clastic wedge on the shallow overpressure can be ignored in the QDNB. The vertical transfer of the basal overpressures is unlikely because of the lack of faulting in the shallow strata. Oil and gas generation is not a likely process for generating shallow overpressure as these rocks are thermally immature. The most probable mechanism is disequilibrium compaction.

The formation age of the shallow overpressure in the deep water parts of the QDNB can be ascertained by basin modeling. The modeling result shows that the excess pressure isoline of 5 MPa lies at the top of the Yinggehai Fm. as shown in **Figure 11**. The modeled pressure coefficient is about 1.2 when the excess pressure is 5 MPa at the depth of 2,268 m. The results of modeling agree with the other indicators of a shallow overpressure in the deep water indicated by Well B and overpressure prediction shown in **Figure 5** and **Figure 8**. The basin modeling (presented in **Figure 11**) suggests that the overpressure formed at about 5.5 Ma, during the deposition of the sediment of the Yinggehai and Ledong Fms.

Rapid deposition of low permeability sediment generates pore fluid overpressure because fluids cannot escape as the sediment compacts (Gordon and Flemings, 1998; Flemings et al., 2008; Wang et al., 2016). In order to ascertain if such a disequilibrium compaction process caused the shallow overpressure in the deep water parts of the QDNB, sedimentation rates were calculated at the same seven observation points where stacking velocities were determined in profile C-D (**Figure 9B** and **Table 2**). **Figure 9B** shows that the sedimentation rates of the Ledong and Yinggehai Fms. were greater than those of the Huangliu and Meishan Fms. and that the sedimentation rate of the Ledong Fm. was far greater than that of the Yinggehai Fm. The sedimentation rate of the Ledong Fm. gradually decreased from a value of 871.7 m/Ma in the shallow area to 288.9 m/Ma in the deep area, whereas the maximum sedimentation rate, 237.6 m/Ma, of the Yinggehai Fm. occurred in the deep water area (**Figure 9B**). The lithologic profile in **Figure 9A** shows that mudstone is the main sedimentary rock in the deep water area, and that few faults are evident above the T60 horizon in the QDNB as shown in **Figure 6**. The shallow overpressure in the QDNB was generated in 5.5 Ma, during this period, there deposited the Yinggehai and Ledong Fms. characterized by high sedimentation rates. These indicate that disequilibrium compaction is the primary cause of the shallow overpressure in the QDNB.

TABLE 2 | Sedimentation rates for the various formations and positions.

Item		Well A	SP7321	SP7108	SP6734	SP6201	SP5774	SP5401
Thickness of Formation (m)	Water depth	189.0	380.0	620.0	1,241.0	1,556.0	1,630.0	1,621.0
	Ledong (Fm)	1,569.0	1,408.0	1,203.0	847.0	820.0	660.0	520.0
	Yinggehai (Fm)	615.0	771.0	771.0	879.0	829.0	503.0	348.0
	Huangliu. (Fm)	464.0	546.0	528.0	464.0	270.0	377.0	370.0
	Meishan (Fm)	427.0	395.0	476.0	386.0	248.0	283.0	192.0
Sedimentation rate (m/Ma)	Ledong (Fm)	871.7	782.2	668.3	470.6	455.6	366.7	288.9
	Yinggehai (Fm)	166.2	208.4	208.4	237.6	224.1	135.9	94.1
	Huangliu (Fm)	92.8	109.2	105.6	92.8	54.0	75.4	74.0
	Meishan (Fm)	85.4	79.0	95.2	77.2	49.6	56.6	38.4

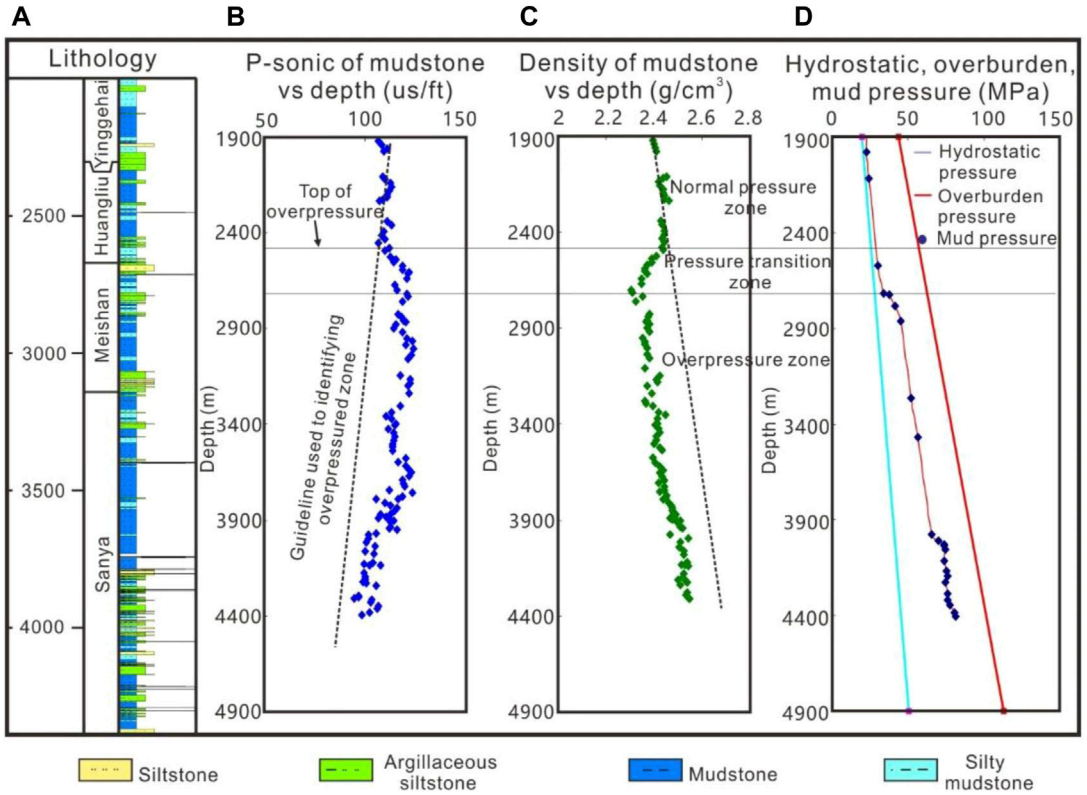

FIGURE 12 | (A) Lithologic profile of Well C **(B)** Pseudo log of sonic P-wave transit times for mudstone. The plot shows the deviation of transit time from the compaction trend below about 2,450 m. **(C)** Plot of log-derived density values for mudstone showing deviation from the compaction trend below about 2,450 m. **(D)** Plot of calculated mud pressures showing a corresponding positive deviation from hydrostatic pressure (overpressure) below about 2,450 m. The decreasing density in the overpressured section of well C indicates that disequilibrium compaction is a primary cause of overpressure in the Qiongdongnan Basin.

Secondly, overpressures generated by disequilibrium compaction are associated with anomalously high porosity (Sayers et al., 2002) and low density compared with normally pressured sediments (Guo et al., 2010). **Figure 12** shows that the decreasing density in the overpressured section of well C indicates that disequilibrium compaction is a primary cause of overpressure in the shallow water parts of the QDNB. Although Well B lies in the deep water area, we believe that the evidence supports our contention that disequilibrium compaction is a primary cause of overpressure in the deep water parts of the QDNB.

CONCLUSION

Through the above analysis, some important conclusions can be drawn.

1) The P-wave sonic and resistivity logs are reliable pressure indicators in the QDNB with all overpressured mudstones having higher P-wave sonic and lower resistivity compared with normally pressured mudstones at a given depth. Thus, the overpressure caused by disequilibrium compaction can be identified by the P-wave sonic and resistivity logs.
2) Pore pressures profiles can be predicted with confidence in the QDNB using the method of "normal compaction trend" based on a calibrated relationship between seismic interval velocities and pressure data from wells.
3) A shallow zone of overpressure is present in the deep water area of the QDNB based on drilling and anomalous seismic interval velocities. The distance between the top of the overpressure and the seabed is 900–1,200 m in the deep water area of the QDNB.
4) Disequilibrium compaction in the deep water is the primary cause of the shallow overpressure in the QDNB, which occurred since about 5.5 Ma.

DATA AVAILABILITY STATEMENT

The original contributions presented in the study are included in the article/Supplementary Material, further inquiries can be directed to the corresponding authors.

AUTHOR CONTRIBUTIONS

JR: Methodology, Investigation, Formal analysis, Writing—Original Draft. LX: Supervision, Funding acquisition, Writing—review and editing. WS: Supervision, Funding acquisition, Conceptualization. WY: Writing—review and editing. RW: Investigation, Formal analysis. YH: Supervision and software. HD: Software.

FUNDING

This work was carried out with support from Key Special for Introduced Talents Team of Southern Marine Science and Engineering Guangdong Laboratory (Guangzhou) [No. GML2019ZD0102].

ACKNOWLEDGMENTS

The authors would like to express their sincere appreciations to Keyu Liu of CSIRO Australia, James Puckette and Mark Tingay of University of Adelaide for their valuable comments and suggestions. Thanks to the editor and reviewers for the suggestions and other assistance for improving this manuscript.

REFERENCES

Abiola, O., and Ayenuro, T. G. (2021). Prediction of Abnormal Pressure from AVO Velocities over "Safety" Field, Onshore Niger Delta, Nigeria. *Petroleum Res.* 6 (1), 26–41. doi:10.1016/j.ptlrs.2020.09.002

Akrout, D., Ahmadi, R., Mercier, E., and Montacer, M. (2021). Present-day Overpressure in Southern Tunisia: Characterization, Possible Causes and Implications for Drilling Operations. *J. Afr. Earth Sci.* 184, 104356. doi:10.1016/j.jafrearsci.2021.104356

Barker, C. (1972). Aquathermal Pressuring: Role of Temperature in Development of Abnormal-Pressure Zones. *AAPG Bull.* 56, 2068–2071. doi:10.1306/819a41b0-16c5-11d7-8645000102c1865d

Berry, F. (1973). High Fluid Potentials in California Coast Ranges and Their Tectonic Significance. *AAPG Bull.* 57, 1219–1249. doi:10.1306/83d90e8a-16c7-11d7-8645000102c1865d

Binh, N. T. T., Tokunaga, T., Nakamura, T., Kozumi, K., Nakajima, M., Kubota, M., et al. (2009). Physical Properties of the Shallow Sediments in Late Pleistocene Formations, Ursa Basin, Gulf of Mexico, and Their Implications for Generation and Preservation of Shallow Overpressures. *Mar. Petroleum Geol.* 26, 474–486. doi:10.1016/j.marpetgeo.2009.01.018

Bradley, J. (1975). Abnormal Formation Pressure. *AAPG Bull.* 59, 957–973. doi:10.1306/83d91efc-16c7-11d7-8645000102c1865d

Bredehoeft, J. D., Wesley, J. B., and Fouch, T. D. (1994). Simulations of the Origin of Fluid-Pressure, Fracture Generation and Movement of Fluids in the Uinta Basin, Utah. *AAPG Bull.* 78, 1729–1747. doi:10.1306/a25ff279-171b-11d7-8645000102c1865d

Carcione, J. M., Helle, H. B., Pham, N. H., and Toverud, T. (2003). Pore Pressure Estimation in Reservoir Rocks from Seismic Reflection Data. *Geophysics* 68, 1569–1579. doi:10.1190/1.1620631

Cobbold, P. R., Mourgues, R., and Boyd, K. (2004). Mechanism of Thin-Skinned Detachment in the Amazon Fan: Assessing the Importance of Fluid Overpressure and Hydrocarbon Generation. *Mar. Petroleum Geol.* 21, 1013–1025. doi:10.1016/j.marpetgeo.2004.05.003

Dasgupta, S., Chatterjee, R., and Mohanty, S. P. (2016). Magnitude, Mechanisms, and Prediction of Abnormal Pore Pressure Using Well Data in the Krishna-Godavari Basin, East Coast of India. *Bulletin* 100, 1833–1855. doi:10.1306/05131615170

Dickinson, G. (1953). Geological Aspects of Abnormal Reservoir Pressures in Gulf Coast Louisiana. *AAPG Bull.* 37, 410–432. doi:10.1306/5ceadc6b-16bb-11d7-8645000102c1865d

Dugan, B., and Flemings, P. B. (2002). Fluid Flow and Stability of the US Continental Slope Offshore New Jersey from the Pleistocene to the Present. *Geofluids* 2, 137–146. doi:10.1046/j.1468-8123.2002.00032.x

Dutta, N. C. (2002). Geopressure Prediction Using Seismic Data: Current Status and the Road Ahead. *Geophysics* 67 (6), 2012–2041. doi:10.1190/1.1527101

Eaton, B. A. (1972). Graphical Method Predicts Geopressure Worldwide. *World oil.* 186, 51–56.

Flemings, P., Long, H., Dugan, B., Germaine, J., John, C., Behrmann, J., et al. (2008). IODP Expedition 308 ScientistsPore Pressure Penetrometers Document High Overpressure Near the Seafloor where Multiple Submarine Landslides Have Occurred on the Continental Slope, Offshore Louisiana, Gulf of Mexico. *Earth Planet. Sci. Lett.* 269, 309–325. doi:10.1016/j.epsl.2007.12.005

Gordon, D. S., and Flemings, P. B. (1998). Generation of Overpressure and Compaction-Driven Fluid Flow in a Plio-Pleistocene Growth-Faulted Basin, Eugene Island 330, Offshore Louisiana. *Basin Res.* 10, 177–196. doi:10.1046/j.1365-2117.1998.00052.x

Guo, X. W., He, S., Liu, K. Y., Song, G. Q., Wang, X. J., and Shi, Z. S. (2010). Oil Generation as the Dominant Overpressure Mechanism in the Cenozoic Dongying Depression, Bohai Bay Basin, China. *AAPG Bull.* 94, 1859–1881. doi:10.1306/05191009179

Hao, F., Li, S., Dong, W., Hu, Z., and Huang, B. (1998). Abnormal Organic-Matter Maturation in the Yinggehai Basin, South China Sea: Implications for Hydrocarbon Expulsion and Fluid Migration from Overpressured Systems. *J. Pet. Geol.* 21 (4), 427–444. doi:10.1111/j.1747-5457.1998.tb00794.x

Hao, F., Li, S. T., Gong, Z. S., and Yang, J. M. (2002). Mechanism of Diapirism and Episodic Fluid Injections in the Yinggehai Basin. *Sci. China Ser. D – Earth Sci.* 45 (2), 151–159. doi:10.1360/02yd9017

Hao, F., Sun, Y. C., Li, S. T., and Zhang, Q. M. (1995). Overpressure Retardation of Organic-Matter Maturation and Petroleum Generation–A Case Study from the Yinggehai and Qiongdongnan Basins, South China Sea. *AAPG Bull.* 79 (4), 551–562. doi:10.1306/8d2b158e-171e-11d7-8645000102c1865d

Hedberg, H. H. (1974). Relation of Methane Generation to Undercompacted Shales, Shale Diapirs, and Mud Volcanoes. *AAPG Bull.* 58, 661–673. doi:10.1306/83d91466-16c7-11d7-8645000102c1865d

Hua, Y., Guo, X., Tao, Z., He, S., Dong, T., Han, Y., et al. (2021). Mechanisms for Overpressure Generation in the Bonan Sag of Zhanhua Depression, Bohai Bay Basin, China. *Mar. Petroleum Geol.* 128, 105032. doi:10.1016/j.marpetgeo.2021.105032

Hunt, J. M. (1990). Generation and Migration of Petroleum from Abnormally Pressured Fluid Compartments. *AAPG Bull.* 74, 1–12. doi:10.1306/0c9b21eb-1710-11d7-8645000102c1865d

Kan, T. K., and Swan, H. W. (2001). Geopressure Prediction from Automatically-derived Seismic Velocities. *Geophysics* 66, 1937–1946. doi:10.1190/1.1487135

Law, B., and Dickinson, W. (1985). Conceptual Model for Origin of Abnormally Pressured Gas Accumulations in Low-Permeability Reservoirs. *AAPG Bull.* 69, 1295–1304. doi:10.1306/ad462bd7-16f7-11d7-8645000102c1865d

Li, C., Luo, X., Zhang, L., Fan, C., Xu, C., Liu, A., et al. (2022). New Understanding of Overpressure Responses and Pore Pressure Prediction: Insights from the Effect of Clay Mineral Transformations on Mudstone Compaction. *Eng. Geol.* 297, 106493. doi:10.1016/j.enggeo.2021.106493

Li, C., Zhang, L., Luo, X., LeiYu, Y. L., Yu, L., Cheng, M., et al. (2021). Overpressure Generation by Disequilibrium Compaction or Hydrocarbon Generation in the Paleocene Shahejie Formation in the Chezhen Depression: Insights from Logging Responses and Basin Modeling. *Mar. Petroleum Geol.* 133, 105258. doi:10.1016/j.marpetgeo.2021.105258

Li, S., Yuan, Y., Sun, W., Sun, D., and Jin, Z. (2016). Formation and Destruction Mechanism as Well as Major Controlling Factors of the Silurian Shale Gas Overpressure in the Sichuan Basin, China. *J. Nat. Gas Geoscience* 1 (4), 287–294. doi:10.1016/j.jnggs.2016.09.002

Liu, H., Yuan, F., Jiang, Y., Zhao, M., Chen, K., Guo, Z., et al. (2019). Mechanisms for Overpressure Generated by the Undercompaction of Paleogene Strata in the Baxian Depression of Bohai Bay Basin, China. *Mar. Petroleum Geol.* 99, 337–346. doi:10.1016/j.marpetgeo.2018.10.001

Liu, J., Liu, T., Liu, H., He, L., and Zheng, L. (2021). Overpressure Caused by Hydrocarbon Generation in the Organic-Rich Shales of the Ordos Basin. *Mar. Petroleum Geol.* 134, 105349. doi:10.1016/j.marpetgeo.2021.105349

Long, H., Flemings, P. B., Germaine, J. T., and Saffer, D. M. (2011). Consolidation and Overpressure Near the Seafloor in the Ursa Basin, Deepwater Gulf of Mexico. *Earth Planet. Sci. Lett.* 305, 11–20. doi:10.1016/j.epsl.2011.02.007

Luo, X. R., Liu, L. J., and Li, X. Y. (2006). Overpressure Distribution and Pressuring Mechanism on the Southern Margin of the Junggar Basin. *Northwest. China. Chin. Sci. Bull.* 51 (19), 2383–2390. doi:10.1007/s11434-006-2126-9

Luo, X. R. (2004). Quantitative Analysis on Overpressuring Mechanism Resulted from Tectonic Stress. *Chin. J. Geophys. – Chin. Ed.* 47 (6), 1086–1093. doi:10.1002/cjg2.608

Luo, X. R., and Vasseur, G. (1996). Geopressuring Mechanism of Organic Matter Cracking: Numerical Modeling. *AAPG Bull.* 80 (6), 856–874. doi:10.1306/64ED88EA-1724-11D7-8645000102C1865D

Luo, X., and Vasseur, G. (1992). Contributions of Compaction and Aquathermal Pressuring to Geopressure and the Influence of Environmental Conditions. *AAPG Bull.* 76, 1550–1559. doi:10.1306/bdff8a42-1718-11d7-8645000102c1865d

Ma, Y. S., Guo, T. L., Zhao, X. F., and Cai, X. Y. (2008). The Formation Mechanism of High-Quality Dolomite Reservoir in the Deep of Puguang Gas Field. *Sci. China Ser. D Earth Sci.* 51, 53–64. doi:10.1007/s11430-008-5008-y

Magara, K. (1975). Reevaluation of Montmorillonite Dehydration as Cause of Abnormal Pressure and Hydrocarbon Migration. *AAPG Bull.* 59, 292–302. doi:10.1306/83d91c7c-16c7-11d7-8645000102c1865d

Mondol, N. H., Bjørlykke, K., Jahren, J., and Høeg, K. (2007). Experimental Mechanical Compaction of Clay Mineral Aggregates-Changes in Physical Properties of Mudstones during Burial. *Mar. Petroleum Geol.* 24, 289–311. doi:10.1016/j.marpetgeo.2007.03.006

Osborne, M. J., and Swarbrick, R. E. (1997). Mechanisms for Generating Overpressure in Sedimentary Basins: a Re-evaluation. *AAPG Bull.* 81, 1023–1041. doi:10.1306/522b49c9-1727-11d7-8645000102c1865d

Parsons, B., and Sclater, J. G. (1977). An Analysis of the Variation of Ocean Floor Bathymetry and Heat Flow with Age. *J. Geophys. Res.* 82, 803–827. doi:10.1029/jb082i005p00803

Pennebaker, E. S. (1968). Seismic Data Indicate Depth, Magnitude of Abnormal Pressure. *World oil.* 166, 73–78.

Plumley, W. J. (1980). Abnormally High Fluid Pressure: Survey of Some Basic Principles. *AAPG Bull.* 64, 414–430. doi:10.1306/2f919409-16ce-11d7-8645000102c1865d

Powers, M. C. (1967). Fluid-release Mechanisms in Compacting Marine Mudrocks and Their Importance in Oil Exploration. *AAPG Bull.* 51, 1240–1254. doi:10.1306/5d25c137-16c1-11d7-8645000102c1865d

Prankada, M., Yadav, K., and Sircar, A. (2021). Analysis of Wellbore Stability by Pore Pressure Prediction Using Seismic Velocity. *Energy Geosci.* 2 (4), 219–228. doi:10.1016/j.engeos.2021.06.005

Radwan, A. E., Abudeif, A. M., Attia, M. M., ElkhawagaAbdelghanya, M. A. W. K., Abdelghany, W. K., and Kasem, A. A. (2020). Geopressure Evaluation Using Integrated Basin Modelling, Well-Logging and Reservoir Data Analysis in the Northern Part of the Badri Oil Field, Gulf of Suez, Egypt. *J. Afr. Earth Sci.* 162, 103743. doi:10.1016/j.jafrearsci.2019.103743

Sayers, C. M., Johnson, G. M., and Denyer, G. (2002). Predrill Pore-pressure Prediction Using Seismic Data. *Geophysics* 67, 1286–1292. doi:10.1190/1.1500391

Schmidt, G. W. (1973). Interstitial Water Composition and Geochemistry of Deep Gulf Coast Shales and Sandstones. *AAPG Bull.* 57, 321–337. doi:10.1306/819a426e-16c5-11d7-8645000102c1865d

Sharp, J. M. (1983). Permeability Controls on Aquathermal Pressuring. *AAPG Bull.* 67, 2057–2061. doi:10.1306/ad4608cd-16f7-11d7-8645000102c1865d

Shi, W., Xie, Y., Wang, Z., Li, X., and Tong, C. (2013). Characteristics of Overpressure Distribution and its Implication for Hydrocarbon Exploration in the Qiongdongnan Basin. *J. Asian Earth Sci.* 66 (apr.8), 150–165. doi:10.1016/j.jseaes.2012.12.037

Shi, X. B., Qiu, X. L., and Xia, K. Y. (2003). Heat Flow Characteristics and its Tectonic Significance of South China Sea. *J. Trop. Oceanogr.* 22 (2), 63–73. (in Chinese with English abstract). doi:10.1016/s1367-9120(03)00059-2

Singha, D. K., and Chatterjee, R. (2014). Detection of Overpressure Zones and a Statistical Model for Pore Pressure Estimation from Well Logs in the Krishna-Godavari Basin, India. *Geochem. Geophys. Geosyst.* 15, 1009–1020. doi:10.1002/2013gc005162

Skempton, A. W. (1970). Consolidation of Clays by Gravitational Compaction. *Q. J. Geol. Soc.* 125, 373–411. doi:10.1144/gsjgs.125.1.0373

Spencer, C. (1987). Hydrocarbon Generation as a Mechanism for Overpressure in Rocky Mountain Region. *AAPG Bull.* 71, 368–388. doi:10.1306/94886eb6-1704-11d7-8645000102c1865d

Tang, J., and Lerche, I. (1993). Geopressure Evolution, Hydrocarbon Generation and Migration in the Beaufort-Mackenzie Basin, Canada: Results from Two-Dimensional Quantitative Modelling. *Mar. Petroleum Geol.* 10, 373–393. doi:10.1016/0264-8172(93)90082-4

Timko, D. J., and Fertl, W. H. (1971). Relationship between Hydrocarbon Accumulation and Geopressure and its Economic Significance. *J. Petroleum Technol.* 23, 923–933. doi:10.2118/2990-pa

Tingay, M. R. P., Hillis, R. R., Swarbrick, R. E., Morley, C. K., and Damit, A. R. (2009). Origin of Overpressure and Pore-Pressure Prediction in the Baram Province, Brunei. *Bulletin* 93, 51–74. doi:10.1306/08080808016

Tingay, M. R. P., Hillis, R. R., Swarbrick, R. E., Morley, C. K., and Damit, A. R. (2007). Vertically Transferred' Overpressures in Brunei: Evidence for a New Mechanism for the Formation of High-Magnitude Overpressure. *Geology* 35, 1023–1026. doi:10.1130/G23906A.1

Tingay, M. R. P., Morley, C. K., Laird, A., Limpornpipat, O., Krisadasima, K., Pabchanda, S., et al. (2013). Evidence for Overpressure Generation by Kerogen-To-Gas Maturation in the Northern Malay Basin. *Bulletin* 97, 639–672. doi:10.1306/09041212032

Wang, X., He, S., Wei, A., Liu, Q., and Liu, C. (2016). Typical Disequilibrium Compaction Caused Overpressure of Paleocene Dongying Formation in Northwest Liaodongwan Depression, Bohai Bay Basin, China. *J. Petroleum Sci. Eng.* 147, 726–734. doi:10.1016/j.petrol.2016.09.014

Wang, X. J., Wu, S. G., Dong, D. D., Gong, Y. H., and Chai, C. (2008). Characteristics of Gas Chimney and its Relationship to Gas Hydrate in the Qiongdongnan Basin. *Mar. Geol. Quat. Geol.* 28 (3), 103–108. (in Chinese with English abstract). doi:10.16562/j.cnki.0256-1492.2008.03.021

Wang, R., Shi, W. Z., Xie, X. Y., Zhang, W., Qin, S., Liu, K., et al. (2020). Clay Mineral Content, Type, and Their Effects on Pore Throat Structure and Reservoir Properties: Insight From the Permian Tight Sandstones in the Hangjinqi Area, North Ordos Basin, China. *Mar. Petroleum Geol.* 115, 104281. doi:10.1016/j.marpetgeo.2020.104281

Wang, R., Liu, K., Shi, W. Z., Qin, S., Zhang, W., Qi, R., et al. (2022). Reservoir Densification, Pressure Evolution, and Natural Gas Accumulation in the Upper Paleozoic Tight Sandstones in the North Ordos Basin, China. *Energies* 15, 1990. doi:10.3390/en15061990

Wu, S. G., Sun, Q. L., Wu, T. Y., Yuan, S. Q., Ma, Y. B., and Yao, G. S. (2009). Polygonal Fault and Oil-Gas Accumulation in Deep-Water Area of Qiongdongnan Basin. *Acta Pet. Sin. A* 30 (1), 22–26. (in Chinese with English abstract). doi:10.7623/syxb200901005

Xu, Q., Shi, W., Xie, Y., Wang, Z., Li, X., and Tong, C. (2017). Identification of Low-Overpressure Interval and its Implication to Hydrocarbon Migration: Case Study in the Yanan Sag of the Qiongdongnan Basin, South China Sea. *Plos One* 12 (9), e0183676. doi:10.1371/journal.pone.0183676

Yuan, Y., Zhu, W., Mi, L., Zhang, G., Hu, S., and He, L. (2009). "Uniform Geothermal Gradient" and Heat Flow in the Qiongdongnan and Pearl River Mouth Basins of the South China Sea. *Mar. Petroleum Geol.* 26, 1152–1162. doi:10.1016/j.marpetgeo.2008.08.008

Yuan, H. M., Wang, Y., and Wang, X. C. (2021). Seismic Methods for Exploration and Exploitation of Gas Hydrate. *J. Earth Sci.* 32 (4), 839–849. doi:10.1007/s12583-021-1502-3

Zhang, F., Lu, X., Botterill, S., Gingras, M., Zhuo, Q., and Zhong, H. (2021). Horizontal Tectonic Stress as a Cause of Overpressure in the Southern Margin of the Junggar Basin, Northwest China. *J. Petroleum Sci. Eng.* 205, 108861. doi:10.1016/j.petrol.2021.108861

Zhang, J. H., Lin, H. L., and Wang, K. Z. (2015). Centrifuge Modeling and Analysis of Submarine Landslides Triggered by Elevated Pore Pressure. *Ocean. Eng.* 109, 419–429. doi:10.1016/j.oceaneng.2015.09.020

Zhang, Y. Q., and Liu, L. (2021). Insights into the Formation Mechanism of Low Water Saturation in Longmaxi Shale in the Jiaoshiba Area, Eastern Sichuan Basin. *J. Earth Sci.* 32 (4), 863–871. doi:10.1007/s12583-020-1353-3

Zhu, W. L. (2007). *Geological Characteristics of Nature Gas Reservoir in Northern Margin Basin of South China Sea*. Beijing: Petroleum Press, 44.

Zou, Y.-R., and Peng, P. a. (2001). Overpressure Retardation of Organic-Matter Maturation: a Kinetic Model and its Application. *Mar. Petroleum Geol.* 18, 707–713. doi:10.1016/s0264-8172(01)00026-5

Zuo, T. N., He, Y. L., Shi, W. Z., Liang, J. Q., Xu, L. T., et al. (2022). Natural Gas Migration Pathways and Their Influence on Gas Hydrate Enrichment in the Qiongdongnan Basin, South China Sea. *Geofluids* 2022, 19. doi:10.1155/2022/1954931

Conflict of Interest: The authors declare that the research was conducted in the absence of any commercial or financial relationships that could be construed as a potential conflict of interest.

Publisher's Note: All claims expressed in this article are solely those of the authors and do not necessarily represent those of their affiliated organizations, or those of the publisher, the editors and the reviewers. Any product that may be evaluated in this article, or claim that may be made by its manufacturer, is not guaranteed or endorsed by the publisher.

frontiers | Frontiers in Earth Science

TYPE Original Research
PUBLISHED 26 July 2022
DOI 10.3389/feart.2022.942895

OPEN ACCESS

EDITED BY
Jinan Guan,
Guangzhou Institute of Energy Conversion (CAS), China

REVIEWED BY
Peiqiang Zhao,
China University of Petroleum, China
Xufei Hu,
China University of Petroleum, China
Zhenyuan Yin,
Tsinghua University, China

*CORRESPONDENCE
Donghui Xing,
xingdh126@126.com

SPECIALTY SECTION
This article was submitted to Sedimentology, Stratigraphy and Diagenesis, a section of the journal Frontiers in Earth Science

RECEIVED 13 May 2022
ACCEPTED 29 June 2022
PUBLISHED 26 July 2022

CITATION
Xing D, Fan Y, Lu H, Lu C, Zhang P, Li H and Ding Y (2022), A combined method for gas-bearing layer identification in a complex sandstone reservoir. *Front. Earth Sci.* 10:942895. doi: 10.3389/feart.2022.942895

A combined method for gas-bearing layer identification in a complex sandstone reservoir

Donghui Xing[1,2,3]*, Yiren Fan[4], Hongfeng Lu[1,2,3], Cheng Lu[5], Peng Zhang[6], Hui Li[7] and Yi Ding[7]

[1]Guangzhou Marine Geological Survey, China Geological Survey, Guangzhou, China, [2]Southern Marine Science and Engineering Guangdong Laboratory (Guangzhou), Guangzhou, China, [3]National Engineering Research Center of Gas Hydrate Exploration and Development, Guangzhou, China, [4]School of Geosciences, China University of Petroleum (East China), Qingdao, China, [5]Center of Oil & Natural Gas Resource Exploration, China Geological Survey, Beijing, China, [6]The First Natural Gas Plant, Changqing Oilfield Company, CNPC, Xi`an, China, [7]Explanation and Development Research Institute, PetroChina Huabei Oilfield Company, Renqiu, China

Langgu Depression is a mature oil and gas exploration area with complicated lithological and physical properties. The varying formation fluid, low-resistivity hydrocarbon-bearing reservoirs, and non-uniform logging series greatly increase the difficulty of gas reservoir identification. The Monte Carlo method is employed to simulate the neutron–gamma logging responses to gas saturation and the influential factors. According to the result, a new gas identification chart eliminating the influence of porosity and formation water salinity is proposed to identify gas reservoirs in the old wells. At the same time, a fluid factor extracted from array acoustic logging and core measurement data is sensitive to the development of gas-bearing layers and useful for the identification of gas reservoirs in the new wells with array acoustic logging. The field examples show that the new combined method greatly improves the ability to identify gas-bearing layers and works well in old well reexamination and new well interpretation.

KEYWORDS

well logging, gas reservoir identification, neutron–gamma logging, array acoustic logging, Biot–Gassmann function

1 Introduction

Langgu Depression is a mature oil and gas exploration area located in the Bohai Bay Basin, China. As a typical complex reservoir involving fault blocks, it is one of the main gas-bearing depressions in the North China Oilfield. With sediments transported from multiple sources, its sedimentary facies zones changed rapidly, and the glutenite migrated drastically in both vertical and horizontal directions, resulting in high anisotropy. Due to the development of the fault blocks, its structure and the relationship between water and oil are very complicated, and the logging response characteristics of different reservoirs are indistinguishable. All of these factors make it hard to determine the development of gas reservoirs correctly (Song et al., 2006; Liu et al., 2012; Zhou et al., 2013).

The identification of gas reservoirs is one of the most important and challenging tasks of formation evaluation, especially in heterogeneous formations with complex minerals, detrital clays, and varying salinity of formation fluid. In spite of this, quite a few achievements have been made in the research on gas reservoirs. Moreover, a great number of methods for identifying gas-bearing layers have been proposed based on the conventional and new logging techniques. These methods include overlapping or cross-plot of log curves (Krief et al., 1990; Brie et al., 1995; Freedman et al., 1998), reservoir reconstruction through the inversion of logging curves (Zhang et al., 2009; Tan et al., 2013), quantitative determination of gas saturation and direct hydrocarbon indicators (DHI) based on elastic and pore space modulus (Hedlin, 2000; Dillon et al., 2003), and selection of parameters sensitive to gas-bearing reservoirs (Goodway et al., 1997; Sun et al., 2000; Xu et al., 2014; Fan et al., 2015). With the continuous development of information processing technology, a number of mathematical methods and intelligent algorithms, including wavelet transform, fuzzy cluster analysis, neural network, and grey modeling, have been widely used in fluid identification (Shi, 2008; Shi et al., 2016; Azudin et al., 2018; Zhang et al., 2018; Zhao et al., 2018). These gas identification methods have achieved good results in practice, and each method has the corresponding suitable formation conditions. In view of the characteristics of Langgu Depression, a gas identification method that can be used under the local formation and logging conditions is urgently needed.

In this study, based on the response characteristics for gas-bearing reservoirs in different logging series, a new gas identification chart is presented to improve the applicability of neutron–gamma logging in gas identification in the old wells. At the same time, an array acoustic logging fluid factor sensitive to the development of gas layer is introduced to identify gas-bearing reservoirs in the new wells where the array acoustic logging technique is widely used.

2 Basic characteristics and exploration status of Langgu Depression

Mainly developed in middle segment of the Shahejie Formation, Langgu Depression is a porous sandstone reservoir with complex lithology and pore structure. Laboratory tests of 90 rock core samples extracted from the field show that the average value of porosity and permeability is 27.4% and 1220 mD, respectively (Figure 1). Previous studies show that the distribution of low-resistivity oil and gas zone, controlled by structure and sedimentation, is regular and random at the same time. In this mature field, different well logging methods are used at different stages of exploration and development. Some wells drilled in the early period of exploration only have acoustic and neutron–gamma logging curves, while in newer wells completed in recent years, the latest logging technologies, such as array acoustic, NMR, and electrical imaging, are used.

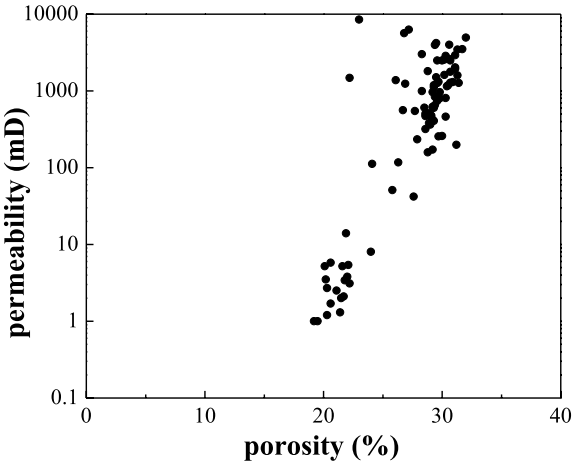

FIGURE 1
Porosity and permeability of 90 cores extracted from Langgu Depression.

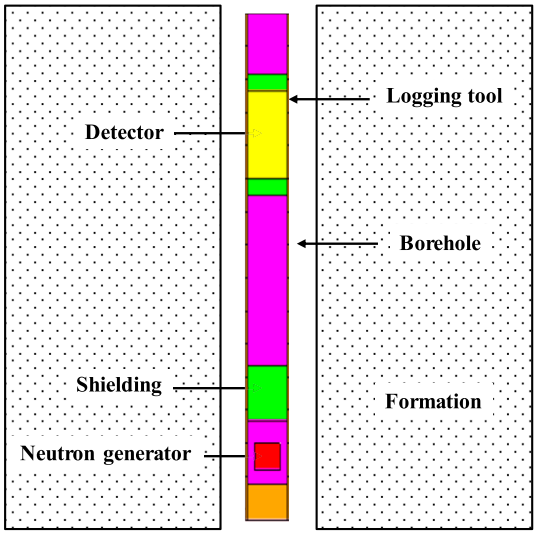

FIGURE 2
MCNP simulation model.

These logging methods have achieved certain effects in the identification of gas-bearing reservoirs, but due to high content of shale and calcium carbonate, the effective porosity and the response of well logging curves to gas decrease greatly. In addition, the vertical distributions of formation fluid chemical and dynamical properties change radically, with formation fluid salinity varying from 1,000 ppm to more than 20,000 ppm. The complex and variable formation fluid characteristics and mud

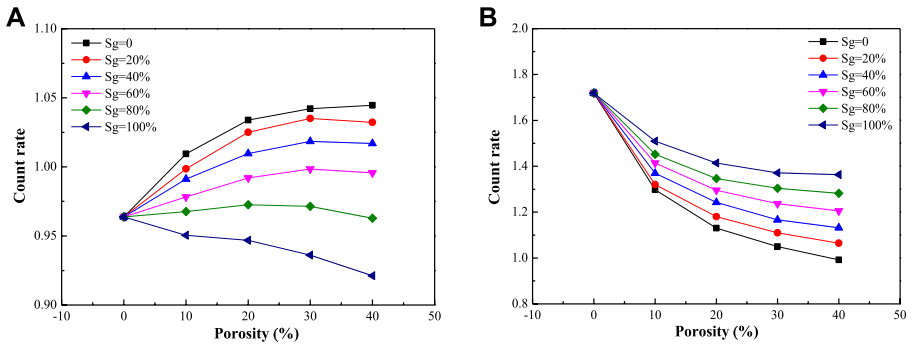

FIGURE 3
Relationship between neutron capture gamma-ray count rate and porosity at various levels of gas saturation. **(A)** Near detector. **(B)** Far detector.

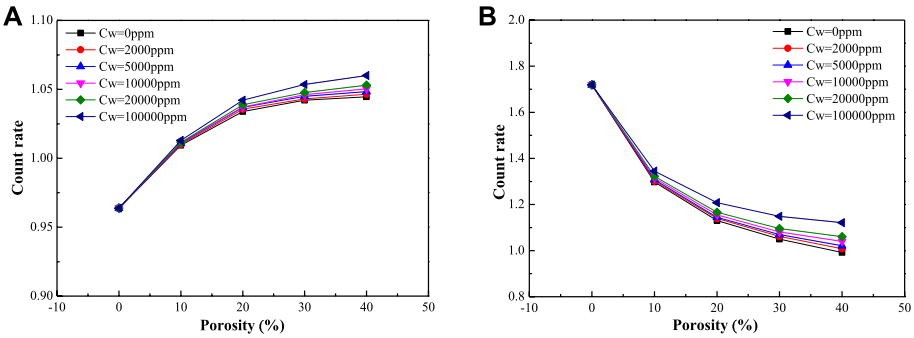

FIGURE 4
Relationship between neutron capture gamma-ray count rate and porosity at different levels of formation fluid salinity. **(A)** Near detector. **(B)** Far detector.

invasion make it difficult to identify the low-resistivity gas layers using resistivity logging. Furthermore, the non-uniform combinations of logging methods used at different stages of exploration and development also increase the difficulty of gas reservoir identification both in old well reexamination and in new well interpretation.

3 Gas layers identification based on neutron–gamma logging

Neutron–gamma logging is often used to identify gas layers because the count rate is sensitive to the presence of gas reservoirs. However, the count rate is greatly affected by two factors, namely, porosity and chloride ion content. The neutron–gamma count rate varies with reservoir porosity, and chlorine, which has a larger capture cross-section than water and gas, may cause the neutron–gamma count rate to increase in reservoirs with high-salinity formation fluid. These factors make it more difficult to determine the development of gas reservoirs with neutron–gamma logging.

To address the aforementioned problems, the response of neutron–gamma logging to gas saturation and the influential factors were studied using the Monte Carlo simulation. Based on the simulation results, a new gas identification chart considering the effects of porosity and formation fluid salinity was developed to improve the ability to identify gas reservoirs, especially in the old wells with very limited logging curves.

3.1 Monte Carlo simulation

3.1.1 Computational model

As an advanced simulation method, the Monte Carlo method can be used to simulate the transport process of continuous energy particles, such as neutrons, photons, and electrons, in arbitrarily shaped media by establishing the corresponding calculation models. Due to its advantages including simple

TABLE 1 Results of the MC simulation with far detector.

C_W/ppm Φ/%	0	2000	5000	10000	20000	100000
0	1.72	1.72	1.72	1.72	1.72	1.72
10	1.30	1.30	1.31	1.31	1.32	1.35
20	1.13	1.14	1.14	1.15	1.17	1.21
30	1.05	1.06	1.07	1.08	1.10	1.16
40	0.99	1.01	1.02	1.04	1.06	1.14

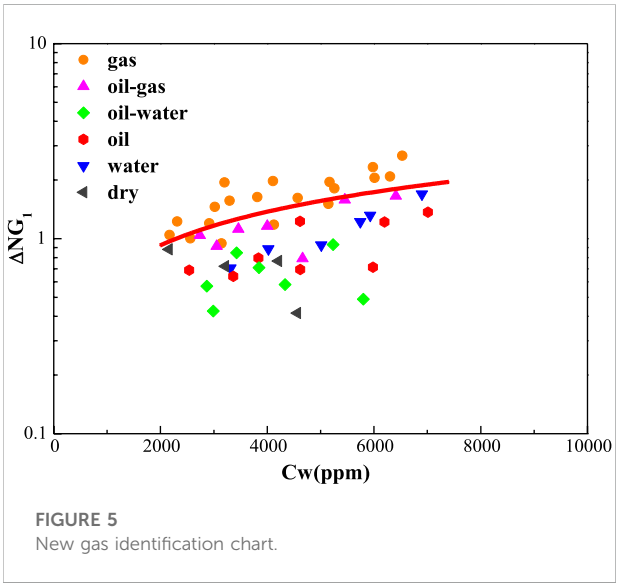

FIGURE 5
New gas identification chart.

structure and strong adaptability, it is widely used in nuclear industry, medicine, and other fields (Briesmeister, 2000). In the area of nuclear logging, the Monte Carlo method is widely used to simulate the attenuation of neutrons in different media and determine the efficiency and response of detectors, playing an important role in the theoretical and practical research on nuclear logging (Zhang and Liu, 2014).

In this study, the Monte Carlo method is employed to simulate the transport process of neutrons in various formations, especially in gas reservoirs, and to study the relationship between the gamma-ray count rate and formation conditions. The simulation model is built based on the Monte Carlo N-Particle Transport Code (MCNP) with the specifications given below.

The borehole (20 cm in diameter) includes a casing and a 3-cm–thick cement sheath, and is filled with fresh water. The formation is filled with formation water and 0.2 g/cc CH_4. The radius is set to 10–70 cm and height to 140 cm. Two detectors are provided for simulation. The distance between the neutron source and the near detector is 30 cm, and the distance between the neutron source and the far detector is 60 cm (Figure 2).

3.1.2 Logging response characteristics

3.1.2.1 The effect of gas saturation on gamma-ray count rate

In the aforementioned simulation model, the formation is a gas-saturated sandstone formation filled with water. When porosity is 0%, 10%, 20%, 30%, and 40%, the level of gas saturation is set to 100%, 80%, 60%, 40%, 20%, and 0% to simulate the neutron capture gamma-ray count rate. The relationship between neutron capture gamma-ray count rate and porosity at different levels of gas saturation is analyzed. The results are shown in Figure 3.

The curves in Figure 3 show that the neutron capture gamma-ray count rate measured by the far detector increases almost linearly with the increase in gas saturation, while the gamma-ray count rate measured by the near detector decreases almost linearly with the increase in gas saturation.

3.1.2.2 The effect of porosity and formation fluid salinity on gamma-ray count rate

The same simulation model with water-saturated sandstone formation is used. When porosity is 0%, 10%, 20%, 30%, and 40%, formation fluid salinity is set to 0, 2,000, 5,000, 10,000, 20,000, and 100,000 ppm, respectively. The relationship between neutron capture gamma-ray count rate and porosity at different levels of formation fluid salinity is analyzed based on the simulation. The results are shown in Figure 4 and Table 1.

As shown in Figure 4, the neutron capture gamma-ray count rate measured by the far detector decreases with the increase in hydrogen index (porosity), while the gamma-ray count rate measured by the near detector increases with the increase in hydrogen index. The neutron capture gamma-ray count rates measured by both the near and the far detectors increase almost linearly with the increase in formation fluid salinity. The data in Table 1 also indicate that in addition to hydrogen index (porosity), formation water salinity is also an important factor affecting the neutron capture gamma-ray count rate. This is because chlorine, which has a larger capture cross-section than water and gas, can result in higher neutron–gamma count rates in reservoirs with high-salinity formation fluids. For this reason, it is difficult to identify gas reservoirs in the formations where the distributions of porosity and formation fluid salinity are complex.

3.2 A new gas identification chart

A new gas identification chart is developed based on the simulation results. A new parameter $\triangle NG_1$ is defined as $\triangle NG_1 = \triangle NG/\Phi$, which means the ratio between the difference in neutron–gamma count rate per unit porosity between target layers and mudstone layers. $\triangle NG$ is defined as $\triangle NG = NG\text{-}NG_0$, that is, the difference in the neutron–gamma count rate

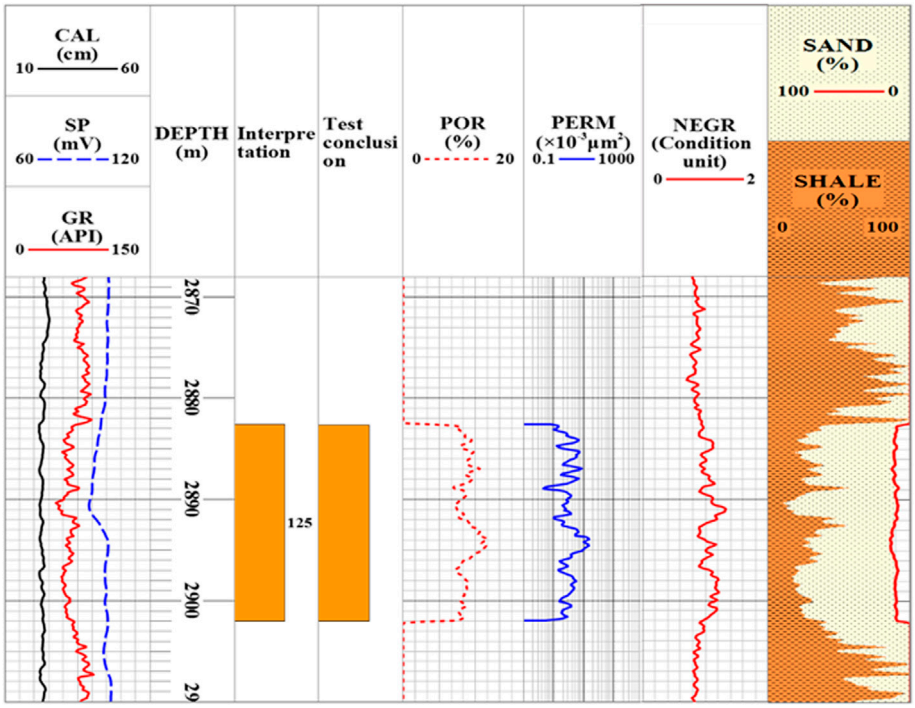

FIGURE 6
Result of gas reservoir prediction with neutron–gamma logging in well A1.

between target layers (NG) and mudstone layers (NG_0). $\triangle NG_1$ is set as the X-axis of the gas identification chart and formation water salinity is set as the Y-axis. The points of gas layers appear in different parts of this chart depending on the levels of gas saturation and formation fluid salinity.

The data of 51 well test layers in 22 old wells from neutron–gamma logging and formation water analysis were used to make the gas identification chart (Figure 5). The points of gas layers in the study area, where the gamma-ray count rate is higher and which are mostly concentrated in the top section of the cross-plot, are obviously different from those of non-gas layers. The dividing line rises upward as formation fluid salinity increases, which is consistent with the result of MCNP simulation.

3.3 Field example

The new gas identification chart is used to evaluate reservoirs based on well logs in Langgu Depression. One of the results is presented in Figure 6. Well A1 is one of the wells used for old well reexamination. Neutron–gamma logging is an important method that can be used because the available logging curves from old wells are limited. The reservoirs are sandstone formations with high density and low porosity. Layer #125 is a tight sandstone reservoir with porosity of about 10%. The value of $\triangle NG_1$ in layer #125 is about 2.4, and the formation fluid salinity is 4650 ppm. Using the new gas identification chart, we interpret this layer as a gas layer, and this interpretation result is identical with the well test result, indicating that neutron–gamma logging is effective in the discovery and evaluation of such gas layers.

4 Gas layer identification based on array acoustic logging

The great advances in exploration technology enable more new logging methods, such as array acoustic logging, to be widely used in new wells. Array acoustic logging can obtain information on the solid matrix and the acoustic velocity of the formation fluid because it is not affected by the salinity of the formation fluid. More importantly, by combining it with conventional logging data, we can obtain the *elastic mechanical* parameters that are sensitive to gas-bearing layers. These parameters can be used to identify and evaluate gas reservoirs. In this study, a method based on fluid factor is derived to improve the ability to identify gas reservoirs in new wells with array acoustic logging curves.

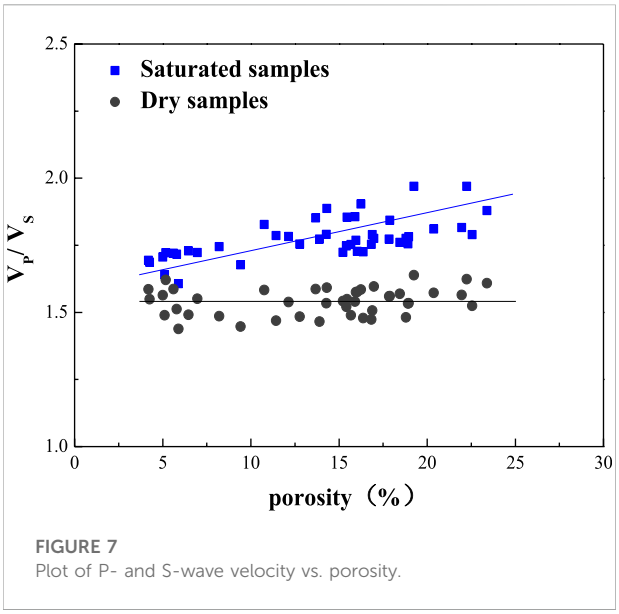

FIGURE 7
Plot of P- and S-wave velocity vs. porosity.

4.1 The Biot–Gassmann theory

Biot and Gassmann identified the relationship between the Lame's coefficients and bulk modulus for saturated and dry rocks (Biot, 1941; Gassmann, 1951)

$$\lambda_{sat} = \lambda_{dry} + \beta^2 M \tag{1}$$

$$K_{sat} = K_{dry} + \beta^2 M \tag{2}$$

where λ_{sat} is the Lame's coefficient for the fluid-saturated rock, λ_{dry} is the Lame's coefficient for the dry rock, β is the Biot coefficient, and M is the modulus. Under low-frequency conditions, Gassmann gave the following equations

$$\beta = 1 - \frac{K_{dry}}{K_m} \tag{3}$$

$$\frac{1}{M} = \frac{\beta - \phi}{K_m} + \frac{\phi}{K_{fl}} \tag{4}$$

where K_m and K_{fl} are the bulk modulus of the matrix material and that of the formation fluid, respectively.

By substituting Eqs 3, 4 into Eq. 2, the following equation can be obtained (Mavko et al., 2009):

$$K_{sat} = K_{dry} + \frac{\left(1 - \frac{K_{dry}}{K_m}\right)^2}{\frac{\phi}{K_{fl}} + \frac{1-\phi}{K_m} - \frac{K_{dry}}{K_m^2}} \tag{5}$$

The term $\beta^2 M$ is defined as pore space modulus K_p (Murphy et al., 1993), which is used to reflect the properties of pore fluid and distinguish the dry rock from the saturated rock. By combining the term $\beta^2 M$ with Biot and Gassmann equations, we can obtain the equation for P-wave velocity V_p, which is written as follows:

$$V_p = \sqrt{\frac{\lambda + 2\mu}{\rho_{sat}}} = \sqrt{\frac{\lambda_{dry} + 2\mu + \beta^2 M}{\rho_{sat}}} \tag{6}$$

$$V_p = \sqrt{\frac{K + \frac{4}{3}\mu}{\rho_{sat}}} = \sqrt{\frac{K_{dry} + \frac{4}{3}\mu + \beta^2 M}{\rho_{sat}}} \tag{7}$$

It can be simplified into the following:

$$V_p = \sqrt{\frac{s + f}{\rho_{sat}}} \tag{8}$$

where ρ_{sat} is the total density of the saturated rock, $s = K_{dry} + \frac{4}{3}\mu$ or $s = \lambda_{dry} + 2\mu$ is the dry-skeleton term, and $f = \beta^2 M$ is a fluid/porosity term. Assuming that $\mu = \mu_{sat} = \mu_{dry}$, the equation for S-wave velocity V_s can be written as follows:

$$V_s = \sqrt{\frac{\mu}{\rho_{sat}}} \tag{9}$$

4.2 Gas identification based on fluid factor

As discussed earlier, the equation for P-wave velocity V_p of the rock can be combined with dry-skeleton term s and fluid/porosity term f. Using these two terms, the equation P- and S-wave impedances, Z_P and Z_S, can be rewritten as follows:

$$Z_p = \rho V_p = \sqrt{\rho(f + s)} \tag{10}$$

$$Z_s = \rho V_s = \sqrt{\rho\mu} \tag{11}$$

Assuming that $c\mu = s$, by extracting factor c, we can obtain the following equations

$$c = \frac{s}{\mu} = \frac{\lambda_{dry}}{\mu} + 2 = \frac{K_{dry}}{\mu} + \frac{4}{3} = \left[\frac{V_p}{V_s}\right]_{dry}^2 \tag{12}$$

$$\rho f = Z_p^2 - cZ_s^2 = \left(\rho V_p\right)^2 - c\left(\rho V_S\right)^2 \tag{13}$$

where ρ is the total density of the rock, which can be obtained from density logging, and V_p and V_s can be obtained from array acoustic logging. ρf is a fluid component that reflects the contribution of the fluid in the pores. Therefore, it was defined as a fluid factor by Russell et al. (2003). The fluid factor can be calculated and used for gas-bearing reservoir identification after the value of c has been found.

Many research studies have been conducted to get an estimate of c. Murphy et al. (1993) found that the average value of K_{dry}/μ ratio for clean quartz sandstones with different porosities was 0.9, in which the value of c is 2.233. Zhang et al. (2015) measured the P- and S-wave velocity for 75 dry sandstones with different porosities and found that the value of c was 2.324. The P- and S-wave velocities of 44 rock core samples taken from Langgu Depression were measured under saturated and dry conditions to find the suitable value of c in this

TABLE 2 Elastic constant ratios of dry cores.

Elastic parameter	$c = (\frac{V_p}{V_s})^2_{dry}$	$(\frac{V_p}{V_s})_{dry}$	σ_{dry}	$\frac{K_{dry}}{\mu}$	$\frac{\lambda_{dry}}{\mu}$
Average	2.375	1.540	0.136	1.033	0.375

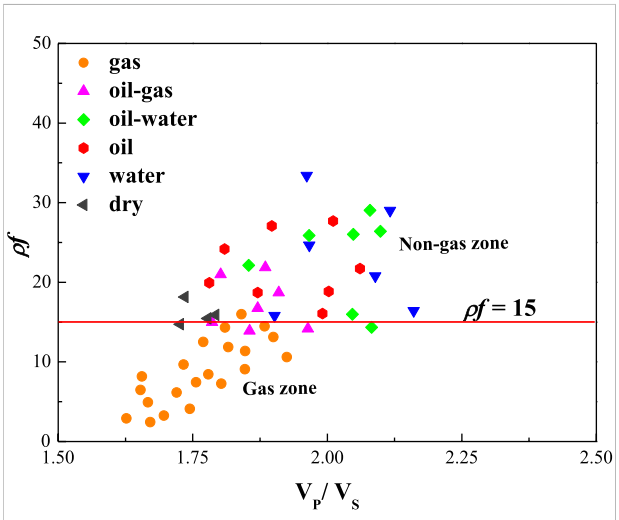

FIGURE 8
Plot of ρf vs. P- and S-wave velocity.

area. The measurement results are shown in Figure 7. From Figure 7, it can be seen that the ratio of P- and S-wave velocity of dry rock cores is mainly within the range of 1.4 to 1.6, and the average value is 1.54. The ratio of V_p/V_s of saturated rock cores is affected by the porosity, and its value increases as porosity increases. Table 1 shows the average value of V_p/V_s and other elastic parameters of the 44 rock core samples. It can be seen from Table 2 that the value of c for samples taken from Langgu Depression is 2.375.

The data of array acoustic logging and density logging of 53 well test layers in 19 new wells were used to calculate fluid factor and V_p/V_s. The results are shown in Figure 8. Figure 8 shows that the points of gas layers are mostly concentrated in the lower left corner of the cross-plot and are obviously different from those of non-gas layers, and the values of V_p/V_s and fluid factor of gas layers are smaller than those of non-gas layers. Most of the fluid factors of gas layers are less than 15, and those of non-gas layers are greater than 15. Therefore, the fluid factor's value of 15 is taken as the dividing line between gas and non-gas layers.

4.3 Field example

The fluid factor was used to identify gas layers in the new wells in which array acoustic logging was carried out. Taking well B1 (Figure 9) in the study area as an example, the first track includes the caliper (CAL), self-potential (SP), and natural gamma (GR), which can reflect the wellbore conditions and the reservoir's lithology. Track 2 displays the well depth of logs. Track 7 contains the compensated neutron (CNL), density (DEN), and acoustic log (AC), which could provide estimates of the reservoir's physical properties, such as porosity (track 5) and permeability (track 6). Track 8 shows high-definition array induction logs, which are commonly used to evaluate the properties of reservoir fluid. We can obtain the value of fluid factor ρf from array acoustic logging and density logging, as shown in track 9, and the fluid factor's value of 15 is taken as the dividing line.

The target tight reservoir in Figure 9 can be divided into five sandstone layers, represented by different icons in track 3. The three layers, 72, 74, and 75, have high porosity and permeability and are characterized by low density, high neutron, and high resistivity. In particular, the value of ρf for these three layers is about 10, which is much lower than the value of the dividing line. In summary, these three layers can be interpreted as good gas layers. The logging data of layer 73 have the same trend, but they are not as clear as those of the three layers, and the value of ρf for this layer is about 12, which is still smaller than 15. Therefore, we interpret this layer as a bad gas layer. The porosity and permeability of layer 76 are lower than those of other layers, no sign of gas in this layer is shown in the traditional logging data, and the value of ρf for this layer is beyond the dividing line. This layer is interpreted to be a dry layer. Layers 72 to 75 are tested together, and the results show they are gas layers. These results are consistent with the conclusion drawn from well log interpretation.

5 Discussion

Neutron–gamma logging is an important method to identify gas layers in old well reexamination due to the limited logging data. However, the results of Monte Carlo simulations show that the capture neutron–gamma ray count rate is significantly influenced by hydrogen index (porosity) and water salinity. Therefore, the new gas identification chart is proposed to eliminate the influences of porosity and formation water salinity.

Array acoustic logging is widely used in new wells, and the fluid factor extracted from it is a good method for gas layer identification in conventional oil and gas fields. In recent years, more and more attention has been paid to natural gas hydrate and its associated gas reservoirs (Boswell and Collett, 2011; Yin et al., 2016; Xie et al., 2022). As a number of NGH reservoirs are present either with a gas layer or water layer, there are similar properties to conventional oil and gas reservoirs in the associated gas reservoirs. Therefore, it is possible for fluid factor to be used in the identification of NGH-associated gas reservoirs under certain circumstances, which needs further study.

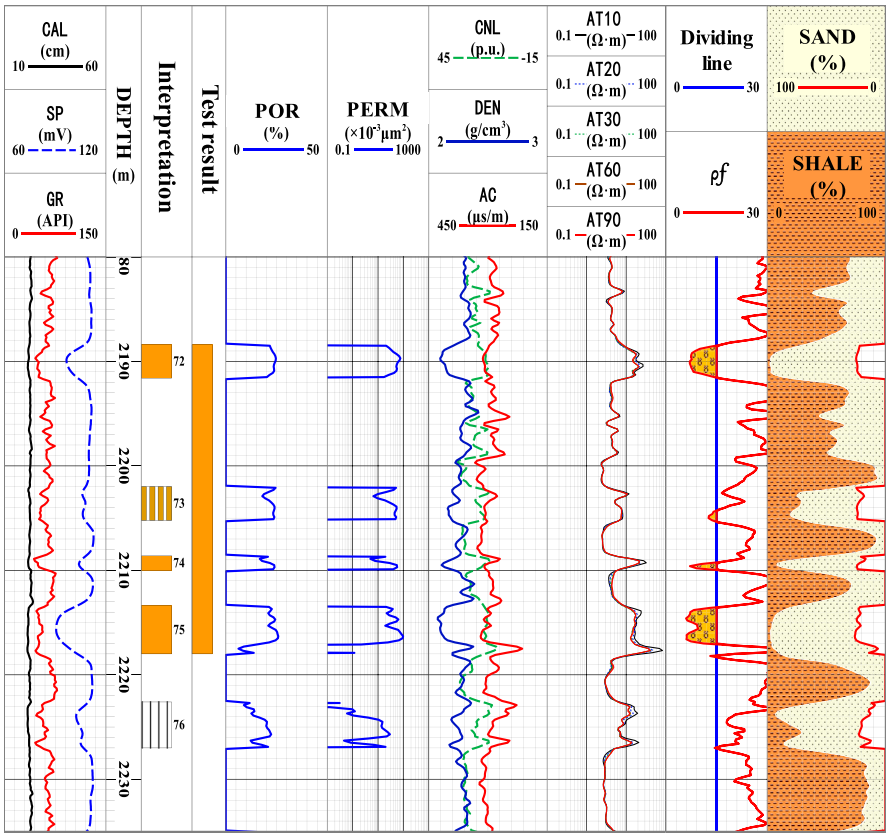

FIGURE 9
Result of gas reservoir prediction with array acoustic logging in well B1.

6 Conclusion

Neutron capture gamma-ray count rate is significantly affected by hydrogen index (porosity) and formation fluid salinity. The new gas identification chart based on neutron–gamma logging can effectively eliminate the effects of porosity and formation fluid salinity and perform well in identifying gas reservoirs, especially in the old wells with limited conventional logging curves.

The fluid factor extracted from array acoustic logging and core measurement data is sensitive to the presence of gas-bearing layers. The new gas identification standard based on the fluid factor is a good way for identifying gas reservoirs in the new wells with array acoustic logging.

The new combined method improves the ability to identify gas-bearing layers and the accuracy of prediction of such layers both in old wells reexamination and in new wells interpretation. It has delivered good results in complex sandstone reservoir such as Langgu Depression and can be used to provide reference for the evaluation of gas reservoirs in other areas.

Data availability statement

The original contributions presented in the study are included in the article/Supplementary Material, and further inquiries can be directed to the corresponding author.

Author contributions

DX, YF, HoL, and CL conceived the method. HuL and YD contributed to the interpretation of the results. DX wrote the manuscript with support from PZ. All authors provided critical feedback and helped shape the research, analysis, and manuscript.

Funding

This work was supported by the Key Special Project for Introduced Talents Team of Southern Marine Science and Engineering Guangdong Laboratory (Guangzhou) (GML2019ZD0105), the Guangzhou Science and Technology Project (202201011463), the National Natural Science

Foundation of China (No. 51991365), and the China Geological Survey Project (Nos. DD20211350 and DD20221700).

Acknowledgments

The authors would like to thank Quanying Zhang from College of Geophysics and Petroleum Resources, Yangtze University, for his warm help in the Monte Carlo simulation.

Conflict of interest

PZ was employed by the Changqing Oilfield Company. HuL and YD were employed by the PetroChina Huabei Oilfield Company.

The remaining authors declare that the research was conducted in the absence of any commercial or financial relationships that could be construed as a potential conflict of interest.

Publisher's note

All claims expressed in this article are solely those of the authors and do not necessarily represent those of their affiliated organizations, or those of the publisher, the editors, and the reviewers. Any product that may be evaluated in this article, or claim that may be made by its manufacturer, is not guaranteed or endorsed by the publisher.

References

Azudin, Y. M., Augustine, A., Afeez, G., Radzuan, J., and Azza, A. (2018). Uncertainty analysis of hydrocarbon in place calculation using 3D seismic and well data during appraisal stage – case study of goldie field, offshore sarawak. *J. Nat. Gas. Sci. Eng.* 57, 238–265. doi:10.1016/j.jngse.2018.06.038

Biot, M. A. (1941). General theory of three-dimensional consolidation. *J. Appl. Phys.* 12, 155–164. doi:10.1063/1.1712886

Boswell, R., and Collett, T. S. (2011). Current perspectives on gas hydrate resources. *Energy Environ. Sci.* 4 (4), 1206–1215. doi:10.1039/c0ee00203h

Brie, A., Pampuri, F., Marsala, A., and Meazza, O. (1995). "Shear sonic interpretation in gas-bearing sands," in SPE annual technical conference and exhibition, Dallas, Texas, October 22–25, 1995. doi:10.2118/30595-MS

Briesmeister, J. F. (2000). *MCNP – a general Monte Carlo N-particle transport Code.* Los Alamos Natl. Lab. Report number: LA-13709-M. doi:10.1016/j.cclet.2011.04.015

Dillon, L., Schwedersky, G., Vásquez, G., Velloso, R., and Nunes, C. (2003). A multiscale DHI elastic attributes evaluation. *Lead. Edge* 22 (10), 1024–1029. doi:10.1190/1.1623644

Fan, Y., Xing, D., Deng, S., Li, R., and Ge, X. (2015). Acoustic properties of low permeability cores and its application to reservoir gas predication. *Xinan Shiyou Daxue Xuebao/Journal Southwest Pet. Univ.* 51 (1), 1–9. doi:10.11885/j.issn.1674-5086.2013.08.11.07

Freedman, R., Minh, C. C., Gubelin, G., J, F. J., Mc Ginness, T., Terry, B., et al. (1998). "Combining nmr and density logs for petrophysical analysis in gas-bearing formations," in SPWLA 39th annual logging symposium, Keystone, Color, 26-28 May.

Gassmann, F. (1951). *Uber die Elastizitat poroser Medien [On the Elasticiy of porous Media]*. Zürich: Inst. für Geophysik an der ETH.

Goodway, B., Chen, T., and Downton, J. (1997). Improved AVO fluid detection and lithology discrimination using Lamé petrophysical parameters; "λρ","μρ",& "λ/μ fluid stack", from P and S inversions. SEG Technical Program Expanded Abstracts 1997. doi:10.1190/1.1885795

Hedlin, K. (2000). Pore space modulus and extraction using AVO. SEG Technical Program Expanded Abstracts 2000. doi:10.1190/1.1815749

Krief, M., Garat, J., Stellingwerf, J., and Ventre, J. (1990). A petrophysical interpretation using the velocities of P and S waves (full-waveform sonic). *Log. Anal.* 31 (6), 355–369.

Liu, H., Jiang, Z., Zhang, R., and Zhou, H. (2012). Gravels in the daxing conglomerate and their effect on reservoirs in the oligocene Langgu depression of the Bohai Bay Basin, North China. *Mar. Pet. Geol.* 29, 192–203. doi:10.1016/j.marpetgeo.2011.07.010

Mavko, G., Mukerji, T., and Dvorkin, J. (2009). *The rock physics handbook. Tools for seismic analysis of porous media*. Statewide Agricultural Land Use Baseline 2015. Cambridge: Cambridge University Press. doi:10.1192/bjp.182.2.123

Murphy, W., Reischer, A., and Hsu, K. (1993). Modulus decomposition of compressional and shear velocities in sand bodies. *Geophysics* 58, 227–239. doi:10.1190/1.1443408

Russell, B. B. H., Hedlin, K., Hilterman, F. J., and Lines, L. R. L. (2003). Fluid-property discrimination with AVO: A biot-gassmann perspective. *Geophysics* 68, 29–39. doi:10.1190/1.1543192

Shi, G. R. (2008). Superiorities of support vector machine in fracture prediction and gassiness evaluation. *Petroleum Explor. Dev.* 35, 588–594. doi:10.1016/S1876-3804(09)60091-4

Shi, Y., Pan, B., Jiang, B., Zhnag, H., Yang, X., Guo, Y., et al. (2016). Application of wavelet analysis in identification of tight sandstone gas reservoirs. *Earth Sci.* 41 (12), 2127–2135. doi:10.3799/dqkx.2016.148

Song, R. C., Zhang, S. N., Dong, S. Y., Zhou, W., Fu, H., Ren, W. B., et al. (2006). "An analysis of the characteristic and controlling factors of the Paleogene glutenite fan in the actic area of the Langgu depression," in *J. Chengdu Univ. Technol. (Sci. Technol. Ed.)*, 33, 587–592. doi:10.1007/s11104-008-9888-6

Sun, X., Shi, Y., and Jiang, Y. (2000). Log interpretation method for low permeability sandstone gas reservoir of Changqing gas field. *Petroleum Explor. Dev.* 27 (5), 115–118.

Tan, F., Li, H., Sun, Z., Yu, X., and Ouyang, M. (2013). Identification of natural gas fractured volcanic formation by using numerical inversion method. *J. Pet. Sci. Eng.* 108, 172–179. doi:10.1016/j.petrol.2013.02.004

Xie, Y., Lu, J., Cai, H., Deng, W., Kuang, Z., Wang, T., et al. (2022). The *in-situ* NMR evidence of gas hydrate forming in micro-pores in the Shenhu area, South China Sea. *Energy Rep.* 8, 2936–2946. doi:10.1016/j.egyr.2022.01.097

Xu, C., Ma, P., Lai, L., Sun, Y., and Li, Z. (2014). Sensitivity parameters of tight sand gas: A case study of lower cretaceous yingcheng formation of yingtai gas field in songliao basin, NE China. *Petroleum Explor. Dev.* 41, 778–783. doi:10.1016/S1876-3804(14)60092-6

Yin, Z., Chong, Z., Tan, H., and Linga, P. (2016). Review of gas hydrate dissociation kinetic models for energy recovery. *J. Nat. Gas Sci. Eng.* 35, 1362–1387. doi:10.1016/j.jngse.2016.04.050

Zhang, F., and Liu, J. (2014). Monte Carlo simulation of PGNAA system for determining element content in the rock sample. *J. Radioanal. Nucl. Chem.* 299, 1219–1224. doi:10.1007/s10967-013-2858-3

Zhang, H., Shi, Y., Zhang, P., Fan, Y., Yang, X., and Li, H. (2015). Identification of low permeability sandstone gas reservoir based on the DSI. *Well Logging Technol.* 39 (5), 591–595.

Zhang, J., Zhang, H., Li, Y., Zheng, C., and Li, Z. (2009). Gas-bearing prediction on tight sandstone gas reservoirs of Xujiahe formation in south Sichuan basin. *Nat. Gas. Ind.* 29 (1), 45–47. doi:10.3787/j.issn.1000-0976.2009.01.011

Zhang, Q., Zhang, F., Liu, J., Wang, X., Chen, Q., Zhao, L., et al. (2018). A method for identifying the thin layer using the wavelet transform of density logging data. *J. Pet. Sci. Eng.* 160, 433–441. doi:10.1016/j.petrol.2017.10.048

Zhao, P., Cai, J., Huang, Z., Huang, Z., and Mehdi Ostadhassan, Ran F. (2018). Estimating permeability of shale-gas reservoirs from porosity and rock compositions. *Geophysics* 83 (5), MR283–MR294. doi:10.1190/geo2018-0048.1

Zhou, L., Cao, Y., Xi, K., Zhao, X., Jin, F., and Dong, X. (2013). Characteristics and genetic mechanism of low-permeability reservoirs of the 4th member of Shahejie formation in Hexiwu structural zone of Langgu sag. *J. China Univ. Petroleum Ed. Nat. Sci.* 37 (3), 8–16. doi:10.3969/j.issn.1673-5005.2013.03.002

frontiers | Frontiers in Earth Science

TYPE Original Research
PUBLISHED 12 August 2022
DOI 10.3389/feart.2022.965898

OPEN ACCESS

EDITED BY
Jinan Guan,
Guangzhou Institute of Energy Conversion (CAS), China

REVIEWED BY
Junqian Li,
China University of Petroleum, China
Zhonggui Hu,
Sequence stratigraphy, China

*CORRESPONDENCE
Feng Changmao,
fengchangm@163.com
Wang Yanlin,
wenhuiwen@163.com

SPECIALTY SECTION
This article was submitted to Marine Geoscience, a section of the journal Frontiers in Earth Science

RECEIVED 10 June 2022
ACCEPTED 05 July 2022
PUBLISHED 12 August 2022

CITATION
Guangjian Z, Changmao F, Yanlin W, Shenghong C, Ming S, Hai Y, Junhui Y, Jing Z and Zhongquan Z (2022), Fault-bounded models of oil–Gas and gas–Hydrate accumulation in the Chaoshan Depression, the South China Sea.
Front. Earth Sci. 10:965898.
doi: 10.3389/feart.2022.965898

Fault-bounded models of oil–Gas and gas–Hydrate accumulation in the Chaoshan Depression, the South China Sea

Zhong Guangjian[1,2], Feng Changmao[1]*, Wang Yanlin[2,3]*, Chen Shenghong[1], Sun Ming[1], Yi Hai[1], Yu Junhui[2,3], Zhao Jing[1] and Zhao Zhongquan[1]

[1]Guangzhou Marine Geological Survey, Guangzhou, China, [2]Southern Marine Science and Engineering Guangdong Laboratory (Guangzhou), Guangzhou, China, [3]Key Laboratory of Ocean and Marginal Sea Geology, South China Sea Institute of Oceanology, Innovation Academy of South China Sea Ecology and Environmental Engineering, Chinese Academy of Sciences, Guangzhou, China

The Dongsha Basin is a large Mesozoic basin extended from the northern South China Sea (SCS) to onshore South China. Though long-term uplift and denudation occurred since the end of the Mesozoic, still thick Mesozoic strata (up to 5,000 m) relict over the Dongsha waters where lies the largest depression, Chaoshan Depression, covering an area of 3.7×10^4 km^2. It was confirmed by a drilling hole, the well LF35-1-1, that high organic carbon-bearing marine Jurassic layers are present in the depression. However, due to the complexity of the superposed Mesozoic and Cenozoic tectonism and poor imaging quality in previous surveys, the petroleum geology remains poorly understood in view of the deep basin structure, the Mesozoic hydrocarbon migration conditions, and the oil–gas accumulation mechanism. In recent surveys, the seismic imaging quality has been significantly improved by employing long and quasi-3D seismic streamer techniques. Correlating with the regional geology onshore the South China, drilling data of the Well LF35-1-1, and well-tying seismic profiles, it is found that two sets of source rocks are developed in the semi-closed gulf during the Upper Triassic-Lower Jurassic and the Upper Jurassic. Their effective thicknesses are estimated as 495 m and 600 m, respectively, being hopeful with high hydrocarbon generation potentials. During the Dongsha Movement that occurred in the late Cenozoic, deep faults have been extensively activated to disturb the overlying sequences, even in some places breaking through the seafloor. A potential trap structure, DS-A, is found in an intra-sag bulge which is bounded by antithetic and synthetic faults. The oil and gas generated in the neighboring sags can migrate along the faults into reservoir layers at higher levels. The antithetic faults also play the role of seal for oil and gas from the hanging wall. Apparent flat bright spots appearing within the DS-A trap indicate likely entrapment of layered petroleum. The synthetic faults on the opposite side of the DS-A structure, although fails to seal oil–gas reservoirs, provide plumbing channels for oil and gas to leak to the shallow layers above which a few pockmarks and mud volcanoes are visible. As the water depth of the continental slope there ranges from 300 m to 2000 m, it is likely for the leaked gas to form natural gas hydrates. A close cogenetic interrelation exists

between the natural gas hydrates at the seafloor and oil–gas reservoirs in the deep.

KEYWORDS

the South China Sea, the Chaoshan Depression, the Mesozoic, tectonic evolution, fault-bounded model, oil–gas accumulation, fault-leakage model, gas–hydrate accumulation

Introduction

Gas hydrate can occur in various morphologies, such as massive, veiny, nodular, and distributive (Lee and Collett, 2009; Bahk et al., 2011; Boswell et al., 2012; Wu et al., 2013; Su et al., 2014, 2020; Liu et al., 2015, 2017; Liang et al., 2016). There are three genetic models of gas hydrate reservoirs, i.e., diffusive model, seeping model, and mixed model depending on whether porosity or fracture operates dominantly in the accumulation process. The gas source of hydrate can be biogenic limited in shallow sedimentary layers or thermogenic hydrocarbon leaked from deep substrates, often oil and gas reservoirs. In terms of potential and higher efficiency in joint exploration and production, the cogenetic gas of hydrate and petroleum has become more attractive.

Hydrates have been discovered over numerous sites in the Cenozoic sedimentary basins (such as the Pearl River Mouth Basin) in the northern SCS. The Chaoshan Depression is the largest Mesozoic depression of the Dongsha Basin bordering the southeast of the Pearl River Mouth Basin, but neither oil–gas nor gas–hydrate have yet been discovered. The drilling results confirmed thin Cenozoic is underlain by thick Mesozoic strata which comprise marine source rock layers. However, the conditions for the formation of hydrates in the Chaoshan Depression have been not clearly expounded. Due to the deep burial of the Mesozoic source layers, it was difficult to clearly reveal the sedimentary filling structure and tectonic deformation characteristics of the basin by poorly imaged seismic reflection in the past. In recent surveys, the Guangzhou Marine Geological Survey (GMGS) has used long and quasi-3D seismic streamers in surveys, which significantly improved the imaging quality of the seismic profiles, revealed the Mesozoic strata in the middle and deep layers more clearly than before, enabling more understanding of the Mesozoic geological structure and petroleum geological conditions of the depression. Based on the latest survey data, it is found that there is a large trap structure (**DS-A** structure) in the low bulge in the central Chaoshan Depression, bounded by antithetic and synthetic faults, which may provide favorable conditions for the formation of oil–gas and hydrates, respectively.

Geological setting

The outcrops onshore South China provinces confirm that a far-reaching transgression began in the early Late Triassic ($\mathbf{T_3^1}$), forming the "Eastern Guangdong Basin" spanning central Guangdong, eastern Guangdong, northern Guangdong, western Fujian, and southern Jiangxi. It was connected with the Dongsha Basin in the northern part of SCS in an advancing trend from sea to land. At the end of the Late Triassic ($\mathbf{T_3^3}$), a brief regression occurred in the East Guangdong Basin. However, in the Early Jurassic, a larger transgression occurred in the East Guangdong Basin, where several hundred meters to nearly 3,000 m of carbonate rocks, clastic rocks, and coal-bearing rock series were deposited. Eastern Guangdong Basin extended to SCS is called Dongsha basin. In the Mid-Late Jurassic, seawater retreated to the northeastern part of SCS, and Mesozoic marine sequences were deposited as evidenced by drill wells in many areas, such as Early Cretaceous marine strata in Well CFC-1 in the central southwestern uplift of Taiwan Basin (Liu, 2001), Mid-Late Jurassic marine strata and Early Cretaceous coastal strata in Well LF35-1-1 on the north slope of Chaoshan Depression (Shao et al., 2007; Wu et al., 2007; Hao et al., 2009). The Mesozoic basins have the characteristics of multi-stage basin formation and multi-stage transformation and are largely superimposed basins formed after the superposition of prototype basins with different evolution characteristics (Zhong et al., 2011).

The Mesozoic basin has experienced long-term structural uplift since the Late Mesozoic and dwindled in the land and sea area in the form of residual depression. Nevertheless, there is a large Mesozoic depression around Dongsha Island where thicker Mesozoic strata are well preserved. The Chaoshan Depression is located on the southeastern side of the Pearl River Mouth Basin in the northern SCS (Figure 1A) covering an area of over 3.7×10^4 km^2. It is the largest Mesozoic residual depression in the northeastern SCS. The Well LF35-1-1 encountered the Mesozoic, of which 1,005m–1369 m is the Cretaceous sand-mudstone section, and 1,369m–1698 m is the Cretaceous tuff section. The 1,698m–2412 m is the Jurassic sand-mudstone section, of which the 1698m–1940m well section is gray–black lamellar mudstone and argillaceous siltstone intercalated with siliceous rock, contains a small amount of micrite limestone, and the rock contains volcanic clastic material; 1940m ~ 2412 m section is composed of gray–black lamellar mudstone and argillaceous siltstone intercalated with sandstone and limestone, and the mudstone is rich in organic matter debris. Radiolarian fossils were found in the 1716m–1839m well section, indicating the deep-sea environment and the Late Jurassic age. Benthic foraminifera fossils are seen in the 2049m–2112 m well

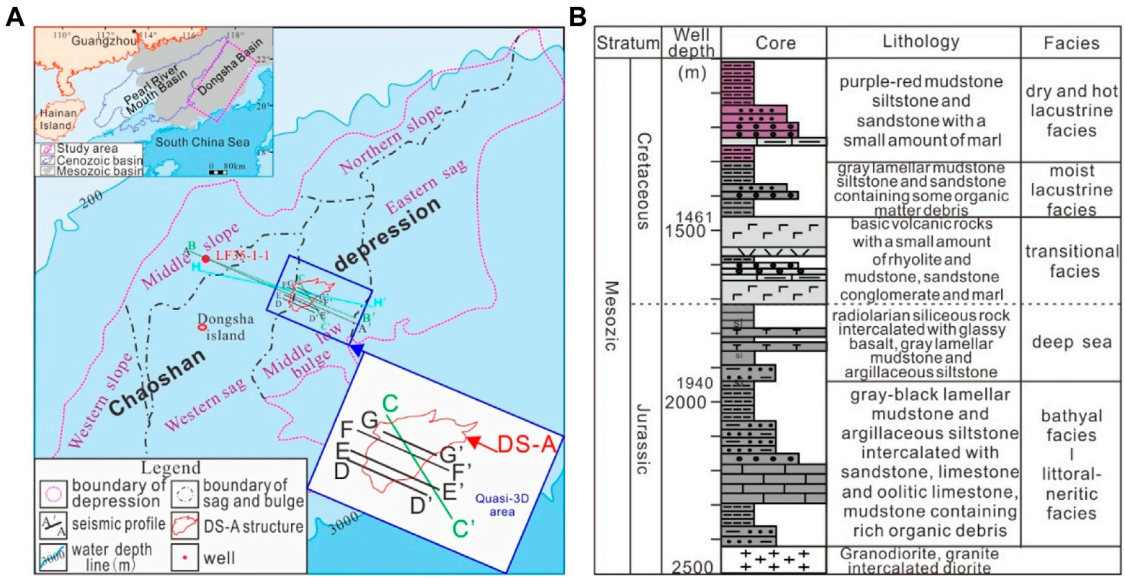

FIGURE 1
Location map and stratigraphic column map. **(A)** Location map of the study area and survey line, structural zoning map of Chaoshan Depression; **(B)** stratigraphic column of well LF35-1-1.

section, indicating this tropical marine shallow water environment. Fossils of sporopollenin can be seen in the 2,187m–2268 m well section, mainly composed of Krassauer and Pseudomonas sporopollenin. This set of sporopollenin fossils appeared in the Middle and Upper Jurassic in southern China, indicating a coastal marsh environment (Shao et al., 2007). Oolitic limestone is seen at 2421 m. Granite-granodiorite intrusions with a small number of diorite intrusions appear in the well section below 2,412 m, and the intrusion period is mainly in the Late Cretaceous (Figure 1B).

Gravity, magnetic and seismic data show weak magmatism over the Chaoshan Depression (Hao et al., 2003). Referring to regional geology, there were mainly two magmatism periods, Yanshanian and Himalayan, respectively. The Himalayan volcanism occurs mainly in the southwest Chaoshan Depression as eruption mainly of intermediate-basic igneous rocks, while the Yanshanian igneous rocks were mainly intrusive in the central and northern slopes as intermediate-acid magmatic rocks (Chen, 2007).

The Chaoshan Depression has experienced weak fracturing in the Late Triassic, depressing in the Jurassic, uplifting in the end Jurassic, rifting in the Cretaceous, uplifting and denudating at the end-Cretaceous, regional thermal subsiding during the Neogene period, and the neo-tectonic Dongsha Movement. The Dongsha Movement occurred at the end of the Middle Miocene and lasted until the early stage of the Late Miocene (Zhao et al., 2012), even to the recent (Yan et al., 2014), leading to the activation of deep faults. It trends generally in the NE direction. Six secondary tectonic units can be divided as the eastern sag, western sag, middle-low uplift, northern slope, central slope, and western slope (Figure 1A). The Mesozoic strata in Chaoshan Depression can be divided into four sequences, $\mathbf{T_3\text{-}J_1}$, $\mathbf{J_2}$, $\mathbf{J_3}$, and **K** (Chen et al., 2005; He et al., 2007, 2013; Shao et al., 2007; Wu et al., 2007; Hao et al., 2009; Feng et al., 2022), developed semi-abyssal-shallow sea ($\mathbf{T_3\text{-}J_1}$), littoral-neritic ($\mathbf{J_2}$), neritic-semi-deep sea ($\mathbf{J_3}$), and sea-land transition-fluvial-lacustrine (**K**) sedimentary layers, the largest in the Mesozoic given the residual sedimentary strata thickness larger than 5000m, it has been deemed resourceful (Wang et al., 2000; Hao et al., 2001, 2004, 2009; Zhou, 2002; Zhou et al., 2003; Zhou et al., 2005; Wang et al., 2009; Duan and Mi, 2012; Zhang et al., 2012; Ji and Zhao, 2014; Hao et al., 2018; Zhang et al., 2018) (Figure 1A).

Data and methods

GMGS has conducted a long array of two-dimensional and quasi-three-dimensional seismic surveys. The most used 2D seismic streamer has 480 channels in 12.5 m spacing. The shooting spacing is 37.5 m using a source capacity of 5,080 cubic inches. The coverage is up to 80-fold.

The seismic data are processed with routine industry procedures and pre-stacked time migration. The focus is on suppression of the turbulence noise, various random noises, linear interferences, and different types of multiples. With the processing, the signals from the shallow, medium, and deep

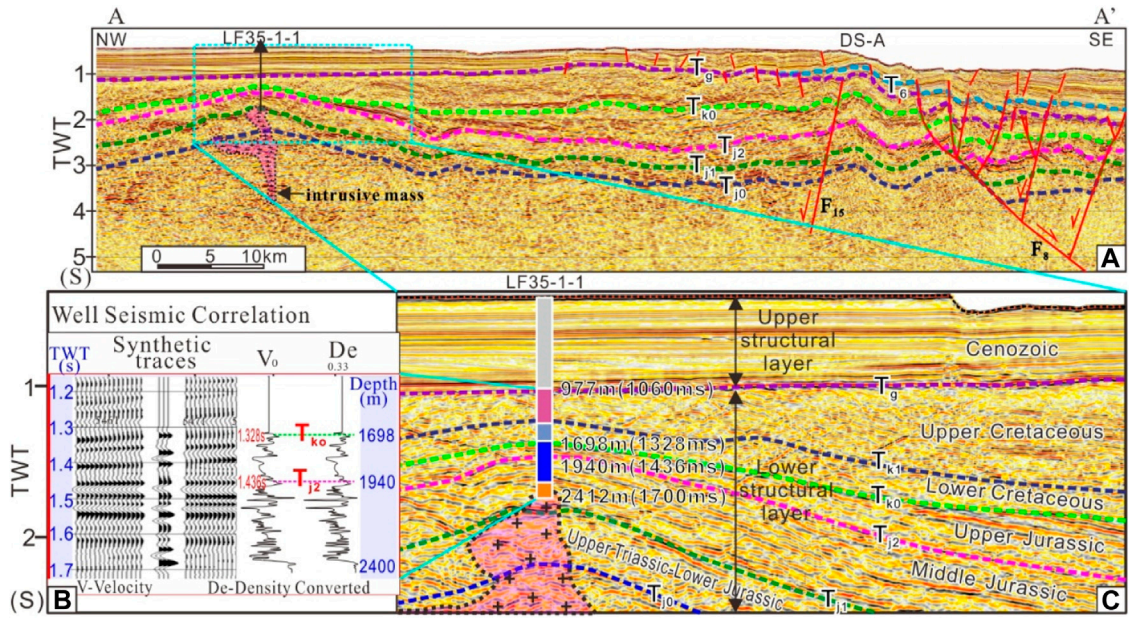

FIGURE 2
Well seismic correlation map. **(A)** Seismic reflection interfaces identified with the Well LF35-1-1; **(B)** well seismic correlation by V and De; **(C)** is the expanded view of **(A)**.

layers are readily discernable, and the wave train characteristics and amplitude characteristics are much clearer than before. The quasi-3D volume regularized with reasonable parameters is also evenly displayed in remarkably enhanced lateral resolution. The improved seismic imaging poses an excellent basis for further analysis of complex geological structures.

The seismic data were interpreted using the GeoFrame software platform. The stratigraphy is interpreted primarily by correlation with the LF35-1-1 well drilled to the north of Dongsha Island (Figure 1A) and analyzed from seismic stratigraphy. Five characteristic seismic reflection interfaces are identified widely over the depression as $\mathbf{T_g}$, $\mathbf{T_{k0}}$, $\mathbf{T_{j2}}$, $\mathbf{T_{j1}}$, and $\mathbf{T_{j0}}$ while the extra two, $\mathbf{T_{k1}}$ and $\mathbf{T_6}$, are identified over local sections (Figure 2).

$\mathbf{T_g}$ is the most obvious unconformity separating the Mesozoic and Cenozoic, which appears at 977 m deep, or two-way time (TWT) of 1,060 ms at the LF35-1-1 column. $\mathbf{T_{k0}}$ is the interface between the Lower Cretaceous and the Upper Jurassic and a strong unconformity interface, its depth is 1698 m corresponding to 1328 ms. $\mathbf{T_{j2}}$ is the interface between the Upper Jurassic and Middle Jurassic with a depth of 1940m corresponding to 1436ms. The upper and lower parts of the interface are in an integrated contact relationship, showing strong reflection characteristics on the seismic profile. $\mathbf{T_{j1}}$ is the interface between the Middle and Lower Jurassic, which has not been revealed by drilling. $\mathbf{T_{j0}}$ is the bottom interface of the Upper Triassic.

Results

One faulted nose structure

Strata over the Chaoshan Depression can be roughly divided on seismic profiles into upper and lower structural layers by the $\mathbf{T_g}$ unconformity (Figure 2). The upper structural layer above shows high-frequency, strong amplitude, and continuous, parallel reflection characteristics, comparable to those in the Pearl River Mouth Basin. The lower structural layer shows low-frequency, medium-weak amplitude, and discontinuous-continuous reflections. It occurs limitedly as an intra-depression deposition, largely in either angularly unconformable or major hiatus contact with the upper layer, indicating that the proto-depression has suffered great uplift and erosion before late subsidence.

The Chaoshan Depression has undergone multi-staged, compressive, and extensional faulting. Compressive faults are only visible in the lower structural layer in limited areal scope, mainly in the northwest and southwest parts. They were active at the end of the Jurassic, usually associated with thrust folding structures. The extensional faults are seen cutting the upper and lower structural layers, more often in the upper structural layer in the continental slope break zone. They fall into three trending groups, i.e., NE, NN, and EW, with the NE-trending faults prevalent over the others (Figure 3A). The extensional faults were active in three periods, the Yanshan Movement to the early

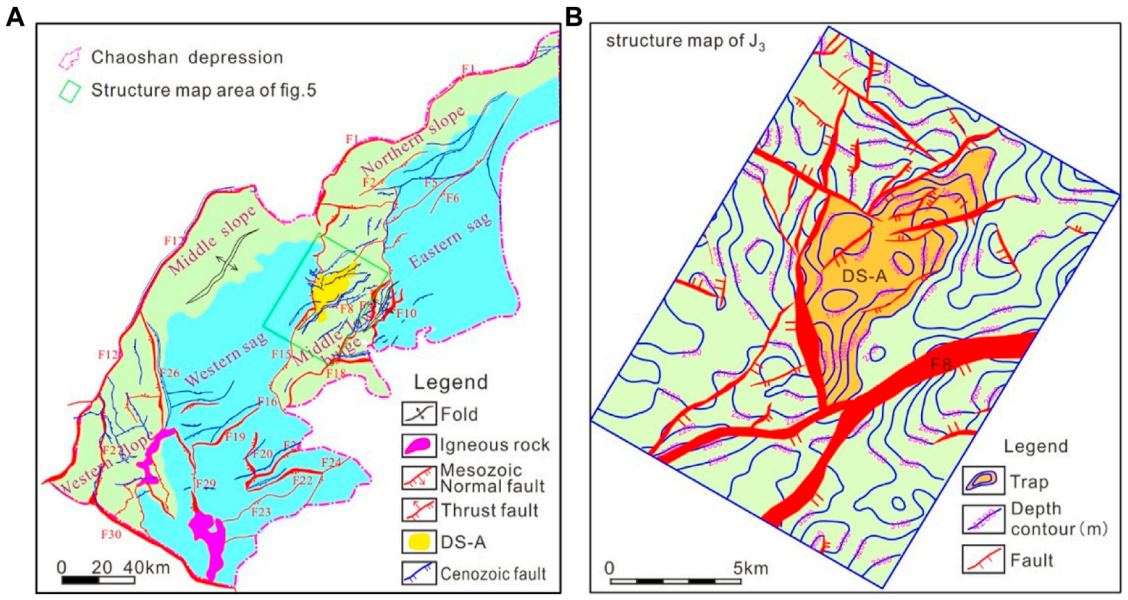

FIGURE 3
Structure map. **(A)** Chaoshan Depression; **(B)** DS-A.

stage of the Himalayan Movement, the late stage of the Himalayan Movement, and the Dongsha Movement (Zhang et al., 2014). The first-stage extensional faults initiated oil–gas migration, while the third-stage faulting can lead to oil–gas leakage from some reservoirs to shallow layers.

A large trap structure, **DS-A**, is found from 2-D profiles and quasi-3D seismic data. It is a fault nose structure composed of multiple fault blocks, fault anticlines, and anticlines. The NE-trending structure is dominated by the wide and gently extruded anticlines, forming a tectonic pattern of alternating uplift and depression belts (Figure 3A). It is located in the west of the central low bulge, covering ~ 300 km^2 (Figure 3B). It began to develop at the end of the Jurassic and was formed in the Late Cretaceous.

Two sets of effective source layers

Two black laminar mudstone intervals between 1940m–2022 m and 2,100m–2400 m in Well LF35-1-1 within the Chaoshan Depression are rich in organic matter. Among them, the thickness of a single mudstone layer in the section from 1940m to 2022 m is generally larger than 6m, with a maximum of 40 m plus and the average at ~20 m. The cumulative thickness of mudstone is 82.28 m. In the mudstones, total organic carbon (TOC) content ranges from 0.18% to 1.15%, averages at 0.67%; HI index ranges from 30 to 118.5 mg/g, with an average of 62.97 mg/g; S1+S2 varies between 0.3–1.71, with an average of 0.98 mg/g; Ro>2.0%; the type of kerogen is mainly of type III, and a few are type II. It is rated as a moderate-good source rock (Figure 4) (Zhong et al., 2007; Yang et al., 2008).

The TOC of the bathyal mudstone of the Shanglongshui Formation (Lower Jurassic) outcropping onshore the South China ranges from 0.5% to 1.71%, with an average of 1.03%, and the TOC of the bathyal mudstone of the Yinpingshan Formation (Lower Jurassic) is 0.64%–1.76%, with an average of 1.31%. The TOC of the neritic-shelf mudstone in the Xiaoshui Formation (Upper Triassic) ranges from 1.17% to 5.43%, with an average of 2.64%. The kerogen types of these three groups are all type II. According to a comprehensive evaluation, source rocks in the Chaoshan Depression can be predicted with great potential for hydrocarbon generation (Zhong et al., 2007).

Correlating the source rock analysis of outcrop on the South China continent and tests of offshore drilling in the Chaoshan Depression, two layers of mudstones deposited in $\mathbf{T_3}$-$\mathbf{J_1}$ bathyal and $\mathbf{J_3}$ neritic—shelf facies are the main source rocks, among which $\mathbf{T_3}$-$\mathbf{J_1}$ source rocks are semi-deep marine facies. The source layers are trustfully established by T well-seismic calibration. They are characteristics of medium-weak amplitude, weak continuity, low frequency, or blank reflection (Figure 4). As a result of seismic interpretation, isopach maps of two effective source layers are compiled. The $\mathbf{T_3}$-$\mathbf{J_1}$ effective source rocks are mainly distributed in the eastern sag, the western sag, and the central low uplift, with a maximum thickness of more than 1000 m and an average thickness of 495 m. The $\mathbf{J_3}$ effective source rocks are mainly distributed in the western sag, with a maximum thickness greater than 1000 m and an average thickness of 600 m (Figure 5).

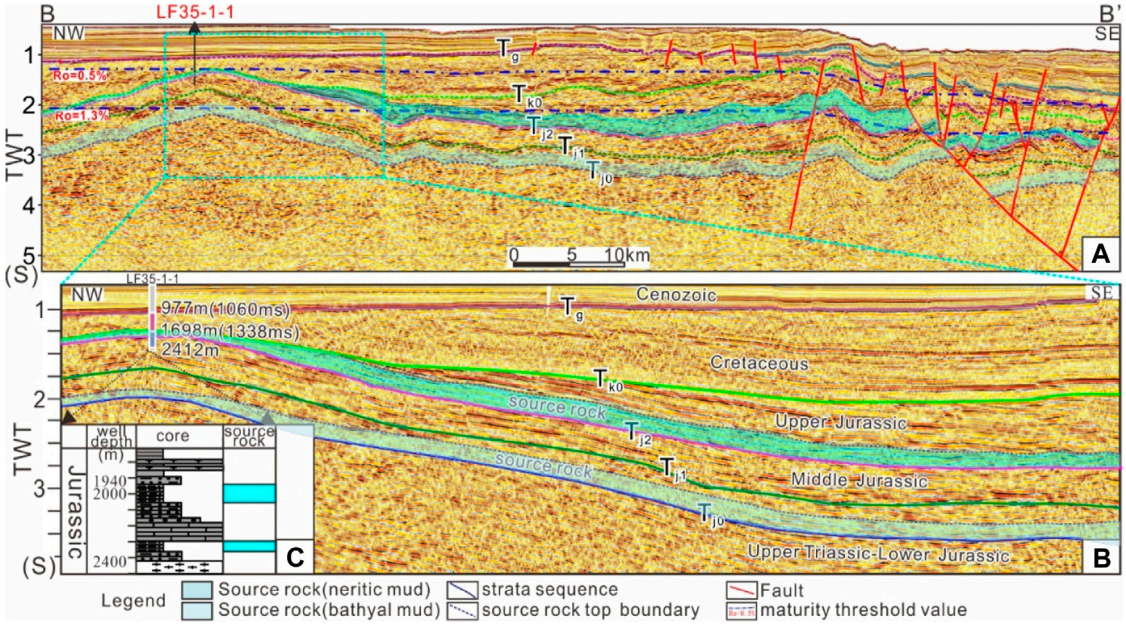

FIGURE 4
Source rocks characteristic of **(A)** two sets of source rocks revealed by seismic, location see Figure 1; **(B)** is the expanded view of **(A)**; **(C)** source rocks revealed by Well LF35-1-1.

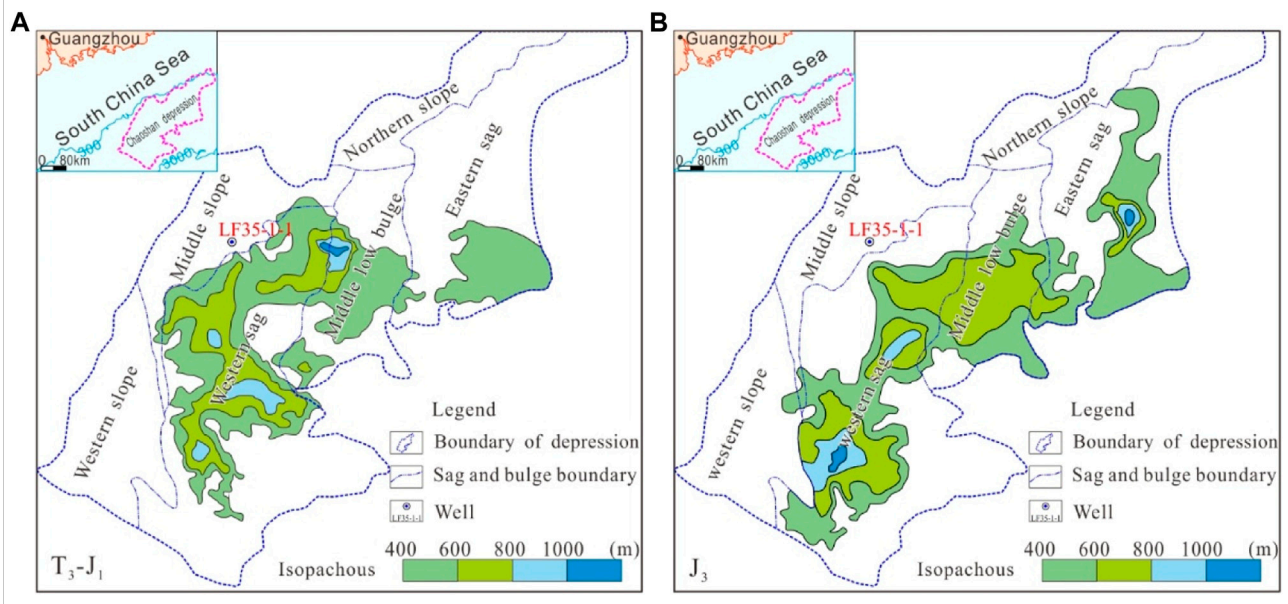

FIGURE 5
Map of mud rock thickness of the two effective source layers in the Chaoshan depression. **(A)** Map of mud rock thickness of T_3-J_1; **(B)** Map of mud rock thickness of J_3.

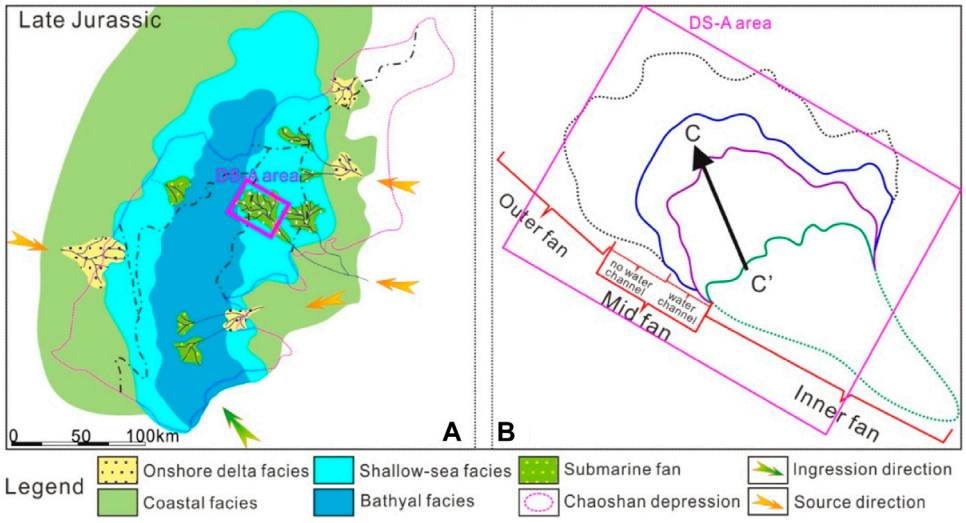

FIGURE 6
Sedimentary facies map in the Chaoshan Depression. **(A)** Map of the Late Jurassic sedimentary facies in the Chaoshan Depression; **(B)** construction of submarine fan.

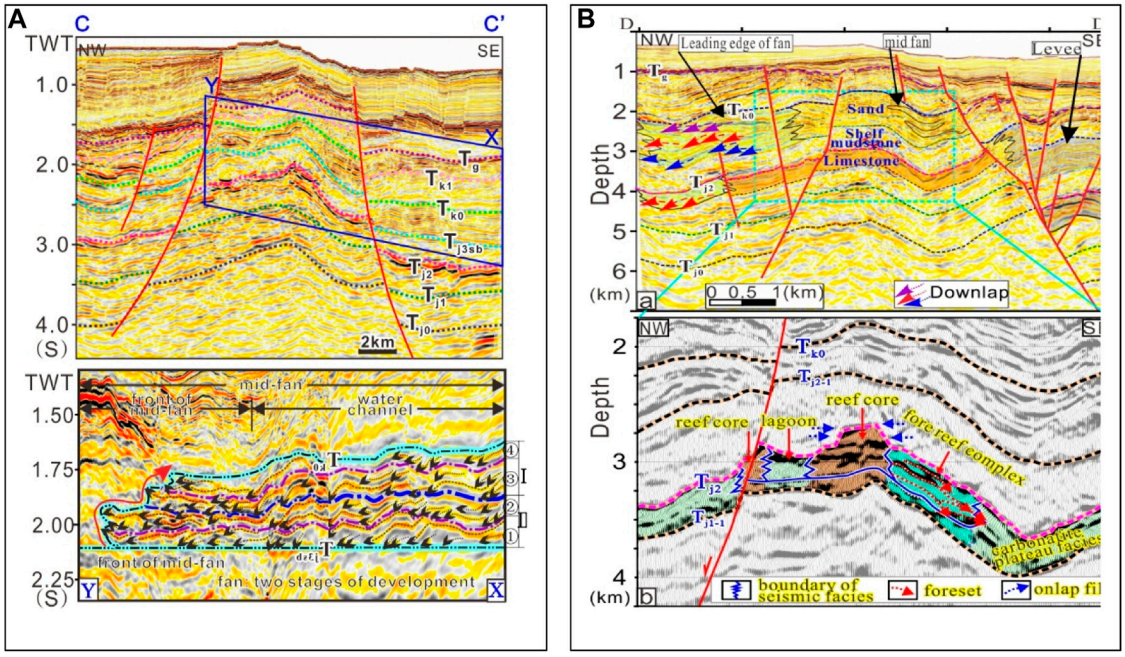

FIGURE 7
Reservoir layer of DS-A, location see Figure 1. **(A)** Interpretation for J_3 fan in DS-A; **(B)** interpretation for J_2 limestone in DS-A.

Three sets of the reservoir layer

There are three sets of reservoirs in the **DS-A** structural area of Chaoshan Depression, i.e., $\mathbf{J_3}$ coastal neritic sandstone, slope fan and submarine fan sandstone, upper $\mathbf{J_2}$ limestone, and $\mathbf{J_{1\text{-}2}}$ sandstone.

At the Well LF35-1-1, the penetrated $\mathbf{J_{2\text{-}3}}$ strata are 714 m thick, in which the total thickness of sandstone is 120 m, and the

maximum thickness of a single layer is 40 m. The sedimentary facies are mainly coastal to deltaic, reef flats, and submarine fans (Figure 6). From the analysis of layer-leveling, sequence stratigraphy, the seismic amplitude attributes of the 3D data volume, and the sand body response characteristics at Well LF35-1-1, a large submarine fan was identified in the upper part of the J_3 in the **DS-A** structure. The bottom of the subsea fan sand body is in sudden contact with the underlying thick bathyal mudstone, and the top is in gradual contact with the overlying thick sea-land transition mudstone, shown by a reflection group of stable and strong amplitude. The prograding features of the sand body along the fan body direction (SE-NW) are clearly visible. The history of the submarine fan can be divided into four stages, of which the second and third stages are the heydays (Figure 7A).

Through well-tied tracking and comparison of the thin layer of oolitic limestone (around 2,421 m) at the top of the Middle Jurassic in Well LF35-1-1, an interface featuring strong amplitude and continuous seismic reflection was traced to below the T_{j2} interface in the **DS-A** structure. The seismic facies between this interface and T_{j2} are blank or sub-parallel weak amplitude reflections (Figure 7B), which can be identified as limestone layers with a thickness of 200m–500 m.

Based on seismic facies analysis, submarine fans were identified in the top of J_3 and the bottom of J_2 in the **DS-A** structure, and a set of stable reflection layers with strong amplitudes appeared in the 3D data volume as a whole, which can be traced continuously. The subsea fan sand is the third set of favorable reservoir rocks in this structure.

Good sealing ability of mudstone

The mudstone encountered in well LF35-1-1 has a large integral thickness, and the maximum thickness of a single layer is greater than 30 m. It should have a good sealing ability and is an important regional cap rock in this area. In addition, many sets of mudstones developed in the Mid-Upper Jurassic, and these mudstones mostly showed continuous or weak continuous, and medium or weak amplitude reflections. By seismic tracking, these mudstones are stable in distribution and can also act as regional cap rocks.

In view of the contact relationship of seismic reflection, it can be found that: 1) **DS-A** structure was completely developed by the early Cretaceous, but suffered strong denudation since the late Cretaceous. The denudation thickness is about 1,100 m; 2) there is no obvious erosion in the Jurassic strata in the **DS-A** structure.

Dual-source and fracture passage

Since the end of the Middle Jurassic, the two sets of source rocks had gradually entered the hydrocarbon generation threshold and had begun to expel hydrocarbons. The **DS-A** structure is adjacent to the western sag on the west side and the eastern sag on the east side. It is a typical intra-sag uplift structure favored with sufficient oil–gas from dual sources for a long duration. There are faults developed in the Mesozoic which cut through the three sets of main source rocks. The oil and gas generated by the Jurassic source rocks in the western and eastern sags can migrate up to J_1 Sandstone, J_2 reef limestone, and J_3 sandstone along the faults, respectively, and multi-layer oil–gas reservoirs finally form at a high point of structural trap (Figure 8). Some Cenozoic faults can further leak the oil and gas to shallow layers. In fact, there are apparent signs of seafloor pockmarks and mud volcanoes around, being indicative of vigorous seep, likely of gas (Figure 9). As the water depth ranges from 300 m to 2000 m, it is highly possible for the leaked gas to form hydrates.

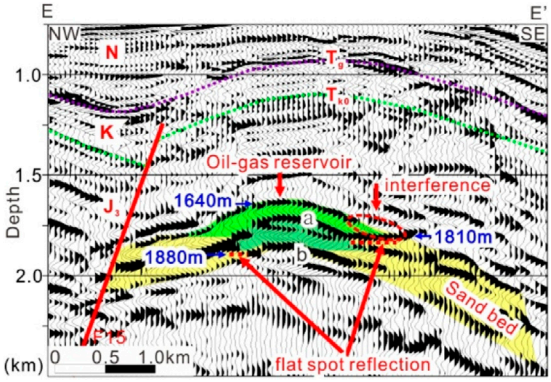

FIGURE 8
Oil–gas reservoir in DS-A.

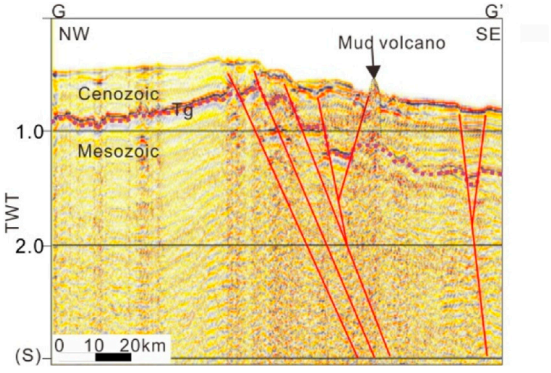

FIGURE 9
Mud volcano nearby DS-A (by courtesy of Yan et al. 2022).

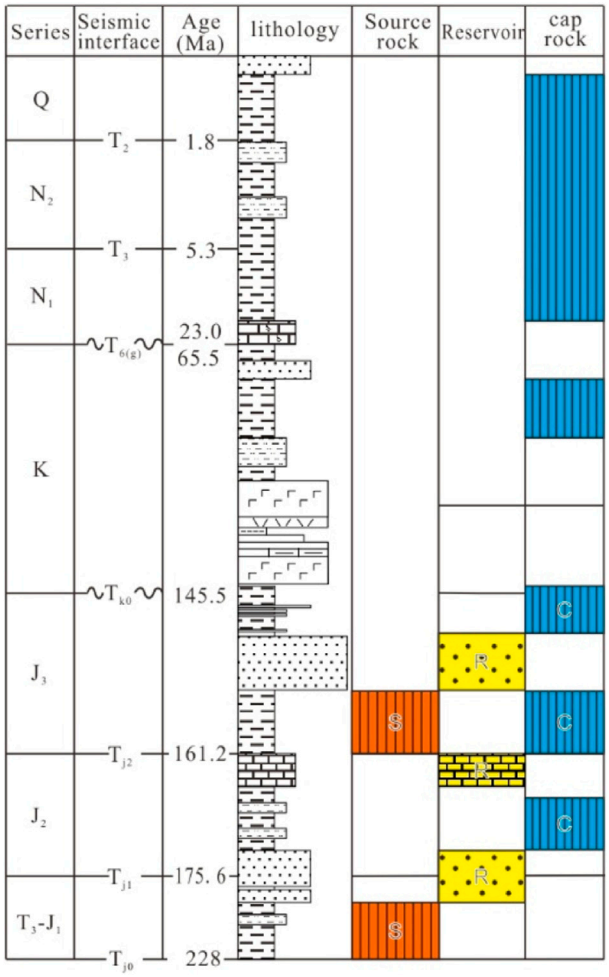

FIGURE 10
Source-reservoir-cap rock combination.

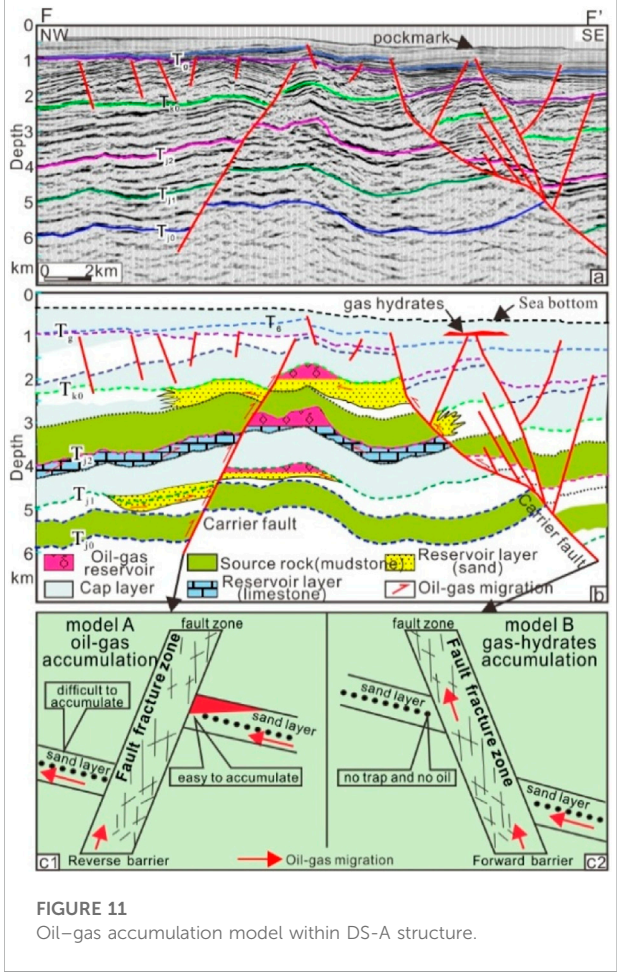

FIGURE 11
Oil–gas accumulation model within DS-A structure.

Discussion

Source-reservoir-cap rock assemblage

According to the mature evolution history of source rocks (Feng et al., 2022), the source rocks at the bottom of the Upper Triassic-Lower Jurassic began to mature at the end of the Late Jurassic, and became highly mature in the middle of the Early Cretaceous. At the same time, the **DS-A** structure began to mature. The source rocks in the lower part of the Upper Jurassic began to mature at the end of the Late Cretaceous, and the **DS-A** structure was established at the same time. At present, all the source rocks in the lower part of the Upper Jurassic have entered high maturity, and the formation of the **DS-A** structural traps has a good relationship with the temporal and spatial configuration of hydrocarbon expulsion and accumulation. According to the tempo-spatial relation (Figure 10), three sets of potentially favorable source-reservoir-cap rock assemblage (**SRCA**) in the Chaoshan Depression can be briefed as 1) $\mathbf{T_3\text{-}J_1}$ bathyal mudstones; J_1 littoral-neritic sandstones; J_2 neritic mudstones; 2) $\mathbf{T_3\text{-}J_1}$ bathyal mudstones; J_3 reef limestone; $\mathbf{J_3}$ neritic and bathyal mudstones; 3) $\mathbf{J_3}$ neritic shelf mudstones; $\mathbf{J_3^2}$—$\mathbf{J_3^3}$ coastal to basin floor fan sand; $\mathbf{J_3}$ neritic and bathyal mudstones.

Antithetic fault-bounded model of oil–gas accumulation

The **DS-A** trap structure started to develop before the peak time of oil–gas migration, fully formed at the end of the Mesozoic when uplift and denudation occurred, and altered during the neotectonics Dongsha Movement. Its formation is accommodated by various faults. Among them, two major faults, antithetic and synthetic, can be recognized as significant for models of potential petroleum reservoir and hydrate accumulation.

The **DS-A** trap sits in the west uptilt flank of a bulged terrain between the Western Sag and the Eastern Sag, which is a typical intra-sag uplift structure. It has developed with two sets of argillaceous source rocks, $\mathbf{T_3}$-$\mathbf{J_1}$ and $\mathbf{J_3}$; the reservoir rocks are submarine fan sand at the top of $\mathbf{T_3}$-$\mathbf{J_1}$ and the bottom of $\mathbf{J_2}$, platform limestone at the top of $\mathbf{J_2}$, and submarine fan sandstone in the middle of $\mathbf{J_3}$. The oil and gas generated in the western and eastern sags can readily migrate along the antithetic faults to accumulate when encountering favorable reservoirs at structural high points over the bulge. In addition, the generated oil and gas can also migrate directly to the upper reservoir through faults (Figure 11). A flat bright spot, ~1 km wide, is visible in Figure 8, which is indicative of a potential layered liquid interface, most likely the realistic existence of gas and oil reservoirs.

Synthetic fault-leakage model of gas-hydrate accumulation

The slope where the Chaoshan Depression sits shows late Cenozoic fault activation. Some of the faults extend from the Mesozoic source rock layers in deep or close to the seafloor, resulting in mud volcanoes (Figure 9) and pockmarks (Figure 11). In fact, much more mud volcanoes have been reported over the Dongsha waters, indicating widespread leakage of oil and gas from the substrates (Yan and Chen, 2009, 2017, 2021; Zhong et al., 2018). As the water depth on the slope ranges from 300 m to 2000 m, the leaked gas can accumulate as a hydrate in the shallow levels (Figure 11, model B).

Conclusion

Based on the latest survey data analysis, Chaoshan Depression has good petroleum geological conditions, and the DS-A structure is a potential trap structure bounded by antithetic and synthetic faults. The oil–gas can migrate along the faults into reservoir layers forming oil–gas reservoir, the oil–gas accumulation is an antithetic fault-bounded model. The synthetic faults provide plumbing channels for oil and gas to form natural gas hydrates, the gas–hydrate accumulation is the synthetic fault-leakage model. A close cogenetic interrelation exists between the natural gas hydrates and oil–gas reservoirs.

1 It can be recognized by seismic correlation with offshore drilling results and onshore outcrops that the main source layers within the Chaoshan Depression comprise the $\mathbf{T_3}$-$\mathbf{J_1}$ and $\mathbf{J_3}$ mudstones, especially, the thick semi-enclosed gulf source rocks of Jurassic which were tested with fairly high organic matter abundance. Three sets of reservoir rock layers are interpreted as, basin-bottom fan sandstone of the Upper Jurassic, limestone of the top mid-Jurassic, and basin floor fan of the upper Lower Jurassic and the bottom Mid-Jurassic. Furthermore, three sets of the source-reservoir-cap assemblage are deemed favorable for petroleum trap **DS-A** within which apparent flat bright spots are visible.

2 The **DS-A** is a nose-shaped structure bounded by antithetic and synthetic faults. It is an intra-sag bulge composed of multiple fault blocks, faulted anticlines, and anticline traps. The faults of different dipping directions play different roles in accumulation models of petroleum and gas hydrates, i.e., the Antithetic Fault-Bounded Model and Synthetic Fault-Leakage Model, respectively. The antithetic faults bounding the uptilt side of the structure displaced the source rock layers in the hanging wall to a low level or contact directly with the sand beds in the footwall, thus enabling source oil and gas to migrate upward or directly into the sand beds reservoir. And the mud smearing along the fault may act as a seal to form reservoirs at high points of the structure.

3 The synthetic faults on the opposite, downdip side of the **DS-A** structure, though incapable of sealing oil–gas reservoirs, provide passages for oil–gas to leak upward to form natural gas hydrates in the shallow layers. Both fault-bounded models are cogenetic in terms of the Mesozoic hydrocarbon sources.

Data availability statement

The original contributions presented in the study are included in the article/supplementary material, further inquiries can be directed to the corresponding authors.

Author contributions

Data processing: ZZ; seismic data interpreting: ZG, FC, and SM; writing-original draft preparation: YH, ZJ, YJ; writing—review and editing: GZ, CF, WY, CS; all authors have read and agreed to the published version of the manuscript.

Funding

Yan Yuning provided a processed seismic profile (Figure 9). Two reviewers are acknowledged for their constructive comments. This research was funded by the National Natural Science Foundation of China (U1901217, 91855101); Key Special Project for Introduced Talents Team of Southern Marine Science and Engineering Guangdong Laboratory (Guangzhou) (GML2019ZD0104, GML2019ZD0201); and Special Support

Program for Cultivating High-level Talents in Guangdong Province (2019BT02H594).

Conflict of interest

The authors declare that the research was conducted in the absence of any commercial or financial relationships that could be construed as a potential conflict of interest.

Publisher's note

All claims expressed in this article are solely those of the authors and do not necessarily represent those of their affiliated organizations, or those of the publisher, the editors, and the reviewers. Any product that may be evaluated in this article, or claim that may be made by its manufacturer, is not guaranteed or endorsed by the publisher.

References

Bahk, J. J., Um, I. K., and Holland, M. (2011). Core lithologies and their constraints on gas-hydrate occurrence in the east sea, offshore korea: Results from the site ubgh1-9. *Mar. Petroleum Geol.* 28 (10), 1943–1952. doi:10.1016/j.marpetgeo.2010.12.003

Boswell, R., Collett, T. S., Frye, M., Shedd, W., McConnell, D. R., and Shelander, D. (2012). Subsurface gas hydrates in the northern Gulf of Mexico. *Mar. Petroleum Geol.* 34 (1), 4–30. doi:10.1016/j.marpetgeo.2011.10.003

Chen, D. F., Su, Z., Feng, D., Lawrence, M. C., et al. (2005). Formation and its controlling factors of gas hydrate reservoir in marine gas vent system. *J. Trop. Oceanogr.* 24 (3), 38–46.

Chen, J. (2007). Geophysical characteristics of the Chaoshan depression and its hydrocarbon exploration potential. *Prog. Geophys.* 22 (1), 147–155.

Duan, J. C., and Mi, H. F. (2012). Seismic facies and sedimentary facies study of mesozoic in chaoshan sag. *Resour. Industries* 14 (1), 100–105. doi:10.13776/j.cnki.resourcesindustries.2012.01.003

Feng, C. M., Zhong, G. J., Sun, M., Lei, Z., Yi, H., and Zhao, Z. (2022). Analysis of the thermogenic gas source of natural gas hydrates over the Dongsha waters in the northern South China sea. *Front. Earth Sci. (Lausanne).* 1, 10. doi:10.3389/feart.2022.873615

Hao, H. J., Lin, H. M., Yang, M. X., Xie, H. Y., and Chen, J. (2001). The mesozoic in chaoshan depression: A new domain of petroleum exploration. *China Offshore Oil Gas (in Chinese)* 15 (3), 157–163.

Hao, H. J., Shi, H. S., Zhang, X. T., Wang, T. C., and Tang, S. L. (2009). Mesozoic sediments and their petroleum geology conditions in chaoshan sag: A discussion based on drilling results from the exploratory well LF35-1-1. *China Offshore Oil and Gas* 21 (3), 151–156.

Hao, H. J., Wang, R. L., Zhang, X. T., Xie, H. Y., and Chen, Z. G. (2004). Mesozoic marine sediment identification and distribution in the eastern Pearl River Mouth Basin. *China Offshore Oil and Gas* 16 (2), 84–88.

Hao, H. J., and Zhang, X. T. (2003). An application of gravimetric and magnetic data in mesozoic petroleum exploration in Chaoshan sag, South China sea. *China Offshore Oil and Gas (Geology)* 17 (2), 128–132.

Hao, H. Y., Zhao, J., Liu, H. S., Zhong, G. J., Ma, W. Y., Xie, P., et al. (2018). Prediction of oil and gas reservoir traps by aromatic hydrocarbons from seabed sediments in Chaoshan depression, South China Sea. *ACTA PETROLEI SINICA* 39 (5), 528–540.

He, J. X., Yan, W., Zhu, Y. H., Zhang, W., Gong, F. X., Liu, S. L., et al. (2013). Biogenetic and sub-biogenetic gas resource potential and genetic types of natural gas hydrates in the northern marginal basins of South China Sea. *Natural Gas Industry* 33 (6), 121–132. doi:10.3787/j.issn.1000-0976.2013.06.023

He, J. X., Yao, Y. J., Ma, W. H., Zhang, S. L., Shi, X. B., Liu, H. L., et al. (2007). Status of oil & gas exploration and analysis of geological character in Mesozoic residual basin, northern South China Sea. *Natural gas geoscience* 18 (5), 635–642.

Ji, Z. Y., Zhao, H. Q., Wang, H. P., and Li, C. L. (2014). The mesozoic petroleum system of chaoshan depression. *Petroleum Geology and Engineering* 28 (3), 9–15.

Lee, M. W., and Collett, T. S. (2009). Gas hydrate saturations estimated from fractured reservoir at Site NGHP-01-10, Krishna-Godavari Basin, India. *J. Geophys. Res.* 114 (B7), B07102. doi:10.1029/2008JB006237

Liang, J. Q., Zhang, G. X., Lu, J. A., Su, P. B., Sha, Z. B., Gong, Y. H., et al. (2016). Accumulation characteristics and genetic models of natural gas hydrate reservoirs in the NE slope of the South China Sea. *Natural Gas Industry* 36 (10), 157–162. doi:10.3787/j.issn.1000-0976.2016.10.020

Liu, C. L., Meng, Q. G., Li, C. F., Sun, J. Y., He, X. L., Yang, S. K., et al. (2017). Characterization of natural gas hydrate and its deposit recovered from the northern slop of the South China Sea. *Earth Science Fronters* 24 (4), 41–50. doi:10.13745/j.esf.yx.2016-12-35

Liu, G. D. (2001). The second exploitation of the oil and gas resources in China. *Progress in Geophysics* 16 (4), 1–3.

Liu, J. L., Wang, S. H., and Yan, W. (2015). Research on coexistence between marine gas hydrate and deep-water oil. *Journal of tropical oceanography* 34 (2), 39–51.

Shao, L., You, H. Q., Hao, H. J., Wu, G. X., Qiao, P. J., Lei, Y. C., et al. (2007). Petrology and depositional environments of mesozoic strata in the northeastern South China sea. *Geological Review* 53 (2), 164–169.

Su, P. B., Liang, J. Q., Zhang, W., Liu, F., Wang, F. F., Li, T. W., et al. (2020). Natural gas hydrate accumulation system in the Shenhu sea area of the northern South China Sea. *Natural Gas Industry* 40 (8), 77–88. doi:10.3787/j.issn.1000-0976.2020.08.006

Su, P. B., Sha, Z. B., Chang, S. Y., Liang, J. Q., Fu, S. Y., et al. (2014). Geological models of gas hydrate formation in the eastern sea area of the Pearl River Mouth Basin. *Natural Gas Industry* 34 (6), 162–168. doi:10.3787/j.issn.1000-0976.2014.06.26

Wang, L. L., Cheng, R. H., Li, F., Zhang, L., and Xu, Z. J. (2009). The mesozoic sedimentary sequences, correlation and geological significance for petroleum of the north margin of South China sea. *Journal of Jilin University (Earth Science Edition)* 39 (2), 175–182. doi:10.13278/j.cnki.jjuese.2009.02.007

Wang, P., Xia, K. Y., and Huang, C. L. (2000). The mesozoic marine sediment distribution and geology-geophysics characteristic at the northeastern of South China continent. *Journal of Tropical Oceanography* 19 (4), 28–35.

Wu, G. X., Wang, R. J., Hao, H. J., and Shao, L. (2007). Microfossil evidence for development of marine Mesozoic in the north of South China Sea. *Marine Geology & Quaternary Geology* 27 (1), 79–85.

Wu, N. Y., Zhang, G. X., Liang, J. Q., Su, Z., Wu, D. D., Lu, H. L, et al. (2013). Progress of gas hydrates research in northern South China Sea. *Adv. New Renew. Energies.* 1 (1), 80–94.

Yan, P., and Chen, D. F. (2009). *New geophysical evidence for gas hydrates in Baiyun Sag in the northern margin of the South China Sea.*

Yan, P., Wang, Y. L., Jin, Y. B., Zhao, M. X., and Zhong, G. J. (2021). Deep-water coral of multiple benthal strategies discovered from mounds in the Dongsha Waters in the South China Sea. *Earth Science Frontiers* 29 (4), 202–210. doi:10.13745/j.esf.sf.2022.1.13

Yan, P., Wang, Y. L., Zheng, H. B., Zhou, D. P., Chen, Z., et al. (2014). Geophysical features of mud volcanoes in the waters southwest of the Dongsha Islands. *Acta Oceanologica Sinica* 7, 142–148.

Yan, P., Wang, Y., Liu, J., Zhong, G., and Liu, X. (2017). Discovery of the southwest Dongsha Island mud volcanoes amid the northern margin of the South China Sea. *Marine and Petroleum Geology* 88 (3), 858–870. doi:10.1016/j.marpetgeo.2017.09.021

Yan, Y. N., Liao, J. P., Yu, J. H., Chen, C., Zhong, G., Wang, Y., et al. (2022). Velocity structure revealing a likely mud volcano off the Dongsha Island, the northern South China sea. *Energies* 15, 195. doi:10.3390/en15010195

Yang, S. C., Tong, Z. G., He, Q., Hao, J. R., et al. (2008). Mesozoic hydrocarbon generation history and igneous intrusion impacts in chaoshan depression, South China sea: A case of LF35-1-1 well. *China Offshore Oil and Gas* 20 (3), 152–156.

Zhang, J. Y., Sun, Z., and Zhang, S. F. (2014). Analysis of mesozoic tectonic deformation in the chaoshan depression of Pearl River Mouth Basin. *Journal of Tropical Oceanography* 33 (5), 41–49.

Zhang, L., Geng, A. S., Wang, L. L., Liao, Y., Xu, G., and Wei, Z. (2012). Assessment of mesozoic source rocks at the margin of South China continent. *Marine Geology & Quaternary Geology* 32 (1), 99–108. doi:10.3724/sp.j.1140.2012.01099

Zhang, Q. L., Zhang, H. F., Zhang, X. T., and Yang, L. L. (2018). The upper Cretaceous prototype basin of the Chaoshan depression in the northern South China Sea and its tectonic setting. *Chinese Journal of Geophysics* 61 (10), 4308–4321.

Zhao, S. J., Wu, S. G., Shi, H. S., Dong, D. D., Chen, D. X., Wang, R., et al. (2012). Structures and dynamic mechanism related to the Dongsha movement at the northern margin of South China Sea. *Progress in geophysics* 27 (3), 1008–1019. doi:10.6038/j.issn.1004-2903.2012.03.022

Zhong, G. J., Wu, S. M., and Feng, C. M. (2011). Sedimentary model of mesozoic in the northern South China sea. *Journal of Tropical Oceanography* 30 (1), 43–48.

Zhong, G. J., Yi, H., Lin, Z., Jin, H. F., and Liu, Z. H. (2007). Characteristic of source rocks and mesozoic in continental slope area of northeastern the south China sea and east Guangdong of China. *Xinjiang Petroleum Geology* 28 (6), 676–680.

Zhong, G. J., Zhang, R. W., Yi, H., Feng, C. M., and Zhao, Z. Q. (2018). The characteristics of shallow gas reservoir developed in the northern continental slope of South China Sea. *Journal of Tropical Oceanography* 37 (3), 80–85.

Zhou, D., Chen, H. Z., Sun, Z., Xu, H. H., et al. (2005). Three Mesozoic sea basins in the eastern and southern South China Sea and their relation to Tethys and Paleo-Pacific domains. *Journal of Tropical Oceanography* 24 (2), 16–25.

Zhou, D. (2002). Mesozoic strata and sedimentary environment in SW Taiwan Basin of NE South China sea and peikang high of Western taiwan. *Journal of Tropical Oceanography* 21 (2), 50–57.

Zhou, D., Yan, J. X., Qiu, Y. X., Chen, H. Z., and Sun, Z. (2003). Rout for the eastern extension of meso-tethys in the Western environs of the south China sea. *Earth Science Frontiers* 10 (4), 469–476.

frontiers | Frontiers in Earth Science

TYPE Original Research
PUBLISHED 25 August 2022
DOI 10.3389/feart.2022.985597

OPEN ACCESS

EDITED BY
Pibo Su,
Guangzhou Marine Geological Survey, China

REVIEWED BY
Jinxiu Yang,
China University of Petroleum, Huadong, China
Xiting Liu,
Ocean University of China, China
Jiapeng Jin,
Pilot National Laboratory for Marine Science and Technology, China

*CORRESPONDENCE
Feng Cai,
caifeng0532@163.com

SPECIALTY SECTION
This article was submitted to Marine Geoscience, a section of the journal Frontiers in Earth Science

RECEIVED 04 July 2022
ACCEPTED 01 August 2022
PUBLISHED 25 August 2022

CITATION
Luo D, Cai F, Li Q, Yan G, Sun Y, Li A and Dong G (2022), Geophysical evidence for submarine methane seepage on the Western slope of Okinawa Trough. *Front. Earth Sci.* 10:985597. doi: 10.3389/feart.2022.985597

Geophysical evidence for submarine methane seepage on the Western slope of Okinawa Trough

Di Luo[1,2], Feng Cai[1,2]*, Qing Li[1,2], Guijing Yan[1,2], Yunbao Sun[1,2], Ang Li[1,2] and Gang Dong[1,2]

[1]Key Laboratory of Marine Hydrocarbon Resources and Environmental Geology, Ministry of Land and Resources, Qingdao Institute of Marine Geology, Qingdao, China, [2]Laboratory for Marine Mineral Resources, Qingdao National Laboratory for Marine Science and Technology, Qingdao, China

Identifying seafloor methane seepage efficiently has important implications for assessing environmental impact, reducing the uncertainty of top seal integrity, understanding the petroleum system, and mitigating the drilling hazards due to shallow gas influx. Pore water geochemistry analyses suggest that the study area has an extremely high methane seepage flux and active methane anaerobic oxidation processes. However, geochemical data cannot provide details about the internal seepages. The geophysical dataset from the Western slope of Okinawa Trough, including 2D high-resolution seismic, sub-bottom profiles, and bathymetry, gives us a good opportunity to understand the detailed characteristics of methane seepages in this study. Geophysical data have revealed numerous methane seepage-related features such as seismic chimneys, pockmarks, submarine domes, and amplitude anomalies, including bright spots and enhanced reflections. Pockmarks and domes are often associated with seismic chimneys, indicating that fluid migration is important in their formation. The various geophysical expressions may represent different stages of methane seepage. Fluid quickly drains, causing severe sediment deformation and forming pockmarks, whereas domes may indicate the early stages of fluid discharge. Chimneys that do not extend to the seafloor may indicate that the venting is gradual and focused. Flares linked to domes or pockmarks may indicate that the fluid migration is active. Several factors triggered the existence of methane seepages on the Western slope of the Okinawa Trough, including tectonic setting, overpressure and rapid sedimentation.

KEYWORDS

Okinawa Trough, seismic chimney, pockmark, bright spot, high-resolution seismic, parametric sub-bottom profile

Introduction

Submarine methane seepage is a geological phenomenon widespread on both active (Netzeband et al., 2010; Tsunogai et al., 2012; Crutchley et al., 2013; Wei et al., 2021) and passive continental margins (Miller et al., 2012; Wenau et al., 2015; Dewangan et al., 2021). Since the discovery of methane seepage into the modern marine environment at the foot of the Florida Escarpment (Paull et al., 1984), the seepage of methane-rich fluids from sediments into the ocean floor or atmosphere has been revealed to be a common feature along continental margins (Williscroft et al., 2017).

Methane seepage has a significant impact on global climate change, the global carbon cycle, ocean acidification, and the chemosynthetic ecosystem (Wei, et al., 2021). Methane is abundant as free bubbles, aqueous methane, and/or gas hydrates in continental margin sediments and is an important component of the global carbon cycle (Suess, 2014; Xu et al., 2021). Their escape from marine sediments could cause oceanic acidification and deoxygenation, as well as amplify climatic warming if they enter the atmosphere (Li et al., 2021). Moreover, several authors have discussed a relationship between methane seepage and gas hydrate reservoirs, such as the Krishna-Godavari offshore basin (Gullapalli et al., 2019), Black Sea (Shnyukov, 2013), offshore western Svalbard (Graves et al., 2017), Taixinan basin (Wang et al., 2018), Hikurangi Margin (Schwalenberg et al., 2010; Krabbenhoeft et al., 2013). Methane in marine sediments is produced by microbial and thermal degradation of organic carbon. If sediment pore fluids become methane saturated and temperature is low while the pressure is relatively high (Graves, et al., 2017), gas hydrate may form. On the other hand, gas hydrate decomposition is an important source of methane (Van Rensbergen et al., 2002). Warming bottom waters have begun to dissociate large amounts of gas hydrate and the resulting methane release may accelerate global warming (Berndt et al., 2014).

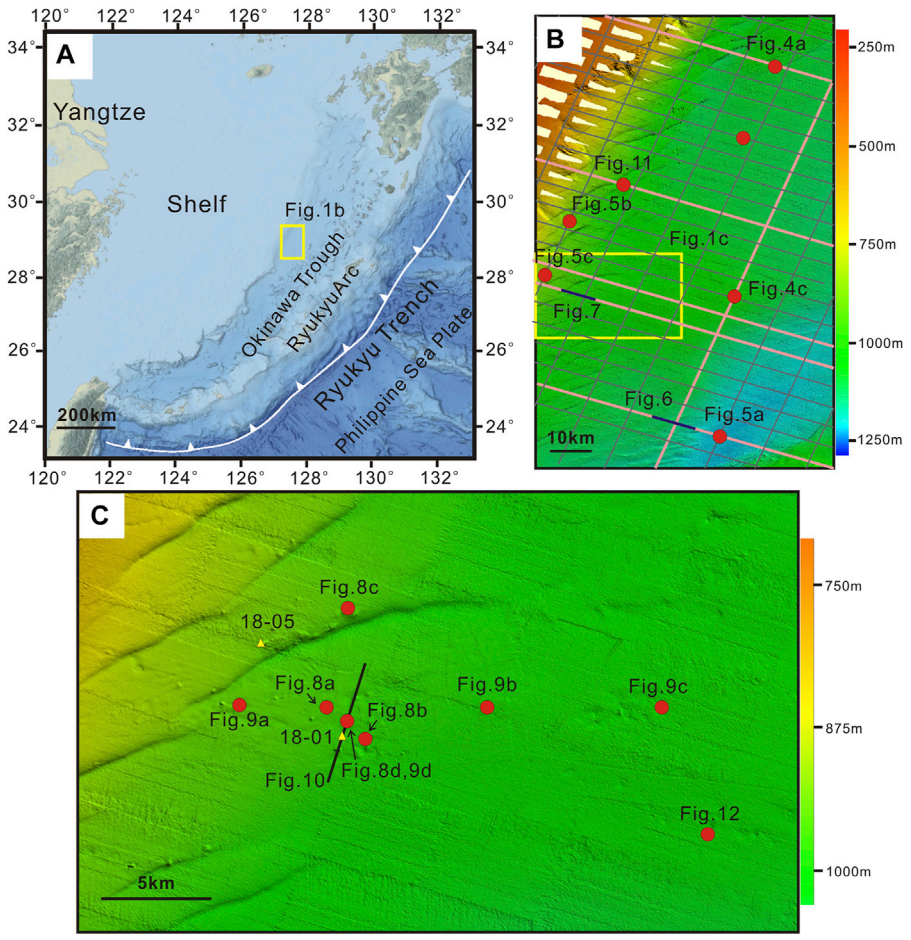

FIGURE 1
(A) Physiographic map of the surrounding sea of Okinawa Trough. The study area is shown with a yellow box. **(B)** The location of seismic lines in black lines and multibeam data in colors. The pink lines denote the locations of seismic lines used in the paper. **(C)** Magnified multibeam data. The location is shown in Figure 1b in the yellow box. For simplicity and clarity, except for Figures 6, 7, 10 we just labeled the location of the geophysical features in each figure with red points.

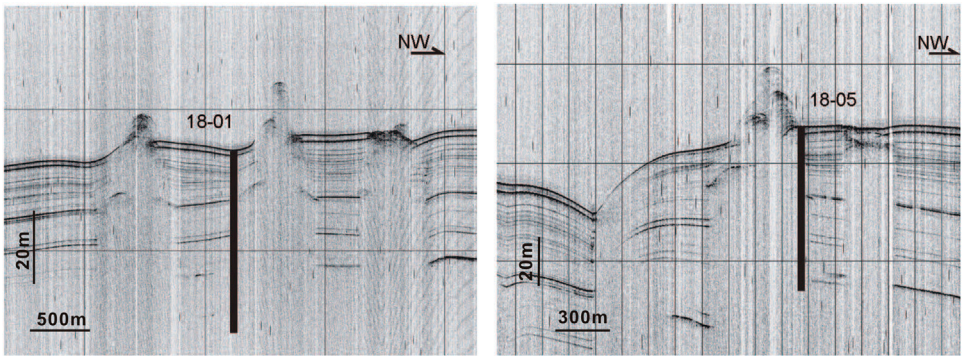

FIGURE 2
Sub-bottom profiles across two drilling sites.

As mentioned above, efficiently detecting and identifying seafloor methane seepage has significant implications (Dixit and Mandal, 2020). Geochemical analysis of pore water or bottom water (Xu et al., 2018), synthetic aperture radar (SAR) (Logan et al., 2010), and seafloor observations such as Remotely Operated Vehicle (Palomino et al., 2016) are conventional practices for detecting methane seepage. However, because of inadequate sampling density and limited investigation depth, these techniques are low-efficiency and only provide shallow-depth information about fluid migration pathways. The seepage and expulsion of methane-rich fluids can create various geological features (Netzeband, et al., 2010). Topographic expressions at the seafloor range from build-ups (e.g. mud volcanoes (Milkov, 2000; Tsunogai, et al., 2012; Magalhaes et al., 2019), mounds [Chun et al., 2011; Somoza et al., 2014; Benjamin and Huuse, 2017) or domes (Koch et al., 2015)] to depressions [e.g., submarine pockmarks (Cathles et al., 2010; Dondurur et al., 2011; Callow et al., 2021)]. Furthermore, many studies revealed that fluid migration pathways were associated with buried underlying structures such as mud diapirs (Rovere et al., 2014; He et al., 2016; Wan et al., 2017), fault systems (Mohammedyasin et al., 2016; Hillman et al., 2020), and seismic chimneys (Kempka et al., 2016; Callow, et al., 2021).

The Okinawa Trough is an active back-arc basin formed by the subduction of the Philippine Sea Plate beneath the Eurasian Plate to the northwest (Figure 1A). Several geological indicators of methane seepage such as abundant authigenic carbonates (Guan et al., 2019; Wang et al., 2019; Guan et al., 2022), concretions, and chimneys (Sun et al., 2015; Xu, et al., 2021) have been discovered along the western slope of the Okinawa Trough. In addition, some mud diapirs (Ning et al., 2009; Xing et al., 2016), and mud volcanoes (Yin et al., 2003) accompanied by fluid flows have been identified from seismic and bathymetric data in the middle and southern sections of the Okinawa Trough. Geochemical data from the pore water of the gravity cores reveals active methane seepage in the vicinity of mud volcanoes (Li et al., 2015; Xu et al., 2018; Xu et al., 2021). In this study, we systematically demonstrate the geophysical properties of methane seepages from the western slope of the Okinawa Trough using high-resolution seismic reflection data (Figure 1B), parametric sub-bottom profiles, and multibeam bathymetric (Figure 1C). A variety of geophysical anomalies associated with methane seepages are interpreted and illustrated.

Geological background

The Okinawa Trough, which extends from the Ilan Plain in northeastern Taiwan to the shallow sea southwest of Kyushu (Sibuet et al., 1987), is an active back-arc basin formed by the subduction of the Philippine Sea Plate beneath the Eurasian Plate to the northwest (Figure 1) (Sibuet et al., 1998). It is divided into northern, middle, and southern segments that are separated by the Tokara Fault and the Miyako Fault zones (Sibuet, et al., 1987). The stages of back-arc evolution in the three segments are very different. The northern Okinawa Trough is experiencing crustal stretching, the middle Okinawa Trough is undergoing propagating rift processes, and the southern Okinawa Trough presents signs of initial ocean crust spreading. The stages of back-arc evolution in the Okinawa Trough vary from continental extension in the northern Okinawa Trough, rifting in the middle Okinawa Trough, and potential seafloor spreading in the southern Okinawa Trough. It is considered to be in the rifting phase prior to the back-arc spreading (Park et al., 1998), and has complex geotectonic features. Along the axis of the middle to southern Okinawa

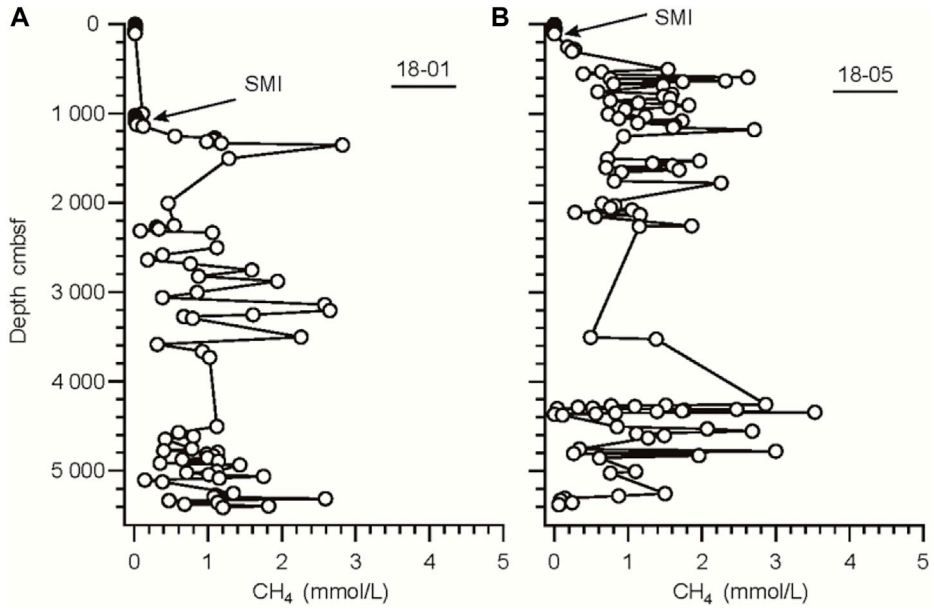

FIGURE 3
Depth profiles of headspace methane concentration in pore water of 18-01 **(A)** and **(B)** 18-05 sites.

Trough, several en-echelon extensional grabens with active faults have been identified (Shinjo and Kato, 2000).

The width of the Okinawa Trough increases from 60 to 100 km in the south to 230 km in the north, while the water depth decreases from 2,300 m to 200 m from south to north (Sibuet et al., 1987; Sibuet et al., 1998; Tsai et al., 2021). The crust and sedimentary layers become gradually thinner along the length of the trough, from 20 to 30 km in the north to 10–12 km in the south (Minami et al., 2022). The northern Okinawa Trough is composed of numerous half-grabens covered by thick terrigenous material layers up to 8 km thick from China's Yangtze and Yellow rivers, whereas the southern Okinawa Trough has a sedimentary cover of up to 2 km. The middle Okinawa Trough has received varying sedimentary supplies from those rivers, and the sedimentary rate has increased considerably over the last 0.5 million years (Sibuet, et al., 1987).

Heat flows in the Okinawa Trough are high (10^2–10^5 mW/m2), which may be caused by present or recent hydrothermal activities associated with the rifting process, according to heat flow studies (Chen et al., 2020). In the southernmost Okinawa Trough, several submarine volcanoes emitting intense gas plumes from the seafloor have been discovered (Tsai, et al., 2021). The geochemical data from pore water on the Western slope of the Okinawa Trough reveals methane seepage in the turbidite deposits is active (Li, et al., 2015) Figure 1b.

Data and methods

Small-scale and high-resolution multichannel seismic

Small-scale and high-resolution marine multichannel seismic detection technology using large energy sparkers seismic source is characterized by a high dominant frequency, wide bandwidth, and high resolution. When compared with traditional method, this technology has the advantages of high resolution (the vertical resolution is up to 1–3 m) and high detection precision (Luo et al., 2017). The high-resolution multichannel seismic data used in this study were acquired using a SIG pulse L5 Sparker with a shooting energy of 20 kJ at every 12.5 m, a 293.75 m streamer (48 channel, 6.25 m group interval) and 12 times stacking fold. The shortest source-receiver distance was 75 m with recording length of 4,000 ms. The data was sampled at an interval of 0.5 ms. Based on the characteristics of the seismic detection technology, targeted processing technologies were applied to improve the quality of seismic data imaging (Luo et al., 2019). Parametric sub-bottom profiles.

The parametric sub-bottom profiles survey is a geophysical method based on acoustic theory to detect shallow formations and structures beneath the seafloor and is one of the important means of marine geological survey. It is useful for identifying the acoustic anomalies of marine sediments.

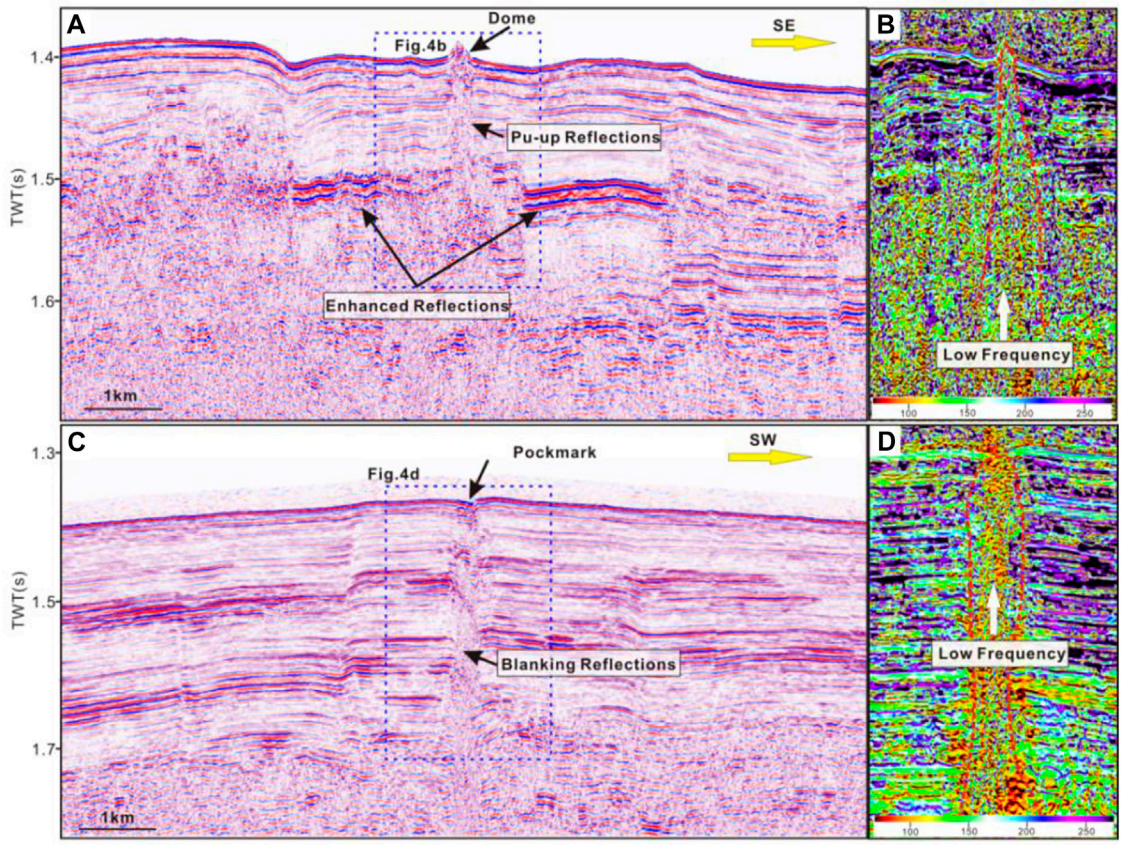

FIGURE 4
Type-A seismic chimneys. **(A,C)** Seismic profiles. A dome or pockmark is observed above chimneys; **(B,D)** The instantaneous frequency attribute profiles, which locations are shown in Figure 4A. Low-frequency anomalies are observed within the chimneys. See locations in Figure 1B.

Sub-bottom profile data used in the study were acquired with the TOPAS PS18 system, with a primary frequency ranging from 2 to 6 kHz. The chirp (Compressed High-Intensity Radar Pulse) technique, which has high penetration, was used for the source pulse. The sound speed of the transducer is 1,500 m/s.

Multibeam bathymetric

The bathymetric data present in this paper was acquired using a Kongsberg Simrad EM122 multi beam echo sounder system. It has a swath angle of 130 and can transmit and receive up to 288 simultaneous beams with a beamwidth of 1 by 1. The sounding frequency of the system is 12 kHz and up to 864 soundings per ping in the dual-swath mode. The data has been processed using QPS Qimera software.

Sediment pore water sampling

The sediment samples for this study were obtained using the seabed drilling rig, with a drilling capacity of 60 m at a water depth of 3,500 m.

According to geophysics data, several mud volcanoes or domes formed on the western slope of the Okinawa Trough, and both boreholes (18-1 and 18-5) are located on the flanks of the mud volcanoes (Figure 2) (Li et al., 2020). The distance between borehole 18-01 and the mud volcano is about 10 m, and borehole 18-05 is located next to the mud volcano.

Pore water was squeezed by pressure filtration, and the sampling interval was 20 cm. Each core section was split into two halves for geochemical analysis and archiving. About 5 cm of thick sediment is used for pore water squeezing. Part of the pore water is used for onboard sulfate, chloride ion, hydrogen sulfide, nutrients (NH4+, NO3−, NO2−, PO43−, SiO2), and total

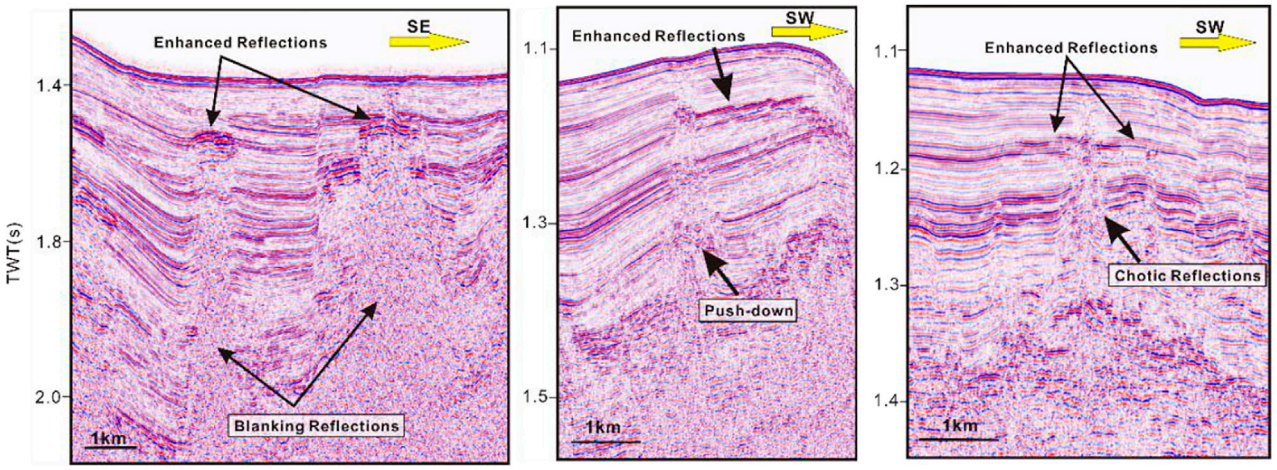

FIGURE 5
Seismic profiles of three type-B seismic chimneys. This type of chimney has no seafloor expressions such as pockmarks or domes. See locations in Figure 1B.

alkalinity determination, and while the other part is sealed and stored at a low temperature for onshore hydrocarbon determination.

The pore water headspace was injected into a gas chromatograph for methane concentration analysis (Agilent 6,850). The carrier gas was nitrogen at a flow rate of 20 ml/min. The precision of the methane analysis is ±3%.

Results

Geochemical constraints on the methane seep activity

In the shallow part, the methane concentration of pore water increased significantly with the increase in depth.

At a depth of 11.44 m below the seafloor, the methane concentration in the headspace of pore water showed a low characteristic of 0.002–0.11 mmol/L in borehole 18-01. Methane concentration rise sharply below 11.44 m, from 0.11 mmol/L at 11.44 m to 2.82 mmol/L (13.54 m). This result indicates that anaerobic oxidation and sulfate reduction of methane are strongly developed at a depth of 11.44 m. The findings reveal that the depth of the Sulfate-Methane Interface (SMI) is 11.44 mbsf. The high values of methane concentration (2.64 and 2.59 mmol/L, respectively) are observed at the depths of 32.08 m and 53.14 mbsf respectively (Figure 3A), indicating the possible migration and occurrence of high-concentration methane fluid in the original formation. In borehole 18-05, the variation in methane concentration in pore water is similar to that in borehole 18-01. The methane concentration remains low in characteristics in shallow depths of 0–1.04 m below the seafloor, while the methane concentration in the strata below 1.04 mbsf increases rapidly, implying that the depth of SMI is 1.04 m. However, at the depths of 5.94, 11.79, 43.42, and 47.79 m, methane concentrations all represented high concentration characteristics (Figure 3B) (Li, et al., 2020).

Seismic chimneys

Methane fluid escapes from conduits can be recognized by seismic and sub-bottom profile data. Seismic chimneys are one of these features. They are vertical to sub-vertical seismic anomalies with circular or elliptical planforms that hydraulically connect deeper stratigraphic layers with the overburden (Karstens and Berndt, 2015). Within seismic chimney structures, seismic amplitude blanking and chaotic reflections are commonly observed (Callow, et al., 2021). Seismic chimneys have been observed extensively on the Western slope of the Okinawa Trough, and they may act as a pathway for methane fluids, allowing upward migration to the seafloor and eventually into the water column. Based on the seismic observations, we classified the seismic chimneys in the study area into four groups.

Type-A chimneys appear to be associated with seafloor domes or pockmarks. In the seismic profiles, the presence of chaotic or blanking reflections has been observed within type-A seismic chimneys. The surrounding reflections bend upwards with reduced amplitude at the lateral margin of chimneys. Type-A chimneys terminate close to the seafloor and are connected to domes or pockmarks. For example, the anomaly of Figure 4A narrows upwards and is terminated with a dome on the seafloor, whereas the chimney shown in Figure 4C is connected to a pockmark on the seafloor. The instantaneous frequency attribute

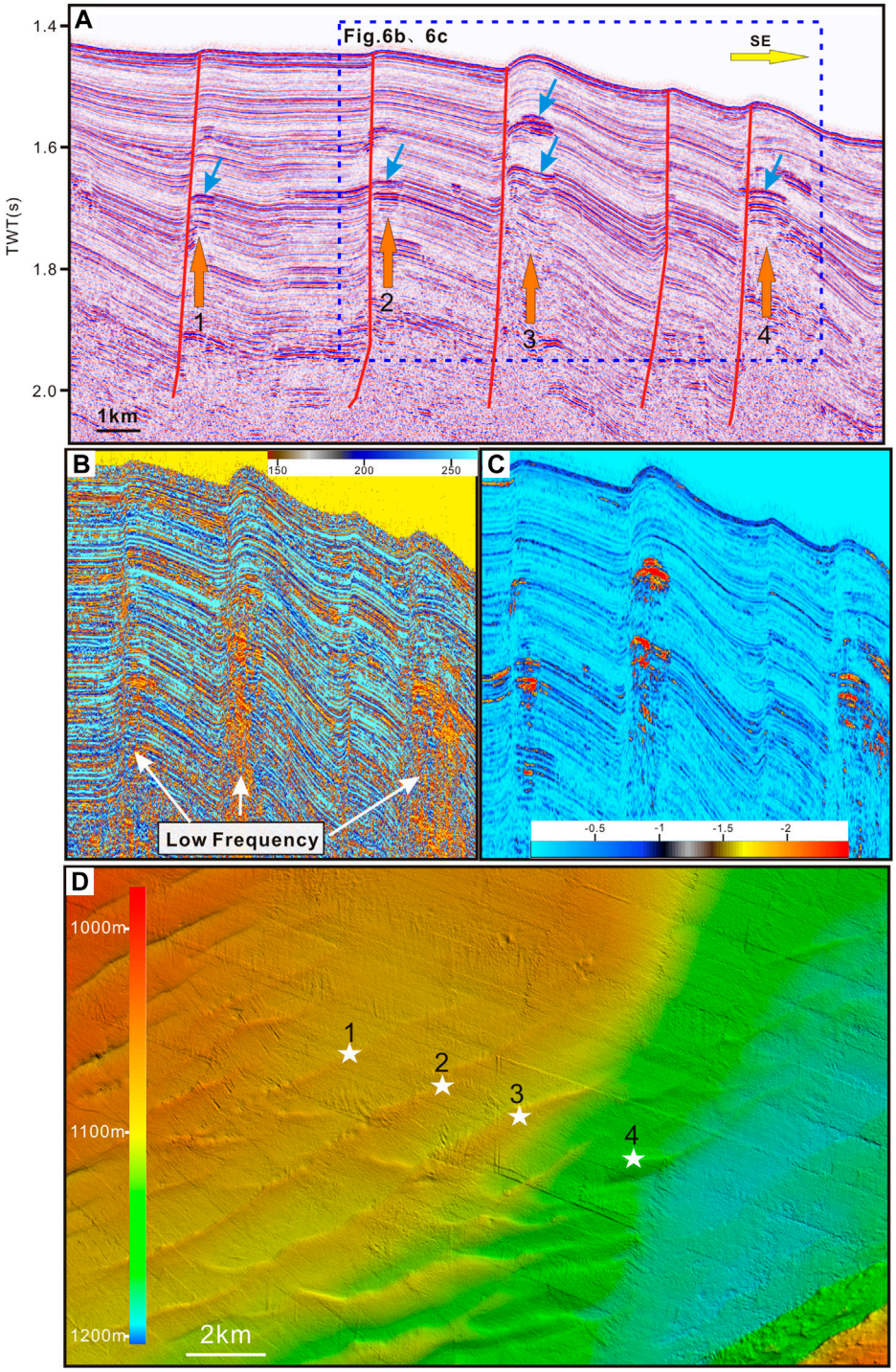

FIGURE 6
Type-C seismic chimneys. **(A)** The seismic profile shows type-C chimneys; **(B)** The Instantaneous frequency attribute profile; **(C)** The high-frequency attenuation attribute profile. The location of **(B)**; **(C)** is shown in Figure 6A. Low-frequency and high-frequency attenuation anomalies are all reveal the presence of fluids. **(D)** Multibeam bathymetry data reveal the relationship between chimneys and faults. White pentacles represent corresponding chimneys in Figure 6A. See locations in Figure 1B.

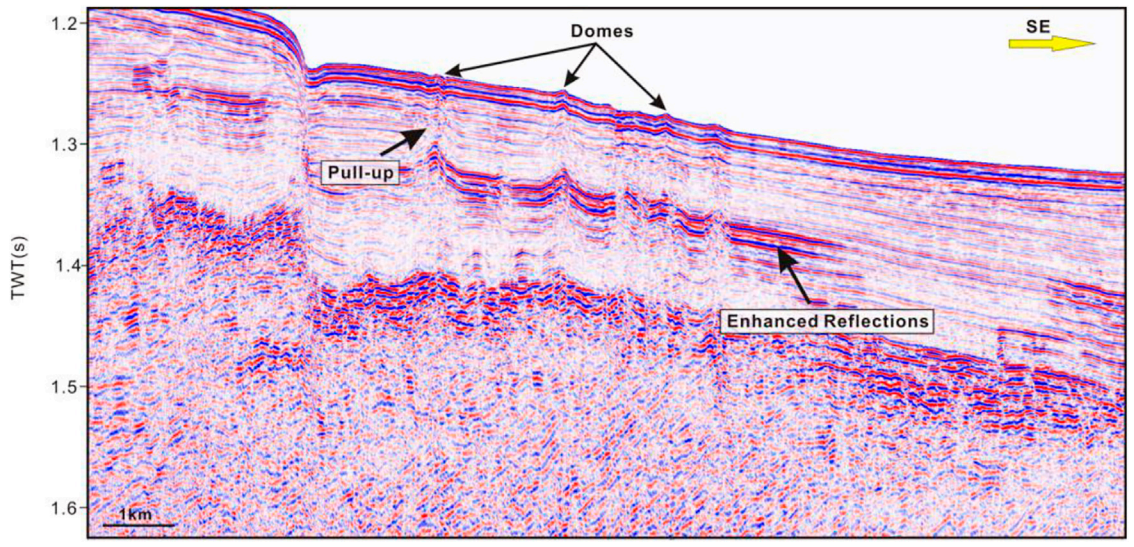

FIGURE 7
Seismic profile shows type-D seismic chimneys. This type of chimney is distinguished by elongated, adjacent to which several enhanced reflections have been observed. See locations in Figure 1B.

is probably the best for mapping frequency variation due to the presence of fluid in the shallow sediments. In the instantaneous frequency profiles (Figures 4B,D), the two chimneys depicted in Figure 4 all present low-frequency anomalies that differ from the surrounding area.

Type-B chimneys are vertically amplitude blanking or chaotic reflections with characteristics similar to type-A, but they do not extend to the seafloor. The majority of them are terminated by high amplitude patches or disturbed zones of comparable width to the underlying distorted zone (Figure 5).

Type-C seismic chimneys are appearing along the deep-seated faults. Reduced reflectivity or chaotic reflections occur within type-C chimneys, and several enhanced reflections or bright spots are sometimes observed within or immediately adjacent to them, like in Figure 6. Four chimneys with chaotic and enhanced reflections along faults are observed in Figure 6, and the distribution of enhanced reflections is limited to the local topographic heights of faults. The instantaneous frequency profile clearly shows low-frequency anomalies along faults, which are speculated to be caused by fluid flow. Due to energy dissipation, seismic waves pass through gas-bearing sedimentary, resulting in a relatively great attenuation effort, particularly for high-frequency signals. The seismic high-frequency attenuation attribute is frequently used to identify fluids by calculating the rate of seismic energy attenuation in the high-frequency band. Therefore, the high value observed in the high-frequency attenuation profile within chimneys suggests that the strata are fluid-rich. Above all, the faulting appears to have aided in decreasing the top seal's integrity or creating a more efficient escape path for the fluids underneath.

Type-D chimneys have elongated, slightly meandering bands and are accompanied by bright spots or enhanced reflections; their seismic signature is similar to that of pipes. Type-D chimneys usually appear in groups, and some of them connect domes on the present-day seafloor (Figure 7).

Seafloor domes

Submarine domes, which are thought to be a precursor of pockmark formation (Koch, et al., 2015), are the most widely observed evidence of potential methane fluid activity on the Western slope of the Okinawa Trough. Some submarine domes have been discovered in the study area (Figure 1). The majority of them are located in water depths ranging from 900 to 980 m. The height of the mud volcanoes ranges from less than 10 m to tens of meters above the seafloor. While the diameters at the base range between 100 and 600 m. The slope of the mud volcanoes varies between 1 and 16°.

The domes in the study area can be classified into three types based on their morphology using multibeam bathymetry. Type-A domes have flat edifices with gentle slopes on their crests, e.g., Figure 8A. The dome rises only about 2–4 m above the surrounding seabed, with slopesranging from 1° to 2°. The diameter of the dome is approximately 250 m. Type-B domes are relatively large and have a crater-like top with a complex, e.g., Figures 8B,C. The dome shown in Figure 8B has two crests: one main crest and the other crest. It rises 3–7 m above the surrounding seafloor and has a diameter of

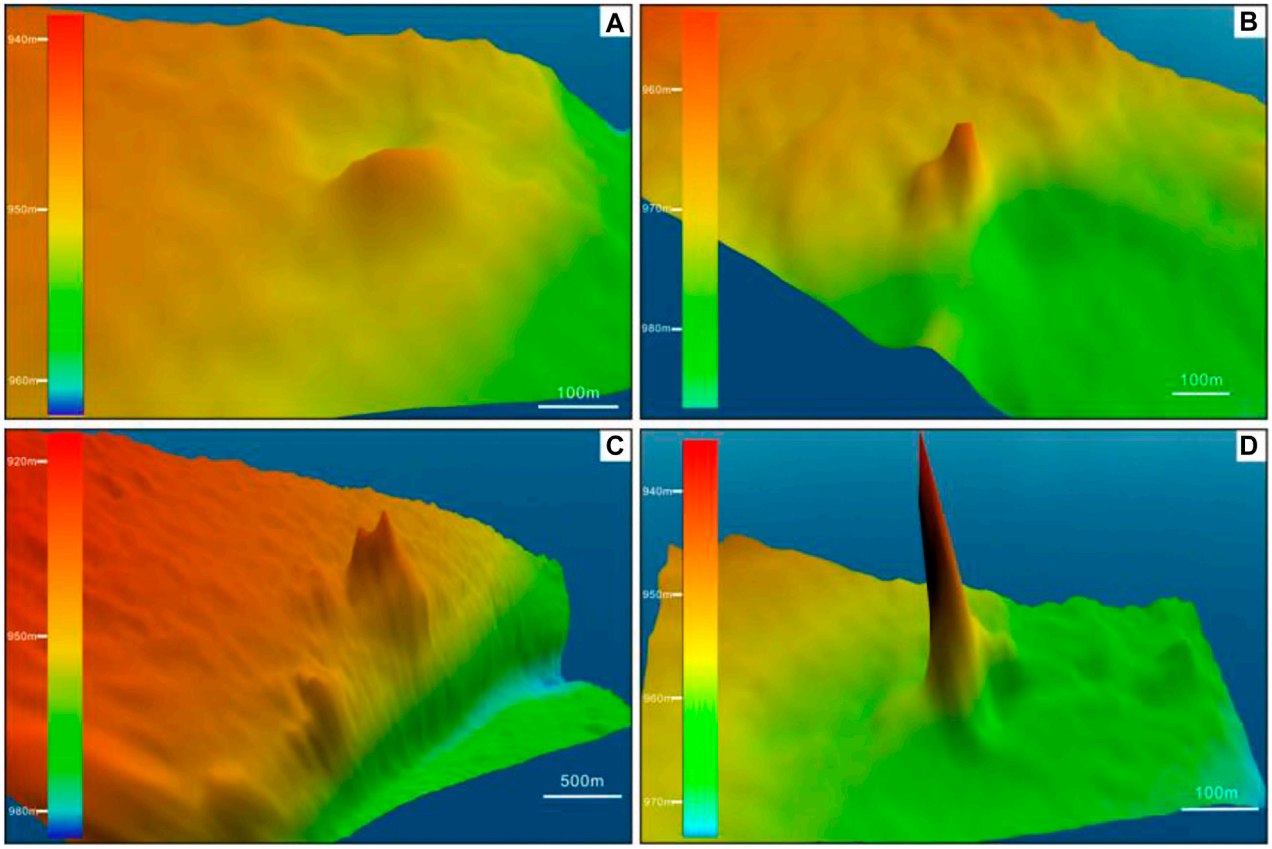

FIGURE 8
Multibeam data of domes. **(A)** An example of a type-A dome, which has flat edifices with gentle slopes on their crests; **(B)** and **(C)** Two examples of type-A domes, which have an irregular shape; **(D)** An example of a type-C dome, which are more conical with a relatively steep slope. See locations in Figure 1C.

about 250 m. The slope angle of type-B is larger than that of type-A, and the slope angle of Figure 8B is about 2°–5°. Figure 8C is the largest dome in the study area, and it also belongs to type-B. It has a more irregular shape. Each flank rises between 9 and 20 m above the seafloor and has a diameter ranging from 300 to 600 m. Type-C domes are more conical with relatively steep slopes. Figure 8D is an example of a type-C dome. The dome is 25 m tall with a 16-degree slope and a diameter of only 130 m. Multibeam bathymetry data reveals that several domes are surrounded by collapse subsidence structures in the study area. Some depressions are annular around the domes, as shown in Figures 9A,B, while the majority are on the side adjacent to the domes, such as Figures 9C,D. The depths of depressions are usually several meters below the seabed.

Sub-bottom profile and high-resolution seismic surveys were conducted in the study area, providing us with an excellent opportunity to better understand the internal characteristics of the submarine domes. Domes are cone-shaped, with internal seismic expressions of blanking or chaotic seismic facies. The majority of the domes in the study area are linked to a seismic chimney, such as the domes shown in Figure 10. The chaotic or blanking reflections in the feeder channels and surrounding strata on both sides of domes exhibit systematically distorted reflectors like pull-up reflections. Parabolic-shaped anomalies in the water column have been observed above domes, whereas flares are also observed in the same place based on multibeam bathymetry. The dome is shown in seismic data (Figure 11) and also presents acoustic flares in multibeam bathymetry data.

Pockmarks

Pockmarks, nearly circular depressions, are related to the escape of fluids and gases through the seafloor and are common on continental margins around the world (Cathles, et al., 2010; Dondurur, et al., 2011). Pockmarks are commonly located in areas where gas is present in near-surface sediments because of their association with the seepage of methane-rich fluids and

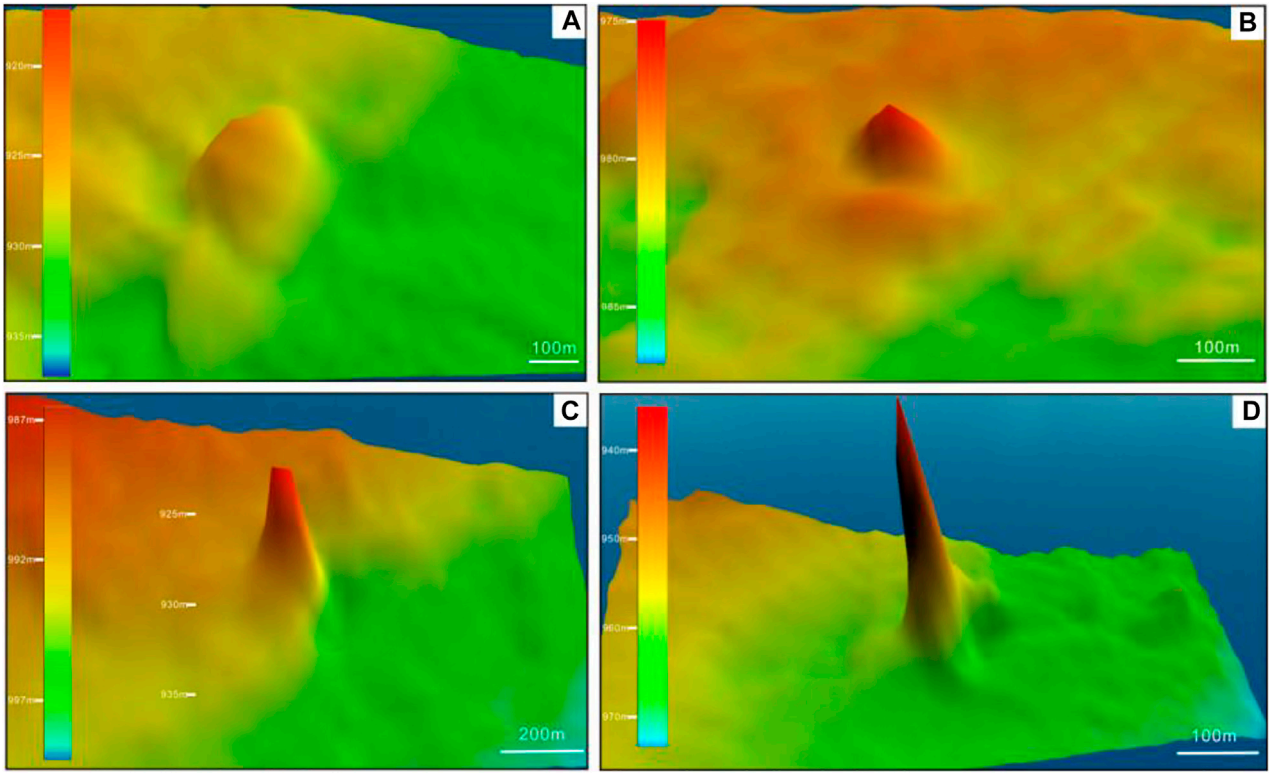

FIGURE 9
Mud volcanoes are surrounded by collapse subsidence structures. See locations in Figure 1C.

gases. Pockmarks form where fluids discharge rapidly enough through seafloor sediments to make them quick. As a result of focused fluid flow, seismic chimneys may, form beneath pockmarks representing feeding channels for the upward migrating fluids and gases (Petersen et al., 2010).

Several pockmarks connected to a chimney have been observed in the study area. Figure 12 depicts an example seismic profile for a pockmark. Below the pockmark, chaotic and push-down reflections have been observed, as well as enhanced reflections on both flanks. In general, there is common agreement in that these push-down reflections are partially explained as velocity effects caused by low-velocity material, such as the migration of fluids or free gas (Bünz et al., 2012).

Bright spots and enhanced reflections

Bright spots and enhanced reflections observed on seismic profiles have been attributed to gas accumulations, which are crucial indicators of methane-related fluids. Bright spots or enhanced reflections in the study area have reversed polarity compared to the seafloor reflection, strongly increased amplitudes compared to the background, and typically with sharp lateral terminations. These amplitude anomalies are commonly found within or surrounding seismic chimneys and the depths of these reflections are viable and do not appear to correlate with specific stratigraphic layers (Figure 4, Figure 5, Figure 6, Figure 7).

Discussion

Origin of methane

The shallow depth of the SMI suggests an extremely high methane seepage flux and active methane anaerobic oxidation processes in both sites. According to the variations features of methane concentration in the pore, the depths of SMI in sites 18-01 and 18-05 are 11.44 and 1.04 m, respectively, indicating high-flux methane fluid seepages. It also confirms that seepages are still active at both sites, as evidenced by gas flares observed in the multibeam data.

Geochemical analysis of pore water molecular ratios and isotopic compositions shows that C1/C2 vary from 960.53 to 1 120.75 in the core 18-01 and from 1 064.66 to 1 546.74 in the

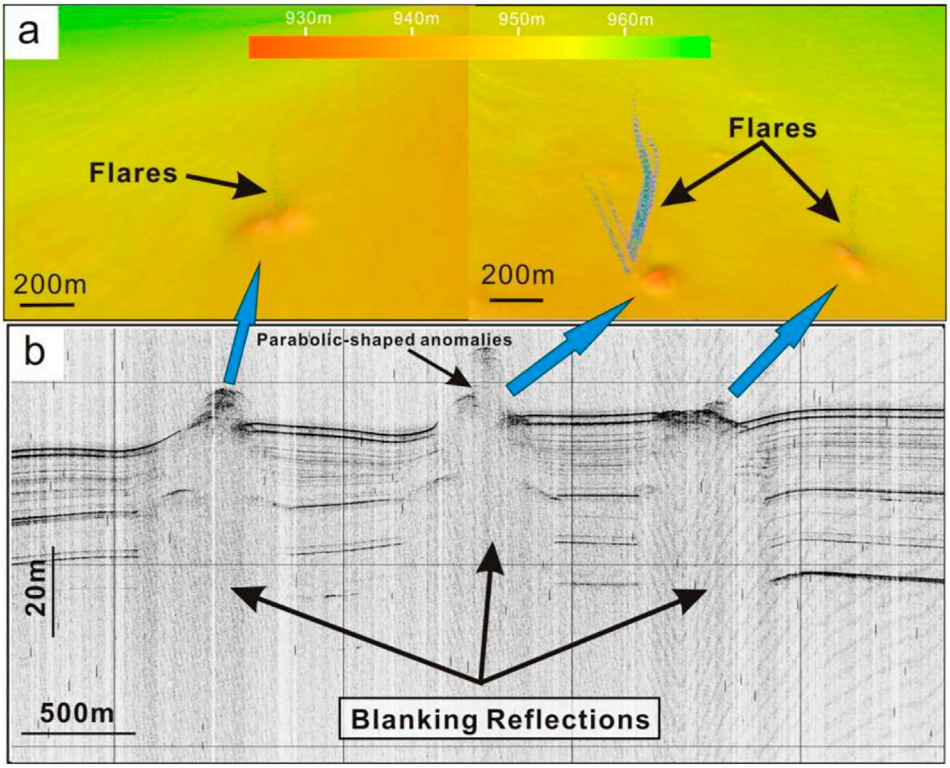

FIGURE 10
Multibeam and sub-bottom profile data show domes. **(A)** Bathymetry data show flares above domes. **(B)** The sub-bottom profile data show parabolic-shaped anomalies above domes. See locations in Figure 1C.

core 18-05, while the carbon isotopic values of pore water methane exhibit a variation from −36.07‰ to −56.60‰ V-PDB in the core 18-01 and from −36.10‰ to −62.92‰ V-PDB in the core 18-05 respectively. We concluded that the pore water methane is derived from a mixture of thermogenic and biogenic sources, primarily thermogenic, based on molecular ratios, stable carbon, and hydrogen isotopic compositions (Li, et al., 2020).

Relationships between observed geophysical anomalies and methane seepages

Seismic chimneys are usually interpreted as focused fluid flow structures that hydraulically connect deeper stratigraphic layers with the overburden. Their formation is believed to be governed by overpressure-induced hydrofracturing of an impermeable cap rock (Karstens and Berndt, 2015).

When methane-rich fluids pass through sediments, the primary sedimentary structures may be physically altered, resulting in the formation of new sediments and structures. Fluid flow reaching the seafloor can cause seabed expressions such as domes and pockmarks. In the study area, domes and pockmarks are frequently found above seismic chimneys, indicating that fluid migration plays an important role in their formation. Chimneys that reach the seafloor forming pockmarks likely indicate recent or active fluid venting (Horozal et al., 2017). Fluids are initially trapped beneath fine-grained sediments, which form a capillary seal, and when they accumulate to a certain thickness, the seal fails, releasing fluids into a chimney, where water is displaced as the chimney moves upward. Then, the surface begins to deform, and the first pockmarks appear when the chimney reaches about halfway to the seafloor. Following that, sediment deformation above the chimney worsen, and pockmarks become more common. The pockmarks merge into a large pockmark with dimensions similar to the chimney. The gas pocket quickly drains when the chimney reaches the surface. Capillary forces draw the water back into the fine layers of the failed portion of the seal by capillary forces, and it is healed. Fluids accumulate beneath it once more, and the chimney formation process may repeat itself if the fluid again accumulates to a thickness (Cathles, et al., 2010). However, Seafloor doming may indicate the early stages of fluid discharge (Horozal, et al., 2017). Accumulation of gaseous

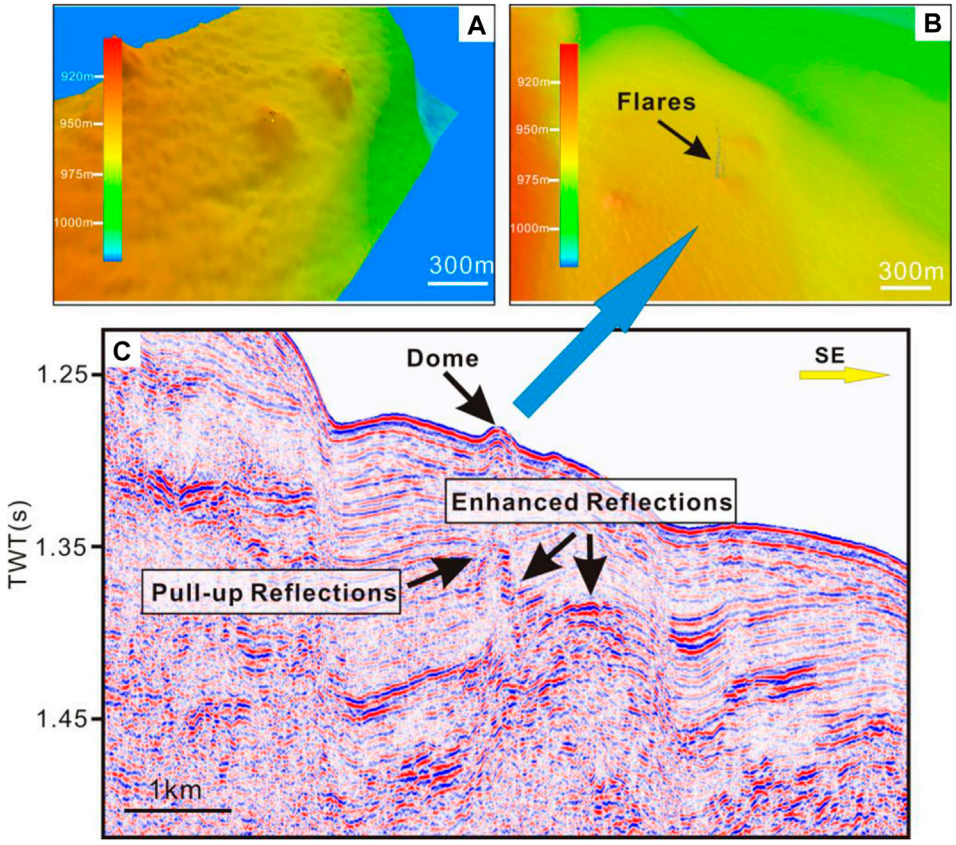

FIGURE 11
Multibeam data and seismic profile show a dome. **(A)** and **(B)** Bathymetry data show flare above the dome. **(C)** The seismic profile data of the dome. Several amplitude anomalies such as pull-up reflections and enhanced reflections were observed around the feeder zone of the dome. See locations in Figure 1C.

methane can generate seabed domes in soft cohesive sediments. The sediment may deform to accommodate the gas as a mechanical response to the increasing accumulation of fluids. Rising pressures from the accumulating fluids produce an upward force, which causes sediment doming (Roy et al., 2019). On the other hand, not all the chimneys extend to the seafloor, forming seafloor expressions, which may indicate that the venting is gradual and focused (Hillman et al., 2018).

In the study area, the multibeam echosounder and sub-bottom profile data have revealed several chimneys that reach the seafloor and form domes or pockmarks linked to flares, indicating that there is active upward migration of fluids occurring (Hillman, et al., 2018). However, there are also domes or pockmarks on the seafloor that are not associated with flares. The absence of flares may suggest that certain seep locations are currently inactive or are not releasing enough fluids, causing an anomaly in the water column (Roy, et al., 2019).

The enhanced reflections and bright spots could be caused by a variety of factors, including variations in lithology and the presence of authigenic carbonate deposits. The presence of free gas in the sediment pore space is another important explanation for enhanced reflections. The presence of free gas can induce p-wave velocity and a increase impedance contrast. This gives rise to an abnormally high amplitude from the top of the free gas zone. We suspect that the enhanced reflections are caused by the local accumulation of free gas within sediments due to their proximity to seismic chimneys.

Possible triggered factors of methane seepages

Multibeam bathymetric data shows that most methane seepages are discovered along steep bathymetric slopes or faults, indicating that the tectonic setting is an important factor triggering the methane seepages. The Okinawa Trough is a back-arc basin formed by extension within the continental lithosphere behind the Ryukyu trench-arc system. Regional extension weakens the overburden, which may result in a

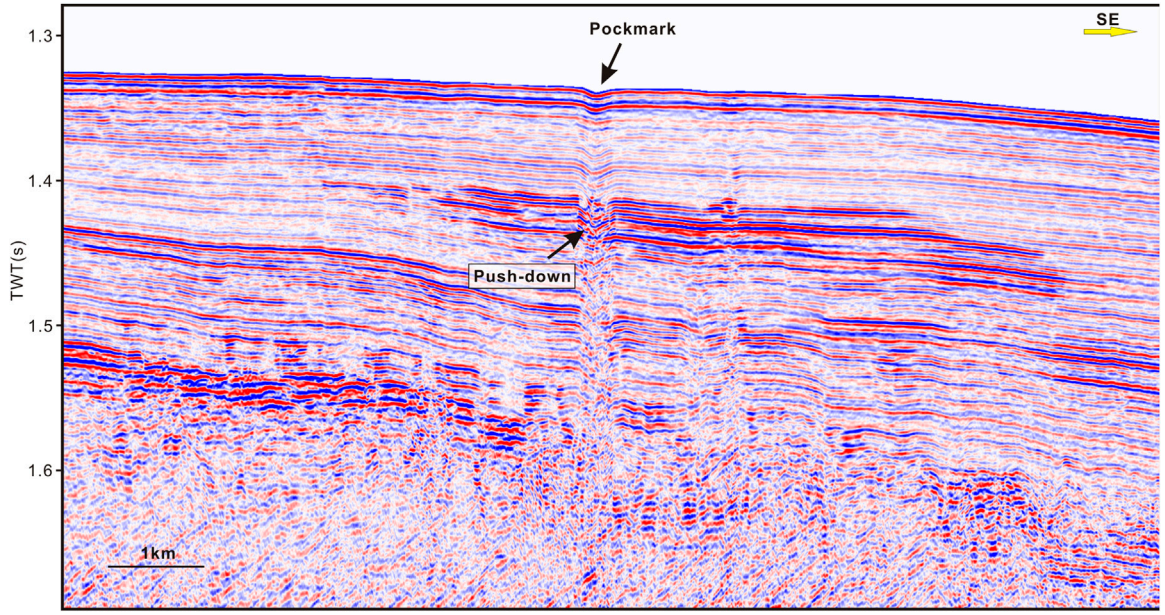

FIGURE 12
Seismic data show a pockmark associated with a seismic chimney. The presence of chaotic and push-down reflections has been observed below the pockmark, and enhanced reflections have been observed on both flanks. See locations in Figure 1C.

local decrease in the tensile strength of the cap rock, thereby reducing its resistance to hydrofracturing. Most chimneys and domes are distrubuted along the steep bathymetric slopes or faults that reveal the relationship. Based on the seismic profiles, numerous high-angle normal faults have developed in the study area. The orientation of these faults is roughly parallel to the great axis of the Okinawa Trough. In the study area, most seeps are associated with faults. Some of them are observed near faults, like Figure 7, Figure 11. Several blanking or chaotic reflections have been observed along faults, as well as enhanced reflections or bright spots that are commonly limited to local topographic heights of faults, like in Figure 6, indicating that faults may play an important role in fluid migration and accumulation.

Not all methane seepages are associated with faults. Several seepages in the study area do not exhibit a clear relationship with faults, as in Figure 12. Besides the tectonic setting, overpressure and rapid sedimentation are also important triggering factors of methane seepages. When the pore-fluid overpressure exceeds the internal forces or lithostatic pressure, vertical hydraulic fracturing may occur (Dimitrov, 2002). Overpressured sediments must be initially isolated by impermeable barriers. Such conduits form the opening of the impermeable barriers and provide a pathway for methane migration from the source. Overpressure generation is likely to be complicated and influenced by many factors (Lei et al., 2011). A rapid sedimentation rate is the main reason for overpressure in sedimentary layers (Milkov, 2000; Dimitrov, 2002; Talukder et al., 2008). The Okinawa Trough deposited a thick Pliocene-Quaternary sedimentary layer, up to thousands of meters. The sedimentary rate is much higher than in the oceans, especially on the Western slope, which could be up to 10–40 cm/ka. During glacial periods, the drop in sea-level caused the continental shelf to narrow. The YangtzeRiver transports a large amount of terrigenous source debris materials directly to the continental slope, where it is rapidly deposited near the Western slope of the Okinawa Trough (Berné et al., 2002). When overburden loads increase dramatically due to high sedimentation, pore fluids cannot be expelled leading to a reduction in pore volume that cannot be balanced. Then, pore fluid will bear part of the load pressure leading to hydrodynamic pressure being higher than the hydrostatic pressure, then producing the overpressure (Talukder et al., 2007).

Conclusion

Pore water geochemical analysis of seabed drilling indicated an extremely high methane seepage flux and active methane anaerobic oxidation processes on the Western slope of the Okinawa Trough. At the same time, numerous methane seepage-related features, such as seismic chimneys, pockmarks, submarine domes, and bright spots or enhanced reflection, have been observed in geophysics data near the drilling sites. These geophysical features are associated with each other. Chaotic or blanking reflections have been observed within seismic chimneys, and several enhanced reflections or bright spots are sometimes observed within or immediately adjacent to them.

Pockmarks and domes are often connected to seismic chimneys, indicating that fluid migration plays an important role in their formation. The different geophysical features may represent different stages of methane seepage. Fluid quickly drains, causing severe sediment deformation and forming pockmarks, whereas domes may be an indication of the early stages of fluid discharge. Chimneys that do not extend to the seafloor may indicate that the venting is gradual and focused. Flares linked to domes or pockmarks may indicate that the fluid migration is active.

Tectonic setting, overpressure, and rapid sedimentation all triggered the existence of methane seepages on the Western slope of the Okinawa Trough. Most chimneys and domes are distributed along the steep bathymetric slopes or faults, revealing that tectonic activity plays an important role in the methane seepages. Besides that, overpressure and rapid sedimentation are important triggering factors of methane seepages which do not exhibit a clear relationship with faults.

Data availability statement

The original contributions presented in the study are included in the article/supplementary material, further inquiries can be directed to the corresponding author.

Author contributions

DL performed the data analyses and wrote the manuscript. FC contributed to the conception of the study; QL contributed to the geochemical analysis of pore water. GY, YS, and GD contributed to acquiring the data used in the study. AL contributed to interpreting the multi-beam bathymetric data.

Funding

This research was financially supported by the Marine S&T Fund of Shandong Province for Pilot National Laboratory for Marine Science and Technology (Qingdao) (No. 2021QNLM020002), the Marine Geology Survey Program of China Geological Survey (No. DD20221707) and the projects of the National Key R&D Program of China (2018YFC0310001).

Conflict of interest

The authors declare that the research was conducted in the absence of any commercial or financial relationships that could be construed as a potential conflict of interest.

Publisher's note

All claims expressed in this article are solely those of the authors and do not necessarily represent those of their affiliated organizations, or those of the publisher, the editors and the reviewers. Any product that may be evaluated in this article, or claim that may be made by its manufacturer, is not guaranteed or endorsed by the publisher.

References

Benjamin, U. K., and Huuse, M. (2017). Seafloor and buried mounds on the Western slope of the Niger Delta. *Mar. Petroleum Geol.* 83, 158–173. doi:10.1016/j.marpetgeo.2017.02.023

Berndt, C., Feseker, T., Treude, T., Krastel, S., Liebetrau, V., Niemann, H., et al. (2014). Temporal constraints on hydrate-controlled methane seepage off svalbard. *Science* 343 (6168), 284–287. doi:10.1126/science.1246298

Berné, S., Vagner, P., Guichard, F., Lericolais, G., Liu, Z., Trentesaux, A., et al. (2002). Pleistocene forced regressions and tidal sand ridges in the East China Sea. *Mar. Geol.* 188 (3), 293–315. doi:10.1016/s0025-3227(02)00446-2

Bünz, S., Polyanov, S., Vadakkepuliyambatta, S., Consolaro, C., and Mienert, J. (2012). Active gas venting through hydrate-bearing sediments on the Vestnesa Ridge, offshore W-Svalbard. *Mar. Geol.* 332–334 (0), 189–197. doi:10.1016/j.margeo.2012.09.012

Callow, B., Bull, J. M., Provenzano, G., Bottner, C., Birinci, H., Robinson, A. H., et al. (2021). Seismic chimney characterisation in the North Sea – implications for pockmark formation and shallow gas migration. *Mar. Petroleum Geol.* 133, 105301. doi:10.1016/j.marpetgeo.2021.105301

Cathles, L. M., Su, Z., and Chen, D. (2010). The physics of gas chimney and pockmark formation, with implications for assessment of seafloor hazards and gas sequestration. *Mar. Petroleum Geol.* 27 (1), 82–91. doi:10.1016/j.marpetgeo.2009.09.010

Chen, L., Chiang, H-T., Wu, J-N., Chiao, L. Y., Shyu, C. T., Liu, C. S., et al. (2020). The focus thermal study around the spreading center of southwestern Okinawa trough. *Tectonophysics* 796, 228649. doi:10.1016/j.tecto.2020.228649

Chun, J-H., Ryu, B-J., Son, B-K., Kim, J. H., Lee, J. Y., Bahk, J. J., et al. (2011). Sediment mounds and other sedimentary features related to hydrate occurrences in a columnar seismic blanking zone of the Ulleung Basin, East Sea, Korea. *Mar. Petroleum Geol.* 28 (10), 1787–1800. doi:10.1016/j.marpetgeo.2011.06.006

Crutchley, G. J., Berndt, C., Geiger, S., Klaeschen, D., Papenberg, C., Klaucke, I., et al. (2013). Drivers of focused fluid flow and methane seepage at south Hydrate Ridge, offshore Oregon, USA. *Geology* 41 (5), 551–554. doi:10.1130/g34057.1

Dewangan, P., Sriram, G., Kumar, A., Mazumdar, A., Peketi, A., Mahale, V., et al. (2021). Widespread occurrence of methane seeps in deep-water regions of Krishna-Godavari basin, Bay of Bengal. *Mar. Petroleum Geol.* 124, 104783. doi:10.1016/j.marpetgeo.2020.104783

Dimitrov, L. I. (2002). Mud volcanoes—The most important pathway for degassing deeply buried sediments. *Earth-Science Rev.* 59 (1), 49–76. doi:10.1016/s0012-8252(02)00069-7

Dixit, A., and Mandal, A. (2020). Detection of gas chimney and its linkage with deep-seated reservoir in poseidon, NW shelf, Australia from 3D seismic data using multi-attribute analysis and artificial neural network approach. *J. Nat. Gas Sci. Eng.* 83, 103586. doi:10.1016/j.jngse.2020.103586

Dondurur, D., Çifçi, G., Drahor, M. G., and Coskun, S. (2011). Acoustic evidence of shallow gas accumulations and active pockmarks in the İzmir Gulf, Aegean sea. *Mar. Petroleum Geol.* 28 (8), 1505–1516. doi:10.1016/j.marpetgeo.2011.05.001

Graves, C. A., James, R. H., Sapart, C. J., Stott, A. W., Wright, I. C., Berndt, C., et al. (2017). Methane in shallow subsurface sediments at the landward limit of the gas hydrate stability zone offshore Western Svalbard. *Geochimica Cosmochimica Acta* 198, 419–438. doi:10.1016/j.gca.2016.11.015

Guan, H., Liu, L., Hu, Y., Li, S., Li, N., Sun, Z., et al. (2022). Rising bottom-water temperatures induced methane release during the middle Holocene in the Okinawa Trough, East China Sea. *Chem. Geol.* 590, 120707. doi:10.1016/j.chemgeo.2022.120707

Guan, H., Sun, Z., Mao, S., Xu, L., Cao, H., Geng, W., et al. (2019). Authigenic carbonate formation revealed by lipid biomarker inventory at hydrocarbon seeps: A case study from the Okinawa Trough. *Mar. Petroleum Geol.* 101, 502–511. doi:10.1016/j.marpetgeo.2018.12.028

Gullapalli, S., Dewangan, P., Kumar, A., Dakara, G., and Mishra, C. (2019). Seismic evidence of free gas migration through the gas hydrate stability zone (GHSZ) and active methane seep in Krishna-Godavari offshore basin. *Mar. Petroleum Geol.* 110, 695–705. doi:10.1016/j.marpetgeo.2019.07.052

He, J. X., Wang, S. H., Zhang, W., Yan, W., and Lu, Z. (2016). Characteristics of mud diapirs and mud volcanoes and their relationship to oil and gas migration and accumulation in a marginal basin of the northern South China Sea. *Environ. Earth Sci.* 75 (15), 1122. doi:10.1007/s12665-016-5894-9

Hillman, J. I. T., Crutchley, G. J., and Kroeger, K. F. (2020). Investigating the role of faults in fluid migration and gas hydrate formation along the southern Hikurangi Margin, New Zealand. *Mar. Geophys. Res.* 41 (1), 8. doi:10.1007/s11001-020-09400-2

Hillman, J. I. T., Klaucke, I., Bialas, J., Feldman, H., Drexler, T., Awwiller, D., et al. (2018). Gas migration pathways and slope failures in the danube fan, Black Sea. *Mar. Petroleum Geol.* 92, 1069–1084. doi:10.1016/j.marpetgeo.2018.03.025

Horozal, S., Bahk, J. J., Urgeles, R., Kim, G. Y., Cukur, D., Kim, S. P., et al. (2017). Mapping gas hydrate and fluid flow indicators and modeling gas hydrate stability zone (GHSZ) in the Ulleung Basin, East (Japan) Sea: Potential linkage between the occurrence of mass failures and gas hydrate dissociation. *Mar. Petroleum Geol.* 80, 171–191. doi:10.1016/j.marpetgeo.2016.12.001

Karstens, J., and Berndt, C. (2015). Seismic chimneys in the Southern Viking Graben – implications for palaeo fluid migration and overpressure evolution. *Earth Planet. Sci. Lett.* 412 (0), 88–100. doi:10.1016/j.epsl.2014.12.017

Kempka, T., Unger, V., and Kühn, M. (2016). Seismic chimney formation induced by upward-migrating methane in the nordland group, southern viking graben. *Energy Procedia* 97, 427–432. doi:10.1016/j.egypro.2016.10.040

Koch, S., Berndt, C., Bialas, J., Haeckel, M., Crutchley, G., Papenberg, C., et al. (2015). Gas-controlled seafloor doming. *Geology* 43 (7), 571–574. doi:10.1130/g36596.1

Krabbenhoeft, A., Bialas, J., Klaucke, I., Crutchley, G., Papenberg, C., and Netzeband, G. L. (2013). Patterns of subsurface fluid-flow at cold seeps: The Hikurangi Margin, offshore New Zealand. *Mar. Petroleum Geol.* 39 (1), 59–73. doi:10.1016/j.marpetgeo.2012.09.008

Lei, C., Ren, J., Clift, P. D., Wang, Z., Li, X., and Tong, C. (2011). The structure and formation of diapirs in the yinggehai–song hong basin, south China sea. *Mar. Petroleum Geol.* 28 (5), 980–991. doi:10.1016/j.marpetgeo.2011.01.001

Li, A., Cai, F., Wu, N., Li, Q., Yan, G., Sun, Y., et al. (2021). Structural controls on widespread methane seeps in the back-arc basin of the Mid-Okinawa Trough. *Ore Geol. Rev.* 129, 103950. doi:10.1016/j.oregeorev.2020.103950

Li, Q., Cai, F., Liang, J., Shao, H., Dong, G., Wang, F., et al. (2015). Geochemical constraints on the methane seep activity in Western slope of the middle Okinawa Trough, the East China Sea. *Sci. China Earth Sci.* 58, 986–995. doi:10.1007/s11430-014-5034-x

Li, Q., Cai, F., Yan, G., Sun, Y., Li, A., Liu, D., et al. (2020). Origin of pore water methane recovered from mud volcanos in the Okinawa Trough. *Mar. Geol. Front.* 36 (9), 79–86. doi:10.16028/j.1009-2722.2020.062

Logan, G. A., Jones, A. T., Kennard, J. M., Ryan, G. J., and Rollet, N. (2010). Australian offshore natural hydrocarbon seepage studies, a review and re-evaluation. *Mar. Petroleum Geol.* 27 (1), 26–45. doi:10.1016/j.marpetgeo.2009.07.002

Luo, D., Cai, F., and Wu, Z. (2017). Numerical simulation for accuracy of velocity analysis in small-scale high-resolution marine multichannel seismic technology. *J. Ocean. Univ. China* 16 (3), 370–382. doi:10.1007/s11802-017-3145-7

Luo, D., Cai, F., Wu, Z., Yan, G., and Du, R. (2019). The key technologies of marine small scale high resolution multichannel seismic high-precision imaging. *Chin. J. Geophys.* 62 (2), 730–742. (in Chinese). doi:10.6038/cjg2019M0178

Magalhaes, V. H., Buffett, B., Archer, D., McGuire, P. C., Pinheiro, L. M., and Gardner, J. M. (2019). Effects of oceanographic changes on controlling the stability of gas hydrates and the formation of authigenic carbonates at mud volcanoes and seepage sites on the Iberian margin of the Gulf of Cadiz. *Mar. Geol.* 412, 69–80. doi:10.1016/j.margeo.2019.03.002

Milkov, A. V. (2000). Worldwide distribution of submarine mud volcanoes and associated gas hydrates. *Mar. Geol.* 167 (1–2), 29–42. doi:10.1016/s0025-3227(00)00022-0

Miller, P., Dasgupta, S., and Shelander, D. (2012). Seismic imaging of migration pathways by advanced attribute analysis, Alaminos Canyon 21, Gulf of Mexico. *Mar. Petroleum Geol.* 34 (1), 111–118. doi:10.1016/j.marpetgeo.2011.09.005

Minami, H., Okada, C., Saito, K., and Ohara, Y. (2022). Evidence of an active rift zone in the northern Okinawa Trough. *Mar. Geol.* 443, 106666. doi:10.1016/j.margeo.2021.106666

Mohammedyasin, S. M., Lippard, S. J., Omosanya, K. O., Johansen, S., and Harishidayat, D. (2016). Deep-seated faults and hydrocarbon leakage in the snøhvit gas field, hammerfest basin, southwestern barents sea. *Mar. Petroleum Geol.* 77, 160–178. doi:10.1016/j.marpetgeo.2016.06.011

Netzeband, G. L., Krabbenhoeft, A., Zillmer, M., Petersen, C., Papenberg, C., and Bialas, J. (2010). The structures beneath submarine methane seeps: Seismic evidence from Opouawe Bank, Hikurangi Margin, New Zealand. *Mar. Geol.* 272 (1–4), 59–70. doi:10.1016/j.margeo.2009.07.005

Ning, X., Shiguo, W., Buqing, S., Bing, L., Liangqing, X., Xiujuan, W., et al. (2009). Gas hydrate associated with mud diapirs in southern Okinawa Trough. *Mar. Petroleum Geol.* 26 (8), 1413–1418. doi:10.1016/j.marpetgeo.2008.10.001

Palomino, D., López-González, N., Vázquez, J-T., Fernandez-Salas, L. M., Rueda, J. L., Sanchez-Leal, R., et al. (2016). Multidisciplinary study of mud volcanoes and diapirs and their relationship to seepages and bottom currents in the Gulf of Cádiz continental slope (northeastern sector). *Mar. Geol.* 378, 196–212. doi:10.1016/j.margeo.2015.10.001

Park, J-O., Tokuyama, H., Shinohara, M., Suyehiro, K., and Taira, A. (1998). Seismic record of tectonic evolution and backarc rifting in the southern Ryukyu island arc system. *Tectonophysics* 294 (1), 21–42. doi:10.1016/s0040-1951(98)00150-4

Paull, C. K., Hecker, B., Commeau, R., Freeman-Lynde, R. P., Neumann, C., Corso, W. P., et al. (1984). Biological communities at the Florida escarpment resemble hydrothermal vent taxa. *Science* 226 (4677), 965–967. doi:10.1126/science.226.4677.965

Petersen, C. J., Bünz, S., Hustoft, S., Mienert, J., and Klaeschen, D. (2010). High-resolution P-Cable 3D seismic imaging of gas chimney structures in gas hydrated sediments of an Arctic sediment drift. *Mar. Petroleum Geol.* 27 (9), 1981–1994. doi:10.1016/j.marpetgeo.2010.06.006

Rovere, M., Gamberi, F., Mercorella, A., Rashed, H., Gallerani, A., Leidi, E., et al. (2014). Venting and seepage systems associated with mud volcanoes and mud diapirs in the southern Tyrrhenian Sea. *Mar. Geol.* 347, 153–171. doi:10.1016/j.margeo.2013.11.013

Roy, S., Senger, K., Hovland, M., Romer, M., and Braathen, A. (2019). Geological controls on shallow gas distribution and seafloor seepage in an Arctic fjord of Spitsbergen, Norway. *Mar. Petroleum Geol.* 107, 237–254. doi:10.1016/j.marpetgeo.2019.05.021

Schwalenberg, K., Haeckel, M., Poort, J., and Jegen, M. (2010). Evaluation of gas hydrate deposits in an active seep area using marine controlled source electromagnetics: Results from Opouawe Bank, Hikurangi Margin, New Zealand. *Mar. Geol.* 272 (1–4), 79–88. doi:10.1016/j.margeo.2009.07.006

Shinjo, R., and Kato, Y. (2000). Geochemical constraints on the origin of bimodal magmatism at the Okinawa Trough, an incipient back-arc basin. *Lithos* 54 (3–4), 117–137. doi:10.1016/s0024-4937(00)00034-7

Shnyukov, E. F. (2013). Mud volcanoes of the Black Sea as a prospecting indicator of methane gas hydrates. *Lithol. Min. Resour.* 48 (2), 114–121. doi:10.1134/s0024490213010045

Sibuet, J. C., Deffontaines, B., Hsu, S. K., Thareau, N., Le Formal, J. P., and Liu, C. S. (1998). Okinawa trough backarc basin: Early tectonic and magmatic evolution. *J. Geophys. Res.* 103 (B12), 30245–30267. doi:10.1029/98jb01823

Sibuet, J-C., Letouzey, J., Barbier, F., Charvet, J., Foucher, J. P., Hilde, T. W. C., et al. (1987). Back arc extension in the Okinawa Trough. *J. Geophys. Res.* 92 (B13), 14041–14063. doi:10.1029/jb092ib13p14041

Somoza, L., León, R., Medialdea, T., Perez, L. F., Gonzalez, F. J., and Maldonado, A. (2014). Seafloor mounds, craters and depressions linked to seismic chimneys breaching fossilized diagenetic bottom simulating reflectors in the central and southern Scotia Sea, Antarctica. *Glob. Planet. Change* 123 (0), 359–373. Part B. doi:10.1016/j.gloplacha.2014.08.004

Suess, E. (2014). Marine cold seeps and their manifestations: Geological control, biogeochemical criteria and environmental conditions. *Int. J. Earth Sci.* 103 (7), 1889–1916. doi:10.1007/s00531-014-1010-0

Sun, Z., Wei, H., Zhang, X., Shang, L., Yin, X., Sun, Y., et al. (2015). A unique Fe-rich carbonate chimney associated with cold seeps in the Northern Okinawa Trough, East China Sea. *Deep Sea Res. Part I Oceanogr. Res. Pap.* 95 (0), 37–53. doi:10.1016/j.dsr.2014.10.005

Talukder, A. R., Bialas, J., Klaeschen, D., Brueckmann, W., Reston, T., and Petersen, J. (2008). Tectonic framework of the mud mounds, associated BSRs and submarine landslides, offshore Nicaragua Pacific margin. *J. Geol. Soc. Lond.* 165, 167–176. doi:10.1144/0016-76492007-012

Talukder, A. R., Bialas, J., Klaeschen, D., Buerk, D., Brueckmann, W., Reston, T., et al. (2007). High-resolution, deep tow, multichannel seismic and sidescan sonar survey of the submarine mounds and associated BSR off Nicaragua Pacific margin. *Mar. Geol.* 241 (1–4), 33–43. doi:10.1016/j.margeo.2007.03.002

Tsai, C-H., Hsu, S-K., Chen, S-C., Wang, S. Y., Lin, L. K., Huang, P. C., et al. (2021). Active tectonics and volcanism in the southernmost Okinawa Trough back-arc basin derived from deep-towed sonar surveys. *Tectonophysics* 817, 229047. doi:10.1016/j.tecto.2021.229047

Tsunogai, U., Maegawa, K., Sato, S., Komatsu, D. D., Nakagawa, F., Toki, T., et al. (2012). Coseimic massive methane release from a submarine mud volcano. *Earth Planet. Sci. Lett.* 341-344, 79–85. doi:10.1016/j.epsl.2012.06.004

Van Rensbergen, P., De Batist, M., Klerkx, J., Hus, R., Poort, J., Vanneste, M., et al. (2002). Sublacustrine mud volcanoes and methane seeps caused by dissociation of gas hydrates in Lake Baikal. *Geol.* 30 (7), 631–634. doi:10.1130/0091-7613(2002)030<0631:smvams>2.0.co;2

Wan, Z., Xu, X., Wang, X., Xia, B., and Sun, Y. (2017). Geothermal analysis of boreholes in the Shenhu gas hydrate drilling area, northern South China Sea: Influence of mud diapirs on hydrate occurrence. *J. Petroleum Sci. Eng.* 158, 424–432. doi:10.1016/j.petrol.2017.08.053

Wang, M., Li, Q., Cai, F., Liang, J., Yan, G., Wang, Z., et al. (2019). Formation of authigenic carbonates at a methane seep site in the middle Okinawa Trough, East China Sea. *J. Asian Earth Sci.* 185, 104028. doi:10.1016/j.jseaes.2019.104028

Wang, X., Liu, B., Qian, J., Zhang, X., Guo, Y., Su, P., et al. (2018). Geophysical evidence for gas hydrate accumulation related to methane seepage in the Taixinan Basin, South China Sea. *J. Asian Earth Sci.* 168, 27–37. doi:10.1016/j.jseaes.2017.11.011

Wei, J., Wu, T., Deng, X., Haider, S. W., Kahkashan, S., and Yang, S. (2021). Seafloor methane emission on the Makran continental margin. *Sci. Total Environ.* 801, 149772. doi:10.1016/j.scitotenv.2021.149772

Wenau, S., Spiess, V., Pape, T., and Fekete, N. (2015). Cold seeps at the salt front in the Lower Congo Basin I: Current methane accumulation and active seepage. *Mar. Petroleum Geol.* 67, 894–908. doi:10.1016/j.marpetgeo.2014.07.032

Williscroft, K., Grasby, S. E., Beauchamp, B., Little, C. T., Dewing, K., Birgel, D., et al. (2017). Extensive early cretaceous (albian) methane seepage on ellef ringnes island, Canadian high arctic. *Geol. Soc. Am. Bull.* 129 (7), 788–805. doi:10.1130/b31601.1

Xing, J., Jiang, X., and Li, D. (2016). Seismic study of the mud diapir structures in the Okinawa Trough. *Geol. J.* 51, 203–208. doi:10.1002/gj.2824

Xu, C., Wu, N., Sun, Z., Zhang, X., Geng, W., Cao, H., et al. (2021). Assessing methane cycling in the seep sediments of the mid-Okinawa Trough: Insights from pore-water geochemistry and numerical modeling. *Ore Geol. Rev.* 129, 103909. doi:10.1016/j.oregeorev.2020.103909

Xu, C., Wu, N., Sun, Z., Zhang, X., Geng, W., Cao, H., et al. (2018). Methane seepage inferred from pore water geochemistry in shallow sediments in the Western slope of the Mid-Okinawa Trough. *Mar. Petroleum Geol.* 98, 306–315. doi:10.1016/j.marpetgeo.2018.08.021

Yin, P., Berné, S., Vagner, P., Loubrieu, B., and Liu, Z. (2003). Mud volcanoes at the shelf margin of the East China Sea. *Mar. Geol.* 194 (3–4), 135–149. doi:10.1016/s0025-3227(02)00678-3

frontiers | Frontiers in Earth Science

TYPE Original Research
PUBLISHED 02 September 2022
DOI 10.3389/feart.2022.990562

OPEN ACCESS

EDITED BY
Pibo Su,
Guangzhou Marine Geological Survey, China

REVIEWED BY
Pin Li,
Shanghai Jiao Tong University, China
Jie Ma,
China National Offshore Oil Corporation, China

*CORRESPONDENCE
Tao Zhang,
ztdrc@sina.com

SPECIALTY SECTION
This article was submitted to Economic Geology, a section of the journal Frontiers in Earth Science

RECEIVED 10 July 2022
ACCEPTED 25 July 2022
PUBLISHED 02 September 2022

CITATION
Wu L, Zhang T, Zhang H, Sui Y, Yu X and Miao M (2022), Economic evaluation of production capacity for natural gas hydrate industrial exploitation in the South China Sea.
Front. Earth Sci. 10:990562.
doi: 10.3389/feart.2022.990562

Economic evaluation of production capacity for natural gas hydrate industrial exploitation in the South China Sea

Linqiang Wu[1,2], Tao Zhang[2]*, Hongtao Zhang[1], Yuzhang Sui[3], Xinghe Yu[4] and Miao Miao[1,5]

[1]School of Earth Sciences and Resource, China University of Geosciences (Beijing), Beijing, China, [2]Development and Research Center, China Geological Survey, Beijing, China, [3]China Geological Survey, Beijing, China, [4]School of Energy, China University of Geosciences (Beijing), Beijing, China, [5]Oil and Gas Survey, China Geological Survey, Beijing, China

Natural gas hydrate (NGH) is a worldwide strategic and prospecting commercial resource in the 21st century. The industrialization of NGH has great strategic significance for the achievement of peak carbon dioxide emissions and carbon neutrality. Prior to its industrialization, an economic evaluation of production capacity for each well per day should be conducted to determine whether it is profitable at different given gas prices. In this study, a new hybrid method based on the discounted cash flow (DCF) method and the energy return on investment (EROI) method is used to estimate the economic production rate of NGH exploitation at four different gas price scenarios. The results show that the lowest production rate to make NGH exploitation economic ranges from 1.96 to 29.60 × 10^4 m^3/d/well. With the change in the number of wells, gas–water ratio, gas price, decreasing rate in production cost, and sensitivity analysis are carried out. It shows that all these key factors have a significantly negative effect on the economic production rate initially, and then the sensitivity to the economic production rate will become lower and lower with the rising value of each key factor.

KEYWORDS

natural gas hydrate (NGH), economic evaluation, discounted cash flow (DCF), energy return on investment (EROI), economic production rate

1 Introduction

Over the past two centuries, industrial civilization has brought about substantial progress but also caused increasingly severe environmental and climate problems. A low carbon transformation of energy use is the key pillar to reducing CO_2 emissions toward a carbon neutral world. Renewable energy like solar and wind energy may dominate our energy mix completely in the future, but considering its tiny contribution to energy supply at present, the timing is still very uncertain (Michael and Arthur, 2019). According to the

BP Statistical Review of World Energy, renewable energy accounts for only about 18% of the world's total primary energy consumption in 2021 (BP, 2022). In the transition to a low-carbon energy future, natural gas is considered a clean, efficient energy source that will likely become an important alternative to coal and oil and a transitional fuel for renewable energy (Javed, 2016; Zheng et al., 2016). With rapid global industrialization, the world's demand for natural gas will grow sharply in the coming decades and will reach 4.9 trillion cubic meters (tcm) by 2040 (Sanja, 2021).

As conventional natural gas resources become depleted, exploration for unconventional gas resources is becoming increasingly important (Vedachalam et al., 2015; Kong et al., 2018). Natural gas hydrate (NGH), an ice-like carrier substance for natural gas formed by gas molecules and water molecules under high-pressure and low-temperature conditions (Sloan and Koh, 2007), is an unconventional gas resource and contains the largest gas resources remaining on the Earth. It is estimated that the gross carbon reserve of NGH is about twice as much as the total reserve of all the other fossil energy including oil, coal, and natural gas (Makogon, 1981; Kvenvolden, 1988; Englezos, 1993). NGH has been discovered worldwide in polar regions, normally associated with onshore and offshore permafrost, and in the sediment of outer continental and insular margins, with 90% of the ocean serving as potential areas for NGH deposits (Kvenvolden, 1993). In theory, when appropriate hydrate expansion factors are considered, 1 m^3 of NGH contains up to 164 m^3 of natural gas at standard conditions (Kvenvolden, 1993). According to preliminary estimates, the total global NGH reserve is approximately 1.5×10^4 tcm (Makogon et al., 2005), which is large enough to replace the increasingly depleted traditional oil and gas resources. As a result, NGH is a worldwide strategic and prospecting commercial resource concerned by many countries in the 21st century (Makogon et al., 2005), and its industrialization has great significance for the world's energy mix optimization, green development, and the achievement of peak carbon dioxide emissions and carbon neutrality.

Natural gas from NGH deposits can be theoretically produced by one or a combination of three main methods (Moridis and Sloan, 2007): 1. depressurization, in which the pressure is reduced below the equilibrium value at the system temperature; 2. thermal stimulation, in which the temperature is raised above the equilibrium value at the system pressure; and 3. injection of inhibitors such as salt and/or alcohol, by which the thermodynamic hydrate stability boundary is shifted to lower temperatures and higher pressures, thus inducing dissociation and gas release. Depressurization is thought to be the most technically efficient means of production from NGH deposits (Walsh et al., 2009; Michael and Arthur, 2019).

Over the last two decades, China has been attaching great importance to research on gas hydrate and has found a total amount of approximately 84 tcm of NGH reserves onshore and offshore, including the South China Sea, the East China Sea, and the Qinghai–Tibet Plateau, nearly 77% of which is distributed in the South China Sea (Tan et al., 2016). In 2013 and 2016, two NGH reserves with natural gas resources of more than 100 billion m^3 each were discovered in the eastern offshore area of the Perl River Mouth basin and Shenhu area in the South China Sea (Yang et al., 2017). The NGH industrialization consists of five general stages, namely, the theoretical research and simulation experiment, the exploratory production test, the experimental production test, the productive production test, and the commercial production stages (Hao, 2022). In 2017, China successfully conducted its first offshore exploratory production test from clayey silt reservoirs, the most widely distributed NGH reservoirs in the world. It lasted for 60 days continuously and stably, yielding cumulative gas production of 30.9×10^4 m^3 (Li et al., 2018). Three years later, the second major leap was evidenced by the experimental production test in 2020. This time it achieved 30 days of continuous gas production and set a new world record for cumulative gas production of 86.14×10^4 m^3 (Ye et al., 2020). Because of these great successes, China has now entered the stage of productive production test and is accelerating its steps to achieve commercial development of NGH by 2030.

Like other conventional and unconventional resources, prior to NGH industrialization, it is necessary to conduct an economic evaluation to determine whether it is profitable or not (Chen et al., 2022a). There exist a lot of factors that can affect the economic feasibility of an NGH exploitation project. Meanwhile, economic production is rare and may be the most important one (Wu et al., 2020). Unfortunately, since now, only a few quantitative analyses of the economic production rate have been carried out. Based on previous studies on NGH industrialization (Yamamoto et al., 2014; Yang et al., 2014; Li et al., 2018; Ye et al., 2020), Wu et al. (2020) proposed that the economic production rate for terrestrial NGH industrial exploitation is 30×10^4 m^3/d/well, while for marine reservoirs, it should be no less than 50×10^4 m^3/d/well. Compared with several trial productions before, both capacities are still two or three orders of magnitude higher than those of pilot production tests (Figure 1). However, the economic production rate for profitable NGH industrial exploitation is not always fixed, and it may decrease with the development of low-cost exploitation technologies.

In recent years, some scholars have started to try to conduct economic evaluations of NGH exploitation, mostly with the method of energy return on investment (EROI) or the method of discounted cash flow (DCF). Kong et al. (2018) carried out an estimation of China's production efficiency of NGH in the South China Sea based on different production capacities. The results show if the production rate for a single well can reach 2.3×10^4 m^3/d with a 12-year production life, the standard energy return on investment is 1.25, indicating the net energy delivered to society by NGH production is positive. Chen et al. (2022b) calculated each EROI of four NGH exploitation

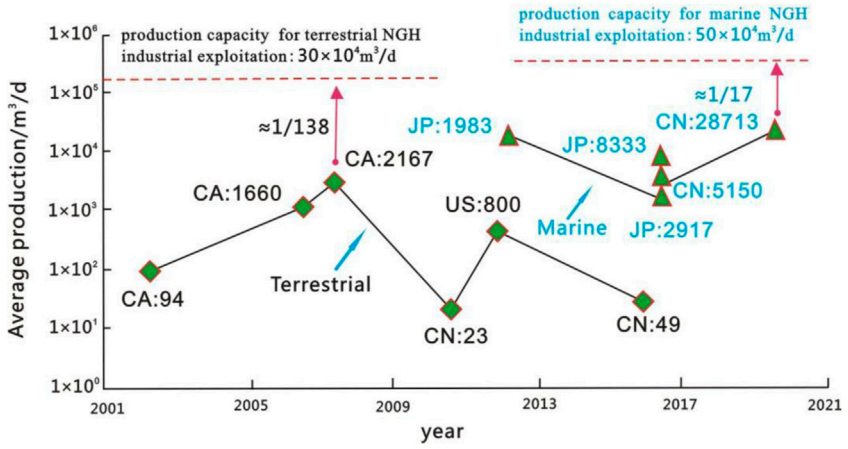

FIGURE 1
Average production capacity of NGH production tests in the world and the economic production rate for terrestrial and marine NGH industrial exploitation (Wu et al., 2020). CN means China, JP means Japan, CA means Canada, and US means the United States. The number after the country abbreviation represents the average daily production capacity of gas hydrates' production tests.

technologies to evaluate the economic potential. She illustrated that compared with thermal simulation, chemical injection, and CO_2 replacement, depressurization is the most economically feasible, with the lowest economic production rate of about 16–25 × 10^4 m^3/d per well. Walsh et al. (2009) presented a preliminary report on the economics of gas production from NGH with the method of discounted cash flow (DCF). According to the results, $12/Mscf (about $10.6/MMBtu) is the lowest gas price that would allow economically viable production from gas hydrates in the absence of associated free gas, while an underlying gas deposit will reduce the viability price estimate to $7.50/Mscf (about $6.62/MMBtu). The results also reported that the production cost for marine hydrate is $3.5–4.00/Mscf (about $3.1–3.5 MMBtu) more expensive than a conventional gas project given a 15% internal rate of return (IRR). Deepak et al. (2019) undertook a techno-economic study of a defined deepwater hypothetical gas hydrate accumulation in the Krishna–Godavari (KG) Basin located along the eastern margin of India. The economic evaluation suggested that when the predicted production rate reaches 600 × 10^4 m^3/d, the production cost will be $9/MMBtu, which means economically viable. Based on the currently assumed production system and gas production behavior, the MH21-S R&D consortium (MH21-S, 2019) described the criteria for NGH commercial production after conducting the economic evaluation of hypothetical hydrate accumulations located in the Nankai Trough, Japan. The calculation results presented that when the LNG price is $10/MMBtu, the production rate per well required for commercial production is about 15 × 10^4 m^3/d or more. Since the technology for commercial exploitation of NGH has not been established yet, exploring the economic production rate is critical to understanding the gap between pilot production tests and the final realization of commercialization. Notably, few studies focusing on the evaluation of the economic production rate for NGH industrial exploitation in the South China Sea have been conducted till now due to the lack of enough field data.

The objective of this article is to estimate the economic production rate required for the industrialization of gas hydrate at different gas prices from an economic point of view and to figure out the key factors affecting production capacity. For evaluation of the economics, calculating capital expenditure (CAPEX) and operating expenditure (OPEX) data are the two fundamental prerequisites. Although the exploitation of marine NGH is similar in many respects to that of offshore conventional gas, there are still some differences in a number of ways, some of which will have a significant effect on the overall economics (Walsh et al., 2009). Unlike conventional gas that can be produced by natural flow, NGH should be first dissociated into a fluid phase (gas and water) that can consume energy (Yamamoto and Nagakubo, 2021). In addition, because the water production from a gas hydrate reservoir could be highly variable, a gas hydrate development will require artificial lift such as electric submersible pumps (ESPs) or gas lift, which will also increase front-end costs in most cases, as well as operating costs over the life of the field (Walsh et al., 2009). On this basis, when the method of discounted cash flow (DCF) is applied, OPEX fully refers to an offshore gas project just as many of the evaluations reviewed previously may cause a large deviation. As for the energy return on investment (EROI) method, it is pretty hard to reasonably calculate CAPEX and OPEX data in energy terms due to the lack of enough available data for trial production tests. As an alternative solution, the authors use a hybrid model, which is widely used in the energy sector (Li and Zhang, 2018, Li and

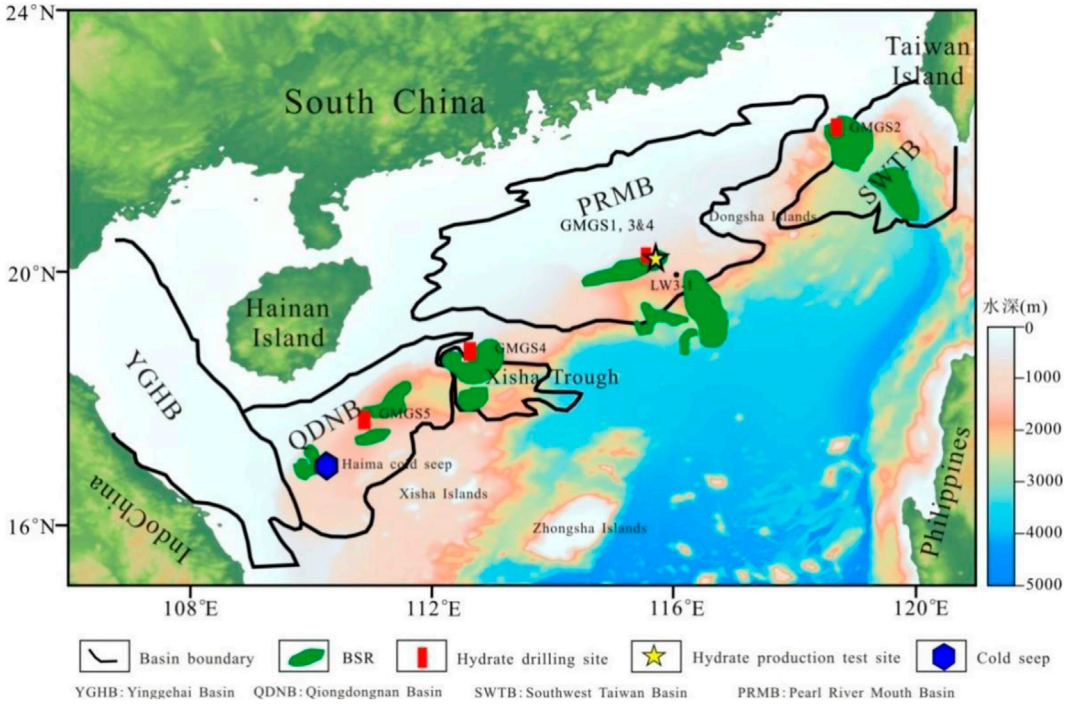

FIGURE 2
Depositional basins and gas hydrate surveying in the northern South China Sea. BSR, bottom simulating reflector (modified from Wu and Wang (2018) and Liang et al. (2019))

Zhang, 2019) and which combines both discounted cash flow (DCF) and energy return on investment (EROI) to estimate the economic production rate required for NGH industrial exploitation at different gas prices. Section 2 describes the method of discounted cash flow (DCF) and energy return on investment (EROI) and proposes a novel DCF-EROI hybrid model. Section 3 makes a range of assumptions for economic evaluation and gives data estimation of key parameters used in the model. Based on Section 3, Section 4 presents the study results and discussion in four different gas price scenarios. Section 5 carries out sensitivity analyses to reduce the uncertainty resulting from the limited data, and Section 6 states the conclusion.

2 Methodology

2.1 Discounted cash flow method

Discounted cash flow (DCF) analysis values of cash flows by bringing them to the present, and its result is known as the net present value (NPV), which is probably the most popular and most sophisticated economic valuation technique to determine whether a project yields a return in excess of the alternative equal risk investment in trade securities (Žižlavský, 2014; Hou, 2016). NPV compares the value of net cash flows today to the value of the same net cash flows in the future, taking inflation and returns into account (Donald, 2012; Bosri, 2019). Here, in this research, expenditure and sales revenue were estimated for hypothetical NGH reservoirs in Shenhu area of the northern South China Sea (Figure 2).

The equation of NPV can be expressed as follows:

$$NPV = \sum_{t=1}^{n} (CI - CO)_t (1 + r)^{-t},$$

where NPV = net present value; CI = cash inflow; CO = cash outflow; $(CI - CO)_t$ = net cash flow generated by innovation project in year t; r = discount rate.

The future net cash flows are computed by subtracting the capital expenditure (CAPEX), operating expenditure (OPEX), and taxes (Tax) from the gas sales revenue (R_gP_g), a product of gas production (R_g) and gas price (P_g). The field tests in China and Japan have demonstrated that conventional offshore gas production facilities can be used for gas hydrate exploitation (Yamamoto et al., 2014; Li et al., 2018; Ye et al., 2020). Therefore, it is reasonable to refer CAPEX, including the cost of production platforms ($C_{platform}$), well drilling and completions (C_{well}), subsea system (C_{subsea}), pipeline construction ($C_{pipeline}$), and field abandonment ($C_{abandonment}$), to those of offshore gas. As mentioned earlier, OPEX can't be fully referred to the cost of offshore gas. It should constitute $OPEX_1$,

referring to the operating cost of offshore gas ($C_{operation}$) and $OPEX_2$, including dissociation costs ($C_{dissociation}$) and artificial lift costs (C_{lift}).

Then, the NPV becomes

$$NPV = \sum_{t=1}^{n} \frac{R_g P_g - \left(C_{platform} + C_{well} + C_{subsea} + C_{pipline} + C_{abandonment} + C_{operation} + C_{dissociation} + C_{lift} + Tax\right)}{(1+r)^t}.$$

Here, the economic production rate, which means the minimum production that is needed to make NGH exploitation financially profitable, is calculated when the final net present value can then be estimated either as zero given a certain discount rate. Then, the economic production rate equals R_g when

$$NPV = \frac{R_g P_g - \left(C_{platform} + C_{well} + C_{subsea} + C_{pipline} + C_{abandonment} + C_{operation} + C_{dissociation} + C_{lift} + Tax\right)}{(1+r)^t}.$$

2.2 Energy return on investment method

The concept of energy return on investment (EROI) was first proposed by Hall and Cleveland (1981). Rather than purely monetarily, the EROI is a useful measure to examine the energetic efficiency of energy processes and systems (Cleveland et al., 1984; Cleveland, 1992).

The equation of EROI can be expressed as follows:

$$EROI = \frac{Energy\ outputs\ (return)}{Energy\ inputs\ (invested)}.$$

Since energy costs (energy outputs and energy inputs) can be converted into currency costs (cash inflow and cash outflow) by dividing the energy intensity, the energy consumed for NGH dissociation ($E_{dissociation}$) and artificial lift (E_{lift}) can be obtained by theoretical estimation.

$E_{dissociation}$ resulted from NGH dissociation is described by energy consumption for each cubic meter of gas produced, which differs for different production methods. For the depressurization method, the energy input is caused by an electric submersible pump (ESP) to lower the pressure during gas production, which can be estimated by Chen et al. (2022b):

$$E_{dissociation} = T_p * P_{ESP} * H_{elec},$$

where T_p = total production time; P_{ESP} = ESP power; H_{elec} = heating value per KWh of electricity.

E_{lift} is lifting energy input for produced fluid. It is a product of the drainage discharge, vertical depth, and corresponding consumption factor (Zeng et al., 2015), as expressed by Kong et al. (2018):

$$E_{lifting} = M_{water} * D_{well} * I_{ESP} * H_{elec},$$

where M_{water} = the amount of water; D_{well} = lifting height, which equals water depth plus well depth; H_{elec} = heating value per KWh of electricity; I_{ESP} = effective power of the electrical submersible pump.

Therefore, according to all the previous equations, $OPEX_2$ can be estimated by

$$OPEX_2 = \left(T_p * P_{ESP} * H_{elec} + M_{water} * D_{well} * I_{ESP} * H_{elec}\right) / * EI,$$

where EI = energy intensity.

3 Assumptions and data estimation

3.1 Assumptions of the model

As the longest gas production period of a marine NGH production test was approximately 2 months in the world (Ye et al., 2020), the long-term gas production behavior is still uncertain, which means there remain various levels of uncertainties such as the number of production wells and the capacity of production facilities for future commercial production. Therefore, for economic evaluation, it is necessary to make a range of assumptions to supplement such uncertain parameters (Table 1).

3.2 Data estimation

As discussed previously, CAPEX and operating expenditure $OPEX_1$ can be referred to an offshore gas project, and they are generated using IHS Energy Que$tor™ planning software and costing database. For $OPEX_2$, it can be estimated by converting energy consumed for NGH decomposition and water lifting into currency. All the key parameters used in this study are referred to simulation and experimental results in the literature (Table 2, 3).

4 Results and discussion

For economic evaluation of gas hydrate exploitation, the economic production rate for each well is one of the most important factors, and it is obviously affected by the market gas price, which has a significant impact on total sales revenue (cash inflows). Due to the variability, it is pretty difficult to predict future gas prices. In this study, four gas price scenarios are assumed with the gas–water ratio set at 100, which is close to the data observed in the first offshore production test of methane hydrates in the eastern Nankai Trough (Yamamoto et al., 2014). The first scenario is at the gas price of $6.15/MMBtu, the average price of China's imported pipeline gas in

TABLE 1 Conditions/assumptions for economic evaluation.

Items	Condition/assumption
Reservoir	Assumed the research is based on hypothetical NGH reservoirs at scientific drilling expedition sites GMGS1, GMGS2, GMGS3, GMGS4, and GMGS 5 conducted by Guangzhou Marine Geological Survey (Figure 2)
	Specific geological conditions, such as porosity and permeability, and production potential are not taken into consideration
Production methods (including production behavior)	Depressurization method is used
	No exchange of heat or fluid between the inside and outside areas
	During the production period, the gas production rate is constant
	Almost has the same production profile as an offshore gas field
Capital expenditure	All the capital investments including drilling wells are completed in the first year
Operating expenditure	Affected by offshore gas technology and the energy consumed for NGH dissociation and gas-water lift
Tax	Tax exemptions due to NGH exploitation are a new industry need of support
Cash inflow	Revenue all comes from gas produced and sold on the domestic market at a given price

TABLE 2 Key parameters used in DCF-EROI analysis.

Parameter	Value	Unit	References
Production life	30	Year	Estimated
Energy intensity	5.994	MJ/$2011	World (2012)
ESP power	50	KW	Wang (2015)
IESP	0.01	kWh/m^3•m	Zeng et al. (2015)
H_{elec}	3.6	MJ/kWh	Kong et al. (2018)

December 2021. The second scenario is assumed at the price of $10/MMBtu, the LNG price used by the MH21-S R&D consortium for economic evaluation. The third one is at $18.93/MMBtu, representing the average price of China's imported LNG in December 2021. The last scenario is at the price of $35.4/MMBtu, the CIF price of China's imported spot LNG in August 2022. Table 4 summarizes the economic production rates at sites GMGS1, GMGS2, GMGS3, GMGS4, and GMGS5 in the South China Sea, changing with the number of production wells in these four scenarios. Compared with the previous economic evaluations resulting from the literature reviewed earlier (Deepak et al., 2019; MH-21S, 2019; Wu et al., 2020), the calculation results are nearly within the same order of magnitude, which implies the economic production rates estimated could be regarded reasonable.

As shown in Table 4, under the same conditions of production life and gas–water ratio, economic production rates in the South China Sea are highly dependent on the gas price, ranging from 1.96 to 29.60 × 10^4 m^3/d/well. Given a certain gas price, the economic production rate needed differs at different sites but not very significantly. This is because the eight NGH sites are located in the similar geological condition with near water depth, costing similar capital expenditure and operating expenditure. In addition, all economic production rates at these sites will decrease with the increase of production wells, which may be resulted from the lower marginal costs for each well. Additionally, Table 4 also shows the effect of gas price and the number of wells on the economic production rate vary from site to site. Here, the GMGS4-SC1 site and GMGS5-W9 are taken for example. In most cases, the economic production rate at the GMGS4-SC1 site is a little lower than that at the GMGS5-W9 site with the same gas price and the number of wells, but this situation will reverse when the LNG price is $35.4/MMBtu, and the number of wells is more than 30. The reason causing such an interesting phenomenon is maybe the sensitivity of gas price and well number on economic production rate changes when these two key factors change by themselves, which will be analyzed in Section 5.

In the case of an actual pipeline gas price of $6.15/MMBtu in late 2021, the gas produced from NGH is certainly not competitive against imported pipeline gas at the current stage. In this scenario, the average economic production rate per well should be about 12.96–29.6 × 10^4 m^3/d, almost 4–10 times higher than the rate recorded in the second production test in Shenhu area, South China Sea (Ye et al., 2020). In other words, there is still a big gap between the gas production efficiency of actual production tests and that required for commercial production.

Based on the LNG price of $10/MMBtu, the economic production rates range from 7.45 to 13.26 × 10^4 m^3/d/well, lower than 15 × 10^4 m^3/d/well estimated by the MH21-S R&D consortium (MH-21S, 2019). This may be caused by the different expected well production life in the two models. In this study, the production life for each well is 30 years, while the parameter used by the MH21-S R&D consortium is 8 years. Considering that most of the life span investigated for simulation of gas hydrate exploitation is about 20–30 years or even longer (Cleveland, 1992; Walsh et al., 2009; Yamamoto and Nagakubo, 2021; Chen et al., 2022a; Chen et al., 2022b), it is more reasonable

TABLE 3 Key parameters for hypothetical NGH reservoirs.

Expedition	Site	Water depth (m)	Mbsf	Expedition time	References
GMGS1	SH2	1,230	200	2007	Yang (2013) and Zhang et al. (2018)
	SH7	1,108	160	2007	Li and Li (2011) and Zhang et al. (2018)
GMGS2	G8	798	80	2013	Wang et al. (2016)
	G16	896	218	2013	Feng et al. (2015)
GMGS3	W19	1,274	156	2015	Sun et al. (2017) and Liang et al. (2022)
	W11	1,274	206	2015	Zhang et al. (2019)
GMGS4	SC1	1,286	150	2016	Wei et al. (2018), Zhang et al. (2019)
GMGS5	W9	1722	168	2018	Liang et al. (2019)

TABLE 4 Economic production rates for NGH industrial exploitation at different natural gas prices, changed with the number of production wells.

Gas price		Pipeline gas $6.15/MMBtu					LNG $10/MMBtu				
Site	Well	20	30	40	50	60	20	30	40	50	60
Economic production rate threshold (10^4 m^3/day/well)											
GMGS1	SH2	22.74	17.98	16.66	16.97	15.87	11.59	9.53	8.61	8.65	8.20
	SH7	21.27	16.90	15.64	15.92	14.90	11.24	9.26	8.37	8.41	7.97
GMGS2	G8	18.38	14.73	13.58	13.77	12.96	10.43	8.63	7.80	7.81	7.45
	G16	19.55	15.51	14.26	14.54	13.58	10.65	8.73	7.87	7.92	7.49
GMGS3	W19	22.99	18.24	16.93	17.24	16.14	11.72	9.67	8.74	8.79	8.34
	W11	23.28	18.39	17.05	17.37	16.24	11.72	9.64	8.71	8.75	8.29
GMGS4	SC1	23.85	19.06	17.78	18.10	17.00	12.14	10.09	9.18	9.21	8.77
GMGS5	W9	29.60	23.26	21.83	22.23	20.78	13.26	10.95	9.93	9.96	9.45
Gas price		**LNG $18.93/MMBtu**					**LNG $35.4/MMBtu**				
Site	**Well**	**20**	**30**	**40**	**50**	**60**	**20**	**30**	**40**	**50**	**60**
Economic production rate threshold (10^4 m^3/day/well)											
GMGS1	SH2	5.26	4.33	3.85	3.93	3.67	2.67	2.20	1.96	1.99	1.86
	SH7	5.21	4.29	3.83	3.90	3.65	2.67	2.20	1.96	2.00	1.87
GMGS2	G8	5.06	4.19	3.74	3.79	3.57	2.64	2.19	1.95	1.98	1.86
	G16	5.03	4.13	3.67	3.74	3.49	2.59	2.13	1.89	1.93	1.80
GMGS3	W19	5.32	4.39	3.92	3.99	3.73	2.70	2.23	1.99	2.02	1.89
	W11	5.29	4.35	3.87	3.94	3.69	2.68	2.20	1.96	2.00	1.87
GMGS4	SC1	5.51	4.57	4.11	4.18	3.92	2.79	2.32	2.08	2.12	1.99
GMGS5	W9	5.63	4.65	4.15	4.23	3.95	2.79	2.30	2.05	2.09	1.96

to assume a longer production life span of about 30 years for economic evaluation.

In the scenario of the LNG price of $18.93/MMBtu, it may look pretty promising to exploit gas hydrate with the economic production rate per well 3.67–5.63× 10^4 m^3/d, which can be achieved by some enhancement recovery methods like dual horizontal wells, etc. (MH-21S, 2019; Wu et al., 2020). In addition, when the LNG price is as high as $35.4/MMBtu, it means gas hydrate could be commercially developed with the lowest production rate needed of only 1.86 × 10^4 m^3/d. However, considering the longest production life in trial tests to now is just about 60 days (Li et al., 2018), and the maximum gas produced from production tests over the last two decades is only a total of 8.6 × 10^5 m^3 (Ye et al., 2020), there is still a long way to extract natural gas from NGH at a production rate of 1.86 × 10^4 m^3/d

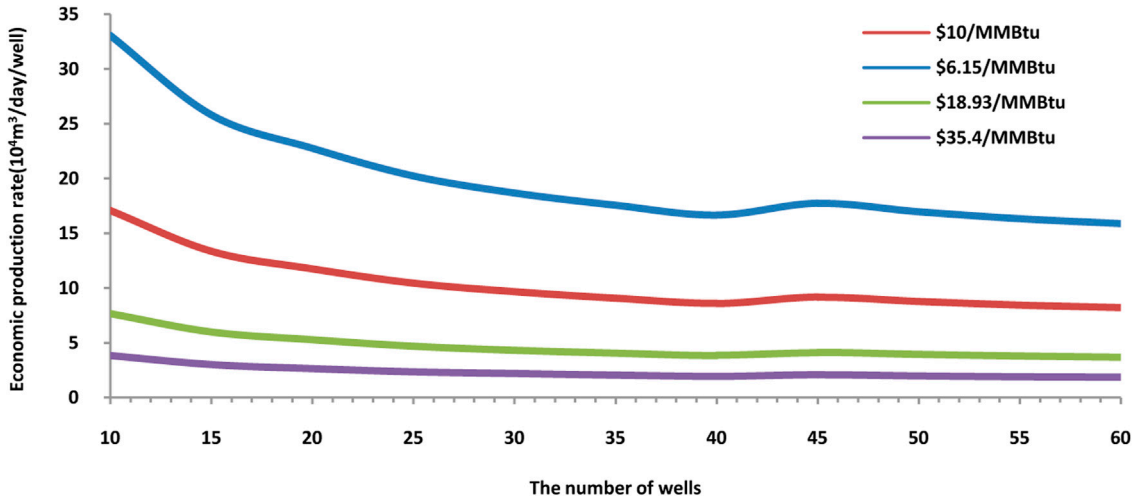

FIGURE 3
Sensitivity analysis of the number of wells on economic production rates at different gas prices with the gas–water ratio set at 100.

for nearly 30 years, which will have a cumulative gas production of about 122.2×10^8 m^3.

5 Sensitivity analysis

High economic production rate results from high cash inflows and low cash outflows over the production life span. As discussed earlier, a lot of factors can affect cash flows, such as the number of wells, gas price, production life, gas-water ratio, etc. In this section, taking the GMGS1-SH2 site as an example for the discussion, a sensitivity analysis is conducted to better understand the effect of four key factors on economic production rate.

As shown in Figure 3, when the number of wells increases, all economic production rates would generally decrease. However, the degree of decline is quite different for different gas prices. The lower the gas price, the faster the economic production rate drops with the rising number of wells. This may be explained by the fact that lower gas price causes lower cash inflows, making the economic production rate more sensitive to cash outflows resulting from drilling more wells. Meanwhile, even at the same gas price, the economic production rate also varies at different levels. Initially, when the number of producing wells increases, the curve of the economic production rate will decline and become more and more flat. While, when the well number reaches about 40, the economic production rate suddenly goes up and then goes down again when the well number arrives at about 47. After that, the curve will become nearly horizontal very slowly. A reasonable interpretation for the variation is that if the number of production wells is less than 40, wells may share the same facilities such as platforms or FPSO (floating production storage and offloading), resulting in the marginal cost for drilling a new well becomes less. Once the well number hits the threshold, another new platform may be needed, and more expenditure will cost.

When the gas–water ratio changes, the energy input for the artificial lift will be different, causing the gas production cost to fluctuate. Similar to the sensitivity analysis on the number of wells, we refine the gas–water ratio to analyze its sensitivity to economic production rate. Figure 4 shows that with the rise of the gas–water ratio, the economic production rate will rapidly drop down from a very high peak and, then the magnitude of the decline becomes smaller and smaller. This is because when the assumed gas price is lower than the cost of lifting produced water, it is impossible to compensate the production cost by sales revenue, no matter how much natural gas is produced. On the other hand, if the gas price is higher than the unit production cost, the higher the gas–water ratio, the less impact it will have on the economic production rate. When the gas–water ratio is higher than 200, the impact is very low; if it is as high as 1,000 or more, the effect of the gas–water ratio can be negligible.

As discussed previously, gas price will directly determine cash inflows. A high gas price means a low economic production rate needed based on the same conditions. Figure 5 illustrates the negative correlation between the economic production rate and natural gas price. Apparently, with a lower number of wells, the gas price has a higher sensitivity to the economic production rate. However, when the number of production wells is more than 40, the gas

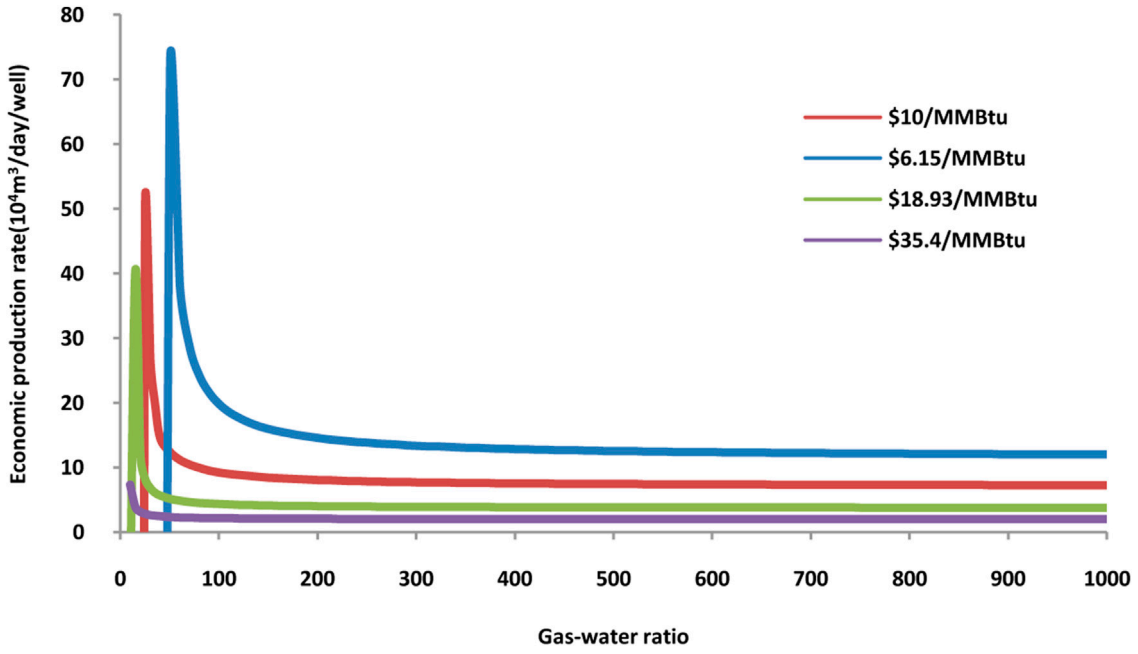

FIGURE 4
Sensitivity analysis of the gas–water ratio on economic production rate at different gas prices with the number of wells set at 30.

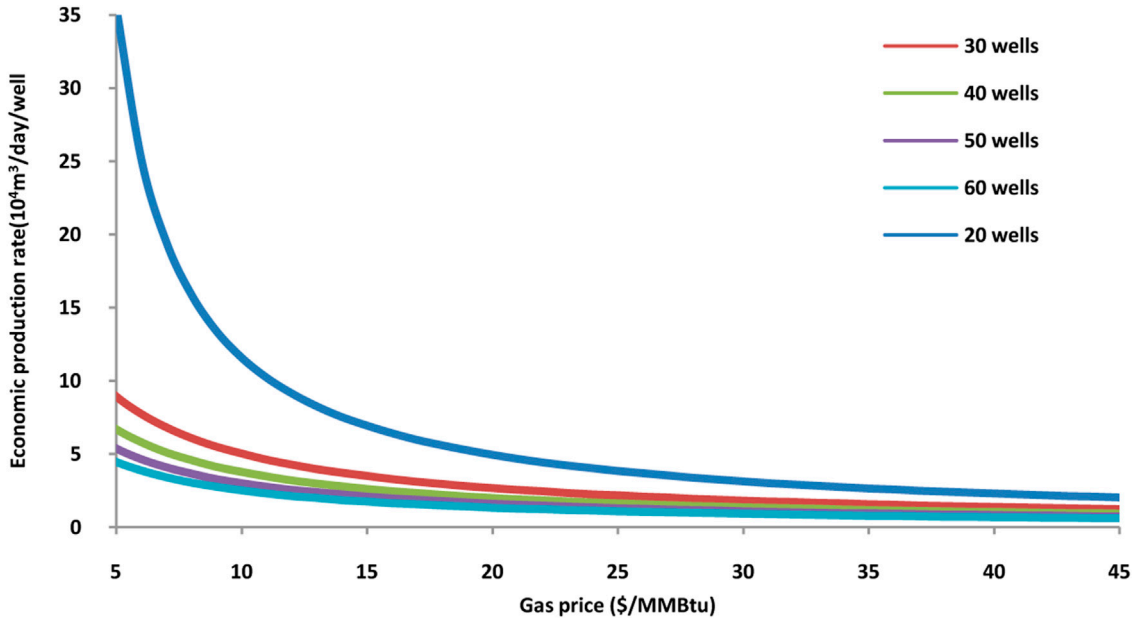

FIGURE 5
Sensitivity analysis of the gas price on economic production rate with the different number of wells with the gas–water ratio set at 100.

price has no obvious effect on the economic production rate.

To accelerate the pace of hydrate industrialization, promoting production capacity and reducing the production cost through technological progress are the two main ways. Figure 6 describes the impact of different rates of decreasing production costs on the economic production rate. Gas price

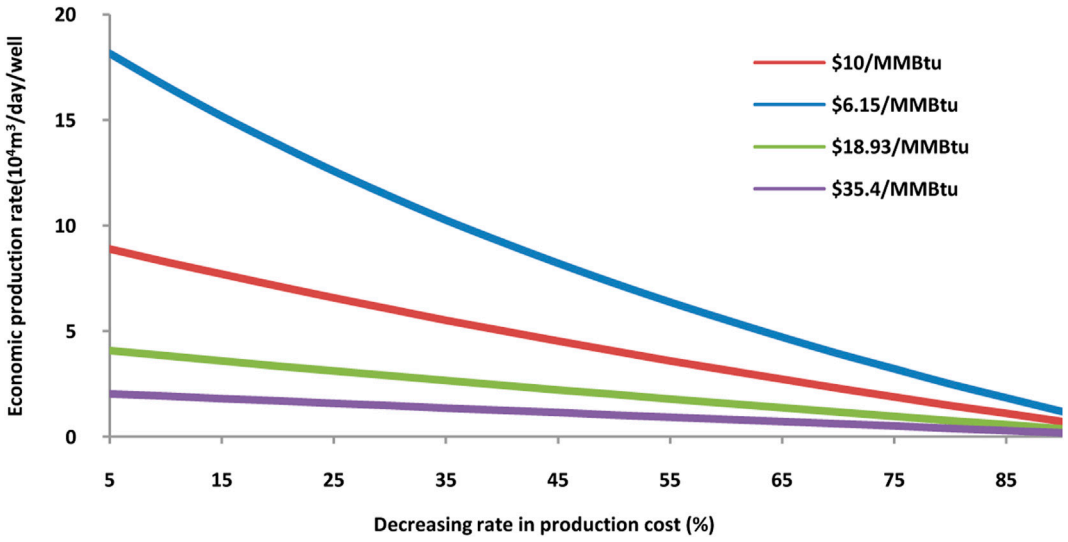

FIGURE 6
Sensitivity analysis of the decreasing rate on economic production rate at different gas prices with the gas–water ratio and the number of wells set at 100 and 30, respectively.

fluctuations make the economic production rate go down at different rates. Similar to the gas–water ratio and the number of wells, the lower gas price has stronger negative correlations with the economic production rate. Based on the previous analysis, it is reasonable to conclude that at a lower natural gas price, it is more necessary to develop gas hydrate exploitation technology to reduce production costs.

6 Conclusion

NGH is a strategic resource with a huge natural gas production potential. The industrialization of NGH has great significance for the achievement of peak carbon dioxide emissions and carbon neutrality. Economic evaluation is a prerequisite for NGH industrial exploitation. In this study, the economic production rate for industrial exploitation of NGH in different parameter scenarios, such as gas price, the number of wells, gas–water ratio, and decreasing rate in production cost, is estimated with a new hybrid method based on the discounted cash flow (DCF) method and the energy return on investment (EROI) method, and the following results are obtained:

1) The economic production rate of natural gas hydrate at sites GMGS1, GMGS2, GMGS3, GMGS4, and GMGS5 in the South China Sea is quantified in four scenarios with different gas prices. Changing the number of wells from 20 to 60, the economic production rate ranges from 1.96 to 29.60 × 10^4 m^3/d/well.
2) In a low gas price market, drilling more wells can decrease the economic production rate quickly at first, but when the number of wells reaches a certain number, it has little effect on the economic production rate.
3) Gas–water ratio has a limited impact on economic production when it is higher than 200. To make gas hydrate exploitation profitable, the lowest gas price must be higher than the cost for lifting produced water.
4) Gas price has a strong negative correlation with the economic production rate. Higher gas prices usually mean more cash inflows and lower economic production rate needed.
5) Reducing gas production costs is necessary to make gas hydrate exploitation competitive against other kinds of natural gas, especially at a low gas price.

Data availability statement

The original contributions presented in the study are included in the article/Supplementary Material; further inquiries can be directed to the corresponding author.

Author contributions

LW: methodology, formal analysis, and writing—original draft. TZ: review and editing. HZ: supervision. YS: figure drawing. XY: editing and supervision. MM: figure drawing.

Funding

This work was supported by the Geological Survey Project of the China Geological Survey (No. DD20221828) and the Think-tank Project of the China University of Geosciences (No. 505104004).

Acknowledgments

The authors would like to express their sincere appreciation to the editor and reviewers for the suggestions and other assistance in improving this manuscript.

Conflict of interest

Authors LW, TZ, YS, and MM were employed by the Development and Research Center, China Geological Survey, China Geological Survey, and Oil and Gas Survey, China Geological Survey.

The remaining authors declare that the research was conducted in the absence of any commercial or financial relationships that could be construed as a potential conflict of interest.

Publisher's note

All claims expressed in this article are solely those of the authors and do not necessarily represent those of their affiliated organizations, or those of the publisher, the editors, and the reviewers. Any product that may be evaluated in this article, or claim that may be made by its manufacturer, is not guaranteed or endorsed by the publisher.

References

Bosri, R. (2019). Evaluation of managerial techniques: NPV and IRR. *UITS J.*

BP (2022). *BP statistical Review of world energy*.

Chen, X. J., Lu, H. L., Gu, L. J., Shang, S. L., Zhang, Y., Huang, X., et al. (2022a). Preliminary evaluation of the economic potential of the technologies for gas hydrate exploitation. *Energy* 243, 123007. doi:10.1016/j.energy.2021.123007

Chen, X. J., Lu, H. L., Zhang, J., Ye, J., and Xie, W. (2022b). Economic critical resources for the industrial exploitation of natural gas hydrate. *Acta Geol. Sin. (Beijing)* 96, 663–673. doi:10.1111/1755-6724.14927

Cleveland, C. J., Costanza, R., Hall, C. A., and Kaufmann, R. (1984). Energy and the US economy: a biophysical perspective. *Science* 225, 890–897. doi:10.1126/science.225.4665.890 http://www.jstor.org/stable/1693932

Cleveland, C. J. (1992). Energy quality and energy surplus in the extraction of fossil fuels in the U.S. *Ecol. Econ.* 6, 139–162. doi:10.1016/0921-8009(92)90010-P

Deepak, M., Kumar, P., Singh, K., and Yadav, U. S. (2019). Techno-economic forecasting of a hypothetical gas hydrate field in the offshore of India. *Mar. Pet. Geol.* 108, 741–746. doi:10.1016/j.marpetgeo.2018.11.016

Donald, D. (2012). *Mergers, acquisitions, and other restructuring activities*.

Englezos, P. (1993). Clathrate hydrates. *Ind. Eng. Chem. Res.* 32 (7), 1251–1274. doi:10.1021/ie00019a001

Feng, J. C., Wang, Y. Z., Li, X. S., Li, G., Zhang, Y., and Chen, Z. Y. (2015). Production performance of gas hydrate accumulation at the GMGS2-site 16 of the pearl river mouth basin in the South China sea. *J. Nat. Gas. Sci. Eng.* 27, 306–320. doi:10.1016/j.jngse.2015.08.071

Hall, C. A., and Cleveland, C. J. (1981). *Energy return on investment for United States petroleum, coal, and uranium*.

Hao, Z. G. (2022). Exploring natural gas hydrates toward a carbon-neutral world. *China Geol.* 5, 1–4. doi:10.31035/cg2022022

Hou, X. Y. (2016). *Adaptability of hydrate reservoir developing method and economic evaluation*. MA thesis: China University of Petroleum East China. (In Chinese with English abstract).

Javed, A. (2016). Analysis of energy security, environmental emission and fuel import costs under energy import reduction targets: a case of Pakistan. *Renew. Sustain. Energy Rev.* 65, 1065–1078. doi:10.1016/j.rser.2016.07.037

Kong, Z. Y., Jiang, Q. Z., Dong, X. C., Wang, J., and Wan, X. (2018). Estimation of China's production efficiency of natural gas hydrates in the south china Sea. *J. Clean. Prod.* 203, 1–12. doi:10.1016/j.jclepro.2018.08.262

Kvenvolden, K. A. (1993). Gas hydrates—Geological perspective and global change. *Rev. Geophys.* 31, 173–187. doi:10.1029/93RG00268

Kvenvolden, K. A. (1988). Methane hydrate — a major reservoir of carbon in the shallow geosphere? *Chem. Geol.* 71, 41–51. doi:10.1016/0009-2541(88)90104-0

Li, G., and Li, X. S. (2011). Numerical simulation for gas production from hydrate accumulated in shenhu area, south china sea, using huff and puff method. *CIESC J.* 62, 459–468. (In Chinese with English abstract)

Li, J. F., Ye, J. L., Qin, X. W., Wu, N. Y., Hu, H. L., Xie, W. W., et al. (2018). The first offshore natural gas hydrate production test in South China Sea. *China Geol.* 1, 5–16. doi:10.31035/cg2018003

Li, P., and Zhang, J. S. (2018). A new hybrid method for China's energy supply security forecasting based on ARIMA and XGBoost. *Energies* 11, 1687. doi:10.3390/en11071687

Li, P., and Zhang, J. S. (2019). Is China's energy supply sustainable? New research model based on the exponential smoothing and GM(1, 1) methods. *Energies* 12, 236. doi:10.3390/en12020236

Liang, J., Meng, M. M., Liang, J. Q., Ren, J. F., He, Y. L., Li, T. W., et al. (2022). Drilling cores and geophysical characteristics of gas hydrate-bearing sediments in the production test region in the shenhu sea, south China sea. *Front. Earth Sci. (Lausanne).* 10, 911123. doi:10.3389/feart.2022.911123

Liang, J. Q., Zhang, W., Lu, J. G., Wei, J. G., Kuang, Z. G., and He, Y. L. (2019). Geological occurrence and accumulation mechanism of natural gas hydrates in the eastern qiongdongnan basin of the South China Sea: insights from site GMGS5-W9-2018. *Mar. Geol.* 418, 106042. doi:10.1016/j.margeo.2019.106042

Makogon, I. (1981). *Hydrates of natural gas*. OklahomaTulsa: PennWell Books.

Makogon, Y. F., Holditch, S. A., and Makogon, T. Y. (2005). Natural gas-hydrates a potential energy source for the 21st century. *J. Pet. Sci. Eng.* 56, 14–31. doi:10.1016/j.petrol.2005.10.009

Mh-21S (2019). *Japan's methane hydrate R&D program,comprehensive report of phase 2 & 3 research results*.

Michael, D. M., and Arthur, H. J. (2019). *Exploration and production of oceanic natural gas hydrate: Critical factors for commercialization*. Second Edition. Switzerland: Springer.

Moridis, G. J., and Sloan, E. D. (2007). Gas production potential of disperse low-saturation hydrate accumulations in oceanic sediments. *Energy Convers. Manag.* 48, 1834–1849. doi:10.1016/j.enconman.2007.01.023

Sanja, P. (2021). *Rystad energy: 2020 gas production exceeded demand*. https://www.offshore-energy.biz/rystad-energy-2020-gas-production-exceeded-demand/.

Sloan, E. D., and Koh, C. A. (2007). *Clathrate hydrates of natural gases*. CRC Press.

Sun, J. X., Zhang, L., Ning, F. L., Lei, H. W., Liu, T. L., Hu, G. W., et al. (2017). Production potential and stability of hydrate-bearing sediments at the site GMGS3-W19 in the South China sea: a preliminary feasibility study. *Mar. Pet. Geol.* 86, 447–473. doi:10.1016/j.marpetgeo.2017.05.037

Tan, Z. F., Pan, G., and Liu, P. K. (2016). Focus on the development of natural gas hydrate in China. *Sustainability* 8, 520. doi:10.3390/su8060520

Vedachalam, N., Srinivasalu, S., Rajendran, G., Ramadass, G., and Atmanand, M. (2015). Review of unconventional hydrocarbon resources in major energy consuming countries and efforts in realizing natural gas hydrates as a future source of energy. *J. Nat. Gas. Sci. Eng.* 26, 163–175. doi:10.1016/j.jngse.2015.06.008

Walsh, M. R., Hancock, S. H., Wilson, S. J., Patil, S. L., Moridis, G. J., Boswell, R., et al. (2009). Preliminary report on the commercial viability of gas production from natural gas hydrates. *Energy Econ.* 31, 815–823. doi:10.1016/j.eneco.2009.03.006

Wang, X. W. (2015). Efficiency optimization design of oil production system using electric submersible pumps. *Petroleum Eng. Constr.* 41, 29–32. (In Chinese with English abstract). doi:10.3969/j.issn.1001-2206.2015.02.008

Wang, Y., Feng, J. C., Li, S., Zhang, Y., and Li, G. (2016). Evaluation of gas production from marine hydrate deposits at the GMGS2-site 8, pearl River Mouth basin, South China sea. *Energies* 9, 222. doi:10.3390/en9030222

Wei, J. G., Fang, Y. X., Lu, H. L., Lu, H. F., Lu, J. G., Liang, J. Q., et al. (2018). Distribution and characteristics of natural gas hydrates in the Shenhu sea area, South China sea. *Mar. Pet. Geol.* 98, 622–628. doi:10.1016/j.marpetgeo.2018.07.028

World, B. (2012). *World Bank SE4ALL database. Energy intensity of industrial sector 2012*.

Wu, N. Y., Li, Y. L., Wang, Y. Z., Sun, J. Y., and Huang, L. (2020). Prospect of marine natural gas hydrate stimulation theory and technology system. *Nat. Gas. Ind.* 40, 100–115. (In Chinese with English abstract). doi:10.3787/j.issn.1000-0976.2020.08.008

Yamamoto, K., and Nagakubo, S. (2021). Review of energy efficiency of the gas production technologies from gas hydrate-bearing sediments. *Front. Energy Res.* 9. doi:10.3389/fenrg.2021.741715

Yamamoto, K., Terao, Y., Fujii, T., Ikawa, T., Seki, M., and Matsuzawa, M. (2014). "Operational overview of the first offshore production test of methane hydrates in the Eastern Nankai Trough," in *Paper presented at the offshore technology conference*.

Yang, S. W., Lang, X. M., Wang, Y. H., Wen, Y. G., and Fan, S. S. (2014). Numerical simulation of Class 3 hydrate reservoirs exploiting using horizontal well by depressurization and thermal co-stimulation. *Energy Convers. Manag.* 77, 298–305. doi:10.1016/j.enconman.2013.09.046

Yang, S. W. (2013). *Simulation and energy efficiency analysis of gas production from hydrates*. PhD dissertation. Guangzhou: South China University of Technology. (In Chinese with English abstract).

Yang, S. X., Liang, J. Q., Liu, C. G., and Sha, Z. B. (2017). Progresses of gas hydrate resources exploration in sea area. *Geol. Surv. China* 4, 1–8. doi:10.19388/j.zgdzdc.2017.02.01

Ye, J. L., Qin, X. W., Xie, W. W., Lu, H. L., Qiu, H. j., et al. (2020). The second natural gas hydrate production test in the South China Sea. *China Geol.* 3, 197–209. doi:10.31035/cg2020043

Zeng, Y. B., Liao, Y. H., Jia, H., Yu, Z. Q., and Wu, S. W. (2015). Marine oil production exectirc submersible pump production opitmization method and its application. *Petrochem. Technol.* 22 (05), 105–106.

Zhang, W., Liang, J. Q., He, J. X., Cong, X. R., Su, P. B., et al. (2018). Differences in natural gas hydrate migration and accumulation between GMGS1 and GMGS3 drilling areas in the Shenhu area, northern South China Sea. *Nat. Gas. indursty* 38, 138–149. (In Chinese with English abstract). doi:10.3787/j.issn.1000-0976.2018.03.017

Zhang, W., Liang, J. Q., Wei, J. G., Su, P. P., Lin, L., Huang, W., et al. (2019). Origin of natural gases and associated gas hydrates in the Shenhu area, northern South China Sea: results from the China gas hydrate drilling expeditions. *J. Asian Earth Sci.* 183, 103953. doi:10.1016/j.jseaes.2019.103953

Zheng, R. C., She, H. B. Y., Babu, P., Linga, P., and Li, X. S. (2016). Review of natural gas hydrates as an energy resource: Prospects and challenges. *Appl. Energy* 162, 1633–1652. doi:10.1016/j.apenergy.2014.12.061

Žižlavský, O. (2014). Net present value approach: Method for economic assessment of innovation projects. *Procedia - Soc. Behav. Sci.* 156, 506–512. doi:10.1016/j.sbspro.2014.11.230

frontiers | Frontiers in Earth Science

TYPE Original Research
PUBLISHED 08 September 2022
DOI 10.3389/feart.2022.968504

OPEN ACCESS

EDITED BY
Lihua Zuo,
Texas A&M University Kingsville,
United States

REVIEWED BY
Jiasheng Wang,
China University of Geosciences
Wuhan, China
Hongxiang Guan,
Ocean University of China, China

*CORRESPONDENCE
Niu Li,
liniu@scsio.ac.cn
Xiaoming Sun,
eessxm@mail.sysu.edu.cn

SPECIALTY SECTION
This article was submitted to Sedimentology, Stratigraphy and Diagenesis,
a section of the journal
Frontiers in Earth Science

RECEIVED 14 June 2022
ACCEPTED 12 August 2022
PUBLISHED 08 September 2022

CITATION
Feng J, Luo M, Liang J, Yang S, Wang H, Li N and Sun X (2022), Possible links with methane seepage and gas hydrate dynamics inferred from authigenic barite records in the northern south china sea.
Front. Earth Sci. 10:968504.
doi: 10.3389/feart.2022.968504

Possible links with methane seepage and gas hydrate dynamics inferred from authigenic barite records in the northern south china sea

Junxi Feng[1,2,3,4], Min Luo[5], Jinqiang Liang[1,2,4], Shengxiong Yang[1,2], Hongbin Wang[6], Niu Li[7]* and Xiaoming Sun[3]*

[1]MLR Key Laboratory of Marine Mineral Resources, Guangzhou Marine Geological Survey, Guangzhou, China, [2]Southern Marine Science and Engineering Guangdong Laboratory (Guangzhou), Guangzhou, China, [3]School of Marine Sciences, Sun Yat-sen University, Guangzhou, China, [4]Natural Gas Hydrate Engineering Technology Center, China Geological Survey, Guangzhou, China, [5]Shanghai Engineering Research Center of Hadal Science and Technology, College of Marine Sciences, Shanghai Ocean University, Shangha, China, [6]Qingdao Institute of Marine Geology, China Geological Survey, Qingdao, China, [7]Key Laboratory of Ocean and Marginal Sea Geology, South China Sea Institute of Oceanology, Innovation Academy of South China Sea Ecology and Environmental Engineering, Chinese Academy of Sciences, Guangzhou, China

Numerous methane seepage events occurred in periods of low or falling sea level since 330 ka BP, which is attributed to decrease in hydrostatic pressure and subsequent gas hydrate dissociation in the northern South China Sea (SCS). The seepage intensity likely decrease due to gas hydrate stabilization once there was a relatively high-stand sea level. However, there are few geochemical records of decline in upward methane flux in the northern South China Sea. Here, combing porewater and solid-phase analyses, the geochemical cycling of barium was investigated in two piston cores from sites HD109 and HD319 within two areas with inferred gas hydrate occurrence in the Taixinan Basin of the northern SCS, in order to track the net decrease in the upward methane flux and to estimate the total duration time of these events in the studied sediments. The results indicate that there are four intervals with barium enrichments in the sediment section overlying the occurrent sulfate-methane transition zone (SMTZ) at both cores, suggesting the SMTZs have downward migrated through time. Based on the excess barium contents and the diffusive Ba^{2+} fluxes above the current SMTZ, we estimate the total time for barium accumulation at both cores is about ten thousand years. It is suggested that some methane seepage events temporarily enhance the upward flux of methane, inducing anaerobic oxidation of methane and associated SMTZ close to the sediment surface before the Holocene. After the most intensive seepage event ceased in the post-glacial period, the upward methane flux decreased and the SMTZ migrated downward gradually, preserving enrichments of diagenetic barite. Overall, these new data confirm the episodic decrease in upward methane flux recorded by authigenic barite after the last glacial maximum, which is likely related to the stabilization of underlying gas hydrate reservoir. This study may fill in the gap of the

geochemical records of the variations in methane seepage and gas hydrate system during the post-glacial period in the northern SCS.

KEYWORDS

authigenic barite, methane seepage, anaerobic oxidation of methane, gas hydate, South China Sea

Introduction

Substantial amounts of methane existing as dissolved and free gas, as well as ice-like gas hydrates are hosted within the sediments in continental margins (Judd and Hovland, 2007). Dissolved and free gas can migrate from underlying reservoirs to the subsurface sediments through specific fluid conduits like faults and fractures (Boetius and Wenzhöfer, 2013). The majority of dissolved methane upward migrated is consumed by anaerobic oxidation of methane (AOM) mediated by a microbial consortium in the sulfate-methane transition zone (SMTZ) where both seawater sulfate and methane are consumed (AOM: $CH_4 + SO_4^{2-} \rightarrow HCO_3^- + HS^- + H_2O$) (Barnes and Goldberg, 1976; Boetius et al., 2000; Wu et al., 2022). The AOM typically induces formation of several types of authigenic minerals including carbonate (e.g., Peckmann and Thiel, 2004), pyrite (e.g., Peckmann et al., 2001) and barite (e.g., Torres et al., 1996; Torres et al., 2003; Castellini et al., 2006; Feng and Roberts, 2011).

Authigenic barite is widely used as a valuable proxy for tracing past methane fluxes in marine sediments (Dickens, 2001; Griffith and Paytan, 2012). The barium in authigenic barite is mostly derived from biogenic barite particles which form in the water column during the decomposition of organic substances and are transported to the seafloor. The sedimentary barite particles become undersaturated and decompose into barium (Ba^{2+}) and sulfate (SO_4^{2-}) ions when they are buried below the SMTZ. The released Ba^{2+} then migrates upward and enters the sulfate-bearing zone where authigenic barites form again just above the SMTZ ($Ba^{2+} + SO_4^{2-} \rightarrow BaSO_4$; Torres et al., 1996). The diagenetic barite is significantly different in the size from normal microcrystalline biogenic particles, especially in methane-rich sediments where it can grow to as large as several 10 μm (Torres et al., 1996). Sometimes at active methane seeps, massive barite deposits, e.g., chimneys, as high as 10 m in height can form on the seafloor (Greinert et al., 2002). Therefore, massive authigenic barite and barium element enrichments in sediment column can be utilized as a useful proxy to constrain the changes in the position of SMTZ and the duration time of methane release activities in the geological past (e.g., Dickens, 2001; Riedinger et al., 2006; Snyder et al., 2007a; Snyder et al., 2007b; Nöthen and Kasten, 2011; Kasten et al., 2012; Sauer et al., 2017; Schneider et al., 2018; Yao et al., 2020; Wood et al., 2021). Interestingly, significant barium enrichments occurred widespreadly at the times of some huge paleo-climatic perturbations, including the Paleocene-Eocene thermal maximum (Dickens et al., 2003), Permian-Triassic extinction (Burger, et al., 2019), and Ediacaran Shuram excursion (Cui et al., 2021). The formation of these barium enrichments may be attributed to massive input of dissolved barium from subsurface gas hydrate reservoirs due to gas hydrate dissociation and further authigenic barite precipitation (Dickens et al., 2003; Burger, et al., 2019; Frieling et al., 2019).

There are widespread methane-rich fluid seepages on the northern continental slope of the South China Sea (SCS) as uncovered by authigenic carbonates sampled at over thirty sites (Feng et al., 2018). There are only two active seep areas–"Haima seeps" and "Site F" found in the northern SCS so far (Feng and Chen, 2015; Liang et al., 2017). The majority of the authigenic carbonates in the northern SCS precipitate either during the periods of sea-level lowstands or corresponding to the times with falling sea-level prior to the Last Glacial Maximum (LGM) (Tong et al., 2013; Han et al., 2014; Yang et al., 2018; Maoyu Wang et al., 2022). It is thus suggested that gas hydrate dissociation took place during sea-level lowstands or falling stages resulting from reduced hydrostatic pressures, which in turn led to methane seepage and formation of authigenic minerals close to the seafloor in the northern SCS (Tong et al., 2013; Han et al., 2014; Li et al., 2016; Lin et al., 2016; Xie et al., 2019). At the post-glacial age, the upward methane flux seemed to decrease significantly on a regional scale (Lin et al., 2016). However, extensive seep activities also occurred during the sea-level highstand associated with Marine Isotope Stage (MIS) 5e (133.3–112.7 ka BP) and MIS 1 (since 14 ka BP) (Feng and Chen, 2015; Liang et al., 2017; Chen et al., 2019). These seepage events derived from gas hydrate dissociation were probably attributed to a climate-driven rise in bottom water temperature (Chen et al., 2019). The mechanisms controlling seepage activity are still controversial. More geochronologic evidences, especially the records of decline in upward methane flux during the deglaciation periods, are required to better understand the driving mechanisms. To date, there are few reports on this kind of geochemical records (e.g., Luo et al., 2015; Lin et al., 2016; Hu et al., 2017), which limits our understanding of the evolution of subsurface methane release in the northern SCS.

In this study, we investigate the downcore variation in Ba content in the sediments and dissolved porewater Ba^{2+} concentrations in two piston cores HD109 and HD319 in

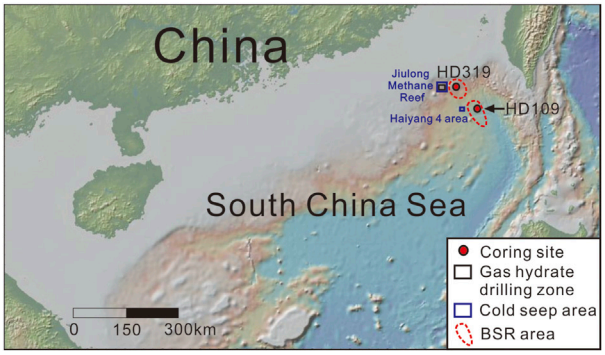

FIGURE 1
Map showing the location of the sediment cores HD109 and HD319 (red dots) in this study. Red dash circle is the BSR-occurring area mapped by Ge et al. (2010) and Wu et al. (2013).

the northeastern SCS, in order to trace the changes in the position of SMTZ and access the present-day and past upward methane fluxes. A numerical transport-reaction model is used to stimulate the geochemical data of pore fluids in order to estimate the present-day methane fluxes. The data of Ba content in both pore fluids and sediments are used to calculate the time required for the formation of authigenic barium enrichments at both sites.

Geological background

The northern SCS is classified as a Cenozoic passive continental margin. The study area is located on the lower slope and at the bottom of the Taixinan Basin (Figure 1) (McDonnell et al., 2000; Suess, 2005). The thickness of sediment in the Taixinan Basin can reach 10 km, where complex faults, fractures, and mud diapirs are well developed. Thus, these conditions favor methane-rich fluid seepage and gas hydrate accumulation (McDonnell et al., 2000; Suess, 2005; Wu et al., 2007). Widespread bottom simulating reflectors (BSR) representing the bottom of the gas hydrate stability zone was observed (e.g., McDonnell et al., 2000; Suess, 2005; Li et al., 2013; Li et al., 2015; Kuang et al., 2018; Bai et al., 2019). In addition, plenty of seep sites have been discovered in this region with water-depth ranging from ~200 to ~3,300 m, including the giant Jiulong Methane Reef with seep carbonates covering ~430 km^2, the Haiyang four area as well as the Site F with active seepage (e.g., Chen et al., 2005; Suess, 2005; Han et al., 2008; Tong et al., 2013; Xudong Wang et al., 2022). Abundant gas hydrates in shallow sediments were successfully recovered from the Jiulong Methane Reef area (Zhang et al., 2015), which validated that methane-rich fluid seepage and gas hydrates were common along the passive margin of the Taixinan Basin.

Materials and methods

Sampling and analytical methods

Two piston cores (HD109 and HD319) were retrieved from two areas with BSR occurrence in the Taixinan Basin during the cruises of the R/V "*Haiyang IV*" in 2003 and 2004, respectively. Site HD109 is located at the bottom of the Taixinan Basin, whereas site HD319 is located on the lower continental slope of this basin (Figure 1). The coordinate positions of these sites were shown in Chen et al. (2006). The lengths of the cores are 771 and 730 cm, respectively (Table 1). The sediments at these cores consist mainly of dark-green, unconsolidated clayey silt and silty clay with several quartz grains. The sand contents are 3 and 1% at the cores HD109 and HD319, respectively, which are much lower than that of the turbidite deposit at nearby site. Therefore, there are only normal deep-sea sediments at the two cores (Chen et al., 2006).

After collection, the engineers cut the cores into sections at intervals of 100 cm from top to bottom, and stored them in a cold room (4°C). The top 20 cm sediments of each sediment section were used to measure headspace gas contents onboard. Around 10 ml of sediments were put into 20-ml empty vials onboard to replace the 10-ml headspace required for the chromatograph injection. The hydrocarbon gas concentrations were measured onboard using the gas chromatograph method (Agilent 7890N). The precision for methane concentration was ±2.5%.

After retrieval of the cores HD109 and HD319, porewater samples were immediately collected from slices of the cores at intervals of 100 cm via a pumping vacuum extraction device at room temperature, then transferred to sealed plastic bottles and stored at 4 °C in April 2003 and May 2004, respectively. Porewater samples of the core HD109 were collected again for further study at intervals of 20 cm after the cruise in May 2003. The offshore analyses of porewater samples were performed at Nanjing University in August 2003 and September 2004, respectively. Dissolved sulfate (SO_4^{2-}) and calcium ion (Ca^{2+}) were determined by the standard methodology of ion chromatography (Metrohm 790 IC). The relative standard deviation was less than 2%. The concentrations of Ba^{2+} and I in porewater samples were analyzed by inductively coupled plasma mass spectrometry (ICP-MS, Finnigan Element II). Before measurement, samples were prepared by diluting in 2% HNO_3 (for Ba^{2+}) or aqua ammonia (for I) with rhodium (Rh) as an internal standard. The analytical precisions were calculated to be <5% for Ba and <2% for I.

The calcium (CaO), aluminium (Al_2O_3) and silicon (SiO_2) contents of the sediment samples were measured *via* PANalytical AXIOSX X-ray fluorescence spectrometry. The analytical precisions were smaller than 2%. After digesting the sediment samples via HCl, HF, and $HClO_4$ acid mixture, the total contents of Ba in sediments were measured via a PerkinElmer Optima 4300DV ICP-OES. The analytical precision was better than 2%.

TABLE 1 Location of the studied sites.

Site	Water depth (m)	Bottom water temperature	Core length (cm)
HD109	3218	~2	771
HD319	1730	~3	730

The contents of total organic carbon (TOC) were analyzed via the potassium dichromate wet oxidation method, with the relative standard deviation better than 1.5%.

Numerical modelling

A 1-D, steady-state, reaction-transport model is used to simulate the depth profiles of solid-phase particulate organic carbon (POC), headspace CH_4, dissolved SO_4^{2-}, Ca^{2+} and Ba^{2+} concentration. The model is based on the following partial differential equations for solid (Eq. 1) and dissolved (Eq. 2) species (Berner, 1980; Wallmann et al., 2006):

$$(1-\Phi)\frac{\partial C_s}{\partial t} = -\frac{\partial\left((1-\Phi)\cdot v_s \cdot C_s\right)}{\partial x} + (1-\Phi)\cdot \Sigma R \quad (1)$$

$$\Phi\frac{\partial C_d}{\partial t} = \frac{\partial\left(\Phi\cdot D_s\cdot\frac{\partial C_d}{\partial x}\right)}{\partial x} - \frac{\partial\left(\Phi\cdot v_p\cdot C_d\right)}{\partial x} + \Phi\cdot\Sigma R + \Phi\cdot\alpha(C_0 - C_l) \quad (2)$$

where C_s and C_d (μmol cm^{-3}) is the concentration of solid and dissolved species, respectively, x (cm) is depth, t (yr) denotes time, Φ denotes porosity, D_s (cm^2 yr^{-1}) denotes the molecular diffusion coefficient corrected for tortuosity, v_p (cm yr^{-1}) denotes the burial velocity of porewater, v_s (cm yr^{-1}) denotes the burial velocity of solids, ΣR is the sum of the rates of biogeochemical reactions considered in the model, α is the mixing rate of bottom water and porewater, C_0 and C_l are the solute concentrations at the sediment-water interface (SWI) and at any depth within the mixing zone, respectively.

Porosity was assumed to decrease with depth under steady-state compaction:

$$\Phi = \Phi_f + \left(\Phi_0 - \Phi_f\right)\cdot e^{-px} \quad (3)$$

where Φ_0 and Φ_f (both dimensionless) are the porosity at SWI and below the depth of compaction, respectively. Moreover, p (cm^{-1}) is the attenuation coefficient for porosity. Since externally imposed fluid advection at the SWI is absent, the velocity of porewater and solids is directed downward under steady-state compaction relative to the SWI:

$$v_p = \frac{\Phi_f\cdot\omega}{\Phi} \quad (4)$$

$$v_s = \frac{\left(1-\Phi_f\right)\cdot\omega}{1-\Phi} \quad (5)$$

where ω ($cmyr^{-1}$) denotes the sedimentation rate.

Depth-dependent molecular diffusive coefficients of dissolved species are calculated based on the equation of Boudreau (1997):

$$D_s = \frac{D_m}{1-ln\ (\Phi)^2} \quad (6)$$

where D_m is the molecular diffusion coefficient at the local temperature, salinity and pressure.

The irrigation rate α, is described as a non-local transport of solutes:

$$\alpha = \alpha_0\cdot\frac{\exp\ (L_{irr} - x/\alpha_1)}{1+\exp\ (L_{irr} - x/\alpha_1)} \quad (7)$$

where α_0 (yr^{-1}) denotes the irrigation intensity coefficient, L_{irr} (cm) is the maximum depth of irrigation, α_1 (cm) is the parameter pointing to the degree of attenuation for bubble irrigation just below the depth of L_{irr}.

The dominant biogeochemical reactions included in the model are organoclastic sulfate reduction (OSR), AOM, *in situ* methanogenesis (MG), and authigenic carbonate precipitation (CP). This model does not consider the reactions of authigenic barite precipitation and dissolution. Instead, the differences between the measured and modelled depth profiles of Ba^{2+} concentration, is used to trace the diagenetic reactions of barite at times of sampling (cf. Vanneste et al., 2013). Additionally, other reactions, including aerobic respiration, denitrification, iron reduction, and manganese reduction via organic matter remineralization are not considered in the model as these processes only occur within the top of sediment (~10–20 cm below the SWI). The reaction rate expressions are shown in Table 2, and the net reaction terms of one solid (POC) and three dissolved species (SO_4^{2-}, Ca^{2+} and CH_4) are given in Table 3. All the parameters in the model are shown in Table 4.

The simulating length of the cores are 1,000 cm for HD109 and 1,500 cm for HD319, respectively. Measured values at the top of sediment are used as upper boundary conditions for all species (Dirichlet boundary). A zero concentration gradient (Neumann-type boundary) was set at the lower boundary for all the species except for Ba^{2+}. The lower boundary condition for Ba^{2+} is imposed as a fixed value. The model was calculated by the NDSolve object of

TABLE 2 Kinetic reaction rate laws in the model.

Rate	Kinetrc rale law[a]
Total POC degradation (wt% C yr^{-1})	$R_{POC} = (0.16 \cdot (a_0 + \frac{x}{v_s})^{-0.95}) \cdot POC$
Organic matter degradation by sulfate reduction (mmol cm^{-3} yr^{-1} of SO_4^{2-})	$R_{OSR} = 0.5 \cdot R_{POC} \cdot \frac{[SO_4^{2-}]}{[SO_4^{2-}]+K_{SO_4^{2-}}} / f_{POC}$
Methanogenesis (mmol cm^{-3} yr^{-1} of CH_4)	$R_{MG} = 0.5 \cdot R_{POC} \cdot \frac{K_{SO_4^{2-}}}{[SO_4^{2-}]+K_{SO_4^{2-}}} / f_{POC}$
Anaerobic oxidation of methane (mmol cm^{-3} yr^{-1} of CH_4)	$R_{AOM} = k_{AOM} \cdot [SO_4^{2-}][CH_4]$
Authigenic carbonate precipitation (mmol cm $^{-3}$ yr^{-1} of Ca^{2+})	$R_{CP} = k_{Ca} \cdot (\frac{[Ca^{2+}] \cdot [CO_3^{2-}]}{K_{SP}} - 1)$

[a]Notation: R_{POC} (wt% C yr^{-1}): POC degradation rate, a_0 (yr): initial age of organic matter in uppermost sediment, v_s (cm yr^{-1}): burial velocity of solids, x (cm): depth in the sediment, Kc: inhibition constant for POC degradation, POC (wt%): POC content in sediment. R_{OSR} (mmol cm^{-3} yr^{-1} of SO_4^{2-}): OSR rate, $[SO_4^{2-}]$: SO_4^{2-} concentration, $K_{SO_4^{2-}}$: Michaelis–Menten constant for the inhibition of sulfate reduction at low sulfate concentrations, f_{POC}: convert between POC (wt%) and DIC (mmol cm^{-3} of pore fluid). f_{POC}= $MW_C/10\Phi/(1-\Phi)/\rho_S$, where MW_C is the molecular weight of carbon (12 g mol^{-1}), ρ_S is the density of dry sediments, and Φ is the porosity. R_{MG} (mmol cm^{-3} yr^{-1} of CH_4): methanogenesis rate. R_{AOM} (mmol cm^{-3} yr^{-1} of CH_4): AOM rate, k_{AOM}: rate constant of AOM, $[CH_4]$: dissolved CH_4 concentration. R_{CP} (mmol cm^{-3} yr^{-1} of Ca^{2+}): authigenic carbonate precipitation rate, k_{Ca} (molcm^{-3} yr^{-1}): rate constant of CP, K_{SP} ($mol^2.l^2$): thermodynamic equilibrium constant at the seafloor condition, $[Ca^{2+}]$ and $[CO_3^{2-}]$: Ca^{2+} and CO_3^{2-} concentrations, respectively.

TABLE 3 Reaction terms of species considered in the model.

Species	Rate
Particulate organic carbon (POC)	$-R_{POC}$
Sulfate (SO_4^{2-})	$-R_{OSR}-R_{AOM}$
Calcium (Ca^{2+})	$-R_{CP}$
Methane (CH_4)	$R_{MG}-R_{AOM}$

MATHEMATICA V. 12.0. All simulations were run for 10^6 years to reach steady state with a mass conservation of >99 %.

Estimating the time for authigenic barite accumulation

The background Ba content (C_0) is about 440 ± 10 mg kg^{-1} and 500 ± 10 mg kg^{-1} at the cores HD109 and HD319, respectively (Figure 3). Using this content as the lower limit, the depth-integrated total amount of excess Ba in the barium enrichment layer was obtained by the expression below:

$$S_{Ba} = \int_u^v (C_x - C_0) \cdot \rho \cdot (1 - \Phi) dx \quad (8)$$

where C_x is the barium content within the peaks from a depth interval from u to v, ρ and Φ are the average grain density and porosity of the sediments.

To calculate the diffusive Ba^{2+} fluxes throughout the SMTZ, Eqs. (9) was used assuming a steady state condition (Schulz, 2006):

$$J_{Ba} = -\Phi D_s \frac{dC_{Ba}}{dx} \quad (9)$$

where J_{Ba}: Ba^{2+}diffusive flux (μmol m^{-2} yr^{-1}), Φ: porosity of sediment, D_S: diffusion coefficient of sediment (m^2 s^{-1}), C_{Ba}: Ba^{2+} concentration (μmol L^{-1}), and x: sediment depth (m). Averages of sediment porosity from 0.65 to 0.75 is applied (Suess, 2005; Huang et al., 2008). The diffusion coefficient D_s is calculated from the diffusion coefficient in free solution (D_0) of 4.41×10^{-6} cm^2 s^{-1} (2 °C) for HD109 and 4.59×10^{-6} cm^2 s^{-1} (3 °C) for HD319, according to Schulz (2006).

Under the assumption of a constant upward Ba^{2+} flux into the sulfate reduction zone, the time (t) required to precipitate the barium pool was calculated as below:

$$t = S_{Ba}/J_{Ba} \quad (10)$$

Results

Geochemical trend of pore fluids

Depth profiles of headspace CH_4, porewater SO_4^{2-}, Ca^{2+}, Ba^{2+}, I concentrations and $\delta^{13}C_{CH4}$ or $\delta^{13}C_{DIC}$ at cores HD109 and HD319 are presented in Figure 2, and the specific data are provided in Table 5. At core HD109, the SO_4^{2-} concentrations keep almost constant as about 28 mM except four abnormal values above 350 cmbsf. Below this depth, it gradually declines to 1.9 mM at the depth of 680 cmbsf and remains at this low level till the base of the cor (Figure 2A). The CH_4 concentrations remain at low levels (0.4–2.1 μM) above 520 cmbsf, followed by a rapid increase to 239.4 μM at 771 cmbs (Figure 2A). The Ca^{2+} concentrations keep relatively constant at the seawater value (~10 mM) with some degree of variations above 300 cmbsf and then decrease to 2.2 mM at 750 cmbsf with some abnormal peaks below 600 cmbs (Figure 2B). The dissolved

TABLE 4 The dataset of specific parameters and boundary conditions used in the model.

Parameter	HD109	HD319	Unit
Temperature (T)[a]	2	3	°C
Salinity (S)	35	35	PSU
Pressure (P)	32.7	17.6	MPa
Density of dry solids (ρ_s)	2.6	2.6	g cm^{-3}
Density of porewater (ρ_{pw})	1.033	1.033	g cm^{-3}
Sedimentation rate (ω)[b]	0.01	0.01	cm yr^{-1}
Porosity at sediment-water interface (Φ_0)[c]	0.7	0.7	
Porosity in compacted sediments (Φ_f) [c]	0.7	0.7	
Depth attenuation coefficient for porosity (p)	0	0	cm^{-1}
Initial age of POC (a_0)[d]	50	50	Kyr
Michaelis–Menten constant for POC degradation ($K_{SO_4^{2-}}$)[e]	1×10^{-4}	1×10^{-4}	mM
Rate constant for AOM (k_{AOM})[d]	30	30	cm^3 yr^{-1} $mmol^{-1}$
Depth of gas bubble irrigation (L_{irr})	280	200	Cm
Irrigation coefficient at the surface (α_0)	0.1	0.1	yr^{-1}
Attenuation coefficient for decrease in bubble irrigation (α_1)[e]	5	5	Cm
Rate constant for carbonate precip./dissol. (k_{Ca})	1.3×10^{-6}	3×10^{-7}	mmol cm^{-3} yr^{-1}
Upper boundary condition for SO_4^{2-}	29	26	mM
Upper boundary condition for Ca^{2+}	10.3	10.3	mM
Upper boundary condition for Ba^{2+}	1.5	1.9	μM
Lower boundary condition for SO_4^{2-}	$\partial C/\partial x = 0$	$\partial C/\partial x = 0$	-
Lower boundary condition for Ca^{2+}	$\partial C/\partial x = 0$	$\partial C/\partial x = 0$	-
Lower boundary condition for Ba^{2+}	25	25	μM

[a]alculated using an empirical formula.
[b]Chen et al. (2006).
[c]Wang et al. (2000).
[d]Wallmann et al. (2006).
[e]Chuang et al. (2013).

Ba^{2+} concentrations remain low (<2 μM) in the uppermost 500 cm. Below this depth, Ba^{2+} concentrations increase to highest value (40 μM) in ~680 cmbsf with some fluctuation (Figure 2C). The I concentrations are also relatively constant at a low level (~16 μM) above 300 cmbsf and increase to 108 μM at the bottom of the core with some fluctuation (Figure 2D).

Similar to core HD109, the SO_4^{2-} and Ca^{2+} concentrations vary little in the upper 100 cmbsf. Below this depth, they gradually decline to 7.1 and 5.8 mM at the bottom of core HD319, respectively (Figures 2F,G). The CH_4 concentrations vary little from 0.2 to 0.4 μM above 600 cmbsf, followed by a sharp increase to 169.3 μM at the bottom of the corFigure 2F 2f). The dissolved Ba^{2+} concentrations remain low values in the upper 600 cmbsf and rise to the highest value (12.7 μM) at 710 cmbs Figure 2H. The dissolved I concentrations increase slightly above 300 cmbsf and then increase sharply to 54.4 μM at the bottom of the core Figure 2I.

Geochemical trend of sediments

Depth profiles of Ba content, Ba/Al ratios, CaO, Al_2O_3, SiO_2 and TOC contents in the sediments of cores HD109 and HD319 are presented in Figure 3, and the raw data are shown in Table 6. Total Ba contents range from 420 to 758 mg kg^{-1} at core HD109 and from 448 to 1,147 mg kg^{-1} at core HD319. The total solid-phase Ba content below 560 cmbsf of core HD109 and throughout core HD319 remains almost constant, fluctuating at 440 ± 10 mg kg^{-1} and 500 ± 10 mg kg^{-1}, and is thus assumed as the 'background' values of solid-phase Ba conten Figure 3A. Above 560 cmbsf of core HD109, the Ba contents are higher and at least four layers of Ba enrichments are recognized. The Ba contents were normalized to Al for purpose of deducting lithologic changes. The depth intervals of Ba enrichments are ca. 40–160 cmbsf, 200–240 cmbsf, 240–300 cmbsf and 320–560 mbsf, respectively. The maximum Ba concentrations in these layers are 698, 758, 596 and 595 mg kg^{-1}, respectively. Similar to core HD109, there are also four layers with Ba enrichment at the core HD319 (Figure 3F). The depth

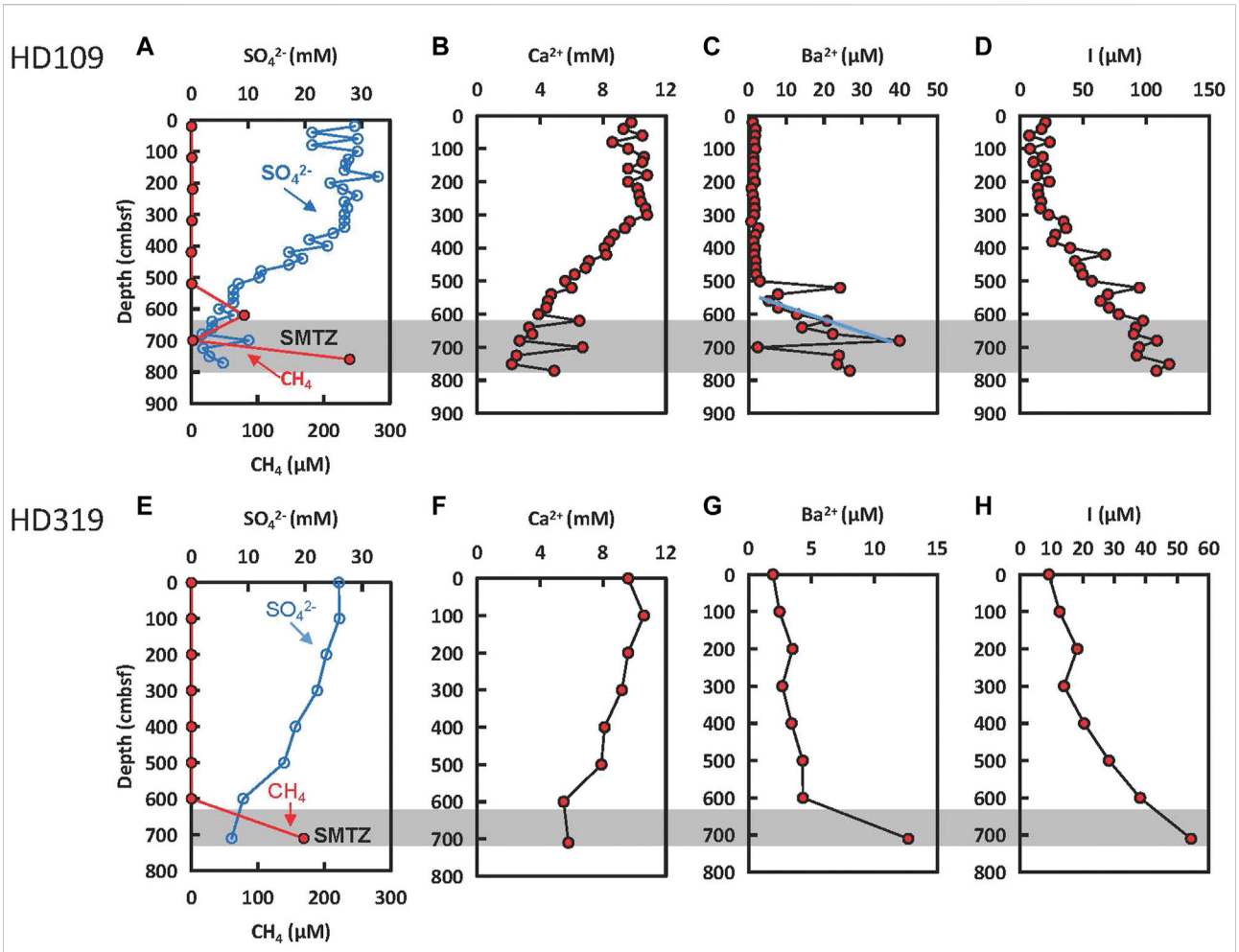

FIGURE 2
Depth profiles of headspace CH_4, porewater SO_4^{2-}, Ca^{2+}, Ba^{2+}, I- concentrations at cores HD109 **(A–D)** and HD319 **(E–H)**. The shaded portions of the graphs refer to the current sulfate-methane transition zones (SMTZ). The blue solid line marks the gradient used for Ba^{2+} flux calculation.

intervals of Ba enrichments are ca. 280–320 cmbsf, 400–420 cmbsf, 580–600 cmbsf and 620–660 mbsf, respectively. The maximums of Ba concentration within these zones are 1,147, 729, 905 and 944 mg kg^{-1}, respectively.

The major element contents at the core HD109 are 1.5–5.7% for CaO, 14.3–17.4% for Al_2O_3, and 54.9–61.8% for SiO_2, respectively Figures 3B–D. The contents of CaO, Al_2O_3 and SiO_2 at the core HD319 are 2.7%–8.4%, 14.3%–18.3% and 51.0–58.1%, respectively Figures 3G–I. The TOC contents range from 0.7 to 1.5% at core HD109 and from 0.6 to 1.1% at core HD319, respectively Figures 3E,J.

Modelling results

The modelled profiles and turnovers are exhibited in Figure 4 and Table 7, respectively. The steady-state stimulation results matched the downcore trend of POC, SO_4^{2-}, and Ca^{2+} concentrations at the cores HD109 and HD319 with prominent differences between modelled and measured concentrations of CH_4 owing to rapid degassing at the time of sampling (Figure 4). The OSR rates were 19.4 and 21.5 mmol m^{-2} yr^{-1} for cores HD109 and HD319, respectively. In comparison, the AOM is the main pathway of sulfate reduction, which rates were 172.2 and 45.3 mmol m^{-2} yr^{-1} for the two cores, respectively. Authigenic carbonate precipitation was induced by the OSR and AOM reactions, which rates were 31.8 and 7.3 mmol m^{-2} yr^{-1} for the two cores (Table 7). Additionally, the modelled Ba^{2+} concentrations are higher than the measured Ba^{2+} values above the SMTZ at both cores, suggesting that dissolved Ba^{2+} had been taken up into the solid phase when pore fluid samples were collected. In contrast, porewater Ba^{2+} concentrations excess the modelling Ba^{2+} values at depth interval of 600–770 cmbsf of the core

TABLE 5 Headspace CH_4, porewater SO_4^{2-}, Ca^{2+}, Ba^{2+}, I^- concentrations of cores HD109 and HD319.

Core ID	Depth (cmbsf)	SO_4^{2-} (mM)	Ca^{2+} (mM)	Ba^{2+} (μM)	I (μM)	CH_4 (μM)
HD109[a]	20	28.8	9.8	1.1	20.2	0.4
	40	21.3	9.3	1.9	17.1	
	60	29.3	10.5	1.8	7.4	
	80	21.3	8.6	1.5	23.6	
	100	29.3	9.6	1.8	7.9	
	125	27.7	10.6	1.3	18	0.8
	140	27.2	10.5	1.4	10.8	
	160	27	9.6	1.6	20.4	
	180	32.9	10.8	1.2	13.3	
	200	24.5	9.6	1.7	23.3	
	220	26.7	10.2	0.8	14.2	2.1
	240	29.2	10.3	1.1	14.6	
	260	27	10.4	1.6	16.7	
	280	27.5	10.7	1.6	16.2	
	300	27	10.8	1.5	22.6	
	320	27	9.7	0.7	34.6	1.1
	340	27	9.4	2.6	36.6	
	360	25	8.7	1.8	28	
	380	20.8	8.4	1.3	25.7	
	400	24	8.1	1.7	39.7	
	420	17.2	8.2	1.5	67.4	0.2
	440	19.6	7.1	1.9	43.7	
	460	17.2	6.9	1.9	47.5	
	480	12.3	6.2	2.1	49.6	
	500	12	5.6	3.0	56.9	
	520	8.3	6	24.2	94.5	0.8
	540	7.4	4.7	7.8	69.6	
	560	7.4	4.5	5.4	63.8	
	580	7.4	4.4	7.8	70.5	
	600	4.9	3.9	12.8	78.2	
	620	7.4	6.5	20.8	97.4	80.0
	640	3.7	3.3	14.2	91.8	
	660	3.7	3.5	22.3	90.1	
	680	1.9	2.7	40.0	108.4	
	700	10.1	6.7	2.4	94.2	2.4
	725	2.1	2.5	24.0	92.5	
	751	3.2	2.2	23.5	118.1	
	771	5.6	4.9	26.8	108	239.4
HD319	0	25.9	9.6	1.9	9.2	0.2
	100	26	10.6	2.5	12.6	0.3
	200	23.7	9.6	3.5	18.2	0.4
	300	22.1	9.2	2.7	14	0.4
	400	18.3	8.1	3.4	20.4	0.4
	500	16.3	7.9	4.3	28.3	0.3
	600	9.1	5.5	4.3	38.2	0.3
	710	7.1	5.8	12.7	54.4	169.3

[a]The data of pore water SO_4^{2-} and headspace CH_4 concentrations are cited from Lin et al. (2017).

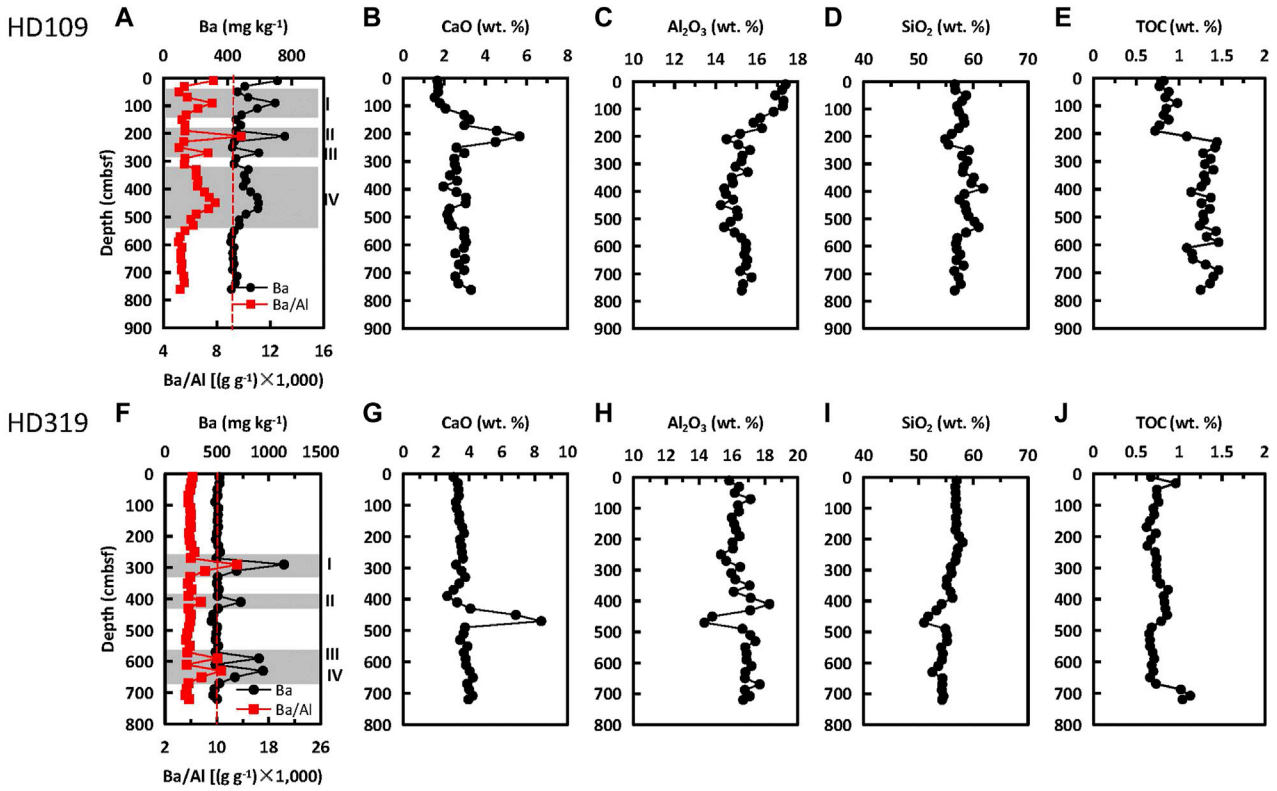

FIGURE 3
Depth profiles for the contents of Ba **(A,F)**, CaO **(B,G)**, Al_2O_3 **(C,H)**, SiO_2 **(D,I)**, TOC **(E,J)** and Ba/Al ratio **(A,F)** at cores HD109 and HD319. The shaded intervals I to IV **(A,F)** refer to Ba fronts. The red vertical lines **(A,F)** refer to the background values of Ba.

HD109, suggesting that Ba^{2+} had been released from the sedimentary barite to the pore fluids (c.f. Vanneste et al., 2013).

Timing of authigenic barite front accumulation

Given a fixed upward Ba^{2+} diffusive flux into the sulfate reduction zone, the accumulation time for the measured barium peaks at cores HD109 and HD319 can be estimated. Considering that porosity data are not available but are important for flux calculation, we referred to the measured porosity data in the nearby Haiyang four area (Suess, 2005; Huang et al., 2008) and applied a porosity of 65, 70, and 75% to show how sensitive the results are to the variations in porosity. The variation of the time for Ba enrichment due to different porosities is presented in Table 8. The calculation results suggest that four Ba fronts from the top to the current SMTZ at core HD109 have persisted for 2.5–4.8 ka, 1.4–2.8 ka, 0.8–1.6 ka and 4.7–9.0 ka. In addition, the duration times for the four Ba fronts from the top to bottom at core HD319 are 3.7–7.1 ka, 1.0–1.9 ka, 1.9–3.7 ka and 3.2–6.1 ka. The calculation results underline that the barite fronts at both cores have been accumulating since the last ten thousand years, with four major peaks accumulation for several thousand years. If we take non-steady-state conditions into consideration, which include the burial input of Ba as well as the output of Ba from the front through burial, the accumulation time could be underestimated (Snyder et al., 2007b). Nevertheless, these conditions can be neglected in this study, due to the relatively short durations for each seepage events and the rather low sedimentation rates in the study area (Chen et al., 2006).

Discussion

Origin of barium fronts

Increase in solid-phase Ba contents in sediments may depend on a variety of factors. For instance, elevated Ba content might be due to high contents of aluminosilicate minerals where barium is

TABLE 6 Contents of TOC, CaO, SiO_2, Al_2O_3 and Ba in the sediments and Ba^{2+} concentration in pore fluids of core HD109 and HD319.

Core ID	Depth	Ba	CaO	Al_2O_3	SiO_2	TOC
	(cmbsf)	(mg kg^{-1})	(%)	(%)	(%)	(%)
HD109	10	712	0.8	17.4	56.6	0.82
	30	508	1.1	17.2	56.7	0.77
	50	462	0.5	16.9	58.7	0.88
	70	529	1.0	17.3	58.0	0.84
	90	698	1.1	17.3	57.0	0.98
	115	586	1.8	16.8	57.3	0.85
	130	488	2.7	16.2	58.2	0.82
	150	453	3.4	15.8	58.4	0.88
	170	483	3.9	16.3	57.3	0.77
	190	452	5.9	15.2	56.1	0.72
	210	758	7.2	14.5	54.9	1.09
	230	442	6.1	15.1	55.5	1.44
	250	430	2.7	15.7	59.2	1.42
	270	596	1.9	15.3	58.0	1.28
	290	453	1.3	15.3	58.9	1.37
	310	440	1.9	15.0	58.3	1.30
	330	530	1.8	15.6	58.1	1.40
	350	505	1.7	14.8	60.1	1.29
	370	516	1.8	14.8	59.7	1.31
	390	498	1.5	14.4	61.8	1.26
	410	544	3.6	14.5	58.4	1.14
	430	586	3.6	14.9	57.5	1.37
	450	595	3.9	14.3	58.5	1.26
	470	590	3.6	15.0	58.7	1.36
	490	515	2.5	15.1	59.1	1.28
	510	473	3.1	14.7	60.2	1.29
	530	474	2.8	14.4	61.0	1.24
	550	442	5.5	14.9	58.7	1.43
	570	426	4.9	15.3	57.1	1.32
	590	420	4.8	15.5	56.8	1.46
	610	441	4.8	15.5	57.0	1.09
	630	432	4.3	15.4	57.6	1.15
	650	435	4.8	15.5	56.9	1.16
	670	441	3.9	15.5	58.2	1.31
	690	431	4.5	15.2	56.6	1.46
	715	460	4.1	15.8	57.3	1.40
	741	450	4.3	15.3	57.7	1.36
	761	424	5.0	15.3	56.6	1.25
HD319	10	524	3.1	15.8	57.0	0.67
	30	525	3.3	16.4	56.7	0.96
	50	503	3.4	16.2	56.8	0.74
	70	507	3.4	17.1	56.8	0.74
	90	483	3.2	16.4	56.7	0.76
	110	514	3.3	16.4	57.1	0.70
	130	509	3.4	16.0	56.8	0.71
	150	504	3.4	16.1	56.9	0.66
	170	511	3.6	16.2	56.8	0.62
	190	499	3.7	16.5	57.4	0.73
	210	491	3.5	16.0	58.1	0.67
	230	512	3.5	16.1	57.2	0.63
	250	530	3.6	15.3	57.0	0.72
	270	495	3.6	15.6	56.7	0.74
	290	1147	3.2	16.5	55.9	0.73
	310	690	3.6	16.0	56.0	0.74
	330	507	3.8	16.2	55.2	0.74
	350	498	3.4	17.1	55.2	0.78
	370	518	3.1	16.1	55.8	0.87
	390	506	2.7	17.1	56.2	0.82
	410	729	3.3	18.3	54.2	0.83
	430	510	4.1	17.1	53.3	0.84
	450	465	6.9	14.8	51.8	0.86
	470	448	8.4	14.3	51.0	0.79
	490	503	3.8	16.6	54.9	0.68
	510	492	3.7	17.1	55.2	0.65
	530	487	3.5	17.4	55.2	0.66
	550	513	3.9	16.8	54.1	0.66
	570	486	3.7	16.9	54.4	0.69
	590	905	3.8	16.9	54.3	0.71
	610	486	3.8	17.2	53.6	0.68
	630	944	4.1	16.8	52.5	0.70
	650	674	4.2	16.8	54.4	0.66
	670	523	3.9	17.7	54.3	0.73
	688	478	4.0	16.8	54.3	1.02
	708	465	4.2	17.1	54.5	1.13
	720	501	4.0	16.7	54.3	1.04

hosted in crystal lattices. It is shown that Ba contents in detrital aluminosilicates can reach up to 1,000 mg kg^{-1} (Dymond et al., 1992). The sediments of cores HD109 and HD319 are consisted of four primary components: clay, quartz, feldspar and biogenic calcium carbonate (Chen et al., 2006). Significant variations in the distribution of these components would thus lead to marked changes in Si, Al and Ca contents in the sediments. Nevertheless, the contents of these elements do not vary considerably throughout the Ba fronts at the two cores except for the Ba fronts II at core HD109. There is a pronounced Ca peak across the Ba front (Figure 3). The Si, Al and Ca contents at core HD109 indicate normal hemipelagic background deposition and is inferred to be controlled by the glacial-interglacial cycles. An increase in the Ca contents was caused by an increase in the

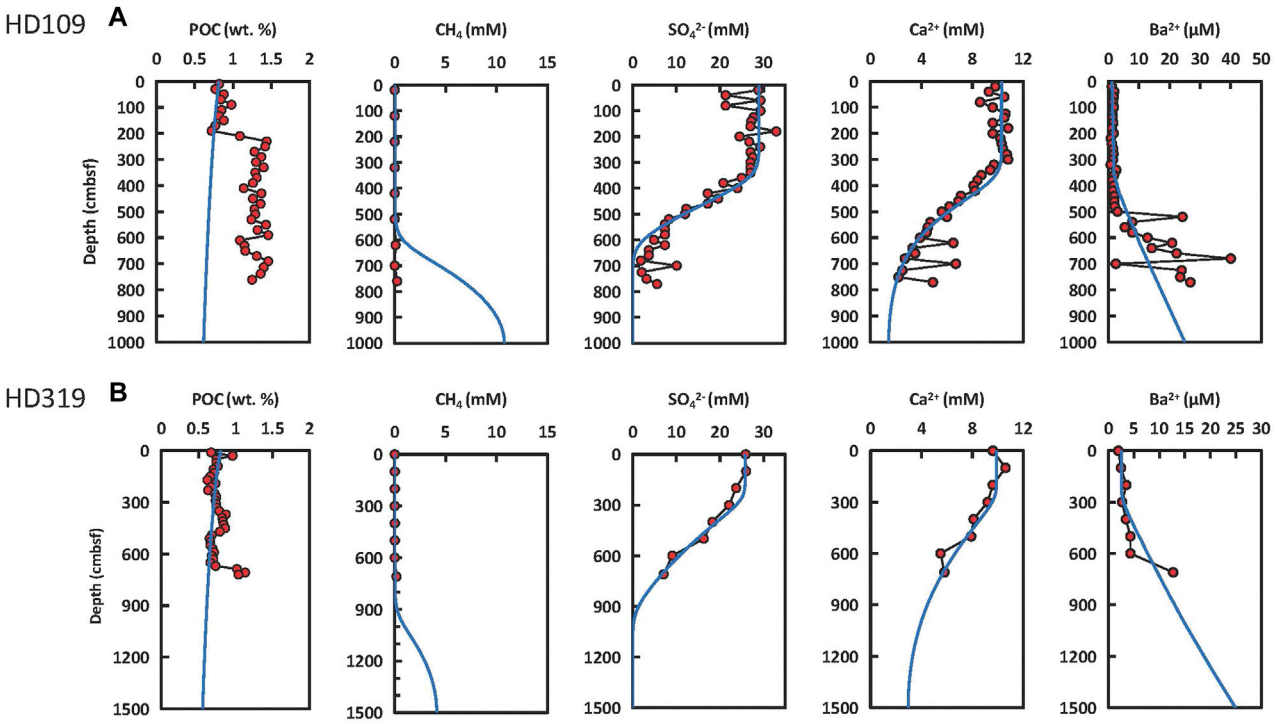

FIGURE 4
Measured data (dots) and simulated results from the steady-state model (curves) of cores HD109 **(A)** and HD319 **(B)**. Downward concentrations of POC, CH4, SO42–, Ca2+ and Ba2+ are shown.

TABLE 7 Depth-integrated turnover rates according to the steady-state modelling.

Turnover	HD109	HD319	Unit
F_{POC}: total POC mineralization	24.1	26.1	mmol m^{-2} yr^{-1} of C
F_{OSR}: sulfate reduction via POC degradation	19.4	21.5	mmol m^{-2} yr^{-1} of SO_4^{2-}
F_{ME}: methane formation via POC degradation	4.6	4.6	mmol m^{-2} yr^{-1} of CH_4
F_{GS}: methane gas dissolution	188.1	45.5	mmol m^{-2} yr^{-1} of CH_4
F_{AOM}: anaerobic oxidation of methane	172.2	45.3	mmol m^{-2} yr^{-1} of CH_4
F_{CP}: authigenic $CaCO_3$ precipitation	31.8	7.3	mmol m^{-2} yr^{-1} of C
Sulfate consumed by AOM	89.9	67.8	%
Percentage of CH_4 consumed by AOM	89.4	90.4	%
Percentage of CH_4 flux from depth	97.6	90.8	%

relative abundance of foraminifera during the transition from Pleistocene to Holocene (Chen et al., 2006). Furthermore, variations in Ba/Al ratios with depth at the two cores are virtually identical to those of solid-phase Ba contents (Figure 3), with the co-occurrence of obvious peaks of Ba content and Ba/Al ratio. The similar variation trend of the two proxies indicates that the formation of Ba fronts was not associated with variations in primary composition of sediment. In summary, the Ba contents and Ba/Al ratios for normalization are both considerably higher than the background values at the cores HD109 and HD319 (Figure 3A,F), which implies that the Ba fronts are derived from mineral authigenesis rather than of detrital origin. Collectively, it is suggested that the Ba front is attributed to the occurrence of barite but not a Ba-rich carbonate phase (Figure 3).

The Ba of the authigenic barite is usually regarded as deriving from biogenic barite which becomes dissolved in sulfate-free pore fluids (Torres et al., 1996; McManus et al., 1998). Decaying

TABLE 8 Calculation of accumulation time of Ba fronts at cores HD109 and HD319.

Core ID	Layer	Porosity (%)	D_0 of Ba ($\times 10^{-6}$ cm^2 s^{-1})	Ba gradient[a] (mol cm^{-4})	Ba flux (mol cm^{-2} a^{-1})	Size of Ba front (g cm^{-2})	Accumulation time (ka)
HD109	I	65	4.41	3.01E−10	1.46E−08	9.73E−03	4.8
	II					5.55E−03	2.8
	III					3.19E−03	1.6
	IV					1.80E−02	9.0
							Total: 18.2
	I	70	4.41	3.01E−10	1.71E−08	8.34E−03	3.6
	II					4.76E−03	2.0
	III					2.73E−03	1.2
	IV					1.54E−02	6.6
							Total: 13.3
	I	75	4.41	3.01E−10	1.99E−08	6.95E−03	2.5
	II					3.97E−03	1.4
	III					2.28E−03	0.8
	IV					1.28E−02	4.7
							Total: 9.5
HD319	I	65	4.59	3.01E−10	1.52E−08	1.48E−02	7.1
	II					3.91E−03	1.9
	III					7.64E−03	3.7
	IV					1.28E−02	6.1
							Total: 18.8
	I	70	4.59	3.01E−10	1.78E−08	1.27E−02	5.2
	II					3.35E−03	1.4
	III					6.55E−03	2.7
	IV					1.10E−02	4.5
							Total: 13.8
	I	75	4.59	3.01E−10	2.07E−08	1.06E−02	3.7
	II					2.80E−03	1.0
	III					5.46E−03	1.9
	IV					9.17E−03	3.2
							Total: 9.8

[a]Assumed to be constant over time. Grain density: 2.6 g cm^{-3}.

biological debris induces the formation of biogenic barite particles in the water column, which then is buried in the sediments (Dymond et al., 1992; Paytan et al., 1993; Gingele and Dahmke, 1994). Hence, the fluxes of biogenic barite burial in the sediments depend on the regional productivity in the water column, and generally higher barite fluxes on the continental margins (Von Breymann et al., 1992). Correspondingly, there are elevated Ba^{2+} concentrations in the pore fluids in continental margin sediments. To date, the concentrations of porewater Ba^{2+} at the typical seep sites, such as Monterey Bay, Peru Margin, San Clemente Fault, and Carlos Ribeiro mud volcano, are considered to mainly originate from the dissolution of biogenic barite and range from 8 to 146 μM (Torres et al., 1996; Torres et al., 2002; Naehr et al., 2000; Vanneste et al., 2013). In addition, the Ba contents in the Ba fronts at the mud volcanos in the Gulf of Mexico are as high as 14,600–23,000 mg kg^{-1}, corresponding to the very high Ba^{2+} concentration in the pore water at these sites (up to 1.2 mM) (Castellini et al., 2006). The excess Ba was released from the dissolution of detrital K-feldspar in sandstone layers (Castellini et al., 2006). In this study, the porewater barium concentrations measured at the cores HD109 and HD319 (up to ~40 μM) are within the range of biogenic barite provenance, suggesting that the dissolved barium at these cores is mainly derived from biogenic barite.

Present-day methane and barium cycle

The sulfate depletion in porewater and the elevated methane concentration at the lower section of the cores HD109 and

HD319 indicate the occurrence of sulfate reduction-driven AOM in the shallow sediments of both sites (Figure 2). There is a relatively broad zone (~600–700 cmbsf) of methane and sulfate co-existence at the core HD109. It is suggested that methane tailing in the sulfate zone may result from incomplete AOM, which may be caused by the dynamic processes of reactive intermediates related to AOM (Dale et al., 2008; Holmkvist et al., 2011).

The porewater profiles of the two cores show a kink-type feature, similar to those observed at other sites in the northern SCS (Yang et al., 2010; Chuang et al., 2013; Feng et al., 2019; Feng et al., 2020; Hu et al., 2019). As the concentrations of the primary dissolved species in porewaters above the kink are close to bottom seawater values, the plausible mechanism for the occurrence of kink-type profiles is probably attributed to seawater intrusion due to hydrological and physical processes (Hensen et al., 2003; Hong et al., 2017). By using a reaction-transport model, the dissolved methane fluxes toward the SMTZ are calculated to be 188.1 mmol m^{-2} yr^{-1} for HD109 and 45.5 mmol m^{-2} yr^{-1} for HD319, respectively (Table 7). According to the modelling results, ~90 and 68% of dissolved sulfate are consumed by AOM at cores HD109 and HD319, respectively. Moreover, the simulation results show that the depth-intergrated AOM rates at both cores are about 10–37 times of the *in situ* methanogenesis rates (Table 7). Hence, the relative contribution ratios of external methane source to the total methane budget are 98 and 91% at cores HD109 and HD319, respectively, indicating that the major part of methane was derived from one or more subsurface reservoirs. A previous study showed that the dissolved gas extracted by headspace from the cores HD109 and a nearby core of HD319 consists only of methane, with $\delta^{13}C$ values of CH_4 ranging from -101.5‰ to -77.6‰ and from -77.8‰ to -57.8‰ below 100 cmbsf. This indicates that the external methane in the shallow sediments is of microbial origin (Fu, 2005). A comprehensive study indicated that microbial methane is predominant in the passive margin offshore southwestern Taiwan. The permeability of fluid channeling may determine the amount of microbial methane incorporated from shallow depth (Chen et al., 2017).

Profiles of Ba^{2+} concentration in pore fluids of the cores HD109 and HD319 resemble to those reported at other methane-rich systems, which are considered to be caused by barite precipitation slightly above or at the SMTZ (Torres et al., 1996; Dickens, 2001; Aloisi et al., 2004; Castellini et al., 2006; Snyder et al., 2007a; Snyder et al., 2007b; Vanneste et al., 2013). The modelling results for the data of Ba^{2+} show that the measured dissolved Ba^{2+} concentrations are lower than those predicted by the model above the SMTZ (Figure 4). These results indicate Ba^{2+} has been removed from the pore waters and taken up into the sediments as barite in sulfate-bearing layers above the SMTZ (Vanneste et al., 2013). The modern depth of active authigenic barite generation just above the SMTZ is indicated by minima in porewater Ba^{2+} (Figure 2). Therefore, the solid-phase Ba front IV at core HD109 may denote an active authigenic barite front (Torres et al., 1996; Vanneste et al., 2013). Additionally, as the sulfate is absent in the pore fluids below the SMTZ, Ba^{2+} is most likely released after previous barite dissolution (Torres et al., 1996). In this case, there is no Ba front below the current SMTZ at the core HD109 (Figure 3), which confirms the dissolution of barite and release of Ba^{2+} in dissolved sulfate-free sediments. It is also supported by the modelling results, as the measured dissolved Ba^{2+} concentrations are higher than those predicted by the model at and below the SMTZ (Figure 4).

It is notable that there are obvious differences in the modelling results and the *in-situ* analytic results of solid phase POC, headspace CH_4, porewater SO_4^{2-} and Ca^{2+} (Figure 4). The modeled POC profiles do not match the measured one below ~50 cmbsf, possibly suggesting a non-steady POC deposition with various POC flux or/and sedimentation rate. The POC flux at sediment surface was often higher in the pre-Holocene period and thus more POC could be deposited at this time (Luo et al., 2015). In addition, the obvious differences between modelled and measured concentrations of CH_4 could be attributed to rapid degassing at the time of sampling (Feng et al., 2019, 2020). Since the porewater samples of the core HD109 were collected again for further study at intervals of 20 cm after the cruise, the unusually high SO_4^{2-} concentrations at the bottom of this core may be caused by the oxidation of dissolved sulfide produced by AOM after core retrieval (Lin et al., 2017). Dissolved hydrogen sulfide and solid-phase iron sulfide could be oxidized quickly to dissolved sulfate under aerobic and anaerobic conditions and lead to decreases in the porewater pH, further causing carbonate dissolution and Ca^{2+} release (Liu et al., 2019). Therefore, the occurrence of elevated Ca^{2+} concentrations at the bottom of the core HD109 may result from the dissolution of carbonate in the sediments. Despite some changes in the geochemical composition of pore fluids might occur before analysing the concentrations of major ions and trace elements, the redox zones and the major biogeochemical processes concerned in this study can still be identified according to the measured geochemical data.

Implications for the history of methane seepage

It is suggested that decline in the methane released flux could potentially verified by the formation of paleo-barite fronts located above the current position of the authigenic barite front (Dickens, 2001). Therefore, the diagenetic Ba enrichment is suggested to be useful to quantitatively trace the net downward movement of the SMTZ and the changes in upward methane flux due to its unique accumulation

mechanism (e.g., Dickens, 2001; Riedinger et al., 2006; Snyder et al., 2007a; Snyder et al., 2007b; Nöthen and Kasten, 2011; Kasten et al., 2012; Vanneste et al., 2013). The calculation results display that the Ba fronts at both cores have been accumulating since the last ten thousand years, including four episodes for several thousand years. In addition, substantial amounts of authigenic pyrites are also discovered at both cores. Most of the pyrite aggregates are black in color and tubular in shape, which consist of clustered framboids (Lu, 2007; Lin et al., 2017). A paragenetic sequence of pyrite crystal growth was observed at the core HD109, which starts as framboidal pyrite with numerous uniform microcrystals, followed by radial overgrowth, and later formed euhedral crystals (Lin et al., 2017). Three zones of ^{34}S enrichment in authigenic pyrites at the core HD109 (at 170 cmbsf, from 450 to 600 cmbsf, 730 to 765 cmbsf depth) show obvious offsets in respect to the present-day SMTZ, suggesting that these zones reflect the positions of paleo-SMTZ. Pyritization during diagenetic processes was revealed, as overgrowths and euhedral pyrite crystals have much higher $\delta^{34}S$ values in comparison with framboids (Lin et al., 2017). Moreover, the $\delta^{13}C$ values of bulk carbonate at core HD319 range from -2.04‰ to -0.02‰ and there is a negative excursion of $\delta^{13}C_{carbonate}$ at the bottom of the core, which suggests the addition of methane-derived authigenic carbonate into the sedimentary inorganic carbon pool within the current SMTZ (Lu, 2007).

In this study, the solid-phase Ba peaks together with the authigenic ^{34}S-enriched pyrite above the present-day SMTZ at the core HD109 both indicate that the sulfidization front was located closer to the seabed in the past (Lin et al., 2017). The uppermost Ba enrichment (Figure 3) implies that the SMTZ was once located at ~1.5 mbsf in the past. However, the depth distribution of the Ba fronts implies that the SMTZ migrated downward by ~4 m with time since the most intense methane seepage, leaving behind the accumulation of diagenetic barite. Hence, the estimations in this study suggest that intense methane seepage occurred around the Pleistocene/Holocene transition, then the upward methane flux have decreased episodically in the post-glacial period.

Indeed, because of sediment burial, the Ba fronts formed in the past would move downward subsequently after the downward migration of the SMTZ. Therefore, the "paleo" Ba fronts should have accumulated at shallower depths in the past. Given the sedimentation rates of 10 cm/kyr during MIS1 for core HD109 and HD319 (Chen et al., 2006), the shallowest "paleo" Ba fronts at ~1.5 mbsf at core HD109 and at ~3.3 mbsf at core HD319 should locate close to the seafloor when they were accumulating in about ten thousand years ago. Alternatively, the SMTZ may not move downward continuously but rather fluctuated over the sediment layer, given the intermittent characteristics of methane seepage and the possible pulses of upward methane flux in a highly dynamic condition (Lin et al., 2017).

Uranium-series ages of seep carbonates indicated that intensive seep activities intermittently occurred from 144.5 ± 12.7 ka to 11 ka in the northeastern SCS (Tong et al., 2013; Han et al., 2014; Feng and Chen, 2015; Chen et al., 2019; Maoyu Wang et al., 2022). The intensive seepage events occurred either during the times of sea-level lowstands or during the periods of sea-level fall before the LGM (Tong et al., 2013; Han et al., 2014; Yang et al., 2018). Previous studies suggest that gas hydrate decomposed during sea-level lowstands or falling stages due to decreases in hydrostatic pressure, and finally resulted in subsurface methane release and the SMTZ upward movements in the northern SCS (Tong et al., 2013; Han et al., 2014; Li et al., 2016; Lin et al., 2016; Xie et al., 2019). In the post-glacial period, the upward methane flux seemed to decrease significantly on a regional scale (Luo et al., 2015; Lin et al., 2016). However, intense seep activities also took place during the sea-level highstand at time of MIS 5e (133.3–112.7 ka BP) and MIS 1 (since 14 ka BP) (Feng and Chen, 2015; Liang et al., 2017; Chen et al., 2019). An increase in bottom water temperature likely triggerred gas hydrate dissociation and associated methane seepage activities (Chen et al., 2019). Overall, the mechanisms for seepage activity are still under debated. More chronologic data of seep activities, especially the records of seepage during the deglaciation periods, are needed to better understand the forcing affecting seep activity.

In this study, the patterns of authigenic Ba fronts above the present-day SMTZ imply the downward migration of the paleo-SMTZ, while the estimation results suggest that the net decline in methane flux on the lower slope and at the bottom of the Taixinan Basin since about ten thousand years ago. Our modelling result shows that the released methane in shallow sediments was supplied from deeper sources, probably from underlying gas hydrate reservoir (Table 7). A study on a nearby sediment core (973–4) also indicated that the methane release flux had decreased since the last deglaciation, which was likely attributed to the decrease in the scale of gas hydrate decomposition (Zhang et al., 2018). The height of global sea level increased by more than 90 m since this period (Hanebuth et al., 2011). In theory, the rise of sea level led to an enhancement in the hydrostatic pressure and a decrease in the salinity, which further resulted in the thickening of the gas hydrate stability zone and the decline in the upward methane flux under a balanced pressure field (Sloan and Koh, 2007). Previous studies showed that even a moderate sea-level rise (<1 m) might significantly inhibit gas seepage at deep-water depths (>1,000 m) (Hsu et al., 2013; Sultan et al., 2020). *In situ* seafloor observations at the nearby cold seeps showed that the cold seeps in Jiulong Methane Reef and Haiyang four area were almost dormant at present day (Suess, 2005; Han et al., 2008; Huang et al., 2008; Wang et al., 2018). Therefore, the gradual decrease in upward methane flux on a regional scale is likely related to the stabilization of gas hydrate system in the northern SCS. This study suggest that

methane released fluxes in the northeastern SCS are highly variable both in spatial dimension and in temporal dimension, and provide new evidence in the driving mechanism of methane seepage in the post-glacial period.

Conclusion

In this study, we identify four intervals with authigenic barite front above the present-day SMTZ and use these Ba fronts to quantitatively track the net downward migration of the SMTZ at cores HD109 and HD319. Based on the estimation of the diffusive Ba^{2+} fluxes and the excess barium contents, microbial methane seepage probably occurred since about ten thousand years ago. It is proposed that methane seepage is more active during the LGM, inducing the SMTZ close to the seafloor. The upward methane flux then decreased and the SMTZ migrated downward gradually in hundreds to thousands of years in the post-glacial period. Consistent with other studies on the history of cold seep, our finding also imply that the gas hydrate system may be more stable during the post-glacial period in the northern SCS. This new case study indicates that methane seep activities on the northeastern slope of SCS are highly variable, and provides new insights on the evolution of methane seepage in the post-glacial period.

Data availability statement

The original contributions presented in the study are included in the article, further inquiries can be directed to the corresponding authors.

Author contributions

JF and NL conceived and designed the research, while JF wrote the manuscript. NL and ML analyzed the data and refined the manuscript. JL, SY, and HW provided the metadata and funding. XS provided scientific supervision. All authors agree with the final version of the manuscript.

Funding

This study was supported by the Guangdong Basic and Applied Basic Research Foundation (Grant: 2019A1515110306, 2022A1515011822), the Natural Science Foundation of China (Grant: 41876038), the Key Special Project for introduced Talents Team of Southern Marine Science and Engineering Laboratory (Guangzhou) (Grant: GML2019ZD0102), the Major Program of Guangdong Basic and Applied Research (Grant: 2019B030302004), the PI Project of Southern Marine Science and Engineering Guangdong Laboratory (Guangzhou) (Grant: GML2020GD0802), and the National Special Project on Gas Hydrate of China (Grant: DD20220224).

Conflict of interest

The authors declare that the research was conducted in the absence of any commercial or financial relationships that could be construed as a potential conflict of interest.

Publisher's note

All claims expressed in this article are solely those of the authors and do not necessarily represent those of their affiliated organizations, or those of the publisher, the editors and the reviewers. Any product that may be evaluated in this article, or claim that may be made by its manufacturer, is not guaranteed or endorsed by the publisher.

References

Aloisi, G., Wallmann, K., Bollwerk, S. M., Derkachev, A., Bohrmann, G., and Suess, E. (2004). The effect of dissolved barium on biogeochemical processes at cold seeps. *Geochim. Cosmochim. Acta* 68, 1735–1748. doi:10.1016/j.gca.2003.10.010

Bai, C., Zhang, G., Liang, J., Yang, Z., Yan, W., Zhu, D., et al. (2019). Deep-water sediment waves as a special gas hydrate reservoirs in the Northeastern South China Sea. *Mar. Pet. Geol.* 101, 476–485. doi:10.1016/j.marpetgeo.2018.12.031

Barnes, R. O., and Goldberg, E. D. (1976). Methane production and consumption in anoxic marine sediments. *Geol.* 4, 297–300. doi:10.1130/0091-7613(1976)4<297:mpacia>2.0.co;2

Berner, R. (1980). "Early Diagenesis: A theoretical approach," in *Princeton series in geochemistry* (Princeton, USA: Princeton University Press).

Boetius, A., Ravenschlag, K., Schubert, C. J., Rickert, D., Widdel, F., Gieseke, A., et al. (2000). A marine microbial consortium apparently mediating anaerobic oxidation of methane. *Nature* 407, 623–626. doi:10.1038/35036572

Boetius, A., and Wenzhöfer, F. (2013). Seafloor oxygen consumption fuelled by methane from cold seeps. *Nat. Geosci.* 6, 725–734. doi:10.1038/ngeo1926

Boudreau, B. P. (1997). *Diagenetic models and their implementation: Modelling transport and reactions in aquatic sediments.* Berlin, Germany: Springer, 414.

Burger, B. J., Estrada, M. V., and Gustin, M. S. (2019). What caused earth's largest mass extinction event? New evidence from the permian-triassic boundary in northeastern Utah. *Glob. Planet. Change* 177, 81–100. doi:10.1016/j.gloplacha.2019.03.013

Castellini, D. G., Dickens, G. R., Snyder, G. T., and Ruppel, C. D. (2006). Barium cycling in shallow sediment above active mud volcanoes in the Gulf of Mexico. *Chem. Geol.* 226, 1–30. doi:10.1016/j.chemgeo.2005.08.008

Chen, D., Huang, Y., Yuan, X., and Cathles, L. M. (2005). Seep carbonates and preserved methane oxidizing archaea and sulfate reducing bacteria fossils suggest recent gas venting on the seafloor in the northeastern South China Sea. *Mar. Pet. Geol.* 22, 613–621. doi:10.1016/j.marpetgeo.2005.05.002

Chen, F., Su, X., Lu, H., Zhu, Y., Liu, J., and Liao, Z. (2006). Lithologic features of sediments characterized by high sedimentation rates since the last glacial maximum from Dongsha area of the South China Sea. *Mar. Geol. Quat. Geol.* 26 (6), 9–17. (In Chinese with English abstract).

Chen, N. C., Yang, T. F., Hong, W. L., Chen, H. W., Chen, H. C., Hu, C., et al. (2017). Production, consumption, and migration of methane in accretionary prism of southwestern Taiwan. *Geochem. Geophys. Geosyst.* 18 (8), 2970–2989. doi:10.1002/2017gc006798

Chen, F., Wang, X., Li, N., Cao, J., Bayon, G., Peckmann, J., et al. (2019). Gas hydrate dissociation during sea-level highstand inferred from U/Th dating of seep carbonate from the South China Sea. *Geophys. Res. Lett.* 46 (23), 13928–13938. doi:10.1029/2019gl085643

Chuang, P. C., Dale, A. W., Wallmann, K., Haeckel, M., Yang, T. F., Chen, N. C., et al. (2013). Relating sulfate and methane dynamics to geology: Accretionary prism offshore SW Taiwan. *Geochem. Geophys. Geosyst.* 14 (7), 2523–2545. doi:10.1002/ggge.20168

Cui, H., Kaufman, A. J., Xiao, S., Zhou, C., Zhu, M., Cao, M., et al. (2021). Dynamic interplay of biogeochemical C, S and Ba cycles in response to the Shuram oxygenation event. *J. Geol. Soc. Lond.* 179 (2), 1–31. jgs2021-081. doi:10.1144/jgs2021-081

Dale, A. W., Regnier, P., Knab, N. J., Jørgensen, B. B., and Van Cappellen, P. (2008). Anaerobic oxidation of methane (AOM) in marine sediments from the skagerrak (Denmark): II. Reactiontransport modeling. *Geochimica Cosmochimica Acta* 72, 2880–2894. doi:10.1016/j.gca.2007.11.039

Dickens, G. R., Fewless, T., Thomas, E., and Bralower, T. J. (2003). "Excess barite accumulation during the Paleocene-Eocene Thermal Maximum: Massive input of dissolved barium from seafloor gas hydrate reservoirs," in *Causes and consequences of globally warm climates in the early paleogene*. Editior S. L. Wing, P. D. Gingerich, B. Schmitz, and E. Thomas (Boulder, Colorado, Geological Society of America Special Paper) 369, 11–23.

Dickens, G. R. (2001). Sulfate profiles and barium fronts in sediment on the blake ridge: Present and past methane fluxes through a large gas hydrate reservoir. *Geochim. Cosmochim. Acta* 65, 529–543. doi:10.1016/s0016-7037(00)00556-1

Dymond, J., Suess, E., and Lyle, M. (1992). Barium in deep-sea sediment: A geochemical proxy for paleoproductivity. *Paleoceanography* 7 (2), 163–181. doi:10.1029/92pa00181

Feng, D., and Chen, D. (2015). Authigenic carbonates from an active cold seep of the northern South China Sea: New insights into fluid sources and past seepage activity. *Deep Sea Res. Part II: Top. Stud. Oceanogr.* 122, 74–83. doi:10.1016/j.dsr2.2015.02.003

Feng, D., and Roberts, H. H. (2011). Geochemical characteristics of the barite deposits at cold seeps from the northern Gulf of Mexico continental slope. *Earth Planet. Sci. Lett.* 309, 89–99. doi:10.1016/j.epsl.2011.06.017

Feng, D., Qiu, J. W., Hu, Y., Peckmann, J., Guan, H., Tong, H., et al. (2018). Cold seep systems in the South China Sea: An overview. *J. Asian Earth Sci.* 168, 3–16. doi:10.1016/j.jseaes.2018.09.021

Feng, J., Yang, S., Wang, H., Liang, J., Fang, Y., and Luo, M. (2019). Methane source and turnover in the shallow sediments to the west of Haima cold seeps on the northwestern slope of the South China Sea. *Geofluids* ID1010824, 1–18. doi:10.1155/2019/1010824

Feng, J., Li, N., Luo, M., Liang, J., Yang, S., Wang, H., et al. (2020). A quantitative assessment of methane-derived carbon cycling at the cold seeps in the Northwestern South China Sea. *Minerals* 10 (3), 1–23. doi:10.3390/min10030256

Frieling, J., Peterse, F., Lunt, D. J., Bohaty, S. M., Sinninghe Damsté, J. S., Reichart, G. J., et al. (2019). Widespread warming before and elevated barium burial during the Paleocene-Eocene Thermal Maximum: Evidence for methane hydrate release? *Paleoceanogr. Paleoclimatol.* 34, 546–566. doi:10.1029/2018pa003425

Fu, S. (2005). Characteristics of the different hydrocarbon gases in marine sediments and their geochemical significances. *Earth Sci. Front.* 12 (3), 253–257.

Ge, L., Jiang, S. Y., Swennen, R., Yang, T., Yang, J. H., Wu, N. Y., et al. (2010). Chemical environment of cold seep carbonate formation on the northern continental slope of South China Sea: Evidence from trace and rare earth element geochemistry. *Mar. Geol.* 277, 21–30. doi:10.1016/j.margeo.2010.08.008

Gingele, F., and Dahmke, A. (1994). Discrete barite particles and barium as tracers of paleoproductivity in South Atlantic sediments. *Paleoceanography* 9, 151–168. doi:10.1029/93pa02559

Greinert, J., Bollwerk, S. M., Derkachev, A., Bohrmann, G., and Suess, E. (2002). Massive barite deposits and carbonate mineralization in the derugin basin, sea of okhotsk: Precipitation processes at cold seep sites. *Earth Planet. Sci. Lett.* 203 (1), 165–180. doi:10.1016/s0012-821x(02)00830-0

Griffith, E. M., and Paytan, A. (2012). Barite in the ocean–occurrence, geochemistry and palaeoceanographic applications. *Sedimentology* 59, 1817–1835. doi:10.1111/j.1365-3091.2012.01327.x

Han, X., Suess, E., Huang, Y., Wu, N., Bohrmann, G., Su, X., et al. (2008). Jiulong methane reef: Microbial mediation of seep carbonates in the South China sea. *Mar. Geol.* 249, 243–256. doi:10.1016/j.margeo.2007.11.012

Han, X., Suess, E., Liebetrau, V., Eisenhauer, A., and Huang, Y. (2014). Past methane release events and environmental conditions at the upper continental slope of the South China sea: Constraints by seep carbonates. *Int. J. Earth Sci.* 103, 1873–1887. doi:10.1007/s00531-014-1018-5

Hanebuth, T. J. J., Voris, H. K., Yokoyama, Y., Saito, Y., and Okuno, J. i. (2011). Formation and fate of sedimentary depocentres on Southeast Asia's Sunda Shelf over the past sea-level cycle and biogeographic implications. *Earth. Sci. Rev.* 104, 92–110. doi:10.1016/j.earscirev.2010.09.006

Hensen, C., Zabel, M., Pfeifer, K., Schwenk, T., Kasten, S., Riedinger, N., et al. (2003). Control of sulfate pore-water profiles by sedimentary events and the significance of anaerobic oxidation of methane for the burial of sulfur in marine sediments. *Geochim. Cosmochim. Acta* 67, 2631–2647. doi:10.1016/s0016-7037(03)00199-6

Holmkvist, L., Kamyshny, A., Vogt, C., Vamvakopoulos, K., Ferdelman, T. G., and Jørgensen, B. B. (2011). Sulfate reduction below the sulfate-methane transition in Black Sea sediments. *Deep Sea Res. Part I: Oceanogr. Res. Pap.* 58, 493–504. doi:10.1016/j.dsr.2011.02.009

Hong, W. L., Torres, M. E., Carroll, J., Crémière, A., Panieri, G., Yao, H., et al. (2017). Seepage from an arctic shallow marine gas hydrate reservoir is insensitive to momentary ocean warming. *Nat. Commun.* 8, 15745. doi:10.1038/ncomms15745

Hsu, S. K., Wang, S. Y., Liao, Y. C., Yang, T. F., Jan, S., Lin, J. Y., et al. (2013). Tide-modulated gas emissions and tremors off SW Taiwan. *Earth Planet. Sci. Lett.* 369, 98–107. doi:10.1016/j.epsl.2013.03.013

Hu, Y., Chen, L., Feng, D., Liang, Q., Xia, Z., and Chen, D. (2017). Geochemical record of methane seepage in authigenic carbonates and surrounding host sediments: A case study from the South China sea. *J. Asian Earth Sci.* 138, 51–61. doi:10.1016/j.jseaes.2017.02.004

Hu, Y., Luo, M., Liang, Q., Chen, L., Feng, D., Yang, S., et al. (2019). Pore fluid compositions and inferred fluid flow patterns at the Haima cold seeps of the South China Sea. *Mar. Pet. Geol.* 103, 29–40. doi:10.1016/j.marpetgeo.2019.01.007

Huang, Y., Suess, E., and Wu, N. (2008). *Methane and gas hydrate geology of the northern South China sea: Sino-German cooperative so-177 cruise report*. Beijing, China: Geological Publishing House.

Judd, A. G., and Hovland, M. (2007). *Submarine fluid flow, the impact on geology, biology, and the marine environment*. Cambridge, England: Cambridge University Press.

Kasten, S., Nöthen, K., Hensen, C., Spieß, V., Blumenberg, M., and Schneider, R. R. (2012). Gas hydrate decomposition recorded by authigenic barite at pockmark sites of the northern Congo Fan. *Geo-Mar. Lett.* 32, 515–524. doi:10.1007/s00367-012-0288-9

Kuang, Z., Fang, Y., Liang, J., Lu, J. A., and Wang, L. (2018). Geomorphological-geological-geophysical signatures of high-flux fluid flows in the eastern Pearl River Mouth Basin and effects on gas hydrate accumulation. *Sci. China Earth Sci.* 61, 914–924. doi:10.1007/s11430-017-9183-y

Li, L., Lei, X., Zhang, X., and Sha, Z. (2013). Gas hydrate and associated free gas in the Dongsha area of northern South China Sea. *Mar. Pet. Geol.* 39, 92–101. doi:10.1016/j.marpetgeo.2012.09.007

Li, L., Liu, H., Zhang, X., Lei, X., and Sha, Z. (2015). BSRs, estimated heat flow, hydrate related gas volume and their implications for methane seepage and gas hydrate in the Dongsha region, northern South China Sea. *Mar. Pet. Geol.* 67, 785–794. doi:10.1016/j.marpetgeo.2015.07.008

Li, N., Feng, D., Chen, L., Wang, H., and Chen, D. (2016). Using sediment geochemistry to infer temporal variation of methane flux at a cold seep in the South China Sea. *Mar. Pet. Geol.* 77, 835–845. doi:10.1016/j.marpetgeo.2016.07.026

Liang, Q., Hu, Y., Feng, D., Peckmann, J., Chen, L., Yang, S., et al. (2017). Authigenic carbonates from newly discovered active cold seeps on the northwestern slope of the South China Sea: Constraints on fluid sources, formation environments, and seepage dynamics. *Deep Sea Res. Part I: Oceanogr. Res. Pap.* 124, 31–41. doi:10.1016/j.dsr.2017.04.015

Lin, Q., Wang, J., Taladay, K., Lu, H., Hu, G., Sun, F., et al. (2016). Coupled pyrite concentration and sulfur isotopic insight into the paleo sulfate–methane transition zone (SMTZ) in the northern South China Sea. *J. Asian Earth Sci.* 115, 547–556. doi:10.1016/j.jseaes.2015.11.001

Lin, Z., Sun, X., Strauss, H., Lu, Y., Gong, J., Xu, L., et al. (2017). Multiple sulfur isotope constraints on sulfate-driven anaerobic oxidation of methane: Evidence from authigenic pyrite in seepage areas of the South China Sea. *Geochim. Cosmochim. Acta* 211, 153–173. doi:10.1016/j.gca.2017.05.015

Liu, C., Jiang, S., Su, X., Huang, C-Y., Zhou, Y., Bian, X., et al. (2019). An effective method to distinguish between artificial and authigenic gypsum in marine sedimentsffective method to distinguish between artifcial and authigenic gypsum

in marine sediments. *Mar. Pet. Geol.* 110, 706–716. doi:10.1016/j.marpetgeo.2019.07.044

Lu, H. (2007). *Mineralogical and geochemical studies on sediments from dongsha area, South China sea: Evidences for gas hydrate occurrence*. Dissertation. Sun Yat-sen University, 174.

Luo, M., Dale, A. W., Wallmann, K., Hensen, C., Gieskes, J., Yan, W., et al. (2015). Estimating the time of pockmark formation in the SW Xisha Uplift (South China Sea) using reaction-transport modeling. *Mar. Geol.* 364, 21–31. doi:10.1016/j.margeo.2015.03.006

Maoyu Wang, M., Chen, T., Feng, D., Zhang, X., Li, T., Robinson, L. F., et al. (2022). Uranium-thorium isotope systematics of cold-seep carbonate and their constraints on geological methane leakage activities. *Geochim. Cosmochim. Acta* 320, 105–121. doi:10.1016/j.gca.2021.12.016

McDonnell, S., Max, M., Cherkis, N., and Czarnecki, M. (2000). Tectono-sedimentary controls on the likelihood of gas hydrate occurrence near Taiwan. *Mar. Pet. Geol.* 17, 929–936. doi:10.1016/s0264-8172(00)00023-4

McManus, J., Berelson, W. M., Klinkhammer, G. P., Johnson, K. S., Coale, K. H., Anderson, R. F., et al. (1998). Geochemistry of barium in marine sediments: Implications for its use as a paleoproxy. *Geochim. Cosmochim. Acta* 62, 3453–3473. doi:10.1016/s0016-7037(98)00248-8

Naehr, T. H., Stakes, D. S., and Moore, W. S. (2000). Mass wasting, ephemeral fluid flow, and barite deposition on the California continental margin. *Geology* 28, 315–318. doi:10.1130/0091-7613(2000)028<0315:mweffa>2.3.co;2

Nöthen, K., and Kasten, S. (2011). Reconstructing changes in seep activity by means of pore water and solid phase Sr/Ca and Mg/Ca ratios in pockmark sediments of the Northern Congo Fan. *Mar. Geol.* 287, 1–13. doi:10.1016/j.margeo.2011.06.008

Paytan, A., Kastner, M., Martin, E. E., Macdougall, J. D., and Herbert, T. (1993). Marine barite as a monitor of seawater strontium isotope composition. *Nature* 366, 445–449. doi:10.1038/366445a0

Peckmann, J., Reimer, A., Luth, U., Luth, C., Hansen, B. T., Heinicke, C., et al. (2001). Methane-derived carbonates and authigenic pyrite from the northwestern Black Sea. *Mar. Geol.* 177, 129–150. doi:10.1016/s0025-3227(01)00128-1

Peckmann, J., and Thiel, V. (2004). Carbon cycling at ancient methane–seeps. *Chem. Geol.* 205, 443–467. doi:10.1016/j.chemgeo.2003.12.025

Riedinger, N., Kasten, S., Gröger, J., Franke, C., and Pfeifer, K. (2006). Active and buried authigenic barite fronts in sediments from the Eastern Cape Basin. *Earth Planet. Sci. Lett.* 241, 876–887. doi:10.1016/j.epsl.2005.10.032

Sauer, S., Crémière, A., Knies, J., Lepland, A., Sahy, D., Martma, T., et al. (2017). U-Th chronology and formation controls of methane-derived authigenic carbonates from the Hola trough seep area, northern Norway. *Chem. Geol.* 470, 164–179. doi:10.1016/j.chemgeo.2017.09.004

Schneider, A., Panieri, G., Lepland, A., Consolaro, C., Crémière, A., Forwick, M., et al. (2018). Methane seepage at Vestnesa Ridge (NW Svalbard) since the last glacial maximum. *Quat. Sci. Rev.* 193, 98–117. doi:10.1016/j.quascirev.2018.06.006

Schulz, H. D. (2006). "Quantification of early Diagenesis: Dissolved constituents in pore water and signals in the solid phase," in *Marine geochemistry* (Berlin, Heidelberg: Springer), 73–124.

Sloan, E. D., Jr., and Koh, C. (2007). in *Clathrate hydrates of natural GasChemical industries*. third ed. (CRC Press).

Snyder, G. T., Dickens, G. R., and Castellini, D. G. (2007a). Labile barite contents and dissolved barium concentrations on blake ridge: New perspectives on barium cycling above gas hydrate systems. *J. Geochem. Explor.* 95, 48–65. doi:10.1016/j.gexplo.2007.06.001

Snyder, G. T., Hiruta, A., Matsumoto, R., Dickens, G. R., Tomaru, H., Takeuchi, R., et al. (2007b). Pore water profiles and authigenic mineralization in shallow marine sediments above the methane-charged system on Umitaka Spur, Japan Sea. *Deep Sea Res. Part II: Top. Stud. Oceanogr.* 54, 1216–1239. doi:10.1016/j.dsr2.2007.04.001

Suess, E. (2005). *RV SONNE cruise report SO 177, sino-German cooperative Project, South China sea continental margin: Geological methane budget and environmental effects of methane emissions and gas hydrates*. IFM-GEOMAR Reports.

Sultan, N., Plaza-Faverola, A., Vadakkepuliyambatta, S., Buenz, S., and Knies, J. (2020). Impact of tides and sea-level on deep-sea Arctic methane emissions. *Nat. Commun.* 11, 1–10. doi:10.1038/s41467-020-18899-3

Tong, H., Feng, D., Cheng, H., Yang, S., Wang, H., Min, A. G., et al. (2013). Authigenic carbonates from seeps on the northern continental slope of the South China Sea: New insights into fluid sources and geochronology. *Mar. Pet. Geol.* 43, 260–271. doi:10.1016/j.marpetgeo.2013.01.011

Torres, M. E., Bohrmann, G., and Suess, E. (1996). Authigenic barites and fluxes of barium associated with fluid seeps in the Peru subduction zone. *Earth Planet. Sci. Lett.* 144, 469–481. doi:10.1016/s0012-821x(96)00163-x

Torres, M. E., McManus, J., and Huh, C. A. (2002). Fluid seepage along the san Clemente Fault scarp: Basin-wide impact on barium cycling. *Earth Planet. Sci. Lett.* 203, 181–194. doi:10.1016/s0012-821x(02)00800-2

Torres, M. E., Bohrmann, G., Dubé, T. E., and Poole, F. G. (2003). Formation of modern and Paleozoic stratiform barite at cold methane seeps on continental margins. *Geol.* 31, 897–900. doi:10.1130/g19652.1

Vanneste, H., James, R. H., Kelly-Gerreyn, B. A., and Mills, R. A. (2013). Authigenic barite records of methane seepage at the Carlos Ribeiro mud volcano (Gulf of Cadiz). *Chem. Geol.* 354, 42–54. doi:10.1016/j.chemgeo.2013.06.010

Von Breymann, M. T., Brumsack, H. J., and Emeis, K. C. (1992). *Proceedings of the ocean drilling Program scientific results*. in *Deposition and Diagenetic Behavior of Barium in the Japan Sea*, vol. 127/128. Ocean Drilling Program.

Wallmann, K., Aloisi, G., Haeckel, M., Obzhirov, A., Pavlova, G., and Tishchenko, P. (2006). Kinetics of organic matter degradation, microbial methane generation, and gas hydrate formation in anoxic marine sediments. *Geochim. Cosmochim. Acta* 70, 3905–3927. doi:10.1016/j.gca.2006.06.003

Wang, P., Prell, W. L., and Blum, P. (2000). *Proceedings of the ocean drilling Program,* initial reports, 184. Ocean Drilling Program.

Wang, X., Liu, B., Qian, J., Zhang, X., Guo, Y., Su, P., et al. (2018). Geophysical evidence for gas hydrate accumulation related to methane seepage in the Taixinan Basin, South China Sea. *J. Asian Earth Sci.* 168, 27–37. doi:10.1016/j.jseaes.2017.11.011

Wood, R. S., Lepland, A., Ogliore, R. C., Houghton, J., and Fike, D. A. (2021). Microscale $\delta^{34}S$ heterogeneities in cold seep barite record variable methane flux off the Lofoten-Vesterålen Continental Margin, Norway. *Earth Planet. Sci. Lett.* 574, 117164. doi:10.1016/j.epsl.2021.117164

Wu, S., Wang, X., Wong, H. K., and Zhang, G. (2007). Low-amplitude BSRs and gas hydrate concentration on the northern margin of the South China Sea. *Mar. Geophys. Res.* 28, 127–138. doi:10.1007/s11001-007-9020-y

Wu, D., Wu, N., Zhang, M., Guan, H., Fu, S., and Yang, R. (2013). Relationship of sulfate-methane interface (SMI), methane flux and the underlying gas hydrate in Dongsha area, northern South China Sea. *Earth Science–Journal China Univ. Geosciences* 38, 1309–1320. doi:10.1007/s11430-012-4545-6

Wu, N., Xu, C., Li, A., Cao, H., Chen, Y., Zhang, X., et al. (2022). Oceanic carbon cycle in a symbiotic zone between hydrothermal vents and cold seeps in the Okinawa Trough. *Geosystems Geoenvironment* 1 (3), 1–11. doi:10.1016/j.geogeo.2022.100059

Xie, R., Wu, D., Liu, J., Sun, T., Liu, L., and Wu, N. (2019). Evolution of gas hydrates inventory and anaerobic oxidation of methane (AOM) after 40ka in the Taixinan Basin, South China Sea. *Deep Sea Res. Part I: Oceanogr. Res. Pap.* 152, 103084. doi:10.1016/j.dsr.2019.103084

Xudong Wang, X., Guan, H., Qiu, J. W., Xu, T., Peckmann, J., Chen, D., et al. (2022). Macro-ecology of cold seeps in the South China sea. *Geosystems Geoenvironment* 1 (3), 1–11. doi:10.1016/j.geogeo.2022.100081

Yang, T., Jiang, S., Ge, L., Yang, J., Wu, N., Zhang, G., et al. (2010). Geochemical characteristics of pore water in shallow sediments from Shenhu area of South China Sea and their significance for gas hydrate occurrence. *Chin. Sci. Bull.* 55, 752–760. doi:10.1007/s11434-009-0312-2

Yang, K., Chu, F., Zhu, Z., Dong, Y., Yu, X., Zhang, W., et al. (2018). Formation of methane-derived carbonates during the last glacial period on the northern slope of the South China Sea. *J. Asian Earth Sci.* 168, 173–185. doi:10.1016/j.jseaes.2018.01.022

Yao, H., Niemann, H., and Panieri, G. (2020). Multi-proxy approach to unravel methane emission history of an Arctic cold seep. *Quat. Sci. Rev.* 244, 106490. doi:10.1016/j.quascirev.2020.106490

Zhang, G., Liang, J., Yang, S., Zhang, M., Holland, M., Schultheiss, P., et al. (2015). Geological features, controlling factors and potential prospects of the gas hydrate occurrence in the east part of the Pearl River Mouth Basin, South China Sea. *Mar. Pet. Geol.* 67, 356–367. doi:10.1016/j.marpetgeo.2015.05.021

Zhang, J., Lei, H., Chen, Y., Kong, Y., Kandasamy, S., Ou, W., et al. (2018). Carbon and oxygen isotope composition of carbonate in bulk sediment in the southwest Taiwan Basin, South China Sea: Methane hydrate decomposition history and its link to mud volcano eruption. *Mar. Pet. Geol.* 98, 687–696. doi:10.1016/j.marpetgeo.2018.08.031

frontiers | Frontiers in Earth Science

TYPE Original Research
PUBLISHED 08 September 2022
DOI 10.3389/feart.2022.991208

OPEN ACCESS

EDITED BY
Pibo Su,
Guangzhou Marine Geological Survey, China

REVIEWED BY
Shuanshi Fan,
South China University of Technology, China
Gang Li,
Guangzhou Institute of Energy Conversion (CAS), China

*CORRESPONDENCE
Yi Qiao,
qiaoyiswpu@163.com

SPECIALTY SECTION
This article was submitted to Marine Geoscience, a section of the journal Frontiers in Earth Science

RECEIVED 11 July 2022
ACCEPTED 28 July 2022
PUBLISHED 08 September 2022

CITATION
Wei N, Qiao Y, Liu A, Zhao J, Zhang L and Xue J (2022), Study on structure optimization and applicability of hydrocyclone in natural gas hydrate exploitation. *Front. Earth Sci.* 10:991208. doi: 10.3389/feart.2022.991208

Study on structure optimization and applicability of hydrocyclone in natural gas hydrate exploitation

Na Wei[1,2], Yi Qiao[1,2]*, Anqi Liu[3], Jinzhou Zhao[1,2], Liehui Zhang[1,2] and Jin Xue[1,2]

[1]State Key Laboratory of Oil and Gas Reservoir Geology and Exploitation, Southwest Petroleum University, Chengdu, China, [2]State Key Laboratory of Natural Gas Hydrate, Beijing, China, [3]Geological Explorations and Development Institute, Chuan Qing Drilling Engineering Company Limited, Chengdu, China

With the development of economy and industry, the consumption of fossil energy is gradually increasing. Currently, natural gas hydrates (NGH) are considered to be an ideal alternative energy due to its large reserve and high energy density. However, the separation of hydrate slurry is a critical step in the exploitation of NGH. In this study, the optimization of the structural parameters based on the conventional three-phase hydrocyclone was carried out using numerical simulation and orthogonal design. At the same time, the separation efficiency criterion E was defined to evaluate the separation efficiency by calculating the sum of the discharge efficiency of water and gas. Analysis of the effect of individual structural factors on the flow field distribution characteristics inside the hydrocyclone using the single factor analysis method. The results showed that: with the combination of structural parameters of s was 2 mm^2 × 12 mm^2, d_z was 28 mm, h was 20 mm, and l_i was 28 mm, the maximum E of the three-phase hydrocyclone was 1.46. The effect significance of each structural parameter on the separation efficiency from the highest to the lowest was the s, d_z, h, and l_i. In the single-factor analysis, when the s was 2 mm^2 × 12 mm^2, the tangential velocity, axial velocity, and CH_4 volume fraction in the flow field reached the maximum of 13.65 m/s, 4.35 m/s, and 12.4%, respectively. But the minimum water phase volume fraction was 69.9% under this structural parameter condition. When the d_z was 36 mm, the maximum decrease value of axial velocity in the flow field was 3.57 m/s, the maximum CH_4 volume fraction was 12.4%, and the water volume fraction reached a minimum of 66.3%. The l_i and the h only had significant effects on the axial velocity and the water volume fraction, respectively. The axial velocity reached a maximum of 4.75 m/s when the l_i was 32 mm, and the water phase volume fraction reached a maximum of 77.9% when the h was 10 mm. The study of the structural parameters and flow field characteristics of this three-phase hydrocyclone applicable to the solid fluidization exploitation of NGH provides some guidance and suggestions for the separation of hydrate slurry after solid fluidization exploitation of NGH.

KEYWORDS

natural gas hydrate, three-phase hydrocyclone, structural parameter optimization, flow field characteristics, solid fluidization exploitation

1 Introduction

With the development of economy and industry, the consumption of fossil energy is increasing year by year. According to statistics, the total global first-time energy consumption in 2018 was 14,301 million tons of oil equivalent, of which oil accounted for 31%, coal for 26%, and natural gas for 23% (Zou et al., 2016; Liang et al., 2020). The massive consumption of fossil fuels posed a great limitation to industrial and economic development and caused serious environmental pollution. Therefore, finding an alternative energy source with large reserves is the key to solving the current energy problem. Natural gas hydrates (NGH) is a kind of natural gas resource buried in the alpine permafrost and deep sea bottom, which has the characteristics of large reserve, wide distribution, high energy density, and clean combustion (Song et al., 2014; Wang et al., 2020). It is estimated that the proven reserves of NGH are $0.82\ m^3 \times 10^{13}\ m^3$–$2.10\ m^3 \times 10^{15}\ m^3$ (at STP conditions), which is twice as much as the total reserves of fossil energy such as coal, oil, and natural gas (Li and Miao, 2014; Wei et al., 2020; Chang et al., 2021). NGH is an ice-like crystal structure composed of guest molecules under certain temperature and pressure conditions, and 1 m^3 of NGH can store about 164 m^3 of natural gas in the standard state (Chong et al., 2016; Chen et al., 2019). As a result, NGH is an alternative energy source with great potential.

At present, the exploitation of NGH is the focus of research in various countries. The United States, Canada, Japan, Russia, and China have all conducted test exploitation studies on NGH (Zhao et al., 2021; Chen et al., 2020). The methods applied by countries in the process of NGH test exploitation include depressurization, thermal excitation, chemical injection, and so on (Chuang et al., 2001; Song et al., 2015; Aminnaji et al., 2017; Cui et al., 2018). The depressurization method is to change the pore pressure of the hydrate reservoir, so that the reservoir pressure in the exploitation area is lower than the pressure condition for hydrate formation, thereby inducing the decomposition of NGH and releasing methane gas (Wang et al., 2018). The depressurization method does not require external energy and is considered to be the most economical method for the exploitation of NGH. However, according to the law of conservation of energy, in the process of exploiting NGH using the depressurization method, the decomposition of hydrate needs to absorb a lot of heat, which leads to the secondary generation of NGH, and then clogs the pipeline, resulting in low exploitation efficiency (Wang, 2019; Liu et al., 2021). The thermal excitation method is to inject heat into the NGH exploitation formation, so that the temperature of the formation is higher than the phase equilibrium temperature of NGH. The thermal exploitation method can control the decomposition rate of NGH by controlling the injection heat (Zhan et al., 2014; Wang et al., 2017). However, the method results in significant energy loss and high exploitation costs. The chemical injection method is to inject chemical reagents into the exploitation reservoir through special equipment, so as to change the phase equilibrium conditions of NGH in the reservoir to induce hydrate decomposition. However, this method is easy to cause environmental pollution and has the problem of high exploitation costs (Yang et al., 2019; Hou et al., 2021).

In order to solve the problems existing in the process of NGH exploitation, Zhou (Zhou et al., 2017a; Zhao et al., 2017) proposed solid fluidization exploitation method for NGH. The solid fluidization method is to crush the hydrate mineral into fine particles by means of high-pressure jet or mechanical crushing, and then mix it with seawater and transport it to the offshore platform through closed pipelines for later separation and treatment (Zhou et al., 2014). The solid fluidization method can exploit the hydrate reservoir *in situ* in the hydrate exploitation area and transport the hydrate particles through a closed environment. The phase equilibrium conditions of NGH are not broken during the whole exploitation process, and the uncontrollable decomposition of hydrate in shallow submarine without enclosed structure is changed to the artificially controlled decomposition of hydrate in the closed system (Zhou et al., 2017b). This method avoids the problems of formation collapse, greenhouse gas leakage, and high exploitation cost caused by traditional NGH exploitation methods, and is a highly efficient, green and controllable NGH exploitation method (Wei et al., 2018). The solid fluidization exploitation of NGH is to exploit the hydrate reservoir in a closed environment. During the exploitation process the seabed sediment is transported to the offshore platform along with the hydrate particles. Meanwhile, hydrate particles will decompose CH_4 with temperature and pressure change during transport (Huang, 2018). Therefore, when the hydrate particles and sediment are moved to the offshore platform through the closed pipeline, the mixture in the pipeline is a three-phase mixture of gas-liquid-solid. So, the separation of the three-phase mixture is an important step in the solid fluidization exploitation of NGH.

At present, the main methods for separating hydrate slurry include gravity sedimentation separation (Wang et al., 2006), chemical separation (Wan, 2009), and cyclone separation (Dong et al., 2018; Qiu et al., 2019; Wang et al., 2019). The gravity sedimentation separation method relies on the density difference between different phases to make different phase in hydrate slurry settle naturally under the action of gravity, so as to realize the separation of gas, liquid, and solid phase. However, this method has the disadvantages of the large footprint and low separation efficiency. The chemical separation is to add relevant chemical reagents to the hydrate slurry and separate the needed phase by chemical reaction. But this method has high engineering application costs and is prone to environmental pollution. The cyclone separation is to inject the hydrate slurry into the hydrocyclone and the hydrate slurry do circular motion in the spin chamber, due to the density difference between different phases resulting in centrifugal

force difference in the circular motion, so as to achieve the separation of different phases. With the advantages of high separation efficiency, small footprint, and no pollution to the environment, the cyclone separation is the most ideal method to separate hydrate slurry which is exploited by solid fluidization.

The hydrocyclone as the main technical equipment of cyclone separation was widely used in petroleum and petrochemical, environmental protection, chemical, and other fields of multi-phase separation because of the advantages of high efficiency, small size, and fast separation (Liu et al., 2018; Gao, 2021; Song et al., 2021). Up to now, many experts and scholars have done a lot of research on three-phase hydrocyclone. Zhao et al. (2008) studied the separation characteristics of hydrocyclone for fine particles under circulating flow conditions by experiment. The experimental results showed that the separation efficiency was maximum at a cycle period rate of 0.68 and a cyclical flow amplitude rate of 2%. Wu and Liu (2019) studied the effect of the inner cone structure on the separation efficiency of a three-phase hydrocyclone by computational fluid dynamics method, and obtained the optimal combination of inner cone structure. Jiang et al. (2014) used numerical simulation to study the effect of three-phase hydrocyclone overflow tube on the separation performance, which provided implications for the optimization of three-phase hydrocyclone structures. Zheng (2005) proposed a hydrocyclone for gas-water-sand three-phase separation by connecting solid-liquid cyclone and gas-liquid cyclone in series, and analyzed the flow field distribution characteristics by experiment. The experimental results verified the separation performance of the three-phase hydrocyclone. Chang et al. (2021) designed a hydrocyclone for desanding of NGH in the wellbore. The effect of structural parameters on the flow field distribution inside the device was verified by a combination of numerical simulation and experiments, and the optimal flow rate of this desanding hydrocyclone was obtained. However, up to now, there are few studies on gas-liquid-solid three-phase hydrocyclone applicable to solid fluidization exploitation of NGH.

In this paper, the numerical simulation method was used to study the structural parameters and internal flow field characteristics of the three-phase hydrocyclone which is applicable to solid fluidization exploitation of NGH. In order to ensure the universality and accuracy of the research, the structural parameters of the conventional three-phase hydrocyclone were optimized by the orthogonal design, and the structural parameters of the three-phase hydrocyclone applicable to the solid fluidization extraction of NGH were obtained. The effects of the gas outlet depth length (l_i), tangential inlet area (s), drain hole height (h), and inverted cone diameter (d_z) on the separation efficiency of the hydrocyclone were also studied. The separation efficiency criterion of the three-phase hydrocyclone for NGH was defined based on the gas output and sand output of the optimized three-phase hydrocyclone. At the same time, the effect of single-factor change on the internal flow field distribution characteristics of the three-phase hydrocyclone was investigated by changing the individual structural parameters of the hydrocyclone. This study has some engineering guidance on hydrate slurry separation in the solid fluidization exploitation of NGH.

2 Materials and methods

2.1 Physical model

In this paper, based on the three-phase hydrocyclone designed by Xu et al. (2017), the optimization of structural parameters and flow field analysis of the three-phase hydrocyclone applicable to the solid fluidization exploitation of NGH were carried out. The structure of the gas-water-sand three-phase hydrocyclone was shown in Supplementary Figure S1.

Hydrate mineral becomes hydrate particles with sediment after solid fluidization exploitation. In the process of transporting hydrate particles from the seabed to the sea surface through a closed pipeline, as the pressure decreases and the temperature increases, the hydrate particles decompose into a three-phase mixture of gas, water, and sand. The mixture is injected into the spin chamber from the tangential inlets at a certain initial velocity, and makes a circular motion along the inner wall of the spin chamber to form a strong vortex. Due to the different densities among different phases, the centrifugal force generated by the three phases of air, water, and sand in the process of circular motion is different. Among them, the density of the sand is the largest, and the centrifugal force generated during the circular motion is the largest, so the sand is distributed on the side wall of the spin chamber, and finally discharged from the sand outlet, an annulus between the outer wall of the spin chamber and the water outlet. The density of the gas is the smallest, and the centrifugal force generated during the circular motion is the smallest, so the gas is distributed at the axis of the spin chamber. However, due to the inverted cone at the axis of the spin chamber, the gas is pushed into the gas outlet and finally discharged from the hydrocyclone under the action of the inverted cone. The density of water is between gas and sand, which is distributed between them in the spin chamber, and enters the interior of the inverted cone through the drain hole and is finally discharged from the hydrocyclone by the water outlet.

In this paper, a three-dimensional model was used to study the structural parameters and flow field characteristics of three-phase hydrocyclone applicable to solid fluidization exploitation of NGH. In the study of swirl flow field, compared with the two-dimensional model, the three-dimensional model can express the velocity change in three directions, thus showing the separation

among different phases, and the flow field characteristics can be expressed more accurately. The structural parameters of the three-phase hydrocyclone were shown in Supplementary Table S1.

2.2 Mathematical model

2.2.1 Governing equation

The fluid in the three-phase hydrocyclone can be regarded as a viscous incompressible fluid, which follows the basic governing equation. Continuity equation, momentum conservation equation and energy conservation equation, as shown in the following Eqs 1–3 (Elsayed and Lacor, 2011; Wang et al., 2015; Zhang et al., 2019; Bu et al., 2021):

Continuity equation

$$\frac{\partial}{\partial x_j}\left(\rho u_j\right) = 0 \tag{1}$$

Momentum conservation equation

$$\frac{\partial}{\partial x_j}\left(\rho u_i u_j\right) = -\frac{\partial p}{\partial x_i} + \frac{\partial}{\partial x_j}\left(\mu \frac{\partial u_i}{\partial x_j}\right) + (\rho - \rho_a) g_j \tag{2}$$

Energy conservation equation

$$\frac{\partial}{\partial x_j}\left(\rho u_j T\right) = \frac{1}{C_p}\frac{\partial}{\partial x_j}\left(k_t \frac{\partial T}{\partial x_j}\right) + \frac{C_{pv} - C_{pa}}{C_p}\left[\frac{\partial}{\partial x_j}\left(\frac{\mu_t}{\sigma_c}\right)\frac{\partial \omega}{\partial x_i}\right]\frac{\partial T}{\partial x_j} \tag{3}$$

2.2.2 Turbulence modeling

In this paper, the numerical simulation was performed *via* commercial software Ansys Fluent 2020. The internal flow field of the hydrocyclone is regarded to be a strong complex swirl field, so the choice of turbulence model has an important effect on the accuracy of numerical simulation results. Among the turbulence models, the Reynolds stress model (RSM) is considered to be suitable for the simulation of turbulent flow fields such as anisotropic flow and three-dimensional flow, taking into account the additional stress caused by streamline curvature and the anisotropy and three-dimensional effect of turbulence. Therefore, the RSM is used to simulate the internal flow field of the three-phase hydrocyclone.

The RSM is based on the average Reynolds number theory, and the governing equations as is shown in the following Eqs 4–10 (Xu, 2012; Wang, 2020):

Reynolds stress transport equation:

$$\frac{\partial}{\partial t}\left(\rho \overline{u'_i u'_j}\right) + \frac{\partial}{\partial x_k}\left(\rho u_k \overline{u'_i u'_j}\right) = D_{T,ij} + P_{ij} + \varphi_{ij} - \varepsilon_{ij} \tag{4}$$

Turbulent kinetic energy diffusion term equation:

$$D_{T,ij} = -\frac{\partial}{\partial x_k}\left(\rho \overline{u'_i u'_j u'_k} + \overline{p u'_j}\delta_{jk} - \mu \frac{\partial}{\partial x_k}\overline{u'_i u'_j}\right) \tag{5}$$

Molecular viscous diffusion term equation:

$$D_{L,ij} = \frac{\partial}{\partial x_k}\left[\mu \frac{\partial}{\partial x_k}\left(\overline{u'_i u'_j}\right)\right] \tag{6}$$

Shear stress equation:

$$P_{ij} = \rho\left(\overline{u'_i u'_k}\frac{\partial u_j}{\partial x_k} + \overline{u'_j u'_k}\frac{\partial u_i}{\partial x_k}\right) \tag{7}$$

Buoyancy generation term equation:

$$G_{ij} = -\rho\beta\left(g_i \overline{u'_j \theta} + g_j \overline{u'_i \theta}\right) = \beta \frac{\mu_t}{0.85}\left(g_i \frac{\partial T}{\partial x_j} + g_j \frac{\partial T}{\partial x_i}\right) \tag{8}$$

Pressure strain term equation:

$$\Phi_{ij} = -0.18\rho\frac{\varepsilon}{k}\left(\overline{u'_i u'_j} - \frac{2}{3}k\delta_{ij}\right) - 0.6\left(p_{ij} - \frac{2}{3}p\delta_{ij}\right) + f(k, \varepsilon, n_x, d) \tag{9}$$

Viscous dissipative term equation:

$$\varepsilon_{ij} = 2\mu \overline{\frac{\partial u'_i}{\partial x_k}\frac{\partial u'_j}{\partial x_k}} \tag{10}$$

2.3 Numerical method and grid generation

The finite volume method was used to solve the problem, and the control equation was discretized based on the pressure-based solver. The Mixture model was selected to study the internal flow field characteristics of the three-phase hydrocyclone and the Semi-Implicit Method for Pressure-Linked Equations (SIMPLE) algorithm was used to solve the discrete equation. SIMPLE algorithm is one of the most widely used flow field calculation methods for solving incompressible flow field in engineering. The core of this method is to use a "prediction-correction" process to solve the Navier-Stokes equations by calculating the pressure field on the basis of an interleaved grid. Considering the effect of gravity on the separation, the gravity acceleration was set as 9.81 m/s^{-2}. Set 1,000 steps per iteration to be saved as a data file in the calculation activity, and the total number of steps for the iteration was 10,000 steps. At the same time, in order to ensure the calculation accuracy, the convergence residual error was set as 10^{-6}.

Meshing the 3D model of three-phase hydrocyclone. In order to ensure the accuracy of the numerical simulation and reduce the calculation time, four grid levels were divided and the grid independence test was carried out.

2.4 Boundary conditions

In this study, water and CH_4 were set as continuous phases and sand as discrete phases. The density of water was 998.2 kg/m^3, and the viscosity was 0.001 pa·s, the density of methane was 0.68 kg/m^3. In order to avoid the particle diameter has an influence on the separation of each phase, the density of sand was 2,700 kg/m^3, and the particle diameter was 50 μm. The volume fractions of water, CH_4 and sand were 0.7, 0.1, and 0.2 respectively. The boundary condition of the tangential inlets of the three-phase hydrocyclone was set as the velocity inlet, and the incident velocity of the gas, water, and sand was consistent under the same structural parameters. The gas outlet, water outlet, and sand outlet were all set as outflow, and the flow ratios were set as 0.6, 0.2, and 0.2, respectively. The wall of the three-phase hydrocyclone was set as wall, the wall roughness was 0, and there was no slip wall boundary.

2.5 Simulation scenarios

In this paper, the numerical simulation method was used to optimize the structural parameters and analyze the internal flow field of the three-phase hydrocyclone applicable to solid fluidization exploitation of NGH. Firstly, taking the actual working conditions of the solid fluidization exploitation process of NGH as the standard, based on the conventional three-phase hydrocyclone, the orthogonal design was used to optimize the structural parameters. Through investigation, it was known that the structural parameters of the gas outlet tube, tangential inlets, and inverted cone structure have a significant effect on the separation efficiency of hydrocyclone. Therefore, the optimization parameters mainly include five factors in this study: gas outlet depth length (l_i), inverted cone length (l_z), tangential inlet area (s), drain hole height (h), and inverted cone diameter (d_z), and each factor were set at five levels. If all five factors and five levels are combined with each other for a full-scale test, the number of tests is 5^5=3,125. In order to reduce the number of tests and ensure the accuracy and scientifically in the statistical analysis process, the orthogonal design was used to calculate and analyze the optimization test process of the structural parameters of the three-phase hydrocyclone. The orthogonal design is an efficient, fast, and concise mathematical statistical method that adopts standardized orthogonal table and scientifically arranges and analyzes multi-factor problems according to the equilibrium discrete orthogonal principle (Zhong et al., 2019; Chen, 2020).

In the process of orthogonal design, the orthogonal table with six factors and five levels was selected according to the number of factors and levels. Each factor was set as a single column, and an empty column was set as reflect the error caused by random factors. Therefore, $L_{25}(5^6)$ orthogonal table was selected, as shown in Supplementary Table S2. Numerical simulations were carried out for a total of 25 combinations of structural parameters from OD1 to OD25 according to Supplementary Table S2. Defined the dimensionless parameter E as the criterion for evaluating the separation efficiency of different combinations of structural parameters, and E is the sum of the ratio of gas outlet discharge to inlet gas injection and the ratio of sand outlet discharge to inlet sand injection, as shown in Eq. 11.

$$E = \frac{G_{out}}{G_{all}} + \frac{S_{out}}{S_{all}} \tag{11}$$

The results of orthogonal design were analyzed by direct analysis and analysis of variance, and the effect degree of different factors on orthogonal design results and the optimal factor combination case were obtained. Meanwhile, by calculating the mean square of each factor and the mean square of the empty column respectively, and comparing the mean square of each factor with the mean square of the empty column, a factor that was less than the mean square of the empty column was classified as an error column. Finally, the optimal structure parameters combination was obtained, and the effect degree of each factor on the results of the orthogonal design was evaluated.

Secondly, taking the three-phase hydrocyclone with the optimal parameters combination as the basic case. The control variable method based on single factor analysis was used to study the effect of single structural parameter change on the internal flow field characteristics of three-phase hydrocyclone. In this study, the numerical simulation was also used to study the effects of the four structural parameters which included gas outlet depth length (l_i), tangential inlet area (s), drain hole height (h), and inverted cone diameter (d_z) on the internal flow field characteristics of three-phase hydrocyclone. In order to ensure the universality and accuracy of the research, the level changes of each structural parameter were evenly distributed, as shown in Supplementary Table S3.

In the process of using numerical simulation to study the effect of structural parameters change on flow field characteristics, Case 1 was set as the basic case. Among all 13 Cases, the tangential inlet area (s) of Case2–Case4 range from 2 mm^2 × 12 mm^2–8 mm^2 × 18 mm^2, and the inverted cone diameter (d_z) of Case5–Case7 range from 24 to 36 mm. The gas outlet depth length (l_i) of Case8–Case10 range from 20 to 32 mm, and the drain hole height (h) of Case11–Case13 range from 10 to 15 mm. These cases were used to study the effects of the tangential inlet area (s), the inverted cone diameter (d_z), gas outlet depth length (l_i), and the drain hole height (h) on the distribution characteristics of the internal flow field of three-phase hydrocyclone.

According to the principle of cyclone separation, the mixture is injected into the three-phase hydrocyclone from the tangential inlets and makes a circular motion in the spin chamber. And in this study, the numerical simulation was carried out base on a three-dimensional physical model, so the characteristics of the flow field on any axial section were consistent. In the analysis of

the internal flow field, the X-Y section was selected as the analysis section. The mixture formed a strong swirl in the spin chamber, and the gas was discharged under the action of the inverted cone and the depth section of the gas outlet. Meanwhile, the density difference between the liquid and the solid leads to the centrifugal force difference in the circular motion, thus realizing the preliminary separation of the solid and liquid in the spin chamber. According to the orthogonal design in Supplementary Table S2, the maximum of gas outlet depth length (l_i) and inverted cone length (l_z) were 32 mm and 108 mm, respectively. Therefore, in order to analyze the flow field distribution characteristics of different phases between the end of the gas outlet tube and the tip of the inverted cone, the monitoring line L_{Am}, L_{Bm}, L_{Cm} was set at an equal distance of 43, 63, and 83 mm from the top of the spin chamber. In the process of separation, the liquid entered the inverted cone through the drain hole and was discharged through the water outlet at the bottom of hydrocyclone. The sand moved downward along the outer surface of the inverted cone and was discharged through the sand outlet at the bottom of the spin chamber. In order to monitor the separation results of liquid and sand, a monitoring line L_{Dm} was set up at the bottom of the spin chamber. The position of the analysis section and the monitoring lines was shown in Supplementary Figure S2.

Finally, by analyzing the distribution and changing trend of velocity field, CH_4 volume fraction and water volume fraction on the analysis section and the monitoring line, thus the effect of the change of structural parameters on flow field distribution and separation efficiency were obtained. In this study, in order to ensure the accuracy of the visibility of the numerical simulation results, the Ansys's post-processing software was used to process the simulation results, and the ratio of chart processing size to model size was 1:1.

3 Result and discussion

3.1 Grid independence

During the meshing process, the physical model was meshed with four levels of 549618, 670520, 782246, and 869326 respectively. The static pressure distribution on monitoring line L_{Am} was analyzed under different grid levels, as shown in Supplementary Figure S3. The static pressure distribution curve with grid levels of 549618, 670520, 782264 was polynomial fitted, and the correlation coefficient R^2 was 0.9954. It is proved that the number of grids has little effect on the numerical simulation results under these levels of grid number. When the number of grids is 869326, the static pressure distribution on monitoring line L_{Am} changes greatly. In order to reduce calculation time and ensure the accuracy of numerical simulation, the fluid domain of three-phase hydrocyclone was divided into about 670000 grid elements, and the grid generation results is shown in Supplementary Figure S4.

3.2 Model validation

The experimental results of Xu were used to verify the accuracy of the numerical simulation. The experimental platform was designed according to the actual situation of the construction site, so the numerical calculation model reestablished according to Xu's experimental situation in this paper. The spin chamber length of the three-phase hydrocyclone is 238 mm, the main diameter is 45 mm, the inverted cone length is 96 mm, the drain hole height is 10 mm, and the tangential inlet area is 4 mm^2 × 14 mm^2. Other structural parameters are consistent as those of the experimental device. In the experiment, the flow rate was set as 4.83 m^3/h, and the pressure drop distribution was studied when the flow ratio of the gas outlet varies in the range of 56%–64%. Therefore, the Reynold stress model and the Mixture model were used in the numerical simulation and the same physical model and boundary conditions were established as in the experiment. The distribution of the experimental results and numerical simulation results of the gas outlet pressure drop under the condition of the gas outlet flow ratio varies from 56% to 64% is shown in Supplementary Figure S5. As shown in Supplementary Figure S5, the overall smaller numerical simulation results compared to the experimental results were due to the simplification of the real process of separation in the numerical simulation. A polynomial fit between the experimental results and numerical simulation was carried out, the correlation coefficient R^2 was 0.942. This verified the accuracy of the numerical simulation results.

3.3 Analysis of orthogonal design results

3.3.1 Direct analysis

The separation efficiency criterion E of OD1-OD25 was calculated by Eq. 11, and the E of 25 groups was obtained as shown in Supplementary Figure S6. As shown in Supplementary Figure S6, the maximum value of E for OD20 is 1.46 and the minimum value of E for OD24 is 1.1. According to the distribution results of E, when the combination of factors is $A_4B_5C_1D_4E_2$, that is when the gas outlet depth length is 28 mm, the tangential inlet area is 2 mm^2 × 12 mm^2, the inverted cone diameter is 28 mm, the inverted cone length is 108 mm, and the drain hole height is 20 mm, the sum of the ratio of gas outlet discharge to inlet gas injection and the ratio of sand outlet discharge to inlet sand injection is the largest of three-phase hydrocyclone. The separation efficiency of the hydrocyclone is the largest under this structure factors combination.

In order to verify the distribution results of the above E and study the effect of a certain level of a single factor on the test results, K_x was defined as the sum of the test results of the level

number is x which belongs to a certain factor column. For example, K_1 represents the sum of the E of all the test results with the level number 1 in a single factor column. In order to study the effect of the level change of various factors on the test results, R was defined as the range. Where a larger R for a factor indicates that the level of that factor has a greater effect on the test results. R can be expressed as Eq. 12.

$$R = K_{x\,max} - K_{x\,min} \tag{12}$$

The K_x and R of each factors of OD1-OD25 were calculated, and the results as shown in Supplementary Table S4.

In the orthogonal design of this paper, the separation efficiency of the three-phase hydrocyclone was evaluated by the E. The larger the E is, the higher the comprehensive efficiency of the gas and water discharge of the hydrocyclone is, that is, the higher the separation efficiency is. As shown in Supplementary Table S4, the distribution of K_x in A (l_i) factor column is K_4> K_3> K_1> K_2> K_5, in B (l_z) factor column is K_5> K_1> K_2> K_3> K_4, in C(s) factor column is K_1> K_3> K_2> K_4> K_5, in D (h) factor column is K_4> K_3> K_2> K_5> K_1, in E (d_z) factor column is K_2> K_1> K_3> K_4> K_5. According to the calculation results of K_x, the optimal factor combination can be obtained as $A_4B_5C_1D_4E_2$. The calculation results of K_x is consistent as that of Eq. 11, which shows that the separation efficiency is the highest when the gas outlet depth length is 28 mm, the tangential inlet area is 2 mm^2 × 12 mm^2, the inverted cone diameter is 28 mm, the inverted cone length is 108 mm, and the drain hole height is 20 mm. The calculation accuracy of Eq. 11 is also verified.

The R of each factors in Supplementary Table S4 was analyzed. The R of factor B (l_z) is less than that of empty column, indicating that the effect of factor B (l_z) on the orthogonal design results is less than that of the test error, and the change of level cannot have a significant effect on the orthogonal design results. Therefore, factor B (l_z) is classified as error. The R of factor A(li), C(s), D(h), and E(d_z) are larger than that of empty column, indicating that these four factors have a significant effect on the orthogonal design results. Among them, R_C>R_E>R_D>R_A, it is proved that the tangential inlet area has the most significant effect on the separation efficiency, and gas outlet depth length has the least effect on the separation efficiency of the three-phase hydrocyclone.

3.3.2 Analysis of variance

In order to analyze the error of the orthogonal design and accurately estimate the significance of each factor on the orthogonal design, the analysis of variance of the orthogonal design results was carried out.

3.3.2.1 Calculation of sum of squares of deviations

In the process of carrying out the orthogonal design, the change of the factor level and the test error is the main reason for the difference between the orthogonal design results. In order to reflect the overall difference of the orthogonal design results, SS_T was defined as the total sum of squares of deviation. The larger the SS_T is, the greater the difference of each orthogonal design results. SS_T can be expressed as Eq. 13.

$$SS_T = \sum_{i=1}^{n}(E_i - \bar{E})^2 = \sum_{i=1}^{n}E_i^2 - \frac{1}{n}\left(\sum_{i=1}^{n}E_i\right) = Q - P \tag{13}$$

The sum of the squares of the deviations of each factor was defined as SS_j (j = A, B, C, D, E, and Empty column). SS_j can be expressed as Eq. 14.

$$SS_j = \frac{r}{n}\left(\sum_{x=1}^{r}K_x^2\right) - \frac{T^2}{n} = \frac{r}{n}\left(\sum_{x=1}^{r}K_x^2\right) - P \tag{14}$$

In Eqs 13, 14, $\bar{E}$ is the average value of E, T is the sum of E, Q is the sum of E^2, and P is the average value of the square of the sum of E. $\bar{E}$, T, Q, P can be expressed as Eqs 15–18.

$$\bar{E} = \frac{1}{n}\sum_{i=1}^{n}E_i \tag{15}$$

$$T = \sum_{i=1}^{n}E_i \tag{16}$$

$$Q = \sum_{i=1}^{n}E_i^2 \tag{17}$$

$$P = \frac{1}{n}\left(\sum_{i=1}^{n}E_i\right)^2 = \frac{T^2}{n} \tag{18}$$

The total sum of squares of deviation was calculated by using Eq. 13, and SS_T was obtained of 0.1567, and the sum of squares of deviation of each factors were calculated by using Eq. 14, the SS_A, SS_B, SS_C, SS_D, SS_E, $SS_{Empty\ column}$ were obtained of 0.0156, 0.0079, 0.0571, 0.0148, 0.0473, and 0.014, respectively.

Because the empty column was set as reflect the error caused by random factors in the orthogonal design process. In the aforementioned direct analysis, the R of factor B was 0.217, which was smaller than that of the empty column of 0.294. In the calculation of sum of squares of deviation, the SS_B was 0.0079 which was smaller than $SS_{Empty\ column}$ of 0.014. It indicates that the effect of factor B on the results of orthogonal design is less than that of error on the results of orthogonal design, so factor B is classified as error. The sum of squares of deviation of the test error was defined as SS_{error}, and it was calculated as shown in Eq. 19.

$$SS_{error} = SS_{Empty\,coloum} + SS_B \tag{19}$$

3.3.2.2 Calculation of degree of freedom

The total freedom degree of the sum of total deviation square was defined as df_T, the freedom degree of the deviations square sum of each factor was defined as df_j, and the freedom degree of error was defined as df_{error}. The df_T, df_j, df_{error} can be expressed as Eqs 20–22.

$$df_T = Total\ number\ of\ tests - 1 = n - 1 \quad (20)$$

$$df_j = level\ Number\ of\ factors - 1 = r - 1 \quad (21)$$

$$df_{error} = df_{Empty\ column} + df_B \quad (22)$$

The total freedom degree was calculated by using Eq. 20, and df_T was obtained of 24. The freedom degree of each factors were calculated by using Eq. 21, and df_A, df_B, df_C, df_D, df_E, $df_{Empty\ column}$ were obtained of 4. The freedom degree of error was calculated by using Eq. 22, and df_{error} was obtained of 8.

3.3.2.3 Calculation of mean square

The mean square of each factor was defined as MS_j (j = A, B, C, D, E, Empty column). The mean square of error was defined as MS_{error}. MS_j, and MS_{error} can be expressed as Eqs 23, 24.

$$MS_j = \frac{SS_j}{df_j} \quad (23)$$

$$MS_{error} = \frac{SS_{error}}{df_{error}} \quad (24)$$

The mean square of each factor were calculated by using Eq. 23, and MS_A, MS_B, MS_C, MS_D, MS_E, $MS_{Empty\ column}$ were obtained of 0.0039, 0.0020, 0.0143, 0.0037, 0.0118, 0.0027, respectively. According to the calculation results of Eq. 23, MS_B = 0.0020 is less than $MS_{Empty\ column}$ = 0.0035. Therefore, factor B is classified as error, which is consistent as the result of intuitive analysis and the result of sum of squares of deviations calculation.

The mean square of error was calculated by using Eq. 24, the MS_{error} was obtained of 0.0027.

3.3.2.4 Calculation of F

The F of each factors was defined as F_j (j = A, C, D, E), F_j can be expressed as Eq. 25.

$$F_j = \frac{MS_j}{MS_e} \quad (25)$$

Calculated from Eq. 25, F_A = 1.4261, F_C = 5.2085, F_D = 1.3536, F_E = 4.3135.

3.3.2.5 Significance test

For the given significance level α, the significance of each factor was tested by comparing the F_j and F. If the F_j is greater than F_α (df_j, df_e), it is proved that this factor has a significant effect on the results of orthogonal design. Therefore, in this paper four levels of α = 0.025, α = 0.05, 0.95, and α = 0.975 were chosen to carry out the significance test. By querying the F distribution table, it was found that $F_{0.025}$ (4,8) = 5.05, $F_{0.05}$(4,8) = 3.84, $F_{0.95}$(4,8) = 0.166, $F_{0.975}$(4,8) = 0.111. The significance test results were compared, as shown in Supplementary Table S5.

As shown in Supplementary Table S5, F_A, F_C, F_D, F_E are all greater than F_α. According to the principle of significance test, A(l_i), C(s), D(h), E(d_z) all have significant effect on the results of orthogonal design. Among them, the factor C(s) has the most significant effect on the results of the orthogonal design, and the results of the analysis of variance are consistent with the results of the direct analysis.

The structural parameters of the three-phase hydrocyclone applicable to solid fluidization exploitation of NGH were optimized by the orthogonal design, and the results of orthogonal design were verified by the direct analysis and the analysis of variance. The test results showed that the gas outlet depth length, the tangential inlet area, the drain hole height, and the inverted cone diameter all had a significant effect on the separation efficiency of the three-phase hydrocyclone. Among them, the effect significance of each factor on the separation efficiency of three-phase hydrocyclone was $s>d_z>h>l_i$. At the same time, the dimensionless parameter E for evaluating the separation efficiency was defined by synthesizing the efficiency of water and sand discharge of the three-phase hydrocyclone. Taking E as the evaluation criterion, it was obtained that when the gas outlet depth length was 28 mm, the tangential inlet area was 2 mm^2 × 12 mm^2, the inverted cone diameter was 28 mm, the inverted cone length was 108 mm, and the drain hole height was 20 mm, the separation efficiency of hydrocyclone separator was the optimal.

3.4 Analysis of the influence of the change of single structural parameters on the distribution characteristics of flow field

In the aforementioned study, the orthogonal design was used to optimize the structural parameters based on the conventional three-phase hydrocyclone, and the optimal combination of structural parameters of three-phase hydrocyclone applicable to solid fluidization exploitation of NGH was obtained. In order to study the effect of the individual structural parameters changes on the separation performance. Based on the significance of the effects of different structural parameters on the separation efficiency obtained from the orthogonal design results, the effect of four structural parameters of s, d_z, l_i, and h on the velocity field, CH_4 volume fraction and water volume fraction distribution law in the flow field were investigated by numerical simulation.

3.4.1 Analysis of flow field distribution with different s of hydrocyclone

When the s of the three-phase hydrocyclone changes, the tangential velocity distribution in the flow field is shown in Supplementary Figure S7. In Supplementary Figures S7A,B,C show the results of tangential velocity distribution at monitoring line L_{Am}, L_{Bm}, L_{Cm}, respectively. As shown in Supplementary Figure S7A, the tangential velocity distribution of Case1–Case4 on monitoring line L_{Am} shows a symmetrical distribution law that increases gradually from the axis to the sidewall with the axial position x = 0 as the symmetrical center. It

indicates that the NGH slurry makes a circular motion around the axis after entering the spin chamber of hydrocyclone from the tangential inlets. However, due to the wall surface roughness of spin chamber was set as 0 and the wall surface had no slip during the numerical simulation, the tangential velocity decreases sharply near the radial position of ±22.5 mm. The maximum tangential velocity of Case 1 in circular motion is 13.65 m, and the maximum tangential velocity of Case 4 in circular motion is 4.80 m/s. The difference between the maximum tangential velocity of Case 1 and that of Case 4 is 8.85 m/s. It is proved that the circular motion of hydrate slurry is the fastest in the spin chamber when s is 2 mm^2 × 12 mm^2, which leads to greater difference of centrifugal force between different phases and better precision of separation. Meanwhile, according to the distribution law shown in Supplementary Figure S7A, under the same flow rate, the incident velocity of the hydrate slurry at the tangential inlets decrease gradually with the increase of s, which leads to the decrease of the maximum tangential velocity of each case on monitoring line L_{Am}. However, the maximum tangential velocity appears near the radial position of ±21.3 mm, which proves that the increase of s has no significant effect on the distribution position of the tangential velocity.

Supplementary Figure S7B shows the distribution of tangential velocity on monitoring line L_{Bm} with different s of hydrocyclone. Compared with the distribution of the tangential velocity on monitoring line L_{Am}, the positional distribution of the tangential velocity on monitoring line L_{Bm} does not change, but the maximum tangential velocity in each case has decreased. The maximum tangential velocity of Case1–Case4 decreases 11.72, 7.31, 5.46, and 4.27 m/s respectively. Among them, the tangential velocity reduction of Case 1 is maximum of 1.93 m/s, and the tangential velocity reduction of Case 4 is minimum of 0.53 m/s.

The distribution of tangential velocity on monitoring line L_{Cm} under different s conditions is shown in Supplementary Figure S7C. The maximum tangential velocity of Case1–Case4 on monitoring line L_{Cm} is 9.99, 6.41, 4.88, and 3.90 m/s, respectively. Compared with the tangential velocity distribution on monitoring line L_{Am}, 3.66, 2.08, 1.27, and 0.9 m/s are decreased respectively. Within the axial range of 43–83 mm from the top of the three-phase hydrocyclone, the tangential velocity decrease of Case1 is the largest, and the tangential velocity decrease of Case4 is the least. The maximum tangential velocity is distributed near the radial position of ±21.3 mm, which proves that the position of the maximum tangential velocity distribution is not affected by s in the axial distance.

The axial velocity distribution in the flow field is shown in Supplementary Figure S8. As shown in Supplementary Figure S8A, the axial velocity on monitoring line L_{Am} shows a distribution law from increasing to decreasing to increasing again from the edge to the axial center of the flow field. The rapid increase of the axial velocity near the edge of the flow field from 0 m/s is due to the fact that the boundary conditions of the spin chamber wall was set to be no wall slip and the roughness is 0 during the numerical simulation. In Case1–Case4, the maximum axial velocity appears at the radial position of 0 mm, and the maximum axial velocity of Case1 is 4.35 m/s. It shows that the axial velocity of the fluid in the flow field is the fastest at the axis of the spin chamber of the three-phase hydrocyclone. As shown in Supplementary Figure S8A, the Case1–Case4 appears a "reverse flow" moving toward the gas outlet near the axis of the flow field with the zero axial velocity line as the dividing line. The "reverse flow" of Case1–Case4 is distributed in the range of the radial position of ±15.3, ±14.2, ±13.5, and ±12.7 mm, respectively. Because the fluid domain in the spin chamber is cylindrical, the position where the Case1–Case4 "reverse flow" occurs can be regarded as a circle with a radius of 15.3, 14.2, 13.5, and 12.7 mm, respectively. On monitoring line L_{Am}, the distribution range of the "reverse flow" of Case1 is the largest in the radial position, and that of Case4 is the smallest in the radial position.

The axial velocity distribution on monitoring line L_{Bm} is shown in Supplementary Figure S8B. Because the inverted cone is fixed in the axial position of the flow field of the three-phase hydrocyclone. The axial velocity of Case1 and Case2 is affected by the inverted cone, which shows a small decrease near the radial position of 0 mm. The axial velocity distribution of Case3 and Case4 is not affected by the inverted cone. However, compared with monitoring line L_{Am}, the maximum axial velocity of each case on monitoring line L_{Bm} decreases 0.92, 0.92, 1.19, and 1.14 m/s respectively. Similarly, the "reverse flow" of Case1–Case4 is distributed in the circular flow field with a radius of 13.3 mm with the zero axial velocity line as the dividing line. Compared with the axial velocity distribution on monitoring line L_{Am}, the "reverse flow" radius of Case1–Case3 distribute on monitoring line L_{Bm} decrease 2, 0.9 and 0.2 mm, respectively. And the "reverse flow" radius of Case4 distributes on monitoring line L_{Bm} increases 0.6 mm.

Supplementary Figure S8C shows the axial velocity distribution curve on monitoring line L_{Cm}. The axial velocity distribution of Case1–Case4 at the axis is decreased by the effect of inverted cone, and the position of the maximum axial velocity in each case tends to approach the radial center with the increase of s. The maximum axial velocities of Case1 and Case4 at radial positions of 5.4 mm and 4.69 mm are 3.11 m/s and 1.27 m/s, respectively, which decreases 0.5 m/s and 0.59 m/s compared with monitoring line L_{Am}. As shown in Supplementary Figure S8C, although the axial velocity of the "reverse flow" at the axis of each case has decreased, its minimum value is still greater than that of the 0 m/s, indicating that the "reverse flow" still exists in the position of monitoring line L_{Cm}. At this time, the radius of "reverse flow" in each case is roughly the same, but it is decreased compared with that in the position of monitoring line L_{Am}. It indicates that the axial velocity decreases and the distribution range decreases gradually with the increase of axial distance.

As shown in Supplementary Figures S9A,B,C, in order to study the effect of hydrocyclone with different s on the distribution of CH_4 in the flow field, the volume fraction distribution of CH_4 on monitoring lines L_{Am}, L_{Bm}, and L_{Cm} were analyzed. On monitoring line L_{Am}, the volume fraction of CH_4 of Case1 is maximum of 12.4%, and the volume fraction of CH_4 of case 4 is minimum of 11.9%. The CH_4 volume fraction of case1 in the radial range of ±22 mm is higher than 10%, which proves that CH_4 accumulates in the axial position of 43 mm and radial range of ±22 mm. The volume fraction of CH_4 in the radial range of ±20.1 mm, ±19.2 mm, ±18.5 mm of Case2–Case4 is higher than 10%, and the radial accumulation range is smaller than that of Case1. That is, with the increase of s from 2 mm^2 × 12 mm^2 to 8 mm^2 × 18 mm^2, the tangential velocity and axial velocity gradually decrease, and the volume fraction of CH_4 at monitoring line L_{Am} gradually decreases, but the CH_4 accumulation position is closer to the axis.

The CH_4 volume fraction distribution on monitoring line L_{Bm} under different s conditions is shown in Supplementary Figure S9B. The distribution of CH_4 volume fraction at monitoring line L_{Bm} is roughly the same as that at monitoring line L_{Am}. The volume fraction of CH_4 in the radial range of ±21.4 mm of Case 1 is more than 10%, and this distribution range is larger than that of Case 2–Case 4. At the same time, the minimum CH_4 volume fraction of Case 1 at the edge is 9.23%, which is higher than that of other cases at the edge. It is proved that when s is 2 mm^2 × 12 mm^2, it has the most significant effect on the distribution of CH_4 in the flow field at the axial position of 63 mm.

Supplementary Figure S9C shows the CH_4 volume fraction distribution on monitoring line L_{Cm} under different s conditions. On monitoring line L_{Cm}, the maximum CH_4 volume fraction of Case 1–Case 4 are all 12.5% and are all located at the radial position of 0 mm. Compared with monitoring lines L_{Am} and L_{Bm}, the maximum CH_4 volume fraction of Case 2–Case 4 increase by 0.2%, 0.3%, and 0.6%, respectively. It indicates that as the axial distance from the top of the three-phase hydrocyclone increases from 43 to 83 mm, the accumulation of CH_4 in Case2–Case4 also increases gradually. However, the CH_4 volume fraction in the radial range of ±20.4 mm of Case1 is more than 10%, and the distribution range is still larger than that of Case2–Case4. It shows that at monitoring line L_{Cm}, when s is 2 mm^2 × 12 mm^2, it has the most significant effect on the distribution of CH_4 in the flow field.

The water volume fraction distribution on monitoring line L_{Dm} under different s conditions is shown in Supplementary Figure S10. In Case1–Case4, in order to compare with Case2–Case4, taking Case1 as basic case according to the results of orthogonal design. It can be seen from Supplementary Figure S10 that the water volume fraction distribution of Case3 and Case1 on monitoring line L_{Dm} is roughly the same, indicating that the separation efficiency of the three-phase hydrocyclone is the same when the other structural parameters are the same and the tangential inlet area is 2 mm^2 × 12 mm^2 and 6 mm^2 × 16 mm^2, respectively. The water volume fraction of Case1 on monitoring line L_{Dm} is 69.9%. Compared with the water volume fraction of Case1, the water volume fraction of Case4 increased by 5.5% with a maximum of 75.4% at monitoring line L_{Dm}. It indicates that the distribution of water is the most concentrated and the water volume fraction is the largest when the tangential inlet area is 8 mm^2 × 18 mm^2.

3.4.2 Analysis of flow field distribution with different d_z of hydrocyclone

The curves of the effect of three-phase hydrocyclone with different d_z on the tangential velocity distribution in the flow field are shown in Supplementary Figure S11. Case1 is set as the basic case and Case5–Case7 is set as the variation group. The tangential velocity changes on monitoring lines L_{Am}, L_{Bm}, and L_{Cm} were analyzed. As shown in Supplementary Figure S9, the maximum tangential velocity of each case at different monitoring line positions all appear at the edge of the flow field and shows the characteristics of central symmetrical distribution with the radial position of 0 mm as the symmetry center. From the local enlargement, we can see that the tangential velocity of different cases on the same monitoring line is roughly the same, but the tangential velocity of the same case is different on different monitoring lines, and the maximum tangential velocity shows the distribution law of decreasing from monitoring line L_{Am} to L_{Cm}. In each case, the tangential velocity is distributed about 13.6 m/s at monitoring line L_{Am} and about 9.98 m/s at monitoring line L_{Cm}, and the maximum tangential velocity decreases 3.62 m/s. It indicates that the decrease of tangential velocity is due to the increase of axial distance, and d_z has no significant effect on tangential velocity in the flow field.

The axial velocity distribution of Case1 and Case5–Case7 on each monitoring line under different d_z conditions is shown in Supplementary Figure S12. When the axial velocity is greater than 0 m/s and the axial position is within the range of monitoring line L_{Am} to L_{Cm}, the axial velocity at the edge of the flow field of each case decreases gradually under different d_z conditions, but the axial velocity distribution is the same in other positions. It shows that when the axial velocity is greater than 0 m/s, the axial position will affect the axial velocity distribution, but d_z will not affect the axial velocity. It indicates that when the axial velocity is greater than 0 m/s, the axial velocity distribution will be affected by the change of axial position, but the axial velocity will not be affected by d_z. When the axial velocity is less than 0 m/s, the axial velocity at the center of the flow field decreases gradually as the axial distance from the top of the three-phase hydrocyclone increases from 43 to 83 mm within the axial range of monitoring line L_{Am} to L_{Cm}. The maximum axial velocities of Case1 and Case5–Case7 at monitoring line L_{Am} are 4.35, 3.55, 4.0, and 3.91 m/s, respectively, and at monitoring line L_{Cm}, the axial velocities of each case at the radial position of

0 mm are 1.13, 1.15, 0.54, and 0.34 m/s respectively. Among them, the axial velocity decrease of Case7 is the largest, indicating that the axial velocity in the flow field is affected most when d_z is 36 mm.

The CH_4 distribution on each monitoring line in the flow field under different d_z conditions is shown in Supplementary Figure S13. The CH_4 volume fraction of Case1 and Case5–Case7 decreases gradually from the radial center to the edge on each monitoring line. It indicates that during the circular motion of the hydrate slurry in the spin chamber, the centrifugal force is the smallest due to the smallest density of CH_4, so that the CH_4 is distributed at the center of the axis. From the local enlargement, it is known that in the axial range between monitoring line L_{Am} and L_{Cm}, with the increase of the axial distance, the CH_4 volume fraction increases gradually at the radial position of 0 mm, and the CH_4 volume fraction of each case reaches the maximum at monitoring line L_{Cm}. On monitoring line L_{Cm}, the CH_4 volume fraction of Case5 is minimum of 12.46%, the CH_4 volume fraction of case 7 is maximum of 12.49%. The CH_4 volume fraction distribution increases with the increase of d_z. It indicates that under the condition that other structural parameters are the same, the increase of the inverted cone diameter reduces the fluid domain between the spin chamber side wall and the inverted cone, and causes the hydrate slurry to move along the surface of the inverted cone, thus increasing its circular motion radius, and then increasing the centrifugal force to promote the separation efficiency of the CH_4.

In order to study the effect of the change of structural parameters d_z on water separation, the water volume fraction distribution curves on monitoring line L_{Dm} under different d_z conditions as shown in Supplementary Figure S14. In Case1 and Case5–Case7, the d_z of Case5 is minimum of 24 mm and the d_z of case 7 is maximum of 36 mm. As shown in Supplementary Figure S14, with the increase of d_z from 24 to 36 mm, the water volume fraction at a radial position of 0 mm on monitoring line L_{Dm} decrease from 70.7% to 66.3%. It indicates that with the increase of the inverted cone diameter, the annular area between the inverted cone and the side wall of the spin chamber gradually decreases, and there is not enough space to separate the water and sand, resulting in the larger the d_z, the lower the water separation efficiency.

3.4.3 Analysis of flow field distribution with different l_i of hydrocyclone

The tangential velocity distribution curves in the flow field under different l_i conditions are shown in Supplementary Figure S15. As shown in Supplementary Figure S15, compared to Case1, there is no significant difference in the tangential velocity distribution of Case8–Case10 on the same monitoring line. It indicates that the change of l_i has no significant effect on the distribution of tangential velocity in the flow field. The maximum tangential velocity of each case appears near the radial position of ±21.2 mm. As shown in local enlargement, the maximum tangential velocity of Case8–Case10 on monitoring lines L_{Am}, L_{Bm}, and L_{Cm} are 14.2, 11.9, and 10.2 m/s respectively, which is not significantly different from that of Case1. It also indicates that the change of l_i has no significant effect on the tangential velocity.

The axial velocity distribution of Case1 and Case8–Case10 on monitoring lines L_{Am}, L_{Bm}, and L_{Cm} under different l_i conditions is shown in Supplementary Figures S16A,B,C, respectively. According to the results of orthogonal design and the setting of structural parameters, the l_i of each case is distributed evenly within 20–32 mm. As shown in Supplementary Figure S16A, as l_i increases from 20 to 32 mm, the maximum axial velocity on monitoring line L_{Am} increases from 3.46 to 4.75 m/s. It shows that the increase of the gas outlet depth length is beneficial to the movement of the gas to the gas outlet. When the axial velocity is greater than 0 m/s, the axial velocity distribution of each case is the same. It is proved that the change of l_i only has a significant effect on the axis.

As shown in Supplementary Figure S16B. As the axial distance from the top of the three-phase hydrocyclone increases from 43 to 83 mm, the effect of the change of the structural parameter l_i on the axial velocity distribution in the flow field is gradually decreased. On monitoring line L_{Bm}, the axial velocity of Case1 and Case9-Case10 is about 3.30 m/s at the radial position of 0 mm, but the axial velocity of Case8 is the smallest of 2.69 m/s at the radial position of 0 mm. It indicates that when l_i is 20 mm, its effect on the axial motion of the gas in the flow field is weakened obviously.

The axial velocity distribution on monitoring line L_{Cm} is shown in Supplementary Figure S16C. With the increase of axial distance, the effect of gas outlet depth length on the flow field gradually disappears. On monitoring line L_{Cm}, under the condition of the same other structural parameters of Case1 and Case8–Case10, the effect of l_i on the flow field is weakened, and there is no significant difference in the axial velocity distribution of each case.

The CH_4 distribution on monitoring line under different l_i conditions is shown in Supplementary Figure S17. On each monitoring line, CH_4 shows the distribution law of accumulation in the radial center, and the CH_4 volume fraction is more than 10% in the radial range of ±20.9 mm. However, there is no significant difference in the CH_4 volume fraction distribution under different l_i conditions on the same monitoring line, indicating that the change of structural parameters l_i has no significant effect on the CH_4 volume fraction distribution in the flow field.

Supplementary Figure S18 shows the water volume fraction distribution curves on monitoring line L_{Dm} under different l_i conditions. As shown in Supplementary Figure S18, the water volume fraction distribution of Case1 and Case8–Case10 on monitoring line L_{Dm} is the same, showing the distribution characteristics of increasing gradually from the edge to the axis. The maximum water volume fraction is 70.2% at the

radial position of 0 mm. It shows that the change of the structural parameter l_i has no significant effect on the separation of the water phase.

3.4.4 Analysis of flow field distribution with different *h* of hydrocyclone

Supplementary Figure S19 shows the tangential velocity distribution under different h conditions. From the local enlargement in Supplementary Figure S19, it can be seen that the maximum tangential velocity shows a gradual decrease in the axial distance of 40 mm from monitoring line L_{Am} to monitoring line L_{Cm}. However, the tangential velocity also shows the distribution characteristic that is not affected by h on the same monitoring line. It indicates that the change of h has no significant effect on the radial separation of gas-liquid-solid mixture.

The axial velocity distribution of Case1 and Case11–Case13 on different monitoring lines under different h conditions is shown in Supplementary Figure S20. When the axial velocity is less than 0 m/s, the axial velocity at the edge of the same monitoring line is the same in different cases, but with the increase of the axial position, the axial velocity at the edge decreases gradually. When the axial velocity is less than 0 m/s, in the axial range between monitoring line L_{Am} and L_{Cm}, as the axial distance from the top of the three-phase hydrocyclone increases from 43 to 83 mm, the axial velocity decreases gradually at the radial center. However, the axial velocity distribution on the same monitoring line is not affected by the change of the structural parameter h. It indicates that the drain hole height only affects the transport of the separated phase, but it has no effect on the velocity distribution in the flow field and the separation process of multiphase.

Supplementary Figure S21 shows the CH_4 distribution curve on monitoring line under different h conditions. Because the parameter h is the height of the drain hole, and the drain hole is the tangential inlets arranged on the inverted cone structure. According to the structural characteristics of the drain hole, it will not affect the circular motion of the fluid in the flow field. Therefore, when other structural parameters are the same, the change of h has no significant effect on the CH_4 distribution in the flow field. However, due to the centrifugal force difference caused by the density difference between different phases in the circular motion, the CH_4 still moves toward the radial center, and the maximum CH_4 volume fraction appears at the radial position of 0 mm at different monitoring lines.

The water volume fraction distribution on monitoring line L_{Dm} under different h conditions is shown in Supplementary Figure S22. Among Case1 and Case11–Case13, Case11 has the largest water volume fraction on monitoring line L_{Dm}, and the maximum water volume fraction of Case11 is 77.9% at the radial position of 0 mm. Compared with Case1, the water volume fraction of Case12 and Case13 has no obvious change, and the maximum water volume fraction distribution are all about 70.5%. It shows that h = 10 mm is the optimal structure parameter for the separated water to enter the drain hole, and the hydrate slurry is separated completely at this position. When h is greater than 10 mm, the position of the drain hole is close to the top of the three-phase hydrocyclone, where the hydrate slurry has not been completely separated, and the water will carry part of the sand phase into the drain hole, so that the mixture discharged from the water outlet contains sand.

4 Conclusion

In this paper, the optimal structural parameter combination of the three-phase hydrocyclone applicable to solid fluidization exploitation of NGH was obtained. The effect of the optimized structural parameters on the internal flow field characteristics of the three-phase hydrocyclone was studied. Based on the above results and discussion, the following conclusions were drawn.

(1) By using the orthogonal design, the structure optimization was carried out based on the conventional three-phase hydrocyclone and defined the dimensionless parameter E as the criterion of separation efficiency. The effect significance of different structural parameters on separation efficiency from high to low was: $s>d_z>h>l_i$. When the maximum E was 1.46, the optimal structural parameters combination was that the tangential inlet area(s) was 2 mm^2 × 12 mm^2, the inverted cone diameter (d_z) was 28 mm, the drain hole height (h) was 20 mm and the gas outlet depth length (l_i) was 28 mm. A new structure of hydrocyclone applicable to solid fluidization exploitation of NGH was obtained, which provides a reference for the engineering practice of hydrate slurry separation.

(2) When the s was in the range from 2 mm^2 × 12 mm^2 to 8 mm^2 × 18 mm^2, the tangential velocity, axial velocity and CH_4 volume fraction in the flow field were all negatively correlated with the s. The three parameters all reached the maximum when the s was 2 mm^2 × 12 mm^2, in which the tangential velocity was 13.65 m/s, the axial velocity was 4.35 m and the CH_4 volume fraction was 12.4%. The water volume fraction distribution was positively correlated with s. When the s was 8 mm^2 × 18 mm^2, the water volume fraction at the water outlet was 75.4%. Therefore, if the water separation efficiency is improved, it is suggested that the s should be set as 8 mm^2 × 18 mm^2.

(3) When the d_z was 36 mm, the maximum attenuation of axial velocity was 3.57 m/s, the maximum CH_4 volume fraction was 12.46% and the minimum water volume fraction was 66.3%. The change of d_z has no significant effect on tangential velocity. Therefore, when the flow rate is

constant in engineering practice, the separation efficiency of water and CH_4 can be adjusted by changing the d_z.

(4) The change of l_i had no effect on the tangential velocity, CH_4 volume fraction distribution and water volume fraction distribution in the flow field. The axial velocity increases with the increase of l_i and reaches the maximum of 4.75 m/s when the l_i was 32 mm. The l_i had a significant effect on the axial migration of CH_4. In engineering practice, the l_i should be appropriately increased to improve the separation efficiency of CH_4.

(5) The h had on effect on the tangential velocity, axial velocity and CH_4 volume fraction distribution in the flow field. With the increase of the h, the water volume fraction of the water outlet decreased gradually. When the h was 10 mm, the water volume fraction of the water outlet was maximum of 77.9%. The h had no significant effect on the flow field distribution, but different h had a significant effect on monitoring the separation position and separation efficiency of the water in engineering practice.

Data availability statement

The original contributions presented in the study are included in the article/Supplementary Material, further inquiries can be directed to the corresponding author.

Author contributions

NW: Resources, project administration, funding acquisition. YQ: Conceptualization, methodology, software, formal analysis, data curation, writing-original draft, writing-review and editing. AL: Investigation. JZ: Project administration, funding acquisition. LZ: Project administration, funding acquisition. JX: Investigation, visualization.

Funding

The research is funded by National Natural Science Foundation of China (No. U20B6005-05), National Key Research and Development Program (No. 2021YFC2800903), 111 Project (No. D21025), Open Fund Project of State Key Laboratory of Oil and Gas Reservoir Geology and Exploitation (No. PLN2021-01, PLN2021-02, PLN2021-03), High-end Foreign Expert Introduction Program (No. G2021036005L), National Natural Science Foundation of China (No. 51874252).

Conflicts of interest

Author AL is employed by Geological Explorations and Development Institute, Chuan Qing Drilling Engineering Company Limited.

The remaining authors declare that the research was conducted in the absence of any commercial or financial relationships that could be construed as a potential conflict of interest.

Publisher's note

Supplementary material

The Supplementary Material for this article can be found online at: https://www.frontiersin.org/articles/10.3389/feart.2022.991208/full#supplementary-material

References

Aminnaji, M., Tohidi, B., Burgass, R., and Atilhan, M. (2017). Gas hydrate blockage removal using chemical injection in vertical pipes. *J. Nat. Gas Sci. Eng.* 40, 17–23. doi:10.1016/j.jngse.2017.02.003

Bu, F. X., Liu, Y., Liu, Y. B., Xu, Z., Chen, S. Q., Jiang, M. H., et al. (2021). Leakage diffusion characteristics and harmful boundary analysis of buried natural gas pipeline under multiple working conditions. *J. Nat. Gas Sci. Eng.* 94, 104047. doi:10.1016/j.jngse.2021.104047

Chang, Y. L., Ti, W. Q., Wang, H. L., Zhou, S. W., Li, J. P., Wang, G. R., et al. (2021). Hydrocyclone used for *in-situ* sand removal of natural gas-hydrate in the subsea. *Fuel* 285, 119075. doi:10.1016/j.fuel.2020.119075

Chen, B. B., Sun, H. R., Li, K. H., Wang, D. Y., and Yang, M. J. (2019). Experimental investigation of natural gas hydrate production characteristics via novel combination modes of depressurization with water flow erosion. *Fuel* 252, 295–303. doi:10.1016/j.fuel.2019.04.120

Chen, X. P., Shen, Q., Ma, X. C., Li, A., and Zhan, M. (2020). Overview of natural gas hydrate test mining at domestic and Foreign. *Guangdong Chem. Ind.* 47, 95–96.

Chen, Z. (2020). *Design and simulation research of wellhead oil-water-sand cyclone*. dissertation/master's thesis. Jingzhou: Yangtze University.

Chong, Z. R., Yang, S. H. B., Babu, P., Linga, P., and Li, X. S. (2016). Review of natural gas hydrates as an energy resource: Prospects and challenges. *Appl. Energy* 162, 1633–1652. doi:10.1016/j.apenergy.2014.12.061

Chuang, J., Ahmadi, G., and Smith, D. H. (2001). Natural gas production from hydrate decomposition by depressurization. *Chem. Eng. Sci.* 56, 5801–5814. doi:10.1016/s0009-2509(01)00265-2

Cui, Y. D., Lu, C., Wu, M. T., Peng, Y., Yao, Y. B., and Luo, W. J. (2018). Review of exploration and production technology of natural gas hydrate. *Adv. Geo-Energy Res.* 2, 53–62. doi:10.26804/ager.2018.01.05

Dong, H., Wu, K. S., Kuang, Y. C., and Dai, M. L. (2018). Study on separation law of hydrate slurry in hydrocyclone based on CFD-DEM. *J. Zhejiang Univ. Eng. Sci.* 52, 11811–11820. doi:10.3785/j.issn.1008-973X.2018.09.023

Elsayed, K., and Lacor, C. (2011). The effect of cyclone inlet dimensions on the flow pattern and performance. *Appl. Math. Model.* 35, 1952–1968. doi:10.1016/j.apm.2010.11.007

Gao, J. M. (2021). *Research on coalescence and breakage characteristics of oil droplets in hydrocyclone under the condition of gas-containing*. dissertation/master's thesis. Daqing: Northeast Petroleum University.

Hou, L., Yang, J. H., Liu, Z. X., and Jiao, J. (2021). Current status and suggestions on development of marine gas hydrate technologies in China. *World Pet. Ind.* 28, 17–22.

Huang, T. (2018). *Fundamental theory study on gas-liquid-solid three-phase flow in natural gas hydrate transportation pipelines in deep water*. dissertation/doctor's thesis. Chengdu: Southwest Petroleum University.

Jiang, M. H., Li, Y. S., Zhao, L. X., Xu, B. R., and Cheng, Q. L. (2014). Numerical simulation on overflow pipe structure of a degassing/desanding three-phase separation hydrocyclone. *Petro-Chemical Equip.* 43, 10–13. doi:10.3969/j.issn.1000-7466.2014.05.003

Li, L. S., and Miao, Q. (2014). Review on natural gas hydrate exploration and development technology. *Oil Gas Field Dev.* 32, 66–71. doi:10.3969/j.issn.1006-553932014.01.018

Liang, L., Sun, J., Yue, M. J., and Geng, H. L. (2020). Comparative analysis of global energy consumption mix in recent ten years. *World Pet. Ind.* 27, 41–47.

Liu, H., Gao, Y., Pei, X. H., Zheng, G. X., and Zheng, L. C. (2018). Progress and prospect of downhole cyclone oil-water separation with single-well injection-production technology. *Acta Pet. Sin.* 39, 463–471. doi:10.7623/syxb201804010

Liu, L. L., Li, Y. L., Zhang, X. H., Luo, D. S. H., and Liu, C. L. (2021). Experimental study on gas hydrate system state evolving during depressurization. *J. Eng. Geol.* 29, 916–1925. doi:10.13544/j.cnki.jep.2021-0695

Qiu, S. Z., Wang, G. R., Wang, G. S., Zhou, S. W., Liu, Q. Y., Zhong, L., et al. (2019). Effects of hydrocyclone separation on purification of natural gas-hydrate slurry and sand remove. *Chin. J. Process Eng.* 19, 64–72. doi:10.12034/j.issn.1009-606X.218154

Song, M. H., Zhao, L. X., Xu, B. R., Liu, L., and Zhang, S. (2021). Discussion on technology of improving separation efficiency of liquid-liquid hydrocyclone. *Chem. Industry Eng. Prog.* 40, 6590–6603. doi:10.16085/j.issn.1000-6613.2020-2545

Song, Y. C., Chen, C. X., Zhao, J. F., Zhu, Z. H., Liu, W. G., Yang, M. J., et al. (2015). Evaluation of gas production from methane hydrates using depressurization, thermal stimulation and combined methods. *Appl. Energy* 145, 265–277. doi:10.1016/j.apenergy.2015.02.040

Song, Y. C., Yang, L., Zhao, J. F., Liu, W. G., Yang, M. J., Li, Y. H., et al. (2014). The status of natural gas hydrate research in China: A review. *Renew. Sustain. Energy Rev.* 31, 778–791. doi:10.1016/j.rser.2013.12.025

Wan, L. H. (2009). *Study on dissociation features of gas hydrate in the presence of chemicals*. dissertation/doctor's thesis. Guangzhou: Guangzhou Institute of Energy Conversion, Chinese Academy of Science.

Wang, A., Yan, X. K., Wang, L. J., Cao, Y. J., and Liu, J. T. (2015). Effect of cone angles on single-phase flow of a laboratory cyclonic-static microbubble flotation column: PIV measurement and CFD simulations. *Sep. Purif. Technol.* 149, 308–314. doi:10.1016/j.seppur.2015.06.004

Wang, B., Fan, Z., Wang, P. F., Liu, Y., Zhao, J. F., and Song, Y. C. (2018). Analysis of depressurization mode on gas recovery from methane hydrate deposits and the concomitant ice generation. *Appl. Energy* 227, 624–633. doi:10.1016/j.apenergy.2017.09.109

Wang, B. (2019). *Study on mining characteristics and effiiciency optimization of naturel gas hydrate resources via depressurization*. dissertation/doctor's thesis. Dalian: Dalian University of Technology.

Wang, D. F., Wang, G. R., Zhong, L., and Qiu, S. Z. (2019). Effects of numbers of inlets on characteristics of flow field and separation performance of natural gas hydrate slurry in hydrocyclone. *Shipbuild. China* 60, 161–169. doi:10.3969/j.issn.1000-4882.2019.04.018

Wang, G. D., He, L. M., Lv, Y. L., and Chen, Z. Y. (2006). Study on oil-water separating behavior of gravity separator. *Acta Pet. Sin.* 27, 112–115. doi:10.7623/syxb200606025

Wang, H. (2020). *Experimental study on separation performance of three-phase cyclone in underground coal mine*. dissertation/master's thesis. Qingdao: Shandong University of Science and Technology.

Wang, W. C., Wang, X. Y., Li, Y. X., Liu, S., Yao, S. P., and Song, G. C. (2020). Study on the characteristics of natural gas hydrate crystal structures during decomposition process. *Fuel* 271, 117537. doi:10.1016/j.fuel.2020.117537

Wang, Y., Feng, J. C., Li, X. S., and Zhang, Y. (2017). Experimental investigation of optimization of well spacing for gas recovery from methane hydrate reservoir in sandy sediment by heat stimulation. *Appl. Energy* 207, 562–572. doi:10.1016/j.apenergy.2017.06.068

Wei, N., Zhao, J. Z., Sun, W. T., Zhou, S. W., Zhang, L. H., Li, Q. P., et al. (2018). Non-equilibrium multiphase wellbore flow characteristics in solid fluidization exploitation of marine gas hydrate reservoirs. *Nat. Gas. Ind.* 38, 90–99. doi:10.3787/j.issn.1000-0976.2018.10.013

Wei, N., Zhou, S. W., Cui, Z. J., Zhao, J. Z., Zhang, L. H., and Zhao, J. (2020). Evaluation of physical parameters and construction of a parameter classification system for natural gas hydrate in the northern South China Sea. *Nat. Gas. Ind.* 40, 59–67. doi:10.3787/j.issn.1000-0976.2020.08.004

Wu, Y. M., and Li, L. Y. (2019). Numerical simulation of inner cone structure of gas-liquid-solid three-phase cyclone separator. *Jiangxi Chem. Ind.*, 101–103. doi:10.14127/j.cnki.jiangxihuagong.2019.02.029

Xu, B. R., Jiang, M. H., and Zhao, L. X. (2017). Effect of production fluid viscosity on the performance of three phase separation hydrocyclone. *J. Mech. Eng.* 53, 175–182. doi:10.3901/jme.2017.08.175

Xu, Y. X. (2012). *Numerical simulation and analysis of the separation process in the hydrocyclone*. dissertation/doctor's thesis. Shanghai: East China University of Science and Technology.

Yang, L., Liu, Y. L., Zhang, H. Q., Xiao, B., Guo, X. W., Wei, R. P., et al. (2019). The status of exploitation techniques of natural gas hydrate. *Chin. J. Chem. Eng.* 27, 2133–2147. doi:10.1016/j.cjche.2019.02.028

Zhan, M. S., Liu, S. X., Zhang, Y. M., Sun, G. G., and Weng, L. (2014). Methane hydrate formation and thermal based dissociation behavior in silica glass bead porous media. *Ind. Eng. Chem. Res.* 53, 6840–6854. doi:10.1021/ie4036737

Zhang, C. E., Cui, B. Y., Wei, D. Z., and Lu, S. S. (2019). Effects of underflow orifice diameter on the hydrocyclone separation performance with different feed size distributions. *Powder Technol.* 355, 481–494. doi:10.1016/j.powtec.2019.07.071

Zhao, J. Z., Zhou, S. W., Zhang, L. H., Wu, K. S., Guo, P., Li, Q. P., et al. (2017). The first global physical simulation experimental systems for the exploitation of marine natural gas hydrates through solid fluidization. *Nat. Gas. Ind.* 37, 15–22. doi:10.3787/j.issn.1000-0976.2017.09.002

Zhao, K. B., Sun, C. Q., and Wu, C. Z. (2021). Research progress of natural gas hydrate development technologies. *Oil Drill. Prod. Technol.* 43, 7–14. doi:10.13639/j.odpt.2021.01.002

Zhao, L. X., Jiang, M. H., and Wang, Y. (2008). Experimental study of a hydrocyclone under cyclic flow conditions for fine particle separation. *Sep. Purif. Technol.* 59, 183–189. doi:10.1016/j.seppur.2007.06.009

Zheng, J. (2005). *Study the gas-liquid-sand three-phase hydrocyclone*. dissertation/master's thesis. Dalian: Dalian University of Technology.

Zhong, L. C., Zhang, Y. S., Wang, T., Ji, Y., Norris, P., and Pan, W. P. (2019). Optimized methods for preparing activated carbon from rock asphalt using orthogonal experimental design. *J. Therm. Anal. Calorim.* 136, 1989–1999. doi:10.1007/s10973-018-7855-x

Zhou, S. W., Chen, W., and Li, Q. P. (2014). The green solid fluidization development principle of natural gas hydrate stored in shallow layers of deep water. *China Offshore Oil Gas* 26, 1–7.

Zhou, S. W., Chen, W., Li, Q. P., Zhou, J. L., and Shi, H. S. (2017a). Research on the solid fluidization well testing and production for shallow non-diagenetic natural gas hydrate in deep water area. *China Offshore Oil Gas* 29, 1–8. doi:10.11935/j/issn.1673-1506.2017.04.001

Zhou, S. W., Zhao, J. Z., Li, Q. P., Chen, W., Zhou, J. L., Wei, N., et al. (2017b). Optimal design of the engineering parameters for the first global trial production of marine natural gas hydrates through solid fluidization. *Nat. Gas. Ind.* 37, 1–14. doi:10.3787/j.issn.1000-0976.2017.09.001

Zou, C. N., Zhao, Q., Zhang, G. S., and Xiong, B. (2016). Energy revolution: From a fossil energy era to a new energy era. *Nat. Gas. Ind. B* 36, 1–11. doi:10.1016/j.ngib.2016.02.001

Nomenclature

Nomenclature

df Freedom degree

d_z Inverted cone diameter (mm)

D_{ij} Diffusion term

E Separation efficiency evaluating criterion

F F value

g Gravitational acceleration (m/s2)

G_{all} Gas volume injected in tangential inlets (%)

G_{out} Gas volume exhausted from gas outlet (%)

G_{ij} Buoyancy generating term

h Drain hole height (mm)

k_t Fluid thermal conductivity

Kx Sum of the test results of the level number is x which belongs to a certain factor column

l_i Gas outlet depth length (mm)

l_z Inverted cone length (mm)

L Monitoring lines

MS Mean square of each factor

P Fluid pressure (Pa)Average value of the square of the sum of E

P Fluid pressure (Pa)Average value of the square of the sum of E

P_{ij} Stress generation term

Q Sum of E2

R Range

s Tangential inlet area (mm2)

S_{out} Sand volume exhausted from sand outlet (%)

S_{all} Sand volume injected in tangential inlets (%)

SS Sum of squares of deviation

T Sum of E

u Velocity (m/s)

Greek letters

μ Fluid viscosity

ε_{ij} Viscous dissipative term

ρ Density

Φ_{ij} Pressure strain generating term

Subscript

all Volume fraction of phase

i Directions

j Directions

out Volume fraction of phase at outlet

x position

frontiers | Frontiers in Earth Science

TYPE Original Research
PUBLISHED 09 September 2022
DOI 10.3389/feart.2022.986647

OPEN ACCESS

EDITED BY
Pibo Su,
Guangzhou Marine Geological Survey, China

REVIEWED BY
Changcheng Han,
Xinjiang University, China
Cunfei Ma,
China University of Petroleum, Huadong, China
Weifeng Zhu,
Dagang oilfield, China

*CORRESPONDENCE
Cuixia Qu,
329865708@qq.com

SPECIALTY SECTION
This article was submitted to Marine Geoscience, a section of the journal Frontiers in Earth Science

RECEIVED 05 July 2022
ACCEPTED 12 August 2022
PUBLISHED 09 September 2022

CITATION
Li H, Liu J, Qu C, Song H and Zhuang X (2022), A method for calculating gas hydrate saturation by dual parameters of logging.
Front. Earth Sci. 10:986647.
doi: 10.3389/feart.2022.986647

A method for calculating gas hydrate saturation by dual parameters of logging

Haiyan Li, Jundong Liu, Cuixia Qu*, Hongye Song and Xueliang Zhuang

Tianjin branch of CNLC Logging Co. LTD., Tianjin, China

Natural gas hydrates, which only occur in geological environments with special conditions, are characterized by physical properties unique from those of oil and gas, rendering current methods of measuring saturation, such as the conventional Archie formula or the sonic velocity method, inaccurate. Therefore, to obtain a reliable saturation value of natural gas hydrates, we propose a two-parameter calculation model of resistivity and acoustic interval transit time based on logging data. The saturation results calculated using the two-parameter calculation model were far more accurate than those of the core experiment results, with the proposed model having an average relative error of 7%, whereas that of the conventional Archie formula was 24%. These results indicate that the logging two-parameter model effectively improves the calculation accuracy of gas hydrate saturation. The saturation calculation model is based on objective theory and has wide adaptability, which provides a reliable foundation for future hydrate resource evaluation, exploration, and development in the study area.

KEYWORDS

natural gashydrates, saturation, logging, resistivity, acoustic interval transit time

Introduction

Natural gas hydrate, also known as solid methane, is an ice-like solid compound formed from hydrocarbon gas molecules, such as methane or water molecules, under low temperature and high pressure. Due to its occurrence under special environmental conditions and physical properties unique from oil and gas, resource evaluation and development of natural gas hydrates is challenging. Specifically, the current quantitative evaluation of gas hydrate reservoir parameters basically follows the theoretical method of oil and gas exploration, which can produce inaccurate results due to the property differences in natural gas hydrates versus oil and gas. Logging technology can directly obtain the information of *in-situ* formation and is one of the most effective methods used currently to identify and evaluate natural gas hydrate reservoirs (Wang et al., 2003; Murray et al., 2006; Collet, 2013; Zhong et al., 2020). The most common methods for calculating saturation parameters of natural gas hydrates are the resistivity method and the sonic velocity method (Guo et al., 2011; Su et al., 2014; Xiao and Bai., 2015; Zhu et al., 2019). The resistivity method requires the determination of the rock-electrical parameters

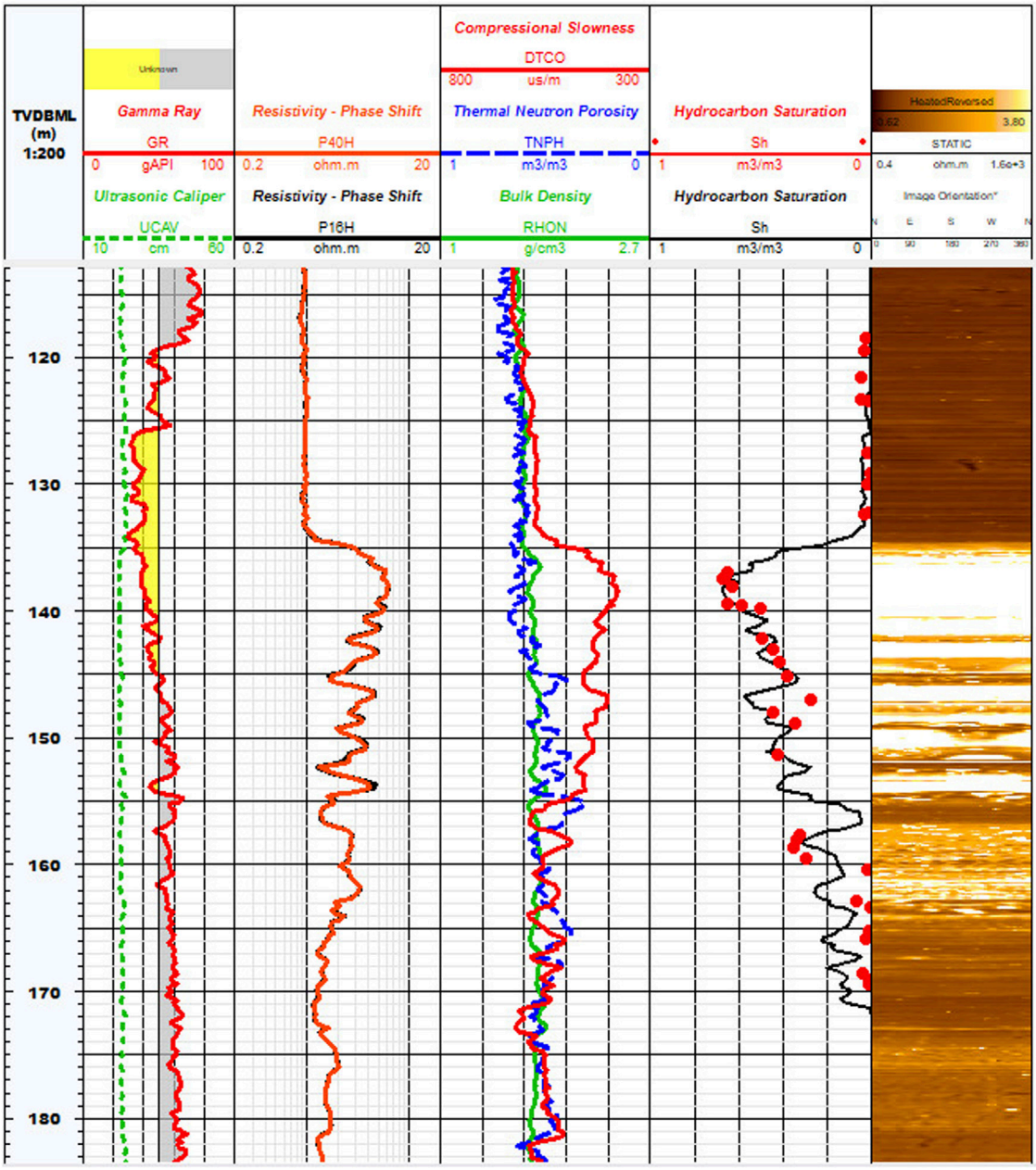

FIGURE 1
Logging map of gas hydrate reservoir of well ** in Shenhu Area, South China Sea.

of the reservoir and then use the Archie formula to calculate the saturation. The sonic velocity method is used to calculate saturation based on sonic velocity measurements of hydrated sediments, which is then combined with empirical or petrophysical models (Wang et al., 2010; Sun et al., 2011). However, natural gas hydrates decompose readily from the *in-situ* formation, making it difficult to obtain rock electrical parameters through experimentation. In addition to the influence of hydrate saturation, the sonic velocity of hydrate-bearing reservoirs is also sensitive to the limestone composition, compaction degree, and microscopic distribution pattern of hydrate in sediments. Thus, the loose and unconsolidated silty clay distribution of the marine hydrate reservoir lends to possible error. In this study, we propose a two-parameter logging model to calculate natural gas hydrate saturation by studying the logging data of several natural gas hydrates in the South China Sea, in an effort to improve the reliability and accuracy of hydrate saturation parameters.

Logging the response characteristics of natural gas hydrate

Lithology of the hydrate reservoir in the Shenhu area of South China Sea is mainly clay siltstone with loose and unconsolidated strata (Zhang et al., 2017). The range of logging depth is about 30–235 m below the seabed. Conventional logging curves are generally constructed based on parameters such as hole diameter, gamma ray, resistivity, acoustic interval transit time, compensated neutron, and compensated density. Figure 1 shows a partial LWD curve of well SH**in the study area. The hydrate-rich section of the reservoir is located at 133–155 m. Compared with the upper and lower strata without hydrates, the curve response features are as follows: lower gamma ray, significantly higher resistivity, lower compensative neutrons, higher density, and significantly shorter acoustic interval transit time. Additionally, the hydrate-rich stratus is highlighted in the micro-resistivity scanning image. The hydrate saturation data points obtained from the core experiment are also in good agreement with them. These characteristics, along with support from the hydrate saturation data points obtained from the core experiment, clearly indicate the existence of hydrate.

High resistivity and low acoustic interval transit time are the most typical characteristics of a hydrate reservoir. Natural gas hydrate is similar to ice, and the process of freezing may result in a "salt elimination" effect. Therefore, pure natural gas hydrate is not conductive, and the formation of hydrate occupies a certain formation pore, which hinders the migration of conductive fluid in the formation, ultimately resulting in a sharp increase in the resistivity of the hydrate-bearing layer (Li and Xiao., 2013; Ning et al., 2013; Zhou et al., 2020). As shown in the LWD diagram of gas hydrate in the study area (Figure 1), the resistivity of the hydrate-developed interval (133–155 m; the third channel) increased sixfold from 1.0 Ω m at the top of the hydrate-bearing layer to 6.2 Ω m and then fell back to 1.3 Ω m through the bottom of the hydrate layer. In addition, natural gas hydrate has a high acoustic velocity, which should lead to a significant decrease in the acoustic interval transit time of the reservoir. Figure 1 shows that the acoustic interval transit time (the fourth DTCO) of the hydrated layer (13–155 m) decreases from 575 μs/m at the top of the hydrated layer to 380 μs/m followed by an increase to 580 μs/m at the bottom of the hydrated layer.

Data and methods

Establishment of the two-parameter saturation calculation model

Due to the high resistivity of natural gas hydrate, most studies have equated it with oil and gas when calculating saturation. The saturation of natural gas hydrate is commonly calculated using the resistivity measurement value and Archie formula (Eq. 1; Wang et al., 2021; Malinverno. et al., 2008).

$$S_h = 1 - \sqrt[n]{\frac{ab\,R_w}{\varnothing^m R_t}} \tag{1}$$

where Sh: The saturation of natural gas hydrate, %; Rw: resistivity of formation water, Ω·m; Rt: resistivity of the formation, Ω·m. φ: porosity of formation, %. a, b: Rock-related coefficients, m: cementation index of the formation; n: saturation index.

The Archie formula is the saturation calculation law established from many core experiments, used to obtain saturation parameters for pure sandstone formations with uniform intergranular pores (Zhang et al., 2018; Lei et al., 2022). The marine natural gas hydrate reservoir has the "non-Archie" characteristics of loose and unconsolidated formation, high shale content, and non-uniform saturation distribution. Additionally, natural gas hydrate decomposes easily once it leaves the *in-situ* formation, making it difficult to accurately obtain the rock electrical parameters a, b, m, and n in the formula through the laboratory (Hyndman. et al., 1999; Goldberg. et al., 2010). Therefore, the Archie formula cannot obtain effective saturation parameters of the hydrate.

The sonic velocity method is mainly used to calculate hydrate saturation using a time average equation (Eq. 2):

$$\frac{1}{V_p} = \frac{\varnothing(1-S)}{V_w} + \frac{\varnothing S}{V_h} + \frac{1-\varnothing}{V_m} \tag{2}$$

where Vp: P-wave velocity of hydrate-bearing sediments, m/s. φ: core porosity, %; S: saturation of hydrate, %; Vw, Vh, and Vm: P-wave velocities of water, pure hydrate, and skeleton, respectively, m/s.

The premise of calculating hydrate saturation using the time average equation is that the theoretical logging acoustic value is composed of pore water, rock skeleton, and hydrate (Chen et al., 2013). However, the actual acoustic value is not only dependent on these media itself, but also on the contact mode between media, such as the degree of formation compaction and the microscopic distribution of hydrate in pores. Therefore, it is necessary to establish a calculation method that can more accurately calculate hydrate saturation.

The proposed model

The formation of natural gas hydrate occurs at a certain temperature, pressure, pore space, and gas source. The occurrence position in the formation depends on the coupling of the above factors, but has no direct relationship with a single factor. However, due to the typical response characteristics of natural gas hydrate with high resistivity and low acoustic interval transit time, it can also be effectively identified by logging data

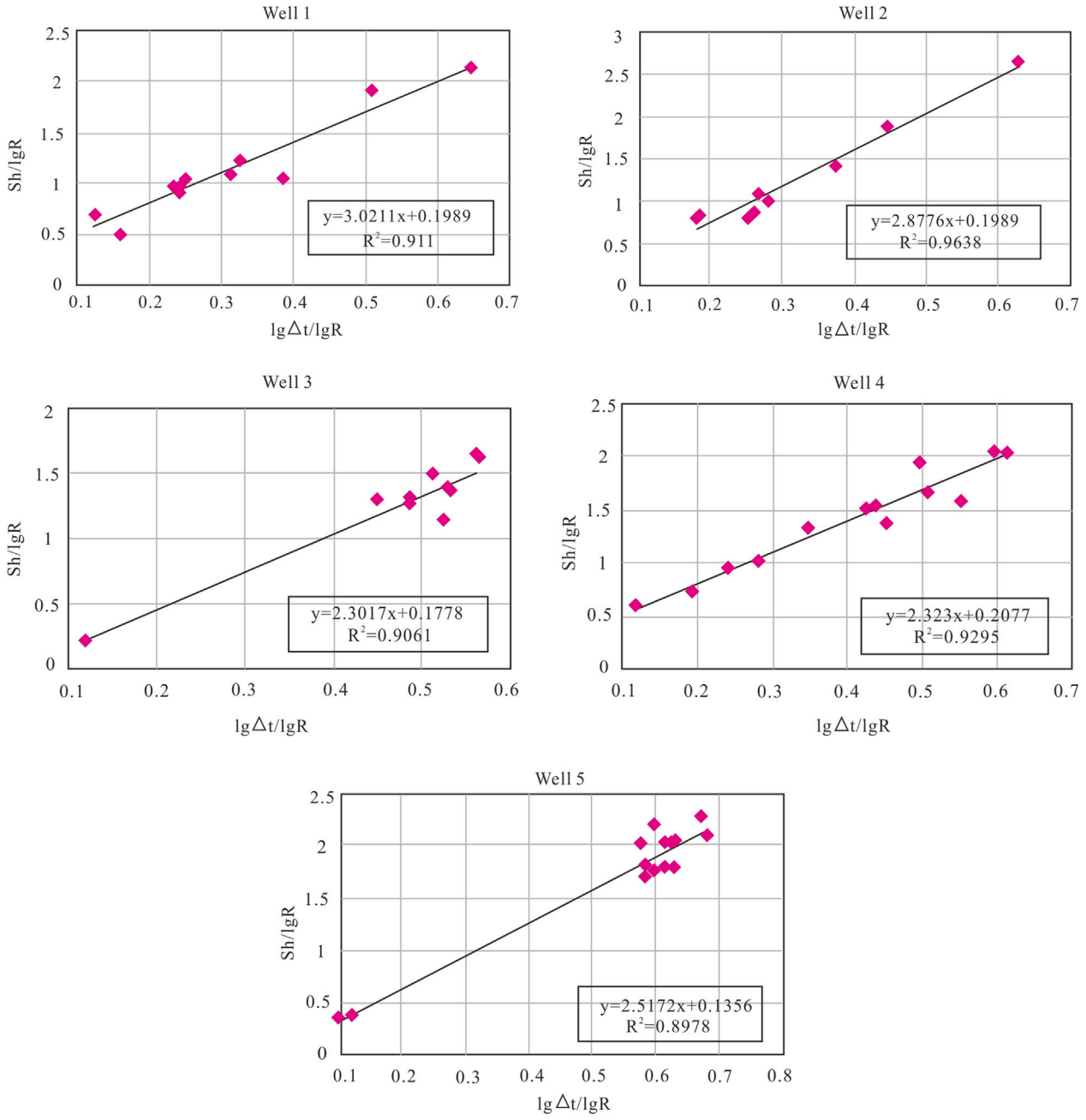

FIGURE 2
The coefficient fitting diagram of five wells in study area.

under multi-factor control. Under this premise, the quantitative calculation model of hydrate saturation is constructed using resistivity and acoustic time difference, which collectively is referred to as the tow-parameter saturation model. The calculation formula is as follows:

$$S_h = a\lg\left(\frac{RT}{RT_b}\right) + b\lg\left(\frac{AC_b}{AC}\right) \quad (3)$$

where RT: deep resistivity logging value of hydrate formation, Ω·m; RTb: deep resistivity of formation without hydrate, Ω·m;

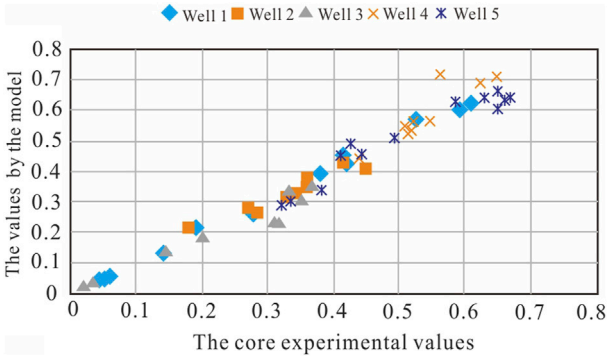

FIGURE 3
Comparison between saturation calculated by two-parameter model and core experimental data.

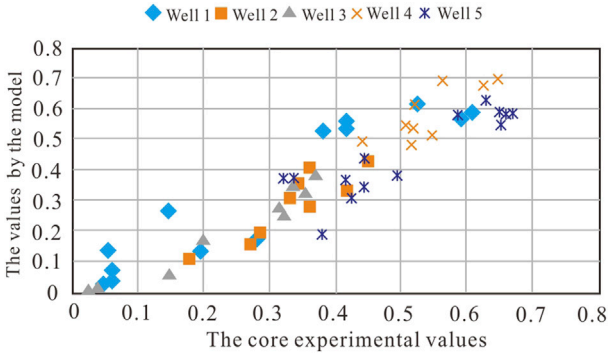

FIGURE 4
Comparison between saturation calculated by Arichie formula and core experimental data.

AC: acoustic interval transit time logging value of hydrate formation, Us/m; ACb: acoustic interval transit time of formation without hydrate, μs/m; the above resistivity value and acoustic interval transit time can be obtained from the logging curves; A and b: constant coefficients of the two-parameter saturation model.

The coefficients fitting

The coefficients a and b in the two-parameter saturation model are obtained by linear fitting.

First, let $\boldsymbol{lgR} = \boldsymbol{lg}\left(\frac{RT}{RT_b}\right)$, $\boldsymbol{lg\Delta t} = \boldsymbol{lg}\left(\frac{AC_b}{AC}\right)$ in Eq. 3, and divide both sides by lgR at the same time, the following Eq. 4 can be obtained:

$$\boldsymbol{S_h/lgR = a + b(lg\Delta t/lgR)} \tag{4}$$

Formula (4) belongs to the form of linear function $y = a + bx$, so the values of coefficients a and b can be fitted by linear regression to determine the saturation calculation formula. The specific process of fitting the values of coefficients a and b is as follows:

The core experimental data of hydrate saturation of five wells in Shenhu Sea of the study area were selected to fit the coefficients. RT, RTb, AC, and ACb are the logging values of these five wells, and Sh is the core experimental data of hydrate saturation. According to the above logging values and core experimental values, a correlation diagram (Figure 2) was established with lg△t/lgR as the abscissa and Sh/lgR as the ordinate. According to the correlation, five groups of fitting coefficient values could be obtained. By calculating the arithmetic average, the values of coefficient a and b are 0.2 and 2.6, so the two-parameter saturation calculation model of natural gas hydrate in this area can be rewritten as:

$$\boldsymbol{S_h = 0.2lg\left(\frac{RT}{RT_b}\right) + 2.6lg\left(\frac{AC_b}{AC}\right)} \tag{5}$$

This saturation calculation model is very simple and widely applicable. First, based on the objective change of reservoir physical characteristics caused by hydrate development, the hydrate saturation can be calculated by using resistivity and acoustic interval transit time logging values. Second, this method avoids the difficult process of obtaining the empirical coefficients in the laboratory, and reduces the influence of strata, lithology, and microscopic factors on measurement outputs. In the specific application process, the correlation coefficient needs to be established according to the actual characteristics. In addition, due to the influence of deposition and structure, lithology and physical properties usually change in a well, and the base value can be segmented to improve the calculation accuracy of hydrate saturation. In terms of coefficient fitting, when more wells are selected, the more accurate the coefficients a and b, and the more reliable the saturation parameters.

Discussion

Analysis of calculation accuracy

To verify the reliability of the two-parameter saturation calculation model, the model calculation results of five wells in the study area were compared with the core experimental values and the values calculated by Archie formula (Figures 3–5, respectively). The rock-electrical parameters in Archie formula were derived from the data of Zhao et al., 2021. The comparison results show that the average relative error of saturation

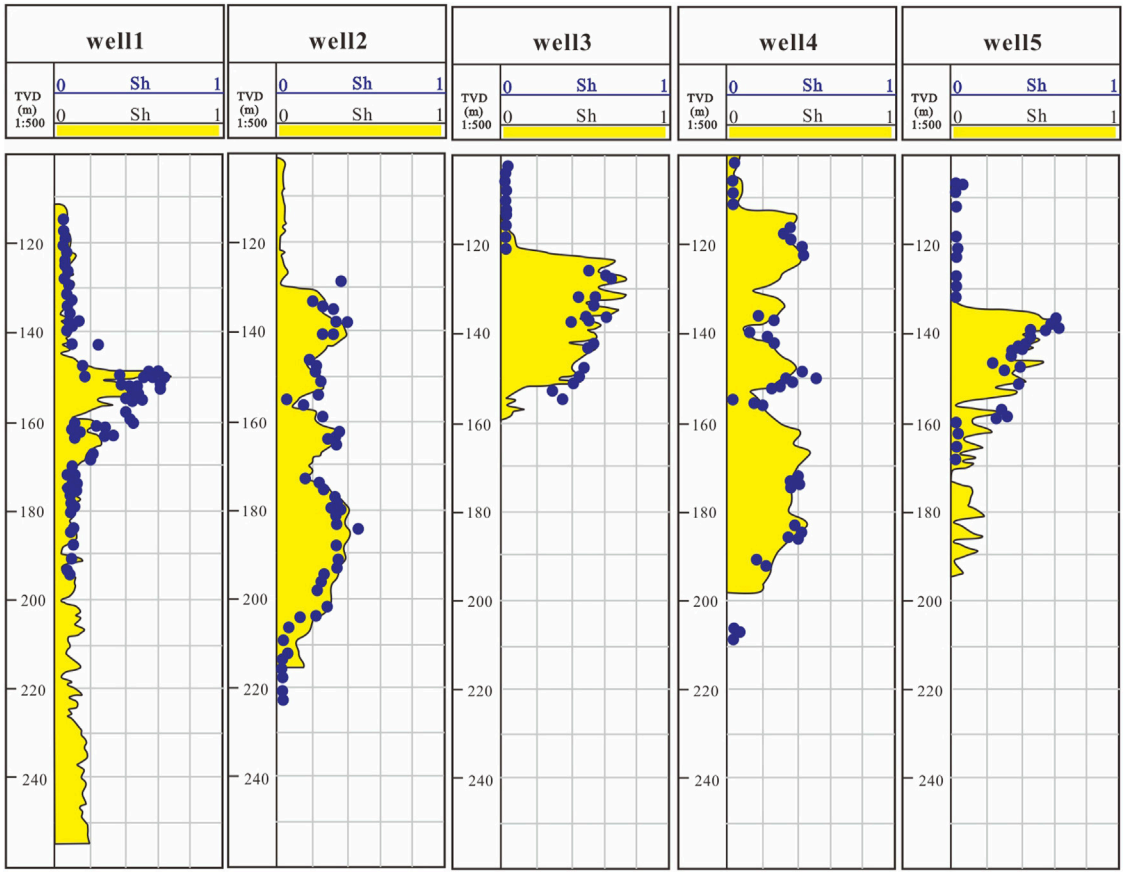

FIGURE 5
Comparison between calculation results of two-parameter saturation model and core experimental data of five wells in the study area.

calculated by the two-parameter model is 7%, which is highly consistent with the core experiment results (Figures 3, 5), whereas the average relative error calculated by the conventional Archie formula is 24%, which is significantly larger than that of the core experiment results (Figure 4). Therefore, the two-parameter saturation model can effectively improve the calculation accuracy of gas hydrate saturation.

Conclusion

Unlike conventional oil and gas reservoirs, marine natural gas hydrate reservoirs are characterized by loose and unconsolidated formation, solid hydrate, and easy decomposition. It is difficult to obtain rock-electrical parameters in the laboratory, and there are many influencing factors of logging acoustic value, resulting in relatively poor reliability of hydrate saturation parameters calculated by Archie formula or the sonic velocity method. According to the objective phenomenon of obvious changes in reservoir physical properties caused by hydrate development, a logging two-parameter calculation model based on resistivity and acoustic interval transit time was proposed, and the continuous acquisition of hydrate saturation parameters based on logging data was realized. By comparing results with those of the core experimental data, the calculation results of the two-parameter model were significantly better than those of the Archie formula, indicating that the two-parameter model effectively improves the calculation accuracy of gas hydrate saturation. The method is simple and has wide adaptability, but in the specific application process, the correlation coefficient should be adjusted according to the characteristics of the actual area, and segmented values should be taken to obtain reliable saturation calculation values.

Data availability statement

The original contributions presented in the study are included in the article/Supplementary Material, further inquiries can be directed to the corresponding author.

Author contributions

HL: Investigation, data analysis. JL: Results supervision. CQ: Research and article writing. HS: Logging data processing and interpretation. XZ: Figure drawing.

Conflict of interest

The authors were employed by CNLC Logging Co. LTD.

Publisher's note

All claims expressed in this article are solely those of the authors and do not necessarily represent those of their affiliated organizations, or those of the publisher, the editors and the reviewers. Any product that may be evaluated in this article, or claim that may be made by its manufacturer, is not guaranteed or endorsed by the publisher.

References

Chen, Y. F., Li, D. L., Liang, D. Q., Zhou, X. B., and Wu, N. Y. (2013). Relationship between gas hydrate saturation and resistivity in sediments of the South China Sea. *Acta Pet. Sinca* 34 (3), 509–512.

Collet, T. S. (2013). A review of well-log analysis techniques used to assess gashydrate-bearing reservoirs. *Geophys. Monogr. Ser.* 124, 189–210.

Goldberg, D. S., Kleinberg, R. L., Weinberger, J. L., Malinverno, A., and Collett, T. S. (2010). "Evaluation of natural gas-hydrate systems using borehole logs[M]," in *Geophysical characterization of gas hydrates* (Tulsa: Society of Exploration Geophysics), 239–261.

Guo, Y., Qiao, S., and Lu, W. (2011). Vertical distribution of gas hydrate in Shenhu area of the South China sea based on acoustic velocity. *Mar. Geol. Front.* 27 (7), 8–11. doi:10.16028/j.1009-2722.2011.07.001

Hyndman, R. D., Yuan, T., and Moran, K. (1999). The concentration of deep sea gas hydrates from downhole electrical resistivity logs and laboratory data. *Earth Planet. Sci. Lett.* 172 (1/2), 167–177. doi:10.1016/s0012-821x(99)00192-2

Lei, Y. N., Wu, S. G., Sun, J., and Wang, G. J. (2022). Review on comprehensive geophysical identification methods of marine natural gas hadrate. *J. Central South Univ. Sci. Technol.* 53 (3), 864–878. doi:10.11817/j.issn.1672-7207.2022.03.009

Li, X., and Xiao, L. Z. (2013). *Geophysical characteristics and logging evaluation of natural gas hydrate*. Beijing: Petroleum Industry Press, 15–84.

Malinverno, A., Kastner, M., Torres, M. E., and Wortmann, U. G. (2008). Gas hydrate occurrence from pore water chlorinity and downhole logs in a transect across the northern Cascadia margin (Integrated Ocean Drilling Program Expedition 311). *J. Geophys. Res.* 113 (B8), B08103. doi:10.1029/2008jb005702

Murray, D. R., Fukuhara, M. R., Osawa, O. R., and Endo, T. R. (2006). Namikawa. Saturation acoustic properties growth habit and state of stress of a gashydrate reservoir from well logs. *Petrophysics* 47 (2), 129–137.

Ning, F. L., Liu, L., Li, S., Zhang, K., Jiang, G. S., Wu, N. Y., et al. (2013). Well logging assessment of natural gas hydrate reservoirs and relevant influential factors. *Acta Pet. Sin.* 34 (3), 591–606. doi:10.7623/syxb201303026

Su, Z., C, Y. C., Yang, R., Wu, N. Y., Chen, D. F., Yang, S. X., et al. (2014). Research on the formation model of gas hydrate deposits in the Shenhu Area, northern South China Sea. *Chin. J. Geophys.* 57 (5), 1664–1674. (in Chinese). doi:10.6038/cjg20140529

Sun, Z. D. Jia, C. Z. and Li, X. F. (2011). *Unconventional oil and gas exploration and development (volume II)*. Beijing: Petroleum Industry Press, 1285–1286.

Wang, X. J., Wu, S. G., Liu, X. W., Guo, Y. Q., Lu, J. A., Yang, S. X., et al. (2010). Estimation of gas hydrate saturation based on resistivity logging and analysis of estimation error. *Geoscience* 24 (5), 993–999. doi:10.19657/j.geoscience.1000-8527.2010.05.001

Wang, Y. J., Wei, W., Xing, C. L., Han, W. F., and Gao, L. (2021). Measurement of hydrate saturation in sediments based on dual parameters from TDR. *Adv. new Renew. energy* 9 (5), 403–410. doi:10.3969/j.issn.2095-560X.2021.05.006

Wang, Z. W., Li, Z. B., and Liu, J. H. (2003). Logging identification and evalution methods for gas hydrate. *Mar. Geol. Quat. Geol.* 23 (2), 97–101. doi:10.16562/j.cnki.0256-1492.2003.02.015

Xiao, G., and Bai, Y. (2015). *The key technology of gas hydrate exploration and development*. Wuhan: Wuhan University Press, 1–20.

Zhang, J., Luo, J., Xia, Y., Hu, W. L., Zhang, G. D., He, C. Y., et al. (2018). Limitation analysis and modification of the Archic equation. *Chin. J. Geophys.* 61 (1), 311–322. (in Chinese).

Zhang, W., Liang, J. Q., Lu, J. A., Wei, J. G., Su, P. B., Fang, Y. X., et al. (2017). Accumulation features and mechanisms of high saturation natural gas hydrate in Shenhu Area, northern South China Sea. *Petroleum Explor. Dev.* 44 (5), 708–719. doi:10.1016/s1876-3804(17)30082-4

Zhao, J., Shi, Z. F., Li, Y. P., Xiang, X. R., Li, J., and Wei, N. (2021). Simulation of conductivity characteristics of gas hydrate reservoirs and its saturation calculation. *Nat. Gas. Geosci.* 32 (9), 1261–1269.

Zhong, G. F., Zhang, D., and Zhao, L. X. (2020). Ourrent states of well-logging evaluation of deep-sea gas hydrate-bearing sedimenb by international scientific ocean drilling (DSDP/ODP/IODP) programs. *Nat. Gas. Ind.* 40 (8), 25–44.

Zhou, J., Song, Y. J., Jiang, Y. J., Sun, Q. S., and Jing, Y. Q. (2020). The research progress of well logging evaluation of marine natural gas hydrate. *J. Southwest Petroleum Universty Sci. Technol. Ed.* 42 (2), 85–92. doi:10.11885/j.issn.1674-5086.2019.10.10.01

Zhu, T., Xing, L. C., Qi, Y., Liu, C. L., Meng, Q. G., and Liu, L. L. (2019). Development of measurement and control software for gas hydrate electrical-acoustic joint detection apparatus with LabVIEW. *Comput. Meas. Control* 27 (6), 124–129.

frontiers | Frontiers in Earth Science

TYPE Review
PUBLISHED 27 September 2022
DOI 10.3389/feart.2022.997337

OPEN ACCESS

EDITED BY
Zhifeng Wan,
Sun Yat-sen University, China

REVIEWED BY
Ren Wang,
CNPC Engineering Technology R & D Company Limited, China
Jiafei Zhao,
Dalian University of Technology, China

*CORRESPONDENCE
Na Wei,
weina8081@163.com
Jun Pei,
asharey@yeah.net

SPECIALTY SECTION
This article was submitted to Marine Geoscience, a section of the journal Frontiers in Earth Science

RECEIVED 18 July 2022
ACCEPTED 05 September 2022
PUBLISHED 27 September 2022

CITATION
Wei N, Pei J, Zhao J, Zhang L, Zhou S, Luo P, Li H and Wu J (2022), A state-of-the-art review and prospect of gas hydrate reservoir drilling techniques. *Front. Earth Sci.* 10:997337. doi: 10.3389/feart.2022.997337

A state-of-the-art review and prospect of gas hydrate reservoir drilling techniques

Na Wei[1,2]*, Jun Pei[1,2]*, Jinzhou Zhao[1,2], Liehui Zhang[1,2], Shouwei Zhou[1,2], Pingya Luo[1], Haitao Li[1,2,3] and Jiang Wu[1,2]

[1]State Key Laboratory of Oil and Gas Reservoir Geology and Exploitation, Southwest Petroleum University, Chengdu, China, [2]State Key Laboratory of Natural Gas Hydrate, Beijing, China, [3]State Key Laboratory of Coal Mine Disaster Dynamics and Control, Chongqing University, Chongqing, China

Securing energy means grasping the key link in the national development and security strategy. Under the goals of carbon peak and carbon neutrality, the overall tendency of energy development is to increase the proportion of natural gas while stabilizing oil consumption, and the global primary energy is entering the era of natural gas. Gas hydrate in deep seabed shallow strata and extremely cold permafrost regions has piqued the interest of researchers due to its abundant resources, widespread distribution, and high energy density. Although the drilling of hydrate wells is still fraught with unknowns and challenges due to the technological barriers between countries, complex on-site working conditions, and unique physical chemical properties, accumulation forms, and occurrence characteristics of gas hydrate, more than ten successful trial productions around the world have opened the door of hope for the development of this potentially new energy. The gas hydrate reservoir drilling technique is the frontier and hotspot of scientific and technological innovation and competitiveness around the globe today, reflecting the level of oil and gas technical advancement. At the national level, it possesses strategic and revolutionary features. Innovative drilling techniques, scientific well location layout, appropriate wellbore structure and well trajectory design, efficient drilling fluid, qualified drilling and completion equipment, and successful pressure-temperature preserved coring may all provide a strong guarantee for the successful completion of gas hydrate wells. This review comprehensively reviews the drilling techniques and engineering measures that can be used to develop gas hydrate. It focuses on the research advancement of important hydrate drilling technologies and the enlightening significance of these developments in the application of hydrate drilling. This work will deliver valuable experience as well as comprehensive scientific information for gas hydrate exploration and drilling.

KEYWORDS

gas hydrate, hydrate reservoir, drilling technique, drilling fluid, wellbore structure, drilling equipment, pressure coring technique, challenge

Introduction

The primary issue of energy development has always been how energy-consuming countries efficiently secure national energy security as well as national economic and social development. Exploring alternative energy is critical for the demand for clean energy at present due to the depletion of traditional energy and the increase in energy demand (Li et al., 2016a; Thakur, 2010). However, alternative energy sources such as electricity, nuclear energy, and geothermal energy are insufficient to supply the world's fast-increasing energy demand. Accordingly, fossil fuels such as oil and natural gas are expected to remain the fundamental energy sources in the future. Deep oil and gas, offshore oil and gas, unconventional oil and gas, low-grade oil and gas, and enhanced oil and gas recovery of developed fields are the key areas of oil and gas resource exploration and development in the future (Heidari et al., 2022; Li et al., 2020a; Isaac et al., 2022). Natural gas, as the fastest-growing fossil fuel in the twenty-first century, will not only help us achieve a low-carbon future but will also serve as a link between today's primary fossil fuels and future renewable energy (Sahu et al., 2020). According to the BP Statistical Review of World Energy 2022 (71st edition), the global oil consumption in 2022 is still lower than the level in 2019, while natural gas consumption is greater than in 2019, breaking the 4 trillion cubic meter threshold for the first time (BP, 2022). The trend of weak oil and strong gas is more obvious. With the consumption of conventional gas reservoirs, unconventional natural gas sources such as gas hydrate, shale gas, and tight gas have become increasingly significant due to their high potential (Song et al., 2014; Vedachalam et al., 2015; Zou et al., 2018). Gas hydrate, also known as combustible ice (*see* Figure 1), is one of the most elusive natural hydrocarbons (John et al., 2020). They can pose a significant danger to deep-water oil and gas operations while also representing a potentially huge untapped clean energy supply (Pelley, 2008; Dong and Zeng, 2017). As an important alternative energy, its commercialization will play a major role in driving the energy production and consumption revolution, as well as providing a way to handle the challenges of security, the economy, and low-carbon energy.

It is estimated that 97–99% of the discovered gas hydrate resources in the world are located in the ocean, and only 1–3% are distributed on land (Merey and Chen, 2022). Gas hydrate also exists in deep-water areas of some inland seas and lakes, such as the Black Sea and Lake Baikal (Gerivani et al., 2020; Yevgeny et al., 2021). Nevertheless, people are more concerned about the gas hydrate stability zone (GHSZ) with considerable thickness in the ocean because the thick layered hydrate-bearing sediments generally do not appear in the inland seas and lakes. Deepwater drilling is one of the key elements of offshore oil and gas engineering (Li et al., 2020b). Although the globe has extensive expertise in conventional oil and gas drilling operations, deep sea drilling experience in unconventional oil and gas deposits, particularly gas hydrate, remains limited (Wang and Gao, 2022). In the past decades, many drilling expeditions for gas hydrate in marine sediments have been successfully carried out around the world. The well-known hydrate drilling expeditions include the Deep Sea Drilling Project (DSDP), the Ocean Drilling Program (ODP), the Integrated Ocean Drilling Program (IODP), the International Ocean Discovery Program (IODP), the Gulf of Mexico Gas Hydrate Joint Industry Project (GOM JIP), the National Gas Hydrate Program (NGHP), the program of Guangzhou Marine Geological Survey (GMGS), the program of Ulleung Basin Gas Hydrate (UBGH), and the hydrate investigation activities carried out by the Research Consortium for Methane Hydrate Resources in Japan (MH21), and the Ministry of Economy, Trade and Industry (MITI) (Winters et al., 2008; Hsiung et al., 2019; Zhong

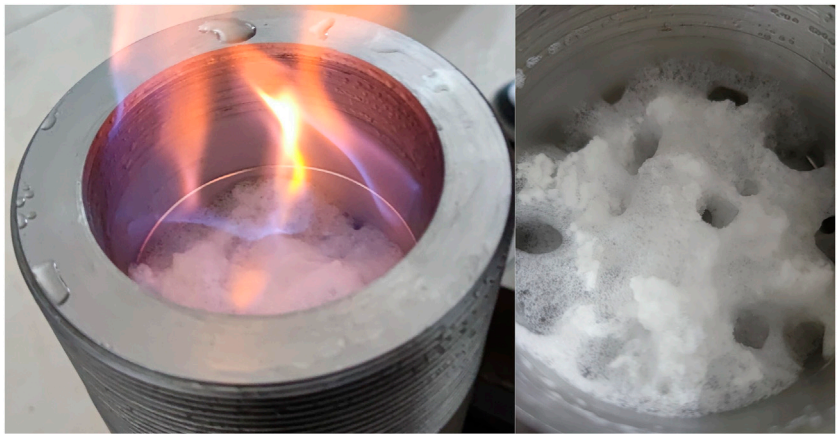

FIGURE 1
Gas hydrate produced in laboratory.

et al., 2021; Park et al., 2022; Xu et al., 2022). Although these drilling operations are located on the shallow surface of the seabed, drilling hydrate wells is considered extremely challenging due to the complex environment in deep water and the thermodynamic properties of the hydrate. From October 2019 to April 2020, the China Geological Survey organized and carried out the second offshore gas hydrate pilot production with the depressurization method (Ye et al., 2020). Based on the previous depressurization pilot production, this round of pilot production broke through horizontal well drilling and production techniques, making China the first country in the world to deploy this technique for offshore gas hydrate pilot production. Nonetheless, there is a significant gap between this trial production and the goal of long-term, safe, stable and efficient industrialized development and utilization of gas hydrate reservoirs. Therefore, international research teams are working hard to develop efficient drilling techniques to exploit gas hydrate sources in a long-term and stable manner. It is known with certainty that laboratory, virtual simulation, and fieldwork have provided an impetus for the development of gas hydrate drilling technology. However, when it comes to the current situation of drilling technology, it is found that only a few reviews comprehensively summarized the development of hydrate drilling techniques.

In this review, the latest gas hydrate drilling technologies and further research and development opportunities are summarized and introduced, including the gas hydrate drilling techniques, wellbore structure, drilling fluid system, equipment and tools, coring techniques, and field application, *etc*. Meanwhile, we point out the gaps and put forward some suggestions for future studies, which can provide insightful guidance for comprehensively understanding the drilling of the gas hydrate reservoirs.

Overview of gas hydrate

Under high pressure and low temperature, methane and/or other small non-polar or slightly polar hydrocarbons can form hydrates with water. Some inorganic small molecules, such as CO_2 and H_2S, are also very efficient hydrate formers. Gas hydrate reservoir development typically requires four basic conditions, namely the presence of a water phase, a channel and/or space for fluid migration and accumulation (Zhang et al., 2021a), as well as a low-temperature and high-pressure environment and a suitable gas source. Therefore, one of the prerequisites for the production of large-scale gas hydrate deposits is the geological structure that faults, fractures, and porous strata may deliver hydrocarbon gases from deep (Liang et al., 2019). The formation of faults and fractures is closely related to tectonic activities, sedimentary responses, and over-pressurized fluids. Non-local gas sources along fault paths have been confirmed to play a role in gas hydrate formation in the South China Sea, the Gulf of Mexico, *etc*. (Zeng et al., 2022). The analysis of gas hydrate systems and environmental assessment in these areas rely heavily on fluid flow migration, accumulation process, and sealing integrity. For example, the widely distributed faults in Baiyun Sag in the Pearl River Mouth Basin have strong geological activity, which has experienced three evolutionary stages of rifting, transition, and subsidence (Liang et al., 2022a). Natural gas diffusion and advection in deep sediment supply a significant amount of gas to the Shenhu area. In Woolsey Mound in the northern Gulf of Mexico, hydrocarbon fluids migrate from deep reservoirs thousands of meters deep through faults and fractures to shallow sediments with high porosity and/or fractured formations (Macelloni et al., 2015). Deep fluid seepage channels typically penetrate the overlying strata in these locations, producing hydrocarbon gas and causing geochemical anomalies such as isotope anomalies, pore water ion concentration anomalies, organic carbon and water content abnormalities (Hu et al., 2017; Monteleone et al., 2022). To identify gas hydrate, geophysical methods such as multi-channel seismic surveys, seabed profiles, and controlled source electromagnetic (CSEM) are frequently used (Minshull et al., 2020; Liang et al., 2020; Crutchley et al., 2010). Bottom-simulating reflectors (BSR), a special physical interface generated by seismic profiles, are the earliest and most widely used, reliable, and intuitive geophysical markers to confirm the occurrence of gas hydrate (Foschi et al., 2019; Colin et al., 2020). Seabed geological sampling, microbial exploration techniques, and seabed visual exploration techniques such as remotely operated vehicles (ROV), ocean floor observation systems (OFOS), TV grabs, and deep-towed systems provide a more robust foundation for determining the presence of gas hydrate (Su et al., 2020). Logging while drilling (LWD) has been widely used in drilling to acquire parameters such as resistivity, acoustic waves, porosity, radioactivity, electromagnetic characteristics, and saturation (Saumya et al., 2019; Boswell et al., 2020; Kim et al., 2022). Whereas pressure coring is the most direct, accurate, and persuasive method in gas hydrate exploration, which is primarily used to recover unspoilt rock columns to study the formation mechanism, shape, accumulation type, and physical chemical properties of gas hydrate, etc. (Gaafar et al., 2015; Wang et al., 2020a; Singh et al., 2022a).

According to the research, about 90% of the ocean and about 27% of the land have favorable conditions for the generation of gas hydrate (Ruan et al., 2012), thus the ocean is the primary target of gas hydrate exploration and development. Fracture systems through the sealing structures, which connect to the ocean and bring in seawater will lead to hydrate dissociation due to the low concentration of CH_4 in seawater (Kvamme and Saeidi, 2021). If the seafloor openings of the fractures are at hydrate-forming depths and temperatures are within the range of hydrate generation, hydrate mounds will form on the seafloor. This type of seafloor hydrate mound can be found all over the world and gives rise to bio-geo ecosystems. Large-scale active cold spring

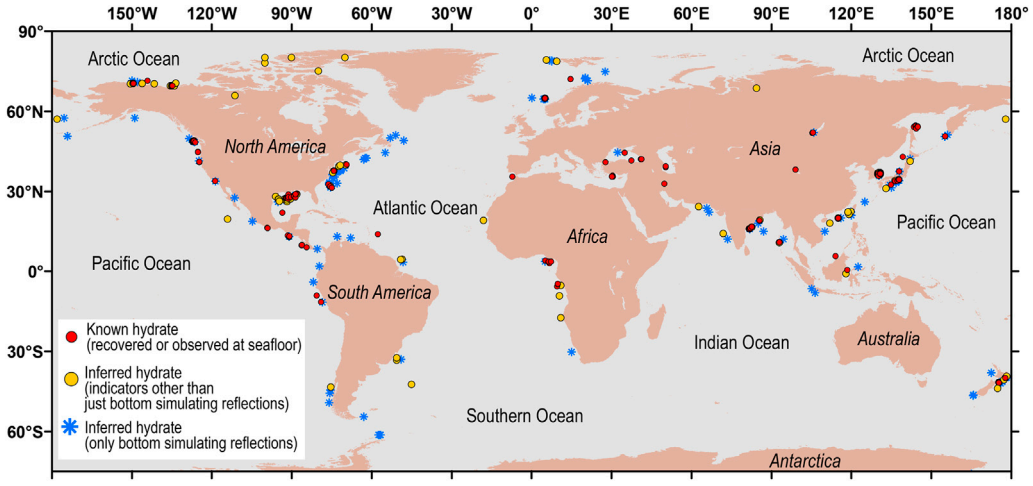

FIGURE 2
Schematic diagram of gas hydrate distribution (reproduced from Ruppel (Ruppel, 2020)).

TABLE 1 Distribution of gas hydrate resources (Sain and Gupta, 2012; Liu et al., 2019a; Sahu et al., 2020; Chibura et al., 2022).

Study areas	Investigative techniques	Estimated gas reserves, m^3	Study areas	Investigative techniques	Estimated gas reserves, m^3
Blake Ridge, United States	BSR and amplitude blank zone	5.70×10^{13}	South Shetland Islands on the edge of Antarctica	BSR	2.30×10^{12}
North Slope of Alaska, United States	BSR and gas and fluid bursts	2.40×10^{12}	Nankai Trough, Japan	BSR	1.10×10^{12}
Offshore Gulf of Mexico	BSR and gas and fluid bursts	1.14×10^{14}	Qinghai-Tibet Plateau, China	Digital bathymetry along with BSR	1.20×10^{12}–2.40×10^{14}
Offshore the eastern United States	BSR and gas and fluid bursts	2.68×10^{14}	Pearl River Mouth Basin, China	Digital bathymetry along with BSR	6.50×10^{13}
Mackenzie Delta, Canada	BSR with deep-tow acoustics/ geophysics system (DTAGS)	0.24–8.70×10^{13}	Qiongdongnan Basin, China	BSR and amplitude blank zone	5.70×10^{12}
Canadian Arctic Islands	BSR with DTAGS	0.19–6.20×10^{14}	Indian Exclusive Economic Zone (including Bay of Bengal and Andaman Sea)	Digital bathymetry along with BSR	1.90×10^{15}
The edge of the Atlantic Canada	BSR with DTAGS	1.90–7.80×10^{13}	Mesoyaha, Russia	BSR	$2.4 \times 10^{10} m^3$
The edge of the Canadian Pacific	BSR with DTAGS	0.32–2.40×10^{13}	Ulleung Basin, South Korea	BSR	2.48×10^{13}

outcrops, for instance, were found on the seafloor of the W01 and Haima sites in the Qiongdongnan Basin, as well as a large number of live mussels, shrimp, crabs, and buried authigenic carbonates, carbonate crusts (He et al., 2022). Gas hydrate occurs in submarine sediments on the active and passive continental margins in nature, as well as permafrost. It is found most commonly in accretionary wedges on active continental margins and geological structures such as mud volcanoes, mud diapirs, gas chimneys, structural faults, polygonal faults, and pipes on passive continental margins (Hu et al., 2021). The hydrate reservoirs found in marine environment are distributed around the world (Chong et al., 2016; Ruppel, 2020; Hu et al., 2021), as shown in Figure 2. Data from seismic observation and gas hydrate drilling projects show that gas hydrate resources are abundant throughout the world, with an estimated 0.2–3×10^{18} m^3 (Singh et al., 2022b). Table 1 shows the estimation of gas hydrate resources in some parts of the world (Sain and Gupta, 2012; Liu et al., 2019a; Sahu et al., 2020; Chibura et al., 2022). According to the conservative estimation of Pang et al. (Pang et al., 2022), the amount of

technically recoverable gas hydrate resources on the planet could range from 190×10^{12} m^3 to 700×10^{12} m^3.

Production methods and drilling challenges

Depressurization, thermal stimulation, inhibitor injection, CO_2 replacement, and solid-state fluidization methods are currently being used in field experiments for gas hydrate development (Olga et al., 2022; Wei et al., 2022; Zhou et al., 2022). The depressurization method refers to the dissociation of gas hydrate into gas by reducing the pressure of the hydrate reservoir in equilibrium (extracting formation fluid or exploiting underlying free gas). This method has a simple process and low cost, but there are problems such as slow production, sand production, and geological stability (Liu et al., 2019b; Yang et al., 2019; Liu et al., 2022; Olga et al., 2022). The thermal stimulation method refers to the dissociation of gas hydrate into natural gas by increasing the reservoir temperature to break the phase equilibrium (heating by hot fluid, microwave, electromagnetic energy, or solar energy) (Roostaie and Leonenko, 2020a; Roostaie and Leonenko, 2020b; Liu et al., 2022). This approach is easy to control, efficient, and pollution-free, however, it is expensive due to high energy consumption, heat loss, low injection rate, and weather sensitivity. The inhibitor injection method makes the gas hydrate easier to decompose into natural gas (Sung et al., 2002; Demirbas, 2010). This method is simple and convenient, and the energy consumption of injection at the initial stage of production is low, but it has the problems of high cost, slow reaction, low efficiency, environmental pollution, *etc*. In an environmentally friendly way, CO_2 or other gas that is more likely to form hydrate under reservoir conditions is used to replace the methane molecules in the hydrate crystal structure. This CO_2 replacement method can reduce geomechanical hazards, reduce water yield, and be environmentally friendly, but it has problems such as slow speed, low injection rate, low replacement rate, *etc*. (Uchida et al., 2005; Fakher et al., 2019; Heydari and Peyvandi, 2020). The solid-state fluidization method breaks the solid gas hydrate in the formation first and then fluidizes it into hydrate slurry by mechanical means, and then lifts it to the surface treatment facilities through the transmission pipeline (Zhou et al., 2018; Wei et al., 2019a; Zhou et al., 2022). This method constructs an artificially closed area with controllable hydrate dissociation, which can realize the exploitation of gas hydrate in deep water and shallow sediment. However, the key theory, process, and technology are still in the experimental stage. Technical feasibility, market acceptance, and environmental permission are the three decisive factors for the realization of commercial exploitation of resources. To ensure production safety and the improvement of development efficiency, new mining techniques or combined mining techniques like the depressurization-solid fluidization combined method, CO_2 replacement assisted depressurization method, electric heating assisted depressurization method, and inhibitor injection-replacement combined method should be further studied.

In permafrost and marine environments, many gas hydrate drilling operations have been completed successfully during the past decades (Dallimore et al., 2002; Chuvilin et al., 2020; Zhang et al., 2020; Liang et al., 2022b). Presently, over 150 gas hydrate wells have been drilled around the world (Makogon, 2010; Zhang et al., 2020). Most gas hydrate drilling activities, including those in the United States, China, India, and South Korea, aim to demonstrate the presence of hydrates in the target area and identify their properties. Hence, most of the hydrate wells deployed around the world are exploration wells, with only a few pilot production wells scattered throughout the Mackenzie Delta in Canada, the North Slope of Alaska in the United States, the Messoyakha in Russia, the Nankai Trough in Japan, the Qilian Mountains in China, and the South China Sea (Sun et al., 2021; Sun et al., 2022). The drilling of these pilot production wells has provided valuable experience for the production operations of the whole industry. However, the technological barriers between countries, complex on-site working conditions, and unique physical chemical properties, accumulation forms, and occurrence characteristics of gas hydrate make the drilling of hydrate wells still full of unknowns and challenges. So far, the natural gas produced in the trial production has not yet crossed the industrialization threshold (Wu et al., 2021; Chen et al., 2022), as shown in Figure 3.

Most hydrate drilling operations are offshore, so the risks and challenges faced by drilling hydrate wells are similar to those of most deep-water drilling operations. In addition to the formation stability problems of weak formation cementation, poor diagenesis, and low strength, there are numerous other problems caused by deep-water drilling tripping fluctuation pressure, deep-water string vibration, shallow gas, shallow water flow, and deep-sea harsh environment (Khabibullin et al., 2011a; Khabibullin et al., 2011b; John et al., 2020; Huang et al., 2020; Li et al., 2021a). The gas hydrate in the Shenhu area of China occurs 203–277 m below the mudline. The predicted equivalent density of fracture pressure of the target layer is only 1.14–1.15 g/cm^3, and the equivalent density of pore pressure is 1.03–1.05 g/cm^3 (Hou et al., 2022). The narrow mud density window, or perhaps a zero density window, induced by high collapse pressure and low fracture pressure in shallow formation makes controlling downhole pressure difficult, and it is very easy to create downhole mishaps such as leakage and collapse. We must consider the occurrence as well

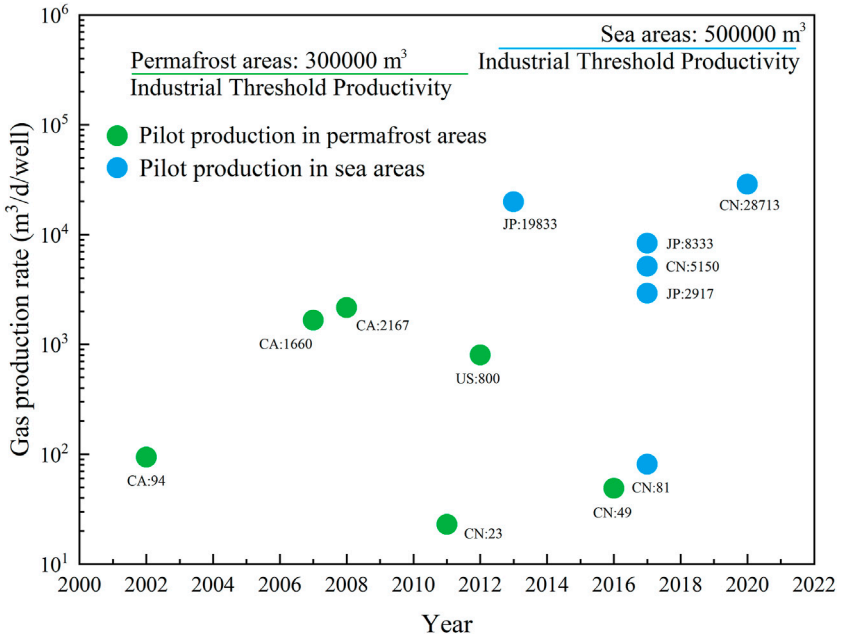

FIGURE 3
The daily production capacity of gas hydrate pilot production has not yet crossed the industrialization threshold (modified from (Wu et al., 2021; Chen et al., 2022)).

as the specific physical and chemical features of gas hydrate when drilling the hydrate reservoirs. The change of phase equilibrium increases the danger of gas hydrate dissociation. So when drilling hydrate wells, great attention should be paid to maintaining the low temperature and high pressure state of the reservoir, or making it more stable by changing the phase equilibrium of gas hydrate. Some common problems and challenges related to gas hydrate dissociation recorded in previous drilling operations include but are not limited to the following (Prassl et al., 2004; Khabibullin et al., 2011b; Li et al., 2018a; Wang et al., 2020b; Li et al., 2021b; Hou et al., 2022). The extremely narrow safe density window, for example, makes downhole temperature and pressure control more difficult than in other deep-water operations; Temperature and pressure fluctuations (swabbing, surge, *etc.*) during tripping or downhole tool movement lead to hydrate dissociation; Hydrate dissociation leads to a loose reservoir framework and aggravates wellhead/wellbore/formation stability problems; Environmental and engineering disasters caused by gas escape and leakage after hydrate dissociation; The secondary formation of gas hydrate near or in the wellbore; Complex multiphase flow of hydrate containing fluid in a wellbore; Rheological property of the drilling fluid; Gas hydrate form around the drill string (riser and casing) or on surface equipment (wellhead, BOP, kill line, and choke manifold). In a nutshell, hydrate drilling seeks to be successful, good, fast, and economical. All engineering measures should be taken to prevent gas hydrate dissociation or secondary formation during operation and to ensure that secondary disasters caused by gas hydrate dissociation are under control.

Gas hydrate drilling techniques

Drilling a gas hydrate reservoir can generally use the slightly overbalanced drilling method, which means keeping the pressure in the borehole slightly higher than the formation pore pressure (but less than the formation fracture pressure) to prevent the wellbore instability caused by the dissociation of gas hydrate and subsequent methane overflow. Driven by the pressure difference between the bottom hole and the formation, the drilling fluid continuously seeps into the formation during the invasion process. In this process, there is not only fluid migration and material transfer but also changes in temperature, pressure, and pore water salinity (Ning, 2005; Fereidounpour and Vatani, 2014; Dong et al., 2022). The change in salinity will cause the deviation of the hydrate phase equilibrium curve, and the change in equilibrium conditions will cause the dissociation of gas hydrate, which is likely to cause uncontrollable drilling risks (Ning et al., 2013a; Ning et al., 2013b). Therefore, in order to effectively protect the reservoir and avoid gas hydrate dissociation during drilling, the drilling technique must be strictly evaluated for necessity,

feasibility and technical economy according to the actual situation of the target area.

The development of drilling technology is changing with each passing day. At present, the developed drilling techniques applicable to gas hydrate reservoirs mainly include managed pressure drilling (MPD), casing while drilling (CWD), coiled tubing drilling (CTD), LWD, etc. (Wu et al., 2021; Merey and Chen, 2022). By actively managing the annulus pressure profile, MPD, an adaptive drilling method, can considerably improve drilling controllability, solve the issue of a narrow density window, and lower the likelihood of accidents (Pui et al., 2017). Compared with overbalanced drilling, MPD can effectively reduce reservoir damage, wellbore instability and operating costs. Halliburton, Schlumberger and Baker Hughes have more than 40 years of theoretical and practical experience in this field. In the field experiment of gas hydrate exploration well Hot Ice #1 in the Arctic region of Alaska, the well control and blowout preventer equipment (BOPE) stack was managed by MPD technique (Kadaster et al., 2005). Dual gradient drilling (DGD), a method of MPD, limits the total hydrostatic pressure through the density of two different annular fluids in the wellbore to avoid exceeding the fracture pressure gradient. Thereinto, riserless DGD is an economical, efficient, and safe gas hydrate drilling method, which can improve the integrity and safety of drilling (Rosenberg et al., 2022). The drilling vessel or platform used in the riserless drilling has lighter loads, allowing drilling in deeper oceans. It has low drilling cost and less likely to jam the drilling tools. However, some unavoidable problems need to be solved. For example, the exposed drill pipe has a long suspension section in the sea water, so high-strength drill pipe shall be selected; The drilling rig shall be provided with the function of drilling string motion compensator. China and other developing countries are still in the early stages of research and development in this field. With the acceleration of the development of deep-sea oil and gas resources in various maritime sovereign countries, the research and development of DGD and key equipment are imminent. International commercialization of DGD techniques has occurred, and the DGD system represented by Riserless Mud Recovery (RMR), Subsea Mudlift Drilling (SMD), DeepVision, Subsea Pumping System (SSPS), and Hollow Glass Spheres (HGS) has been established (Chen et al., 2007; Naser et al., 2022). Concentric drill pipe reverse circulation DGD technique, riser level control DGD technique, riserless subsea pump lifting DGD technique, dual density drilling technique, and other DGD schemes have been developed at the same time. To employ DGD to produce deep-water oil and gas hydrate safely and effectively, we need to create a dual gradient drilling technique with more versatility. Southwest Petroleum University has proposed a new technology for safe drilling of deep-water gas hydrate with double-layer pipe DGD system and structural scheme, but it has not yet reached the level of commercial application (Wang et al., 2019a).

As early as around 2004, Hannegan et al. (Hannegan, 2005; Hannegan et al., 2005; Todd et al., 2006) put forward the view that MPD is suitable for gas hydrate drilling, and believed that CWD may have a unique application in gas hydrate drilling. CWD applies torque and weight on bit (WOB) by replacing drill pipe with casing, and runs casing while drilling, thus saving time and operation cost (Sánchez and Al-Harthy, 2011). The CWD and casing-bit system allows drilling through the problem area at a relatively low flow rate and setting casing to avoid hole enlargement (Motghare and Musale, 2017). The lower flow rate also makes it possible to use smaller and lighter drilling equipment. In addition, the plastering effect in CWD can form a filter cake with low porosity and low permeability on the wellbore. This effect can reduce or prevent leakage, expand the safe density window of drilling fluid, improve borehole stability and reduce formation damage effectively, which is critical for the design of gas hydrate drilling engineering (Briner et al., 2015). CWD has been verified by a large number of practices and has been successfully applied to gas hydrate drilling operations in the Canadian Arctic permafrost (Vrielink et al., 2008). Managed pressure casing drilling (MPCD) is built on MPD and leverages CWD techniques to handle the problem of downhole high pressure management in the process of open hole logging after tripping out, ensuring that the pressure control mechanism is in place (Balanza et al., 2015). At present, MPCD has been successfully applied in well Gao 124 - Geng 30, well Gao 132 -Geng 33, well Bei 3 - Ding 5 - Geng P34 and well Bei 3-342 - Geng P51 in Daqing Oilfield (Liu et al., 2020; Liu et al., 2021), and it is expected to be applied to gas hydrate drilling in China in the future.

CTD technique also shows its potential in this field. In 2016, the small hole (small diameter) directional drilling technique, one of the CTD techniques, was first applied to the gas hydrate production wells in the Muli permafrost area, Qinghai (Li et al., 2017a), making China the first country to successfully connect two wells in high-altitude areas using this technology. CTD technique is also used in the drilling of gas hydrate well during the solid fluidization production in the South China Sea. Moreover, LWD, which can drill and log at the same time, is extremely useful in identifying and evaluating producible gas hydrate deposits, as well as acquiring and quantifying critical parameters of gas hydrate production. Due to its widely application in the mineral exploration, it is also recommended to use reverse circulation drilling (RC) technology in gas hydrate drilling (Zhang et al., 2015). As summarized in Table 2, these drilling techniques have their pros and cons. Specific techniques and processes need to be selected according to the actual situation.

Wellbore structure and well trajectory

Because gas hydrate mostly occurs in the semi-consolidated or even unconsolidated mud and sand layer on the seabed, the reservoir after hydrate dissociation is likely to cause wellbore instability. Proper wellbore structure, wellbore trajectory, and borehole reaming are not only conducive to the stability of the wellbore but also help to improve the productivity of gas hydrate. Before designing the well structure and well trajectory, it is necessary to ascertain the potential drilling location of

TABLE 2 Characteristics of drilling technologies suitable for gas hydrate exploration and development.

Name	Strengths	Weaknesses
MPD	*1*) accurately control of borehole pressure, *2*) reduce the well construction cycle, *3*) reduce formation instability and collapse, *4*) prevent lost circulation and well kick, *5*) reduction in casing number and hole size, *6*) reduce damage to reservoir, and *7*) the drilling cost is reduced significantly	*1*) a difficult operation procedure; *2*) no samples or logs obtained; *3*) potentially a large amount of drilling fluid; and *4*) difficulties in removing the drilling strings from the hole
CWD	CWD can *1*) shorten the well construction cycle, *2*) reduce downhole accidents, *3*) improve hydraulic parameters, annulus upward velocity, and wellbore cleaning conditions, *4*) simplify the structure and reduce drilling rig volume, and *5*) reduce drilling costs, compared with drill pipe drilling	*1*) capital investment for CWD rig is still high, *2*) fatigue failure most likely to occur in casing string with high doglegs, *3*) high torque and drag, *4*) hydraulics system problems for CWD in deeper intervals, and *5*) lighter and more durable drill bits are required
CTD	*1*) equipped with electric logging lines or other signal telemetry options, *2*) small footprint and greater mobility, *3*) continuous circulation without stopping the pump and the well control stack makes the safety performance better, *4*) suitable for the underbalanced drilling (UBD), gas-liquid multiphase drilling and air drilling, and *5*) fewer service personnel are needed; *6*) Quicker trip times	*1*) inability to rotate, *2*) short service life caused by coiled tubing fatigue, *3*) reduced pump rates, torque, and WOB, *4*) restricted wellbore size, *5*) short service life caused by coiled tubing fatigue, *6*) higher costs to change the coiled tubing and maintain a drilling-fluid system, and *7*) limited equipment and limited experience manpower base

exploration wells or production wells according to the exploration and research results of BSR, GHSZ, formation temperature and pressure, reservoir properties, plume, hydrate mound, *etc*. Thereafter, design the casing program based on the downhole pressure profile and pressure balance.

Gas hydrate development is currently at the exploratory and pilot production stages worldwide. The chosen drilling location's geological characteristics are not very complicated. Most exploration wells adopt open hole drilling without a riser, and the designed well type and well structure are relatively simple. Only China has so far broken through in the drilling and production techniques of horizontal wells in the gas hydrate field experiment. For comparison, other explorations or pilot production wells are vertical wells. During the second gas hydrate production test in the South China Sea with the depressurization method, the maximum bending degree of the horizontal wellbore reached 15.2°/30 m (Ye et al., 2020). By increasing the contact area between the wellbore and the reservoir and expanding the gas hydrate dissociation area, the hydrate dissociation rate and productivity were greatly improved during this field experiment.

Both domestic and international academics have theoretically analyzed and demonstrated different well types and well layouts strategies, such as vertical wells, horizontal wells, and multilateral branch wells. Moridis et al. (Moridis et al., 2008) studied the productivity improvement of horizontal wells in different types of hydrate reservoirs compared with vertical wells at the earliest. Since then, a large number of experiments and theoretical studies have emphasized the advantages of horizontal wells in gas hydrate production. Li et al. used the parallel version of the TOUGH+HYDRATE code to simulate the gas production of the two-point horizontal well system of permafrost hydrate in the Qilian Mountains and evaluate its commercial feasibility (Li et al., 2015). The stimulation measures under different well structures have been compared by many scholars since the production efficiency of gas hydrate is one of the most concerning issues. Jin et al. recently used TOUGH+HYDRATE and GMS software to research the new radial multi-branch horizontal wells in the Shenhu area to improve the gas production rate (Jin et al., 2022). It was found that as the well's overall length increases, radial branch horizontal wells produce more water and gas. The production of gas and water from multi-branch wells is greatly influenced by depth, while the rate at which hydrates dissociate is hardly affected.

Figures 4, 5 show the information of wellbore structure and well trajectory adopted in several gas hydrate pilot production experiments. Figures 4A–E respectively show the structure of production wells of the first offshore pilot production in Japan, the second offshore pilot production in Japan, the first offshore solid fluidization pilot production in China, the first offshore depressurization pilot production in China, and the second offshore depressurization pilot production in China. It can be seen from these trial productions that the current drilling depth of offshore gas hydrate is about 1000–1400m, the test depth is 200–500 m. Except for the solid fluidization production well, 914.4 mm conductors are used in the first spud, and 339.7 and 244.5 mm casings are used in the second spud and the third spud, respectively. Figures 5A–C depict the well Ignik Sikumi # 1 in Alaska, the well Mallik 5L-38 in Mackenzie Delta, and the well SK in Qilian Mountains. Similarly to marine hydrate drilling, hydrate drilling in permafrost regions mainly adopts vertical well structures at present. For example, the vertical well Mount Elbert # 1 on the North Slope of Alaska was drilled to the hydrate formation using a 12 1/4-inch bit, water-based mud, and LWD tools (Sun et al., 2011). The 9 5/8-inch diameter casing was fixed slightly below the bottom of the permafrost (594 m). The drilling of gas hydrate layer was further drilled with a 7 7/8-inch bit and oil-based mud. Coring from the bottom of the casing to a depth of 760 m, then the drilling was deepened to 914 m. The hole was reamed to a diameter of 8 3/4 inches at last.

So far, the most complex gas hydrate production wells are SK-0, SK-1, and SK-2 in the Muli permafrost area of the Qilian Mountains. The well trajectory is divided into three sections, as shown in Figure 5C, namely the vertical section, the build-up section, and the horizontal section. The measuring while drilling

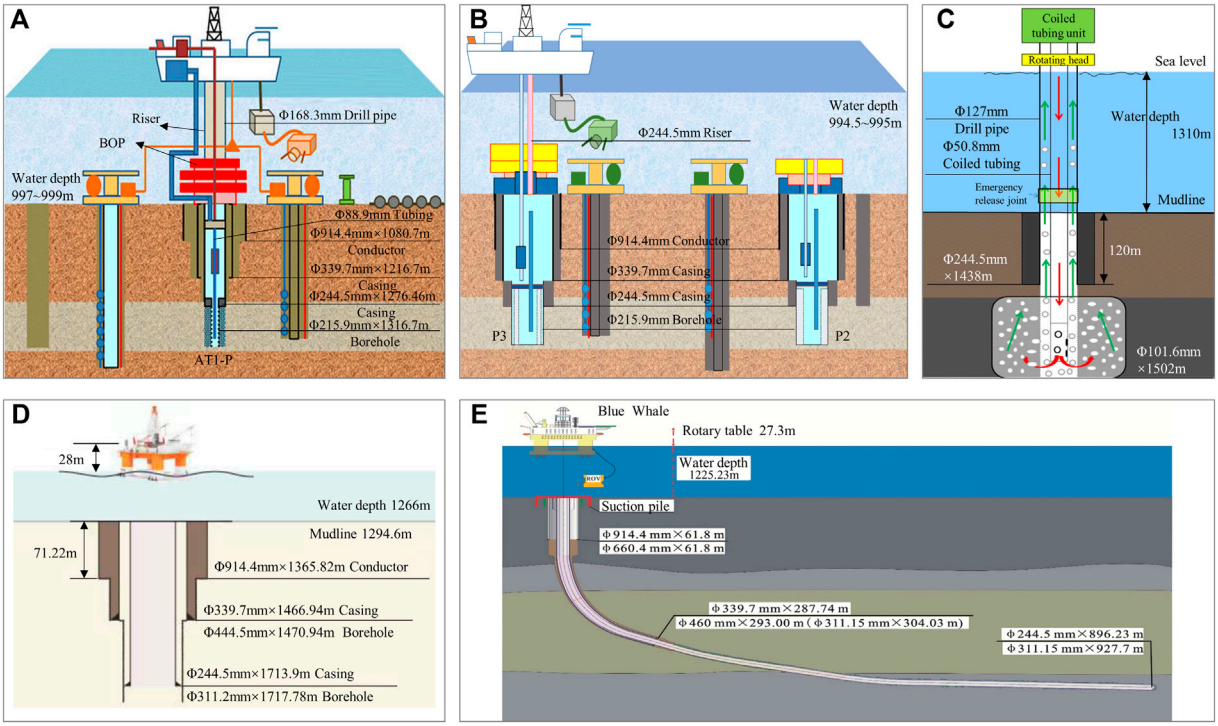

FIGURE 4
Wellbore structures of offshore gas hydrate pilot production wells. **(A)** the first offshore pilot production well in Japan, **(B)** the second offshore pilot production well in Japan, **(C)** the first offshore solid fluidization pilot production well in China, **(D)** the first offshore depressurization pilot production well in China, and **(E)** the second offshore depressurization pilot production well in China. (Matsuzawa et al., 2014; Yamamoto et al., 2014; Li et al., 2019; Yamamoto et al., 2019; Ye et al., 2020).

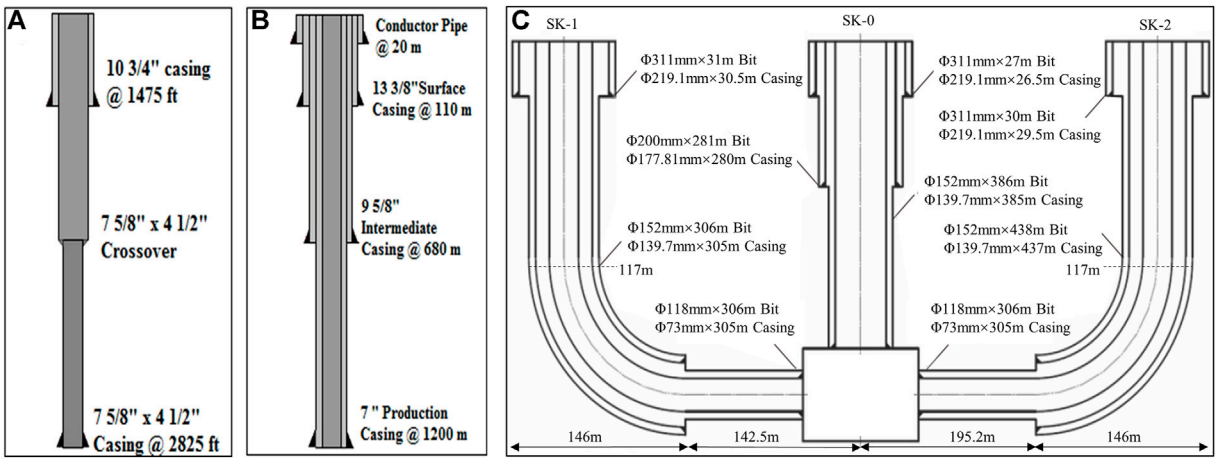

FIGURE 5
Wellbore structures of permafrost gas hydrate pilot production wells. **(A)** the well Ignik Sikumi # 1 in Alaska, **(B)** the well Mallik 5L-38 in Mackenzie Delta, and **(C)** the well SK in Qilian Mountains. (Merey, 2016; Li et al., 2017b; Merey, 2019; Zhu et al., 2020).

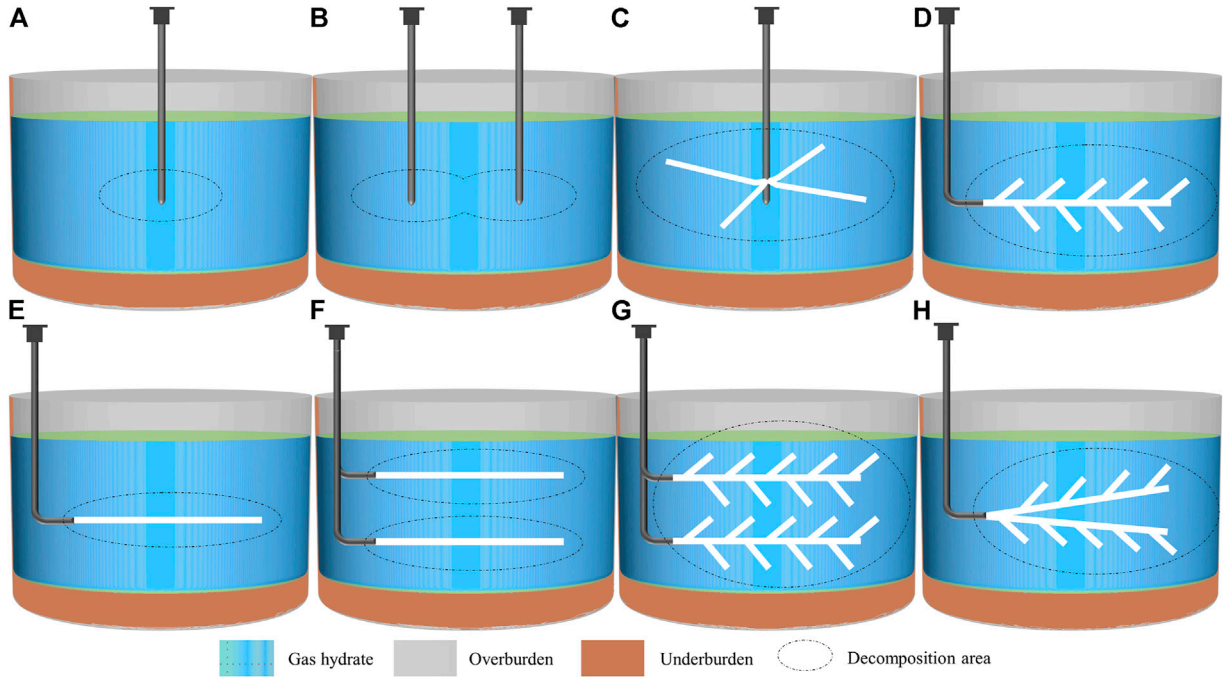

FIGURE 6
Wellbore structure model of gas hydrate production well to improve gas production efficiency. **(A)** Single vertical well, **(B)** dual vertical wells, **(C)** radial lateral well, **(D)** fishbone well, **(E)** single horizontal well, **(F)** dual horizontal wells, **(G)** dual fishbone well, and **(H)** dual branch multilateral horizontal well.

(MWD) technique was used to control the wellbore trajectory in butt joint horizontal well drilling, and the drilling in the build-up section and horizontal section was completed by a single-bend positive displacement motor (PDM) and a polycrystalline diamond compact (PDC) bit (Li et al., 2017b). The build-up section of well SK-1 started from the depth of 95 m. In the first curve section, the buildup rate was controlled at about 10.5°/30 m. When drilling to a depth of about 300 m, the inclination angle increases to 64°. The buildup rate in the later curve section was controlled at about 9°/30 m until the hole depth reached 340 m and drilling passed through the first layer of gas hydrate. The maximum inclination angle of well SK-1 was 83, and the length of the horizontal section was designed to be short. Lastly, SK-1 extended to the bottom hole butt-joint area of SK-0. The build-up section of the SK-2 well was designed to continuously increase the inclination angle. The kick-off point was set at a well depth of 80 m, and the buildup rate in the curve section was controlled at about 10°/30 m. The SK-2 connected with SK-1 and SK-0 in the butt-joint area at last. The completion of SK-1 and SK-2 has greatly promoted the development of hydrate experimental technology and numerical simulation technology under different well types in China and even other countries in the world.

Generally speaking, marine hydrate drilling faces softer formation, poorer drillability, and greater difficulty in casing running when compared to hydrate drilling in permafrost. In the weakly cemented formation on the seabed, the orientation of horizontal wells and the extension of horizontal sections are more difficult. We therefore need to accelerate the progress of marine hydrate drilling and production. It will be important to build a theory of increasing production and a technology system to address the issue of gas hydrate development efficiency. Complex wells significantly enhance the exposed area of gas hydrate as well as the controlled reserves of wells, thus increasing output and also the production efficiency of single wells. Directional wells, multi-branch wells, cluster wells, complex well patterns, *etc.*, as shown in Figure 6, may be the main ways to increase the production of gas hydrate in the future (Ning et al., 2022), (Mahmood and Guo, 2021), (Zhang et al., 2022), (Yu et al., 2021), (Li et al., 2013), (Ye et al., 2021), (Li et al., 2011). Accordingly, the complex wells also put forward higher requirements for gas hydrate well structure and well trajectory.

Drilling fluid system

During the drilling of hydrate reservoirs, the drilling fluid in the wellbore will exchange material and energy with seawater. The original pressure and temperature field will be disturbed by the circulating drilling fluid interacting with the hydrate

TABLE 3 Gas hydrate drilling fluid system (Burger et al., 2006; Collett et al., 2015; Merey, 2016; Merey, 2019; Wu et al., 2021).

Location	Well name	Well type	Water depth, m	Buried depth, m	Drilling fluid type
Permafrost	Mallik 3L-38	Production well	—	810–1105	Lecithin water solution
Permafrost	Mallik 4L-38	Production well	—	800–1095	Lecithin water solution
Permafrost	Mallik 5L-38	Production well	—	805–1105	Lecithin water solution
Permafrost	Qilian DK-1	Exploration well	—	133.5–135.5+142.9–147.7+165.3–165.5	Water-based drilling fluid
Permafrost	Ignik Sikumi #1	Production well	—	525–740	Oil-based drilling fluid
Permafrost	Mount Elbert #1	Production well	—	614–628+649–666	Oil-based drilling fluid
Sea	NGHP 1 7-A	Exploration well	1285	130–150	Sepiolite - seawater
Sea	SHSC-4	Production well	1266	201–251	Water-based drilling fluid
Sea	SHSC2-6	Production well	1225.23	203–277	Water-based drilling fluid
Sea	AT1-P2	Production well	995	261–321	KCl polymer - sepiolite mud
Sea	AT1-P3	Production well	994.5	259.5–320.5	KCl polymer - sepiolite mud
Sea	GOM JIP 1 AT13-1	Exploration well	1290.5	30–246.3	Attapulgite-seawater
Sea	GOM JIP 1 AT14-1	Exploration well	1300.2	180–220	Attapulgite-seawater
Sea	GOM JIP 2 WR 313-G	Exploration well	2000	231–424	Attapulgite-seawater

particles when it enters the hydrate deposit through holes and throats (Chen et al., 2019). As drilling fluid penetrates into the formation, the physical characteristics of the hydrate-bearing sediments will change as a result of the superposition of numerous causes. One of the fundamental characteristics of drilling fluid invasion into hydrate formation is the phase change of gas hydrate, which is also the primary distinction between drilling fluid invasion into gas hydrate formation and conventional oil and gas reservoir. The interaction process between drilling fluid and formation is a process involving the coupling of drilling, rock mechanics, rock mineralogy, chemistry, and dynamics of fluids in porous media (Teymouri et al., 2020; Ruan et al., 2021). This process has an impact on the mechanical, electrical, thermal, and permeability properties of the formation around the wellbore. At the same time, it also changes the geomechanical stability of the formation, the reliability of resistivity logging during drilling, heat transfer, the following gas production rate, etc. (Ning et al., 2013b). This is closely related to many complex downhole issues and is a world-class problem that has not been well solved on a worldwide scale. It is vital to prevent drilling fluid from entering the formation during the deep water drilling and gas hydrate development processes because it poses a severe danger to safe and successful drilling. In the process of Qilian Mountain drilling exploration, for instance, the boreholes of QTZK2 and SK-2 collapsed and were buried due to drilling fluid problems (Gao et al., 2017). Even if the formula and performance of the drilling fluid are adjusted, the wellbore is still unstable during subsequent operations. It can be seen that research and development of drilling fluid systems to solve the key technical challenges of hydrate drilling, whether on land or at sea, is the development direction, frontier subject, and good opportunity for drilling fluid technology.

At present, the commonly recognized method is to maintain the thermodynamic stability of gas hydrate by increasing the well pressure and reducing the mud temperature. This method primarily employs water-based drilling fluid, oil-based drilling fluid, and synthetic-based drilling fluid systems for gas hydrate exploration and drilling (He et al., 2021; Das et al., 2022a). Oil-based drilling fluid is generally used in hydrate drilling activities in permafrost, such as the production well of the Ignik Sikumi oilfield in the United States (Grigg and Lynes, 1992; Schoderbek et al., 2013a). It provides excellent hydrate inhibition performance and antifreeze properties, and will not induce hydrate dissociation. However, there are several drawbacks, such as environmental pollution, excessive costs, and safety issues. It is highlighted that the drilling fluid should have low toxicity, no bioaccumulation, and be harmless to the environment after discharge. Consequently, from the standpoints of inhibitory effects, environmental protection, and cost management, the water-based drilling fluid system is still the best choice for gas hydrate exploration (Liu et al., 2016a). Table 3 shows the gas hydrate drilling fluid system used in some drilling operations. It can be seen that water-based drilling fluids with hydrate inhibitors such as sepiolite, KCl polymer, lecithin, and attapulgite are widely used.

As we know, drilling fluids play an important role in hydrate drilling engineering because they have many functions, such as preventing ice blockage, wellbore lubrication, wellbore cleaning, controlling filtration, and maintaining wellbore stability, etc. (Rana et al., 2021). Reasonable mud density, sufficient inhibition, and sealing ability are the basic indicators for evaluating gas hydrate drilling fluid. Therefore, a low-

temperature hydrate drilling fluid system with strongly inhibitive ability, good sealing ability, and enhanced wellbore stability is the key research direction. Currently, the innovation of water-based hydrate drilling fluid mainly focuses on gas hydrate inhibitors, fluid loss control additives, and rheology modifiers. Gas hydrate inhibitors, one of the most concerned groups, are divided into thermodynamic hydrate inhibitors (THIs), kinetic hydrate inhibitors (KHIs), and antiagglomerant hydrate inhibitors (AAs) (Ke and Chen, 2019; Kiran and Prasad, 2021). The functional mechanism of THIs is to change the thermodynamic balance between water molecules and gas molecules by changing the chemical potential of the aqueous solution or hydrate phase to avoid hydrate generation (Kiran and Prasad, 2021). Methanol, ethylene glycol, sodium chloride, calcium chloride, potassium chloride, potassium formate, and amino acids are typical THIs (Sa et al., 2011). However, oil and gas fields are finding it more difficult to endure the pressures of heavy use and the high cost of THIs. For comparison, injection of low-dose KHIs can reduce the cost and harm to the environment compared with injection of high-dose THIs. KHIs are adsorbed on the surfaces of hydrate particles at the initial stage of hydrate crystallization, nucleation, and growth. Shortly afterwards, the cyclic structure of KHIs combines with the hydrate cavity structure through hydrogen bonds, delaying and interfering with hydrate crystal nucleation and preventing further crystal growth (Mozaffar et al., 2016). KHIs are mostly low molecular weight polymers dissolved in the aqueous phase, including polyvinylpyrrolidone (PVP), polyethylene caprolactam, poly-N-vinyllactam polymers, and hyper-branched polyesteramides (Mozaffar et al., 2016; Roostaei et al., 2021). Another kind of low-dosa agent, AAs, such as quaternary ammonium surfactants, alkylaryl sulfonates, and phosphonium salt surfactants, can emulsify the oil-water phase and disperse the water in the oil phase into small water droplets (Chua and Kelland, 2013; Nagappayya et al., 2015). Although the emulsified water droplets in the oil phase can also form hydrates with gas, the generated hydrates are difficult to agglomerate. Thus, gas hydrate cannot be formed normally. Low dosage hydrate inhibitors (LDHIs), including KHIs and AAs, have attracted more and more attention from the oil and gas industry in recent years because of their low consumption, high economy, and good environmental benefits (Kelland, 2006).

As mentioned above, fluid loss control additives and rheology modifiers are the focus of drilling fluid research. Fluid loss control additives such as bentonite, carboxymethyl cellulose (CMC), polyanionic cellulose (PAC), and starch are the materials in drilling mud to reduce filtration rate and improve mud cake characteristics. Rheology-modifier additives such as xanthan gum (XG), guar gum (GG) and polyacrylamide (PAM) have a great impact on the rheological properties of the drilling fluid formula. Some rheological modifier additives can also be good fluid loss control additives; for instance, the widely used and environmentally friendly additives GG and XG can effectively improve the viscosity of the drilling fluid and reduce the filtration. In recent years, some new materials have been widely used to improve the performance of hydrate drilling fluids. On the one hand, it has been discovered that drilling fluid with nanoparticles has a tiny particle size and a large surface area, which has a promising future. The nanomaterials can effectively seal the pore throat of the reservoir and enhance the stability of the wellbore, thus realizing the role of reservoir protection (Ngata et al., 2022; Zamora-Ledezma et al., 2022). On the other hand, the drilling fluid with polymers has also become one of the most widely used drilling fluid systems after years of development. It has good rheological properties and the ability to maintain wellbore stability (Ghozatloo et al., 2015; Gupta and Sangwai, 2019). Therefore, there are many reports about nanoparticles and polymers in the hydrate drilling fluid in recent years. Liu, Das, Maiti et al. (Liu et al., 2016b; Wang et al., 2017; Zhao et al., 2019; Zhang et al., 2021b; Maiti et al., 2021; Yuha et al., 2021; Das et al., 2022b) have developed some drilling fluids with hydrate inhibition, respectively, and compared and verified the effects of these drilling fluids through experiments. *See* Table 4 for details. A glance at open sources indicates that some traditional ideas and old formulations are not suitable for the new application scenario of hydrate drilling, and new ideas and formulations are emerging. When encountering various complex downhole conditions, only by studying and improving the corresponding drilling fluid technology can we effectively solve the above-mentioned technical problems and challenges encountered in the drilling process. It is necessary to draw on existing experience and comprehensively apply multidisciplinary knowledge to deeply study the mechanism and internal laws behind these problems. The new technology emerging as the times require may effectively solve and improve the overall level of hydrate drilling fluid and completion fluid technology.

Drilling equipment, tools and instruments

Gas hydrate drilling is mainly carried out with the help of general technical equipment in the conventional oil and gas industry, and downhole data is mostly obtained by LWD. The drilling technologies for permafrost hydrate and marine hydrate are distinct because of their varied environments, and as a result, so are the drilling equipment, tools, and instruments that are employed. In most cases, risers are required in the process of marine hydrate pilot production and offshore drilling, but considering the factors such as cost, efficiency, operation window, drilling success rate, etc., most gas hydrate exploration wells are operated on floating drilling vessels or platforms with dynamic positioning systems (DPS) by using riserless drilling technology (i.e., open hole drilling, and the rock cuttings generated are scattered on the seabed), such as

TABLE 4 Gas hydrate drilling fluid developed in recent years.

Drilling fluid formula	Drilling fluid type	Features and advantages	Reference
Seawater + 2% Nano SiO_2 + 3% Bentonite + 1% Sodium CMC + 3% Sulfomethylated phenolic resin + 1% PVP (K90) + 2% KCl	Water-based drilling fluid	With the best density, good low-temperature rheology and sufficient shale hydration inhibition. The hydrate inhibition performance is good. The cost of the gas hydrate drilling fluid is 15–20% lower than that of the drilling fluid used in the South China Sea	Liu et al. (Liu et al., 2016b)
Distilled water + 0.4% CMC + 0.4% PAC + 0.4% XG + 5% KCl + 1% Sarcosine	Water-based drilling fluid	Sarcosine is an environmentally friendly inhibitor. Compared with polyvinyl caprolactam (PVCap) and PVP, the drilling fluid containing sarcosine has better inhibition efficiency, shorter aggregation time, and less fluid loss	Das et al. (Das et al., 2022b)
Distilled water + 4.0% Bentonite + 3.5% NaCl + 6.0% $CaCO_3$ + 0.7% PVP (K90) + 0.4% GG + 0.4 Boron nitride nanoparticles	Water-based drilling fluid	Boron nitride nanoparticles can improve the rheological properties of drilling fluid, and reduce fluid loss and cake thickness	Maiti et al. (Maiti et al., 2021)
2.0% Sodium bentonite + 0.15% XG + 0.2% Hydroxyethyl cellulose + 0.2% Carboxymethyl starch + 2.0% Polyetheramine + 1.5% Liquid Lubricant + 1.0% Ultrafine Calcium Carbonate + 25% NaCl+ 20% Ethylene glycol	Water-based drilling fluid	It has good ultra-low temperature rheology, hydrate inhibitive property and environmental protection, shale inhibition performance and low thermal conductivity, which is conducive to the wellbore stability of Arctic permafrost	Zhang et al. (Zhang et al., 2021b)
Freshwater + 3.0% NaCl, 3.0% KCl and 0.8% XG and 1% of Tetrametylammonium chloride	Water-based drilling fluid	Tetramethylammonium chloride and PVP can delay the formation of gas hydrate in the same order of magnitude, but the former has higher thermal stability in drilling mud than the latter and can provide suitable shear thinning behavior	Yuha et al. (Yuha et al., 2021)
Base mud + 20% NaCl + 0.1% NaOH + 3% Sulfonated phenolic resin + 4% Sulfonated lignite + 0.3% XG	Water-based drilling fluid	Excellent rheological property and low fluid loss. It is a polymer drilling fluid suitable for hydrate drilling in permafrost	Wang et al. (Wang et al., 2017)
Deionized water + 2.0% Bentonite + 0.25% Amphoteric polymer + 0.5% Low-viscosity PAC + 2.0% Sulfonated phenolic resin +5.0% KCl + 10.0% NaCl (Ethylene glycol) + 0.1% PVP + 0.5% Lecithin	Water-based drilling fluid	Stable rheological performance, filtration performance and hydrate inhibition performance. The combination of 0.1 wt% PVP and 0.5 wt% lecithin provided the best inhibitory effect	Zhao et al. (Zhao et al., 2019)

the GMGS1 survey missions (Merey, 2016; Cheng et al., 2019; Merey, 2019). In the process of riserless drilling, the drill bit is directly lowered to the seabed through the drill pipe for drilling, and the drilling fluid is injected through the drill pipe and then directly discharged into the sea water or recovered after returning to the seabed (Aird et al., 2019; Cheng et al., 2019; Hancock et al., 2019; Chen et al., 2021; Kulkarni and Heinze, 2022). The main equipment used includes drilling equipment, DPS, and a mud treatment system. The drilling equipment includes a drilling control system and a lifting system. The DPS includes three modes: DP1, DP2, and DP3(DNV, 2013; Hogenboom et al., 2020). The mud treatment system includes a desilter, a desander, a vibrating screen, a centrifuge, a degasser, and other tools and instruments. As the carriers for these devices, jack-up drilling platforms, semi-submersible drilling platforms, and drilling vessels have become the main platforms for marine resource exploration and development with their flexibility and good adaptability. Therefore, regardless of the drilling technology utilized to explore gas hydrate deposits, large-scale drilling platforms or drilling vessels are indispensable.

Large-scale deep-water rigs are mobile national territory and strategic weapons, and people from all walks of life have paid great attention to them. So far, the drilling vessels or platforms used in hydrate drilling internationally include JOIDES Resolution, Fugro Synergy, Fugro Voyager, Chikyu, REM Etive, Helix Q4000, Hai Yang Shi You 708, Uncle John, Helix Q-4000, Blue Whale I and II, etc. Table 5 displays the parameters of some vessels or platforms (Graham and Reed, 1969; Rabinowitz and Garrison, 1985; Gabitto and Barrufet, 2009; Li et al., 2018b; FUGRO SYNERGY, 2021; Graber et al., 2021; Jin, 2021; Liang et al., 2021). Thereinto, Fugro's geotechnical engineering vessel is a modular drilling unit (FUGRO SYNERGY, 2021), which can provide high-quality geotechnical data and play an important role in several gas hydrate field surveys and scientific drilling activities. And JOIDES Resolution is a specifically designed ODP drilling vessel that is outfitted with laboratories for on-board cores and borehole data processing and analysis. Drilling and coring with ship heave up to 4.9 m is possible with the Active and Passive Heave Compensator (AHC/PHC) systems on JOIDES Resolution (Graber et al., 2021). The schematic diagram of drilling equipment on the JOIDES Resolution is shown in Figure 7. Furthermore, compared to the specifically designed drilling vessels JOIDES Resolution and Chikyu, sister drilling platforms Blue Whale I and Blue Whale II adopt the more advanced DP3 dynamic positioning system, which has reliable, efficient, and sufficient drilling capacity. In addition to those that have been put into commercial operation, some new drilling vessels or platforms are under construction. Recently, China is building a scientific drilling vessel, Meng Xiang, which can be used for gas hydrate exploration and development. In any case, gas hydrate drilling in the ocean is mainly done by large-scale

TABLE 5 Parameters of some drilling vessels (platforms) used for offshore gas hydrate drilling.

Vessel name	Year of built	Size, m	Draft, m	Gross Tonnage, t	Maximum operating water depth, m	Maximum drilling depth, m	Number of power thrusters	Number of crew	DP system	Drilling mode	Scientific influence
GLOMAR CHALLENGER	1968	Length 121 Beam 19 Derrick height 43	6.1	10,500	~6100	~7000	4	68	Not available	Riserless drilling	Glomar Challenger is the only special drilling vessel of DSDP and the world's first vessel that can drill in waters with a water depth greater than 6000 m
JOIDES RESOLUTION	1978	Length 143.3 Beam 21.3	5.5	8817	8235	8385	12	112	DP2	Riserless drilling	JOIDES Resolution is the only special drilling vessel of ODP. It is now one of the scientific drilling platforms of IODP, and once served NGHP.
BAVENIT	1986	Length 85.8 Beam 16.8 Depth 8.43	5.6	3575	2000	2000	4	NA	DP2	Riserless drilling	One of the most advanced exploration and drilling vessels in Russia, and once served GMGS.
CHIKYU	2005	Length 210 Beam 38 Depth 16.2	9.2	56,752	2500 (upgradeable to 4000 m)	10,000	6	200	DP2	Riser drilling, riserless drilling	The scientific drilling vessel with a riser drilling system installed for the first time in the world, and once served MH21 and NGHP.
FUGRO SYNERGY	2009	Length 103.7 Beam 19.7 Depth 10.6	6.3	6593	3000	Not available	4	84	DP2	Riserless drilling	Fugro Synergy is an ultra-deepwater geotechnical drilling vessel, and once served NGHP and UBGH.
FUGRO VOYAGER	2013	Length 82.9 Beam 21.8 Depth 8.15	5.66	4644	3000	Not available	4	60	DP2	Riserless drilling	Fugro Voyager is an ultra-deepwater geotechnical drilling vessel, and once served CMGS.
HAI YANG SHI YOU 708	2011	Length 105 Beam 23.4 Depth 9.6 m	7.4	7847	3000	3600	5	90	DP2	Riserless drilling	The first deepwater engineering research vessel in China
BLUE WHALE I	2016	Length 117 Width 92.7 Height 118	—	43,000	3658	15,240	8	Not available	DP3	Riser drilling, riserless drilling	The largest ultra-deepwater semi-submersible drilling platform in the world
BLUE WHALE II	2017	Length 117 Width 92.7 Height 118	—	43,725	3658	15,250	8	Not available	DP3	Riser drilling, riserless drilling	Sister platform of Blue Whale I. The largest and deepest ultra-deepwater semi-submersible drilling platform in the world

10.3389/feart.2022.997337

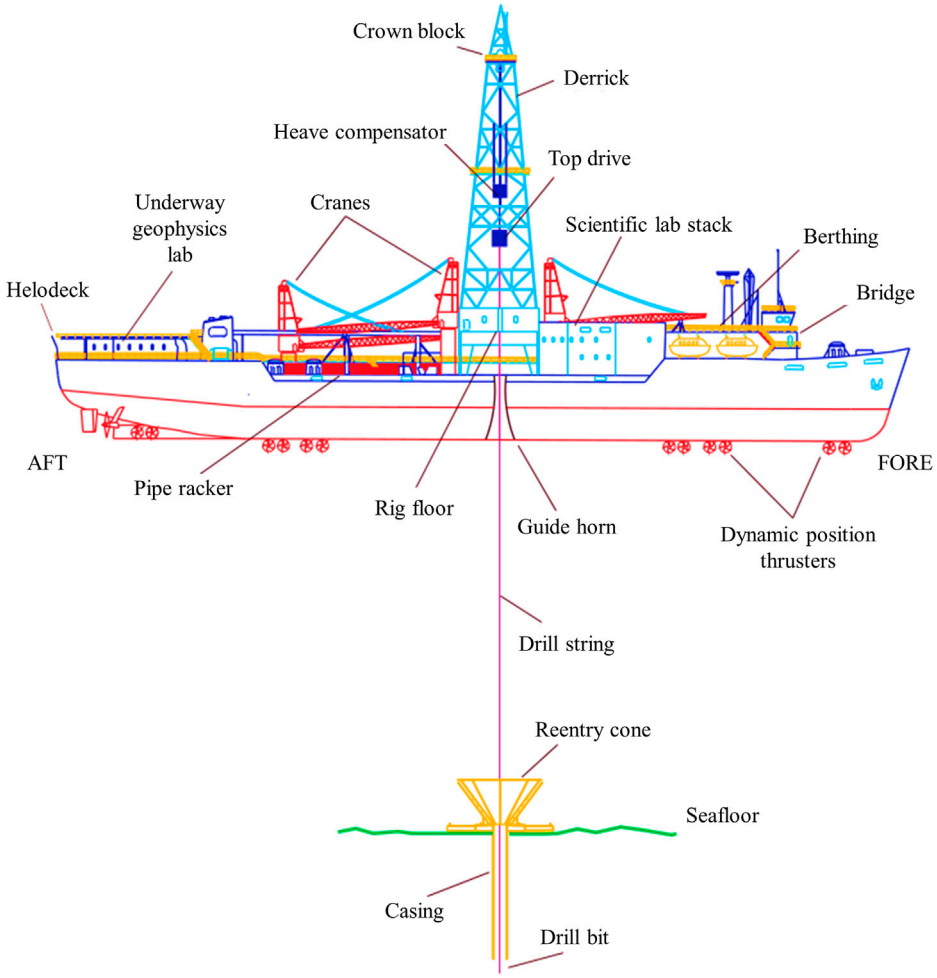

FIGURE 7
Schematic diagram of drilling equipment on R/V JOIDES Resolution (reproduced from (Graber et al., 2021)).

drilling vessels, which virtually increases the exploration cost. In the future, small drilling vessels and submersible drilling equipment with rolled casing shall be developed and improved to reduce costs. MPD, UBD, CWD, and insulated riser drilling, etc., shall be fully applied to solve the problems such as wellhead collapse, wellbore instability and submarine landslide that may be caused in the process of gas hydrate drilling.

Drilling efficiency, well quality, coring quality, and coring efficiency are closely related to the performance of the bit during gas hydrate drilling. To ensure the coring speed and drilling efficiency of the bit, the commonly used drill bits at present include solid carbide bits and polycrystalline diamond composite (PDC) bits. In addition to selecting the drill bits according to the characteristics of formation lithology before drilling, it is also necessary to carry out targeted design and calculation for drill bit contour, hydraulic parameters, tooth layout, tooth cutting parameters, etc. Many research teams have made great contributions to the development and selection of drill bits for hydrate drilling. In 2002, the Mallik 3L-38 well drilled in the Mackenzie Delta used 7.87-inch Reed PMCKP TJ3210 and TJ3212 bits. The Mallik 4L-38 well used 7.87-inch Reed PMCKP TJ3224 and Hughes JG4XP bits and the Mallik 5L-38 well used 8.74-inch Reed PMCKP Hughes GIHXP and Hughes JD4XP bits (Zhang and Zhu, 2011; Merey, 2016; Wu et al., 2021). The Mount Elbert # 1 well in the North Slope of Alaska used 12 1/4-inch bits between the depths of 0 and 594 m. Due to the defects of water-based mud, oil-based drilling fluid and 7 7/8-inch bits were used below the bottom of the permafrost, effectively improving the drilling rate. Similar operations occurred in the Ignik Sikumi field. The target horizon of the Ignik Sikumi #1 well is between 525 and 740 m, and oil-based drilling fluid and 9 7/8-inch Smith XR + PS5130 and Smith XR + CPS5126 bits are used for drilling

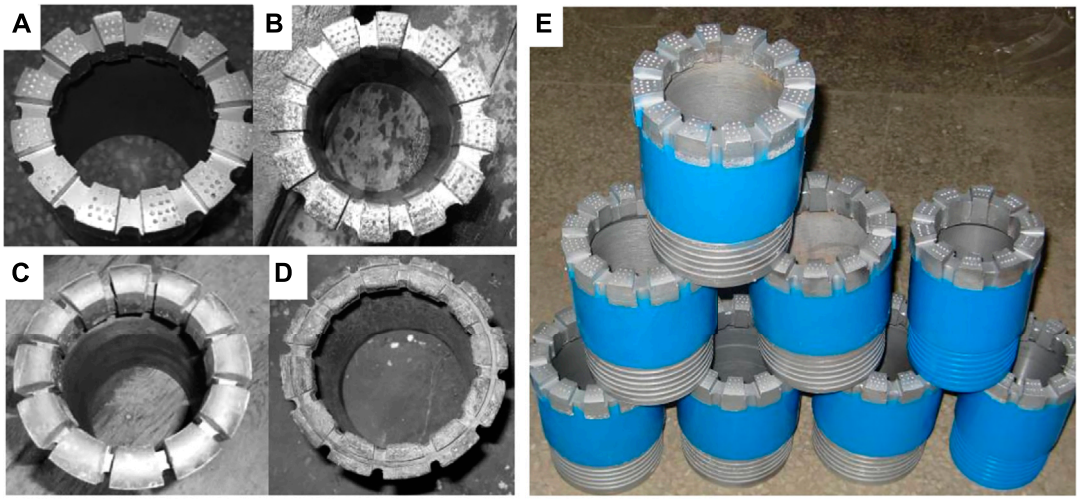

FIGURE 8
Bionic coupling impregnated diamond bit and normal diamond drill bit samples (modified from (Sun et al., 2012)). **(A)** A new bionic coupling impregnated diamond bit, **(B)** a used bionic coupling impregnated diamond bit, **(C)** a new normal diamond drill bit, **(D)** a used normal diamond bit, and **(E)** the front view of bionic coupling impregnated diamond bit samples.

(Schoderbek et al., 2013; Merey, 2016). Ignik Sikumi #1 well is designed for hydrate production experiments by the replacement method and the depressurization method. A state-of-the-art gas mixing skid (GMS) designed by ConocoPhillips was used in the experiment (Boswell et al., 2017). During the production of Ignik Sikumi #1, the specially designed GMS, line heater, pump system, and low gas-rate measurement skid ensure the success of the test. In addition, the research institutions led by Jilin University have successfully applied their wear-resistant bionic coupling impregnated diamond bit to the drilling experiment of the MK-2 hole in Mohe County, China. The non-smooth surface of this bionic bit imitates the characteristics of pits in the front chest and back plates of dung beetles. The bottom surface of the drill bit is designed and manufactured into a non-smooth surface (as shown in Figure 8) (Wang et al., 2016; Gao et al., 2018), which makes the bit more wear-resistant and then improves the rock crushing efficiency and service life. Field tests show that the bionic coupling impregnated diamond bit is more suitable for the exploration and drilling of gas hydrates than the ordinary diamond bit. The average drilling rate is increased by about 30%, and the service life of the bit is increased by more than 37% (Sun et al., 2012). Other hydrate drilling bits also include atypical water jet mining heads specially designed for deep-sea shallow surface weak cemented hydrate solid-state fluidization mining (Wang et al., 2019b; Wang et al., 2020c), the straight-rotating mixed nozzles and the porous and rotating porous jet nozzles for cavitating jet drilling radial horizontal wells (Li et al., 2020c).

To open up the laboratory-exploration-drilling-completion-production-transportation-user chain of gas hydrate development, it is imperative to strengthen the research and application of production equipment systems. For example, the deep-water geotechnical drilling vessel is a major piece of equipment in offshore oil engineering. The design and manufacture of drilling vessels is the integration of many technologies, including ship technology, offshore geophysical exploration technology, drilling technology, and experimental equipment. At present, the drilling of gas hydrates in the ocean is mostly done by large-scale drilling vessels, which virtually increases the cost. In the future, efficient and low-cost drilling equipment combinations should be improved and developed to reduce costs. Devices that should be studied more in the future include but are not limited to economic semi-submersible drilling and production platforms suitable for hydrate exploitation; small drilling vessels; deep-water light drilling systems; seabed drilling tools, riser systems, logging and coring systems, as well as supporting equipment for complex well construction, well trajectory control, pressure control, downhole sand control and other drilling technologies. Table 6 shows the typical technical equipment for offshore gas hydrate drilling (Fu et al., 2020). In the current situation, there is a lack of special equipment for gas hydrate drilling. Conventional oil and gas production equipment plays an important role in hydrate drilling and development and yet they are not perfectly compatible. Moreover, whether the mining technology and equipment used in the short-term pilot production can withstand the test of long-term commercial mining still needs further verification. There will be tougher tests to come.

TABLE 6 Typical equipment system for gas hydrate drilling [modified from 186].

Pilot production area and time	Production method	Equipment system	Development direction
Nankai Trough, Japan, 2013 and 2017	Depressurization	Chikyu + riser + drill pipe + bit + casing + BOP + electric submersible pump + sand control tool + packer + lifting separator	Improve sand control system, separation system, and monitoring system; Reduce the weight of the drilling vessel; Produce gas hydrate by gradient decompression
Shenhu area, South China Sea, 2017	Depressurization	Blue Whale I + riser + drill pipe + bit + coiled tubing + BOP + hydraulic slotting tool + electric submersible pump + sand control sieve tube + packer	Develop a technique for reservoir stimulation in low permeable gas hydrate reservoirs; Sand control; Investigate narrow-density window drilling technology; Solve the problem of dynamic monitoring of hydrate mining
Shenhu area, South China Sea, 2017	Solid state fluidization	HAI YANG SHI YOU 708 + drill pipe + coiled tubing + jet crushing nozzle + + cyclone desander + coring bit	Invent and manufacture high-efficiency crushing tools, special mining tools, special transmission pipes, lifting pumps, and other underwater tools and equipment; Develop multilayer production techniques and equipment
Shenhu area, South China Sea, 2020	Depressurization	Blue Whale II + suction anchor + drill pipe + bit + coiled tubing + BOP + new bypass pre filling sieve tube + electric submersible pump + gas-liquid separator + packer	Study the technical equipment for large-scale hydrate development; Design safe and sustainable production strategy

Gas hydrate drilling coring

Gas hydrate sampling technology consists of seabed sampling and geotechnical drilling (Day, 2006; Ren et al., 2013; Su et al., 2020). The former is used to collect samples of hydrate-bearing sediments on the seabed or in shallow strata, and is a direct method of locating gas hydrate on the sea floor. Seabed samplers mainly include gravity samplers, box samplers, grab samplers, vibration piston samplers, gravity piston samplers, *etc.* (Su et al., 2020). The recoilless piston corer Advanced Piston Corer (APC) used in ODP, the stationary piston corer STACOR developed by France, the Multiple Autoclave Corer (MAC) and Dynamic Autoclave Piston Corer (DAPC) used in R.V. SONNE cruise in Germany, and the pressure tight piston corer (PTPC) developed by Zhejiang University in China all belong to the above categories (Lunne and Long, 2006; Tommasi et al., 2019). The maximum depth that can be reached by seabed sampling is between a few and tens of meters, but the actual sampling depth is influenced by the geological environment in addition to sampler performance. These samplers frequently fail to sustain pressure during sampling and are unable to assist researchers in getting *in-situ* samples from deep hydrate reservoirs. High-quality samples can be taken hundreds of meters underground using gas hydrate drilling and coring techniques. On this account, gas hydrate coring technology is considered to be the most direct way to identify and recover gas hydrate in the deep ocean.

The physical properties of hydrate cores under atmospheric temperature and pressure will be very different from native hydrate-bearing sediments (Xie et al., 2016). However, the geotechnical coring tools used in the past are not equipped with the pressure and temperature preservation (PTP) devices, so it is difficult to obtain gas hydrate cores under natural conditions. This situation calls for stringent technical requirements for coring tools, core analysis and transfer systems. So as not to change the physical and chemical characteristics of samples, these devices must be able to prevent gas hydrate from dissociation. Pressure core analysis is considered to be the keystone of hydrate investigation (Schultheiss et al., 2008), but more importantly, the premise of pressure core analysis is to deploy the pressure coring system in hydrate exploration (Sun et al., 2015a; Li et al., 2016b; Hu et al., 2022). The pressure coring system can maintain the pressure of gas and liquid in the rock sample. Compared with traditional methods, pressure coring can improve the evaluation accuracy and avoid more than 50% gas loss (Li et al., 2021c).

The United States and European countries almost monopolize the development and sales of pressure coring technology and equipment. These professional core samplers usually allow drilling to be controlled from the seabed, drilling vessel or drilling platform. Several representative wireline pressure coring systems have been successfully deployed, including the Pressure Coring Barrel (PCB) developed in DSDP (Peterson, 1984; Sun et al., 2015a); The Pressure Coring Sampler (PCS) (Pettigrew, 1992; Dickens et al., 2000) designed by Pettigrew to replace the PCB, which applies to the drill string size used on JOIDES Resolution; The Hydrate Autoclave Coring Equipment (HYACE) developed by the EU-sponsored HYACINTH program, which is a coring tool system developed based on the experience of using PCS during ODP navigation (Amann et al., 1997); Two wireline coring tools, the HYACE Rotary Corer (HRC) for cutting rotary cores in lithified sediment and the Fugro (Rotary) Pressure Corer (FPC or FRPC) for sampling unlithified sediments, are included in the HYACE; The Pressure Temperature Coring System (PTCS) invented by Aumann & Associates Inc. (AAI) and the Japan National Oil Corporation (JNOC: now the Japan Oil, Gas and Metals National Corporation, JOGMEC) (Qin et al., 2016); Pressure Core Tool with Ball Valve (PCTB) developed by Geotek. Because the core

TABLE 7 Comparison of operation conditions of different pressure coring systems.

Coring tools	Institutions	Core liner length, m	Core diameter, mm	Maximum bearing capacity, MPa	Sealing methods	Coring history
PCB	DSDP	6	5.78	35	Ball valve	DSDP 19/42/44//62/76, Blake Outer Ridge
PCS	ODP	1	4.32	68.97	Ball valve	ODP 124/139/141/146/164/196/201/204, IODP 311, NGHP1
FPC	EU- sponsored HYACINTH program	1	58	25	Flapper valve	ODP 194/201/204, IODP 311, JIP Leg 01, NGHP1, GMGS1, GMGS2, UBGH1, UBGH2, Gumusut-Kakap project
HRC	EU- sponsored HYACINTH program	1	51	25	Flapper valve	ODP 194/201/204, IODP 311, NGHP1, UBGH1, UBGH1
PTCS	JOGMEC	3.5	73	24.13	Ball valve	Mallik 2L-38 well, Kashiwazaki field, MITI Nankai Trough exploration well, 2004 METI Tokai-oki to Kumano-nada drilling campaign, SONNE cruises
Hybrid PCS	JAMSTEC and AAI	3.5	51	34.48	Ball valve	Nagaoka onshore field test well, Nankai Trough AT1-C, Expedition 802 in Nankai Trough Project, GOM JIP 03
PCTB	Geotek Ltd., United Kingdom	3	51	35	Ball valve	GMGS3, GMGS4, GMGS5, NGHP2, UT-GOM2-1
PTPS	China University of Petroleum, Beijing	10	60	30	Flapper valve	HY4-2006-03 voyage
WPTCS	Chinese Academy of Geoscience	1.351.13	38 28	20	Ball valve	Qilian mountain gas hydrate exploration well, Qiangtang basin gas hydrate exploration well
SUCO	TU Clausthal	1.2	50	21	Flapper valve	Gas hydrate campaign in Korea
MDP	Corsyde	1.3	45	20	Flapper valve	The expedition of Guineco-MeBo in 2011

size of PTCS does not match the widely used Geotek's Pressure Core Analysis and Transfer System (PCATS), JAMSTEC and AAI designed and manufactured the Hybrid Pressure Coring System (Hybrid PCS) using PTCS technology (Kubo et al., 2014; Yamamoto, 2015). Other drilling coring devices used in the field include the pressure and temperature preservation system (PTPS) developed by the China University of Petroleum (Beijing) and Southwest Petroleum University (Zhu et al., 2013), Wire-line pressure and temperature core system (WPTCS) developed by the Chinese Academy of Geoscience (Zhang et al., 2014), SUGAR corer (SUCO) in South Korea, and MeBo-Druckkern-Probennehmer (MDP) used in Nigeria Delta during the SUGAR 1 (Abid1 et al., 2015). *See* Table 7 for the comparison of their operation conditions (Kubo et al., 2014; Zhu et al., 2013; Zhang et al., 2014; Abid1 et al., 2015; Zhu et al., 2011; Bohrmann et al., 2007; Chen et al., 2013; Dickens et al., 2003; Inada and Yamamoto, 2015; Yang et al., 2017; Schultheiss et al., 2009; Ryu et al., 2013; Flemings et al., 2019). A glance at open sources indicates that FPC, HRC, Hybrid PCS, and PCTB are the main coring tools used in large hydrate drilling activities in the past decade. In 2010, the researchers recovered 25 pressure cores using FPC, FRC, and FRPC equipped on the D/V Fugro Synergy during UBGH2 (Ryu et al., 2013). In June 2012, MH21 used Hybrid PCS equipped on the D/V Chikyu to conduct pressure coring (Yamamoto, 2015). During the NGHP2 in 2015, 17 holes were drilled and/or cored with conventional coring tools (HPCS/ESCS) or pressure coring tools (PCTB) equipped on the D/V Chikyu (Kumar et al., 2019). During the GMGS5 in 2018, the conventional coring tools and PCTB on the Fugro Voyager drill vessel were used to coring at four drilling sites: W01, W07, W08, and W09 (Wei et al., 2019b). Here we can see that the driving force for the continued development of pressure coring technology comes largely from national programs.

Delivering high-quality, pressure-sealed, temperature-preserved gas hydrate samples is the tireless pursuit of exploration drilling. However, it is found that there are still many deficiencies in the coring tools after a rough comparison. Due to the limitations of the harsh environment in the drilling process, the use of the coring tools is restricted by the mechanical strength and tightness (Abid1 et al., 2015; Wang et al., 2015; Sun et al., 2015b). The most likely situation is that mechanical valves, sealing rings, and other seals cannot seal *in-situ* gas hydrate samples effectively, resulting in partial or complete loss of physical, chemical, and biological information. The pressure bearing range of the commercially used coring tools is 20–30 MPa and the maximum pressure does not exceed 70 MPa. The ice valves developed based on *in-situ* drilling fluid can improve the pressure-preserved performance of the valve to the level of 25 MPa or even higher 47 MPa (LuoPeng et al., 2015; Li et al., 2016b; Zhang et al., 2016). Although there have been some new designs that claim to increase the maximum bearing capacity of pressure corers above 100 MPa in recent years

(Li et al., 2021c), they have not been applied in engineering. On the other hand, to reduce the influence of temperature change on the core, temperature preservation devices are added to the pressure-preserved drilling tools. This poses another world-class difficulty. That is, the key to the temperature preservation coring technology of gas hydrate is to prevent the temperature from rising, which is contrary to the previous temperature preservation technology. PCS, PCB, FPC, HRC, MAC, and DAPC do not have the function of temperature preservation, and the later developed PTCS, Hybrid PCS, PCTB, PTPS, WPTCS, and hole-bottom freezing sampling (HBFS) drilling tools (Sun et al., 2018; Guo et al., 2020) use vacuum insulation, thermal insulation material, cooling medium, thermoelectric-refrigeration technique, or external cooling device for temperature preservation. The heat preservation effect is limited. Higher core recovery needs to overcome pressure-related defects, and gas hydrate temperature-preservation coring techniques should be further developed, especially the active temperature-preservation techniques.

Conclusion

Drilling techniques are a series of practical technologies that combine empirical rules, qualitative judgment, and semi-quantitative interpretation. Successful, good, fast, and economical has always been the goal of drilling. However, with the development of oil and gas exploration and development of unconventional, low permeability, deep-water, and other complex oil and gas fields, drilling engineering is facing a series of problems and challenges in terms of safety, economy, and efficiency. Risks and challenges such as temperature and pressure fluctuations, drill string vibration, shallow water and gas flow, safe mud density window, wellhead/wellbore stability, flow assurance, methane leakage, etc. are still and will be difficult problems faced by hydrate drilling for a long time. Although the focus of this paper is to drill gas hydrate in the marine environment, especially in deep water, these situations also apply to drilling gas hydrate on land. The measures taken by the drilling project, whether on land or in the ocean, are to minimize the changes in the *in-situ* temperature and pressure of the reservoir to prevent hydrate dissociation. Thus, to avoid accidents such as wellbore instability and reservoir collapse. It is recommended to adopt the micro overbalance drilling method and develop drilling fluid with excellent performance to deal with the risk of drilling fluid invasion and hydrate dissociation in drilling activities.

Over the years, certain experience has been accumulated in scientific theory, technical equipment, engineering construction, environmental impact assessment in the field of gas hydrate. However, it is still necessary to develop advanced drilling technology and innovative drilling systems for use in the challenging conditions of drilling hydrate reservoirs. Through reasonable well layout, scientific well design, qualified casing and tubing, efficient drilling fluid, pressure-temperature preserved hydrate coring, successful completion, and sustainable development measures, methane can be produced safely and efficiently from hydrate reservoirs. Anyway, we must give full play to the advantages and characteristics of industry, universities, and research institutes. Multidisciplinary knowledge and the latest achievements in other fields should be comprehensively applied to overcome these difficulties. Only by deeply studying their mechanisms and internal laws can they be effectively solved. This requires proposing new scientific problems, establishing new theoretical viewpoints, developing new methods, new materials, new tools, and forming new technologies.

Author contributions

NW: Investigation, writing–original draft, review and editing, supervision, funding acquisition. JP: Investigation, methodology, writing - original draft, review and editing. JZ: Conceptualization, investigation, review. LZ: Investigation, methodology, visualization. SZ: Methodology, investigation, review. PL: Investigation, methodology, review. HL: Investigation. JW: Writing - editing. NW and JP contributed equally to this work and share first authorship.

Funding

This work was financially supported by the National Natural Science Foundation of China (U20B6005-05, 51874252), National Key Research and Development Program of China (2021YFC2800903), Sichuan High-end Foreign Talent Introduction Project (SYZ202124), High-end Foreign Experts Recruitment Plan of China (G2021036005L), 111 Project (D21025), and Open Fund of State Key Laboratory of Oil and Gas Reservoir Geology and Exploitation (Southwest Petroleum University) (PLN 2021-01, PLN 2021-02, PLN 2021-03).

Acknowledgments

The authors would like to thank the reviewers and editors for their helpful comments and suggestions.

Conflict of interest

The authors declare that the research was conducted in the absence of any commercial or financial relationships that could be construed as a potential conflict of interest.

Publisher's note

References

Abid1, K., Spagnoli, G., Teodoriu, C., and Falcone, G. (2015). Review of pressure coring systems for offshore gas hydrates research. *Uw. Tech. Int. J. Soc. Uw. Tech.* 33, 19–30. doi:10.3723/ut.33.019

Aird, P. (2019). *Chapter 12 - deepwater "riserless" drilling*, Editor(s): P. Aird and D. Drilling, Oxford, United Kingdom: Gulf Professional Publishing, 441–475.

Amann, H., Hohnberg, H. J., and Reinelt, R. (1997). HYACE—A novel autoclave coring equipment for systematic offshore gashydrate sampling. *Dtsch. Wiss. Ges. für Erdgas Kohle e.V. (DGMK)* 9706, 37–49.

Balanza, J. A., Justiniano, L. C., and Poletzky, I. (2015). "Implementation of managed pressure casing drilling and managed pressure cementing techniques in unconventional reservoirs," in SPE/IADC Drilling Conference and Exhibition, London, England, UK, March 17–19, 2015.

Bohrmann, G., Pape, T., and participants., C. (2007). Report and preliminary results of R/V METEOR cruise M72/3, istanbul–trabzon–istanbul. Marine gas hydrates of the eastern Black Sea. *Berichte, Fachbereich Geowiss. Univ. Brem. Nr.* 261, 176pp.

Boswell, R., Hancock, S., Yamamoto, K., Collett, T., Pratap, M., and Lee, S. R. (2020). *Natural gas hydrates: Status of potential as an energy resource*. Amsterdam, Netherlands: Elsevier, 111–131. Future Energy.

Boswell, R., Schoderbek, D., Collett, T. S., Ohtsuki, S., White, M., and Anderson, B. J. (2017). The iḡnik Sikumi field experiment, Alaska North Slope: Design, operations, and implications for CO2–CH4 exchange in gas hydrate reservoirs. *Energy fuels.* 31 (1), 140–153. doi:10.1021/acs.energyfuels.6b01909

Bp (2022). *Statistical review of world energy*. 71st edition. London: BP.

Briner, A., Busaidi, Y., Adawi, A., Hilditch, R., Sanchez, F., Sanderson, M., et al. (2015). "CwD technology improves economics in tight gas exploration project in the sultanate of Oman". In: Paper presented at the Abu Dhabi International Petroleum Exhibition and Conference, November 9–12, 2015, Abu Dhabi, UAE.

Burger, J., Gupta, D., Jacobs, P., and Shillinglaw, J. (2006). Overview on hydrate coring, handling and analysis. DOE Report, DE-FC26–02NT41327.

Chen, G. M., Yin, Z. M., Xu, L. B., and Jiang, S. Q. (2007). *Rev. Deep. dual gradient Drill. Technol.* 34 (2), 246–252. (in Chinese with English Abstract).

Chen, J. W., Fan, W., Bingham, B., Chen, Y., Gu, L. Y., and Li, S. L. (2013). A long gravity-piston corer developed for seafloor gas hydrate coring utilizing an *in situ* pressure-retained method. *Energies* 6 (7), 3353–3372. doi:10.3390/en6073353

Chen, L., and Merey, S. (2021). Chapter 13 - emerging technologies in methane hydrate projects, Editor(s): L. Chen and S. Merey, *Oceanic methane hydrates*, Oxford, United Kingdom: Gulf Professional Publishing, 349–390.

Chen, X. J., Lu, H. L., Gu, L. J., Shang, S. L., Zhang, Y., Huang, X., et al. (2022). Preliminary evaluation of the economic potential of the technologies for gas hydrate exploitation. *Energy* 243, 123007. doi:10.1016/j.energy.2021.123007

Chen, Y., Sun, B. J., Gao, Y. H., Liu, K., Li, H., and Zhao, X. X. (2019). Pressure effects on heat transfer in hydrate-bearing deposit with drilling fluid invasion by lab simulation. *Int. J. Green Energy* 16 (10), 770–777. doi:10.1080/15435075.2019.1641104

Cheng, W., Ning, F. L., Sun, J. X., Liu, Z. C., Jiang, G. S., and Li, X. D. (2019). A porothermoelastic wellbore stability model for riserless drilling through gas hydrate-bearing sediments in the Shenhu area of the South China Sea. *J. Nat. Gas Sci. Eng.* 72, 103036. doi:10.1016/j.jngse.2019.103036

Chibura, P. E., Zhang, W., Luo, A. J., and Wang, J. (2022). A review on gas hydrate production feasibility for permafrost and marine hydrates. *J. Nat. Gas Sci. Eng.* 100, 104441. doi:10.1016/j.jngse.2022.104441

Chong, Z. R., Yang, S. H. B., Babu, P., Linga, P., and Li, X. S. (2016). Review of natural gas hydrates as an energy resource: Prospects and challenges. *Appl. Energy* 162, 1633–1652. doi:10.1016/j.apenergy.2014.12.061

Chua, P. C., and Kelland, M. A. (2013). Study of the gas hydrate anti-agglomerant performance of a series of n-Alkyl-tri(n-butyl)ammonium bromides. *Energy fuels.* 27 (3), 1285–1292. doi:10.1021/ef3018546

Chuvilin, E., Ekimova, V., Davletshina, D., Sokolova, N., and Bukhanov, B. (2020). Evidence of gas emissions from permafrost in the Russian arctic. *Geosciences* 10 (10), 383. doi:10.3390/geosciences10100383

Colin, F., Ker, S., Riboulot, V., and Sultan, N. (2020). Irregular BSR: Evidence of an ongoing reequilibrium of a gas hydrate system. *Geophys. Res. Lett.* 47 (20), 1–10. doi:10.1029/2020gl089906

Collett, T., Riedel, M., Boswell, R., Presley, J., Kumar, P., Sathe, A., et al. (2015). U.S. Geological Survey Scientific Investigations Report 2012–5054[R]. Denver, CO: USGS. Indian national gas hydrate program expedition 01 report.

Crutchley, G. J., Pecher, I. A., Gorman, A. R., Henrys, S. A., and Greinert, J. (2010). Seismic imaging of gas conduits beneath seafloor seep sites in a shallow marine gas hydrate province, Hikurangi Margin, New Zealand. *Mar. Geol.* 272 (1), 114–126. doi:10.1016/j.margeo.2009.03.007

Dallimore, S. R., Collett, T. S., Weber, M., and Uchida, T. (2002). Drilling program investigates permafrost gas hydrates. *Eos Trans. AGU.* 83 (18), 193–198. doi:10.1029/2002eo000129

Das, S., Mahto, V., Udayabhanu, G., Lall, M., Singh, K., and Deepak, M. (2022). Experimental evaluation of Sarcosine as an eco-friendly green hydrate inhibitor for the drilling of gas hydrate bearing formations. *J. Petroleum Sci. Eng.* 208, 109764. doi:10.1016/j.petrol.2021.109764

Das, S., Mahto, V., Udayabhanu, G., Lall, M., Singh, K., and Deepak, M. (2022). Experimental evaluation of Sarcosine as an eco-friendly green hydrate inhibitor for the drilling of gas hydrate bearing formations. *J. Petroleum Sci. Eng.* 208, 109764. doi:10.1016/j.petrol.2021.109764

Day, R. W. (2006). *Subsurface exploration. Fundation engineering handbook*. New York, United States: McGraw-Hill.

Demirbas, A. (2010). Methane hydrates as potential energy resource: Part 2–methane production processes from gas hydrates. *Energy Convers. Manag.* 51 (7), 1562–1571. doi:10.1016/j.enconman.2010.02.014

Dickens, G. R., Schroeder, D., and Hinrichs, K. U.; the Leg 201 Scientific Party (2003). "The pressure core sampler (PCS) on Ocean Drilling Program Leg 201: general operations and gas release," in *Proceedings ODP, initial reports 201*. S. L. D'Hondt, B. B. Jørgensen, and D. J. Miller Editors et al. (College Station, TX: Ocean Drilling Program), 1–22.

Dickens, G. R., Wallace, P. J., Paull, C.K., and Borowski, W. S. (2000). Detection of methane gas hydrate in the pressure core sampler (PCS): Volume-pressure-time relations during controlled degassing experiments. *Proc. Ocean. Drill. Progr. Sci. Results* 164, 113–126.

DNV (2013). *Dynamic positioning systems with enhanced reliability*. Høvik: Det Norske Veritas AS.

Dong, H., and Zeng, G. (2017). Flammable ice' — Extract with caution. *Nature* 546, 599. doi:10.1038/546599a

Dong, L., Wan, Y. Z., Li, Y. L., Liao, H. L., Liu, C. L., Wu, N. Y., et al. (2022). 3D numerical simulation on drilling fluid invasion into natural gas hydrate reservoirs. *Energy* 241, 122932. doi:10.1016/j.energy.2021.122932

Fakher, S., Elgahawy, Y., and Abdelaal, H. (2019). "A comprehensive review on gas hydrate reservoirs: formation and dissociation thermodynamics and rock and fluid properties," in International Petroleum Technology Conference, Beijing, China, March 26–28, 2019.

Fereidounpour, A., and Vatani, A. (2014). An investigation of interaction of drilling fluids with gas hydrates in drilling hydrate bearing sediments. *J. Nat. Gas Sci. Eng.* 20, 422–427. doi:10.1016/j.jngse.2014.07.006

Flemings, P., Phillips, S. C., Boswell, R., Collett, T. S., Cook, A. E., Dong, T., et al. (2019). Pressure coring a Gulf of Mexico deep-water turbidite gas hydrate reservoir: Initial results from the university of Texas–Gulf of Mexico 2-1 (UT-GOM2-1) hydrate pressure coring expedition. *Am. Assoc. Pet. Geol. Bull.* 104 (9), 1847–1876. doi:10.1306/05212019052

Foschi, M., Aanoni, M., Cartwright, J. A., and Idiz, E. (2019). Microbial vs thermogenic gas hydrates in the South falkland basin: BSR distribution and fluid origin. *Mar. Petroleum Geol.* 102, 695–703. doi:10.1016/j.marpetgeo.2019.01.023

Fu, Q., Wang, G. R., Zhou, S. W., Zhong, L., and Wang, L. Z. (2020). Development of marine natural gas hydrate mining technology and equipment. *Chin. J. Eng. Sci.* 22 (6), 32–39. (in Chinese with English Abstract). doi:10.15302/j-sscae-2020.06.005

Fugro Synergy (2021) Fugro SYNERGY. Available at: https://media.fugro.com/media/docs/default-source/about-fugro-doc/vessels/fugro-synergy_a4_lr.pdf?sfvrsn=9cfa0c1a_26.

Gaafar, G. R., Tewari, R. D., and Zain, Z. M. (2015). "Overview of advancement in core analysis and its importance in reservoir characterisation for maximising recovery," in SPE Asia Pacific Enhanced Oil Recovery Conference, Kuala Lumpur, Malaysia, August 11–13, 2015 (Kuala Lumpur, Malaysia: Society of Petroleum Engineers), 222–238.

Gabitto, J., and Barrufet, M. (2009). Gas hydrates research programs: An international review.

Gao, K., Sun, Y. H., Ren, L. Q., Cao, P. L., Li, W. T., and Fan, H. K. (2018). Design and analysis of ternary coupling bionic bits. *J. Bionic Eng.* 5, 53–59. doi:10.1016/s1672-6529(08)60072-4

Gao, Y. H., Liang, J., Liu, H. S., Zhang, S. Y., Chen, L., and Chen, B.H. (2017). Analysis and research on gas hydrate drilling fluid application in Qilian Muli area, Qinghai Province. *J. Qinghai Univ. Sci.* 35 (3), 52–57+64. (in Chinese).

Gerivani, H., Putans, V. A., Merklin, L. R., and Modarres, M. H. (2020). Characteristics of features formed by gas hydrate and free gas in the continental slope and abyssal plain of the Middle Caspian Sea. *Mar. Georesources Geotechnol.* 39 (4), 419–430. doi:10.1080/1064119x.2019.1709585

Ghozatloo, A., Hosseini, M., and Shariaty-Niassar, M. (2015). Improvement and enhancement of natural gas hydrate formation process by Hummers' graphene. *J. Nat. Gas. Sci. Eng.* 27, 1229–1233. doi:10.1016/j.jngse.2015.09.069

Graber, K. K., Pollard, E., Jonasson, B., and Schulte, E. (2021) Overview of Ocean Drilling program engineering tools and hardware. http://www-odp.tamu.edu/publications/tnotes/tn31/jr/jr.htm.

Graham, J. R., and Reed, J. A., II (1969). Glomar challenger deep sea drilling vessel. *J. Petroleum Technol.* 21 (10), 1263–1274. doi:10.2118/2180-pa

Grigg, R. B., and Lynes, G. L. (1992). Oil-based drilling mud as a gas-hydrates inhibitor. *SPE Drill. Eng.* 7 (1), 32–38. doi:10.2118/19560-pa

Guo, W., Zhang, P. Y., Yang, X., Lei, J., Sun, Y. H., Rui, J., et al. (2020). Development and application of hole-bottom freezing drilling tool for gas-hydrate-bearing sediment sampling. *Ocean. Eng.* 203, 107195. doi:10.1016/j.oceaneng.2020.107195

Gupta, P., and Sangwai, J. S. (2019). formation and dissociation kinetics of methane hydrate in aqueous oilfield polymer solutions (polyacrylamide, xanthan gum, and guar gum) and their performance evaluation as low-dosage kinetic hydrate inhibitors (LDHI). *Energy fuels.* 33 (7), 6335–6349. doi:10.1021/acs.energyfuels.9b01204

Hancock, S., Boswell, R., and Collett, T. (2019). "Development of deepwater natural gas hydrates," in Paper presented at the Offshore Technology Conference, Houston, Texas, May 6–9, 2019.

Hannegan, D. M. (2005). "Methane hydrate drilling technology," in Paper presented at the Offshore Technology Conference, Houston, Texas, USA, May 2–5, 2005.

Hannegan, D. M., Todd, R. J., Pritchard, D. M., and Jonasson, B. (2005). "MPD-uniquely applicable to methane hydrate drilling," in Paper presented at the SPE/IADC Underbalanced Technology Conference and Exhibition, Houston, Texas, USA, October 11–12, 2004.

He, Y. L., Liang, J. Q., Kuang, Z. G., Deng, W., Ren, J. F., Lai, H. F., et al. (2022). Migration and accumulation characteristics of natural gas hydrates in the uplifts and their slope zones in the Qiongdongnan Basin. *China, China Geol.* 5 (2), 234–250.

He, Y., Long, Z., Lu, J. S., Shi, L., Yan, W., and Liang, D. (2021). Investigation on methane hydrate formation in water-based drilling fluid. *Energy fuels.* 35 (6), 5264–5270. doi:10.1021/acs.energyfuels.0c04409

Heidari, H., Akbari, M., Souhankar, A., and Hafezi, R. (2022). Review of global energy trends towards 2040 and recommendations for Iran oil and gas sector. *Int. J. Environ. Sci. Technol. (on line)* 19, 8007–8018. doi:10.1007/s13762-022-03963-w

Heydari, A., and Peyvandi, K. (2020). Study of biosurfactant effects on methane recovery from gas hydrate by CO2 replacement and depressurization. *Fuel* 272, 117681. doi:10.1016/j.fuel.2020.117681

Hogenboom, S., Rokseth, B., Vinnem, J. E., and Utne, I. B. (2020). Human reliability and the impact of control function allocation in the design of dynamic positioning systems. *Reliab. Eng. Syst. Saf.* 194, 106340. doi:10.1016/j.ress.2018.12.019

Hou, Y., Liu, C. S., and Liu, D. (2022). Drilling fluid technology of horizontal well in shallow soft formation of natural gas hydrate in sea area, (in Chinese). *Drill. Eng.* 49 (2), 16–21.

Hsiung, K. H., Saito, S., Kanamatsu, T., Sanada, Y., and Yamada, Y. (2019). Regional stratigraphic framework and gas hydrate occurrence offshore eastern India: Core-log-seismic integration of National Gas Hydrate Program Expedition 02 (NGHP-02) Area-B drill sites. *Mar. Petroleum Geol.* 108, 206–215. doi:10.1016/j.marpetgeo.2018.06.021

Hu, C. Y., Yang, T. F., Burr, G. S., Chuang, P. C., Chen, H. W., Walia, M., et al. (2017). Biogeochemical cycles at the sulfate-methane transition zone (SMTZ) and geochemical characteristics of the pore fluids offshore southwestern Taiwan. *J. Asian Earth Sci.* 149, 172–183. doi:10.1016/j.jseaes.2017.07.002

Hu, G. W., Bu, Q. T., Lyu, W. J., Wang, J., Chen, J., Li, Q., et al. (2021). A comparative study on natural gas hydrate accumulation models at active and passive continental margins. *Nat. Gas. Ind. B* 8 (2), 115–127. doi:10.1016/j.ngib.2021.03.001

Hu, Y. Q., Xie, J., Xue, S. N., Xu, M., Fu, C. H., He, H. L., et al. (2022). Research and application of thermal insulation effect of natural gas hydrate freezing corer based on the wireline-coring principle. *Petroleum Sci.* 19 (3), 1291–1304. doi:10.1016/j.petsci.2021.11.019

Huang, T. J., Zhang, Y., Wang, Y., Li, X. S., and Chen, Z. Y. (2020). An experimental drilling apparatus used for evaluating drilling risks related to natural gas hydrate. *MethodsX* 7, 101019. doi:10.1016/j.mex.2020.101019

Inada, N., and Yamamoto, K. (2015). Data report: Hybrid Pressure Coring System tool review and summary of recovery result from gas-hydrate related coring in the Nankai Project. *Mar. Petroleum Geol.* 66, 323–345. doi:10.1016/j.marpetgeo.2015.02.023

Isaac, O. T., Pu, H., Oni, B. A., and Samson, F. A. (2022). Surfactants employed in conventional and unconventional reservoirs for enhanced oil recovery—a review. *Energy Rep.* 8, 2806–2830. doi:10.1016/j.egyr.2022.01.187

Jin, C. Y. (2021). Research report on technologies and equipment for exploitation of marine combustible ice resources. *IOP Conf. Ser. Earth Environ. Sci.* 647, 012117. doi:10.1088/1755-1315/647/1/012117

Jin, G. R., Peng, Y. Y., Liu, L. H., Su, Z., Liu, J., Li, T., et al. (2022). Enhancement of gas production from low-permeability hydrate by radially branched horizontal well: Shenhu Area, South China Sea. *Energy* 253, 124129. doi:10.1016/j.energy.2022.124129

John, J., Sin, G. H., Steve, M., and Jim, F. (2020). A case study of natural gas hydrates (NGH) in offshore NW Sabah: Identification, shallow geohazard implication for exploration drilling, extraction challenges and potential energy resource estimation. *Bull. Geol. Soc. Malays.* 70, 57–75. doi:10.7186/bgsm70202005

Kadaster, A. G., Millheim, K. K., and Thompson, T. W. (2005). "The planning and drilling of hot ice #1 - gas hydrate exploration well in the alaskan arctic," in The SPE/IADC Drilling Conference, Amsterdam, Netherlands, February 23–25, 2005.

Ke, W., and Chen, D. Y. (2019). A short review on natural gas hydrate, kinetic hydrate inhibitors and inhibitor synergists. *Chin. J. Chem. Eng.* 27 (9), 2049–2061. doi:10.1016/j.cjche.2018.10.010

Kelland, M. A. (2006). History of the development of low dosage hydrate inhibitors. *Energy fuels.* 20 (3), 825–847. doi:10.1021/ef050427x

Khabibullin, T., Falcone, G., and Teodoriu, C. (2011). Drilling through gas-hydrate sediments: Managing wellbore-stability risks. *SPE Drill. Complet.* 26 (2), 287–294. doi:10.2118/131332-pa

Khabibullin, T., Falcone, G., and Teodoriu, C. (2011). Drilling through gas-hydrate sediments: Managing wellbore-stability risks. *SPE Drill. Complet.* 26 (02), 287–294. doi:10.2118/131332-pa

Kim, G. Y., Yi, B. Y., Kang, N. K., Yoo, D. G., and Lee, Yong, M. J. (2022). Comparison of logging-while-drilling and wireline logging data from gas hydrate-bearing deep-sea sediments, the Ulleung Basin, East Sea. *Explor. Geophys.* 53 (1), 92–103. doi:10.1080/08123985.2021.1898942

Kiran, B. S., and Prasad, P. S. R. (2021). Inhibition of methane hydrates using biodegradable additives. *ACS Omega* 6 (12), 8261–8270. doi:10.1021/acsomega.0c06328

Kubo, Y., Mizuguchi, Y., Inagaki, F., and Yamamoto, K. (2014). A new hybrid pressure-coring system for the drilling vessel <i>Chikyu</i>. *Sci. Dril.* 17 (17), 37–43. doi:10.5194/sd-17-37-2014

Kulkarni, N., and Heinze, L. (2022). "Assess the impact of shallow water flow geohazard on drilling operations in the riserless sections of deepwater well construction," in Paper presented at the SPE Canadian Energy Technology Conference, Calgary, Alberta, Canada, March 16–17, 2022.

Kumar, P., Collett, T. S., Shukla, K. M., Yadav, U. S., Lall, M. V., and Vishwanath, K. (2019). India national gas hydrate program expedition-02: Operational and technical summary. *Mar. Petroleum Geol.* 108, 3–38. doi:10.1016/j.marpetgeo.2018.11.021

Kvamme, B., and Saeidi, N. (2021). A zero emission scheme for producing energy from natural gas hydrates and conventional natural gas. *Petroleum* 7 (4), 364–384. doi:10.1016/j.petlm.2021.10.003

Li, B., Li, X. S., Li, G., and Chen, Z. Y. (2015). Evaluation of gas production from Qilian Mountain permafrost hydrate deposits in two-spot horizontal well system. *Cold Regions Sci. Technol.* 109, 87–98. doi:10.1016/j.coldregions.2014.08.002

Li, C., Xie, H. P., Gao, M. Z., Chen, L., Zhao, L., Li, C. B., et al. (2021). Novel designs of pressure controllers to enhance the upper pressure limit for gas-hydrate-bearing sediment sampling. *Energy* 227, 120405. doi:10.1016/j.energy.2021.120405

Li, G., Li, X. S., Yang, B., Duan, L. P., Huang, N. S., Zhang, Y., et al. (2013). The use of dual horizontal wells in gas production from hydrate accumulations. *Appl. Energy* 112, 1303–1310. doi:10.1016/j.apenergy.2013.03.057

Li, G. S., Tian, S. C., and Zhang, Y. Q. (2020). Research progress on key technologies of natural gas hydrate exploitation by cavitation jet drilling of radial wells. *Petroleum Sci. Bull.* 5 (3), 349–365. (In Chinese with English abstract).

Li, H. T., Ge, Z. L., Wei, N., Sun, W. T., Zhang, Y., Xue, J., et al. (2021). Research on intelligent judgment method of natural gas hydrate drilling risk. *Petroleum* 7 (4), 439–450. doi:10.1016/j.petlm.2021.10.014

Li, H. Y., Zhang, M., Lau, H. C., and Fu, S. W. (2020). China's deepwater development: Subsurface challenges and opportunities. *J. Petroleum Sci. Eng.* 195, 107761. doi:10.1016/j.petrol.2020.107761

Li, J. F., Ye, J. L., Qin, X. W., Qiu, H. J., Wu, N. Y., Lu, H. L., et al. (2018). The first offshore natural gas hydrate production test in South China Sea. *China Geol.* 1 (1), 5–16. doi:10.31035/cg2018003

Li, L. J., Peng, J. M., Gao, Q., Sun, M, Z., Liu, Y., Li, M., et al. (2016). Pressure retaining method based on phase change for coring of gas hydrate-bearing sediments in offshore drilling. *Appl. Therm. Eng.* 107, 633–641. doi:10.1016/j.applthermaleng.2016.06.174

Li, L. L., Yang, J., Zhou, G. D., Yan, L., Yin, Q. S., Zhou, B., et al. (2018). "A new method based on simulation experiment to evaluate subsea wellhead stability of drilling from gas hydrate sediments in deep water," in Paper presented at the Offshore Technology Conference, Houston, Texas, USA, April 30–May 3, 2018.

Li, L., Yang, J., Zou, X., Yan, L., Zhang, C. C., Yang, P. Y., et al. (2021) "Monitoring technology of gas hydrate in polar drilling," in Paper presented at the The 31st International Ocean and Polar Engineering Conference, Rhodes, Greece, June 20–25, 2021.

Li, Q. M., Zhang, Y. Q., Yin, H., et al. (2017). Application of horizontal docking well drilling technology in gas hydrate test production. *Explor. Eng. Soil Drill. Tunneling)* 44 (8), 13–17. (in Chinese with English Abstract).

Li, W. L., Gao, D. L., and Yang, J. (2019). Challenges and prospects of well drilling and completion in Marine gas hydrate formation. *Oil Drill. Prod. Technol.* 41 (6), 681–689. (in Chinese).

Li, X. M., Zhang, Y. Q., Yin, H., Liang, J., Wang, H. B., et al. (2017). Application of drilling technology of horizontally butted well for gas hydrate trial-producing. *Explor. Eng. Soil Drill. Tunneling* 44 (8), 13–17. (in Chinese with English Abstract).

Li, X. S., Xu, C. G., Zhang, Y., Ruan, X. K., Li, G., and Wang, Y. (2016). Investigation into gas production from natural gas hydrate: A review. *Appl. Energy* 172, 286–322. doi:10.1016/j.apenergy.2016.03.101

Li, X. S., Zhang, Y., Li, G., Chen, Z. Y., and Wu, H. J. (2011). Experimental investigation into the production behavior of methane hydrate in porous sediment by depressurization with a novel three-dimensional cubic hydrate simulator. *Energy fuels.* 25 (10), 4497–4505. doi:10.1021/ef200757g

Liang, J. Q., Deng, W., Lu, J. A., Kuang, Z. G., He, Y. L., Zhang, W., et al. (2020). A fast identification method based on the typical geophysical differences between submarine shallow carbonates and hydrate bearing sediments in the northern South China Sea. *China Geol.* 3 (1), 16–27. doi:10.31035/cg2020021

Liang, J. Q., Zhang, W., Lu, J. A., Wei, J. G., Kuang, Z. G., and He, Y. L. (2019). Geological occurrence and accumulation mechanism of natural gas hydrates in the eastern Qiongdongnan Basin of the South China Sea: Insights from site GMGS5-W9-2018. *Mar. Geol.* 418, 106042. doi:10.1016/j.margeo.2019.106042

Liang, Q. Y., Xiao, X., Zhao, J., Zhang, W., Li, Y., Wu, X. M., et al. (2022). Geochemistry and sources of hydrate-bound gas in the Shenhu area, northern south China sea: Insights from drilling and gas hydrate production tests. *J. Petroleum Sci. Eng.* 208, 109459. doi:10.1016/j.petrol.2021.109459

Liang, T., Chen, Y. L., and Zhao, Y. (2021) "Introduction to the drilling system of "Chikyu" drilling vessel"," in The 20th National Exploration Engineering (Geotechnical drilling engineering) academic Exchange conference, Xining, Qinghai, China.

Liu, J., Yang, R., Wu, D. D., and Jin, G. R. (2019). Estimation of microbial hydrate resources based on hydrocarbon generation material balance method:Case study of deep water area in southwestern Qiongdongnan Basin. *Nat. Gas. Geosci.* 30 (04), 539–548. (in Chinese with English Abstract).

Liu, S. Y., Li, H. Y., Wang, B., and Sun, B. J. (2022). Accelerating gas production of the depressurization-induced natural gas hydrate by electrical heating. *J. Petroleum Sci. Eng.* 208, 109735. doi:10.1016/j.petrol.2021.109735

Liu, T. L., Jiang, G. S., Zhang, P., Sun, J., Sun, H., Wang, R., et al. (2016). A new low-cost drilling fluid for drilling in natural gas hydrate-bearing sediments. *J. Nat. Gas Sci. Eng.* 33, 934–941. doi:10.1016/j.jngse.2016.06.017

Liu, X. F., Liu, C. H., and Wu, J. J. (2019). Dynamic characteristics of offshore natural gas hydrate dissociation by depressurization in marine sediments. *Geofluids* 2019, 1–11. doi:10.1155/2019/6074892

Liu, Y. M., Fang, M., Jiang, Y. F., Li, T. F., Yang, X. T., Wang, L. S., et al. (2021). Field test of scattered renewal well controlled pressure casing drilling and completion technology in the third mining block. *West-China Explor. Eng.* 33 (08), 43–46+49. (in Chinese).

Liu, Y. M., Yang, Z. G., Yang, J. S., Ma, X. W., Huo, D., and Geng, J. W. (2020). Research and field test of controlled pressure casing drilling technology. *Drill. Prod. Technol.* 43 (4), 1–3. (in Chinese).

Lunne, T., and Long, M. (2006). Review of long seabed samplers and criteria for new sampler design. *Mar. Geol.* 226, 145–165. doi:10.1016/j.margeo.2005.07.014

Luo, Y. J., Peng, J. M., Sun, M. Z., Sun, Q., Ji, T. K., et al. (2015). An ice-valve-based pressure-coring system for sampling natural hydrate-bearing sediments: Proof-of-concept laboratory studies. *J. Nat. Gas Sci. Eng.* 27, 1462–1469. doi:10.1016/j.jngse.2015.10.011

Macelloni, L., Lutken, C. B., Garg, S., Simonetti, A., D'Emidio, M., Wilson, R. M., et al. (2015). Heat-flow regimes and the hydrate stability zone of a transient, thermogenic, fault-controlled hydrate system (Woolsey Mound northern Gulf of Mexico). *Mar. Petroleum Geol.* 59, 491–504. doi:10.1016/j.marpetgeo.2014.09.010

Mahmood, M. N., and Guo, B. Y. (2021). Productivity comparison of radial lateral wells and horizontal snake wells applied to marine gas hydrate reservoir development. *Petroleum* 7 (4), 407–413. doi:10.1016/j.petlm.2021.10.004

Maiti, M., Bhaumik, A. K., and Mandal, A. (2021). Performance of water-based drilling fluids for deepwater and hydrate reservoirs: Designing and modelling studies. *Petroleum Sci.* 18 (6), 1709–1728. doi:10.1016/j.petsci.2021.09.001

Makogon, Y. F. (2010). Natural gas hydrates – a promising source of energy. *J. Nat. Gas Sci. Eng.* 2 (1), 49–59. doi:10.1016/j.jngse.2009.12.004

Matsuzawa, M., Terao, Y., Hay, B., Wingstrom, L., Duncan, M., and Ayling, I. (2014). "A completion system application for the world's first marine hydrate production test," in Paper presented at the Offshore Technology Conference, Houston, Texas, USA, May 5–8, 2014.

Merey, Ş., and Chen, L. (2022). Numerical comparison of different well configurations in the conditions of the 2020-gas hydrate production test in the Shenhu Area. *Upstream Oil Gas Technol.* 9, 100073. doi:10.1016/j.upstre.2022.100073

Merey, Ş. (2016). Drilling of gas hydrate reservoirs. *J. Nat. Gas Sci. Eng.* 35, 1167–1179. doi:10.1016/j.jngse.2016.09.058

Merey, Ş. (2019). Evaluation of drilling parameters in gas hydrate exploration wells. *J. Petroleum Sci. Eng.* 172, 855–877. doi:10.1016/j.petrol.2018.08.079

Minshull, T. A., Marín-Moreno, H., Betlem, P., Bialas, J., Buenz, S., Burwicz, E., et al. (2020). Hydrate occurrence in europe: A review of available evidence. *Mar. Pet. Geol.* 111, 735–764. doi:10.1016/j.marpetgeo.2019.08.014

Monteleone, V., Marín-Moreno, H., Bayrakci, G., Best, A., Shaon, F., Hossain, M. M., et al. (2022). Seismic characterization and modelling of the gas hydrate system in the northern Bay of Bengal, offshore Bangladesh. *Mar. Petroleum Geol.* 141, 105690. doi:10.1016/j.marpetgeo.2022.105690

Moridis, G. J., Reagan, M. T., and Zhang, K. (2008). "The use of horizontal wells in gas production from hydrate accumulations," in Paper presented at the Proceedings of the 6th International Conference on Gas Hydrates, Vancouver, British Columbia, Canada.

Motghare, P. D., and Musale, A. (2017). "Unconventional hydrocarbons: Gas hydrates - drilling challenges and suitable technology," in Paper presented at the SPE Oil and Gas India Conference and Exhibition, Mumbai, India, April 4–6, 2017.

Mozaffar, H., Anderson, R., and Tohidi, B. (2016). Reliable and repeatable evaluation of kinetic hydrate inhibitors using a method based on crystal growth inhibition. *Energy fuels.* 30 (12), 10055–10063. doi:10.1021/acs.energyfuels.6b00382

Nagappayya, S. K., Lucente-Schultz, R. M., Nace, V. M., and Ho, V. M. (2015). Antiagglomerant hydrate inhibitors: The link between hydrate-philic surfactant behavior and inhibition performance. *J. Chem. Eng. Data* 60 (2), 351–355. doi:10.1021/je500611d

Naser, G., Bin, G., and Sajjad, N. (2022). Evaluating the effect of new gas solubility and bubble point pressure models on PVT parameters and optimizing injected gas rate in gas-lift dual gradient. *Drilling* 15 (3), 1212.

Ngata, M. R., Yang, B. L., Aminu, M. D., Iddphonce, R., Omari, A., Shaame, M., et al. (2022). Review of developments in nanotechnology application for formation damage control. *Energy fuels.* 36 (180), 80. doi:10.1021/acs.energyfuels.1c03223

Ning, F. L., Chen, Q., Sun, J. X., Wu, X., Cui, G. D., Mao, P., et al. (2022). Enhanced gas production of silty clay hydrate reservoirs using multilateral wells and reservoir reformation techniques: Numerical simulations. *Energy* 254, 124220. (Part A). doi:10.1016/j.energy.2022.124220

Ning, F. L., Zhang, K. N., Wu, N. Y., Li, G., Jiang, G. S., et al. (2013). Invasion of drilling mud into gas-hydrate-bearing sediments. Part I: Effect of drilling mud properties. *Geophys. J. Int.* 193, 1370–1384. doi:10.1093/gji/ggt015

Ning, F. (2005). *Research on wellbore stability in gas hydrate formation*. China: China University of Geosciences.

Ning, F., Wu, N., Yu, Y., Zhang, K., Jiang, G., Zhang, L., et al. (2013). Invasion of drilling mud into gas-hydrate-bearing sediments. Part II: Effects of geophysical properties of sediments. *Geophys. J. Int.* 193, 1385–1398. doi:10.1093/gji/ggt016

Olga, G., Sergei, M., and Pavel, S. (2022). Key areas of gas hydrates study: Review. *Energies* 15 (5), 1799. doi:10.3390/en15051799

Pang, X. Q., Jia, C. Z., Chen, Z. X., Shi, H. S., Chen, Z. H., Hu, T., et al. (2022). Reduction of global natural gas hydrate (NGH) resource estimation and implications for the NGH development in the South China Sea. *Petroleum Sci.* 19 (1), 3–12. doi:10.1016/j.petsci.2021.12.006

Park, S. Y., Son, B. K., Choi, J., Jin, H., and Lee, K. (2022). Application of machine learning to quantification of mineral composition on gas hydrate-bearing sediments, Ulleung Basin, Korea. *J. Petroleum Sci. Eng.* 209, 109840. doi:10.1016/j.petrol.2021.109840

Pelley, J. (2008). Gas hydrates on the front burner: Flammable ice could create a bridge to a sustainable energy future. *Environ. Sci. Technol.* 42 (20), 7550–7551. doi:10.1021/es802250e

Peterson, M. N. A. (1984). Deep sea drilling project development engineering technical report note 16. La Jolla, CA: OSTI.GOV.Design and operation of a wireline pressure core barrel.

Pettigrew, T. L. (1992). Design and operation of a wireline pressure core sampler (PCS), Ocean drilling program technical note 17.

Prassl, W. F., Peden, J. M., and Wong, K. W. (2004). "Mitigating gas hydrate related drilling risks: A process-knowledge management approach," in Paper presented at the SPE Asia Pacific Oil and Gas Conference and Exhibition, Perth, Australia, October 18–20, 2004.

Pui, G., Bhandari, J., Arzaghi, E., Abbassi, R., and Garaniya, V. (2017). Risk-based maintenance of offshore managed pressure drilling (MPD) operation. *J. Petroleum Sci. Eng.* 159, 513–521. doi:10.1016/j.petrol.2017.09.066

Qin, H. W., Cai, Z., Hu, H. M., Wang, J. J., Ye, W., and Chen, Y. (2016). Numerical analysis of gravity coring using coupled Eulerian-Lagrangian method and a new corer. *Mar. Georesources Geotechnol.* 34 (5), 403–408. doi:10.1080/1064119x.2014.958880

Rabinowitz, P. D., and Garrison, L. E. (1985). *Operational and laboratory capabilities of "JOIDES resolution*. College Station, TX: Texas A & M University.

Rana, A., Khan, I., and Saleh, T. A. (2021). Advances in carbon nanostructures and nanocellulose as additives for efficient drilling fluids: Trends and future perspective—a review. *Energy fuels.* 35 (9), 7319–7339. doi:10.1021/acs.energyfuels.0c04341

Ren, H., Han, L. J., Xu, J. L., and Wu, Z. H. (2013). "Research on marine gas hydrate drilling sampler of China," in *Paper presented at the tenth ISOPE ocean mining and gas hydrates symposium* (Poland: Szczecin).

Roostaei, M., Javanmardi, J., Rasoolzadeh, A., and Mohammadi, A. H. (2021). Experimental determinations of the complete inhibition, the slow growth, and the rapid failure regions of methane hydrate formation in the presence of polyvinylpyrrolidone and polyvinylcaprolactam aqueous solutions. *Energy fuels.* 35 (5), 3780–3787. doi:10.1021/acs.energyfuels.0c03562

Roostaie, M., and Leonenko, Y. (2020). Analytical investigation of gas production from methane hydrates and the associated heat and mass transfer upon thermal stimulation employing a coaxial wellbore. *Energy Convers. Manag.* 209, 112616. doi:10.1016/j.enconman.2020.112616

Roostaie, M., and Leonenko, Y. (2020). Gas production from methane hydrates upon thermal stimulation, an analytical study employing radial coordinates. *Energy* 194, 116815. doi:10.1016/j.energy.2019.116815

Rosenberg, S., Kotow, K., Wakefield, J., Sampietro, S., and Hulett, B. (2022). "Riserless casing drilling for mitigation of shallow hazards - a paradigm shift in deepwater well construction," in *Paper presented at the IADC/SPE international drilling conference and exhibition* (Galveston, Texas, USA).

Ruan, X. K., Li, X. S., and Xu, C. G. (2021). A review of numerical research on gas production from natural gas hydrates in China. *J. Nat. Gas. Sci. Eng.* 85, 103713. doi:10.1016/j.jngse.2020.103713

Ruan, X. K., Yang, M. J., Li, Y. H., Song, Y. C., and Liang, H. F. (2012). A review on the selection of extraction technologies for different forms of natural gas hydrate reservoirs. *Nat. Gas Explor. Dev.* 35 (2), 39–43+88. (in Chinese).

Ruppel, C. (2020). Map of gas hydrate locations . Available at: https://www.usgs.gov/media/images/map-gas-hydrate-locations-known-and-inferred.

Ryu, B. J., Collett, T. S., Riedel, M., Kim, G. Y., Chun, J., Bahk, J. J., et al. (2013). Scientific results of the second gas hydrate drilling expedition in the Ulleung basin (UBGH2). *Mar. Petroleum Geol.* 47, 1–20. doi:10.1016/j.marpetgeo.2013.07.007

Sa, J. H., Lee, B. R., Park, D. H., Han, K., Chun, H. D., and Lee, K. H. (2011). Amino acids as natural inhibitors for hydrate formation in CO2 sequestration. *Environ. Sci. Technol.* 45 (13), 5885–5891. doi:10.1021/es200552c

Sahu, C., Kumar, R., and Sangwai, J. S. (2020). Comprehensive review on exploration and drilling techniques for natural gas hydrate reservoirs. *Energy fuels.* 34 (10), 11813–11839. doi:10.1021/acs.energyfuels.0c02202

Sain, K., and Gupta, H. (2012). Gas hydrates in India: Potential and development. *Gondwana Res.* 22 (2), 645–657. doi:10.1016/j.gr.2012.01.007

Sánchez, F., and Al-Harthy, M. H. (2011). Risk analysis: Casing-while-Drilling (CwD) and modeling approach. *J. Petroleum Sci. Eng.* 78 (1), 1–5. doi:10.1016/j.petrol.2011.04.017

Saumya, S., Narasimhan, B., Singh, J., Yamamoto, H., Vij, J., Sakiyama, N., et al. (2019). Acquisition of logging-while-drilling (LWD) multipole acoustic log data during the India national gas hydrate program (NGHP) expedition 02. *Mar. Petroleum Geol.* 108, 562–569. doi:10.1016/j.marpetgeo.2018.10.011

Schoderbek, D., Farrell, H., Hester, K., Howard, J., Raterman, K., Silpngarmlert, S., et al. (2013). *ConocoPhillips gas hydrate production test final technical report*. Houston, TX: ConocoPhillips Co.

Schultheiss, P., Holland, M., and Humphrey, G. (2009). Wireline coring and analysis under pressure: Recent use and future developments of the HYACINTH system. *Sci. Dril.* 7 (7), 44–50. doi:10.5194/sd-7-44-2009

Schultheiss, P., Holland, M., and Roberts, J. (2008). "Pressure core analysis: The keystone of a gas hydrate investigation," in Proceedings of the 6th International Conference on Gas Hydrates Vancouver, British Columbia, July 6-10, 2008.

Singh, R. P., Lall, D., and Vishal, V. (2022). Prospects and challenges in unlocking natural-gas-hydrate energy in India: Recent advancements. *Mar. Petroleum Geol.* 135, 105397. doi:10.1016/j.marpetgeo.2021.105397

Song, Y., Yang, L., Zhao, J., Liu, W., Yang, M., Li, Y., et al. (2014). The status of natural gas hydrate research in China: A review. *Renew. Sustain. Energy Rev.* 31, 778–791. doi:10.1016/j.rser.2013.12.025

Su, P. B., Liang, J. Q., Zhao, Q. X., Lu, J. A., Su, X., and Yang, T. (2020). *Exploration technology of natural gas hydrate resources in sea area*. Beijing: Science Press.

Sun, W. T., Pei, J., Wei, N., Zhao, J. Z., Xue, J., Zhou, S. W., et al. (2021). Sensitivity analysis of reservoir risk in marine gas hydrate drilling. *Petroleum* 7 (4), 427–438. doi:10.1016/j.petlm.2021.10.013

Sun, W. T., Wei, N., Zhao, J. Z., Kvamme, B., Zhou, S. W., Zhang, L. H., et al. (2022). Imitating possible consequences of drilling through marine hydrate reservoir. *Energy* 239, 121802. doi:10.1016/j.energy.2021.121802

Sun, Y., Goldberg, D., Collett, T., and Hunter, R. (2011). High-resolution well-log derived dielectric properties of gas-hydrate-bearing sediments, Mount Elbert gas hydrate stratigraphic test well, Alaska north slope. *Mar. Pet. Geol.* 28, 450–459. doi:10.1016/j.marpetgeo.2010.03.001

Sun, Y. H., Ma, Y. L., Huang, S. H., Gao, K., Liu, B. C., Li, X. Y., et al. (2012). Development and application of bionic coupling impregnated diamond bit for gas hydrate exploration. *J. Jilin Unviersity Earth Sci. Ed.* 42 (S3), 295–300. (in Chinese with English Abstract).

Sun, Y. H., Wang, Y., Guo, W., Jia, R., Chen, G., and Zhang, P. (2018). Hole-bottom freezing technique based on phase change heat transfer for gas-hydrates sampling: Efficiency optimization of refrigeration change of phase. *Appl. Therm. Eng.* 130, 722–734. doi:10.1016/j.applthermaleng.2017.11.012

Sun, Y. H., Wang, Y., Lü, X. S., Jia, R., and Guo, W. (2015). Hole-bottom freezing method for gas hydrate sampling. *J. Nat. Gas Sci. Eng.* 25, 271–283. doi:10.1016/j.jngse.2015.05.011

Sun, Y., Wang, Y., Lü, X., Jia, R., and Guo, W. (2015). Hole-bottom freezing method for gas hydrate sampling. *J. Nat. Gas. Sci. Eng.* 25, 271–283. doi:10.1016/j.jngse.2015.05.011

Sung, W., Lee, H., and Lee, C. (2002). Numerical study for production performances of a methane hydrate reservoir stimulated by inhibitor injection. *Energy sources.* 24 (6), 499–512. doi:10.1080/00908310290086527

Teymouri, M., Sanchez, M., and Santamarina, J. C. (2020). A pseudo-kinetic model to simulate phase changes in gas hydrate bearing sediments. *Mar. Pet. Geol.* 120, 104519. doi:10.1016/j.marpetgeo.2020.104519

Thakur, N. K. (2010). Gas hydrates as alternative energy resource - seismic methods. *Curr. Sci.* 99 (2), 181–189.

Todd, R. J., Hannegan, D. M., and Harrall, S. (2006). "New technology needs for methane hydrates production," in Paper presented at the Offshore Technology Conference, Houston, Texas, USA, May 1–4, 2006.

Tommasi, P., Avalle, A., Budillon, F., Romeo, R., Caburlotto, A., Conforti, A., et al. (2019). Evaluation of disturbance induced on soft offshore sediments by two types of gravity piston coring techniques. *Mar. Geol.* 417, 106005. doi:10.1016/j.margeo.2019.106005

Uchida, T., Ikeda, I. Y., Takeya, S., Kamata, Y., Ohmura, R., Nagao, J., et al. (2005). Kinetics and stability of CH4–CO2 mixed gas hydrates during formation and long-term storage. *ChemPhysChem* 6 (4), 646–654. doi:10.1002/cphc.200400364

Vedachalam, N., Srinivasalu, S., Rajendran, G., Ramadass, G. A., and Atmanand, M. A. (2015). Review of unconventional hydrocarbon resources in major energy consuming countries and efforts in realizing natural gas hydrates as a future source of energy. *J. Nat. Gas Sci. Eng.* 26, 163–175. doi:10.1016/j.jngse.2015.06.008

Vrielink, H. J., Bradford, J. S., Basarab, L., and Ubaru, C. C. (2008). "Successful application of Casing-While-Drilling technology in a Canadian Arctic permafrost application," in Paper presented at the IADC/SPE Drilling Conference, Orlando, Florida, USA, March 4–6, 2008.

Wang, C., Liu, Y. P., Hou, W., Liu, C., Zheng, Y. Y., and Wang, G. R. (2020). "Dynamic risk analysis on offshore natural gas hydrate production test based on DBN-GO method," in Paper presented at the The 30th International Ocean and Polar Engineering Conference, Virtual, October 11–16, 2020.

Wang, G. R., Huang, R., Zhong, L., Wang, L, Z., Zhou, S, W., and Liu, Q. Y. (2019). An optimal design of crushing parameters of marine gas hydrate reservoirs in solid fluidization exploitation. *Nat. Gas. Ind. B* 6 (3), 257–261. doi:10.1016/j.ngib.2018.10.006

Wang, G. R., Zhong, L., Liu, Q. Y., and Zhou, S. W. (2019). Research on deep-sea oil and gas hydrate exploitation technology based on double gradient double tube. *Ocean Eng. Equip. Technol.* 201, 225–233.

Wang, L., Li, Y., Wu, P., Shen, S., Liu, T., Leng, S., et al. (2020). Physical and mechanical properties of the overburden layer on gas hydrate-bearing sediments of the South China sea. *J. Pet. Sci. Eng.* 189, 107020. doi:10.1016/j.petrol.2020.107020

Wang, L. Z., Wang, G. R., Mao, L. J., Fu, Q., and Zhong, L. (2020). Experimental research on the breaking effect of natural gas hydrate sediment for water jet and engineering applications. *J. Petroleum Sci. Eng.* 184, 106553. doi:10.1016/j.petrol.2019.106553

Wang, S., Zhang, C., and Yuan, C. P. (2017). Rheological properties of polymer drilling fluid developed for permafrost natural gas hydrate drilling[J]. *Chem. Technol. Fuels Oils* 53 (2), 274–285.

Wang, Y. B., and Gao, D. L. (2022). Study on the marine environment limiting conditions of deepwater drilling for natural gas hydrate. *Appl. Energy* 312, 118802. doi:10.1016/j.apenergy.2022.118802

Wang, Y., Sun, Y. H., Lv, X. S., Jia, R., and Guo, W. (2015). Hole-bottom freezing method for gas hydrate sampling. *J. Nat. Gas. Sci. Eng.* 25, 271–283. doi:10.1016/j.jngse.2015.05.011

Wang, Z. Z., Gao, K., Sun, Y. H., Zhang, Z. H., Zhang, S. Y., Liang, Y., et al. (2016). Effects of bionic units in different scales on the wear behavior of bionic impregnated diamond bits. *J. Bionic Eng.* 13 (4), 659–668. doi:10.1016/s1672-6529(16)60337-2

Wei, J. G., Liang, J. Q., Lu, J. G., Zhang, W., and He, Y. L. (2019). Characteristics and dynamics of gas hydrate systems in the northwestern South China Sea - results of the fifth gas hydrate drilling expedition. *Mar. Petroleum Geol.* 110, 287–298. doi:10.1016/j.marpetgeo.2019.07.028

Wei, N., Zhao, J. Z., Sun, W. T., Zhou, S. W., Zhang, L. H., Li, Q. P., et al. (2019). Non-equilibrium multiphase wellbore flow characteristics in solid fluidization exploitation of marine gas hydrate reservoirs. *Nat. Gas. Ind. B* 6 (3), 282–292. doi:10.1016/j.ngib.2018.10.008

Wei, W. N., Li, B., Gan, Q., and Li, Y. L. (2022). Research progress of natural gas hydrate exploitation with CO_2 replacement: A review. *Fuel* 312, 122873. doi:10.1016/j.fuel.2021.122873

Winters, W. J., Dugan, B., and Collett, T. S. (2008). Physical properties of sediments from Keathley Canyon and Atwater Valley, JIP Gulf of Mexico gas hydrate drilling program. *Mar. Petroleum Geol.* 25 (9), 896–905. doi:10.1016/j.marpetgeo.2008.01.018

Wu, N. Y., Li, Y. L., Wan, Y. Z., Sun, J. Y., Huang, L., and Mao, P. X. (2021). Prospect of marine natural gas hydrate stimulation theory and technology system. *Nat. Gas. Ind. B* 8 (2), 173–187. doi:10.1016/j.ngib.2020.08.003

Xie, H. P., Liu, T., Gao, M. Z., Chen, L., Zhou, H. W., Ju, Y., et al. (2016). Research on *in-situ* condition preserved coring and testing systems. *Petroleum Sci.* 18 (6), 1840–1859. doi:10.1016/j.petsci.2021.11.003

Xu, Z., Hu, T., Pang, X. Q., Wang, E. Z., Liu, X. H., Wu, Z. Y., et al. (2022). Research progress and challenges of natural gas hydrate resource evaluation in the South China Sea. *Petroleum Sci.* 19 (1), 13–25. doi:10.1016/j.petsci.2021.12.007

Yamamoto, K. (2015). Overview and introduction: Pressure core-sampling and analyses in the 2012–2013 MH21 offshore test of gas production from methane hydrates in the eastern Nankai Trough. *Mar. Petroleum Geol.* 66, 296–309. doi:10.1016/j.marpetgeo.2015.02.024

Yamamoto, K., Terao, Y., Fujii, T., Ikawa, T., Seki, M., Matsuzawa, M., et al. (2014). "Operational overview of the first offshore production test of methane hydrates in the Eastern Nankai Trough," in Paper presented at the Offshore Technology ConferenceMay 5–8, 2014, Houston, Texas, USA.

Yamamoto, K., Wang, X. X., Tamaki, M., and Suzuki, K. (2019). The second offshore production of methane hydrate in the Nankai Trough and gas production behavior from a heterogeneous methane hydrate reservoir. *RSC Adv.* 9 (45), 25987–26013. doi:10.1039/c9ra00755e

Yang, M. J., Gao, Y., Zhou, H., Chen, B. B., and Li, Y. H. (2019). Gas production from different classes of methane hydrate deposits by the depressurization method. *Int. J. Energy Res.* 43 (10), 5493–5505. doi:10.1002/er.4669

Yang, S., Liang, J., Lei, Y., Gong, Y., Xu, H., Wang, H., et al. (2017). GMGS4 gas hydrate drilling expedition in the South China Sea. *Fire Ice Methane Hydrate Newsl.* 17, 1–5.

Ye, H. Y., Wu, X. Z., and Li, D. Y. (2021). Numerical simulation of natural gas hydrate exploitation in complex structure wells: Productivity improvement analysis. *Mathematics* 9 (18), 2184. doi:10.3390/math9182184

Ye, J. L., Qin, X. W., Xie, W. W., Lu, H. l., Ma, B. j., Qiu, H. j., et al. (2020). The second natural gas hydrate production test in the South China Sea. *China Geol.* 3 (2), 197–209. doi:10.31035/cg2020043

Yevgeny, S., Volodymyr, K., and Valentina, Y. (2021). Mud-volcanic deposits of methane gas hydrates" in the Black Sea. *E3S Web Conf.* 230, 01005. doi:10.1051/e3sconf/202123001005

Yu, T., Guan, G. Q., Abudula, A., Wang, D. Y., and Song, Y. C. (2021). Numerical evaluation of free gas accumulation behavior in a reservoir during methane hydrate production using a multiple-well system. *Energy* 218, 119560. doi:10.1016/j.energy.2020.119560

Yuha, Y. B. M., Lal, B., Bavoh, C. B., and Keong, L. K. (2021). A comparison study on the performance between Tetrametylammonium chloride and PolyvinylPyrrolidone as drilling mud additives for gas hydrates. *Mater. Today Proc.* 47 (6), 1258–1262. doi:10.1016/j.matpr.2021.02.791

Zamora-Ledezma, C., Narváez-Muñoz, C., Guerrero, V. H., Medina, E., and Meseguer-Olmo, L. (2022). Nanofluid formulations based on two-dimensional nanoparticles, their performance, and potential application as water-based drilling fluids. *ACS Omega* 7 (24), 20457–20476. doi:10.1021/acsomega.2c02082

Zeng, Z. W., Zhu, H. T., Yang, X. H., and Cao, X. R. (2022). Three-dimensional seismic analysis of a polygonal fault system (PFS) in the Northern Carnarvon Basin, Australia: Implications for fluid flow migration and gas hydrate system. *J. Petroleum Sci. Eng.* 215, 110602. doi:10.1016/j.petrol.2022.110602

Zhang, J. H., Fan, B., and Liu, R. J. (2020). Current situation and drilling technology of gas hydrate drilling. *Sci. Technol. Eng.* 20 (35), 14343–14351. (in Chinese).

Zhang, L., Feng, R., Geng, S. H., Meng, M. M., Li, X., Ren, B., et al. (2021). Influence of geological structures on hydrate accumulation in subsea shallow formations. *J. Nat. Gas Sci. Eng.* 90, 103898. doi:10.1016/j.jngse.2021.103898

Zhang, P. P., Zhang, Y. Q., Zhang, W. H., and Tian, S. C. (2022). Numerical simulation of gas production from natural gas hydrate deposits with multi-branch wells: Influence of reservoir properties. *Energy* 238, 121738. (Part A). doi:10.1016/j.energy.2021.121738

Zhang, X. X., Peng, J. M., Sun, M. Z., Gao, Q., and Wu, D. Y. (2016). Development of applicable ice valves for ice-valve-based pressure corer employed in offshore pressure coring of gas hydrate-bearing sediments. *Chem. Eng. Res. Des.* 111, 117–126. doi:10.1016/j.cherd.2016.05.001

Zhang, Y. B., Qiu, Z. S., Zhao, X., Zhong, H., Huang, W., and Mu, J. (2021). Experimental study on ultra-low temperature drilling fluid in Arctic permafrost. *Polar Sci.* 28, 100645. doi:10.1016/j.polar.2021.100645

Zhang, Y. Q., Liang, J., Li, K., Wang, H. B., Li, X. M., and Wu, J. X. (2014). Research progress of drilling coring and mining on the permafrost natural gas hydrates in China. *Procedia Eng.* 73, 362–367. doi:10.1016/j.proeng.2014.06.210

Zhang, Y. Q., Zhang, L. X., and Wang, H. B. (2015). "The reverse circulation (RC) drilling techniques for the mineral resources exploration and production in ocean," in *Paper presented at the eleventh ocean mining and gas hydrates symposium* (Hawaii, USA: Kona). Paper Number: ISOPE-M-15-207.

Zhang, Y. Q., and Zhu, Y. H. (2011). Research and application of the natural gas hydrate drilling technique in Qilian Mountain permafrost. *Geol. Bull. China* 30 (12), 1904–1909. (in Chinese with English Abstract).

Zhao, X., Qiu, Z. S., Zhao, C., Xu, J., and Zhang, Y. (2019). Inhibitory effect of water-based drilling fluid on methane hydrate dissociation. *Chem. Eng. Sci.* 199, 113–122. doi:10.1016/j.ces.2018.12.057

Zhong, G. F., Zhang, D., and Zhao, L. X. (2021). Current states of well-logging evaluation of deep-sea gas hydrate-bearing sediments by the international scientific ocean drilling (DSDP/ODP/IODP) programs. *Nat. Gas. Ind. B* 8 (2), 128–145. doi:10.1016/j.ngib.2020.08.001

Zhou, S. W., Li, Q. P., Chen, W., Zhou, J. L., Wei, N., Guo, P., et al. (2018). Optimal design of the engineering parameters for the first global trial production of marine natural gas hydrates through solid fluidization. *Nat. Gas. Ind. B* 5 (2), 118–131. doi:10.1016/j.ngib.2018.01.004

Zhou, S. W., Li, Q. P., Lv, X., Fu, Q., and Zhu, J. (2022). Key issues in development of offshore natural gas hydrate. *Front. Energy* 14 (3), 433–442. doi:10.1007/s11708-020-0684-1

Zhu, H. Y., Liu, Q. Y., Deng, J. E., Wang, G. R., Xiao, X. H., Jiang, Z. L., et al. (2011). Pressure and temperature preservation techniques for gas-hydrate-bearing sediments sampling. *Energy* 36 (7), 4542–4551. doi:10.1016/j.energy.2011.03.053

Zhu, H. Y., Liu, Q. Y., Wang, G. R., Xiao, X. H., Zhu, X. H., Jiang, Z. L., et al. (2013). A pressure and temperature preservation system for gas-hydrate-bearing sediments sampler. *Petroleum Sci. Technol.* 31 (6), 652–662. doi:10.1080/10916466.2010.531352

Zhu, Y. H., Zhang, Y. Q., Fang, H., Lu, Z. Q., Pang, S. J., Zhang, S., et al. (2020). Research progress of natural gas hydrate in China. *Geol. Surv. China* 7 (04), 1–9. (in Chinese).

Zou, C. N., Yang, Z., He, D. B., Wei, Y. S., Li, J., Jia, A., et al. (2018). Theory, technology and prospects of conventional and unconventional natural gas. *Petroleum Explor. Dev.* 45 (04), 604–618. doi:10.1016/s1876-3804(18)30066-1

frontiers | Frontiers in Earth Science

TYPE Original Research
PUBLISHED 27 September 2022
DOI 10.3389/feart.2022.1014976

OPEN ACCESS

EDITED BY
Zhifeng Wan,
Sun Yat-sen University, China

REVIEWED BY
Jiliang Wang,
Institute of Deep-Sea Science and Engineering (CAS), China
Yajuan Yuan,
South China Normal University, China
Junxi Feng,
Guangzhou Marine Geological Survey, China

*CORRESPONDENCE
Huaiyan Lei,
lhy@xmu.edu.cn

SPECIALTY SECTION
This article was submitted to Sedimentology, Stratigraphy and Diagenesis,
a section of the journal Frontiers in Earth Science

RECEIVED 09 August 2022
ACCEPTED 31 August 2022
PUBLISHED 27 September 2022

CITATION
Kong Y, Lei H, Cheng W, Wang B, Pan F and Huang F (2022), Shifting microbial communities perform anaerobic oxidation of methane and methanogenesis in sediments from the Shenhu area of northern south China sea during long-term incubations.
Front. Earth Sci. 10:1014976.
doi: 10.3389/feart.2022.1014976

Shifting microbial communities perform anaerobic oxidation of methane and methanogenesis in sediments from the Shenhu area of northern south China sea during long-term incubations

Yuan Kong[1], Huaiyan Lei[2]*, Weidong Cheng[2], Bin Wang[2], Fulong Pan[2] and Fanfan Huang[2]

[1]Fujian Key Laboratory on Conservation and Sustainable Utilization of Marine Biodiversity, Fuzhou Institute of Oceanography, Minjiang University, Fuzhou, China, [2]Department of Geological Oceanography, College of Ocean & Earth Science, Xiamen University, Xiamen, China

Microbial communities and their associated metabolic activities, methanogenesis and anaerobic oxidation of methane (AOM), are the key components of carbon biocycles in continental margin sediments. The composition and diversity of microbial communities in a methanic environment have been widely investigated, but identifying direct correlations between microbial communities and their activities remains a challenge. Here, we investigated shifting microbial communities that performed methanogenesis and AOM in long-term incubations (the longest is up to 199 days). AOM, methanogenesis, sulfate reduction and iron reduction occurred during the incubation, and 16S rRNA gene sequencing showed that some bacteria were maintained or even enriched during the incubation compared to the environmental samples. In contrast, archaeal diversity was reduced, and only some uncultured archaea belonging to the phylum Bathyarchaeota were enriched after treatment with a high sulfate concentration (29.38 mM), suggesting that sulfate might promote their enrichment. Well-known anaerobic methanotrophic archaea (ANME) were not detected, and SEEP-SRB1, which is in syntrophy with ANME, decreased to approximately zero after the incubation. The abundance of known methanogens, such as genera *Methanococcoides* and *Methanosarcina*, increased slightly in some incubations but was still present at a low relative abundance (<0.15%). Incubation with a lower sulfate concentration (4 mM) and higher iron content resulted in greater $\delta^{13}CO_2$ accumulation, indicating that iron may be the additional electron acceptor for AOM. Based on these results, other unknown or unconventional phylotypes or pathways of methanogenesis and AOM may occur during the incubation. Thus, the diversity of methanogens and anaerobic methanotrophs warrants further investigation.

KEYWORDS

anaerobic oxidation of methane, methanogenesis, microbial communities, incubation, marine sediments

1 Introduction

Marine sediments on continental margins often contain substantial concentrations of organic carbon, which can be used by microbes for methane production (Ferry and Lessner, 2008; Zhuang et al., 2018). The produced methane may be gaseous sources of methane hydrate (Paull et al., 1994; Davie and Buffett, 2003) or even migrates out of the sedimentary column to the seawater or atmosphere (Reeburgh, 2007; Ferry and Lessner, 2008). However, most methane produced by microbe methanogenesis or seeping from gas hydrate is removed by microbial-mediated anaerobic oxidation of methane (AOM) (Reeburgh, 2007; Regnier et al., 2011; Egger et al., 2018). Therefore, AOM is considered the major biological sink of methane in marine sediments (Hinrichs and Boetius, 2003), and methanogenesis and AOM are the key components of carbon biogeocycles in continental margin sediments (Barnes and Goldberg, 1976).

AOM depends on the reduction of electron acceptors, such as SO2- 4 (Martens and Berner, 1974; Joye et al., 2004), NO- 3/NO- 2 (Ettwig et al., 2010) and Fe^{3+}/Mn^{4+} (Beal et al., 2009; Joye, 2012; Egger et al., 2015). Moreover, the discovery of the artificial electron acceptor, 9,10-anthraquinone-2,6-disulfonate (AQDS), in marine sediments enabled anaerobic methanotrophic archaea (ANME) to survive alone. And that suggests potential independence of respiratory AOM (Rotaru and Thamdrup, 2016; Scheller et al., 2016). The microbes known to be responsible for sulfate-dependent AOM are ANME and sulfate-reducing bacteria (SRB) (Hinrichs et al., 1999; Boetius et al., 2000; Orphan et al., 2001). Candidatus *Methylomirabilis oxyfera* (*M. oxyfera*) and Candidatus *Methanoperedens nitroreducens* (*M. nitroreducens*) are responsible for nitrate dismutation-coupled AOM (Ettwig et al., 2010). Candidatus *Methanoperedens ferrireducens* can use Fe^{3+} as the terminal electron acceptor to mediate AOM (Cai et al., 2018) and members of the Methanoperedenaceae, Candidatus *Methanoperedensmanganicus* and Candidatus *Methanoperedens manganireducens*, can be responsible for Mn (IV)-dependent AOM (Leu et al., 2020). Moreover, studies using culture-independent biomolecular techniques have shown that the dominant microorganisms vary in the niche where AOM may occur, including subsurface sediments within the sulfate-methane transition zone (SMTZ) from gas hydrate-bearing areas and cold seep system sediments and the total prokaryotic population of ANME increases or is missing in the SMTZ. Bacterial groups, such as the JS1 group, Planctomycetes, and Chloroflexi are not typically associated with AOM and are also enriched in these environments (Inagaki et al., 2006; Reed et al., 2009; Pachiadaki and Kormas, 2013; Yanagawa et al., 2014; Gong et al., 2017; Cui et al., 2019). These findings prompted questions regarding the AOM and the microorganisms responsible.

Hence, we performed incubations with sediments from three different sites in potential gas hydrate-bearing areas in the northern South China Sea, and we treated the mixtures with $^{13}CH_4$. Because the sediments from the three sites included in the incubations received a large amount of organic carbon inputs (>1%) (Supplementary Table S1), we treated the incubations with a low sulfate condition characteristic of the SMTZ to eliminate the potential utilization of other substrates (mainly organic matter) in addition to methane, as previously reported (Webster et al., 2011). However, as we reported in a previous study, AOM might be conducted above the SMTZ, where the sulfate concentration is relatively high (up to 18.76 mM) (Kong et al., 2021). We also established incubations treated with a high sulfate concentration to assess other potential microbial activities and their effects on microbial diversity and abundance. After the incubation, we used high-throughput sequencing data from microbial 16S rRNA gene amplicons in the incubation slurries and related environmental samples to analyze the shifting microbial communities and their implications.

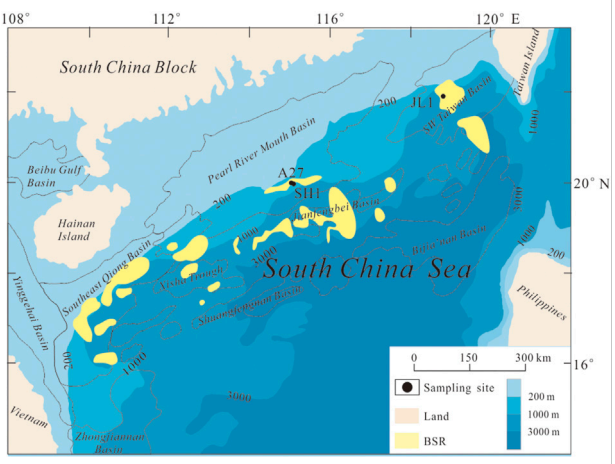

FIGURE 1
Sampling site. The bottom stimulating reflector (BSR) distribution is delineated from previous literature (Wu N. et al., 2013).

2 Materials and methods

2.1 Sampling site and geochemical setting

Three sediment cores were collected during the "NORC 2018-05" cruise conducted by the "TAN KAH KEE" research vessel in 2018 in the northeastern South China Sea. The A27 and SH1 sites were sampled at sea water depths of 677 m below sea level (mbsl) and 1,451 mbsl, respectively, within the bottom stimulating reflector (BSR, one of the signs to determine the potential gas hydrate-bearing) distribution in the Shenhu area (Figure 1). This area is considered a location favorable for gas hydrate formation and conservation (Lu et al., 2011), and gas

hydrate has been recovered during multiple drilling expeditions (Wu et al., 2011; Zhang et al., 2015; Zhang et al., 2017). The depth of sulfate-methane transition (SMT) in this area ranges from 7.7 m below the sea floor (mbsf) to 87.9 mbsf, and most of the SMT is shallower than 50 mbsf (Wu L. et al., 2013). The SMT at sites A27 and SH1 was predicted to be located at depths of 10.76 mbsf and 9.63 mbsf, respectively, according to the linear fitting of SO2- 4 concentrations from 4 mbsf (Kong et al., 2021). The JL1 site was sampled at a sea water depth of 3,011 mbsl near the 973-4 site, which has been reported to be influenced by gas hydrate decomposition and AOM, and the SMT was located at 9 mbsf (Liu et al., 2018; Zhang et al., 2018). We selected sediments at 4.9–5.0 mbsf from A27, 4.2–4.3 mbsf from SH1 and 5.05–5.15 mbsf from JL1, and we used samples from A27 to assess the effects of the sulfate concentration on the activities, diversity and abundance of microbial communities. According to our preliminary research, the depths of all these sediments did not reach the SMT (Liu et al., 2018; Zhang et al., 2018; Kong et al., 2021) but still they had the ability to perform AOM (Kong et al., 2021). The detailed geochemical conditions of the sampling layers are included in the Supplementary material (Supplementary Table S1).

2.2 Sample collection and storage

After retrieval, the sediment core was cut into two halves. One of the two halves was used to collect environmental samples for DNA extraction. Samples were cut with a sterile knife, stored in a sterile centrifuge tube, placed into a liquid nitrogen tank after the collection of 10 samples and transferred to a −80°C freezer after one sediment core was sampled. The other half was used to collect incubation and other geochemical samples. The incubation sediment samples were sliced at intervals of 10 cm with a sterile knife, placed into two sterile Zip-lock homogenous plastic bags with no headspace and preserved at 4°C in a deck refrigerator. All sampling was performed in the laboratory of the cabin during the voyage. After the field expedition, DNA samples were transported on dry ice, and the incubation samples were transported on ice to the Marine Geological Laboratory, Department of Geological Oceanography, Xiamen University where they were stored at −80°C or 4°C.

2.3 Incubation experiment

The incubation experiments were started 4 months after sampling. For the initial experimental protocol, 7 experimental and control incubation bottles were prepared for each study sediment core. We periodically extracted the headspace gas from one experimental and one control bottle and then opened it to take water and mud samples for major ion and microbial tests. However, after three tests, the headspace gas test results were unstable but showed obvious $^{13}CO_2$ accumulation, indicating that this scheme was not feasible. Therefore, we changed the protocols to periodically extract the headspace gas and supernatant from one bottle and test the indicators. Therefore, we randomly selected one of the remaining culture bottles from every site as the parallel experiment for the third test culture bottle. So each culture group (two parallel experiments and one control) was pretreated as follows (calculated according to the modified experimental protocol): 51 g of wet sediments (~45 ml) in each selected layer was homogenized in 135 ml of bottom seawater (treated with or without $BaCl_2$), then 5 ml of this suspension were extracted each time and placed separately into 3 culture bottles, and finally 60-ml suspension was distributed in approximately 110-ml culture bottles. The approximate ratio of sediment to medium was selected according to previously reported incubation studies (Beal et al., 2009; Segarra et al., 2013; Egger et al., 2015). The bottom seawater was collected at site A27 using a conductivity-temperature-depth (CTD) instrument. The sulfate concentration of the bottom seawater was 29.38 mM. The bottom seawater treated with $BaCl_2$ was filtered twice with membrane filters (0.2 μm) after being well mixed to remove $BaSO_4$, resulting in approximately 4 mM sulfate. All bottom seawater samples treated with or without $BaCl_2$ were filter-sterilized and degassed with N_2 (99.999%; the same nitrogen was used throughout the study) before mixing with sediments. After the contents were mixed, the culture bottles were sealed with airtight butyl rubber stoppers and secured with open-top Al screw caps. After sealing, the contents were purged with nitrogen for 20 min. After all pretreatment procedures, 50 ml of labeled methane (99% $^{13}CH_4$ and 1% $^{12}CH_4$) and nitrogen were injected into the headspace of the experimental and control groups, respectively, to yield 2 bar overpressures (volume headspace ≈50 ml). Each incubation was numbered (see details in Table 1) and incubated in the dark at 20°C with shaking (300 r/min).

2.4 Headspace sampling and analysis

Headspace samples were taken periodically. The CO_2 content and the $\delta^{13}C$-CO_2 in the headspace of all samples were analyzed with a gas chromatograph (Agilent 6,820, United States) coupled to a mass spectrometer (Delta V Advantage, Thermo Fisher, Bremen, Germany). The analysis column was a Poraplot Q-type capillary column, and He was used as the carrier gas. The heating procedure was as follows: an initial temperature of 50°C, a constant temperature for 2 min, an increase in temperature 180°C at a rate of 25°C/min, and a constant temperature for 8 min. The assay was repeated three times. The test results are presented as the content of $\delta^{13}C_{CO2}$ (in ‰ vs. Vienna Peedee Belemnite (VPDB); precision and accuracy were ±0.2‰) and R, which was defined as $^{13}C/^{12}C$. The headspace CH_4 concentration

TABLE 1 Conditions and serial number of each incubation sample.

Samples		Experimental group	Conditions			Control group	Conditions		
Sites	Depths/ mbsf		SW	SW*	$^{13}CH_4$		SW	SW*	N_2
SH1	4.2–4.3	SH1_mc1		√	√	SH1_cntl		√	√
		SH1_mc2		√	√				
JL1	5.05–5.10	JL1_mc1		√	√	JL1_cntl		√	√
		JL1_mc2		√	√				
A27	4.9–5.0	A27s_mc1	√		√	A27s_cntl	√		√
		A27s_mc2	√		√				
		A27_mc1		√	√	A27_cntl		√	√
		A27_mc2		√	√				

SW*, bottom seawater treated with $BaCl_2$, filtered twice with membrane filters (0.2 μm) to remove $BaSO_4$ and filter-sterilized, resulting in approximately 4 mM sulfate; mc, methane consuming group; cntl, control groups; mc1 and mc2 are the duplicate samples in the methane-consuming groups.

in the control groups was analyzed in the final sampling period with a gas chromatograph (with a pyrolysis furnace at 960°C and reducing furnace at 600°C) coupled to a mass spectrometer using a HP-PLOT Q column with helium as the carrier gas (flow rate of 1.5 ml/min). The measurement error was< 3% (obtained by repeated the test testing twice for each sample). The CH_4 concentrations in the headspace were then converted to dissolved CH_4 contents as previously reported (Johnson et al., 1990). All tests were performed at the Third Institute of Oceanography, Ministry of Natural Resources.

Because $^{13}CH_4$ was the only stable isotope tracer added during the incubation, we defined that the $^{13}CO_2$ that formed in the headspace was fully converted from $^{13}CH_4$ oxidation. The fractional abundances of $^{13}CO_2$ [$^{13}F=^{13}C/(^{12}C+^{13}C)$] were used to quantify the AOM activity as previously reported (Beal et al., 2009; Scheller et al., 2016; Bray et al., 2017). The AOM rates were calculated during the period of the linear increase in $^{13}CO_2$ formation (Beal et al., 2009; Egger et al., 2015; Scheller et al., 2016; Bray et al., 2017). However, accurate quantification of the concentration of inorganic carbon formed from methane oxidation is challenging (Scheller et al., 2016). Therefore, we estimated inorganic carbon formed from the total headspace CO_2 and the dissolved CO_2 in the incubation liquid, which were calculated according to Henry's law based on only the loss due to each headspace sampling procedure.

2.5 Supernatant sampling and analysis

Supernatant samples were collected after every headspace sampling procedure and allowed to stand until the supernatant was clarified. Approximately 2 ml of supernatant liquid was drawn out by the disposable syringe with a long sterile needle (20G, inner, 0.6 mm, outter, 0.9 mm). The supernatant liquid was used to analyze the SO2- 4 concentration by ion chromatography (IC) in a 100-fold diluted sample (0.01 ml of supernatant liquid with 9.99 ml of de-oxygenated UHQ water) as Zhang et al. (2015) and the Fe^{2+} concentration was measured by the UV spectrophotometry in a 5-fold diluted sample (0.5 ml of supernatant liquid with 2 ml of ion chromatography). Utilized 0-phenanthroline reacted with Fe^{2+} then colorated, a wave-length of 510 nm was determined by UV-absorption spectroscopy. Linear and well reproducible calibration curves were obtained in the concentration range of 0–5 mg/L Fe^{2+} standard solution made by Fe^{3+} standard solution with 10% Hydroxylamine Hydrochloride. The standard deviation of this method was found less than 2%.

2.6 Community DNA extraction and purification

We collected 2.5 ml of slurry from every incubation after the final headspace gas sample was collected, and we centrifuged the samples at 12,000 g for 5 min and removed the supernatant. DNA was extracted from 0.5 g of sediment using the E.Z.N.A. Soil DNA Kit (OMEGA, United States) according to the manufacturer's instructions.

2.7 PCR amplification and 16S rRNA gene amplicon sequencing

The V4 regions of the 16S rRNA genes were amplified using the ArBa515F (5′-GTGCCAGCMGCCGCGGTAA-3′) and Arch806R (5′-GGACTACVSGGGTATCTAAT-3′) primers, which target conserved sequences present in bacteria and archaea (Bates et al., 2011). Based on the preliminary

experiments, we used the TransGen AP221-02: TransStart Fastpfu DNA Polymerase (20 μL) system, and the minimum number of thermal cycles was set to 27. The thermal cycling conditions were as follows: initial denaturation at 95°C for 3 min; 27 cycles of denaturation at 95°C for 30 s, annealing at 55°C for 30 s and extension at 72°C for 45 s; elongation at 72°C for 10 min; and a hold at 10°C. The correct size of the amplicons (~250 bp) was verified by 2% agarose gel electrophoresis and purification using Diffinity RapidTips (Sigma-Aldrich, United States). Purified amplicons were sequenced using the Illumina MiSeq platform at Majorbio Bio-Pharm Technology Co., Ltd., Shanghai, China, according to standard protocols.

The methyl coenzyme reductase subunit A (*mcrA*) geneencodes the key enzyme in methane metabolism in all well-known methanogens (Luton et al., 2002). We amplified the functional *mcrA* gene after final headspace sampling using the 5′-GGTGGTGTMGGATTCACACARTAYGCWACAGC-3′ and 5′-TTCATTGCRTAGTTWGGRTAGTT-3′ primers as previously reported (Luton et al., 2002). The Double Taq Plus Master Mix (10 μL) system was used, and the minimum number of thermal cycles was set to 37. The thermal cycling conditions were as follows: initial denaturation at 95°C for 3 min; 37 cycles of denaturation at 95°C for 30 s, annealing at 53°C/55°C/58°C for 30 s and extension at 72°C for 45 s; elongation at 72°C for 10 min; and a hold at 10°C.

2.8 Phylogenetic analyses

Raw fastq files were quality-filtered using QIIME61 (version 1.9.1 http://qiime.org/install/index.html). Reads that were unable to be assembled were rejected. Operational taxonomic units (OTUs) were clustered by UPARSE (version 11 http://drive5.com/uparse/) with 97% similarity. After quality filtering and clustering, OTUs at the 97% identity level were obtained, and phylotypes were assigned an identity based on comparisons with sequences in the SILVA (SSU111) database (http://www.arb-silva.de). After each sample was normalized to the minimum OTUs, the alpha diversity, Good's coverage, beta diversity, composition and abundance analyses of the libraries were completed. The data preprocessing and OTU-based analysis were performed using Mothur (version v.1.30.1 http://www.mothur.org/wiki/Schloss_SOP#Alpha_diversity) and the R language toolkit at the free online Majorbio I-Sanger Cloud Platform (www.i-sanger.com).

2.9 Sequencing results and deposition

Source sequences are available in the Sequence Read Archive (SRA) database under the accession number PRJNA627291.

3 Results

3.1 Biogeochemical process in incubations

Initially, we used incubations injected with N_2 in the headspace as the controls for incubations injected with $^{13}CH_4$. At the end of the incubation period, however, CH_4 concentrations were present in the headspace of the control groups. This result indicated that methanogenesis occurred in the controls during the incubation. Compared to the controls, the experimental groups exhibited a significant accumulation of $^{13}CO_2$ in the headspace gas, indicating that the AOM occurred. Meanwhile, the SO2- 4 and Fe^{2+} concentrations in the supernatant of each incubation fluctuated revealing that sulfate reduction and iron reduction occurred during the incubation.

Methanogenesis: At the end of the 117-days incubation, we measured the headspace methane content of all control groups. Methane production rates were calculated over the period of linear increase of the dissolved CH_4 concentration. The headspace of all control groups contained a certain methane concentration (52.56–193.81 ppm, Table 2). The A27s group produced less methane than theA27, and the SH1 group produced more methane than the A27 group. The methane production rate in each group was calculated. SH1_cntl had the highest methane production (81.67 nmol/g/yr) followed by A27_cntl (62.27 nmol/g/yr), A27s_cntl (58.86 nmol/g/yr) and JL1_cntl (22.15 nmol/g/yr).

Anaerobic methane oxidation: Using the calculation method mentioned in the Methods section, the headspace gas tests and calculations are provided in the supplementary material (Supplementary Table S2). As shown in Figure 2, all the experimental groups showed much greater $^{13}CO_2$ enrichment but much lower total CO_2 production than the control groups. The headspace CO_2 concentration did not change accordingly with $^{13}F_{CO2}$. Moreover, the A27s group produced more CO_2 than the A27 group. However, the patterns among A27, SH1 and JL were difficult to distinguish. We determined the AOM rate in the experimental group to be 4.5353–27.0239 nmol/g/yr. At each stage, the AOM rate in group A27 was higher than that in the other two site groups, and the A27s group showed a slightlly higher AOM rate than the A27 group.

Sulfate reduction: The sulfate concentration in the supernatant showed a fluctuating trend during the incubation (Figure 3A). A clear pattern of change was not observed in the comparison. However, a clear decreasing was detected in some experimental groups (A27, A27s, and SH) at the end of incubation.

Iron reduction: Figure 3B shows the increasing trend for the Fe^{2+} concentration in the supernatant at the early stage, especially during the period from 94 to 117 days, and the Fe^{2+} content increased rapidly. However, the Fe^{2+} concentration decreased in all experimental groups. In addition, the Fe^{2+} concentration in the supernatant exhibited a decreasing trend in almost of the

TABLE 2 Headspace CH_4 content and calculation of dissolved CH_4 in the control groups.

Sample numbers	Test results/ppm	Calculated results/μmol/L
JL1_cntl	52.56	2.3015
SH1_cntl	193.81	8.4865
A27s_cntl	139.69	6.1167
A27_cntl	147.78	6.4710

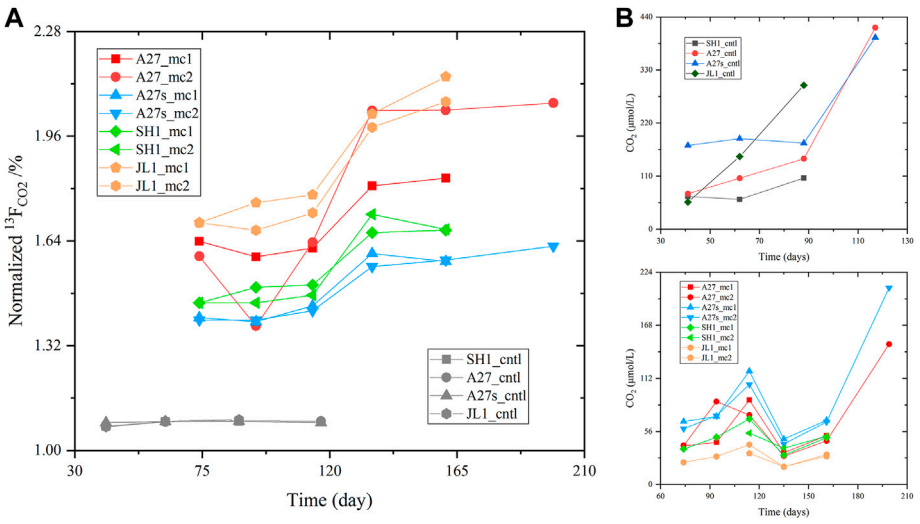

FIGURE 2
Time course of tested **(A)** normalized $^{13}F_{CO2}$ ($^{13}CO_2/(^{12}CO_2+^{13}CO_2)$, which was calculated based on the $\delta^{13}C$-CO_2 measured during the incubation period) and **(B)** CO_2 concentrations in the headspace. The serial number of each incubation sample and its corresponding incubation conditions are listed in Table 1.

control groups (Figure 3B). The trends in all experimental groups indicated that iron reduction occurred during the first 117 days. The decreasing Fe^{2+} concentration in the late stage (after 117 days) may have been caused by precipitation with other elements.

3.2 Microbial taxonomy

3.2.1 Taxonomic composition

To determine the differences of microbial diversity after the incubation, 16S rRNA gene libraries were constructed with the DNA extracted from the 8 slurry samples and 3 corresponding environmental sediment samples collected at the following depths: 5.0 mbsf in the A27 core, 4.2 mbsf in the SH1 core and 5.15 mbsf in the JL1 core. A total of 621,679 sequences were obtained after quality filtering. After clustering, each sample was normalized to the minimum sequences (35,449), and 389,939 sequences were included in the final OTU table (Supplementary Table S3). Estimators of alpha diversity were calculated after normalization, and Good's coverage indexes were 0.9785–0.9961 (Supplementary Table S4), indicating an adequate sequencing depth, which was further confirmed by rarefaction analysis (Supplementary Figure S5).

The species richness (Chao 1 and sobs indexes) and evenness (Shannon and Simpson indexes) of the microbial communities showed a decreasing trend in the slurry samples compared to those in the environmental sediment samples (Figure 4). Groups amended with sufficient SO2- 4 (A27s and A27s_cntl, 29.38 mM) showed higher values than those amended with low SO2- 4 concentrations (A27 and A27_cntl, 4 mM), and the experimental groups (A27_mc, A27s_mc, SH1_mc and JL1_mc) typically showed lower values than controls (A27_cntl, A27s_cntl, SH1_cntl and JL1_cntl).

The cluster analysis reflected the effects of incubation conditions for the incubation slurries and environmental sediment communities. The incubation slurries amended with different SO2- 4 concentrations were distinctly separated from one another (Figure 5A).

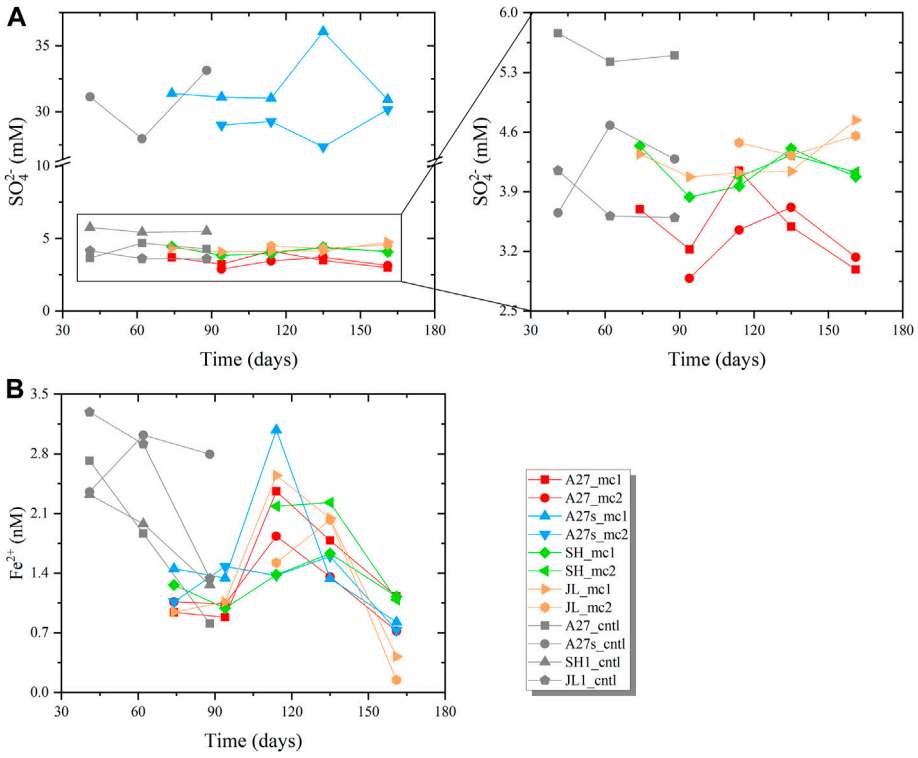

FIGURE 3
Time course of **(A)** the measured SO2- 4 concentrations and **(B)** Fe^{2+} concentrations in the supernatant liquid. The enlarged graph in **(A)** on the right shows the detailed changes observed in incubations with treated bottom seawater. Because the incubation scheme was modified, the supernatant of the control groups was only sampled three times, and the sampling times were inconsistent with the experimental group.

Seventy-four prokaryotic phyla were identified from the 16S rRNA gene sequences (Supplementary Table S3). Phyla with less than 0.5% abundance were classified as others, and the abundance of each phylum is shown in Figure 5B. The changes in community structure after incubation were mainly focused on the abundance of bacteria. The proportion of the phyla Proteobacteria, Bacteroidetes, Firmicutes, Actinobacteria, Latescibacteria, and Gemmatimonadetes increased after the incubation, and the proportions of other bacteria decreased but were maintained at a certain value. In contrast, the abundances of archaea were mainly reduced after incubation. Archaea sequences belonging to Bathyarchaeota, Lokiarchaeota, Hadesarchaea, Euryarchaeota, Thaumarchaeota, and Woseearchaeota (DHVEG-6) were maintained after incubation.

The 5 most dominant OTUs of bacteria in the incubation samples belonged to the genera *Pseudomonas*, *Halomonas*, *Marinobacter*, family Sva1033 and order Clostridiales. The 5 most dominant OTUs of archaea in the incubation samples belonged to the phyla Bathyarchaeota, Lokiarchaeota, and Hadesarchaea. Only OTU2228 and OTU 5554 were enriched after the incubation, and they belonged to uncultured or unclassified Bathyarchaeota. The lineages of OTU 2228 and OTU 5554 were similar to those of the MCG-B and MCG-C groups, respectively (Figure 6B). The proportion of OTU 2228 increased from 7.40% (A27_env) before incubation to 9.23% (A27s_mc) in the A27 incubations amended with sufficient sulfate. OTU 5554 was slightly enriched in JL1_mc (from 0.06% in the environmental sample to 0.10% in the slurry) and was maintained at a certain proportion in other groups. The proportion of other OTUs belonging to the phylum Bathyarchaeota were slightly decreased but maintained certain abundances during the incubation (Figure 6A). Enriched OTUs of phylum Bathyarchaeota were present in the experimental and control sediments amended with a sufficient sulfate concentration (29.38 mM), and a higher proportion of phylum Bathyarchaeota was present in groups treated with a sufficient sulfate concentration (29.38 mM) compared to groups treated with a low sulfate concentration (4 mM).

3.2.2 Diversity and community structure of methanogens and ANME

Well-known ANME sequences were not detected in any of the samples. Well-known methanogens in the phylum Euryarchaeota, genera *Methanococcoides*, *Methanobrevibacter*, *Methanosarcina* and *Methanobacterium* were detected in the incubation groups (Supplementary Table S3). However, the proportion of these genera were low, and the highest value

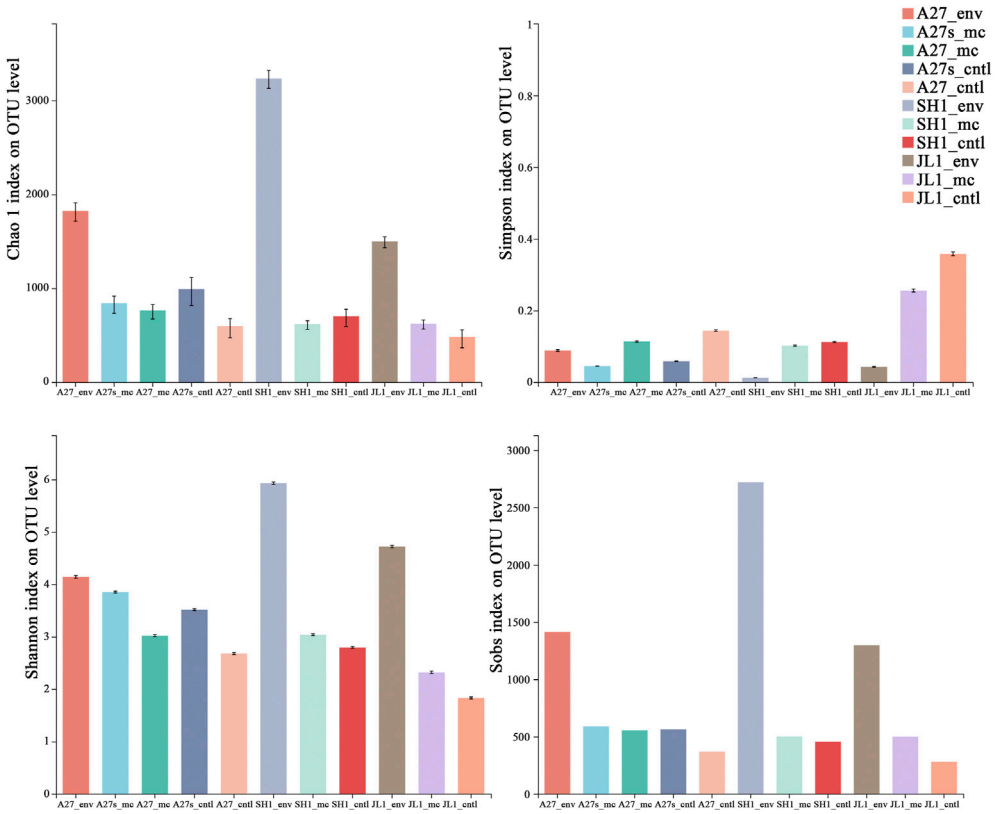

FIGURE 4
Alpha diversity estimators of microbial community 16S gene sequences at the OTU level for environmental sediment samples (sampling site_env) and the related incubation slurry samples amended with $^{13}CH_4$ (sampling site_mc) and N_2 (sampling site_cntl).

was only 0.15% (A27s_mc). Compared to the environmental samples, the abundance of some methanogens belonging to uncultured or unclassified species in the genera *Methanococcoides* and *Methanosarcina* increased, but none were present across all samples from the control groups. We also attempted toamplify *mcrA* from the DNA samples from all incubation slurries under three different annealing conditions (50/55/58°C), but all failed. Considering the amount of sample available, we did not perform further experiments.

3.2.3 Taxonomic comparison

We divided the 11 samples into the following 3 groups to perform the one-way ANOVA: environmental group (Env), incubation group amended with $^{13}CH_4$ (Exp) and incubation group amended with N_2 (Cntl). In terms of the top 15 relative abundances of microorganisms at the phylum level, the phyla Proteobacteria and Chloroflexi presented significant differences ($0.01 < p$ value < 0.05)between the three groups of samples (Figure 7A). In terms of the top 15 relative abundances of microorganisms at the genus level, the genera *Halomonas*, *Marinobacter*, and norank genus in MSBL9 presented significant differences ($0.001 < p$ value < 0.05) among the three groups (Figure 7B).

No significant differences in archaea and bacteria were observed at the phylum level between the experimental groups and control groups. At the genus level, however, the low abundance genera *Alcanivorax*, *Streptomyces*, *Filomicrobium* and *Pelomonas* presented significant differences (Supplementary Figure S6). We also compared the differences in microbial communities between the two experimental incubation slurries and their controls treated with different sulfate concentrations. A higher proportion of archaea was present in the experiment and control samples treated with high sulfate concentrations (29.38 mM) (Supplementary Figure S7).

4 Discussion

4.1 Enriched microorganisms and implications

In the present study, the enriched microorganisms differed from those previously reported in previous studies using incubations to detect AOM (Beal et al., 2009; Webster

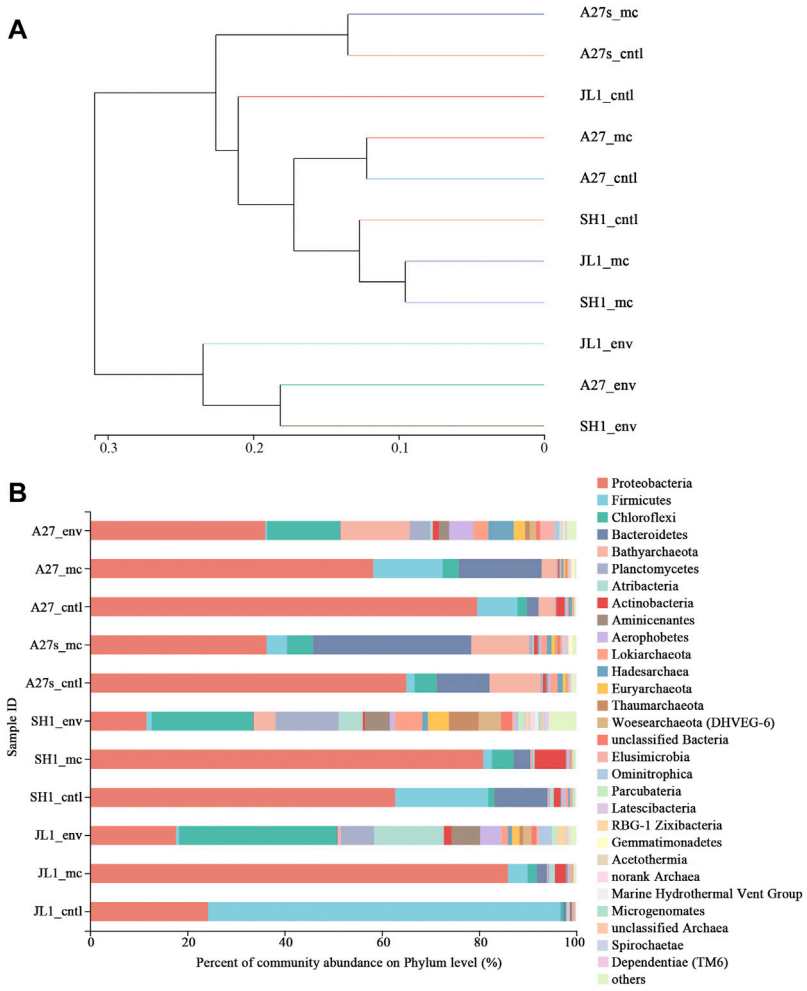

FIGURE 5
Comparison of microbial communities among all samples. **(A)** Hierarchical cluster analysis using pairwise weighted UniFrac distances. The scale bar between branches represents the distance between samples. **(B)** Community abundance of microorganisms at the phylum level for environmental sediment samples (sampling site_env) and the related incubation slurry samples amended with $^{13}CH_4$ (sampling site_mc) and N_2 (sampling site_cntl). Taxa with abundances <0.5% were included in "others".

et al., 2011). The most striking feature of the enriched microorganisms was the overwhelming dominance of bacteria, including the uncultured or unclassified species in *Pseudomonas, Halomonas*, *Marinobacter*, *Sva* 1,033 and Desulfobulbaceae, but none were widely enriched across all incubation slurries. These phylogenetic groups are presentin various marine sediments and are regularly detected in methanic environments (Reed et al., 2002; Inagaki et al., 2006), but their abundance is relatively low. AOM, methanogenesis, sulfate reduction and iron reduction occurred during the incubation in the present study. Thus, the enrichment of these unclassified or uncultured species in our anaerobic incubation indicated that they may be directly or indirectly involved in these biogeochemical processes.

Notably, ANME sequences were not present in any of the samples. However, an abundance of labeled methane was oxidized anaerobically during the incubation. Previous studies have shown that ANME are not present in some geochemical environments where AOM dominates (Lin et al., 2014; Yanagawa et al., 2014; Katayama et al., 2016). Some researchers have speculated that the dominant phylum Bathyarchaeota might participate directly or indirectly in AOM in methane-rich environments (Lin et al., 2014; Katayama et al., 2016; Fan et al., 2017; Cui et al., 2019). Moreover, Bathyarchaeota might have the potential for methane metabolism (Evans et al., 2015). In addition, researchers have recently speculated that Bathyarchaeota express genes encoding MCR enzymes that are potentially required for alkane metabolism rather than methane metabolism (Laso-Pérez et al., 2016; Evans et al.,

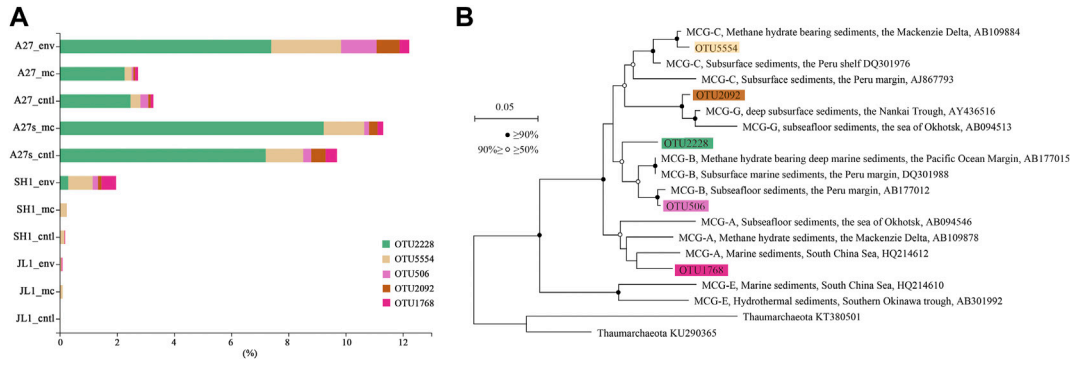

FIGURE 6
Community abundance and lineage of enriched OTUs in the phylum Bathyarchaeota. **(A)**. The top five OTUs in the phylum Bathyarchaeota. **(B)**. Neighbor-joining 16S rRNA gene tree showing the placement of representative members of Bathyarchaeotal relative to environmental sequences, including genes recovered from marine sediments. Thaumarchaeota 16S rRNA sequences from reference genomes were used as an outgroup. Bathyarchaeota (formerly MCG) groups are mainly based on a previous classification (Meng et al., 2014). The stability of the topology was evaluated by bootstrapping (1,000 replicates). Nonparametric support values are indicated with white (≥70%) and black (≥90%) circles. The environmental context and National Center for Biotechnology Information (NCBI) accession numbers are shown. Scale bars indicate the expected number of substitutions per site.

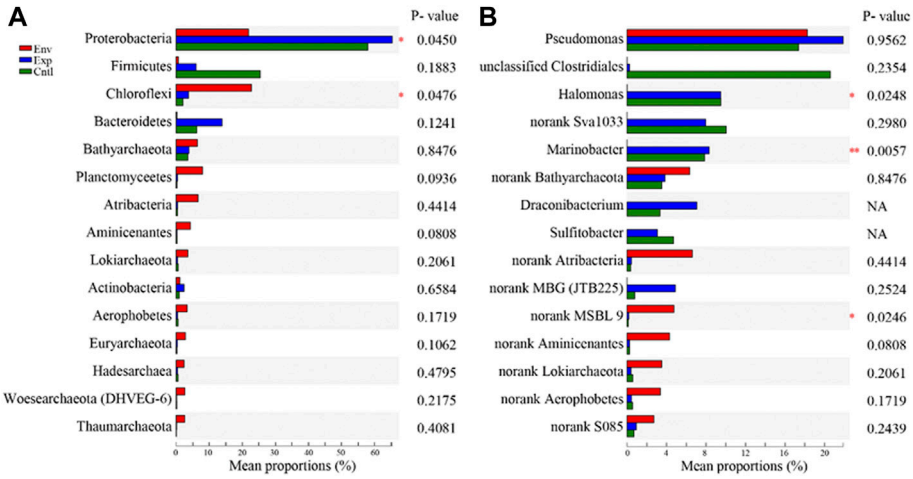

FIGURE 7
Statistical comparison of the relative abundances **(A)** at the phylum level and **(B)** at the genus level among the environmental sediment samples (Env) and the related incubation slurries amended with $^{13}CH_4$ (Exp)and N_2 (Cntl). One-way ANOVA was used to evaluate the significance of differences between the indicated groups. *p <0.05 and **p <0.01.

2019). In the present study, the phylum Bathyarchaeota was enriched in experimental groups with no ANME, and AOM still occurred during the incubation further confirming the hypothesis that Bathyarchaeota may participate in AOM in some way.

In addition, methanogens have been previously reported to perform AOM (Soo et al., 2016), and they contain the *mcrA* gene, which conducts AOM through "reverse methanogenesis" (Hallam et al., 2004). After incubation in the present study, the abundance of some methanogens belonging to uncultured or unclassified species in the genera *Methanococcoides* and *Methanosarcina* increased in the A27 experimental groups but was still considered relatively low (<0.15%). However, this change was not universal in all culture groups. The other control groups that produced a certain amount of methane contained fewer or no methanogen sequences, which may explain why we failed to amplify the *mcrA* gene. Thus, these findings suggested that other unknown or unconventional

phylotypes or pathways may perform AOM and methanogenesis during the incubation. The uncultured or unclassified lineage belonging to the phylum Bathyarchaeota may be the most promising lineage and is worthy of further investigation.

4.2 Impact of the sulfate concentration on the incubation

Webster et al. (2011) suggested that a low sulfate concentration promotes the enrichment of representative SMTZ prokaryotes. However, we only detected some of the representative SMTZ bacteria, such as *Gammaproteobacteria*, *Deltaproteobacteria*, *Firmicutes*, and *Bacteroidetes*, and the bacteria not known to be involved in AOM, such as *Actinobacteria* (Harrison et al., 2009), were enriched in thelow concentration of sulfate (4 mM) group. We also found that the sulfate concentration exerted a marked effect on archaeal community enrichment/maintenance as reflected by the higher proportion of archaea sequences in the slurries amended with high concentrations of sulfate (29.38 mM) group. The enrichment of some lineages of the phylum Bathyarchaeota in slurries amended with high concentration of sulfate (29.38 mM) suggested that sulfate promotes their enrichment.

Sulfate reduction related AOM has been suggested to be the most strongly cooperative metabolic process that controls methane emissions from marine sediments (Barnes and Goldberg, 1976; Iversen and Jorgensen, 1985; Nauhaus et al., 2002; Knittel and Boetius, 2009). SR-AOM is presumed to be most active in the SMTZ where sulfate is depleted to approximately zero and the AOM rate is the highest (Iversen and Jorgensen, 1985). In our incubations, more $^{13}CH_4$ was oxidized in the experimental groups with a low concentration of sulfate (A27, ~4 mM) than in those with a high concentration of sulfate (A27s, 29.38 mM), but we did not determine whether a high sulfate concentration reduces the AOM rate or whether electron acceptors other than sulfate are used during the incubation, leading to a higher AOM rate. Because a high concentration of iron was present in the sediment, reactive iron reduction in sediments may have stimulated sulfate-driven AOM (Sivan et al., 2014) or coupled to AOM to remove large amounts of CH_4 (Egger et al., 2015). Thus, a reasonable assumption is that iron may be involved in the AOM during the incubation. Iron reduction was observed in all groups in the initial period of incubation, the Fe^{2+} levels were clearly increased and, even showed a rapid increasing trend from 74 to 117 days in this stage. The iron reduction rate was similar to the AOM rate in the A27 and SH1 groups. Our major element test and sequential reactive iron extraction results showed that the incubation of sediments of A27 contained a higher reactive iron content (1.33%) and total iron (6.18%) than those of SH1 (0.67 and 4.82%, respectively) (Supplementary Table S1). If iron is merely a stimulant, the iron content does not exert much of an effect on the AOM rate. However, iron may be the electron acceptor, which is energetically more favorable than sulfate in AOM (Beal et al., 2009; Ettwig et al., 2010; Joye, 2012). Therefore, we suggest that the higher reactive iron content led to the anaerobic oxidation of additional methane, resulting in higher AOM rates in the two groups incubated with lower sulfate concentrations.

Numerous bacterial genera enriched in our incubations have been identified to reduce ferric iron, including the dominant and enriched genus *Pseudomonas* (Johnson and Mcginness, 1991; Naganuma et al., 2006), the genus *Halomonas* (Hajizadeh et al., 2015) and the genus *Shewanella* (Kim et al., 1999; Weber et al., 2006; Wang et al., 2008). The enriched family Sva1033, which is most closely related to *Desulfuromonas palmitatis*, has been reported to be a dissimilatory iron reducer capable of oxidizing long-chain fatty acids (Coates et al., 1995) and is hypothesized to undergo metabolic switching from metal reduction to sulfate reduction (Buongiorno et al., 2019). An investigation of microbial communities in metal reduction-coupled AOM incubations has suggested that metal-reducing bacteria play a vital role in metal-dependent AOM (Beal et al., 2009). The same conclusion has been proposed based on investigations of the microbial community in methanic sediments (Li et al., 2019). Thus, the enriched dissimilatory iron-reducing bacteria might directly or indirectly participate in AOM, further suggesting a role for iron reduction in AOM in our incubations.

5 Conclusion

In this study, we reported the incubation results and the shifting diversity and composition of microbial communities. The results of headspace gas indicated that AOM occurred in the experimental groups and that methane production occurred in the control groups during incubations. The enriched microorganisms in our incubations have been reported to degrade organic matter, reduce sulfate, reduce iron and produce methane. However, the well-known ANME, responsible organisms of AOM, were not detected. We propose that the enriched Bathyarchaeata have the potential to perform AOM during incubation. Additionally, more $^{13}CH_4$ was oxidized to $^{13}CO_2$ in the experimental groups treated with low concentrations of sulfate (~4 mM) than in those treated with high concentrations of sulfate (29.38 mM), and more $^{13}CH_4$ was oxidized to $^{13}CO_2$ in the A27 groups, which contained more reactive iron and total iron than SH1 groups. Furthermore, bacteria with dissimilatory iron-reducing metabolism were enriched after incubation. These results suggested that additional electron acceptors may be involved in AOM and that iron is the best candidate. The known methanogens were only detected at low abundance in some samples from the control group, suggesting that methanogenesis may be more phylogenetically widespread than currently appreciated. The

shifting of microbial communities before and after culture in this study provided a better understanding of AOM, methanogenesis and the responsible microorganisms.

Data availability statement

The datasets presented in this study can be found in online repositories. The names of the repository/repositories and accession number(s) can be found in the article/ Supplementary Material.

Author contributions

YK; Data curation, Formal analysis, Investigation, Software, Visualisation, Writing-original draft, Writing-review and editing. HL; Project administration, Supervision, Writing-review and editing, Validation. WC; Investigation, Methodology, Data curation, BW; Investigation, Methodology. FP; Investigation, Software, Visualization. FH; Investigation, Formal analysis.

Funding

This work was funded by the National Natural Science Foundation of China (Grant Nos. 41773078 and 41276046), the Fundamental Research Funds of Xiamen University (Grant No. 20720180114) and the China Ocean Mineral Resources Research and Development Association (DY135-B2-13).

Acknowledgments

We would like to thank the National Natural Science Foundation of China (Grant Nos. 41773078 and 41276046) and the Fundamental Research Funds of Xiamen University (Grant Nos. 20720180114) for funding this study. We would also like to thank the captain, crew and scientists of the NORC 2018–05 voyage for the gravity core sampling.

Conflict of interest

The authors declare that the research was conducted in the absence of any commercial or financial relationships that could be construed as a potential conflict of interest.

Publisher's note

All claims expressed in this article are solely those of the authors and do not necessarily represent those of their affiliated organizations, or those of the publisher, the editors and the reviewers. Any product that may be evaluated in this article, or claim that may be made by its manufacturer, is not guaranteed or endorsed by the publisher.

Supplementary material

The Supplementary Material for this article can be found online at: https://www.frontiersin.org/articles/10.3389/feart.2022.1014976/full#supplementary-material

References

Barnes, R. O., and Goldberg, E. D. (1976). Methane production and consumption in anoxic marine sediments. *Geology* 4 (1976), 297–300. doi:10.1130/0091-7613(1976)4<297:MPACIA>2.0.CO;2

Bates, S. T., Berg-Lyons, D., Caporaso, J. G., Walters, W. A., Knight, R., and Fierer, N. (2011). Examining the global distribution of dominant archaeal populations in soil. *ISME J.* 5 (5), 908–917. doi:10.1038/ismej.2010.171

Beal, E. J., House, C. H., and Orphan, V. J. (2009). manganese- and iron-dependent marine methane oxidation. *Science* 325 (5937), 184–187. doi:10.1126/science.1169984

Boetius, A., Ravenschlag, K., Schubert, C. J., Rickert, D., Widdel, F., Gieseke, A., et al. (2000). A marine microbial consortium apparently mediating anaerobic oxidation of methane. *Nature* 407 (6804), 623–626. doi:10.1038/35036572

Bray, M. S., Wu, J., Reed, B. C., Kretz, C. B., Belli, K. M., Simister, R. L., et al. (2017). Shifting microbial communities sustain multiyear iron reduction and methanogenesis in ferruginous sediment incubations. *Geobiology* 15, 678–689. doi:10.1111/gbi.12239

Buongiorno, J., Herbert, L. C., Wehrmann, L. M., Michaud, A. B., Laufer, K., Røy, H., et al. (2019). Complex microbial communities drive iron and sulfur cycling in arctic fjord sediments. *Appl. Environ. Microbiol.* 85 (14), e00949–00919. doi:10.1128/aem.00949-19

Cai, C., Leu, A. O., Xie, G. J., Guo, J., Feng, Y., Zhao, J. X., et al. (2018). A methanotrophic archaeon couples anaerobic oxidation of methane to Fe(III) reduction. *ISME J.* 12 (8), 1929–1939. doi:10.1038/s41396-018-0109-x

Coates, J. D., Lonergan, D. J., Philips, E. J. P., Jenter, H., and Lovley, D. R. (1995). Desulfuromonas palmitatis sp. nov., a marine dissimilatory Fe(III) reducer that can oxidize long-chain fatty acids. *Arch. Microbiol.* 164 (6), 406–413. doi:10.1007/bf02529738

Cui, H., Su, X., Chen, F., Holland, M., Yang, S., Liang, J., et al. (2019). Microbial diversity of two cold seep systems in gas hydrate-bearing sediments in the South China Sea. *Mar. Environ. Res.* 144, 230–239. doi:10.1016/j.marenvres.2019.01.009

Davie, M. K., and Buffett, B. A. (2003). Sources of methane for marine gas hydrate: Inferences from a comparison of observations and numerical models. *Earth Planet. Sci. Lett.* 206 (1), 51–63. doi:10.1016/S0012-821X(02)01064-6

Egger, M., Rasigraf, O., Sapart, C. J., Jilbert, T., Jetten, M. S., Röckmann, T., et al. (2015). Iron-mediated anaerobic oxidation of methane in brackish coastal sediments. *Environ. Sci. Technol.* 49 (1), 277–283. doi:10.1021/es503663z

Egger, M., Riedinger, N., Mogollón, J. M., and Jørgensen, B. B. (2018). Global diffusive fluxes of methane in marine sediments. *Nat. Geosci.* 11 (6), 421–425. doi:10.1038/s41561-018-0122-8

Ettwig, K. F., Butler, M. K., Paslier, D. L., Pelletier, E., Mangenot, S., Kuypers, M. M. M., et al. (2010). Nitrite-driven anaerobic methane oxidation by oxygenic bacteria. *Nature* 464 (7288), 543–548. doi:10.1038/nature08883

Evans, P. N., Boyd, J. A., Leu, A. O., Woodcroft, B. J., Parks, D. H., Hugenholtz, P., et al. (2019). An evolving view of methane metabolism in the Archaea. *Nat. Rev. Microbiol.* 17 (4), 219–232. doi:10.1038/s41579-018-0136-7

Evans, P. N., Parks, D. H., Chadwick, G. L., Robbins, S. J., Orphan, V. J., Golding, S. D., et al. (2015). Methane metabolism in the archaeal phylum Bathyarchaeota revealed by genome-centric metagenomics. *Science* 350 (6259), 434–438. doi:10.1126/science.aac7745

Fan, X. B., Liang, Q. Y., Niu, M. Y., Yu, T. T., Wang, Y. S., and Wang, F. P. (2017). The diversity and richness of archaea in the northern continental slope of South China Sea. *Microbiol. China* 44 (7), 1589–1601. doi:10.13344/j.microbiol.china.170159

Ferry, J. G., and Lessner, D. J. (2008). Methanogenesis in marine sediments. *Ann. N. Y. Acad. Sci.* 1125 (1), 147–157. doi:10.1196/annals.1419.007

Gong, J., Sun, X., Xu, L., and Lu, H. (2017). Contribution of thermogenic organic matter to the formation of biogenic gas hydrate: Evidence from geochemical and microbial characteristics of hydrate-containing sediments in the Taixinan Basin, South China Sea. *Mar. Petroleum Geol.* 80, 432–449. doi:10.1016/j.marpetgeo.2016.12.019

Hajizadeh, N., Sefidi Heris, Y., Zununi Vahed, S., Vallipour, J., Hejazi, M., Golabi, S., et al. (2015). Fe(III) reduction by halomonas sp. TBZ9 and maribobacter sp. TBZ23, isolated from urmia lake in Iran. *Adv. Environ. Biol.* 8, 59–65.

Hallam, S. J., Putnam, N., Preston, C. M., Detter, J. C., Rokhsar, D., Richardson, P. M., et al. (2004). Reverse methanogenesis: Testing the hypothesis with environmental genomics. *Science* 305 (5689), 1457–1462. doi:10.1126/science.1100025

Harrison, B. K., Zhang, H., Berelson, W., and Orphan, V. J. (2009). Variations in archaeal and bacterial diversity associated with the sulfate-methane transition zone in continental margin sediments (santa barbara basin, California). *Appl. Environ. Microbiol.and Environ. Microbiol.* 75 (6), 1487–1499. doi:10.1128/aem.01812-08

Hinrichs, K.-U., and Boetius, A. (2003). "The anaerobic oxidation of methane: New insights in microbial ecology and biogeochemistry," in *Ocean margin systems*. Editors G. Wefer, D. Billett, D. Hebbeln, B. B. Jørgensen, M. Schlüter, and T. C. E. van Weering (Berlin, Heidelberg: Springer Berlin Heidelberg), 457–477.

Hinrichs, K. U., Sylva, S., Brewer, P., Delong, E., and Hayes, J. (1999). Methane-consuming archaebacteria in marine sediments. *Nature* 398 (6730), 802–805. doi:10.1038/19751

Inagaki, F., Nunoura, T., Nakagawa, S., Teske, A., Lever, M., Lauer, A., et al. (2006). Biogeographical distribution and diversity of microbes in methane hydrate-bearing deep marine sediments on the Pacific Ocean Margin. *Proc. Natl. Acad. Sci. U. S. A.* 103 (8), 2815–2820. doi:10.1073/pnas.0511033103

Iversen, N., and Jorgensen, B. B. (1985). Anaerobic methane oxidation rates at the sulfate-methane transition in marine sediments from Kattegat and Skagerrak (Denmark)1. *Limnol. Oceanogr.* 30 (5), 944–955. doi:10.4319/lo.1985.30.5.0944

Johnson, D. B., and Mcginness, S. (1991). Ferric iron reduction by acidophilic heterotrophic bacteria. *Appl. Environ. Microbiol.* 57 (1), 207–211. doi:10.1128/AEM.57.1.207-211.1991

Johnson, K. M., Hughes, J. E., Donaghay, P. L., and Sieburth, J. M. (1990). Bottle-calibration static head space method for the determination of methane dissolved in seawater. *Anal. Chem.* 62 (21), 2408–2412. doi:10.1021/ac00220a030

Joye, S. B. (2012). A piece of the methane puzzle. *Nature* 491, 538–539. doi:10.1038/nature11749

Joye, S. B., Boetius, A., Orcutt, B. N., Montoya, J. P., Schulz, H. N., Erickson, M. J., et al. (2004). The anaerobic oxidation of methane and sulfate reduction in sediments from Gulf of Mexico cold seeps. *Chem. Geol.* 205 (3), 219–238. doi:10.1016/j.chemgeo.2003.12.019

Katayama, T., Yoshioka, H., Takahashi, H. A., Amo, M., Fujii, T., and Sakata, S. (2016). Changes in microbial communities associated with gas hydrates in subseafloor sediments from the Nankai Trough. *FEMS Microbiol. Ecol.* 92 (8), fiw093–10. doi:10.1093/femsec/fiw093

Kim, B. H., Kim, H. J., Hyun, M. S., and Park, D. H. (1999). Direct electrode reaction of Fe(III)-reducing bacterium, Shewanella putrefaciens. *J. Microbiol. Biotechnol.* 9 (2), 127–131. doi:10.1002/(SICI)1099-1514(199905/06)20:33.0.CO;2-I

Knittel, K., and Boetius, A. (2009). Anaerobic oxidation of methane: Progress with an unknown process. *Annu. Rev. Microbiol.* 63, 311–334. doi:10.1146/annurev.micro.61.080706.093130

Kong, Y., Lei, H. Y., Zhang, Z. L., Cheng, W. D., Wang, B., Pan, F. L., et al. (2021). Depth profiles of geochemical features, geochemical activities and biodiversity of microbial communities in marine sediments from the Shenhu area, the northern South China Sea. *Sci. Total Environ.* 779, 146233. doi:10.1016/j.scitotenv.2021.146233

Laso-Pérez, R., Wegener, G., Knittel, K., Widdel, F., Harding, K. J., Krukenberg, V., et al. (2016). Thermophilic archaea activate butane via alkyl-coenzyme M formation. *Nature* 539 (7629), 396–401. doi:10.1038/nature20152

Leu, A. O., Cai, C., McIlroy, S. J., Southam, G., Orphan, V. J., Yuan, Z., et al. (2020). Anaerobic methane oxidation coupled to manganese reduction by members of the Methanoperedenaceae. *ISME J.* 14 (4), 1030–1041. doi:10.1038/s41396-020-0590-x

Li, J., Li, L., Bai, S., Ta, K., Xu, H., Chen, S., et al. (2019). New insight into the biogeochemical cycling of methane, S and Fe above the sulfate-methane transition zone in methane hydrate-bearing sediments: A case study in the dongsha area, South China sea. *Deep Sea Res. Part I Oceanogr. Res. Pap.* 145, 97–108. doi:10.1016/j.dsr.2019.01.011

Lin, L.-H., Wu, L.-W., Cheng, T.-W., Tu, W.-X., Lin, J.-R., Yang, T. F., et al. (2014). Distributions and assemblages of microbial communities along a sediment core retrieved from a potential hydrate-bearing region offshore southwestern Taiwan. *J. Asian Earth Sci.* 92, 276–292. doi:10.1016/j.jseaes.2014.02.014

Liu, J., Wang, J., Izon, G., Antler, G., Wang, Z., Zhao, J., et al. (2018). Vivianite formation in methane-rich deep-sea sediments from the South China Sea. *Biogeosciences* 15 (20), 6329–6348. doi:10.5194/bg-15-6329-2018

Lu, G., ShaoYong, J., Tao, Y., JingHong, Y., NengYou, W., Zhang, G., et al. (2011). Glycerol ether biomarkers and their carbon isotopic compositions in a cold seep carbonate chimney from the Shenhu area, northern South China Sea. *Chin. Sci. Bull.* 56 (16), 1700–1707. doi:10.1007/s11434-011-4486-z

Luton, P. E., Wayne, J. M., Sharp, R. J., and Riley, P. W. (2002). The mcrA gene as an alternative to 16S rRNA in the phylogenetic analysis of methanogen populations in landfill b bThe GenBank accession numbers for the mcrA sequences reported in this paper are AF414034–AF414051 (see Fig. 2) and AF414007–AF414033 (environmental isolates in Fig. 3). *Microbiol. Read. Engl.* 148, 3521–3530. doi:10.1099/00221287-148-11-3521

Martens, C. S., and Berner, R. A. (1974). Methane production in the interstitial waters of sulfate-depleted marine sediments. *Science* 185 (4157), 1167–1169. doi:10.1126/science.185.4157.1167

Meng, J., Xu, J., Qin, D., He, Y., Xiao, X., and Wang, F. (2014). Genetic and functional properties of uncultivated MCG archaea assessed by metagenome and gene expression analyses. *The ISME Journal* 8 (3), 650–659. doi:10.1038/ismej.2013.174

Naganuma, T., Sato, M., Hoshii, D., Amanomurakami, Y., Iwatsuki, T., and Mandernack, K. W. (2006). Isolation and characterization of Pseudomonas strains capable of Fe(III) reduction with reference to redox response regulator genes. *Geomicrobiol. J.* 23, 145–155. doi:10.1080/01490450600596565

Nauhaus, K., Antje, B., Martin, K., and Widdel, F. (2002). *In vitro* demonstration of anaerobic oxidation of methane coupled to sulphate reduction in sediment from a marine gas hydrate area. *Environ. Microbiol.* 4 (5), 296–305. doi:10.1046/j.1462-2920.2002.00299.x

Orphan, V. J., House, C. H., Hinrichs, K. U., Mckeegan, K. D., and Delong, E. F. (2001). Methane-consuming archaea revealed by directly coupled isotopic and phylogenetic analysis. *Science* 293 (5529), 484–487. doi:10.1126/science.1061338

Pachiadaki, M. G., and Kormas, K. A. (2013). Interconnectivity vs. isolation of prokaryotic communities in European deep-sea mud volcanoes. *Biogeosciences* 10 (5), 2821–2831. doi:10.5194/bg-10-2821-2013

Paull, C. K., Ussler, W., III, and Borowski, W. S. (1994). Sources of biogenic methane to form marine gas hydrates. *Ann. N. Y. Acad. Sci.* 715, 392–409. doi:10.1111/j.1749-6632.1994.tb38852.x

Reeburgh, W. S. (2007). Oceanic methane biogeochemistry. *Chem. Rev.* 107 (2), 486–513. doi:10.1021/cr050362v

Reed, A. J., Dorn, R., Van Dover, C. L., Lutz, R. A., and Vetriani, C. (2009). Phylogenetic diversity of methanogenic, sulfate-reducing and methanotrophic prokaryotes from deep-sea hydrothermal vents and cold seeps. *Deep Sea Res. Part II Top. Stud. Oceanogr.* 56 (19), 1665–1674. doi:10.1016/j.dsr2.2009.05.012

Reed, D. W., Fujita, Y., Delwiche, M. E., Blackwelder, D. B., Sheridan, P. P., Uchida, T., et al. (2002). Microbial communities from methane hydrate-bearing deep marine sediments in a forearc basin. *Appl. Environ. Microbiol.* 68 (8), 3759–3770. doi:10.1128/AEM.68.8.3759-3770.2002

Regnier, P., Dale, A. W., Arndt, S., Larowe, D. E., Mogollón, J., and Cappellen, P. V. (2011). Quantitative analysis of anaerobic oxidation of methane (AOM) in marine sediments: A modeling perspective. *Earth. Sci. Rev.* 106 (1–2), 105–130. doi:10.1016/j.earscirev.2011.01.002

Rotaru, A. E., and Thamdrup, B. (2016). A new diet for methane oxidizers. *Science* 351 (6274), 658. doi:10.1126/science.aaf0741

Scheller, S., Yu, H., Chadwick, G. L., Mcglynn, S. E., and Orphan, V. J. (2016). Artificial electron acceptors decouple archaeal methane oxidation from sulfate reduction. *Science* 351 (6274), 703–707. doi:10.1126/science.aad7154

Segarra, K. E. A., Comerford, C., Slaughter, J., and Joye, S. B. (2013). Impact of electron acceptor availability on the anaerobic oxidation of methane in coastal freshwater and brackish wetland sediments. *Geochimica Cosmochimica Acta* 115 (5), 15–30. doi:10.1016/j.gca.2013.03.029

Sivan, O., Antler, G., Turchyn, A. V., Marlow, J. J., and Orphan, V. J. (2014). Iron oxides stimulate sulfate-driven anaerobic methane oxidation in seeps. *Proc. Natl. Acad. Sci. U. S. A.* 111 (40), 4139–4147. doi:10.1073/pnas.1412269111

Soo, V. W. C., McAnulty, M. J., Tripathi, A., Zhu, F., Zhang, L., Hatzakis, E., et al. (2016). Reversing methanogenesis to capture methane for liquid biofuel precursors. *Microb. Cell. Fact.* 15 (1), 11. doi:10.1186/s12934-015-0397-z

Wang, F., Wang, J., Jian, H., Zhang, B., Li, S., Wang, F., et al. (2008). Environmental adaptation: Genomic analysis of the piezotolerant and psychrotolerant deep-sea iron reducing bacterium Shewanella piezotolerans WP3. *PLOS ONE* 3 (4), 1937–1949. doi:10.1371/journal.pone.0001937

Weber, K. A., Achenbach, L. A., and Coates, J. D. (2006). Microorganisms pumping iron: Anaerobic microbial iron oxidation and reduction. *Nat. Rev. Microbiol.* 4 (10), 752–764. doi:10.1038/nrmicro1490

Webster, G., Sass, H., Cragg, B. A., Gorra, R., Knab, N. J., Green, C. J., et al. (2011). Enrichment and cultivation of prokaryotes associated with the sulphate–methane transition zone of diffusion-controlled sediments of Aarhus Bay, Denmark, under heterotrophic conditions. *FEMS Microbiol. Ecol.* 77 (2), 248–263. doi:10.1111/j.1574-6941.2011.01109.x

Wu, L., Yang, S., Liang, J., Su, X., Fu, S., Sha, Z., et al. (2013). Variations of pore water sulfate gradients in sediments as indicator for underlying gas hydrate in Shenhu Area, the South China Sea. *Sci. China Earth Sci.* 56 (4), 530–540. doi:10.1007/s11430-012-4545-6

Wu, N., Zhang, G., Liang, J., Su, Z., Wu, D., Lu, H., et al. (2013). Progress of gas hydrate research in northern South China sea. *Adv. New Renew. Energy* 1 (1), 80–94. doi:10.3969/j.issn.2095-560X.2013.01.008

Wu, N., Zhang, H., Yang, S., Zhang, G., Liang, J., Lu, J. a., et al. (2011). Gas hydrate system of Shenhu area, northern South China sea: Geochemical results. *J. Geol. Res.* 2011, 1–10. doi:10.1155/2011/370298

Yanagawa, K., Kouduka, M., Nakamura, Y., Hachikubo, A., Tomaru, H., and Suzuki, Y. (2014). Distinct microbial communities thriving in gas hydrate-associated sediments from the eastern Japan Sea. *J. Asian Earth Sci.* 90, 243–249. doi:10.1016/j.jseaes.2013.10.019

Zhang, G., Liang, J., Lu, J. a., Yang, S., Zhang, M., Holland, M., et al. (2015). Geological features, controlling factors and potential prospects of the gas hydrate occurrence in the east part of the Pearl River Mouth Basin, South China Sea. *Mar. Petroleum Geol.* 67, 356–367. doi:10.1016/j.marpetgeo.2015.05.021

Zhang, J., Lei, H., Chen, Y., Kong, Y., Kandasamy, S., Ou, W., et al. (2018). Carbon and oxygen isotope composition of carbonate in bulk sediment in the southwest Taiwan Basin, South China Sea: Methane hydrate decomposition history and its link to mud volcano eruption. *Mar. Petroleum Geol.* 98, 687–696. doi:10.1016/j.marpetgeo.2018.08.031

Zhang, W., Liang, J., Lu, J. a., Wei, J., Su, P., Fang, Y., et al. (2017). Accumulation features and mechanisms of high saturation natural gas hydrate in Shenhu Area, northern South China Sea. *Petroleum Explor. Dev.* 44 (5), 708–719. doi:10.1016/S1876-3804(17)30082-4

Zhuang, G.-C., Heuer, V. B., Lazar, C. S., Goldhammer, T., Wendt, J., Samarkin, V. A., et al. (2018). Relative importance of methylotrophic methanogenesis in sediments of the Western Mediterranean Sea. *Geochimica Cosmochimica Acta* 224, 171–186. doi:10.1016/j.gca.2017.12.024

frontiers | Frontiers in Earth Science

TYPE Original Research
PUBLISHED 28 September 2022
DOI 10.3389/feart.2022.997079

OPEN ACCESS

EDITED BY
Pibo Su,
Guangzhou Marine Geological Survey, China

REVIEWED BY
Junpeng Wang,
China University of Geosciences Wuhan, China
Yonghe Sun,
Chongqing University of Science and Technology, China
Fenquan Xie,
Northeast Petroleum University, China

*CORRESPONDENCE
Lijun Song,
Ljsong@xsyu.edu.cn

SPECIALTY SECTION
This article was submitted to Marine Geoscience, a section of the journal Frontiers in Earth Science

RECEIVED 18 July 2022
ACCEPTED 22 August 2022
PUBLISHED 28 September 2022

CITATION
Song L, Feng X, Yang Y and Li Y (2022), Distribution, development, transformation characteristics, and hydrate prospect prediction of the rift basins of northwest Zealandia in the Southwest Pacific.
Front. Earth Sci. 10:997079.
doi: 10.3389/feart.2022.997079

Distribution, development, transformation characteristics, and hydrate prospect prediction of the rift basins of northwest Zealandia in the Southwest Pacific

Lijun Song*, Xuliang Feng, Yushen Yang and Yamin Li

School of Earth Sciences and Engineering, Xi'an Shiyou University, Xi'an, China

As the last area with unknown oil exploration potential, Zealandia has attracted the attention of petroleum scientists. Under the constraint of the known rift distribution, the gravity and magnetic anomaly data are utilized to predict the distribution of rift basins, and the balanced cross-section technique and basin simulation technique are utilized to analyze the development of the rift basins and hydrocarbon generation history of source rocks for the hydrate prospect prediction of the rift basins of northwest Zealandia. The time of rifting in Zealandia varies greatly from place to place, and it has experienced extensive rifts, migrated to the east of the Lord Howe Ridge, migrated to the west of the Lord Howe Ridge, migrated to the west of the Dampier Ridge, and finally migrated to both sides of the Lord Howe Ridge and then experienced multiple stages of compression transformation and deep burial transformation. The Upper Cretaceous coal source rock in the rift II stage has entered the wet gas generation stage in the deep part of the rift or deeper rift on the eastern side of the Lord Howe Ridge, and the coal-generated wet gas may migrate along the fault and form a gas hydrate in the shallow seabed stable zone.

KEYWORDS

thermal history simulation, natural gas hydrate, prospect prediction, Zealandia, development characteristics of the rift basins

1 Introduction

Zealandia is a hidden landmass in the southwestern Pacific Ocean, which is 94% submerged beneath the oceanic waters (Mortimer et al., 2016), as a result of widespread Late Cretaceous breakup, crustal thinning, and consequent isostatic balance. With the deepening of geological and geophysical investigation, especially with the discovery of the granites and metamorphic rocks in the pre-Cretaceous basement (Suggate et al., 1978; Beggs et al., 1990; Tulloch et al., 1991, 2009; Gamble et al., 1993; McDougall et al., 1994; Mortimer et al., 1997, 1998, 2006, 2008a, 2008b, 2014, 2015) and the discovery of

synchronal volcanic records from the Late Cretaceous (Tulloch et al., 2009; Mortimer et al., 2014), a great deal of knowledge on the distribution, structure, and cracking process of the continental block has been obtained for the in-depth discussions (Corredorfo, 1996; Ringis, 1972; Shaw, 1979; Stock and Molnar, 1982; Luyendyk, 1995; Lafoy et al., 2005; Schellart et al., 2006; Mortimer et al., 2006). Zealandia is considered to be a consistent continent with an area of 4.9 Mkm^2 (Mortimer et al., 2016), consisting of a series of grabens and horsts (Gaina et al., 1998). Also, the continental block is considered to be a product of the breakup of the continent Gondwana in the Late Cretaceous. Following the breakup of the continent Gondwana, the continental block experienced extensive rifting and plastic thinning and then sank under the ocean with the influence of gravity isostasy.

There is abundant evidence for gas hydrates in the Fairway Basin and Taranaki Basin, such as diapir structures and BSRs (Claypool and Kaplan, 1974; Kvenvolden, 1995; Exon et al., 1998; Collot et al., 2009; Kroeger et al., 2017). Owning to the limitation to data, a deep understanding of the distribution, the extensional process, the law of the later reformation, and the prospect of the exploration of the hydrate is still lacking. In recent years, with the development of seismic exploration and ocean drilling, it has shown that it has an important potential for gas hydrate exploration in view of the Upper Cretaceous coal-measure source rocks from drillings (Van de Beuque et al., 2003; Kroeger et al., 2017), especially the findings of BSR (bottom simulating reflection) and diapir and crater in the Fairway (Exon et al., 1998) and Taranaki basins (Auzende et al., 2000; Pierrick et al., 2015; Kroeger et al., 2017).

As the last area with unknown oil exploration potential, it has attracted the attention of energy scientists. In view of the fact that hydrocarbon gases can form hydrates in the shallow seabed, they migrated from the mature hydrocarbon generation of coal-measure source rocks. So this article is under the constraint of the known rift distribution, using gravity and magnetic anomaly data to predict the distribution of rift basins and combining with the results of seismic interpretation, the balanced cross-section

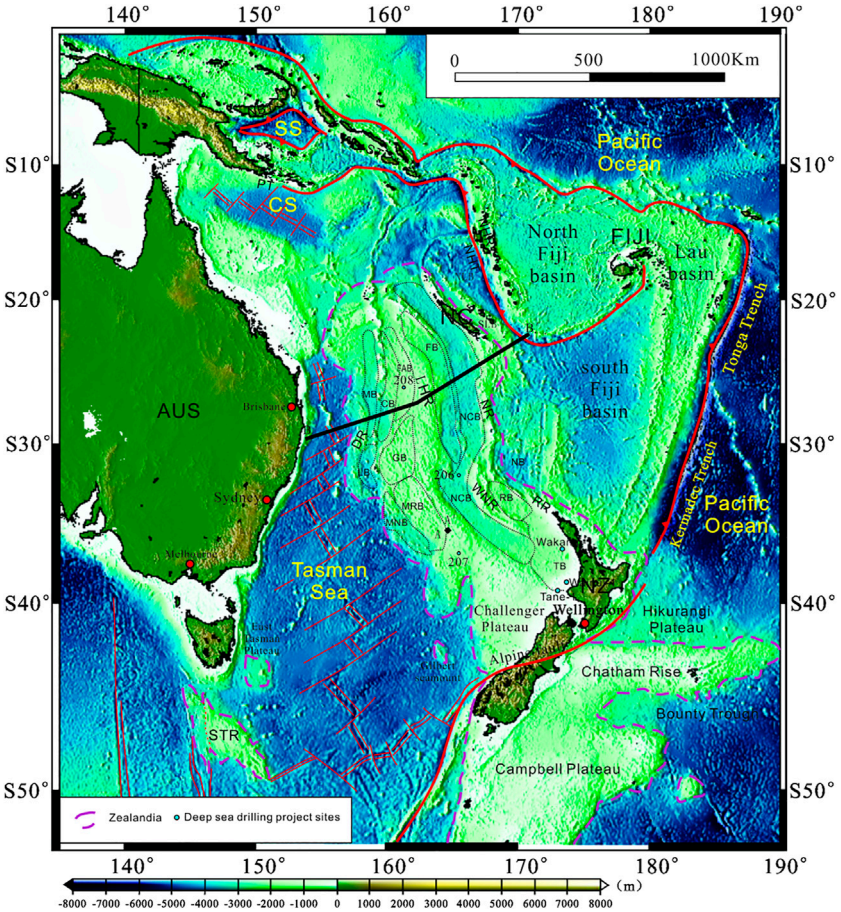

FIGURE 1
Tectonic location and division of tectonic units of the continent of Zealandia.

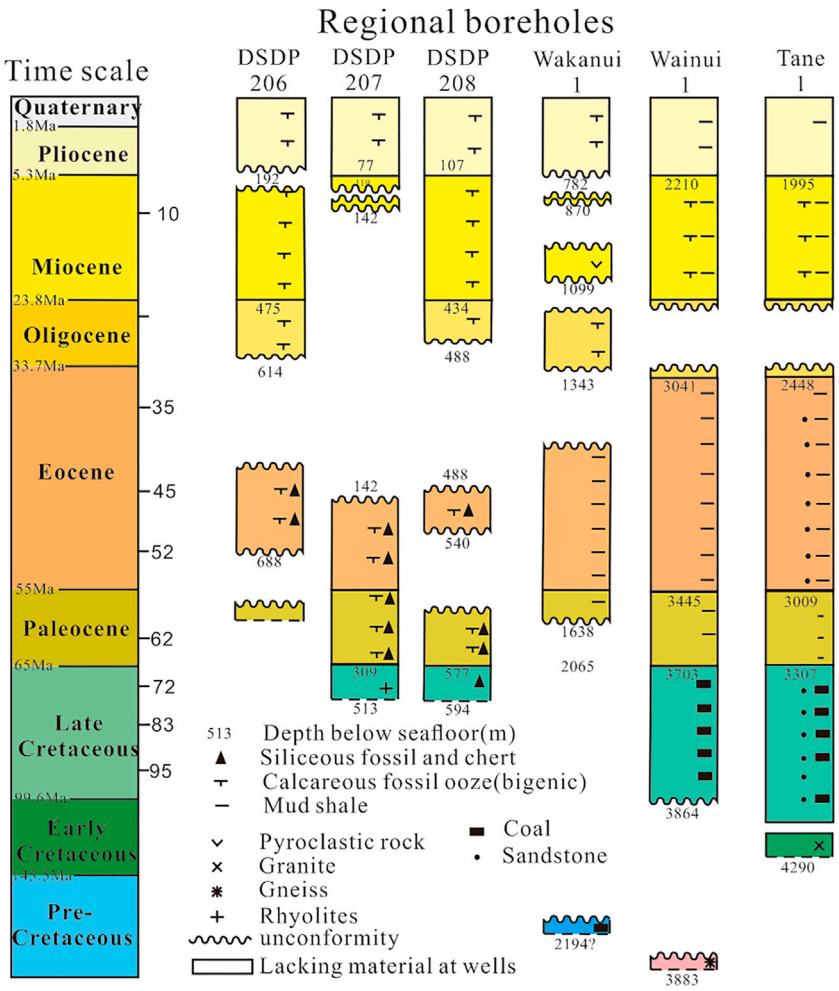

FIGURE 2
Comprehensive histogram of formation drilling (Willcox and Sayers, 2002; Stagg et al., 2002; Van de Beuque et al., 2003; Collot et al., 2009).

technique, and basin simulation technique to analyze the development law of the lacunae and hydrocarbon generation history of source rocks for the hydrate prospect prediction.

2 Regional geological background

Zealandia is located between the Australian Plate in the west and the Pacific Plate in the east. Specifically, it is located in the sea area between the trench of New Britain–San Cristobal–New Hebrides and the Tasman Sea–Coral Sea on the eastern edge of Australia (Figure 1).

Bathymetric map of the southwestern Pacific region showing data used for this study. Countries (AUS: Australia, NZ: New Zealand, and NC: New Caledonia); rises (LHR: Lord Howe Rise, DR: Dampier Ridge, WNR: West Norfolk Ridge, NR: Norfolk Ridge, RR: Reinga Ridge, STR: South Tasman Ridge, and NHR, New Hebrides Ridge); seas (CS: Coral Sea and SS: Solomon Sea); back-arc basins (TB: Taranaki Basin, RB: Reinga Basin, NCB: New Caledonia Basin, NLB: North Loyalty Basin, FAB: Faust Basin, FB: Fairway Basin, CB: Capel Basin, MB: Middleton Basin, GB: Gower Basin, MOB: Moore Basin, MNB: Monowai Basin, and LB: Lord Howe Basin); troughs (PT: Pocklington Trough, NBT: New Britain Trough, and NHT: New Hebrides Trench). A-A′ and B-B′ are seismic profile positions (the same as follows).

There are a number of basins, basin-bounding plateaus, and elongated ridges in Zealandia, which were mainly rifted from the eastern margin of the Gondwana continent in the Late Cretaceous. The ridges and plateaus are underlain by extended continental crust (e.g., Dampier Ridge, Lord Howe Rise, Challenger Plateau, Norfolk Ridge, Campbell Plateau, and Chatham Rise). Most of the basins (Fairway Basin, Capel Basin, and Reinga Basin) are mainly located between the Lord

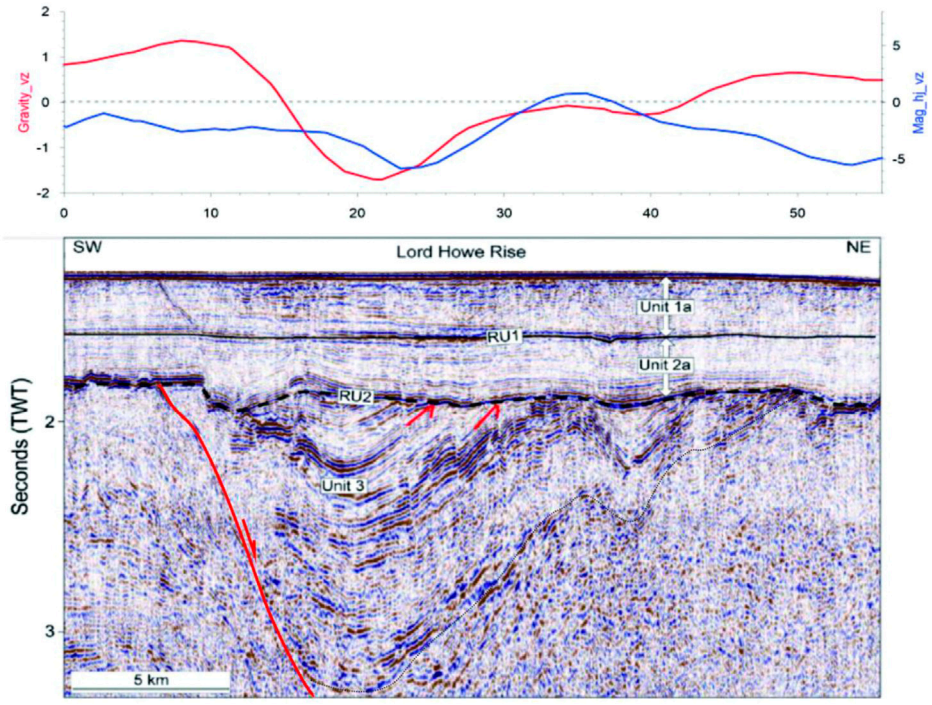

FIGURE 3
Seismic profile with gravity–magnetic anomalies.

Howe Rise and the Norfolk Ridge or on the east and west sides, which are mainly covered by mid to Late Cretaceous rift valley-related sediments and volcanic and Cenozoic pelagic sediments (Figure 2).

1) Initial continental rift stage (~120–95 Ma)

This Zealandia extension and the formation of its internal rift basin groups were mainly followed by episodic opening from early to middle Cretaceous to present, as a direct consequence of hinge-retreat of the subducting Pacific Plate and collapse of the overriding Zealandia toward the retreating hinge of the Pacific Plate. It can be roughly divided into the following five stages.

From the early to middle Cretaceous, there is a strong, widespread east-west to northeast-southwest-directed extension in the eastern margin of Gondwana, resulting from east to northeast-directed rollback of west to southwest-dipping subduction of the Pacific Plate. A set of pyroclastic rocks deposited in these rift basins during this period overlain the pre-Cretaceous metamorphic or granite basement (Van de Beuque et al., 2003). In the Late Cretaceous Cenomanian (~95 Ma), the overriding Zealandia extension ceased in relative plate motion from the collision between Zealandia and the Pacific Plate (Veevers, 2000a, b).

2) Pulsatile continental breakup and drift stage (95–52 Ma)

From the Late Cretaceous (~95Ma) to Early Eocene (~52Ma), the eastern margin of Gondwana continues to widespread rifting, primarily due to the west-directed subduction and east-directed rollback of the Pacific Plate (up to at least 1,200 km) (Schellart et al., 2006), accommodating opening of the New Caledonia, South Loyalty, Coral Sea, and Pocklington back-arc basins and partly accommodating spreading in the Tasman Sea. From 73 Ma to 68 Ma, the spreading rifting occurred between the Lord Howe Ridge and Dampier Ridge in the South Tasman Sea. Subsequently, the spreading rifting ridge then jumped to the west of the Dampier Ridge and continued to expand northward (Ringis, 1972), leading to the formation of the Coral Sea from 62 Ma to 52 Ma in the northern Tasman Sea (Gaina et al., 1999).

3) Pulsatile compressional tectonic stage (52–22.3 Ma)

In the Eocene, the convergent motion between the Pacific Plate and Zealandia increased gradually due to the northward migration of Australia and Zealandia. This convergence process resulted in the cessation of the expansion of the Coral Sea (~52Ma) (Gaina et al., 1999), Tasman Sea (~52 Ma) (Gaina et al., 1998), and the south Loyalty–Santa Cruz–Pocklington

Basin (~55Ma) (Schellart et al., 2006) and also caused the oceanic crust of the back-arc basin of the new back-arc basin subducting toward the New Caledonia island arc. Subsequently, New Caledonia–Pocklington subduction zone was formed in Paleocene to earliest Eocene (~50–45 Ma) (Cluzel et al., 2001).

This convergence shortening event was represented by the formation of the high-pressure/low-temperature (HP/LT) rocks from the Pouebo metamorphic terrane in northern New Caledonia, the original rock of which was formed in ~85–55 Ma (Spandler et al., 2005) and for which peak high-pressure metamorphism has been dated at ~44Ma (Spandler et al., 2005). This subduction and convergence process continued until the earliest Miocene and eventually led to the obduction of ophiolite remnants and terranes in the South Loyalty back-arc basin along the newly formed New Caledonia–Pocklington subduction zone, which was formed in the Eocene to Early Miocene (~38–33.7 Ma) (Cluzel et al., 2001).

This subduction–convergence event also has an obvious response in the sedimentary record, which caused the two angular unconformity contacts with the underlying Paleocene and between the Eocene and Oligocene. These angular unconformity contact relationships are revealed in drilling DSDP 206, 207, and 208 (Van de Beuque et al., 2003). With the weakening of subduction-compression, the rift basins entered the stage of stress relaxation depression and deposited a set of nannofossil ooze, chalk, and volcanic ash in Oligocene.

4) Shear extrusion tectonic stage (23.3–5 Ma)

Since 23 Ma, with the Southeast Indian Ocean Ridge extending eastward, the Resolution Ridge began to form due to seafloor expansion and mantle uplift, which led to the Alpine rupture of the North and South Islands of New Zealand. With the striking southwestward extension of the Campbell Plateau relative to the Challenger Plateau in New Zealand, the dextral lithospheric Alpine fault zone was gradually formed by left-lateral strike-slip (Kamp, 1986), which led to the multi-stage compression and denudation reformation in south Zealandia (Figure 2).

With the rapid southeastward expansion movement of the Southeast Indian Ocean Ridge, which merged with the Southwest Pacific Ridge, Zealandia was completely separated from the surrounding Antarctic at 10 Ma.

5) Thermogravimetric equilibrium subsidence stage (5–0 Ma)

From the latest Miocene or Pliocene to the present, especially owning to subducting westward and retreating eastward of the Pacific Plate (up to ~400 km of rollback distance) (Schellart et al., 2006), Zealandia was strongly thermal and extensionally subsided and concealed under the sea, covered by thick deep-sea ooze deposits, accompanying with the extension of the Lau back-arc Basin.

3 Methods

3.1 Rift distribution identification method and process

3.1.1 Principle of rift identification and data source

The sedimentary strata in rift basins are characterized by large thickness variations, lateral discontinuity, and local distribution. Therefore, the gravity anomalies often caused by them should be local low-gravity anomalies. Since most of the rifted sedimentary layers in rift basins are non-magnetic or weakly magnetic, their magnetic anomalies should also be local low-magnetic anomalies. However, given that the magnetism of the metamorphic basement of the Zealandia plate may vary greatly when using the local anomalies of gravity and magnetism to identify the distribution of rifted layers in this area, gravity is the main force, and magnetism is the supplement.

Gravity satellite altimetry gravity anomaly data come from the latest satellite gravity data covering the world provided by the University of California, San Diego, and the Scripps Oceanographic Institute, version 23.1. Data sources and descriptions are available at http://topex.ucsd.edu/cgi-bin/get_data.cgi. The gravity potential field was processed in m or km. The magnetic data come from EMAG2 (the Earth Magnetic Anomaly Grid), which is the result of data splicing of different observation forms (aerial magnetic survey and marine ship survey) in different regions. The network degree of air magnetic survey and marine ship survey is different, and the average grid degree of data is 2′×2’. See https://www.ngdc.noaa.gov/docucomp/page?xml = NOAA/NESDIS/NGDC/MGG/Geophysical_Models/iso/xml/EMAG2.xml &view=getDataView&header=none for data source and description.

Modified from (Bache et al., 2013), the section location is shown in Figure 1.

3.1.2 Method and process of rift distribution identification

By comparing the locations of the rift basin in both the plane and the profile with those identified by the seismic profile, the local gravity and magnetic anomalies would be determined for the purpose of identifying the distribution of rift basins. The identification method and process of the Northwest Zealandia rift basin are as follows.

First, the extraction of the gravity anomaly of the sedimentary layer and the calculation of the pole magnetic anomaly were performed. The Bouguer gravity anomaly was calculated by subtracting the seawater gravity anomaly from the free space gravity anomaly, which is obtained by forward modeling from seafloor topography data. The density of seawater is 1.03×10^3 kg/m^3, and the average density of the rift sedimentary layer is 2.30×10^3 kg/m^3. The gravity anomaly of

the sedimentary layer was obtained by subtracting the Moho gravity anomaly from the Bouguer gravity anomaly, and the fluctuation of the Moho was forwardly calculated by the Moho depth data in CRUST1.0, with the density difference between the crust and mantle being 0.5×10^3 kg/m^3. Affected by the oblique magnetization, the position of the geological body does not correspond to that of the magnetic force ΔT anomaly. Therefore, the pole magnetic anomaly was calculated by the method of changing the magnetic dip angle. According to the comprehensive histogram of regional formation drilling, the stratigraphic unit age in the seismic profile (Figure 3 and Bache et al., 2013) is revised. Unit 1a: Oligocene to Pleistocene deposits (?); unit 2a: Paleocene to Eocene sedimentary rocks (?); unit 3: Late Cretaceous Rift seismic unit (inference from rift sequence characteristics); RU1 and RU2: regional unconformities.

Second, the extraction of rift weight and magnetic anomalies was performed. In order to determine the range of local gravity and magnetic anomalies, the vertical first-order derivative of the gravity anomaly and the vertical first-order derivative of the polarized magnetic force anomaly are obtained at different extension heights through, respectively, calculating the vertical first-order derivatives of the sedimentary layer gravity anomaly and the pole magnetic anomaly by the upward continuation method to suppress the high-frequency interference. By comparing the different calculation results with the positions of the rifts identified by the seismic data (Figure 3), the vertical first-order derivative of gravity and magnetic anomalies is determined, which is most consistent with the seismic rift distribution results (Figure 4).

Finally, the identification of the distribution of the rift sedimentary layer. Considering the best vertical first-order derivative determined in the second step as the basic data, combined with the seismic profiles collected in the study area as constraints, the plane distribution of the rift layer in the study area was comprehensively identified (Figure 5), mainly by utilizing the negative region of the vertical first-order derivative of the gravity anomaly and supplementally utilizing the negative region of the vertical first-order derivative of polarized magnetic force anomaly.

The green shaded area represents the rift location identified by gravity and magnetic anomalies; the blue shaded area is the rift location identified by Bache et al. (2013) using seismic profiles. The detailed name of the basin is shown in Figure 1.

3.2 Time-depth conversion and selection of boundary conditions for thermal simulation

For modeling hydrocarbon generation history, conversion of data (including reflection seismic profiles) from time domain (two-way travel time, TWT) to depth domain (meters) was carried out by 3D-Move software. The model used in this study was based on a regional model using velocity data from the speed of velocity layers (Kroeger et al., 2017). PetroMod modeling is a well-established method to forward model the evolution of sedimentary basins by restoring the original basin conditions and adding sediment through time (Naeth et al., 2005; Beha et al., 2008; Hantschel and Kauerauf, 2009; Ondrak et al., 2009). Forward modeling is often used to reconstruct the thermal evolution of the hydrocarbon generation history of source rocks (Kroeger et al., 2017). The modern average heat flow value on the source rocks' thermal evolution modeling is derived from Foucher and Scient (2006) and Kroeger et al. (2017), which is 55 mW/m^2. The heat flow values of paleo-geological historical periods are comprehensively determined according to the dynamic background of the basin (Allen and Allen, 1990). The parameters of formation lithology are calculated according to the drilling data, and paleo-depth parameters are obtained from sedimentary facies analysis.

4 Results and discussion

4.1 Formation, evolution, and transformation of rift basins

The rifting time in Zealandia varies greatly from place to place; however, the migration of the rifting has obvious regularity. It has experienced extensive rifts, migrated to the east of the Lord Howe Ridge, migrated to the west of the Lord Howe Ridge, migrated to the west of the Dampier Ridge, and finally migrated to both sides of the Lord Howe Ridge and then experienced multiple stages of compression transformation and deep burial transformation. For a single rift basin in Zealandia, it can be roughly divided into the volcanic eruption rift I stage, rift II stage, rift III stage, compression transformation stage, stress relaxation subsistence stage, shear compression deformation stage, and thermal-gravity equilibrium subsidence stage (Figure 6). The initial profile of the evolution section was modified from the seismic profile line 206/04 (Van de Beuque et al., 2003).

4.1.1 Early Cretaceous intracontinental volcanic rift I stage (c.120–95 Ma)

At the initial continental rifting stage during the early Cretaceous (Barremian-Cenomanian), a large number of alkaline non-marine volcaniclastic and volcanic rocks were deposited in each rift basin all over Zealandia, with possible coal and lacustrine sediments as the result of the incipient extensional rifting. On the Lord Howe Rise, there is direct evidence of this volcanic phase in DSDP site 207, which penetrated subaerial to shallow marine rhyolite tuffs and flows (Van de Beuque et al., 1996). There is a depositional hiatus in Cenomanian between the volcanic rift I sequence and its

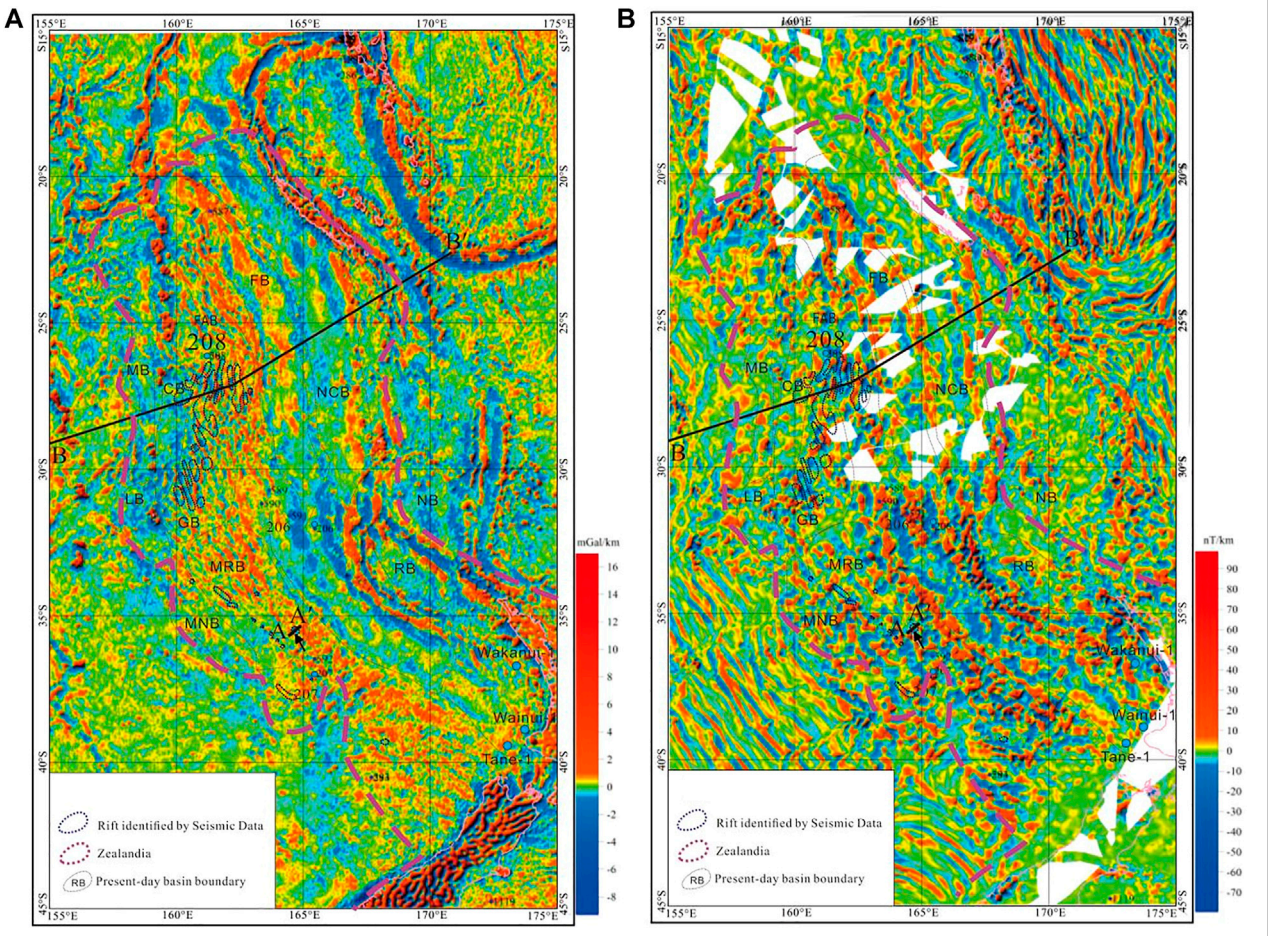

FIGURE 4
First-order vertical derivative of **(A)** gravity and **(B)** magnetic anomaly reduced to the pole. The solid black line pointed by the white arrow locates the position of the seismic section in Figure 3. **(A)** First-order vertical derivative of gravity anomaly. **(B)**. First-order vertical derivative of magnetic anomaly reduced to the pole. The white area is the data blank area. Abbreviation of basin name (see Figure 1).

overburden system in response to the collision between Zealandia and the Pacific Plate (Veevers, 2000a,b).

4.1.2 Late Cretaceous Cenomanian–Campanian rift II stage (95–83 Ma)

In the Late Cretaceous (Cenomanian–Campanian, 95–83 Ma), the rift basins were mainly developed on the east side of the Lord Howe Ridge, which was filled with a set of continental or marine-continental coal-bearing volcanic clastic rocks, grading upward to a shallow marine clastic-dominated succession (Gibson et al., 2015). Drillings of Tane-1 and Wainui-1 and outcrops onshore New Caledonia revealed that coal seams and carbonaceous mudstones were developed in the southern end of the New Caledonia basin and the northwest sea basin of New Zealand on the east side of the Lord Howe Ridge (Paris and Lille, 1977; Stagg et al., 2002).

4.1.3 Late Cretaceous (Campanian)-earliest Eocene rift III stage (83-52Ma)

Since the Late Campanian in the Late Cretaceous, rifting migrated to the west of Lord Howe ridge and rifted from south to north. From the Late Cretaceous (Campanian) to Eocene, the rift basins were mainly filled with siliciclastic to calcareous sandstones and mudstones of marginal marine to neritic origin, grading upward to fine-grained bathyal sediments in the deeper depocenters of rift basins (Gibson et al., 2015). Then, the deep-sea calcareous ooze was deposited in the Paleocene.

4.1.4 Earliest Eocene to early Oligocene extrusion transformation stage (52–33.7 Ma).

From earliest Eocene to early Oligocene, this convergence along the eastern margin of Zealandia from New Guinea to New Zealand caused rift basin inversion and compressional uplift

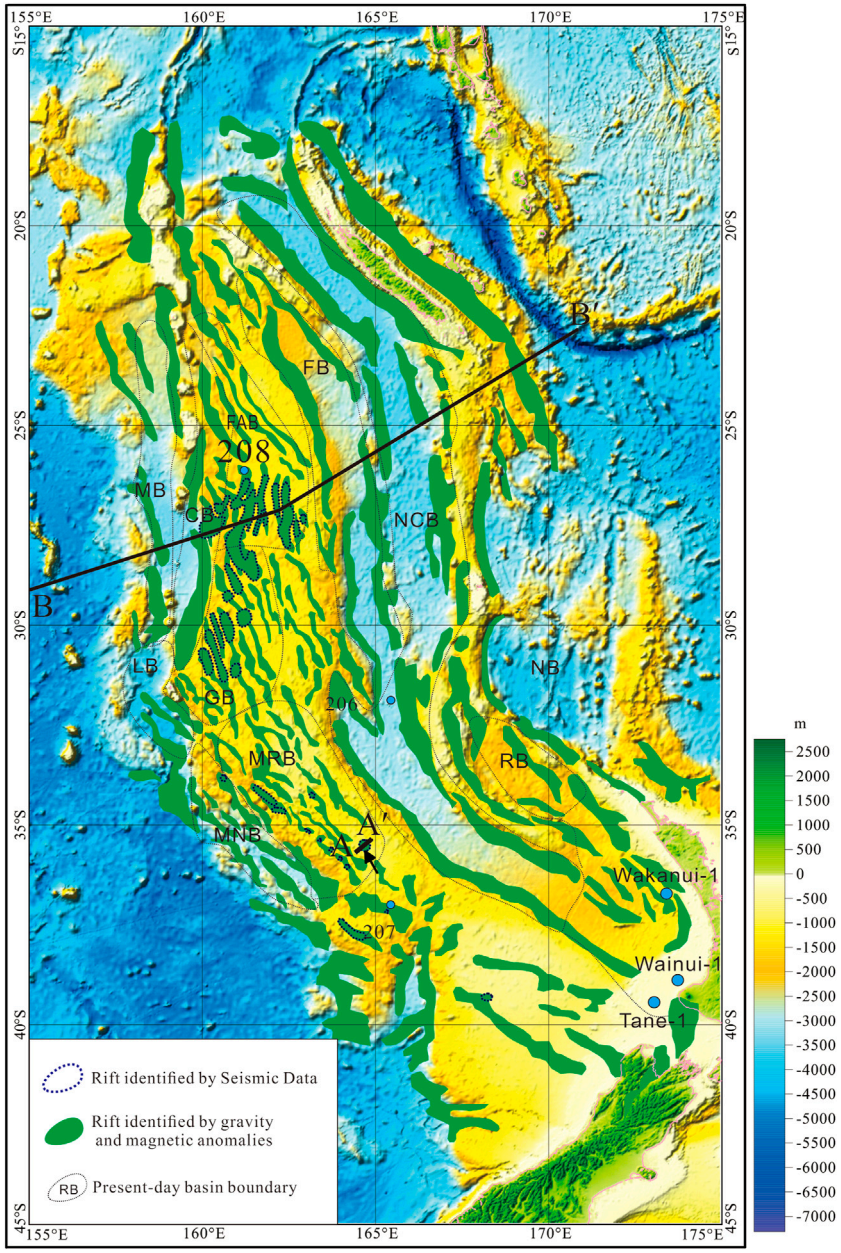

FIGURE 5
Identified rift distribution and its location map.

denudation, manifesting as the absence of upper Eocene and even middle-lower Oligocene in the majority of the rift basins in the Lord Howe Rise (Stagg et al., 2002; Van de Beuque et al., 2003).

4.1.5 Mid-late Oligocene stress relaxation subsistence transformation stage (33.7-23.3 Ma)

With the weakening of subduction-compression, the rift basins entered the stage of stress relaxation depression and thermal subsidence transformation stage and were filled with a set of nannofossil ooze, chalk, and volcanic ash in the Oligocene (Gaina et al., 1998; Gibson et al., 2015).

4.1.6 Miocene shear compression extrusion transformation stage (23.3–5 Ma).

In the Miocene, the plate boundary began to propagate through New Zealand as a convergent boundary, initiated by Neogene clockwise rotation of the Pacific subduction system (Van de Beuque et al., 2003). Since the late Miocene, oblique

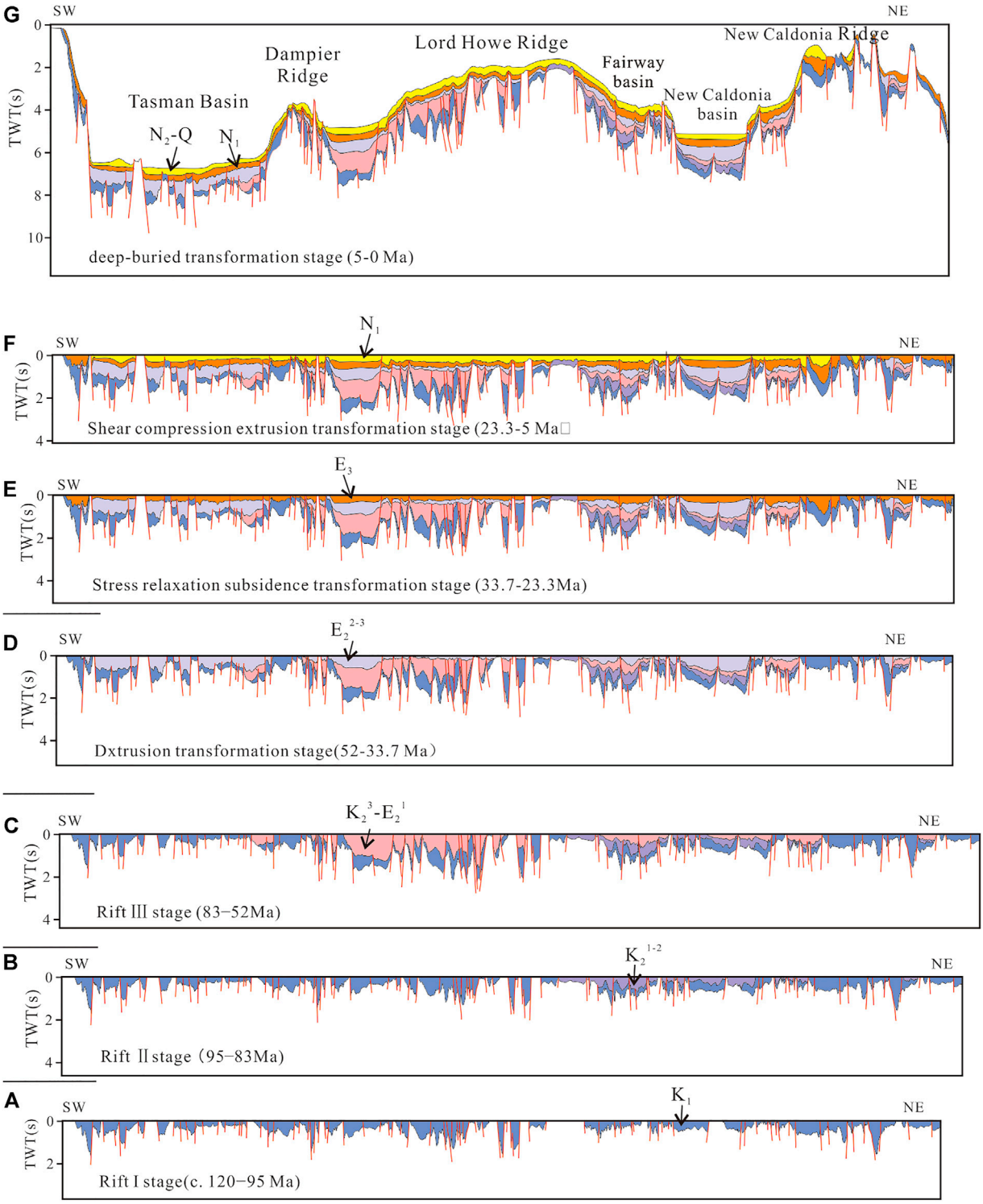

FIGURE 6
Formation, evolution, and transformation map of rift basins.

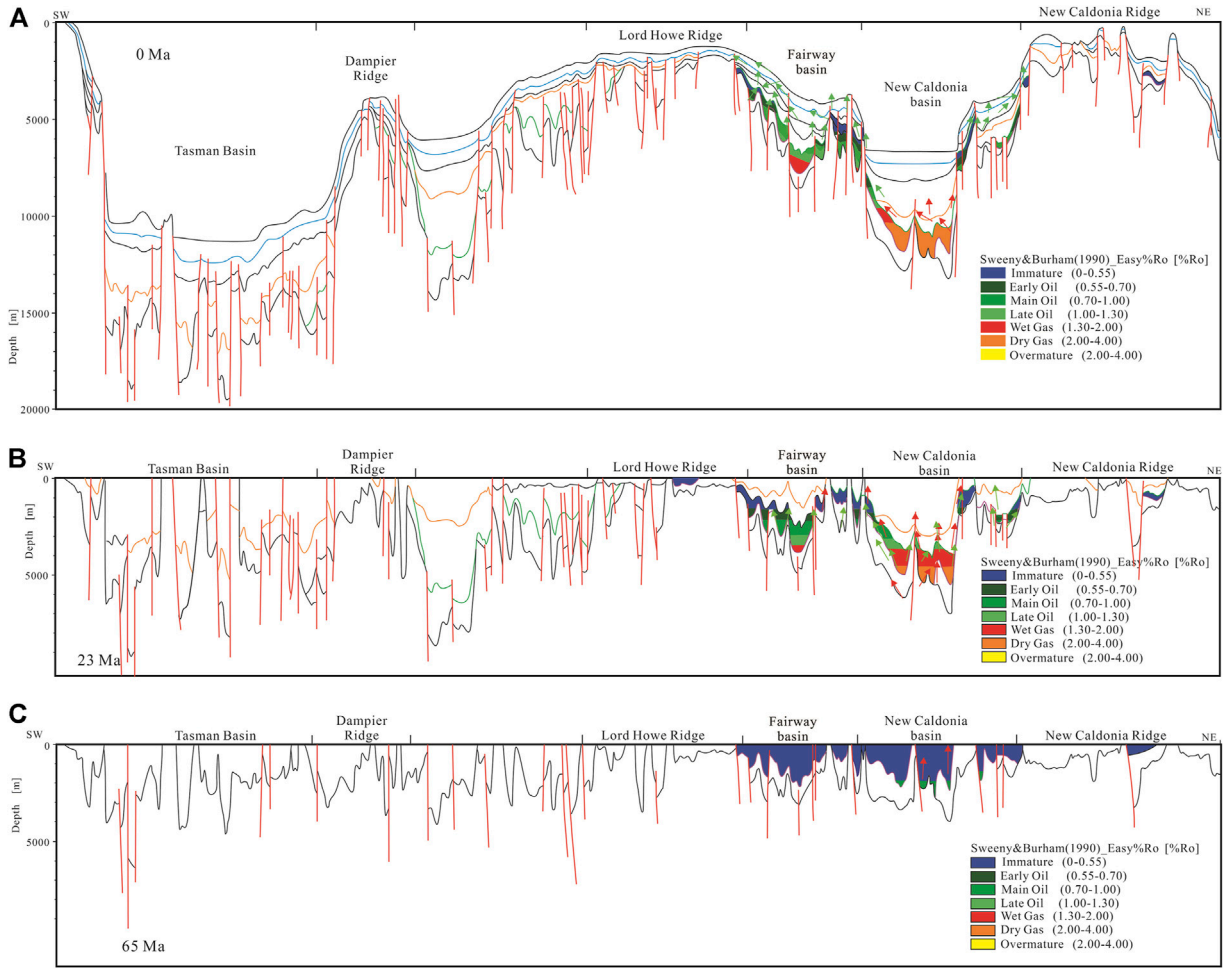

FIGURE 7
Large-section thermal history simulation profile across Zealandia (line 206/04 from Van de (Beuque et al. 2003).

compression along the Alpine Fault caused an uplift of the Macquarie Ridge. This pulsating shear compression resulted in the fold uplift, denudation of rift basins, and Miocene multiple depositional discontinuities in southeastern Zealandia.

4.1.7 Pliocene deep-buried transformation stage (5-0 Ma)

Since the Pliocene, under the regional dynamics of thermal gravity sedimentation, the region in rift basins has been strongly subsiding and was strongly buried by the thick deep-sea ooze.

4.2 Thermal history simulation and analysis

PetroMod thermal history systems modeling predicts that the Upper Cretaceous coal-measure source rocks at the bottom of the rift basins on the east side of the Lord Howe Ridge have entered the gas stage since the Miocene (Figure 7). In the Paleocene, the coal-measure source rock in the deep rifts in the central part of the New Caledonia Basin entered the hydrocarbon generation threshold (Figure 7C). In the Miocene, the coal-measure source rock in the deep rifts in the central part of the Fairway Basin and New Caledonia Basin entered the wet and dry stages, respectively (Figure 7B). At present, the thermal evolution degree of Upper Cretaceous coal-measure source rocks gradually increases from west to east and that at the bottom of the rifts in the Fairway Basin have entered the stage of generating wet gas, while most of the source rocks in the New Caledonia Basin have entered the stage of generating dry gas (Figure 7A).

4.3 Favorable zone forecast

Gas in hydrate deposits may come from thermogenic hydrocarbons deeper in the sediment pile (Claypool & Kaplan, 1974; Kvenvolden, 1995). The general coincidence of BSR-like

distribution with the structural depression and depocenter in the Fairway Basin indicates a thermogenic component to the gas hydrates (Exon et al., 1998; Collot et al., 2009). The observed BSR-like depth of 0.7 s TWT below the seabed is consistent with the calculation of the predicted transition boundary in the eastern Lord Howe Rise and in the New Caledonia Basin based on the recorded thermal gradients (Exon et al., 1998). In the oceanic crust, sediment gas hydrates occur where bottom water temperatures approach 0 °C and water depths exceed about 300 m, and the lower limit of gas hydrate occurrence is up to about 2,000 m below the seafloor, determined by the geothermal gradient (Van de Beuque et al., 2003).

BSR-like are true BSRs in the Fairway and Taranaki basins, a thermogenic hydrocarbon gas source from the buried Upper Cretaceous coal-measure source rock. Such thermogenic gas could be generated from the organic-rich coal sediments in the rift basins and migrated up-dip onto the shallow strata through the Cretaceous-Paleogene extensional faults, perhaps in part beneath a seal of early forming hydrates. The shallow layer of rift basins shows potential for gas hydrate formation and exploration potential on the eastern side of the Lord Howe Rise (Figure 1), when the upper Cretaceous coal-measure source rocks are under the gas generation stage.

5 Conclusion

As the last area with unknown oil exploration potential, it has attracted the attention of energy scientists. Gravity and magnetic anomaly data, balanced cross-section, and thermal history modeling results show the following.

1) The rifting time in Zealandia varies greatly from place to place. It has experienced extensive rifts, migrated to the east of the Lord Howe Ridge, migrated to the west of the Lord Howe Ridge, migrated to the west of the Dampier Ridge, and finally migrated to both sides of the Lord Howe Ridge and then experienced multiple stages of compression transformation and deep burial transformation.
2) For a single rift basin in Zealandia, it can be roughly divided into the volcanic eruption rift I stage, rift II stage, and/or rift III stage, compression transformation stage, stress relaxation subsistence stage, shear compression deformation stage, and thermal-gravity equilibrium subsidence stage.
3) In the Late Cretaceous (Cenomanian-Campanian, 95–83 Ma), the continental or marine-continental coal-bearing clastic rock sequence was mainly developed in the rift basins on the east side of the Lord Howe Ridge.
4) The Upper Cretaceous coal source rocks were deposited, and their burial depth is higher than the gas generation threshold in the Fairway and New Caledonia basins and other basins on the eastern side of the Lord Howe Ridge. The deeply buried source rocks in the central part of the rift have entered the wet-late maturity stage since Cenozoic and may migrate along the fault and form a gas hydrate in the shallow seabed stable zone. The shallow layer of rift basins on the eastern side of the Lord Howe Ridge has the gas hydrate-forming potential.

Data availability statement

The original contributions presented in the study are included in the article/Supplementary Material; further inquiries can be directed to the corresponding author.

Author contributions

XF and the LS completed the writing of this thesis, and YY and YL participated in the clearing and editing of some drawings.

Funding

This study was supported by the Natural Science Foundation of China (No. 41102072) and the China Geological Survey Project (No. DD20160227).

Conflict of interest

The authors declare that the research was conducted in the absence of any commercial or financial relationships that could be construed as a potential conflict of interest.

Publisher's note

References

Allen, P. A., and Allen, J. R. (1990). *Basin analysis:principles and application*. Oxford,England: Blackwell Scientific Publications, 282–283.

Auzende, J. M., Van de Beuque, S., Dickens, G., François, C., Lavoy, Y., Voutay, O., et al. (2000). Deep sea diapirs and bottom simulating reflflector in Fairway Basin (SW Pacific). *Mar. Geophys. Res.* 21, 579–587. doi:10.1023/a:1004848715044

Bache, F., Mortimer, N., Sutherland, R., Collot, J., Rouillard, P., Stagpoole, V., et al. (2013). Seismic stratigraphic record of transition from Mesozoic subduction to continental breakup in the Zealandia sector of eastern Gondwana. *Gondwana Res.* 26, 1060–1078. doi:10.1016/j.gr.2013.08.012

Beggs, J. M., Challis, G. A., and Cook, R. A. (1990). Basement geology of the Campbell plateau: Implications for correlation of the Campbell magnetic anomaly system. *N. Z. J. Geol. Geophys.* 33, 401–404. doi:10.1080/00288306.1990.10425696

Claypool, G. W., and Kaplan, I. R. (1974). "The origin and distribution of methane in marine sediments," in *Natural gases in marine sediments*. Editor I. R. Kaplan (New York: Plenum), 99–139.

Cluzel, D., Aitchison, J. C., and Picard, C. (2001). Tectonic accretion and underplating of mafic terranes in the Late Eocene intraoceanic fore-arc of New Caledonia (Southwest Pacific); geodynamic implications. *Tectonophysics* 340, 23–59. doi:10.1016/s0040-1951(01)00148-2

Collot, J., Herzer, R., Lafoy, Y., and Geli, L. (2009). Mesozoic history of the fairway–aotea basin: Implications for the early stages of Gondwana fragmentation. *Geochem. Geophys. Geosyst.* 10, Q12019. doi:10.1029/2009gc002612

Corredorfo (1996). Three- dimensional geometry and kinematics of the Western thrust front of the eastern Cordillera. *Columbia AAPG SEPM* 5, 29–30.

Exon, N, F., Dickens, G. R., Auzende, J-M., Lafoy, Y., Symonds, P. A., and Van de Beuque, S. (1998). Gas hydrates and free gas on the Lord howe rise. *PESA J.* 26, 148–158.

Foucher, J. P., and Scient, P. (2006). *Rapport de la campagne AUSFAIR/ZoNéCo-12*. à borddu N/O Marion Dufresnes, 12–26.

Gaina, C., Müller, D., Royer, J. Y., Stock, J. M., Hardebeck, J. L., and Symonds, P. (1998). The tectonic history of the Tasman Sea; a puzzle with 13 pieces. *J. Geophys. Res.* 103, 12413–12433. doi:10.1029/98JB00386

Gaina, C., Müller, R. D., Royer, J.-Y., and Symonds, P. (1999). Evolution of the Louisiade triple junction. *J. Geophys. Res.* 104, 12927–12939. doi:10.1029/1999jb900038

Gamble, J. A., Wright, I. C., and Baker, J. A. (1993). Seafloor geology and petrology in the oceanic to continental transition zone of the kermadec-havre-taupo volcanic zone arc system, New Zealand: New Zealand. *N. Z. J. Geol. Geophys.* 36, 417–435. doi:10.1080/00288306.1993.9514588

Gibson, G. M., Roure, F., and Manatschal, G. (2015). Sedimentary basins and crustal processes at continental margins: From modern hyper-extended margins to deformed ancient analogues. *Geol. Soc. Lond. Spec. Publ.* 413, 9–33.

Kamp, P. J. J. (1986). The mid-Cenozoic Challenger rift system of Western New Zealand and its implications for the age of Alpine fault inception. *Geol. Soc. Am. Bull.* 97, 255–281.

Kroeger, K. F., Crutchley, G. J., Hill, M. G., and Pecher, I. A. (2017). Potential for gas hydrate formation at the northwest New Zealand shelf margin - new insights from seismic reflection data and petroleum systems modelling. *Mar. Petroleum Geol.* 83, 215–230. doi:10.1016/j.marpetgeo.2017.02.025

Kvenvolden, K. A. (1995). A review of the geochemistry of methane in natural gashydrate. *Org. Geochem.* 23, 997–1008. doi:10.1016/0146-6380(96)00002-2

Lafoy, Y., Brodien, I., Vially, R., and Exon, N. F. (2005). Structure of the basin and ridge system west of New Caledonia (southwest Pacific): A synthesis. *Mar. Geophys. Res. (Dordr).* 26, 37–50. doi:10.1007/s11001-005-5184-5

Luyendyk, B. (1995). Hypothesis for Cretaceous rifting of East Gondwana caused by subducted slab capture. *Geology* 23, 373–376. doi:10.1130/0091-7613(1995)023<0373:HFCROE>2.3.CO;2

McDougall, I., Maboko, M. A. H., Symonds, P. A., McCulloch, M. T., Williams, I. S., and Kudrass, H. R. (1994). Dampier ridge, Tasman Sea, as a stranded continental fragment. *Aust. J. Earth Sci.* 41, 395–406. doi:10.1080/08120099408728150

Mortimer, N., Campbell, H. J., Tulloch, A. J., King, P. R., Stagpoole, V. M., Wood, R. A., et al. (2016). Zealandia: Earth's hidden continent. *GSA Today* 27–35. doi:10.1130/GSATG321A.1

Mortimer, N., Dunlap, W. J., Palin, J. M., Herzer, R. H., Hauff, F., and Clark, M. (2008b). Ultra-fast early Miocene exhumation of cavalli seamount, northland plateau, southwest Pacific ocean. *N. Z. J. Geol. Geophys.* 51, 29–42. doi:10.1080/00288300809509848

Mortimer, N., Hauff, F., and Calvert, A. T. (2008a). Continuation of the new england orogen, Australia, beneath the queensland plateau and Lord howe rise. *Aust. J. Earth Sci.* 55, 195–209. doi:10.1080/08120090701689365

Mortimer, N., Herzer, R. H., Gans, P. B., Parkinson, D. L., and Seward, D. (1998). Basement geology from three kings ridge to west Norfolk ridge, Southwest Pacific ocean: Evidence from petrology, geochemistry and isotopic dating of dredge samples. *Mar. Geol.* 148, 135–162. doi:10.1016/S0025-3227(98)00007-3

Mortimer, N., Hoernle, K., Hauff, F., Palin, J. M., Dunlap, W. J., Werner, R., et al. (2006). New constraints on the age and evolution of the wishbone ridge, Southwest Pacific cretaceous microplates, and zealandia–west Antarctica breakup. *Geol.* 34, 185–188. doi:10.1130/G22168.1

Mortimer, N., Rattenbury, M., King, P., Bland, K., Barrell, D., Bache, F., et al. (2014). High-level stratigraphic scheme for New Zealand rocks. *N. Z. J. Geol. Geophys.* 57, 402–419. doi:10.1080/00288306.2014.946062

Mortimer, N., Tulloch, A. J., and Ireland, T. R. (1997). Basement geology of Taranaki and wanganui basins, New Zealand: New Zealand. *N. Z. J. Geol. Geophys.* 40, 223–236. doi:10.1080/00288306.1997.9514754

Mortimer, N., Turnbull, R. E., Palin, J. M., Tulloch, A. J., Rollet, N., and Hashimoto, T. (2015). Triassic-jurassic granites on the Lord howe rise, northern Zealandia. *Aust. J. Earth Sci.* 62, 1–8. doi:10.1080/08120099.2015.1081984

Paris, J. P., and Lille, R. (1977). "New Caledonia: Evolution from permian to Miocene, mapping data and hypotheses about geotectonics," in *International symposium on dynamics in southwest pacific, 27 august–2 september 1976, noumea, New Caledonia* (Paris: Editions Technip), 195–208.

Pierrick, R., Julien, C., Rupert, S., Francois, B., Martin, P., Samuel, E., et al. (2015). Seismic stratigraphy and paleogeographic evolution of Fairway basin, northern Zealandia, southwest Pacific: From cretaceous Gondwana breakup to cenozoic Tonga–kermadec subduction. *Basin Res.* 29, 189–212. doi:10.1111/bre.12144

Ringis, J. (1972). *The structure and history of the Tasman Sea and the southeast Australian margin*. Sydney: Ph.D. thesisUniv. of New South Wales.

Schellart, W. P., Lister, G. S., and Toy, V. G. (2006). A Late Cretaceous and Cenozoic reconstruction of the Southwest Pacific region: Tectonics controlled by subduction and slab rollback processes. *Earth-Science Rev.* 76, 191–233. doi:10.1016/j.earscirev.2006.01.002

Shaw, R. D. (1979). *On the evolution of the Tasman Sea and adjacent continental margins*. Sydney, Australia: Ph.D. thesis, University of Sydney, 311.

Spandler, C., Rubatto, D., and Hermann, J. (2005). Late cretaceous-tertiary tectonics of the southwest pacific: Insights from U–Pb sensitive, high-resolution ion microprobe (SHRIMP) dating of eclogite facies rocks from New Caledonia. *Tectonics* 24, TC3003. doi:10.1029/2004TC001709

Stagg, H. M. J., Alcock, M. B., Borissova, I., and Moore, A. M. G. (2002). *Geoscience Australia record*. 2002/25.Geological framework of the southern Lord Howe Rise and adjacent areas

Stock, J., and Molnar, P. (1982). Uncertainties in the relative positions of the Australia, Antarctica, Lord howe, and pacific plates since the late cretaceous. *J. Geophys. Res.* 87 (B6), 4697–4714. doi:10.1029/jb087ib06p04697

R. P. Suggate, G. R. Stevens, and M. T. Te Punga (Editors) (1978). *The geology of New Zealand* (Wellington: New ZealandGovernment Printer), 819.

Tulloch, A. J., Kimbrough, D. L., and Wood, R. A. (1991). Carboniferous granite basement dredged from a site on the Southwest margin of the Challenger plateau, Tasman Sea: New Zealand. *N. Z. J. Geol. Geophys.* 34, 121–126. doi:10.1080/00288306.1991.9514449

Tulloch, A. J., Ramezani, J., Mortimer, N., Mortensen, J., van den Bogaard, P., and Maas, R. (2009). "Cretaceous felsic volcanism in New Zealand and Lord howe rise (Zealandia) as a precursor to final Gondwana break-up," in *Extending a continent: Architecture, rheology and heat budget*. Editors U. Ring and B. Wernicke (Canberra: Geological Society (London) Special Publication), 89–118.

Van de Beuque, S., Stagg, H. M. J., Sayers, J., Willcox, J. B., and Symonds, P. A. (2003). *Geological framework of the northern Lord howe rise and adjacent areas, geoscience Australia record*.

Veevers, J. J. (2000a). Change of tectono-stratigraphic regime in the Australian plate during the 99 Ma (mid-Cretaceous) and 43 Ma (mid-Eocene) swerves of the Pacific. *Geology* 28, 47–50. doi:10.1130/0091-7613(2000)028<0047:cotsri>2.3.co;2

Veevers, J. J. (2000b). "Chapter 16. Mid-cretaceous (99 Ma) and mid Eocene (43 Ma) events in the indo-Australian and antarctic plates and coeval swerves of the Pacific plate," in *Billion-year Earth history of Australia and neighbours in gondwanaland*. Editor J. J. Veevers (Sydney: GEMOC Press), 102–109.

Willcox, J. B., and Sayers, J. (2002). *Geological framework of the central Lord Howe Rise (Gower Basin) region with consideration of its petroleum potential*. Canberra: Geoscience Australia Record.

frontiers | Frontiers in Earth Science

TYPE Original Research
PUBLISHED 30 September 2022
DOI 10.3389/feart.2022.994602

OPEN ACCESS

EDITED BY
Lihua Zuo,
Texas A&M University Kingsville,
United States

REVIEWED BY
Bing Bai,
Beijing Jiaotong University, China
Chen Peipei,
Beijing University of Civil Engineering and Architecture, China

*CORRESPONDENCE
Jun Pei,
asharey@yeah.net
Na Wei,
weina8081@163.com

SPECIALTY SECTION
This article was submitted to Marine Geoscience,
a section of the journal
Frontiers in Earth Science

RECEIVED 15 July 2022
ACCEPTED 06 September 2022
PUBLISHED 30 September 2022

CITATION
Pei J, Wei N, Zhang B, Zhao J, Kvamme B, Coffin RB, Li H and Bai R (2022), Imitating the effects of drilling fluid invasion on the strength behaviors of hydrate-bearing sediments: An experimental study.
Front. Earth Sci. 10:994602.
doi: 10.3389/feart.2022.994602

Imitating the effects of drilling fluid invasion on the strength behaviors of hydrate-bearing sediments: An experimental study

Jun Pei[1,2]*, Na Wei[1,2]*, Boning Zhang[3], Jinzhou Zhao[1,2], Bjørn Kvamme[1], Richard B. Coffin[1], Haitao Li[1,2,4] and Ruiling Bai[1,2]

[1]State Key Laboratory of Oil and Gas Reservoir Geology and Exploitation, Southwest Petroleum University, Chengdu, China, [2]State Key Laboratory of Natural Gas Hydrate, Beijing, China, [3]Chengdu North Petroleum Exploration and Development Technology Co., Ltd., Chengdu, China, [4]State Key Laboratory of Coal Mine Disaster Dynamics and Control, Chongqing University, Chongqing, China

The drilling fluid invasion into hydrate-bearing sediments will change the geomechanical properties of the reservoir and may lead to uncontrolled geological disasters in the worst case. Native sediments are replaced with artificial samples in this study to investigate the effect of drilling fluid invasion on the strength behaviors of hydrate-bearing sediments. The triaxial test is used primarily to assess the strength behaviors of hydrate-bearing sediments at varying temperatures, pressures, and hydrate saturation levels. The process of water-based drilling fluid penetrating into hydrate-bearing sediments is then experimentally imitated under various experimental conditions, with reservoir temperature of 4°C and pore pressure of 10 MPa. The possible repercussions of drilling fluid invasion and hydrate phase transition are identified by testing the mechanical properties of sediments under various invasion times and temperatures. The findings reveal that when hydrate saturation rises from 5% to 35%, the gas hydrate sediments shift from strain hardening to strain softening, with the critical hydrate saturation value of transition is between 15% and 25%. Peak strength increases with increasing hydrate saturation and pressure, and decreases with increasing temperature, whether drilling fluid invasion is present or not. The peak strength, Young's modulus, shear modulus, and secant modulus of hydrate sediments all decreased significantly after drilling fluid invasion, although the Poisson's ratio rose. These mechanical parameters are related to temperature and pressure under the action of drilling fluid. Finally, engineering and research recommendations for reducing the risk of drilling fluid invasion and hydrate dissociation are made based on experimental findings and theoretical analysis. This study innovatively examine the geomechanical mechanical properties of drilling fluid invading hydrate reservoir, which is critical for avoiding production concerns.

KEYWORDS

hydrate-bearing sediments, gas hydrate, triaxial test, geomechanical properties, stress-strain, strength behaviors

1 Introduction

Natural gas hydrate is a caged crystalline compound, commonly known as combustible ice (Sloan and Koh., 2007; Sun et al., 2021). It is known for its abundant energy reserves, wide distribution, high calorific value and high-energy density, which makes it an ideal low-carbon fuel. The special environment of deep-water seafloor can provide suitable temperature and pressure conditions for the generation of natural gas hydrate. The continental shelf, mid-ocean ridge and trench are ideal areas for gas hydrate generation. It is estimated that 20.7% of the global land and 90% of the deep-water seafloor have conditions conducive to the generation of gas hydrate, of which about 95% of the gas hydrate is stored in the deep-sea area (Ye and Liu., 2013; Sun et al., 2021). Currently the reserves of natural gas hydrate in the world has so far proved inconclusive. According to USGS data from the year 2000, the quantity of energy trapped in hydrate is likely more than twice that of all energy in known fossil fuels (coal, oil, and gas) (Kvamme, 2020). The widely quoted view article that could be used to estimate the reserves, provided by Boswell and Collett, yielded a global gas hydrate gas-in-place resources of 3×10^{15} m^3 (Boswell and Collett, 2011; Wang and Wang, 2020). Various signs show that natural gas hydrate may become an alternative energy after shale gas and coalbed methane. Marine gas hydrate with huge reserves will become the main area of exploration and development in the future.

Methane and/or other small non-polar, or slightly polar hydrocarbons can form hydrate with water (or ice) under high pressure and low temperature. Some inorganic pollutants in natural gas, like for instance CO_2 and H_2S, are also very efficient hydrate formers (Chibura et al., 2022). Sources of gas to natural gas hydrate are either from thermogenic degradation of organic material deep down in sediments, or from biogenic degradation of organic material in the upper crust (Stolper et al., 2014; Dai et al., 2017; Liang et al., 2022). The majority of global resources reside in marine sediments beneath the seafloor, at temperatures and pressures within the hydrate stability region (Jang et al., 2019; Cui et al., 2021; Wei et al., 2022). If the seafloor conditions are outside the hydrate forming conditions, this will result in direct fluxes of natural gas to the ocean, and in some cases bubbling of gas all the way to the air (Kvamme and Saeidi, 2021). If the seafloor openings of the fractures are at hydrate forming depths, and temperatures are inside hydrate generation, then an unstable situation will establish. This type of hydrate mounds on the seafloor can be found numerous places round the world and give rise to bio geo ecosystems. In nature, environments such as the permafrost, the submarine sediments on the active and passive continental margins are suitable for hydrate occurrence. It is found that the main occurrence areas of gas hydrate are the accretionary wedges on the active continental margins and geological structures such as cold spring vents, mounds, faults, mud volcanoes and diapirs on the passive continental margins. At present, hydrate reservoirs found in marine environment are mainly distributed along the coast of India, the Sea of Japan, the Nankai Trough, the Gulf of Mexico, the Atlantic coast of the USA, the margin of the Arctic Ocean, the Cascadia margin, the Bering Strait, the South China Sea, the Ulleung Basin, the Niger Delta Basin, the coastal Trinidad and Tobago (Sun et al., 2011; Chong et al., 2016; Hu et al., 2021).

Historically, the interest in offshore natural gas hydrate as an energy source has risen considerably during the latest four decades. The distribution, occurrence, properties, exploration and development methods of gas hydrate have always been the focus of research. Countries that are very interested in gas hydrate include developed countries such as the United States, Canada, Norway, Japan, South Korea and Germany, as well as emerging economies such as China, India and Russia. Significant progress have been made in our understanding of the properties of hydrate reservoir and its exploration and development methods. It is realized that the development of natural gas hydrate, an unconventional energy with great potential, can not only meet the growing energy demand, but also help to reduce carbon dioxide emissions (Lee et al., 2003; Yin and Linga, 2019). However, the traditional oil and gas development technology is not completely applicable to the development of natural gas hydrate. At present, the production methods of natural gas hydrate are mainly depressurization, thermal stimulation, CO_2-CH_4 replacement, chemical inhibitor injection, etc. (Lee et al., 2003; Chong et al., 2016; Li et al., 2016; Yin and Linga, 2019). These methods are faced with problems such as formation instability, sand control and prevention. In recent years, the solid fluidization method proposed by our team has also been widely reported (Zhou et al., 2018a; Wei N. et al., 2019; Zhou et al., 2020). After 2000, these methods have been verified by short-term trial production in the field. In 2002, although the production efficiency was not satisfactory, the trial production experiment conducted in permafrost Mallik for about 5 days verified the effectiveness of the thermal stimulation method for the first time (Yin and Linga, 2019). Then in 2007 and 2008, the depressurization method was used to conduct two trial production in this region, producing 830 and 13,200 m^3 of natural gas respectively (Huang et al., 2009; Yin and Linga, 2019). In 2012, the CO_2-CH_4 replacement method was combined with the depressurization, producing a total of 24,000 m^3 of natural gas on the North Slope of Alaska in

30 days (Wang and Lau, 2020). The trial production of gas hydrate in permafrost areas also includes scientific research in Qilian Mountain, Tibet, China in 2011 and 2016 (Li et al., 2018; Liang et al., 2020). It was not until 2013 that the first trial production project of marine gas hydrate in the world was successfully implemented. The first attempt in the Daini–Atsumi Knoll off Honshu Island produced 119,000 m^3 of methane applying the depressurization method. Four years later, Japan conducted the second production of methane hydrate using two producer wells sequentially in the Nankai Trough (Yamamoto et al., 2019). A key problem in production technology is the limited understanding of the geomechanics of gas hydrate sediments. This problem became very obvious even in the field experiments in Alaska and Nankai Trough. Sediment movement and uncontrolled sand production occurred in both places. Although the initial goals have not been fully achieved, unprecedented achievements have been made and all countries concerned should learn from Japan. After that, China conducted two depressurization production in the South China Sea in 2017 and 2020, producing 309000 and 861,400 m^3 of natural gas respectively (Ye et al., 2020; Zhang et al., 2022). The world's first solid-state fluidization trial production was almost carried out at the same time as China's first depressurization trial production. This new technique for non-diagenetic hydrate has achieved a recovery of up to 80.1% in the first attempt (Zhou et al., 2018b; Zhou et al., 2020). Nevertheless, some technical problems such as sand production, water production, wellbore stability, methane leakage and so on, have not been well solved in the past, which have seriously affected the commercialization of gas hydrate. At present, the study of geomechanical properties and other physical properties of natural gas hydrate reservoir is of great significance for logging evaluation and reservoir stability evaluation of natural gas hydrate reservoir. Considering the possible energy crisis in the future and the great potential of gas hydrate, it is necessary to conduct an in-depth study of these unsolved problems.

The invasion of drilling fluid into hydrate reservoir is an important and unsolved problem. In the drilling process of marine hydrate reservoir, the drilling fluid will penetrate into the hydrate-bearing sediment and displace the original water and gas in the formation due to the pressure difference. As a result, the initial temperature, pressure and salinity conditions of hydrate reservoir will change. Natural gas hydrate are not thermodynamically stable and the existence of commercial concentrations of hydrate is only possible when the hydrate deposits are sealed by clay, shale and other sediments of very low permeability (Cui et al., 2021; Sun et al., 2022). Drilling through hydrate filled sediments will increase the temperature in the regions surrounding the borehole, which is mainly due to the high temperature of the drilling fluid itself and the heat generated by the friction of drilling tools. And the drilling fluid by itself contains ions as well as polar fluids that significantly affect the activity of the water. Both effects will lead to local dissociation of

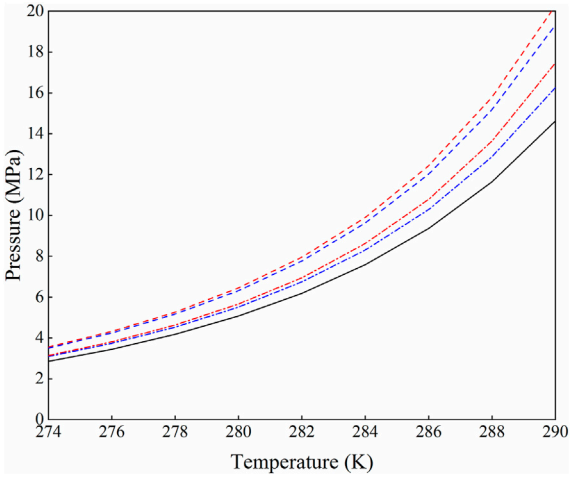

FIGURE 1
The solid curve is hydrate stability limit for hydrate formed from pure water and CH_4, red dash-dot is for hydrate formed from a 2 wt% methanol in water solution and CH_4, blue dash-dot is for hydrate formed from a 2 wt% NaCl in water solution and CH_4, red dashed is for hydrate formed from water in a 5 wt% methanol in water solution and CH_4, and blue dashed is for hydrate formed from water in a 5 wt% NaCl in water solution and CH_4.

hydrate. The water and gas produced by hydrate dissociation, together with the initially invaded drilling fluid, are driven further away from the bottom of the wellbore by the newly entered drilling fluid. As such the invasion of drilling fluid in hydrate reservoir is accompanied by hydrate dissociation and heat transfer. One concern is that released gas can leak through annulus along with the returning drilling mud. Other possible leakage pathways include passages between the outside of the pipeline and the sediments. The impact of the temperature increase is unique for every specific hydrate reservoir and depends on the super saturation, i.e., free energy of the hydrate at actual pressure and temperature relative to free energy of the hydrate at pressure temperature stability conditions. For illustration, we plot stability limits of hydrate in temperature pressure projection and in projection of CH_4 concentration in surrounding water in Figure 1. Increased temperature, reduced pressure or inhibitors that bring the system outside hydrate stability, and keep this condition outside stability, will lead to hydrate dissociation. Like, for instance, the invasion of drilling fluid into hydrate reservoir. In short, these effects cause changes in mechanical, electrical, thermodynamic properties and permeability of the reservoir, affecting the stability of formation and the reliability of logging during drilling. It may lead to poor rheology of drilling fluid and wellbore instability. This complex process will be described and analyzed in detail in the next section.

Evaluating the strength behaviors of hydrate reservoirs and studying the response process of drilling fluid invading the

TABLE 1 Some theoretical research and experimental studies on the physical parameters of drilling fluid invasion into gas hydrate sediments in recent years.

Main contribution	Apparatus/Method	Main parameter	Literature
A three-dimensional thermal-hydro-chemical coupling model, which can be used to analyze the invasion characteristics of drilling fluid and the formation response.	The numerical modeling.	Pore pressure and temperature, hydrate and water saturation, fluid-loss velocity, cumulative filtrate volume, invasion time, permeability, drilling fluid pressure and temperature, etc.	Dong et al. (2022)
Near-wellbore fracture initiation and propagation induced by drilling fluid invasion: a fluid solid coupling study of borehole stability.	The integrated discrete element method (DEM)-computational fluid dynamics (CFD).	Stress-Strain relationship, pore pressure, radial length of instability zone, s stress field, tress difference, invasion fluid pressure, gas hydrate saturation, seabed depth, etc.	Zhu et al. (2021)
The characteristics of drilling fluid invading marine hydrate reservoirs under different drilling fluid parameters and its effect on hydrate dissociation behaviors near the well.	TOUGH + HYDRATE numerical modeling.	Pore pressure, hydrate saturation, salinity, drilling fluid temperature, drilling fluid density, drilling fluid salinity, etc.	Wang et al. (2021)
The hydrate saturation, penetration depth, and influence mechanism of temperature and pressure difference during drilling fluid penetration.	The artificial core preparation device and the gas hydrate mining and fluid migration simulation system.	Porosity, resistivity, pressure, temperature, hydrate saturation, penetration depth, mechanisms, etc.	Zheng et al. (2020)
The distributions of temperature, pressure, saturation and NaCl concentration of pore water around the wellbore at different times after the drilling fluid invaded the reservoir.	The numerical modeling.	Pressure and temperature around the wellbore, hydrate saturation, water saturation, gas saturation, NaCl concentration, intrinsic permeability, etc.	Huang et al. (2020)
Analysis of multi field coupling and optimization of drilling parameters.	Numerical simulation and experimental verification.	Distance from wellbore, drilling fluid density, well depth, drilling temperature, pressure and temperature in the wellbore, flow rate, gas holdup, hydrate particle concentration, etc.	Wei J et al. (2019)
Effects of temperature and thermodynamic inhibitors of water-based drilling fluid on hydrate-bearing samples with different hydrate saturations.	The drilling fluid/NGH-bearing sediment interaction testing system.	Drilling fluid formula (salt-type inhibitors or alcohol-type inhibitors), drilling fluid temperature, P-wave velocity, gas hydrate saturation, hydrate inhibitor concentration, hydrate dissociation time, etc.	Zhang et al. (2017)
The behavior of hydrate under thermal stimulation of drilling fluid was investigated to study the factors affecting wellbore integrity.	An experimental setup of hydrate evaluation test.	Temperature, hydrate dissociation rate, hydrate dissociation front, etc.	Fereidounpour and Vatani, (2014)

formation near the wellbore in drilling is of great significance to logging evaluation, safe drilling, reservoir protection, and gas production. In recent years, researchers from many countries and regions have studied the geomechanical properties of hydrate-bearing sediment during dissociation. Great progress has been made in sample preparation, parameter testing, temperature and pressure control, model verification and so on. So far, a laboratory-field and macro-micro experimental system of hydrate-bearing sediment mechanics have been preliminarily formed. The macroscopic mechanical properties of hydrate deposits are revealed by triaxial experiments based on classical soil mechanics, and the microscopic experiments based on CT, nuclear magnetic resonance (NMR), and scanning electron microscopy (SEM) are helpful to clarify their geomechanical mechanism (Park et al., 2018; Wu et al., 2018; Liu et al., 2019; Tian et al., 2019). In previous studies, the research of drilling fluid invading hydrate reservoir focused on the impact of drilling activities on hydrate reservoirs. The influence of drilling fluid invasion is usually ignored in the design of drilling fluid. To our knowledge, there are many numerical simulation studies on the changes of physical parameters of hydrate-bearing sediments in the process of invasion, but few related experimental studies, especially the impact of drilling fluid invasion on reservoir geomechanical properties. At present, most of the studies on the geomechanical properties of hydrate-bearing sediments are carried out without drilling fluid, and there is a lack of experimental study on the change of reservoir properties after drilling fluid invasion. See Table 1 for some studies on the physical parameters of hydrate-bearing sediments during the invasion process of drilling fluid in recent years.

The commercial application needs further investigations on the geotechnical and mechanical characteristics of hydrate-bearing sediments after drilling fluid intrudes into hydrate reservoirs. For these purposes, laboratory studies is more time-saving and labor-saving than field tests. Using artificial cores as the experimental sample, we will investigate the effects of drilling fluid invasion at various temperatures and invasion times on the geomechanical properties of gas hydrate deposits in this work. The stress-strain and other geomechanical properties of 16 groups of hydrate-bearing sediments under different temperature, pressure and saturation were measured. Then, the invasion temperature and time of drilling fluid was changed under different saturation conditions, and the changes of

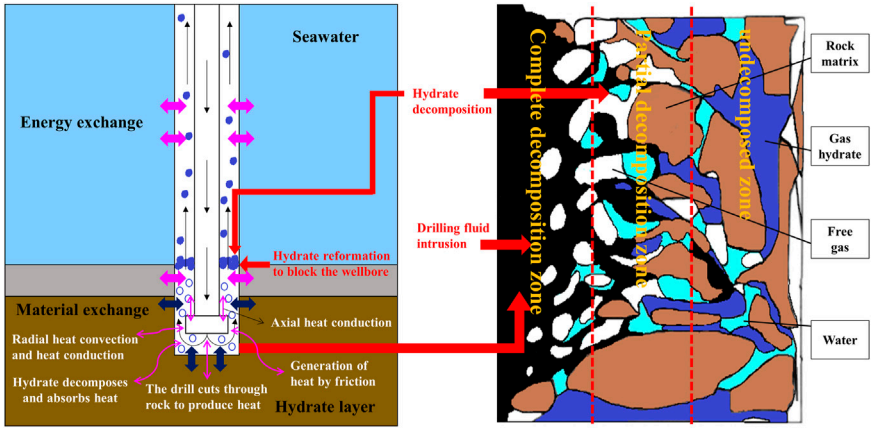

FIGURE 2
Drilling fluid invasion profile around the wellbore. The boundary and distance between zones do not represent the actual boundary and distance.

geomechanical properties after hydrate dissociation were measured experimentally. The hydrate saturation range of the experiment is roughly controlled at 5%–35%. There are two choices of drilling fluid temperature, and there are three levels of invasion time, with a total of 24 groups of drilling fluid invasion experiments. Additionally, the effects and risks caused by hydrate dissociation after drilling fluid invasion during drilling are analyzed and evaluated. Engineering suggestions are put forward to ensure that industrial personnel can perform their work safely and efficiently.

2 Possible effects of hydrate dissociation and reservoir properties due to drilling fluid invasion

Drilling gas hydrate reservoirs is often thought to be dangerous. Common concerns include well plugging, blowout, wellbore stability, formation collapse, and landslides (Merey, 2016). In our previous work, we paid more attention to the engineering parameters, consequences and risks of wellbore multiphase flow in the process of marine gas hydrate drilling (Wei et al., 2018; Wei N. et al., 2019; Sun et al., 2021; Sun et al., 2022). Here we focus on the effects of drilling fluid invasion on the hydrate generation and dissociation. The drilling fluid in the wellbore will exchange material and energy with seawater and the formation during the drilling of hydrate reservoirs. It is critical that the circulating drilling fluid enters the hydrate reservoir through holes and throats and interacts with hydrate particles, causing the initial pressure and temperature field to be disrupted (Chen et al., 2019). The drilling fluid profile around the wellbore can be divided into three components, as shown in Figure 2. When drilling into the hydrate reservoir, the first layer along the invasion direction is the hydrate complete dissociation zone, where there is no hydrate, and drilling fluid, free water, and free gas are the fluids in the formation pores. Solid particles in the drilling fluid are generally deposited in this location, forming mud cake on the wellbore. The hydrate partial dissociation zone is the second layer, where the hydrate is decomposing due to the disturbance brought by the drilling fluid. Gas hydrate, gas (decomposition gas and reservoir gas) and water (including water in the drilling fluid, decomposition water and formation water) coexist in three phases. The last layer is an *in-situ* hydrate formation that is not disturbed by drilling activity.

The drilling fluid profile reveals that when the drilling fluid penetrates the reservoir, the properties of the hydrate-bearing sediments will change due to the composition of the drilling fluid and the dissociation of gas hydrate. The drilling fluid and gas hydrate dissociation will affect the mechanical characteristics, electrical properties, thermal properties, and permeability of the formation near the wellbore, affecting the geomechanical stability of the formation, the reliability of resistivity logging during drilling, and the heat transfer, gas production rate of subsequent production (Ning et al., 2014). These situations were encountered during the Gulf of Mexico Gas Hydrate Joint Industry Project Leg II (JIP Leg II) when drilling the well WR 313 (Collett et al., 2009; Cook et al., 2012). The phase change of gas hydrate is one of the primary characteristics of drilling fluid invasion into hydrate formation, which is also the main difference between drilling fluid invasion into hydrate formation and conventional oil and gas formation. This process is actually a coupling of the temperature field, seepage field, stress field, and chemical field (Teymouri et al., 2020; Ruan et al., 2021). Advanced numerical simulators can be used to solve the coupled thermo-hydro-mechanical-chemical (THMC)

process during the interaction process between drilling fluid and hydrate reservoir (Bai et al., 2021; Bai et al., 2022; Samala and Chaudhuri, 2022). Therefore, the establishment and solution of highly nonlinear and coupled differential equations with great challenges is one of the research hotspots in this field.

The micro overbalance drilling method is generally adopted for drilling hydrate wells, that is, maintaining the pressure in the hole slightly greater than the formation pore pressure and less than the formation fracture pressure to prevent the wellbore instability caused by the dissociation of gas hydrate and methane overflow. The wellbore instability is generally manifested as fracture, collapse (diameter expansion), and diameter reduction. During drilling, the positive pressure difference will cause the drilling fluid filtrate to penetrate into the borehole wall rock, and the pore pressure, temperature, salt content, and water content will increase accordingly (Ning, 2005; Ning et al., 2013). The increase of formation temperature leads to the thermal dissociation of gas hydrates near the wellbore. The dissociation of gas hydrates increases the formation pore pressure and water content. At the same time, the mud and sand particles cemented by gas hydrate collapse, which sharply reduces the mechanical strength of wall rock (Ning et al., 2009; Ning et al., 2013). Drilling fluid invasion and hydrate dissociation will alter pore pressure, pore fluid flow, and hydrate dissociation rate. The effective stress of the wellbore framework and the crushing resistance of the wellbore decrease as the formation pore pressure rises. For fine-grained and soft hydrate sediments, the invasion of drilling mud and the dissociation of gas hydrate may result in the fracturing of hydrate sediments. If the gas produced by dissociation enters the wellbore, it will lead to drilling fluid gasification (Fereidounpour and Vatani, 2014). The water and gas produced by dissociation will not only further increase the water content near the well wall, but also the dissociation of hydrate will improve the formation permeability and increase the invasion rate of drilling fluid, which is not conducive to the formation of filter cake to protect the well wall. Therefore, the process from the opening of the wellbore to the complete dissociation of gas hydrate near the wellbore is the most unstable stage of the wellbore. At the same time, the ions in the drilling fluid intrude into the formation with the filtrate, and ion exchange occurs at the borehole wall. Chemical potential increases the migration and permeability of the filtrate as well as the water dialysis under the capillary force. The multi factor coupling action accelerates the hydration reaction of the argillaceous hydrate reservoir while drastically lowering the mechanical strength of the wall rock. In addition, the heat generated by the friction between the circulating drilling fluid and the wellbore and the drilling tool, the heat generated by the friction between the drilling tool and the wellbore during the up and down movement and the rotation of the drilling tool will increase the temperature around the wellbore and continuously decompose the gas hydrate. The up and down movement of drilling tools will also cause the continual change of bottom hole pressure, resulting in the invasion of drilling fluid and the instability of the wellbore. Because gas hydrates usually occur in the semi-consolidated or even unconsolidated mud and sand layer on the seabed, and the water depth is so large, borehole collapse or fracture will happen more easily than in a typical oil and gas reservoir.

3 Materials and methods

3.1 Soil and sand sample properties

It is generally believed that gas hydrate sediments should be tested *in situ*. However, due to the high cost and technical difficulty of *in-situ* sampling of marine natural gas hydrate, it is necessary to formulate a reasonable and scientific artificial core preparation scheme (Song et al., 2014). The first thing to consider in manual sample preparation is the nature of the sediment. The size, shape, and composition of sediment grains affect the nucleation and growth of gas hydrate. Field exploration and *in-situ* drilling coring found that hydrate saturation increased with the increase of pore volume ratio and particle size (Ito et al., 2015) and it is known that gas hydrate is preferentially accumulated in coarse sand (viz., sandy; mean > 63 μm) (Su et al., 2021). The coring analysis in the east of the Nankai Trough in Japan also verifies a significant positive correlation between gas hydrate saturation and sand content and median particle size (Ito et al., 2015). According to Shepard and Moore (Shepard and Moore, 1954; Kuang et al., 2019) and the sediment particle size standard determined by the geotechnical code, the hydrate-bearing sediment samples from the Krishna Godavari, Mahanadi, and Andaman basins in India are mainly composed of clay and silt particles, with a median grain size of 1.86–186 μm (Guo et al., 2020; Maiti et al., 2022). The gas hydrate drilling cores in the gas hydrate reservoir in the South China Sea are mainly silt and clay. The grain sizes of hydrate-bearing sediment samples are primarily distributed in the range of 0.2–200 μm (Guo et al., 2020; Zhu et al., 2020). The median grain size of sediments in the eastern Nankai Trough of Japan is 4.0–146.4 μm (Kuang et al., 2019). The hydrate-bearing sediment cores obtained from the Hydrate Ridge in the Pacific Ocean (ODP204 voyage) show that gas hydrates mainly occur in 8–26 μm and 50–148 μm of the sediment (Su et al., 2005). Sand and clay minerals were proportionally blended in this investigation to create artificial samples (Luo et al., 2016; Shen et al., 2022).

To imitate the muddy sandy hydrate reservoir, a mixture of kaolin (0–50 μm) and quartz sand (150–230 μm) was utilized. Sand materials with different grain sizes were observed through a

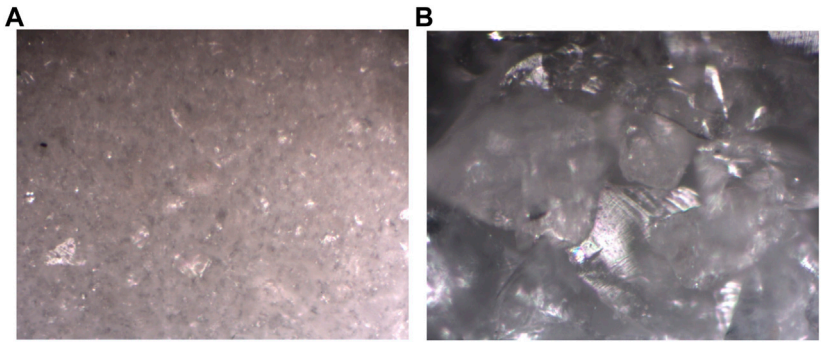

FIGURE 3
Image of soil and sand sample observed under the microscope. **(A)** kaolin (0–50 μm), **(B)** quartz sand (150–230 μm).

TABLE 2 Information of experimental materials for hydrate-bearing sediments.

Material	Source	Main information
Methane	Huate Gas Co., Ltd.	Gas purity>99.9%
Quartz sand, 150–230 μm	Perfemiker	SiO_2: 52.82%, sediment percentage 0.02%, Fe_2O_3 storage temp: 2–8°C, loss on ignition (LOI): 0.2%, 2.6 g/ml at 25 °C (lit.)
Kaolin, 0–50 μm	Perfemiker	Al_2O_3:43.9%, SiO_2: 52.82%, CaO: 0.25%, MgO: 0.19%, K_2O: 0.33%, Na_2O: 0.28%, TiO_2: 1.09%, LOI: 0.04%, Fe_2O_3storage temp: 2–8°C, humidity of experimental environment 68%RH, 2.58 g/ml at 25 °C (lit.)
Distilled water	Guangzhou Yafei water treatment equipment Co., Ltd.	Level 1 water, conductivity ≤0.1 μs/cm

microscope made by Olympus Corporation, as shown in Figure 3. Commercial sand and clay minerals used to prepare artificial samples were purchased from Perfemiker. So far, most of the recovered natural gas hydrate samples are sI methane hydrate. Therefore, methane hydrate with different saturation in sediments has been studied. Methane gas was purchased from Huate Gas Co., Ltd. with a purity of 99.9%. The distilled water for the experiment is from Guangzhou Yafei water treatment equipment Co., Ltd., with conductivity ≤0.1 μs/cm. See Table 2 for specific information of experimental materials. The authors indicated the feasibility of the artificial samples by comparing the mechanical properties of the artificial samples with those of Luo et al. (2016), Li L et al. (2021), Shen et al. (2022).

3.2 Drilling fluid properties

It is critical to avoid drilling fluid invading the reservoir during deepwater drilling and hydrate development since this poses a severe danger to safe and effective drilling. Hydrate reservoir drilling now uses water-based, oil-based, and synthetic-based drilling fluids. The oil-based drilling fluid, such as the production test well of Ignik Sikimu oil field in the United States, has been selected for the hydrate drilling activities in the frozen soil area, because of its good hydrate control performance and anti-freezing performance (Grigg and Lynes, 1992; Schoderbek et al., 2013). However, when all factors such as hydrate inhibition, environmental protection, and cost are taken into account, the water-based drilling fluid system is still the best option for natural gas hydrate exploration (Liu et al., 2016). The sepiolite mud, lecithin-water solution drilling fluid, KCl polymer drilling fluid, and other drilling fluids that are conducive to safe solid carrying and good hydrate inhibition are selected in the hydrate drilling activities in the waters around India, the Mallik permafrost region, the Gulf of Mexico, and the Nankai Trough of Japan (Burger et al., 2006; Collett et al., 2012; Merey, 2016). Therefore, the water-based drilling fluid in this investigation had 10% ethylene glycol, 0.5% lecithin, and 0.5% polyvinylpyrrolidone (PVP) added to it. The drilling fluid is provided by the China University of Petroleum (East China), and the particular formula is protected by intellectual property rights, thus it is not practical to go into detail.

The experimental performance test of drilling fluid shows that the apparent viscosity (AV) of the drilling fluid is 41.5 mPa·s, the plastic viscosity (PV) is 29.0 mPa·s, the yield point (YP) is 13.5 Pa, and the ratio of yield point to plastic viscosity (YP/PV) is

0.47 at 25°C. AV, PV, YP, and YP/PV of drilling fluid at 4°C are 49.0 mPa·s, 34.5 mPa·s, 16.5 Pa, and 0.48 respectively. YP (4°C)/YP (25°C) = 1.22. It can be seen that the viscosity of the drilling fluid increases little at low temperatures, which can reduce the problem of lost circulation caused by serious thickening at low temperatures. The drilling fluid can effectively break rock at a high shear rate and carry rock cuttings at a low shear rate, to purify the bottom of the borehole and ensure wellbore stability. The filtrate loss of drilling fluid is 5.2 ml under normal atmospheric temperature, a pressure difference of 690 kPa, and a test time of 30 min. The filter cake is thin and tough, with a weak sand feeling, good smoothness, no looseness after soaking, and good firmness. After the mud cake in the downhole environment is compacted under the pressure difference, it will effectively stabilize and protect the open hole wall. It is speculated that the wall-building property of the drilling fluid is good.

3.3 Apparatus

The experiment adopts the experimental system developed by Southwest Petroleum University, as shown in Figure 4. The advantage of the device is that the gas hydrate generation experiment and triaxial mechanical test can be completed in the same reactor, which can effectively avoid the dissociation of gas hydrate in the test process. The experimental device includes a reactor, a temperature regulation system, a pressure regulation system, a triaxial mechanics system, a fluid control system, an acoustic and electrical measurement system, and a data acquisition and control system. The reactor is where gas hydrate sediments are created and the sand that represents a reservoir is squeezed into cylinder cores. The sidewall of the inner chamber of the reactor is a black cylindrical rubber cylinder (see Figure 5A). The inside of the reactor is sealed by the rubber cylinder, the upper steel cover, and the lower steel shaft (see Figure 5B) without air leakage. The upper steel cover is provided with a high-pressure resistant visual window, through which one can observe the image in the reactor in real-time through the equipped high-definition camera. The working pressure range of the reactor is 0–35 MPa, and the temperature range is -6–25°C. The temperature regulation system is mainly composed of cooling jackets, two NVOHAI THD-0506 refrigeration units, and supporting refrigeration pipelines. Industrial alcohol is used to reduce the freezing point of water in the water bath device, and to maintain the low-temperature environment inside the reactor and the drilling fluid tank. The reactor and drilling fluid tank are wrapped with a layer of insulation sleeves to avoid heat exchange with the environment. The pressure regulation system includes a gas pressure regulation unit, a confining pressure regulation unit, and an axial pressure regulation unit. Here we refer to the gas pressure regulation unit in particular. The pressure of gas and the pore pressure of gas hydrate sediments are regulated by the gas pressure regulation unit, which is mainly composed of gas injection pipelines, gas pressure regulating valves, and a gas cylinder. The confining pressure regulation unit and the axial pressure regulation unit form part of the triaxial mechanical system. The other part of the triaxial mechanical system mainly includes the loading instrument, the displacement gauge, stress sensor, etc. The system controls the confining pressure and axial pressure in the reactor through the loading instrument, which can provide necessary pressure conditions for the initial preparation of natural gas hydrate, and also provide a guarantee for the determination of mechanical parameters in the later stage of the experiment. The fluid control system includes a gas control unit (i.e., gas pressure regulation unit), a seawater control unit, and a drilling fluid control unit. It is mainly composed of a vacuum pump, two gas cylinder, two gas stabilized pressure pump, a buffer tank, a water tank, a liquid injection pump, and a drilling fluid tank. The acoustic and electrical measurement system includes acoustic wave and resistivity test units. The acoustic wave is transmitted and received by the acoustic probe and displayed on the DS1052E oscilloscope. The resistivity of the hydrate-bearing core is measured by the TH2810B bridge instrument. The data acquisition and control system controls the experimental parameters by computer and records the experimental data and images.

The experimental device is equipped with pressure sensors with an accuracy of ±0.2% of full scale and a range of 0–40 MPa to measure the gas pressure in the reactor and pipeline, and temperature sensors with an accuracy of ±0.05% of full scale and a range of −50 to 150°C to measure the temperature in the reactor and drilling fluid tank. The parameter monitoring instruments of the experimental device also include an XMT instrument cabinet, a high-voltage ultra-clear monitoring camera, and a measuring chamber.

3.4 Experiment procedures

The reservoir lithology of gas hydrate in the deep sea is mainly divided into consolidated diagenetic hydrate and weakly cemented non-diagenetic hydrate. The non-diagenetic gas hydrate is difficult to support the reservoir under external temperature and pressure disturbance due to poor rock and soil cementation in the reservoir. The generation of gas hydrate will enhance the strength of the reservoir, while the decomposed hydrate-bearing sediments is prone to deformation. The weakly cemented sandy samples used in the experimental test are prepared from quartz sand and kaolin (clay). The mass ratio of quartz sand to kaolin in the sample is 0.9:0.1. The quality of soil and sand is 100 g. The weak cemented gas hydrate sample is prepared by the simple quartz sand filling method. The temperature and pressure of the hydrate reservoir are first simulated, and then the triaxial tests of hydrate-bearing sediment are carried out using the

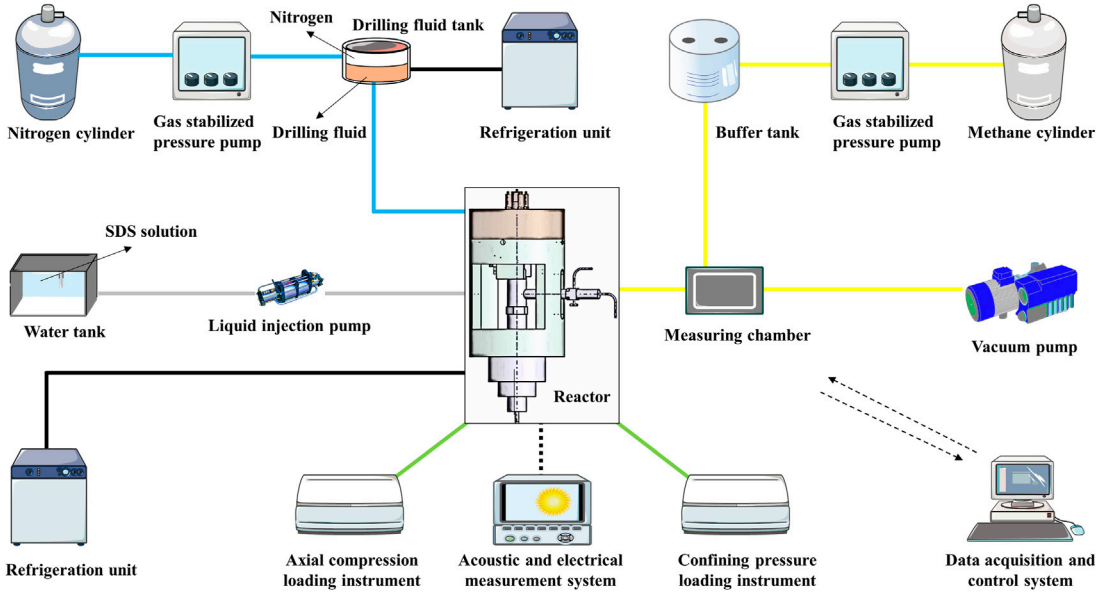

FIGURE 4
Schematic of the experimental system.

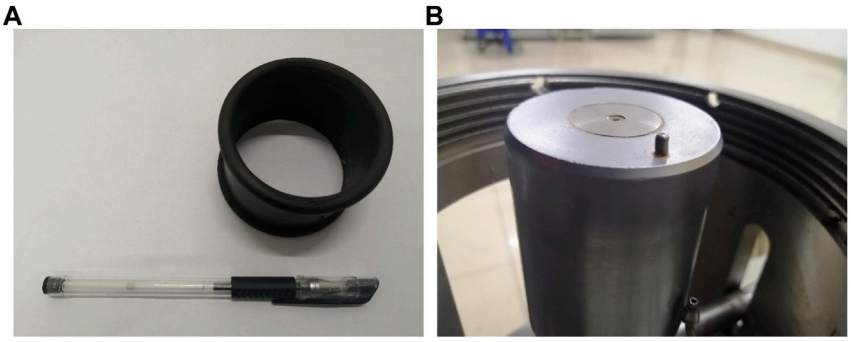

FIGURE 5
The rubber cylinder **(A)** and lower steel shaft **(B)** of gas hydrate reactor. The diameter of the rubber cylinder is 60 mm, and the size of the internal space of the reactor can be reduced with the compression of the lower steel shaft.

prepared samples. The effects of drilling fluid invasion on the strength behaviors of hydrate-bearing sediments are then studied, and changes in mechanical characteristic parameters of hydrate-bearing sediments are observed. The experimental flow of gas hydrate-bearing sediment preparation is shown in Figure 6 and the experiment procedures are as follows.

3.4.1 Step 1: Sample preparation

The selected quartz sand and kaolin are mixed evenly according to the specified ratio, and the bottom and side parts of the sample are wrapped with a thin rubber film before being loaded into the rubber cylinder of the reactor. Cover the reaction chamber with the upper steel cover, secure the upper steel cover and the reactor, and then compact the sand by loading 10 MPa axial pressure on the reactor according to the experimental requirements. The rock sample can be molded into unconsolidated reservoir frameworks depending on the compaction and cementation. Vacuum pumping is essential to prevent the influence of air in the reactor on the natural gas hydrate preparation process. The temperature in the reactor can be controlled by turning on the temperature regulation system

for refrigeration. Then inject quantitative sodium dodecyl sulfate (SDS) solution into the cylindrical porous rock sample in the reactor under appropriate temperature conditions. The mass concentration of SDS solution is 0.03%, which is used to promote the rapid generation of methane hydrate (Wu and Zhang, 2009). After the water is fully penetrated, the gas pressure regulation unit is started to pressurize to keep the pressure in the reactor at the predetermined hydrate generation pressure. When the consumption rate of natural gas is zero, it indicates that methane hydrate has been formed. The prepared hydrate-bearing sediment is used for subsequent mechanical tests. The preparation process of hydrate-bearing sediment is shown in Figure 4. It should be noted that in order to balance the air pressure in the rubber cylinder, it is necessary to keep the confining pressure slightly higher than the internal air pressure in the reactor to maintain the stable shape of the sample.

3.4.2 Step 2: Triaxial tests

The required parameters are set for the conventional triaxial tests after the hydrate-bearing sediment samples with a certain saturation are prepared according to the method described in step 1. The three stresses applied to the cylindrical sample (σ_1, σ_2, and σ_3) are perpendicular to each other, two of which are equal, i.e., the medium principal stress is equal to the minor principal stress ($\sigma_2 = \sigma_3$). $\triangle\sigma$, indicates the deviator stress, which is equal to the difference between axial stress and radial stress ($\triangle\sigma=\sigma_1-\sigma_2$). During the experiments, the operator increases the axial stress and radial confining pressure of the hydrate-bearing sediment sample to the specified confining pressure equivalently (the effective confining pressure is 3 MPa), then keeps the confining pressure unchanged, and continues to increase the axial stress of the sample. The loading speed of the axial load is 0.2 mm/min. The displacement caused by radial and axial deformation of the sample is collected and recorded in the data acquisition and control system. After the experiment, remove the internal air pressure, confining pressure and axial load in sequence. Finally, open the upper steel cover of the reactor and take out the sample.

3.4.3 Step 3: Drilling fluid invasion

Clean up the reactor after the triaxial test, and re-prepare hydrate-bearing sediments with hydrate saturations of A1 to A4 as directed in step 1. The drilling fluid is sucked from the drilling fluid tank into the pipeline using the negative pressure in the pipeline. Then increase the nitrogen pressure through the gas stabilized pressure pump. After the gas pressure rises to the invasion pressure, open the control valve between the drilling fluid injection pipeline and the reactor to inject the hydrate-bearing sediment from the top of the reactor with the drilling fluid at different temperatures at a pressure of 12 MPa. When the invasion time reaches the preset value, the triaxial experiment can be started. The operation process of the triaxial test shall be carried out in strict accordance with the method described in step 2. Although the sample preparation may deviate from the actual value of hydrate saturation under the same conditions, the inevitable random error is acceptable because the experimenters scrupulously follow the same criteria and methods.

3.5 Methane hydrate saturation

At present, the main methods for preparing hydrate-bearing sediment samples include the ice searching method, excess gas method, excess water method, and dissolved gas method (Lijith et al., 2019; Chen et al., 2022). In this study, we choose the excess gas method to make the methane hydrate. The excess gas method entails keeping a certain amount of water in the pores of a rock sample and injecting excess gas under appropriate temperature and pressure conditions to convert all of the water molecules in the pores into structural water molecules of gas hydrate, resulting in the desired hydrate saturation. Under the temperature and pressure conditions in this paper, water will not exist in the form of ice, so the hydrate saturation obtained by this method is accurate and reasonable. Hydrate saturation is a key parameter for reservoir optimization and resource evaluation. The precise computation of hydrate saturation is critical for determining the mechanical properties of the hydrate reservoir under drilling fluid invasion. According to the chemical reaction formula for producing methane hydrate, 1 mol of methane and 5.75 mol of water will be consumed for each 1 mol of methane hydrate generated. Therefore, the water consumed to produce hydrate sediments with specific hydrate saturation can be calculated by the Eq. 1 (Li et al., 2017). Since the concentration of SDS solution is very low, the influence of solute molecules on the quality of water consumed can be ignored. However, about 5% of the excess SDS solution was still added to offset the inevitable loss of water during the experiment. Experiments have validated this strategy, thus it is regarded as reasonable. The verification method of actual saturation during the experiment is shown in Eq. 2 (Shen et al., 2022).

$$m_w = \frac{5.75M_{H_2O}}{5.75M_{H_2O} + M_{CH_4}}\rho_H \phi V S_h \tag{1}$$

$$S_h = \frac{PV_{gas}M_H}{ZRT\rho_H V\phi} \tag{2}$$

where M_{H_2O} and M_{CH_4} respectively represent the molar mass of hydrated methane, g/mol. ρ_H is the density of methane hydrate, g/cm^3. ϕ denotes the porosity of the compacted sediment sample. V is the total volume of the compacted sediment sample, g/cm^3. S_h indicates the hydrate saturation. V_{gas} is the volume of methane gas consumed at temperature T and pressure P, cm^3. M_H is the molar mass of methane hydrate, g/mol. Z indicates the gas compression factor, dimensionless. R denotes the universal gas constant.

TABLE 3 The experimental conditions for the preparation and mechanical test of hydrate-bearing sediments in the non-intrusive state. S_h represents the hydrate saturation, P and T represent the pressure and temperature in the reactor respectively.

Core No.	S_h/%	P/MPa	T/°C	Core No.	S_h/%	P/MPa	T/°C
A1	5	10	4	C1	5	10	8
A2	15			C2	15		
A3	25			C3	25		
A4	35			C4	35		
B1	5	12	4	D1	5	12	8
B2	15			D2	15		
B3	25			D3	25		
B4	35			D4	35		

TABLE 4 The experimental conditions for the mechanical test of hydrate-bearing sediments in the intrusive state. T_{in} and P_{in} represent the drilling fluid temperature and invasion pressure respectively, and t_{in} represent the invasion time.

Gas hydrate-bearing sediment parameters			Drilling fluid invasion parameters		
T/°C	P/MPa	S_h/%	T_{in}/°C	P_{in}/MPa	t_{in}/min
4	10	5/15/25/35	2/8/14	12	10/20

The mechanical test of hydrate-bearing sediments without drilling fluid invasion was carried out and then the drilling fluid invasion experiment was carried out when the simulated reservoir temperature and pore pressure were constant. The hydrate saturation range of this study is roughly controlled at 5%–35%. The reservoir temperature has two options of 4 and 8°C, and the *in-situ* pore pressure has two grades of 10 and 12 MPa. There are three choices of drilling fluid temperature, and two levels of invasion time, with a total of 24 groups of drilling fluid invasion experiments. Note that the equilibrium temperatures of the methane hydrate at 10 and 12 MPa when the triaxial shear test is performed are 13.47 and 15.12°C, respectively, according to the CSMHyd software. The experimental conditions and parameter settings are shown in Tables 3, 4.

4 Results and discussion

4.1 Effect of temperature, pressure, and hydrate saturation on stress-strain behaviors

Temperature, pressure, and hydrate saturation all affect the strength behaviors of hydrate-bearing sediments, according to the mechanism. Figure 7 shows the experimental phenomena observed by the camera before and after hydrate generation under reservoir temperature of 4°C and pore pressure of 12 MPa. The filter screen in Figure 7 is primarily used to prevent mud and sand from leaking and obstructing gas and liquid pipelines, and it has no bearing on the mechanical properties. The stress-strain relationship of hydrate sediments provides the foundation for evaluating reservoir strength parameters and deformation features in the development of gas hydrate resources. 16 groups of experiments were conducted under different temperatures, pressures, and hydrate saturation conditions, and the stress-strain curves under the effective confining pressure of 3 MPa were obtained, as shown in Figure 8. It is noticeable that as the load increases, the sediment deforms and eventually fails. The stress-strain law of hydrate sediments exhibits a trend of transition from strain hardening to strain softening with an increase in hydrate saturation from 5% to 35%, regardless of the temperature and pressure conditions of the environment in which methane hydrate is found. The stress-strain curves of hydrate-bearing sediments have no clear peak points when the hydrate saturation is between 5% and 15%, and they all show the characteristics of strain hardening. The failure characteristics of the sandy sediments with low hydrate saturation can be demonstrated to constitute ductile failure in this investigation. When the hydrate saturation is between 25% and 35%, the stress-strain curves of hydrate sediments show obvious peak points, which are characterized by strain softening. It can be seen from the figure that the peak strength of the strain softened sediments occurs near the strain equal to 1%–2%. When the strain range is less than 1%, the higher the hydrate saturation is, the faster the deviator stress of the hydrate-bearing sediment increases.

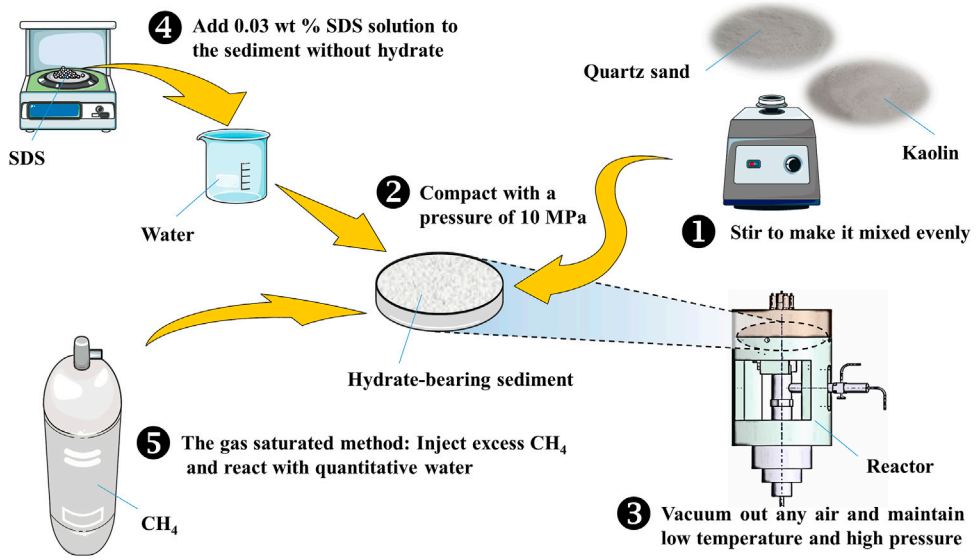

FIGURE 6
The experimental flow of gas hydrate-bearing sediment preparation.

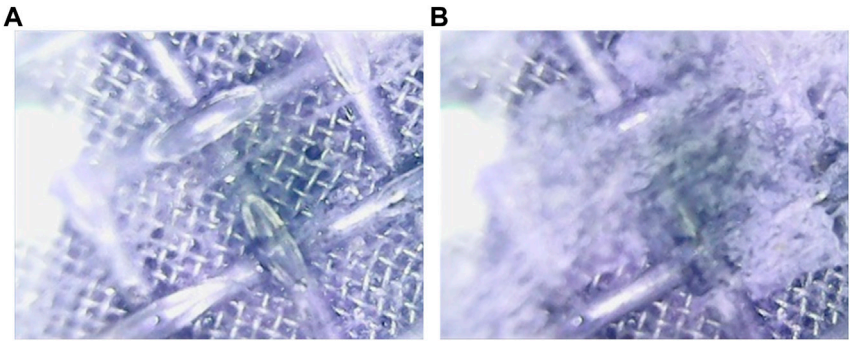

FIGURE 7
Experimental phenomena were observed in the reactor before and after hydrate generation. **(A)** Pre-experiment phenomenon; **(B)** Post-experiment phenomenon.

According to the experimental results, the critical hydrate saturation value of hydrate-bearing sediments for strain hardening and strain softening transition is between 15% and 25%. This result is consistent with the conclusion of Masui et al. (2006), Masui et al. (2008), Zhang et al. (2018).

The peak strength of strain hardened hydrate deposits is defined as the deviator stress at 8% strain. For the hydrate-bearing sediments with strain softening, the peak strength is equal to the value of the highest point of the stress-strain curve. The relationship between peak strength and hydrate saturation is shown in Figure 9. It can be found that with the increase of hydrate saturation, the deviator stress of hydrate-bearing sediments increases, and the stiffness and strength increase significantly. It can be seen from Figures 8, 9 that the strength of hydrate-bearing sediments increases with the decrease of reservoir temperature. This is mainly because the strength of solid hydrate in the pore space increases with the decrease of temperature, further strengthening the cementation between particles (Hyodo et al., 2002). Moreover, Figure 8 also reveals that within the pressure range studied in this study, the strength of hydrate-bearing sediments increases with the increase of pore pressure.

Studies have shown that the mechanical properties of hydrate-bearing sediments mainly depend on the morphology

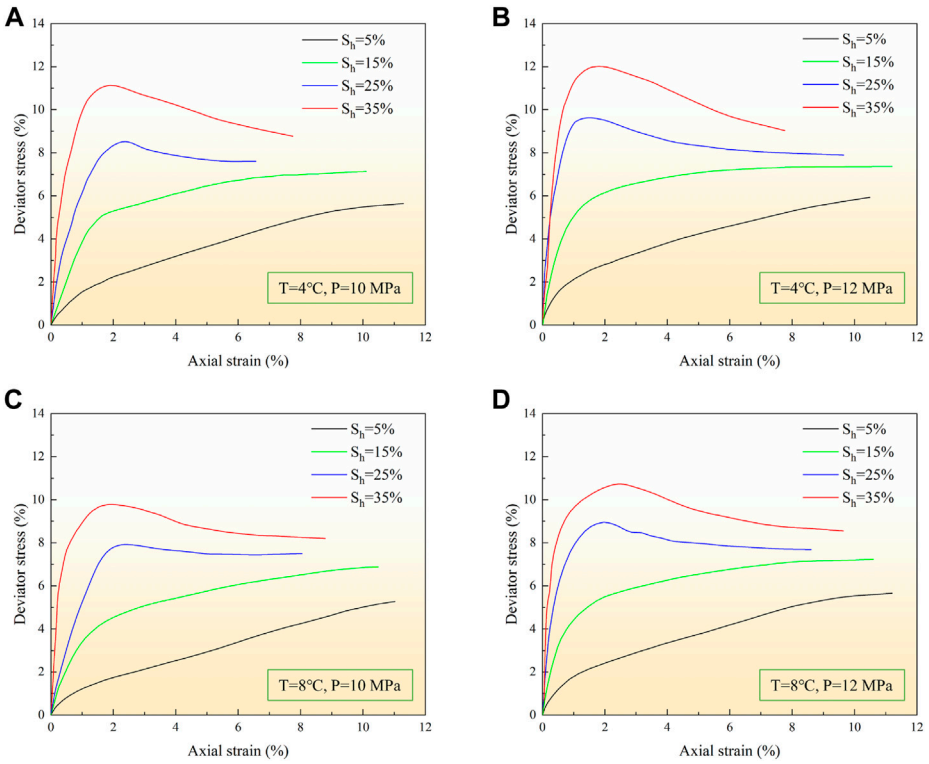

FIGURE 8
Stress strain curves at different temperatures and pressures. **(A)** The stress-strain curve under reservoir temperature of 4°C and pore pressure of 10 MPa. **(B)** The stress-strain curve under reservoir temperature of 4°C and pore pressure of 12 MPa. **(C)** The stress-strain curve under reservoir temperature of 8°C and pore pressure of 10 MPa. **(D)** The stress-strain curve under reservoir temperature of 8°C and pore pressure of 12 MPa.

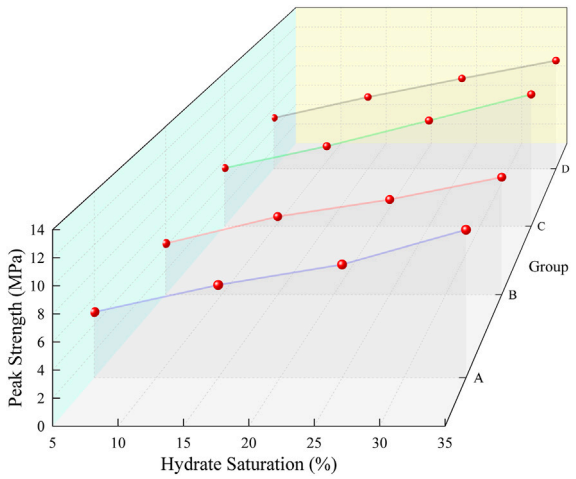

FIGURE 9
The peak strengths of the hydrate-bearing sediments increase with the increase of hydrate saturation.

of gas hydrate in pores. Hydrate-bearing sediments show better geomechanical properties, which is the reason for their greater stability as compared to the native sediments. Therefore, if the dissociation of gas hydrate in the reservoir can be controlled, the formation with high hydrate saturation is less prone to borehole collapse than the formation with low hydrate saturation (Zhang et al., 2017). For coarse-grained sandy sediments, with the increase of hydrate saturation, the hydrate occurrence in the pores transits from pore filling type, and load-bearing type to grain cementing type (Lijith et al., 2019). According to Lijith et al. (2019) the hydrate saturation at which a sudden increase in effective cohesion is observed is defined as breakpoint hydrate saturation (S_{HB}). When the hydrate saturation is 0, the stress increases with the axial strain, and the sample shrinks and becomes dense gradually. When the hydrate saturation is between 0 and S_{HB}, the hydrate growing in pores and on surfaces of rock grains will hinder the rolling and sliding between grains under external forces. These broken, falling, or

crushed hydrates will lead to the expansion of hydrate-bearing sediments and the increase of residual shear strength. When the hydrate saturation is greater than S_{HB}, the hydrate cementation between grains is stronger. At this moment, hydrate saturation has a significant impact on the effective cohesion of hydrate-bearing sediments. This phenomenon is closely related to hydrate growth around rock grains. During the shear process of the samples, the failure plane may extend along with the hydrate or sediment-hydrate boundary, which may eventually lead to the strain softening of hydrate-bearing sediments.

The research shows that under the condition of low hydrate saturation, the relationship between stress-strain behaviors of hydrate-bearing sediments is limited by temperature (Shen et al., 2022), which can be seen from the stress-strain curves with the hydrate saturation of 5% and 15%. When the hydrate saturation is high, the effect of hydrate cementation on the mechanical properties of hydrate-bearing sediment samples is more obvious. The influence of pressure, on the other hand, is stated as follows: the strength of methane hydrate increases as pressure rises, and the change in hydrate crystal strength further affects the cementation strength of hydrate-bearing sediments (Hyodo et al., 2013; Jiang et al., 2015; Shen et al., 2021). This is the conclusion for the stable region of hydrate phase equilibrium. If the temperature and pressure conditions exceed the stable region and the gas hydrate continues to decompose, the stress-strain behavior will be seriously affected. Actually, the mechanical properties of geotechnical materials are inevitably influenced by numerous factors. In addition to the experimental conditions studied in this investigation, the factors that change the stress-strain behaviors of hydrate-bearing sediments also include confining pressure, grain size, porosity, microstructural aspects of soils, etc. (Hyodo et al., 2013; Jiang et al., 2015; Wang et al., 2020; Bai et al., 2021; Shen et al., 2021). We have also seen a surge in research into the thermal, hydraulic, and chemical action processes that affect the stress state variables of hydrate-bearing sediments in recent years (Li Y et al., 2021; Samala and Chaudhuri, 2022; Wang et al., 2022). Accordingly, the further work in this study will include the analysis of the coupling action of multiple fields on the mechanical properties of gas hydrate reservoirs.

4.2 Effects of drilling fluid temperature and invasion time on stress-strain behaviors

External disturbance, which is usually bad, will change the mechanical properties of hydrate-bearing sediments. For example, the increase of ocean temperature caused by global warming leads to the dissociation of hydrate and the escape of gas, causing reservoir stability to deteriorate. Long term field test may lead to reservoir instability, which may lead to geological disasters such as earthquake, tsunami and collapse (Merey, 2016; Wang et al., 2020). When the bit is drilled to the hydrate layer in drilling activities, the drilling fluid continuously infiltrates into the reservoir, driven by the pressure difference between the bottom hole and the formation, causing changes in hydrate saturation, pore pressure, temperature distribution, and physical and mechanical properties. To investigate the strength behaviors of drilling fluid invading hydrate-bearing sediments, we conducted laboratory tests with drilling fluid developed by China University of Petroleum (East China). Based on the experimental data of hydrate-bearing sediments with four hydrate saturations of A1–A4 without drilling fluid invasion, we carried out 24 groups of drilling fluid invasion experiments. The pressure difference between the drilling fluid and the pore pressure is 2 MPa, the drilling fluid temperature is 2, 8, and 14°C respectively, and the invasion time is 0.5 h and 1 h.

Figures 10, 11 respectively show the changes in stress-strain curves and peak strengths of hydrate-bearing sediments after drilling fluid invasion with different hydrate saturation, drilling fluid temperature, and invasion time. The experiment reveals that the invasion of drilling fluid does not change the trend of hydrate-bearing sediment strength increasing as saturation increases. When the hydrate saturation is low, the influence of drilling fluid invasion on the stress-strain curve is small. The trend of weakening the strength properties of sediments seems to increase with the increase of hydrate saturation. In the case of high hydrate saturation, with the increase of drilling fluid invasion time, the sediment shows a trend from brittle failure to ductile failure. The peak strength of hydrate-bearing sediments decreased, with a maximum reduction of 47.71% and a minimum decrease of 7.02%. In this study, the top of the core sample is the first to come into contact with the drilling fluid, so the deformation of the sediment may first occur at the contact interface, similar to the diffusion of drilling fluid from the wellbore to the reservoir shown in Figure 2. The small size of the core sample may explain why the strength of the hydrate-bearing sediment decreased in such a short period. When the hydrate saturation and the intrusive pressure difference are the same, the temperature is the main factor driving this process. It can be seen from Figures 10, 11 that the strength of hydrate-bearing sediments becomes weaker with the increase of drilling fluid temperature or invasion time. This is mainly because the increase in temperature accelerates the hydrate dissociation process, and then the strength of the hydrate-bearing sediment decreases. The higher the temperature of the drilling fluid, the more likely the gas hydrates are to slide, dislocate, fragment, and fall off under the action of triaxial stress. If the temperature of the interface between drilling fluid and hydrate increases and exceeds the phase equilibrium region, the gas hydrate will decompose rapidly due to the increase in

drilling fluid temperature. The gas produced by hydrate dissociation will increase the pore pressure, and the water produced by hydrate dissociation will increase the water saturation. If the sediment contains clay minerals, the reservoir permeability will be lower due to hydration expansion. All these factors will affect the stress-strain curve of hydrate-bearing sediments. It should be noted that even if the drilling fluid temperature is lower than the reservoir temperature, the drilling fluid will cause a change in reservoir strength properties. First of all, the drilling fluid is a complex dispersion system containing a variety of chemicals, including salts, alcohols, and other substances that will change the phase equilibrium curve, thus affecting the stability of the gas hydrate. Secondly, the hydration of water-based drilling fluid will change the rock structure microscopically, and macroscopically, and reduce the cohesion of rock and soil. This complex multi-field coupled process has been verified in some experimental and numerical simulations (Gao et al., 2019; Liao et al., 2021).

4.3 Effects of drilling fluid invasion on other mechanical properties

Figure 12 shows the changes in Poisson's ratio (ν), Young's modulus (E), shear modulus (G), and secant modulus (E_c) with temperature and time after drilling fluid intrudes into hydrate-bearing cores with different hydrate saturations. Figure 13 shows the changes in mechanical parameters before and after drilling fluid invasion. ν is defined as the absolute value of the ratio of the transverse normal strain to the axial normal strain of a material, which is an elastic constant reflecting the transverse deformation of a material. Previous studies have shown that the ν of a hydrate reservoir varies from 0.1 to 0.4, and there is no clear functional relationship between ν and hydrate saturation and confining pressure (Lee and Collett, 2001; Lijith et al., 2019). This is consistent with our results that when there is no drilling fluid invasion, the variation range of ν is 0.19–0.25, which is random. However, when the drilling fluid enters, it can be observed that the change of ν is generally positively correlated with the change in hydrate saturation and invasion times. When the hydrate saturation and invasion times increase, the ν generally increases (with an average increase of 14.56%). Nevertheless, to ensure that the results are applicable, this correlation should be extended to a wider set of parameters.

The various moduli of materials refer to the ratio of stress to strain under force. Corresponding to different stress states, there are different names. The elastic-plastic or plastic deformation characteristics of hydrate-bearing sediments with low hydrate saturation cannot be simply characterized by elastic modulus and other parameters. Since the stress-strain curves have been described, additional analysis is helpful to reveal the impact of drilling fluid invasion on the reservoir. It is considered that the initial stage of hydrate sediment deformation meets the characteristics of elastic deformation in this investigation. E is a physical parameter that represents the ability of solid materials to withstand deformation. It can reflect the cementation ability, bite action, internal friction, and compression resistance between particles in the sample, which is of great significance to the study of sediment deformation. In this paper, E corresponds to the experimental value at 0.5% strain. Therefore, the E of 16 groups of hydrate-bearing sediments before the drilling fluid invasion ranges from 0.167 to 1.742 GPa. It can be seen from that Figure 13B with the increase of the proportion of hydrate in the sediment, its cementation between soil particles is bound to increase. The hydrate cemented with soil particles further improves the elastic mechanical properties of the sediment and enhances its ability to resist plastic deformation. The elastic properties of hydrate-bearing sediment increase greatly when S_h is about 25%. This hydrate saturation value is consistent with the critical saturation value of the effect of hydrate on the overall mechanical properties of sediments (Waite et al., 2009). Compared with the case when S_h is 0, the E of hydrate-bearing sediments after the drilling fluid invation decreases significantly, varying from 0.045 to 1.033 GPa. It can be seen that the E decreases with the increase of invasion time and drilling fluid temperature. At the same time, regardless of whether invasion happens or not, the decreasing value (absolute value) of E increases with increasing hydrate saturation. Assuming that the hydrate-bearing sediments are homogeneous and isotropic, then $G = E/2(1+\nu)$ can be used to calculate the shear modulus. The calculation results are shown in Figures 12C, 13C. As the difference of ν is small, the change of G is consistent with that of elastic modulus. In addition, the secant modulus which can reflect the average stiffness characteristics of hydrate-bearing sediments is analyzed. The E_c in the figure is defined as the secant modulus corresponding to a 1.5% strain. It can be concluded that when the reservoir temperature is 4°C, the pore pressure is 10 MPa, and the hydrate saturation is 5%–35%, the E_c of hydrate-bearing sediments ranges from 0.103 to 0.729 GPa. The E_c of hydrate-bearing sediments increases as hydrate saturation increases under the same effective confining pressure. The pores between soil particles gradually fill in the form of grain cementation as hydrate concentration rises, the cementation between soil particles becomes stronger, and the overall stiffness of hydrate-bearing sediments rises. Similar to Young's modulus, the secant modulus of the hydrate-bearing sediments after drilling fluid invasion decreased significantly, ranging from 0.063 to 0.616 GPa, with a maximum decrease of 62.3% (the invasion at 14°C for 20 min). The stress field around the hole will be redistributed in the actual drilling procedure due to the change in elastic modulus and Poisson's ratio in the hydrate dissociation zone. The main cause of these phenomena is that hydrate dissociation has been going on with the extension of drilling fluid immersion time or the

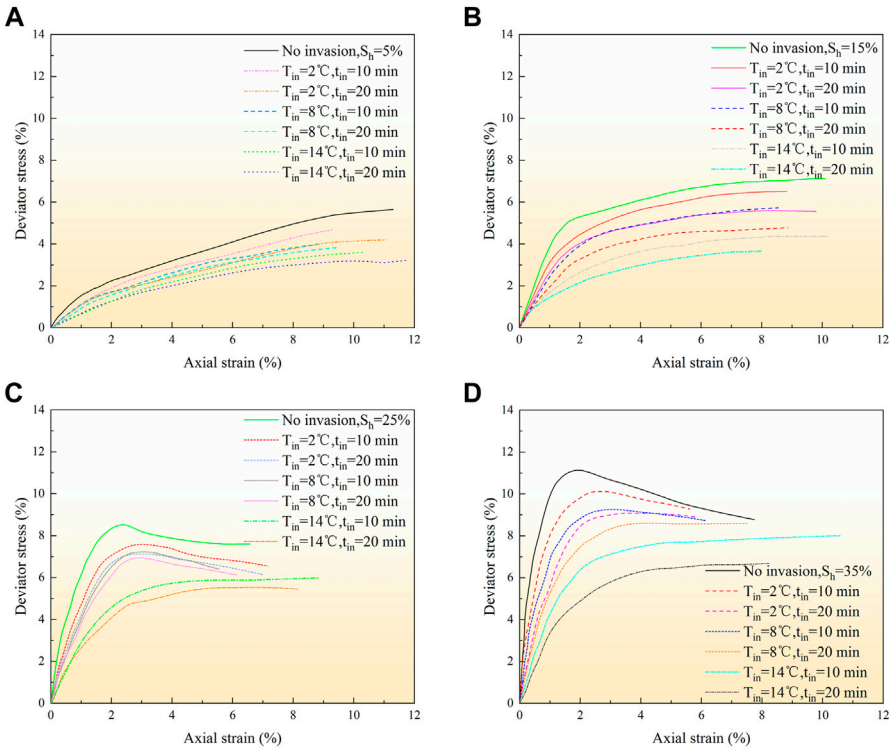

FIGURE 10
Stress-strain curve of hydrate-bearing sediment after drilling fluid invasion. **(A)** The stress-strain curve with 5% hydrate saturation. **(B)** The stress-strain curve with 15% hydrate saturation. **(C)** The stress-strain curve with 25% hydrate saturation. **(D)** The stress-strain curve with 35% hydrate saturation.

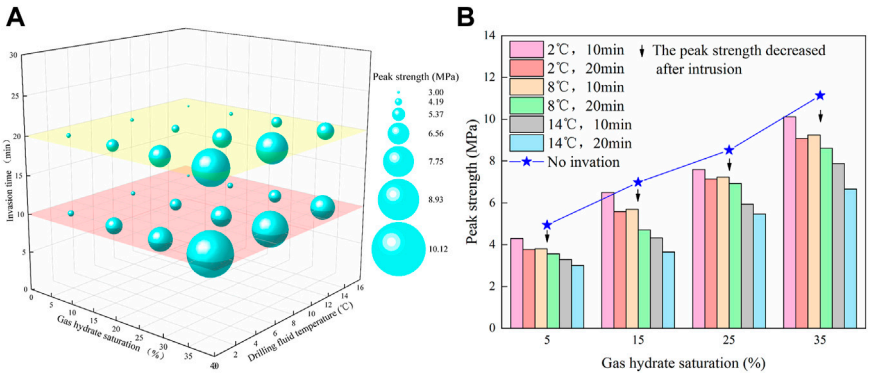

FIGURE 11
The peak strengths of hydrate-bearing sediments after drilling fluid invasion vary with hydrate saturation, drilling fluid temperature, and invasion time. **(A)** The peak strengths of the hydrate-bearing sediments are expressed in terms of bubble size. **(B)** Peak strength variations before and after drilling fluid invasion.

increase of drilling temperature. Furthermore, the argillaceous components of the sidiments are severely hydrated, resulting in a decline in the elastic and strength parameters.

4.4 Suggestions for future research

Driven by the pressure difference between the bottom hole and the formation, the drilling fluid filtrate continuously

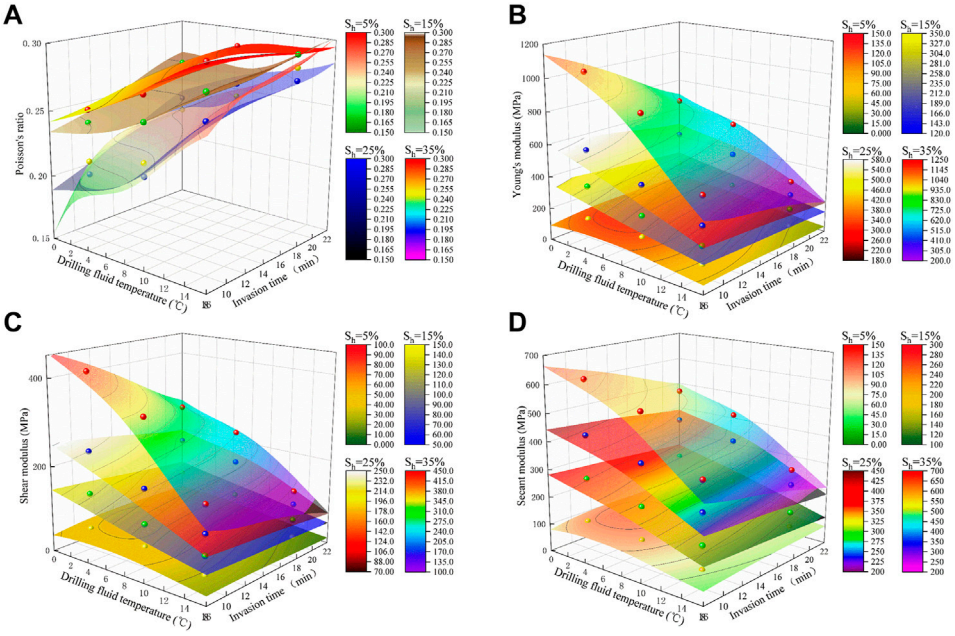

FIGURE 12
Changes of mechanical parameters before and after drilling fluid invasion. **(A)** Poisson's ratio, **(B)** Young's modulus, **(C)** shear modulus, and **(D)** secant modulus.

seeps into the reservoir during the drilling fluid invasion. In addition to fluid migration and material transfer, there are also changes in temperature, pressure, and pore water salinity. The change in salinity will cause the deviation of the hydrate phase equilibrium curve, and the change in temperature and pressure will cause the dissociation of gas hydrate. In summary, the interaction between drilling fluid with a given salinity and inhibitor content and the hydrate reservoir is mostly produced by permeability induced by pressure differences and hydrate dissociation caused by temperature differences. These two factors can have a strong impact on the spatial distribution of physical parameters, thus changing the stress distribution of the wall rock of the wellbore. As a consequence, whether in the calculation of the wall rock stress or during the experimentation phase, it is vital to investigate the impact of these two parameters on the stress field of the wellbore. In view of this, the goal of engineering measures is to reduce changes in *in-situ* temperature and pressure to prevent the dissociation of gas hydrate and risks such as wellbore instability and reservoir collapse. Some recommendations below for future research are made in this paper.

- ➢ Micro overbalance drilling is recommended.
- ➢ Drilling fluid with strong hydrate inhibition performance shall be used.
- ➢ The temperature of the drilling fluid must be reduced.
- ➢ Reduce the filtration loss of the drilling fluid.
- ➢ It is suggested to increase the density of the drilling fluid.
- ➢ Risk monitoring measures are essential.

At present, the study on a specific drilling fluid system for hydrate drilling is still in its early stages, and the low-temperature drilling fluid system with strong hydrate inhibition and plugging property based on deep-water drilling fluid is likely to become the main focus in the future. Theoretical work on the wellbore stability of gas hydrate under the influence of the drilling fluid is now underway. However, most of these studies focus on the construction of wellbore stability models and software coupling simulations. There are few field application technologies, so field experiments and applications should be increased. In addition, bottom-hole temperature and pressure management technology to prevent hydrate dissociation and promote hydrate regeneration could be the key to resolving the problem of safe drilling and production in hydrate reservoirs. And confining pressure is another important factor affecting wellbore stability. It is suggested to conduct experiments under different confining pressures to explore the changes in parameters such as cohesion, internal friction angle, and expansion angle of hydrate-bearing sediments after drilling fluid invasion.

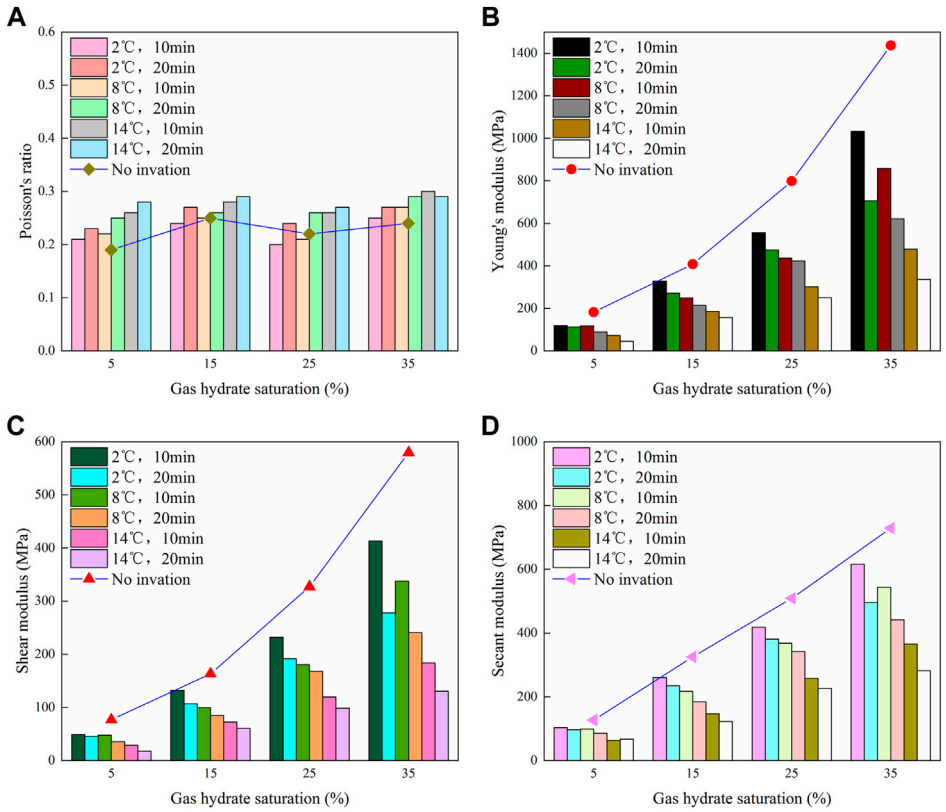

FIGURE 13
Changes of mechanical parameters before and after drilling fluid invasion. **(A)** Poisson's ratio, **(B)** Young's modulus, **(C)** shear modulus, and **(D)** secant modulus.

5 Conclusion

We have studied the effect of drilling fluid invasion on the strength behaviors of hydrate-bearing sediments. To accomplish this, the mechanical properties of hydrate-bearing sediments with different hydrate saturations under constant pressure differences were simulated by changing the drilling fluid temperature and invasion time. Compared with native sediments without gas hydrates, hydrate-bearing sediments show better geomechanical properties. The increase in hydrate saturation can significantly enhance cementation, making its impact on the mechanical properties of sediment samples more obvious. These mechanical properties make it more stable. Our research has shown that the peak strengths of the hydrate-bearing sediment samples increase with increasing hydrate saturation and pressure and decrease with increasing temperature. As the hydrate saturation increases from 5% to 35%, the hydrate-bearing sediments change from strain hardening to strain softening, and the critical hydrate saturation value of the transition is between 15% and 25%. In the hydrate dissociation zone, drilling fluid invasion will change the elastic parameters and strength parameters of the sediment, resulting in poor wellbore stability. With the increase in drilling fluid temperature and invasion time, the peak strength, Young's modulus, shear modulus, and secant modulus decrease, while Poisson's ratio increases. The stress field around the well will be reallocated due to the hydrate dissociation process and the fluid-solid coupling effect. Our study has also shown that the influence of drilling fluid invasion on the mechanical parameters of the wall rock is usually ignored in the design of drilling fluid. Given the risks of drilling fluid invasion and hydrate dissociation in drilling activities, research on drilling fluid invasion mechanisms and performance optimization will help to prevent hydrate dissociation and avoid risks such as wellbore instability and reservoir collapse.

Data availability statement

The original contributions presented in the study are included in the article/supplementary material, further inquiries can be directed to the corresponding authors.

Author contributions

JP: Investigation, methodology, experiment, writing—original draft, review and editing. NW: Investigation, writing—review, supervision, funding acquisition. BZ: Methodology, data curation, experiment, visualization. JZ: Conceptualization, investigation, review. BK: Methodology, investigation, review. RC: Investigation, review. HL: Validation, resources, experiment. RB: Formal analysis, experiment.

Funding

This work was financially supported by the National Natural Science Foundation of China (U20B6005-05, 51874252), National Key Research and Development Program of China (2021YFC2800903), Sichuan High-end Foreign Talent Introduction Project (SYZ202124), High-end Foreign Experts Recruitment Plan of China (G2021036005L), 111 Project (D21025), and Open Fund of State Key Laboratory of Oil and Gas Reservoir Geology and Exploitation (Southwest Petroleum University) (PLN 2021-01, PLN 2021-02, PLN 2021-03).

Acknowledgments

The authors would like to thank the reviewers and editors for their helpful comments and suggestions.

Conflict of interest

BZ is employed by Chengdu North Petroleum Exploration and Development Technology Co., Ltd.

The remaining authors declare that the research was conducted in the absence of any commercial or financial relationships that could be construed as a potential conflict of interest.

Publisher's note

References

Bai, B., Wang, Y., Rao, D. Y., and Bai, F. (2022). The effective thermal conductivity of unsaturated porous media deduced by pore-scale SPH simulation. *Front. Earth Sci.* 10, 943853. doi:10.3389/feart.2022.943853

Bai, B., Zhou, R., Cai, G. Q., Hu, W., and Yang, G. C. (2021). Coupled thermo-hydro-mechanical mechanism in view of the soil particle rearrangement of granular thermodynamics. *Comput. Geotech.* 137, 104272. doi:10.1016/j.compgeo.2021.104272

Boswell, R., and Collett, T. S. (2011). Current perspectives on gas hydrate resources. *Energy Environ. Sci.* 4, 1206–1215. doi:10.1039/c0ee00203h

Burger, J., Gupta, D., Jacobs, P., and Shillinglaw, J. (2006). *Overview on hydrate coring, handling and analysis*. Houston, TX: DOE Report. DE-FC26–02NT41327.

Chen, H., Du, H., Shi, B., Shan, W. C., and Hou, J. Q. (2022). Mechanical properties and strength criterion of clayey sand reservoirs during natural gas hydrate extraction. *Energy* 242, 122526. doi:10.1016/j.energy.2021.122526

Chen, Y., Sun, B. J., Gao, Y. H., Liu, K., Li, H., and Zhao, X. X. (2019). Pressure effects on heat transfer in hydrate-bearing deposit with drilling fluid invasion by lab simulation. *Int. J. Green Energy* 16 (10), 770–777. doi:10.1080/15435075.2019.1641104

Chibura, P. E., Zhang, W., Luo, A. J., and Wang, J. J. (2022). A review on gas hydrate production feasibility for permafrost and marine hydrates. *J. Nat. Gas. Sci. Eng.* 100, 104441. doi:10.1016/j.jngse.2022.104441

Chong, Z. R., Yang, S. H. B., Babu, P., Linga, P., and Li, X. S. (2016). Review of natural gas hydrates as an energy resource: Prospects and challenges. *Appl. Energy* 162, 1633–1652. doi:10.1016/j.apenergy.2014.12.061

Collett, T., Riedel, M., Cochran, J., Boswell, R., Presley, J., Kumar, P., et al. The NGHP Expedition Scientists (2012). *The national gas hydrate Program expedition 01 scientists expedition summary*. Reston, VA: Scientific Investigations Report, 2012–5054.

Collett, T. S., Boswell, R., Frye, M., Shedd, W., Godfriaux, P., Dufrene, R., et al. (2009). "Gulf of Mexico gas hydrate Joint Industry project Leg II—operational summary," in Proceedings of the Drilling and Scientific Results of the 2009 Gulf of Mexico Gas Hydrate Joint Industry Project Leg II. May 2009

Cook, A. E., Anderson, B. I., Rasmus, J., Sun, K. L., Li, Q. M., Collett, T. S., et al. (2012). Electrical anisotropy of gas hydrate-bearing sand reservoirs in the Gulf of Mexico. *Mar. Pet. Geol.* 34 (1), 72–84. doi:10.1016/j.marpetgeo.2011.09.003

Cui, J. L., Sun, Z. F., Kan, J. Y., Jia, S., Sun, C. Y., Chen, G. J., et al. (2021). Study on the factors affecting the sealing performance and mechanical stability of CO_2 hydrate cap during gas production from methane hydrate. *J. Nat. Gas. Sci. Eng.* 93, 104050. doi:10.1016/j.jngse.2021.104050

Dai, J. X., Ni, Y. Y., Huang, S. P., Peng, W. L., Han, W. X., Gong, D. Y., et al. (2017). Genetic types of gas hydrates in China. *Petroleum Explor. Dev.* 44, 887–898. doi:10.1016/s1876-3804(17)30101-5

Dong, L., Wan, Y. Z., Li, Y. L., Liao, H. L., Liu, C. L., Wu, N. Y., et al. (2022). 3D numerical simulation on drilling fluid invasion into natural gas hydrate reservoirs. *Energy* 241, 122932. doi:10.1016/j.energy.2021.122932

Fereidounpour, A., and Vatani, A. (2014). An investigation of interaction of drilling fluids with gas hydrates in drilling hydrate bearing sediments. *J. Nat. Gas. Sci. Eng.* 20, 422–427. doi:10.1016/j.jngse.2014.07.006

Gao, Y. H., Chen, Y., Wang, Z. Y., Chen, L. T., Zhao, X. X., and Sun, B. J. (2019). Experimental study on heat transfer in hydrate-bearing reservoirs during drilling processes. *Ocean. Eng.* 183, 262–269. doi:10.1016/j.oceaneng.2019.04.092

Grigg, R. B., and Lynes, G. L. (1992). Oil-based drilling mud as a gas-hydrates inhibitor. *SPE Drill. Eng.* 7, 32–38. doi:10.2118/19560-pa

Guo, K., Fan, S. S., Wang, Y. H., Lang, X. M., Zhang, W. X., and Li, Y. P. (2020). Physical and chemical characteristics analysis of hydrate samples from northern south China sea. *J. Nat. Gas. Sci. Eng.* 81, 103476. doi:10.1016/j.jngse.2020.103476

Hu, G., Bu, Q., Lyu, W., Wang, J., Chen, J., Li, Q., et al. (2021). A comparative study on natural gas hydrate accumulation models at active and passive continental margins. *Nat. Gas. Ind. B* 8 (2), 115–127. doi:10.1016/j.ngib.2021.03.001

Huang, J. W., Bellefleur, G., and Milkereit, B. (2009). Seismic modeling of multidimensional heterogeneity scales of Mallik gas hydrate reservoirs, Northwest Territories of Canada. *J. Geophys. Res.* 114, B07306. doi:10.1029/2008jb006172

Huang, T. J., Zhang, Y., Li, G., Li, X. S., and Chen, Z. Y. (2020). Numerical modeling for drilling fluid invasion into hydrate-bearing sediments and effects of permeability. *J. Nat. Gas. Sci. Eng.* 77, 103239. doi:10.1016/j.jngse.2020.103239

Hyodo, M., Nakata, Y., Yoshimoto, N., Fukunaga, M., Kubo, K., Nanjo, Y., et al. (2002). "Triaxial compressive strength of methane hydrate," in Proceedings of the Twelfth International Offshore and Polar Engineering Conference, Kitakyushu, Japan, May 2002. ISOPE-I-02-062.

Hyodo, M., Yoneda, J., Yoshimoto, N., and Nakata, Y. (2013). Mechanical and dissociation properties of methane hydrate-bearing sand in deep seabed. *Soils Found.* 53 (2), 299–314. doi:10.1016/j.sandf.2013.02.010

Ito, T., Komatsu, Y., Fujii, T., Suzuki, K., Egawa, K., Nakatsuka, Y., et al. (2015). Lithological features of hydrate-bearing sediments and their relationship with gas hydrate saturation in the eastern Nankai Trough, Japan. *Mar. Pet. Geol.* 66 (2), 368–378. doi:10.1016/j.marpetgeo.2015.02.022

Jang, J. B., Dai, S., Yoneda, J., Waite, W. F., Stern, L. A., Boze, L. G., et al. (2019). Pressure core analysis of geomechanical and fluid flow properties of seals associated with gas hydrate-bearing reservoirs in the Krishna-Godavari Basin, offshore India. *Mar. Pet. Geol.* 108, 537–550. doi:10.1016/j.marpetgeo.2018.08.015

Jiang, M. J., Zhu, F. Y., and Utili, S. (2015). Investigation into the effect of backpressure on the mechanical behavior of methane-hydrate-bearing sediments via DEM analyses. *Comput. Geotech.* 69, 551–563. doi:10.1016/j.compgeo.2015.06.019

Kuang, Y. M., Yang, L., Li, Q. P., Lv, X., Li, Y. P., Yu, B., et al. (2019). Physical characteristic analysis of unconsolidated sediments containing gas hydrate recovered from the Shenhu Area of the South China sea. *J. Pet. Sci. Eng.* 181, 106173. doi:10.1016/j.petrol.2019.06.037

Kvamme, B. (2020). Consistent thermodynamic calculations for hydrate properties and hydrate phase transitions. *J. Chem. Eng. Data* 65, 2872–2893. doi:10.1021/acs.jced.0c00171

Kvamme, B., and Saeidi, N. (2021). A zero emission scheme for producing energy from natural gas hydrates and conventional natural gas. *Petroleum* 7 (4), 364–384. doi:10.1016/j.petlm.2021.10.003

Lee, H., Seo, Y., Seo, Y. T., Moudrakovski, I. L., and Ripmeester, J. A. (2003). Recovering methane from solid methane hydrate with carbon dioxide. *Angew. Chem. Int. Ed.* 42 (41), 5048–5051. doi:10.1002/anie.200351489

Lee, M. W., and Collett, T. S. (2001). Elastic properties of gas hydrate-bearing sediments. *Geophysics* 66 (3), 763–771. doi:10.1190/1.1444966

Li, J. F., Ye, J. L., Qin, X. W., Qiu, H. J., Wu, N. Y., Lu, H. L., et al. (2018). The first offshore natural gas hydrate production test in South China Sea. *China Geol.* 1 (1), 5–16. doi:10.31035/cg2018003

Li L, L. J., Li, X. S., Wang, Y., Qin, C. Z., Li, B., Luo, Y. J., et al. (2021). Investigating the interaction effects between reservoir deformation and hydrate dissociation in hydrate-bearing sediment by depressurization method. *Energies* 14 (3), 548. doi:10.3390/en14030548

Li, X. S., Xu, C. G., Zhang, Y., Ruan, X. K., Li, G., and Wang, Y. (2016). Investigation into gas production from natural gas hydrate: A review. *Appl. Energy* 172, 286–322. doi:10.1016/j.apenergy.2016.03.101

Li Y, Y. L., Dong, L., Wu, N. Y., Nouri, A., Liao, H. L., Chen, Q., et al. (2021). Influences of hydrate layered distribution patterns on triaxial shearing characteristics of hydrate-bearing sediments. *Eng. Geol.* 294, 106375. doi:10.1016/j.enggeo.2021.106375

Li, Y. L., Liu, C. L., Liu, L. L., Huang, M., and Meng, Q. G. (2017). Triaxial shear test and strain analysis of unconsolidated hydrate-bearing sediments. *Nat. Gas. Geosci.* 28 (3), 383–390. In Chinese with English abstract.

Liang, Q. Y., Xiao, X., Zhao, J., Zhang, W., Li, Y., Wu, X. M., et al. (2022). Geochemistry and sources of hydrate-bound gas in the Shenhu area, northern south China sea: Insights from drilling and gas hydrate production tests. *J. Pet. Sci. Eng.* 208, 109459. doi:10.1016/j.petrol.2021.109459

Liang, Y. P., Tan, Y. T., Luo, Y. J., Zhang, Y. Y., and Li, B. (2020). Progress and challenges on gas production from natural gas hydrate-bearing sediment. *J. Clean. Prod.* 261, 121061. doi:10.1016/j.jclepro.2020.121061

Liao, Y. Q., Wang, Z. Y., Chao, M. Z., Sun, X. H., Wang, J. T., Zhou, B. Y., et al. (2021). Coupled wellbore-reservoir heat and mass transfer model for horizontal drilling through hydrate reservoir and application in wellbore stability analysis. *J. Nat. Gas. Sci. Eng.* 95, 104216. doi:10.1016/j.jngse.2021.104216

Lijith, K. P., Malagar, B. R. C., and Singh, D. N. (2019). A comprehensive review on the geomechanical properties of gas hydrate bearing sediments. *Mar. Pet. Geol.* 104, 270–285. doi:10.1016/j.marpetgeo.2019.03.024

Liu, T. L., Jiang, G. S., Zhang, P., Sun, J. X., Sun, H. C., Wang, R., et al. (2016). A new low-cost drilling fluid for drilling in natural gas hydrate-bearing sediments. *J. Nat. Gas. Sci. Eng.* 33, 934–941. doi:10.1016/j.jngse.2016.06.017

Liu, Z. C., Kim, J., Lei, L., Ning, F. L., and Dai, S. (2019). Tetrahydrofuran hydrate in clayey SedimentsLaboratory formation, morphology, and wave characterization. *J. Geophys. Res. Solid Earth* 124 (4), 3307–3319. doi:10.1029/2018jb017156

Luo, T. T., Song, Y. C., Zhu, Y. M., Liu, W. G., Liu, Y., Li, Y. H., et al. (2016). Triaxial experiments on the mechanical properties of hydrate-bearing marine sediments of South China Sea. *Mar. Pet. Geol.* 77, 507–514. doi:10.1016/j.marpetgeo.2016.06.019

Maiti, M., Bhaumik, A. K., and Mandal, A. (2022). Geological characterization of natural gas hydrate bearing sediments and their influence on hydrate formation and dissociation. *J. Nat. Gas. Sci. Eng.* 100, 104491. doi:10.1016/j.jngse.2022.104491

Masui, A., Haneda, H., Yuji, O., and Aoki, K. (2006). "Triaxial compression test on submarine sediment containing methane hydrate in deep sea off the coast off Japan," in Proceedings of the 41st Annual Conference, Tokyo, Japan, July 2006 (Japanese Geotechnical Society).

Masui, A., Miyazaki, K., Haneda, H., Ogata, Y., and Aoki, K. (2008). "Mechanical properties of natural gas hydrate bearing sediments retrieved from eastern Nankai Trough," in Proceedings of the Offshore Technology Conference. OTC-19277-MS.

Merey, S. (2016). Drilling of gas hydrate reservoirs. *J. Nat. Gas. Sci. Eng.* 35, 1167–1179. doi:10.1016/j.jngse.2016.09.058

Ning, F. L. (2005). *Research on wellbore stability in gas hydrate formation*. Lumo Road, Wuhan: China University of Geosciences.

Ning, F. L., Wu, N., Jiang, G., and Zhang, L. (2009). "The effect of gas hydrates dissociation and drilling fluids invasion upon borehole stability in oceanic gas hydrates-bearing sediment," in *Marine Geology and geophysics* (Washington, D.C., United States: American Geophysical Union). OS31A-1207.

Ning, F. L., Wu, N. Y., Yu, Y. B., Zhang, K. N., Jiang, G. S., Zhang, L., et al. (2014). Erratum: Invasion of drilling mud into gas-hydrate-bearing sediments. Part II: Effects of geophysical properties of sediments. *Geophys. J. Int.* 197 (2), 1271. doi:10.1093/gji/ggu061

Ning, F. L., Zhang, K. N., Wu, N. Y., Zhang, L., Li, G., Jiang, G. S., et al. (2013). Invasion of drilling mud into gas-hydrate-bearing sediments. Part I: Effect of drilling mud properties. *Geophys. J. Int.* 193 (3), 1370–1384. doi:10.1093/gji/ggt015

Park, T., Lee, J. Y., and Kwon, T. H. (2018). Effect of pore size distribution on dissociation temperature depression and phase boundary shift of gas hydrate in various fine-grained sediments. *Energy fuels.* 32 (4), 5321–5330. doi:10.1021/acs.energyfuels.8b00074

Ruan, X. K., Li, X. S., and Xu, C. G. (2021). A review of numerical research on gas production from natural gas hydrates in China. *J. Nat. Gas. Sci. Eng.* 85, 103713. doi:10.1016/j.jngse.2020.103713

Samala, R., and Chaudhuri, A. (2022). Coupled THMC modeling of dissociation induced deformation of gas hydrate bearing media. *Comput. Geosci.* 166, 105162. doi:10.1016/j.cageo.2022.105162

Schoderbek, D., Farrell, H., Hester, K., Howard, J., Raterman, K., Silpngarmlert, S., et al. (2013). *ConocoPhillips gas hydrate production test final technical report.* (Houston, Texas: ConocoPhillips Company).

Shen, S., Li, Y. H., Sun, X., Wang, L., and Song, Y. C. (2021). Analysis of the mechanical properties of methane hydrate-bearing sands with various pore pressures and confining pressures. *J. Nat. Gas. Sci. Eng.* 87, 103786. doi:10.1016/j.jngse.2020.103786

Shen, S., Li, Y. H., Sun, X., Wang, L., and Song, Y. C. (2022). Stress behavior of hydrate-bearing sands with changing temperature and hydrate saturation. *J. Nat. Gas. Sci. Eng.* 98, 104389. doi:10.1016/j.jngse.2021.104389

Shepard, F. P., and Moore, D. G. (1954). Sedimentary environments differentiated by coarse-fraction studies. *AAPG Am. Assoc. Pet. Geol.) Bull.* 38 (8), 1792–1802.

Sloan, E. D., and Koh, C. A. (2007). *Clathrate hydrate of natural gases*. 3rd Edition. Boca Raton, Florida, US: CRC Press.

Song, Y. C., Zhu, Y. M., Liu, W. G., Zhao, J. F., Li, Y. H., Chen, Y. F., et al. (2014). Experimental research on the mechanical properties of methane hydrate-bearing sediments during hydrate dissociation. *Mar. Pet. Geol.* 51, 70–78. doi:10.1016/j.marpetgeo.2013.11.017

Stolper, D. A., Lawson, M., Davis, C. L., Ferreira, A. A., Neto, E. V. S., Ellis, G. S., et al. (2014). Formation temperatures of thermogenic and biogenic methane. *Science* 344, 1500–1503. doi:10.1126/science.1254509

Su, M., Luo, K. W., Fang, Y. X., Kuang, Z. G., Yang, C. Z., Liang, J. Q., et al. (2021). Grain-size characteristics of fine-grained sediments and association with gas hydrate saturation in Shenhu Area, northern South China Sea. *Ore Geol. Rev.* 129, 103889. doi:10.1016/j.oregeorev.2020.103889

Su, X., Song, C. B., and Fang, N. Q. (2005). Variation in grain size of sediments above BSR and correlation with the occurrence of gas hydrates on Hydrates Ridge, East Pacific. *Earth Sci. Front.* 12 (1), 234–242. In Chinese with English abstract.

Sun, C. Y., Li, W. Z., Yang, X., Li, F. G., Yuan, Q., Mu, L. A., et al. (2011). Progress in research of gas hydrate. *Chin. J. Chem. Eng.* 19 (1), 151–162. doi:10.1016/s1004-9541(09)60192-0

Sun, W. T., Pei, J., Wei, N., Zhao, J. Z., Xue, J., Zhou, S. W., et al. (2021). Sensitivity analysis of reservoir risk in marine gas hydrate drilling. *Petroleum* 7 (4), 427–438. doi:10.1016/j.petlm.2021.10.013

Sun, W. T., Wei, N., Zhao, J. Z., Kvamme, B., Zhou, S. W., Zhang, L. H., et al. (2022). Imitating possible consequences of drilling through marine hydrate reservoir. *Energy* 239, 121802. doi:10.1016/j.energy.2021.121802

Teymouri, M., Sanchez, M., and Santamarina, J. C. (2020). A pseudo-kinetic model to simulate phase changes in gas hydrate bearing sediments. *Mar. Pet. Geol.* 120, 104519. doi:10.1016/j.marpetgeo.2020.104519

Tian, H. H., Wei, C. F., Yan, R. T., and Chen, H. L. (2019). A NMR-based analysis of carbon dioxide hydrate dissociation process in silt. *Sci. Sin. -Phys. Mech. Astron.* 49 (3), 034615. doi:10.1360/sspma2018-00151

Waite, W. F., Santamarina, J. C., Cortes, D. D., Dugan, B., Espinoza, D. N., Germaine, J., et al. (2009). Physical properties of hydrate-bearing sediments. *Rev. Geophys.* 47 (4), RG4003. doi:10.1029/2008rg000279

Wang, J. J., and Lau, H. C. (2020). Thickness of gas hydrate stability zone in permafrost and marine gas hydrate deposits: Analysis and implications. *Fuel* 282, 118784. doi:10.1016/j.fuel.2020.118784

Wang, L. Z., and Wang, G. R. (2020). Experimental and theoretical study on the critical breaking velocity of marine natural gas hydrate sediments breaking by water jet. *Energies* 13 (7), 1725. doi:10.3390/en13071725

Wang, Q. B., Wang, R., Sun, J. X., Sun, J. S., Lu, C., Lv, K. H., et al. (2021). Effect of drilling fluid invasion on natural gas hydrate near-well reservoirs drilling in a horizontal well. *Energies* 14 (21), 7075. doi:10.3390/en14217075

Wang, Q. L., Wang, Z. M., Li, P., Song, Y. C., and Wang, D. Y. (2022). Numerical modeling of coupled behavior of gas production and mechanical deformation of gas hydrate reservoir in shenhu area, south China sea: Enlightenments for field monitoring and model verification. *Energy* 254, 124406. doi:10.1016/j.energy.2022.124406

Wang, Y., Kou, X., Feng, J. C., Li, X. S., and Zhang, Y. (2020). Sediment deformation and strain evaluation during methane hydrate dissociation in a novel experimental apparatus. *Appl. Energy* 262, 114397. doi:10.1016/j.apenergy.2019.114397

Wei J, J., Cheng, Y. F., Yan, C. L., Li, Q. C., Zou, D. Y., and Zhang, H. W. (2019). Drilling parameter optimizing strategies to prevent hydrate decomposition risks. *Appl. Therm. Eng.* 146, 405–412. doi:10.1016/j.applthermaleng.2018.09.135

Wei, N., Sun, W. T., Meng, Y. F., Liu, A. Q., Zhao, J. Z., Zhou, S. W., et al. (2018). Multiphase non equilibrium pipe flow behaviors in the solid fluidization exploitation of marine natural gas hydrate reservoir. *Energy Sci. Eng.* 6, 760–782. doi:10.1002/ese3.251

Wei N, N., Zhao, J., Sun, W., Zhou, S., Zhang, L., Li, Q., et al. (2019). Non-equilibrium multiphase wellbore flow characteristics in solid fluidization exploitation of marine gas hydrate reservoirs. *Nat. Gas. Ind. B* 6 (3), 282–292. doi:10.1016/j.ngib.2018.10.008

Wei, W. N., Li, B., Gan, Q., and Li, Y. L. (2022). Research progress of natural gas hydrate exploitation with CO2 replacement: A review. *Fuel* 312, 122873. doi:10.1016/j.fuel.2021.122873

Wu, N. Y., Liu, C. L., and Hao, X. L. (2018). Experimental simulations and methods for natural gas hydrate analysis in China. *China Geol.* 1 (1), 61–71. doi:10.31035/cg2018008

Wu, Q., and Zhang, B. Y. (2009). Kinetic promotion of sodium dodecyl sulfate on formation rate of mine gas hydrate. *Procedia Earth Planet. Sci.* 1 (1), 648–653. doi:10.1016/j.proeps.2009.09.102

Yamamoto, K., Wang, X. X., Tamaki, M., and Suzuki, K. (2019). The second offshore production of methane hydrate in the Nankai Trough and gas production behavior from a heterogeneous methane hydrate reservoir. *RSC Adv.* 9 (45), 25987–26013. doi:10.1039/c9ra00755e

Ye, J. L., Qin, X. W., Xie, W. W., Lu, H. L., Ma, B. J., Qiu, H. J., et al. (2020). The second natural gas hydrate production test in the South China Sea. *China Geol.* 3 (2), 197–209. doi:10.31035/cg2020043

Ye, Y. G., and Liu, C. L. (2013). *Natural gas hydrate: Experimental techniques and their applications*. New YorkHeidelberg: Springer Berlin.

Yin, Z. Y., and Linga, P. (2019). Methane hydrates: A future clean energy resource. *Chin. J. Chem. Eng.* 27 (9), 2026–2036. doi:10.1016/j.cjche.2019.01.005

Zhang, H. W., Cheng, Y. F., Shi, J. H., Li, L. D., Li, M. L., Han, X. T., et al. (2017). Experimental study of water-based drilling fluid disturbance on natural gas hydrate-bearing sediments. *J. Nat. Gas. Sci. Eng.* 47, 1–10. doi:10.1016/j.jngse.2017.08.029

Zhang, X. H., Luo, D. S., Lu, X. B., Liu, L. L., and Liu, C. L. (2018). Mechanical properties of gas hydrate-bearing sediments during hydrate dissociation. *Acta Mech. Sin.* 34 (2), 266–274. doi:10.1007/s10409-017-0699-y

Zhang, Y. C., Liu, L. L., Hu, G. W., Bu, Q. T., Li, C. F., Zhang, Z. C., et al. (2022). Formation mechanism, experimental method, and property characterization of grain-displacing methane hydrates in marine sediment: A review. *China Geol.* 5 (2), 345–354. doi:10.31035/cg2022014

Zheng, M. M., Liu, T. L., Jiang, G. S., Wei, M., Huo, Y. X., and Liu, L. (2020). Large-scale and high-similarity experimental study of the effect of drilling fluid penetration on physical properties of gas hydrate-bearing sediments in the Gulf of Mexico. *J. Pet. Sci. Eng.* 187, 106832. doi:10.1016/j.petrol.2019.106832

Zhou, S. W., Li, Q. P., Chen, W., Zhou, J. L., Pang, W. X., He, Y. F., et al. (2018a). "The world's first successful implementation of solid fluidization well testing and production for non-diagenetic natural gas hydrate buried in shallow layer in deep water," in Proceedings of the Offshore Technology Conference, Houston, Texas, USA, April 2018, 2784–2794.

Zhou, S. W., Li, Q. P., Lv, X., Fu, Q., and Zhu, J. L. (2020). Key issues in development of offshore natural gas hydrate. *Front. Energy* 14 (3), 433–442. doi:10.1007/s11708-020-0684-1

Zhou, S. W., Zhao, J. Z., Li, Q. P., Chen, W., Zhou, J. L., Wei, N., et al. (2018b). Optimal design of the engineering parameters for the first global trial production of marine natural gas hydrates through solid fluidization. *Nat. Gas. Ind. B* 5 (2), 118–131. doi:10.1016/j.ngib.2018.01.004

Zhu, H. Y., Dang, Y. K., Wang, G. R., Zhou, S. W., and Fu, Q. (2021). Near-wellbore fracture initiation and propagation induced by drilling fluid invasion during solid fluidization mining of submarine nature gas hydrate sediments. *Pet. Sci.* 18 (6), 1739–1752. doi:10.1016/j.petsci.2021.09.026

Zhu, Y. M., Wang, H., Chen, C., and Luo, T. T. (2020). Effects of sand contents on mechanical characteristics of methane hydrate-bearing sediments in the permafrost. *J. Nat. Gas. Sci. Eng.* 75, 103129. doi:10.1016/j.jngse.2019.103129

frontiers | Frontiers in Earth Science

TYPE Original Research
PUBLISHED 18 January 2023
DOI 10.3389/feart.2022.1018325

OPEN ACCESS

EDITED BY
Lihua Zuo,
Texas A&M University Kingsville,
United States

REVIEWED BY
Jiliang Wang,
Institute of Deep-Sea Science and Engineering (CAS), China
Qian-Zhi Zhou,
Sun Yat-sen University, China

*CORRESPONDENCE
Bin Zhao,
zbin_a@mail.cgs.gov.cn

SPECIALTY SECTION
This article was submitted to Marine Geoscience,
a section of the journal
Frontiers in Earth Science

RECEIVED 13 August 2022
ACCEPTED 31 October 2022
PUBLISHED 18 January 2023

CITATION
Wang X, Liu S, Zhao B, Yao Y, Wu G, Xie R, Fu Y and Ning Z (2023), Quantitative analysis of the risk of hydrogen sulfide release from gas hydrates.
Front. Earth Sci. 10:1018325.
doi: 10.3389/feart.2022.1018325

Quantitative analysis of the risk of hydrogen sulfide release from gas hydrates

Xianqing Wang[1,2,3], Siqing Liu[3], Bin Zhao[3,4]*, Yanfu Yao[1,2,3], Gang Wu[1,2,3], Rui Xie[1,2,3], Yutong Fu[1,2,3] and Zijie Ning[3]

[1]Sanya Institute of South China Sea Geology, Guangzhou Marine Geological Survey, Sanya, China, [2]Academy of South China Sea Geological Science, China Geological Survey, Sanya, China, [3]Guangzhou Marine Geological Survey, Guangzhou, China, [4]Southern Marine Science and Engineering Guangdong Laboratory, Guangzhou, China

The role that H_2S plays in the global sulfur cycle has been studied extensively in recent years. This paper focuses on the influence of H_2S released from gas hydrates on sulfur cycle and establishes a one-dimensional mathematical model to calculate the amount of H_2S released from the dissociation of gas hydrates present in multiple layers in the Qiongdongnan Basin China. The results show that the sulfate and methane transition zone that covers an area of about 100 km^2in the Qiongdongnan Basin contains 2.3 × 10^{12} g of pyrite, which requires 4.06 × 10^{11} mol of H_2S for its formation. The H_2S released from the dissociation of gas hydrates is 5.4 ×10^{11} mol, which is about 1.3 times that needed for the formation of pyrite. Therefore, the H_2S released from the gas hydrates is an important source of H_2S for the formation of pyrite in the sulfate-methane transition zone of Qiongdongnan Basin. According to the flux of H_2S and the partial pressure of O_2 (P_{O2}) in the atmosphere, the critical value of the balance between the flux of H_2S and P_{O2} turns out to be 0.13 mol kg^{-1}·bar^{-1}. Furthermore, considering the effect of global sea-level changes, three risk modes are identified to categorize the amount of H_2S released from the dissociation of gas hydrate into the atmosphere. We classify the periods from 5–12 Ma BP, 25–29 Ma BP, 47–52 Ma, and 57–61 Ma BP into the high-risk mode. Furthermore, the results show that a part of the H_2S released from the gas hydrate dissociation is oxidized by the Fe (III) oxide metal, with much of the metal ions being released into the pore water. Another part of the H_2S is re-oxidized by the O_2 in the ocean, with much of SO_4^{2-} released into the seawater. Therefore, the process also provides metal ions and SO_4^{2-} to pore water or seawater when the H_2S released from gas hydrate diffuses from the bottom. This paper provides new insights into the source of H_2S in the ocean and shows that the H_2S contained in gas hydrates plays an important role in the global sulfur cycle.

KEYWORDS

sulfur cycle, hydrogen sulfide, pyrite formation, anaerobic oxidation, methane

1 Introduction

Pyrites are the most important sulfur sinks and are widely distributed in marine sediments (Lin et al., 2017). They have a significant influence on the sulfur cycle and have resulted in a series of studies involving major scientific issues, such as the evolution of oxygen and the origin of life (Butler et al., 2004; Chen et al., 2006; Formolo and Lyons 2013; Akhoudas et al., 2018). Therefore, many scholars have carried out detailed research on their cause and isotope composition (Hu et al., 2012; Pan et al., 2018). Two pyrite formation pathways have been proposed. One pathway is the polysulfide one:

$$FeS_{(s)} \rightarrow FeS_{(aq)} + S^{2-}_{n\,(aq)} = FeS_{2\,(aq)} + S^{2-}_{n-1}\,(aq) \qquad (1)$$

The other is the H_2S pathway, initially observed as the reaction of pyrrhotite ($Fe_{1-x}S$) with $H_2S_{(aq)}$:

$$FeS_{(s)} \rightarrow FeS_{(aq)} + H_2S_{(aq)} = FeS_{2\,(S)} + H_2\,(g) \qquad (2)$$

There have been many studies related to the formation of pyrite, right from the identification of the macroscopic sedimentary environment to the microscopic microbial culture, and are mainly focused on the redox state of the sedimentary environment and the global C-S-Fe cycle (Peckmann and Thiel 2004; Kraal et al., 2009; Lin et al., 2016). In recent years, the influence of the local depositional environment on the formation of pyrite and its isotopes has received increasing attention, and the idea of using pyrite sulfur isotopes to trace the evolution of depositional environment (such as sea-level changes) has been put forward (Wang et al., 2018a), especially in shallow seas (Peckmann et al., 2001; Lim et al., 2011; Sima et al., 2011). During OSR and SO_4^{2-}-AOM processes, higher HS- concentrations are produced in the pore water and HS- reacts with Fe^{2+} in pore water or sediment to form pyrite. During this process, metal oxides are gradually converted into FeS and finally into pyrite under the action of excessive hydrogen sulfide. Therefore, studying the source of hydrogen sulfide has important scientific significance to understand the change of depositional environments. However, the speciation of H_2S in seawater is complex, with the species most often described in terms of free sulfide (H_2S+ HS^-+ S^{2-}). Furthermore, questions remain regarding the role that H_2S plays in the global sulfur cycle, particularly with respect to its presence in the remote oceanic atmosphere and possible transfer across the air/sea interface. Previous studies have found that the main source of hydrogen sulfide for the formation of pyrite in marine sediments is from the anaerobic oxidation of methane (AOM) and organic sulfur reduction (OSR) (Xie et al., 2019; Wei et al., 2020). The production of hydrogen sulfide also occurs in hydrothermal systems due to geochemical processes (Yao and Millero, 1996). Huene and Pecher, (1999) summarized the H_2S concentrations found in a large number of hydrothermal fluids at various locations in the Pacific and Atlantic oceans, whereas the concentrations ranged from 1.1 to 110 mmol kg^{-1} (Von et al., 1995). However, previous studies have focused more on the mechanism of the formation of hydrogen sulfide and the source of hydrogen sulfide from volcanic eruptions, hydrothermal flux, or from the AOM and OSR (Radford- Knwry and Cutter, 1994, Shen et al., 2008; Wu et al., 2018). Only a handful of studies have focused on hydrogen sulfide contained in hydrates. At present, H_2S has been observed in gas hydrates using Raman spectroscopy at the Hydrate Ridge (Hester et al., 2007), the Nigerian Margin (Chazallon et al., 2007), and the South China Sea (Fang et al., 2019). In marine sediments, there are huge reserves of gas hydrates, which are widely distributed. There are also huge reserves of H_2S in gas hydrates, which are universally present across the Earth. Moreover, H_2S released from gas hydrates has an important influence on the environment. Considering the huge reserves of

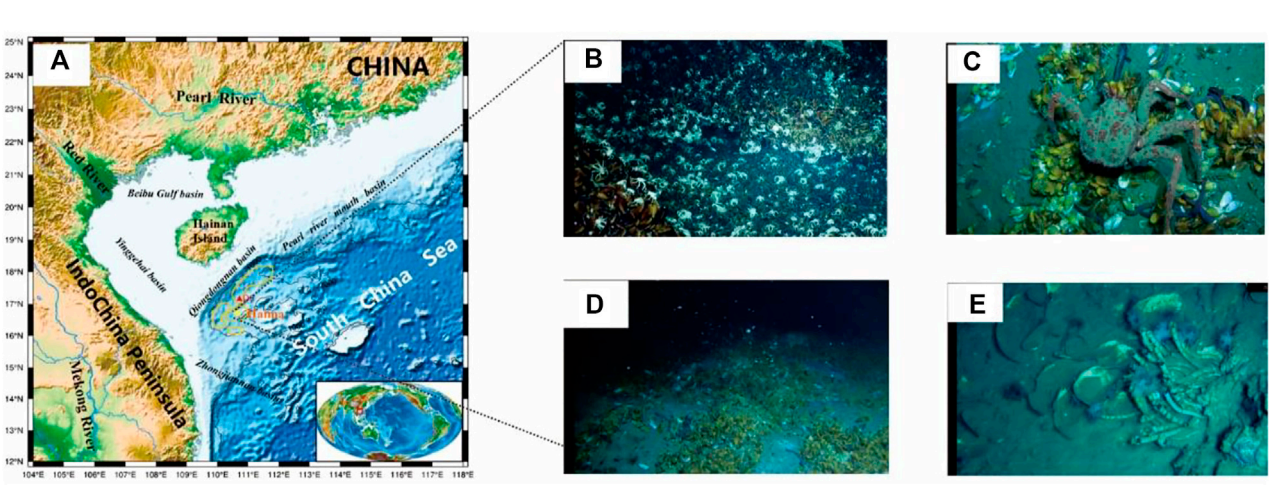

FIGURE 1
The methane seep area was observed in Qiongdongnan Basin. [**(A)**: Study Area, **(B–E)**: Biological status of methane leakage area].

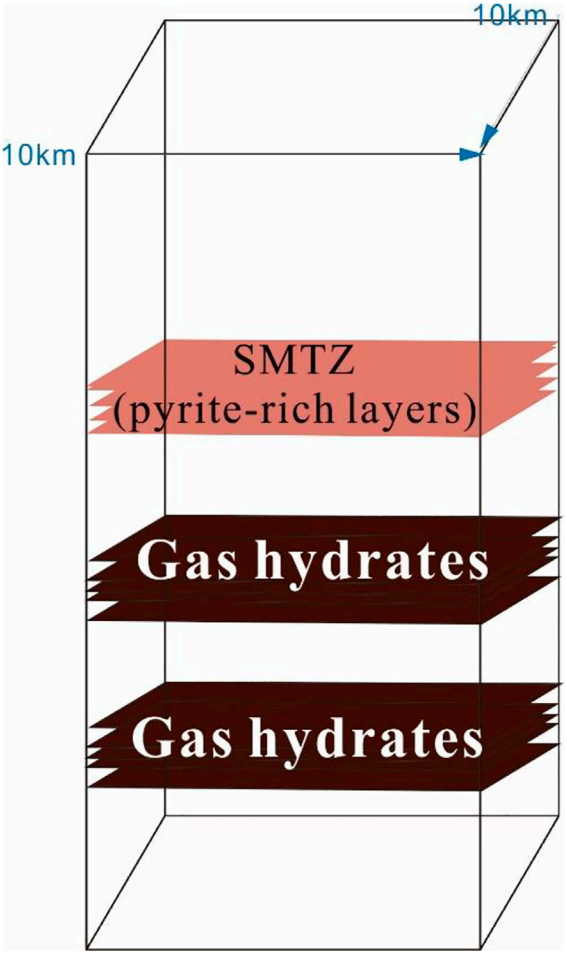

FIGURE 2
The mode distribution of gas hydrate and sulfate methane transition zone.

gas hydrates, the amount of H_2S contained in gas hydrates is also huge. Furthermore, when gas hydrates dissociate, much of the H_2S released from the gas hydrates also affect the environment, the sulfur cycle in the ocean, and the local ecosystem (Kastner et al., 1998). Therefore, it is important to study the role that gas hydrates play in pyrite formation.

2 Geological setting

Qiongdongnan Basin is located in the western part of the northern continental slope of the South China Sea (Figure 1). The northern part of the basin is bound by the Hainan Island, while the west is adjacent to Indochina. Additionally, the east is close to the Pearl River Mouth Basin. The Qiongdongnan Basin covers more than 80,000 km^2, and approximately 60% of the basin has a water depth of more than 300 m (Wang et al., 2015). The seafloor water temperature at the Qiongdongnan Basin is 2°C–3°C, and the mean geothermal gradient is approximately 40°C/km. However, due to the common gas-bearing fluid activity in the Qiongdongnan Basin, the geothermal gradient in the study area is relatively much higher (Yuan et al., 2009). Oil and gas have been discovered in multiple reservoirs in different structural tectonic belts in the Qiongdongnan Basin (QDNB) (Zhang et al., 2014; Wang et al., 2015; W. Zhang et al., 2015; Zhang et al., 2016; Qin et al., 2019). The sediments deposited during the Pliocene and Quaternary possess favorable conditions for hosting biogenic gases, and these were commonly encountered in the strata shallower than 2,300 m during gas logging. In addition, the coal-measure source rocks deposited in the Oligocene are in the thermal evolution stage of mature-to-high-mature, with favorable conditions for thermogenic gas generation (Huang et al., 2015; Huang et al., 2017). Overpressure was common during the formation of QDNB when the rapidly filling sediments deposited in the Cenozoic became deeply buried under compaction (Shi et al., 2019; Wang et al., 2020). The mud diapirs and gas chimneys caused by overpressure are widely distributed in the deep water, providing an important vertical migration pathway for hydrocarbons and for the formation and accumulation of natural gas hydrates (Zhang et al., 2016; Wang et al., 2020). Furthermore, there is a large concentration of bivalve shells in the methane seep area (Figures 1B–E), indicating that the methane flux is higher. Meanwhile, multiple layers of gas hydrate are also found in the study area (Liang et al., 2019) (Figure 2).

3 Methods

In the current study, we used mass conversation equations to calculate the amount of H_2S in the sink and how much H_2S is released from the sink.

The total mass of H_2S at any given time can be described as:

$$\frac{d}{dt}H_2S = H_2S_{RG} + H_2S_{RA} + H_2SS_{RO} + H_2S_{PH} - H_2S_{FP} - H_2S_{RM} - H_2S_O \quad (3)$$

where H_2S_{RG} denotes the H_2S released from gas hydrate dissociation, H_2S_{RA} denotes the H_2S produced from AOM, H_2S_{R0} denotes the H_2S_{RO} produced by OSR, H_2S denotes the H_2S released from hydrothermal sources, H_2S_{FP} denotes the H_2S that reacts with the metal ions to form pyrite, H_2S_{RM} denotes the H_2S that is oxidized by the Fe (III) oxides, and H_2S_O denotes the H_2S that is oxidized by oxygen. In the study area, there is no volcanic and hydrothermal activity. Therefore, in the current paper, the H_2S_{PH} is assumed to be zero.

In the present study, the percentage of H_2S in gas hydrates was confirmed by the relative peak intensities of H_2S to CH_4. in

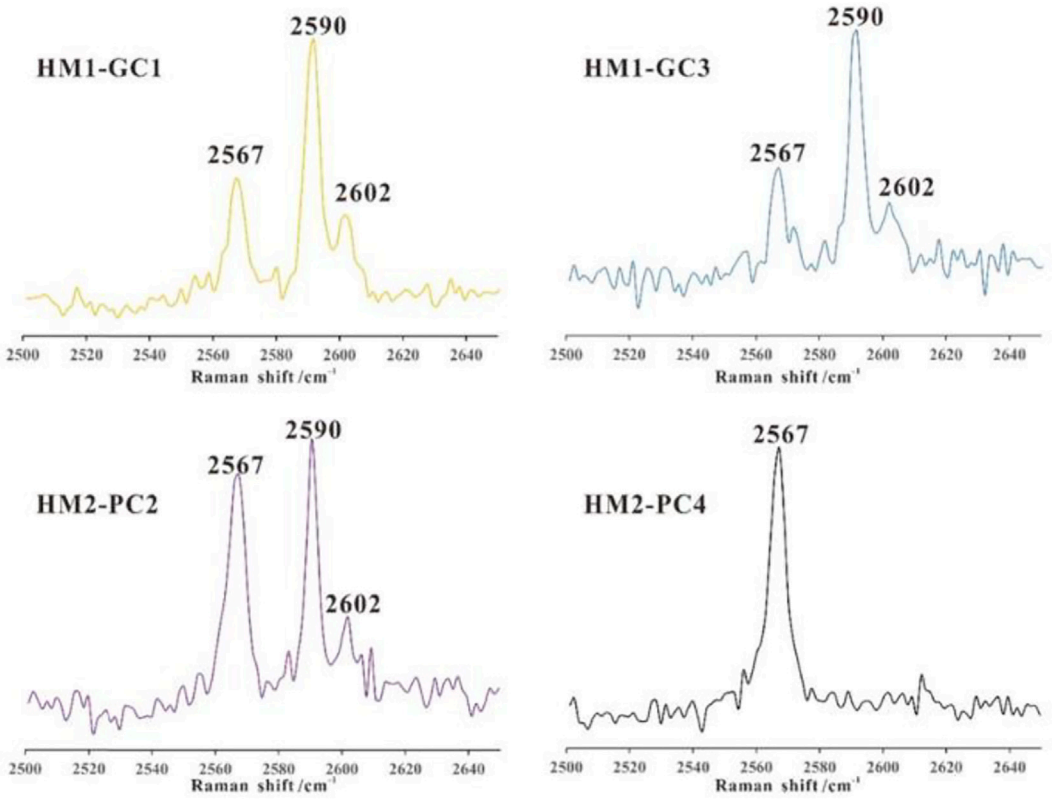

FIGURE 3
The concentration of H_2S in gas hydrate at Qiongdongnan basin (Referend from huang et al., 2017).

Spectroscopy. Moreover, their Raman quantification factor ratios were calibrated using the crystal established absolute cage occupancies of a pure H_2S sample (Figure 3) (Qin and Kuhs 2013), which is similar to the procedures described in (Qin and Kuhs, 2013) for CH_4 hydrate.

The percentage values of the partial pressure of atmospheric oxygen (P_{O2}) are determined by Liu et al. (2021) and the present value of P_{O2} is 212.28 mbar. The geological time of P_{O2} is determined by multiplying the fraction of P_{O2} with 212.28 mbar.

4 Results and discussion

4.1 Influence of the H_2S released from gas hydrates on the formation of pyrite

In marine sediments, the formation of H_2S occurs in a variety of settings. The production of H_2S in the pore water of sediments and the water column of stagnant basins is due to the anaerobic oxidation of methane (Yang et al., 2007). Submarine hydrothermal emissions are also a possible source of H_2S to the ocean. However, previous studies have shown that H_2S released from submarine hydrothermal emissions are not easily transferred into the atmosphere and shallow sediments (Yao and Milero., 1996). Therefore, the organic sulfur reduction (OSR) and anaerobic oxidation of methane (AOM) are the main sources of H_2S for the formation of pyrite (Commeau et al., 1987; Egger et al., 2015; Lin et al., 2015; Xie et al., 2019; Wu 2020; Wu, 2020; Wu, Xie, et al., 2020). However, the question remains as to how to evaluate the quantity of H_2S involved in the process of the formation of pyrites. As we all know, the AOM is widely present in the seepage area of gas hydrates (Wang et al., 2018b). Pyrites are also concentrated in sulfate and methane transition zone. During the process of AOM, the methane diffused from the bottom reacts with the sulfate from the overlying water at the sulfate-methane transition zone (SMTZ). The specific process is as follows:

$$CH_4 + SO_4^{2-} \rightarrow HS^- + HCO_3^- + H_2O \quad (4)$$

From Eq. 4, assuming the same reaction rate conditions, when 1 mol of methane is reduced by the sulfate, 1 mol of HS^- is produced at the same time. However, during the process of pyrite formation, 2 mol HS^- is needed to form 1 mol of pyrite (Peckmann et al., 2001; Canet et al., 2006; Lin et al., 2017). The specific reactions are as follows:

$$Fe^{2+} + HS^- \rightarrow FeS + H^+ \quad (5)$$

$$FeS + H_2S \rightarrow FeS_2 + H_2 \quad (6)$$

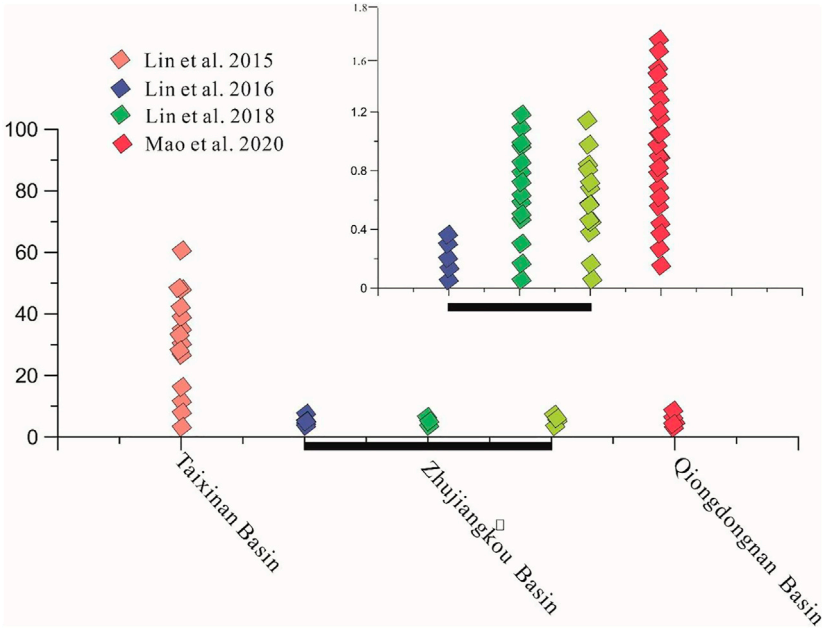

FIGURE 4
Content of pyrite at sulfate and methane transition zone in different sediments basin.

Moreover, 1 mol of hydrogen sulfide is provided by the AOM process, and another 1 mol is provided by another unknown mechanism. The presence of H_2S in the gas hydrates provides an explanation (Qin et al., 2020). Of course, organic sulfur reduction (OSR) also provides part of the missing H_2S. The specific reaction is as follows:

$$2CH_2O + SO_4^{2-} \rightarrow 2HCO_3^- + H_2S \quad (7)$$

However, OSR often takes place in the open environment and shallower sediments as compared to AOM (Xie et al., 2019). Therefore, the hydrogen sulfide produced by the OSR is always diffused upwards under the influence of pressure gradient. Due to this reason, it is difficult for it to be diffused downwards.

In the study area, the SMTZ is mainly distributed at 6–9 mbsf in the Taixinan Basin and the content of pyrite in the sediments is about 1.16%–1.03% at Taixinan Basin (Wu et al., 2019; Wei, et al., 2020). Previous studies have shown that the content of pyrite at the Zhujiangkou Basin, where the SMTZ is present at 5–7 mbsf, is about 2.5%–2.6% (Liu et al., 2016). In the Qiongdongnan Basin, the content of pyrite lies within the range of 1%–3%, and the SMTZ is distributed at about 2–3.9 mbsf. Furthermore, the SMTZ is also very close to the water-sediment seafloor, indicating that the methane flux is high in the Qiongdongnan area (Miao et al., 2021). During the GMGS5 voyages, the methane seep area was found, which covered an area of about 100 km^2 in the Qiongdongnan Basin (Figure 1). In this area, there is a rich concentration of gas hydrates and pyrites in the sediments. Based on the above analysis, the amount of pyrite in the SMTZ deposits in the methane seep area in the Qiongdongnan Basin can be calculated using the following equation

$$Quantity_{pyrite} = Depth_{SMTZ} \times S_{methane\ seep\ area} \times Q_{sediment\ density} \times C_{the\ pyrite\ percent\ of\ sediments} \quad (8)$$

$$Mole\ H_2S = \frac{Quantity_{pyrite}}{m} \times 2 \quad (9)$$

In this paper, m represents the relative molecular weight of pyrite. The depth of the SMTZ is 1.9 m, whereas the cover area is 100 km^2. Moreover, Q ranges from 1.64 to 1.9 g/cm^3 (Zhang et al., 2015; Liang et al., 2019). We selected a sediment density of 1.8 g/cm^3 and a pyrite percentage in the sediment of 2% in the Qiongdongnan Basin (Figure 4) (Mao et al., 2021; A. Haggerty 1991; Lim et al., 2011). The calculated quantity of pyrite is 6.9×10^{12} g. Therefore, the H_2S needed to form pyrite is 4.06×10^{11} mol. The same methods can be applied to calculate the quantity of H_2S released from the gas hydrates (see Eq. 10).

$$Quantity_{gas\ hydrate} = Depth_{gas} \times S \times Q_{sediment\ density} \times Saturation\ of\ gas\ hydrate \quad (10)$$

In this equation, the $Depth_{gas\ hydrate}$ has been confirmed to be deposited at the three sediments sections (18.55–40.42 mbsf, 43.42 to 56.12 mbsf, and 58.6 to 98.42 mbsf) and was based on coring and sampling results

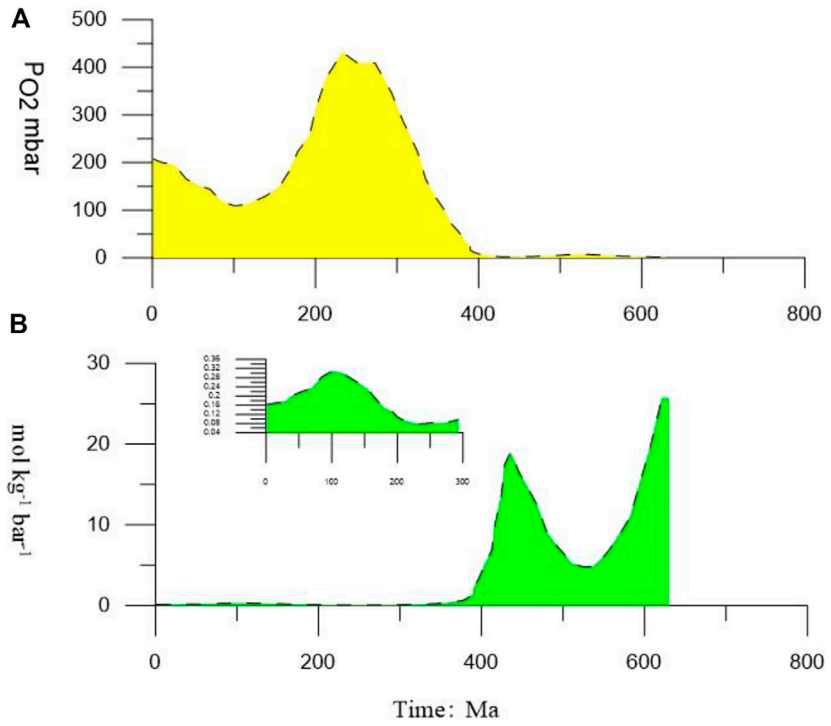

FIGURE 5
(A) Variation in the value of P_{O2} from present to 600 Ma BP. **(B)** Critical values changes from present to 600 Ma BP under the H_2S released from the complete dissociation of the first layer of gas hydrate. Moreover, from the present to 400 Ma, the H_2S released from the complete dissociation of the first layer of gas hydrate hardly moves into the atmosphere.

and pilot hole LWD anomalies, which showed a high resistivity, low density, high gamma-ray values, and elevated acoustic velocity (Liang et al., 2019) Herein, the first Depth $_{gas}$ is 21.87 m, the second Depth $_{gas}$ is 13 m, and the saturation of gas hydrate is 31%. The quantity of gas hydrate in the first layer is 1.22×10^{15} g. The percentage of H_2S in the gas hydrate ranges from 1% to 2%, and, therefore, the quantity of H_2S in the gas hydrate of the first layer is 1.83×10^{13} g. The moles of H_2S released from the dissociation of gas hydrates in the first layer can be calculated using the $_{following}$ equation:

$$Mole\,H_2S = \frac{Quantity_{H2S}}{d} \tag{11}$$

According to this analysis, the released quantity of H_2S is 5.4×10^{11} mol. The H_2S released from the gas hydrate is about 1.3 times the H_2S needed for the formation of pyrite. The calculation results show that the H_2S released from the dissociation of gas hydrates may be the source of H_2S required to form pyrites. What is more, a greater volume and continual release of H_2S from the gas hydrate could cause the H_2S to seep into the water and even into the atmosphere. If so, it is still not clear what its biological and chemical consequences could be.

4.2 Evaluating the concentration of H_2S released from gas hydrates into the ocean and atmosphere

In general, H_2S can be depleted in seawater *via* oxidation. Recognized loss processes include photochemical oxidation, reaction with dissolved oxygen (Millero et al., 1987), After hydrogen sulfide ($HS=H_2S+HS^-+S^{2-}$) is produced, it mainly participates in three types of reaction processes: 1) It gradually diffuses to the seabed and enters the bottom seawater body or oxidizes during the diffusion process. The oxidants in this process include oxygen, Iron oxides and manganese-containing oxides, products include elemental sulfur (S_0), complex sulfides (e.g., $S_2O_3^{2-}$) and sulfates; 2) Combine with organic matter to form organic sulfur; (three is also the most important reaction process, that is, it combines with iron-bearing minerals to form iron-bearing polysulfides and monosulfides and finally converts to pyrite. This is also the main formation mechanism of pyrite in marine sediments. In addition, a large number of laboratory studies have shown that pyrite can also be formed directly without the transformation of iron polysulfides. However, it is not all HS required for pyrite formation comes from SO_4^{2-}-AOM. (Kelly and Kadish, 1982). However, in marine anoxic sediments, the concentration of oxygen and is low. Yao and Millero, 1996 found that elemental sulfur was the dominant

product (95–100%) produced by the oxidation of H_2S by hydrous Fe(III) oxides. In fact, elemental sulfur is seldom found in the marine sediments in the Qiongdongnan Basin. Therefore, in anoxic sediments, the H_2S released from gas hydrates cannot be easily consumed, except in the process of forming pyrite. Nanomolar levels (0.1–2 nM) of H_2S have been found in the surface waters of the oceans (Cutter and Oatts, 1987; Iii and Tsamakis, 1989). However, the mechanism of the production and maintenance of hydrogen sulfide in surface seawater remains unclear. As is discussed in Section 4.1, if the second layer of gas hydrate dissociation results in the release of hydrogen sulfide into seawater, the main controlling factor for the release of hydrogen sulfide into the atmosphere is oxygen. In fact, in anoxic basins, mildly sulfidic deep waters are separated from the atmosphere by an oxygenated surface layer, at the base of which is a sulfide chemocline through which O_2 concentrations fall to zero. Kump et al. (2005) found that a significant buildup of H_2S in the deep sea could have led to toxic emissions of H_2S into the atmosphere, methane accumulation, and global warming Kump et al. (2005). The question is how to evaluate the seepage of H_2S into the water or atmosphere, and that the fundamental characteristic affecting the supply of H_2S into the water or atmosphere is the supply of O_2, whose transport through the surface layer must exceed the upwelling and diffusive flux of the reductant (H_2S) from below. The flux of O_2 must be at least two times the concentration of H_2S given the stoichiometry of the following reaction:

$$H_2S + 2O_2 \rightarrow SO_4^{-2} + 2H^- \tag{12}$$

The fundamental characteristic of a stable chemocline is that the supply of O_2 from the atmosphere across the air-sea interface and its transport through the surface layer must exceed the upwelling and diffusive flux of the reductant (H_2S) from below. Kump et al. (2005) treated the exchange of gases, including O_2, between the atmosphere and ocean by using a piston-velocity formulation, whereby the flux of gases occurs at a rate (in this case, F_{O2}) that is proportional to the contrast in gas concentrations between the atmosphere and surface ocean with the proportionality constant being the piston velocity (k):

$$F_{O2} = \rho_{oce} \cdot k \cdot K_H \ (P_{O2atm} - P_{O2oce}) \tag{13}$$

The supply of H_2S from below by upwelling (F_{H2S}) can be written as

$$F_{H2S} = \rho_{oce} \cdot u \cdot [H_2S]deep \tag{14}$$

where u is the upwelling rate (four in $m \cdot yr^{-1}$), $[H_2S]_{deep}$ is the concentration of H_2S in deep waters (in $mol \cdot kg^{-1}$), ρ_{oce} is the density of seawater (1,002 kg/m^3), and K_H is the Henry's law constant for O_2 (for warm surface waters, K_H is 10^{-3} $mol\ kg^{-1} \cdot bar^{-1}$).

The critical conditions for the balance of O_2 and H_2S must conform to the following equations:

$$F_{O2} = 2F_{H2S} \tag{15}$$

$$\rho_{oce} \cdot k \cdot K_H \ (P_{O2atm} - P_{O2oce}) = 2\,\rho_{oce} \cdot u \cdot [H_2S]deep \tag{16}$$

Given these values, and setting the surface water O_2 partial pressure (P_{O2oce}) to zero, the P_{O2oce} critical ratio of H_2S in the deep to atmospheric O_2, above which the steady-state surface-water O_2 concentration is zero, is given by Eq. 17.

$$\left(\frac{H2S_{deep}}{P_{O2,\,atm}}\right) = \frac{k \cdot KH}{2u} = \frac{1000m\,yr-1 \times 10-3\,mol\,kg-1\,bar-1}{2 \times 4\,m\,yr-1}$$

$$\approx 0.13\ \frac{mol}{kg\,bar} \tag{17}$$

In the study area, the dissociation of the first gas hydrate layer would cause the H_2S to reach 0.135 $mol\ kg^{-1}$, and, at present, $P_{O2\ atm}$ is 212.28 mbar. Hence, $\frac{H2S_{deep}}{P_{O2,\,atm}}_{\ present} = \frac{0.135mol \cdot kg-1}{212.28 \times 10-3bar} \approx 0.64\ \frac{mol}{kg\,bar}$. 0.64 $mol\ kg^{-1} \cdot bar^{-1}$ (Figure 5) is greater than the critical value of 0.13 $mol\ kg^{-1} \cdot bar^{-1}$. Due to this reason, the dissociation of the gas hydrate in the first layer would cause a subsequent release of H_2S that could easily enter the atmosphere in the present condition of P_{O2}. However, during geological time, P_{O2} often changes with time, so at different geological times, the critical values would vary (Table 1). In this paper, we calculated the various critical values from the present to 600 Ma. Our results show that, from 0 to 200 Ma, the H_2S easily seeped into the atmosphere through the dissociation of gas hydrate in the first layer. From 200 to 300 Ma, the calculated $H_2S_{\ deep}/P_{O2}$ values are lower than the standard values. Therefore, it would have been difficult for the H_2S to seep into the atmosphere if the temperature and pressure changed during this geological time.

4.3 Evaluation of the influence of gas hydrate dissociation on H_2S release through geological time

Gas hydrates are sensitive to temperature and pressure (Wan et al., 2022). When these factors change, the gas hydrates can dissociate. Previous studies have shown that gas hydrates are sensitive to sea-level changes (Chown et al., 2000; Blendinger 2004; Bangs and Nathan, 2005; Jang-Jun et al., 2011). A decrease in sea level will cause a corresponding change in the pressure. These pressure changes can gradually cause the gas hydrates to dissociate. In fact, in the sediments with normal methane seepage, it is difficult for the hydrogen sulfide produced by AOM to reach the water, but the existence of methane-hydrogen sulfide hydrate makes large-scale hydrate decomposition that may lead to massive hydrogen sulfide release. At this time, it is particularly important to evaluate the conditions under which the hydrogen sulfide gas reaches the water body. In this study, we assume that the gas hydrate in the first layer is more susceptible to changes in the sea-level, resulting in a

TABLE 1 The partial pressure of atmospheric oxygen level at different geological period.

Geological time	Partial pressure of atmospheric oxygen level (%)	P_{O2mbar}
1.37	99.13	207.22
11.45	99.13	200.10
27.32	96.56	194.35
41.66	93.79	165.08
56.01	79.66	152.14
70.35	73.42	143.95
84.85	69.47	118.76
100.57	57.31	109.13
116.44	52.66	112.36
137.96	54.22	128.86
155.21	62.18	147.77
166.81	71.31	179.12
178.25	86.44	222.88
192.60	107.56	256.35
199.92	123.71	310.73
212.74	149.95	376.64
232.89	181.76	431.94
251.66	208.44	408.67
273.18	197.21	408.67
293.32	197.21	346.11
307.67	167.03	285.54
325.07	137.80	222.88
335.14	107.56	165.08
345.21	79.66	132.28
358.03	63.84	100.58
365.20	48.54	74.28
375.28	35.85	55.02
379.70	26.55	45.39
383.98	21.90	32.65
389.77	15.76	24.75
389.77	11.95	16.41
394.05	7.92	11.81
398.32	5.70	8.98
404.12	4.33	6.63
412.67	3.20	4.90
415.57	2.36	3.52
424.27	1.70	2.47
428.54	1.19	1.93
435.71	0.93	1.78
445.78	0.86	2.04
467.46	0.98	2.68
480.27	1.29	3.72
493.25	1.80	4.63
501.95	2.24	5.33
510.49	2.57	6.46
524.99	3.12	7.01
536.44	3.38	7.01
546.51	3.38	5.93
556.58	2.86	4.90
570.93	2.36	3.72
582.53	1.80	3.07
591.07	1.48	2.40
606.94	1.16	1.72
621.29	0.83	1.31
629.99	0.63	1.31

(Continued in next column)

TABLE 1 (*Continued*) The partial pressure of atmospheric oxygen level at different geological period.

dissociation of the gas hydrate in the first layer. The gas hydrate in the second layer is assumed to be gradually released, causing a 20%, 40%, 60%, 80%, and 100% release of H_2S. Previous studies have shown that the H_2S released from the dissociation of gas hydrates in the first layer easily seeps into the atmosphere, except during 192–307 Ma BP. When 20% of H_2S is released from the gas hydrate in the second layer, it easily seeps into the atmosphere, except from 199 to 325 Ma. When the H_2S released by the dissociation of gas hydrates in the second layer reaches 40%, it also easily seeps into the atmosphere, except from 199 to 273 Ma (Figure 6). When the H_2S released by the dissociation of gas hydrates in the second layer reaches 60%, it easily seeps into the atmosphere, except from 212 to 293 Ma. When the H_2S released by the dissociation of gas hydrates in the second layer reaches 80%, it easily seeps into the atmosphere, except from 212 to 273 Ma. When the H_2S released by the dissociation of gas hydrates in the second layer reaches 100%, it easily seeps into the atmosphere, except from 232 to 273 Ma. For more precise estimates of the risk of H_2S being released into the atmosphere from the dissociation of gas hydrates, we incorporated the effects of sea-level change from 100 Ma BP to today and identified three risk modes: 1) the high-risk mode indicates that the sea level decreased sharply causing large-scale gas hydrate dissociation. The P_{O2} value within this geological period is low. In this case, the H_2S released into the atmosphere is high. 2) The moderate-risk mode indicates that the sea level decreased slower than in the high-risk mode and caused partial gas hydrate dissociation. However, the P_{O2} values during geological time are at a higher level. In this case, the amount of H_2S released into the atmosphere was moderate. 3) The low-risk mode indicates that the sea level is high and the P_{O2} values during this geological period are also high. In

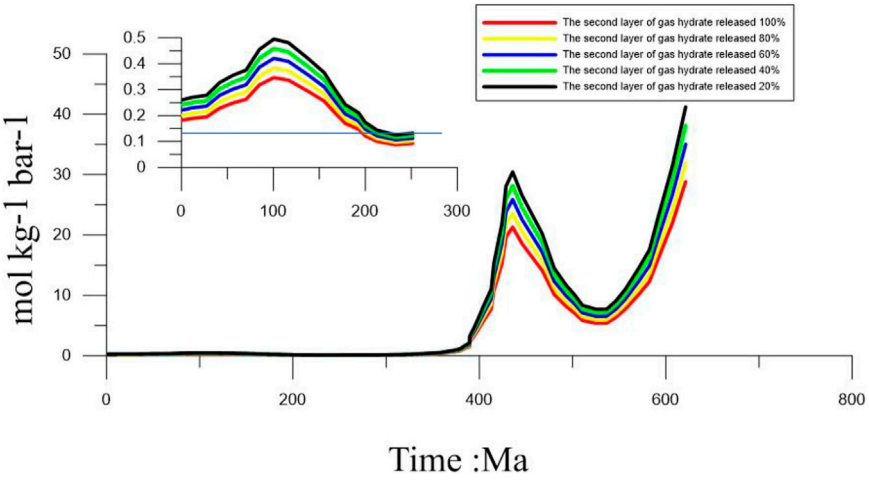

FIGURE 6
Variation in the values from 600 Ma BP under the gradual dissociation of second gas hydrate from 20% to 100%.

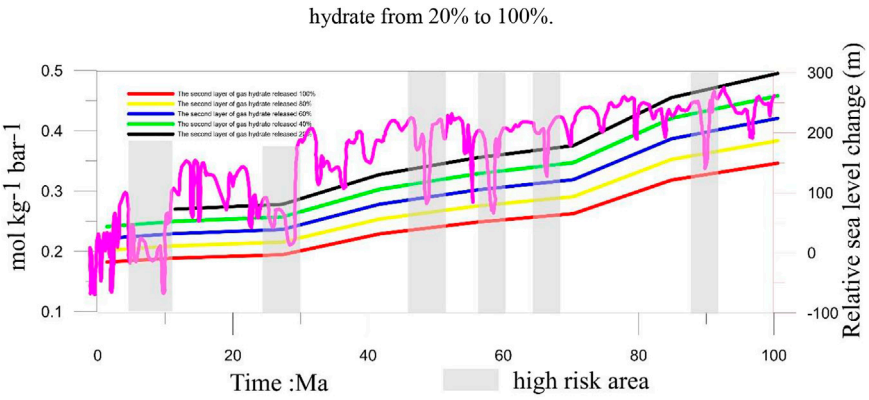

FIGURE 7
Risk ranging from present to 100 Ma BP. The purple curve represents the change in global sea level. The grey area represents the high risk of H_2S going into the atmosphere.

this case, the H_2S released from the gas hydrate would not easily seep into the atmosphere. Based on the three risk modes, we classified 5–12 Ma BP, 25–29 Ma BP, 47–52 Ma, and 57–61 Ma BP into the high-risk mode. In addition, we draw a conclusion through detailed analysis: When geological time of the P_{O2} was low and the gas hydrate's temperature and pressure changed greatly, it caused massive gas hydrate dissociation resulting in a massive amount of H_2S being released from the gas hydrates and diffusing into the pore water from the bottom. During the process, part of the H_2S released from the gas hydrate was oxidized by the Fe (III) oxide metals, and part of it was used to form pyrite. Most of the H_2S entered the ocean and even into the atmosphere. When geological time of the P_{O2} is high, the sea-level changed greatly. Meanwhile, massive H_2S was released from the gas hydrate into the pore water. This released H_2S will diffuse from the bottom. During the process, a small part of H_2S was released from the gas hydrate (being the H_2S source) to form pyrite. However, most of the H_2S will enter the ocean and get re-oxidized to become sulfate by the O_2 in the ocean. Furthermore, the H_2S released from the dissociation of the gas hydrates would be oxidized by Fe (III) oxide metals, with much of these metal ions being released into the pore water. In addition, the H_2S that was re-oxidized by the O_2 in the ocean also released much of the SO_4^{2-}. Therefore, the process also provides metal ions and SO_4^{2-} into pore water or seawater

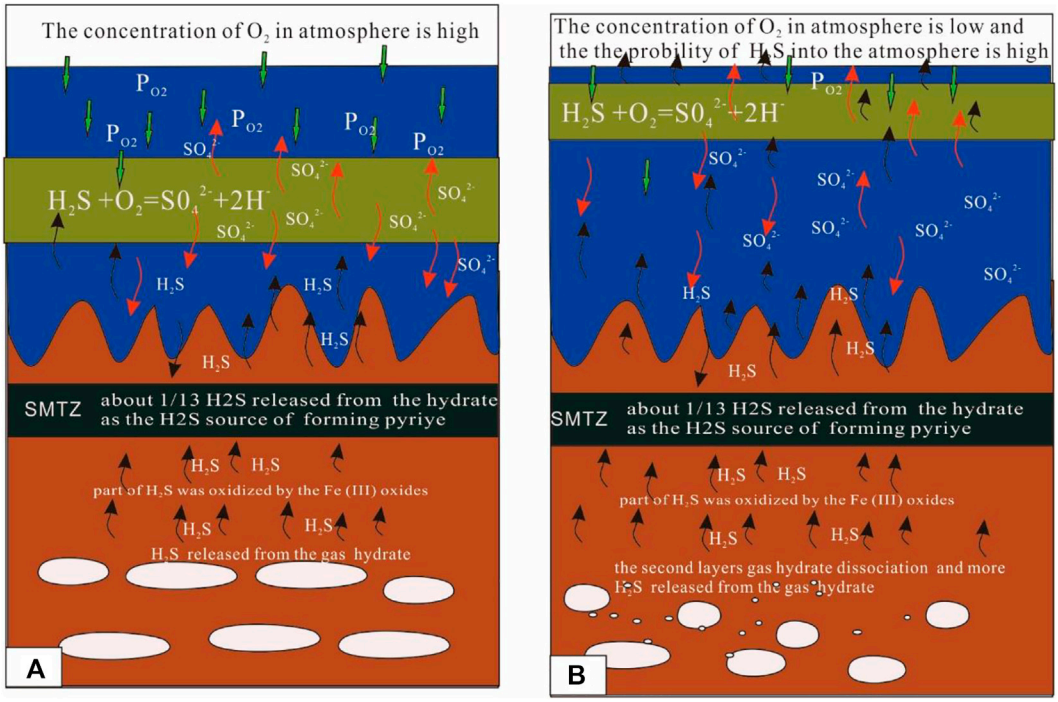

FIGURE 8
Mode of the sulfur cycle. The results show that a part of the H_2S released from the dissociation of the gas hydrate is oxidized by Fe (III) oxide metal, with much of the metal ions being released into the pore water. Another part of the H_2S is re-oxidized by the O_2 in the ocean, with much of SO_4^{2-} released into the seawater. Therefore, the process also provides metal ions and SO_4^{2-} to pore water or seawater when the H_2S released from the gas hydrate diffuses from the bottom. The difference in A and B is the level of P_{O2}. In **(A)**, the P_{O2} is high and the released hydrogen sulfide from the decomposition of hydrate finds it difficult to enter the atmosphere. In **(B)**, the P_{O2} is low and the released hydrogen sulfide from the decomposition of hydrate finds it easy to enter the atmosphere.

when the H_2S released from gas hydrate diffuses from the bottom.

5 Conclusion

It is important to evaluate how H_2S is released from gas hydrates. In this study, we established a one-dimensional mathematical model to calculate the amount of H_2S released from multiple layers of gas hydrates in the Qiongdongnan Basin. We investigated the role that H_2S released from the dissociation of gas hydrates plays on the sulfur cycle. Furthermore, we established the relationship between H_2S released from gas hydrate dissociation and the concentration of H_2S in the atmosphere. Our results show that the sulfate and methane transition zone (SMTZ) in the Qiongdongnan Basin contains 2.3×10^{12} g of pyrite, which requires 4.06×10^{11} mol of H_2S for its formation. The amount of H_2S released from the gas hydrate dissociation is 5.4×10^{11} mol, which is about 1.3 times more than that needed for the formation of pyrite. Therefore, the H_2S released from the dissociation of gas hydrates is an important source of H_2S for the formation of pyrites in the SMTZ in the Qiongdongnan Basin. Based on the flux of H_2S and the partial pressure of O_2 (P_{O2}) in the atmosphere, we calculated the critical value of the balance between the flux of H_2S and P_{O2} to be 0.13 mol $kg^{-1} \cdot bar^{-1}$. Furthermore, considering the effects of global sea-level change, we determined three risk modes to evaluate the possible seepage of H_2S from gas hydrate dissociation into the atmosphere. These are as follows: 1) the high-risk mode indicates that the sea level decreased sharply causing large-scale gas hydrate dissociation. The P_{O2} values during this geological time are low. In this situation, there was a larger amount of H_2S released into the atmosphere. 2) The moderate-risk mode indicates that the sea level decreased gradually and caused partial gas hydrate dissociation. However, the P_{O2} values at this geological time are higher. In this case, the amount of H_2S released into the atmosphere was moderate. 3) The low-risk mode indicates that the sea level is high, and the P_{O2} values at this geological time are also higher (Figure 7). Therefore, it was not easy for the H_2S released from the gas hydrate dissociation to seep into the atmosphere. Based on the three risk modes, we classified 5–12 Ma BP, 25–29 Ma BP, 47–52 Ma, and 57–61 Ma BP into the high-risk mode. Furthermore, the H_2S released from the

gas hydrate was oxidized by Fe (III) oxide metals, with much of the metal ions being released into the pore water. The H_2S that was re-oxidized by the O_2 in the ocean also released a lot of SO_4^{2-} (Figure 8). Therefore, the whole process also provides the raw materials for the process itself. This paper provides new insights into the source of H_2S found in the atmosphere and shows that the H_2S contained in gas hydrates possibly plays an important role in the global sulfur cycle.

Data availability statement

The original contributions presented in the study are included in the article/supplementary material, further inquiries can be directed to the corresponding author.

Author contributions

XW: Conceptualization, Methodology, Writing—Original Draft. SL: Data Curation. BZ: Conceptualization, Supervision, Writing—Review and Editing. YY and GW: Supervision. RX: Writing—Review and Editing. YF and ZN: Funding Acquisition, Resources, Supervision. All authors contributed to the manuscript.

Funding

The research was supported by the Project of Sanya Yazhou Bay Science and Technology City (No. SCKJ-JYRC-2022-14), GuangDong Basic and Applied Basic Research Foundation (No. 2020A1515110405), Geology Investigation Project of China Geological Survey (No. DD20221725), National Natural Science Foundation of China (No. 42106078).

Conflict of interest

The authors declare that the research was conducted in the absence of any commercial or financial relationships that could be construed as a potential conflict of interest.

Publisher's note

All claims expressed in this article are solely those of the authors and do not necessarily represent those of their affiliated organizations, or those of the publisher, the editors and the reviewers. Any product that may be evaluated in this article, or claim that may be made by its manufacturer, is not guaranteed or endorsed by the publisher.

References

Akhoudas, C., Chevalier, N., Blanc-Valleron, M. M., Klein, V., Mendez-Millan, M., Demange, J., et al. (2018). Methane-derived stromatolitic carbonate crust from an active fluid seepage in the Western basin of the sea of marmara: Mineralogical, isotopic and molecular geochemical characterization. *Deep Sea Res. Part II Top. Stud. Oceanogr.* 153, 110–120. doi:10.1016/j.dsr2.2017.12.022

Bangs, N. L. B., Musgrave, R. J., and Trehu, A. M. (2005). Upward shifts in the southern hydrate ridge gas hydrate stability zone following postglacial warming, offshore Oregon. *J. Geophys. Res.* 110, B03102. doi:10.1029/2004jb003293

Blendinger, W. (2004). sea level changes versus hydrothermal diagenesis: Origin of triassic carbonate platform cycles in the dolomites, Italy. *Sediment. Geol.* 178, 141–144. doi:10.1016/j.sedgeo.2005.03.001

Butler, I. B., Bottcher, M. E., Rickard, D., and Oldroyd, A. (2004). Sulfur isotope partitioning during experimental formation of pyrite via the polysulfide and hydrogen sulfide pathways: Implications for the interpretation of sedimentary and hydrothermal pyrite isotope records. *Earth Planet. Sci. Lett.* 228 (3-4), 495–509. doi:10.1016/j.epsl.2004.10.005

Canet, C., Prol-Ledesma, R. M., Escobar-Briones, E., Mortera-Gutiérrez, C., Morales-Puente, P., Linares, C., et al. (2006). Mineralogical and geochemical characterization of hydrocarbon seep sediments from the gulf of Mexico. *Mar. Petroleum Geol.* 23 (5), 605–619. doi:10.1016/j.marpetgeo.2006.05.002

Chazallon, B., Focsa, C., Charlou, J. L., Bourry, C., and Donval, J. P. (2007). A comparative Raman spectroscopic study of natural gas hydrates collected at different geological sites. *Chem. Geol.* 244 (1-2), 175–185. doi:10.1016/j.chemgeo.2007.06.012

Chen, D. F., Dong, F., Zheng, S., Zhi, G. S., Chen, G. Q., and Iii, L. (2006). Pyrite crystallization in seep carbonates at gas vent and hydrate site. *Mater. Sci. Eng. C* 26 (4), 602–605. doi:10.1016/j.msec.2005.08.037

Chown, E. H., N'Dah, E., and Mueller, W. U. (2000). The relation between iron-formation and low temperature hydrothermal alteration in an archean volcanic environment. *Precambrian Res.* 101 (2), 263–275. doi:10.1016/s0301-9268(99)00091-1

Commeau, R. F., Paull, C. K., Commeau, J. A., and Poppe, L. J. (1987). Chemistry and mineralogy of pyrite-enriched sediments at a passive margin sulfide brine seep: Abyssal gulf of Mexico. *Earth Planet. Sci. Lett.* 82 (1-2), 62–74. doi:10.1016/0012-821x(87)90107-5

Cutter, G. A., and Oatts, T. J. (1987). Determination of dissolved sulfide and sedimentary sulfur speciation using gas chromatography-photoionization detection. *Anal. Chem.* 59 (5), 717–721. doi:10.1021/ac00132a008

Egger, M., Rasigraf, O., Sapart, C. J., Jilbert, T., Jetten, M., Roeckmann, T., et al. (2015). Iron-mediated anaerobic oxidation of methane in brackish coastal sediments. *Environ. Sci. Technol.* 49 (1), 277–283. doi:10.1021/es503663z

Fang, Y., Wei, J., Lu, H., Liang, J., Cao, J., Fu, J., et al. (2019). Chemical and structural characteristics of gas hydrates from the haima cold seeps in the qiongdongnan basin of the south China sea. *J. Asian Earth Sci.* 182, 103924. doi:10.1016/j.jseaes.2019.103924

Formolo, M. J., and Lyons, T. W. (2013). Sulfur biogeochemistry of cold seeps in the green canyon region of the gulf of Mexico. *Geochimica Cosmochimica Acta* 119, 264–285. doi:10.1016/j.gca.2013.05.017

Haggerty, J. A. (1991). Evidence from fluid seeps atop serpentine seamounts in the mariana forearc: Clues for emplacement of the seamounts and their relationship to forearc tectonics. *Mar. Geol.* 102 (1-4), 293–309. doi:10.1016/0025-3227(91)90013-t

Hester, K. C., Dunk, R. M., White, S. N., Brewer, P. G., Peltzer, E. T., and Sloan, E. D. (2007). Gas hydrate measurements at hydrate ridge using Raman spectroscopy. *Geochimica Cosmochimica Acta* 71 (12), 2947–2959. doi:10.1016/j.gca.2007.03.032

Hu, Y., Li, H., and Xu, J. (2012). Shallow gas accumulation in a small estuary and its implications: A case history from in and around xiamen bay. *Geophys. Res. Lett.* 39 (24), 2012GL054478. doi:10.1029/2012gl054478

Huang, H., Huang, B., Huang, Y., Li, X., and Tian, H. (2017). Condensate origin and hydrocarbon accumulation mechanism of the deepwater giant gas field in Western south China sea: A case study of lingshui 17-2 gas field in Qiongdongnan basin. *Petroleum Explor. Dev.* 44, 409–417. doi:10.1016/s1876-3804(17)30047-2

Huang, L., Su, Z., and Wu, N. Y. (2015). Evaluation on the gas production potential of different lithological hydrate accumulations in marine environment. *Energy* 91, 782–798. doi:10.1016/j.energy.2015.08.092

Huene, R. V., and Pecher, I. A. (1999). Vertical tectonics and the origins of bsrs along the Peru margin. *Earth Planet. Sci. Lett.* 166 (1-2), 47–55. doi:10.1016/s0012-821x(98)00274-x

Iii, G., and Tsamakis, E. (1989). Concentration and form of dissolved sulfide in the oxic water column of the ocean. *Mar. Chem.* 27 (3-4), 165–177. doi:10.1016/0304-4203(89)90046-7

Jang-Jun, B., Um, I. K., and Holland, M. (2011). Core lithologies and their constraints on gas-hydrate occurrence in the east sea, offshore Korea: Results from the site ubgh1-9. *Mar. Petroleum Geol.* 28 (10), 1943–1952. doi:10.1016/j.marpetgeo.2010.12.003

Kastner, M., Kvenvolden, K. A., and Lorenson, T. D. (1998). Chemistry, isotopic composition, and origin of a methane-hydrogen sulfide hydrate at the cascadia subduction zone. *Earth Planet. Sci. Lett.* 156 (3–4), 173–183. doi:10.1016/s0012-821x(98)00013-2

Kelly, S. L., and Kadish, K. M. (1982). Counterion and solvent effects on the electrode reactions of manganese porphyrins. *Inorg. Chem.* 21, 3631–3639. doi:10.1021/ic00140a010

Kraal, P., Slomp, C. P., Forster, A., Kuypers, M., and Sluijs, A. (2009). Pyrite oxidation during sample storage determines phosphorus fractionation in carbonate-poor anoxic sediments. *Geochimica Cosmochimica Acta* 73 (11), 3277–3290. doi:10.1016/j.gca.2009.02.026

Kump, L. R., Pavlov, A., and Arthur, M. A. (2005). Massive release of hydrogen sulfide to the surface ocean and atmosphere during intervals of oceanic anoxia. *Geol.* 33 (5), 397–400. doi:10.1130/g21295.1

Liang, J., Zhang, W., Lu, J., Wei, J., and He, Y. (2019). Geological occurrence and accumulation mechanism of natural gas hydrates in the eastern Qiongdongnan basin of the South China sea: Insights from site gmgs5-w9-2018. *Mar. Geol.* 418, 106042. doi:10.1016/j.margeo.2019.106042

Lim, Y, C., Lin, S., Yang, T, F., Chen, Y, G., and Liu, C, S. (2011). Variations of methane induced pyrite formation in the accretionary wedge sediments offshore southwestern Taiwan. *Mar. Petroleum Geol.* 28 (10), 1829–1837. doi:10.1016/j.marpetgeo.2011.04.004

Lin, Q., Wang, J. S., Shaoying, F. U., Hongfeng, L. U., Qingtao, B. U., Lin, R. X., et al. (2015). Elemental sulfur in northern south China sea sediments and its significance. *Sci. China Earth Sci.* 58, 2271–2278. doi:10.1007/s11430-015-5182-7

Lin, Q., Wang, J., Taladay, K., Lu, H., Hu, G., Sun, F., et al. (2016). Coupled pyrite concentration and sulfur isotopic insight into the paleo sulfate-methane transition zone (smtz) in the northern south China sea. *J. Asian Earth Sci.* 115, 547–556. doi:10.1016/j.jseaes.2015.11.001

Lin, Z., Sun, X., Strauss, H., Lu, Y., Gong, J., Xu, L., et al. (2017). Multiple sulfur isotope constraints on sulfate-driven anaerobic oxidation of methane: Evidence from authigenic pyrite in seepage areas of the South China sea. *Geochimica Cosmochimica Acta* 211, 153–173. doi:10.1016/j.gca.2017.05.015

Liu, S. W., Lai, Z. P., Wang, Y. X., Fan, X. L., Wang, L. L., Tian, M. Z., et al. (2016). Growing pattern of mega-dunes in the badain jaran desert in China revealed by luminescence ages. *Quat. Int.* 410, 111–118. doi:10.1016/j.quaint.2015.09.048

Liu, X. M., Kah, L. C., Knoll, A. H., Cui, H., Hazen, R. M., Bekker, A., et al. (2021). A persistently low level of atmospheric oxygen in Earth's middle age. *Nat. Commun.* 12 (1), 351. doi:10.1038/s41467-020-20484-7

Mao, S. H., Qin, J. Z., and Li, Y. K. (2021). Re: Mandatory submission of patient identifiable information to third parties: Fgm now, what next? *BMJ* 17 (4), 219–220. doi:10.1136/bmj.h5146

Miao, X., Feng, X., Li, J., and Lin, L. (2021). Tracing the paleo-methane seepage activity over the past 20, 000 years in the sediments of qiongdongnan basin, northwestern south China sea. *Chem. Geol.* 559, 119956. doi:10.1016/j.chemgeo.2020.119956

Millero, F. J., Sotolongo, S., and Izaguirre, M. (1987). Oxidation kinetics of fe(ii) in sea water. *Geochim. Cosmochim. acta* 51, 793–801. doi:10.1016/0016-7037(87)90093-7

Pan, M., Wu, D., Yang, F., Sun, T., Wu, N., and Liu, L. (2018). Geochemical sedimentary evidence from core 973-2 for methane activity near the jiulong methane reef in the northern south China sea. *Interpretation* 6, 1–39. doi:10.1190/INT-2017-0001.1

Peckmann, J., Reimer, A., Luth, U., Luth, C., Reitner, J., Heinicke, C., et al. (2001). Methane-derived carbonates and authigenic pyrite from the northwestern black sea. *Mar. Geol.* 177 (1-2), 129–150. doi:10.1016/s0025-3227(01)00128-1

Peckmann, J., and Thiel, V. (2004). Carbon cycling at ancient methane-seeps. *Chem. Geol.* 205 (3-4), 443–467. doi:10.1016/j.chemgeo.2003.12.025

Qin, J., and Kuhs, W. F. (2013). "Quantitative Raman scattering of guest molecules in gas hydrates and its relevance to gas exchange processes involving N2," in Proceedings of the The Tenth (2013) ISOPE Ocean Mining and Gas Hydrates Symposium, Szczecin, Poland, September 2013.

Qin, X., Liang, Q., Ye, J., Yang, L., Kou, B., Xie, W., et al. (2020). The response of temperature and pressure of hydrate reservoirs in the first gas hydrate production test in south China sea. *Appl. Energy* 278, 115649. doi:10.1016/j.apenergy.2020.115649

Qin, X. W., Zhao, B., Li, F. Y., Zhang, B. J., Wang, H. J., Zhang, R. W., et al. (2019). Deep structure research of the South China sea: Progresses and directions. *China Geol.* 2 (4), 530–540. doi:10.31035/cg2018125

Radford- Knwry, J., and Cutter, G. A. (1994). Biogeochemistry of dissolved hydrogen sulfide species and carbonyl sulfide in the Western north atlantic ocean. *Geochimica Cosmochimica Acta* 58 (24), 5421–5431. doi:10.1016/0016-7037(94)90239-9

Shen, B., Mao, S. H., Kaufman, A. J., Bao, H., Zhou, C., and Wang, H. (2008). Stratification and mixing of a post-glacial Neoproterozoic ocean: Evidence from carbon and sulfur isotopes in a cap dolostone from northwest China. *Earth Planet. Sci. Lett.* 265, 209–228. doi:10.1016/j.epsl.2007.10.005

Shi, Y. H., Liang, Q. Y., Yang, J. P., Yuan, Q. M., Wu, X. M., and Kong, L. (2019). Stability analysis of submarine slopes in the area of the test production of gas hydrate in the south China sea. *China Geol.* 2, 274–284. doi:10.31035/cg2018122

Sima, M., Dold, B., Frei, L., Senila, M., Balteanu, D., and Zobrist, J. (2011). 'Sulfide oxidation and acid mine drainage formation within two active tailings impoundments in the Golden Quadrangle of the Apuseni Mountains, Romania. *J. Hazard. Mater.* 189, 624–639. doi:10.1016/j.jhazmat.2011.01.069

Wan, Z. F., Zhang, W., Ma, C., Liang, J. Q., Li, A., Meng, D. J., et al. (2022). Dissociation of gas hydrates by hydrocarbon migration and accumulation-derived slope failures:an example from the south China sea. *Geosci. Front.* 13 (2), 101345. doi:10.1016/j.gsf.2021.101345

Wang, J., Wu, S., Kong, X., Ma, B., Li, W., Wang, D., et al. (2018a). Subsurface fluid flow at an active cold seep area in the qiongdongnan basin, northern south China sea. *J. Asian Earth Sci.* 168, 17–26. doi:10.1016/j.jseaes.2018.06.001

Wang, J., Wu, S., and Yao, Y. (2018b). Quantifying gas hydrate from microbial methane in the south China sea. *J. Asian Earth Sci.* 168, 48–56. doi:10.1016/j.jseaes.2018.01.020

Wang, S., Magalhães, V. H., Pinheiro, L. M., Liu, J., and Yan, W. (2015). Tracing the composition, fluid source and formation conditions of the methane-derived authigenic carbonates in the gulf of cadiz with rare Earth elements and stable isotopes. *Mar. Petroleum Geol.* 68, 192–205. doi:10.1016/j.marpetgeo.2015.08.022

Wang, X., Liu, B., Jin, J., Lu, J., Zhou, J., Qian, J., et al. (2020). Increasing the accuracy of estimated porosity and saturation for gas hydrate reservoir by integrating geostatistical inversion and lithofacies constraints. *Mar. Petroleum Geol.* 115, 104298. doi:10.1016/j.marpetgeo.2020.104298

Wei, J., Li, J., Wu, T., Zhang, W., Li, J., Wang, J., et al. (2020). Geologically controlled intermittent gas eruption and its impact on bottom water temperature and chemosynthetic communities—a case study in the "HaiMa" cold seeps, south China sea. *Geol. J.* 55 (9), 6066–6078. doi:10.1002/gj.3780

Wu, D., Sun, T., Xie, R., Pan, M., Wu, N., Ye, Y., et al. (2019). Characteristics of authigenic minerals around the sulfate-methane transition zone in the methane-rich sediments of the northern south China sea: Inorganic geochemical evidence. *Int. J. Environ. Res. Public Health* 16 (13), 2299. doi:10.3390/ijerph16132299

Wu, D., Xie, R., Liu, J., Yang, F., Wu, N., Liu, L., et al. (2020). Zone of metal-driven anaerobic oxidation of methane is an important sink for phosphorus in the taixinan basin, south China sea. *Mar. Geol.* 427, 106268. doi:10.1016/j.margeo.2020.106268

Wu, T., Deng, X., Yu, Z., and Wang, L. (2020). Acoustic characteristics of cold-seep methane bubble behavior in the water column and its potential environmental impact. *Acta Oceanol. Sin.* 39 (5), 133–144. doi:10.1007/s13131-019-1489-0

Wu, T., Wei, J., Liu, S., Guan, Y., Zhang, R., Su, M., et al. (2018). Characteristics and formation mechanism of seafloor domes on the north-eastern continental slope of the south China sea. *Geol. J.* 55, 1–10. doi:10.1002/gj.3402

Xie, R., Wu, D., Liu, J., Sun, T., and Wu, N. (2019). Evolution of gas hydrates inventory and anaerobic oxidation of methane (aom) after 40ka in the taixinan basin, south China sea. *Deep Sea Res. Part I Oceanogr. Res. Pap.* 152, 103084. doi:10.1016/j.dsr.2019.103084

Yang, X., Liu, Y., Li, C., Song, Y., Zhu, H., and Jin, X. (2007). Rare Earth elements of aeolian deposits in Northern China and their implications for determining the provenance of dust storms in Beijing. *Geomorphology* 87, 365–377. doi:10.1016/j.geomorph.2006.10.004

Yao, W., and Millero, F. J. (1996). Oxidation of hydrogen sulfide by hydrous fe(iii) oxides in seawater. *Mar. Chem.* 52, 1–16. doi:10.1016/0304-4203(95)00072-0

Yuan, S., Wu, S., Thomas, L., Yao, G., Lv, F., Cao, F., et al. (2009). Fine-grained pleistocene deepwater turbidite channel system on the slope of qiongdongnan basin, northern south China sea. *Mar. Petroleum Geol.* 26 (8), 1441–1451. doi:10.1016/j.marpetgeo.2009.03.007

Zhang, G., Liang, J., Lu, J., Yang, S., Zhang, M., Holland, M., et al. (2015). Geological features, controlling factors and potential prospects of the gas hydrate occurrence in the east part of the pearl river mouth basin, south China sea. *Mar. Petroleum Geol.* 67, 356–367. doi:10.1016/j.marpetgeo.2015.05.021

Zhang, M., Konishi, H., Xu, H., Sun, X., Lu, H., Wu, D., et al. (2014). Morphology and formation mechanism of pyrite induced by the anaerobic oxidation of methane from the continental slope of the ne south China sea. *J. Asian Earth Sci.* 92, 293–301. doi:10.1016/j.jseaes.2014.05.004

Zhang, X. H., Lu, X. B., Chen, X. D., Zhang, L., and Shi, Y. (2016). Mechanism of soil stratum instability induced by hydrate dissociation. *Ocean. Eng.* 122, 74–83. doi:10.1016/j.oceaneng.2016.06.015

Frontiers in Earth Science

Investigates the processes operating within the major spheres of our planet

Advances our understanding across the earth sciences, providing a theoretical background for better use of our planet's resources and equipping us to face major environmental challenges.

Discover the latest Research Topics

See more →

Frontiers

Avenue du Tribunal-Fédéral 34
1005 Lausanne, Switzerland
frontiersin.org

Contact us

+41 (0)21 510 17 00
frontiersin.org/about/contact